The quest for Earth's oldest ice *p. 436*

Origin of lung disease in cystic fibrosis *p. 503*

Dispensing with genes on the Y chromosome *p. 514*

Science

$15
29 JANUARY 2016
sciencemag.org
AAAS



Jupiter rising

Geometric techniques in Babylonian astronomy

pp. 435 & 482

CONTENTS



446 Supergenes in birds

29 JANUARY 2016 • VOLUME 351 • ISSUE 6272

NEWS

IN BRIEF

428 News at a glance

IN DEPTH

430 **CAN GERMANY ENGINEER A COAL EXIT?**
Debate grows over whether nation could eliminate a key but dirty fuel by 2040 *By C. Schrader*

431 **RARE ISOTOPES OFFER CLUES TO THE CHEMISTRY OF THE PLANET**
New lab tools bring exotic isotopic signatures into view
By E. Hand

433 **A FISH BACK FROM THE DEAD**
Understanding how killifish survive months without oxygen could help stroke victims *By E. Pennisi*

434 **RESEARCHERS CLAIM TO FIND HIV SANCTUARIES**
The most powerful antiretrovirals may not reach virus lurking in some tissues *By J. Cohen*

435 **CALCULUS PRECURSOR UNCOVERED IN ANCIENT BABYLON**
Math whizzes left precocious geometric calculations on clay tablets by 50 B.C.E.
By R. Cowen
▸ REPORT P. 482

FEATURES

436 **TIBET'S PRIMEVAL ICE**
The quest for the world's oldest ice could yield a Rosetta Stone for how Asia responds to a changing climate *By J. Qiu*

PHOTO: (BOTTOM LEFT) LONNIE G. THOMPSON



436



444

440 **A CANCER LEGACY**
Once viewed as tragic anomalies, many childhood cancers may have their roots in inherited mutations
By J. Couzin-Frankel

INSIGHTS

BOOKS *ET AL.*

444 **CITY OF THORNS**
By B. Rawlence, reviewed by M. Hynie

PERSPECTIVES

446 **AVIAN SUPERGENES**
Genetic data reveal how two complex bird mating systems evolved
By S. Taylor and L. Campagna

448 **HOW ECOSYSTEMS CHANGE**
Conservation planning must accommodate changes in ecosystem composition to protect biodiversity
By A. E. Magurran

450 **HOW CAN HIGHER-YIELD FARMING HELP TO SPARE NATURE?**
Mechanisms to link yield increases with conservation *By B. Phalan* et al.

452 **PRESCRIPTION DRUGS OBSCURE MICROBIOME ANALYSES**
Patient populations should be stratified for medications when looking for gut microbial signatures of disease
By S. Devkota

453 **TRACKING THE ORIGINS OF TUMORIGENESIS**
A zebrafish model allows visualization of embryonic reprogramming during melanoma initiation
By S. Boumahdi and C. Blanpain
▸ RESEARCH ARTICLE P. 464

LETTERS

456 **A NECROGENOMIC REGISTRY'S POTENTIAL**
By P. L. Hedley and M. Christiansen

456 **TROPICAL DAMS: TO BUILD OR NOT TO BUILD?**
By P. M. Fearnside

457 **TECHNICAL COMMENT ABSTRACTS**

457 **ONLINE BUZZ: TENURE'S TENURE**

DEPARTMENTS

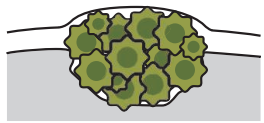
427 **EDITORIAL**
Global science engagement
By Geraldine Richmond

530 **WORKING LIFE**
Battling the bureaucracy hydra
By Jörgen Johansson

Downloaded from on January 31, 2016

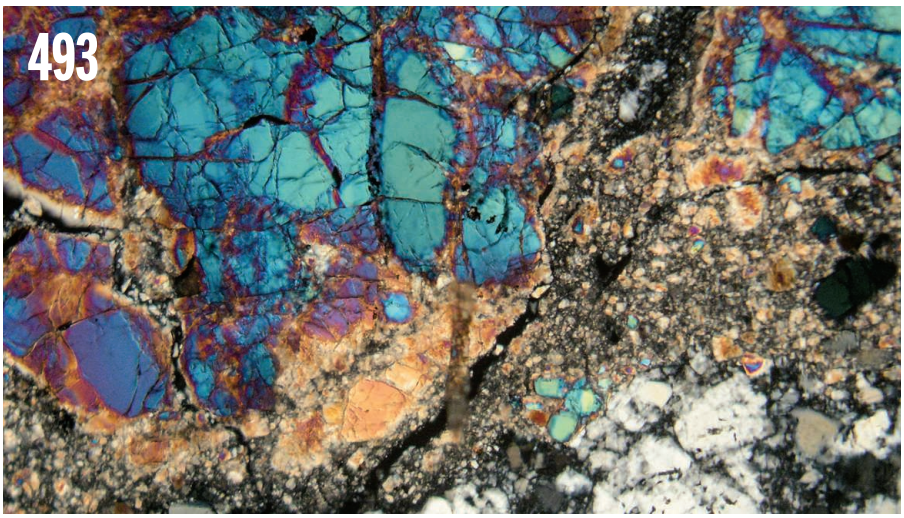
Published by AAAS

CONTENTS



453 & 464
Turning normal cells into cancer cells

29 JANUARY 2016 • VOLUME 351 • ISSUE 6272



RESEARCH

IN BRIEF

461 From *Science* and other journals

RESEARCH ARTICLES

464 MELANOMA INITIATION
A zebrafish melanoma model reveals emergence of neural crest identity during melanoma initiation
C. K. Kaufman et al.
RESEARCH ARTICLE SUMMARY; FOR FULL TEXT: dx.doi.org/10.1126/science.aad2197
▸ PERSPECTIVE P. 453

465 STRESS RESPONSE
Translation from the 5′ untranslated region shapes the integrated stress response
S. R. Starck et al.
RESEARCH ARTICLE SUMMARY; FOR FULL TEXT: dx.doi.org/10.1126/science.aad3867

466 STRUCTURAL BIOLOGY
The 3.8 Å structure of the U4/U6.U5 tri-snRNP: Insights into spliceosome assembly and catalysis
R. Wan et al.

REPORTS

475 SURFACE SCIENCE
Activation of Cu(111) surface by decomposition into nanoclusters driven by CO adsorption
B. Eren et al.

478 OCEANOGRAPHY
Enhanced East Pacific Rise hydrothermal activity during the last two glacial terminations
D. C. Lund et al.

482 HISTORY OF SCIENCE
Ancient Babylonian astronomers calculated Jupiter's position from the area under a time-velocity graph
M. Ossendrijver
▸ NEWS STORY P. 435; PODCAST; VIDEO

485 SUPERCONDUCTIVITY
Emergence of superconductivity in the canonical heavy-electron metal $YbRh_2Si_2$ *E. Schuberth* et al.

488 GEOPHYSICS
Periodic slow slip triggers megathrust zone earthquakes in northeastern Japan
N. Uchida et al.

493 LUNAR FORMATION
Oxygen isotopic evidence for vigorous mixing during the Moon-forming giant impact *E. D. Young* et al.

497 POLYMERS
Simultaneous covalent and noncovalent hybrid polymerizations *Z. Yu* et al.

503 CYSTIC FIBROSIS
Airway acidification initiates host defense abnormalities in cystic fibrosis mice *V. S. Shah* et al.

507 BIOCHEMISTRY
An unprecedented mechanism of nucleotide methylation in organisms containing *thyX T. V. Mishanina* et al.

511 IMMUNOLOGY
Most microbe-specific naïve $CD4^+$ T cells produce memory cells during infection *N. J. Tubo* et al.

514 SEX CHROMOSOME
Two genes substitute for the mouse Y chromosome for spermatogenesis and reproduction *Y. Yamauchi* et al.



ON THE COVER

Replica of a Babylonian tablet (circa 350–150 BCE), which describes the motion of Jupiter (upper left). The tablet is part of the first known use of geometric methods in Babylonian mathematical astronomy, which was previously thought to operate exclusively with arithmetical concepts. See pages 435 and 482. *Photo: © David Sharpe; Tablet: © The Trustees of the British Museum All Rights Reserved; Starfield: © Babak Tafreshi/ Corbis All Rights Reserved*

Science Staff 426
AAAS News & Notes 458
New Products 517
Science Careers 518

SCIENCE (ISSN 0036-8075) is published weekly on Friday, except the last week in December, by the American Association for the Advancement of Science, 1200 New York Avenue, NW, Washington, DC 20005. Periodicals mail postage (publication No. 484460) paid at Washington, DC, and additional mailing offices. Copyright © 2016 by the American Association for the Advancement of Science. The title SCIENCE is a registered trademark of the AAAS. Domestic individual membership and subscription (51 issues): $165 ($74 allocated to subscription). Domestic institutional subscription (51 issues): $1522; Foreign postage extra: Mexico, Caribbean (surface mail) $55; other countries (air assist delivery) $89. First class, airmail, student, and emeritus rates on request. Canadian rates with GST available upon request, GST #1254 88122. Publications Mail Agreement Number 1069624. **Printed in the U.S.A.**
Change of address: Allow 4 weeks, giving old and new addresses and 8-digit account number. **Postmaster:** Send change of address to AAAS, P.O. Box 96178, Washington, DC 20090–6178. **Single-copy sales:** $15.00 current issue, $20.00 back issue prepaid includes surface postage; bulk rates on request. **Authorization to photocopy** material for internal or personal use under circumstances not falling within the fair use provisions of the Copyright Act is granted by AAAS to libraries and other users registered with the Copyright Clearance Center (CCC) Transactional Reporting Service, provided that $35.00 per article is paid directly to CCC, 222 Rosewood Drive, Danvers, MA 01923. The identification code for *Science* is 0036-8075. *Science* is indexed in the *Reader's Guide to Periodical Literature* and in several specialized indexes.

Published by AAAS

Science
AAAS
1200 New York Avenue, NW, Washington, DC 20005
Bateman House, 82-88 Hills Road, Cambridge, UK CB2 1LQ

Editor-in-Chief Marcia McNutt
Executive Editor Monica M. Bradford **News Editor** Tim Appenzeller
Managing Editor, Research Journals Katrina L. Kelner
Deputy Editors Barbara R. Jasny, Andrew M. Sugden(UK), Valda J. Vinson, Jake S. Yeston

Research and Insights

SR. EDITORS Caroline Ash(UK), Gilbert J. Chin, Lisa D. Chong, Julia Fahrenkamp-Uppenbrink(UK), Pamela J. Hines, Stella M. Hurtley(UK), Paula A. Kiberstis, Marc S. Lavine(Canada), Kristen L. Mueller, Ian S. Osborne(UK), Beverly A. Purnell, L. Bryan Ray, Guy Riddihough, H. Jesse Smith, Jelena Stajic, Peter Stern(UK), Phillip D. Szuromi, Sacha Vignieri, Brad Wible, Nicholas S. Wigginton, Laura M. Zahn **ASSOCIATE EDITORS** Brent Grocholski, Keith T. Smith **ASSOCIATE BOOK REVIEW EDITOR** Valerie B. Thompson **ASSOCIATE LETTERS EDITOR** Jennifer Sills **CHIEF CONTENT PRODUCTION EDITOR** Cara Tate **SR. CONTENT PRODUCTION EDITORS** Harry Jach, Lauren Kmec **CONTENT PRODUCTION EDITORS** Jeffrey E. Cook, Chris Filiatreau, Cynthia Howe, Barbara P. Ordway, Catherine Wolner **SR. EDITORIAL COORDINATORS** Carolyn Kyle, Beverly Shields **EDITORIAL COORDINATORS** Joi S. Granger, Lisa Johnson, Anita Wynn **PUBLICATIONS ASSISTANTS** Aneera Dobbins, Jeffrey Hearn, Dona Mathieu, Le-Toya Mayne Flood, Shannon McMahon, Scott Miller, Caitlyn Phillips, Jerry Richardson, Rachel Roberts(UK), Alice Whaley(UK), Brian White **EXECUTIVE ASSISTANT** Anna Bashkirova **ADMINISTRATIVE SUPPORT** Janet Clements(UK), Lizanne Newton(UK), Maryrose Madrid, John Wood(UK)

News

NEWS MANAGING EDITOR John Travis **INTERNATIONAL EDITOR** Richard Stone **DEPUTY NEWS EDITORS** Daniel Clery(UK), Robert Coontz, Elizabeth Culotta, David Grimm, David Malakoff, Leslie Roberts **CONTRIBUING EDITOR** Martin Enserink(Europe) **SR. CORRESPONDENTS** Jeffrey Mervis, Elizabeth Pennisi **NEWS WRITERS** Adrian Cho, Jon Cohen, Jennifer Couzin-Frankel, Carolyn Gramling, Eric Hand, Jocelyn Kaiser, Catherine Matacic, Kelly Servick, Robert F. Service, Erik Stokstad(Cambridge, UK), Emily Underwood **INTERNS** Hanae Armitage, Nala Rogers **CONTRIBUTING CORRESPONDENTS** Michael Balter(Paris), John Bohannon, Ann Gibbons, Mara Hvistendahl, Sam Kean, Eli Kintisch, Kai Kupferschmidt(Berlin), Andrew Lawler, Christina Larson(Beijing), Mitch Leslie, Charles C. Mann, Eliot Marshall, Virginia Morell, Dennis Normile(Shanghai), Heather Pringle, Tania Rabesandratana(London), Gretchen Vogel(Berlin), Lizzie Wade(Mexico City) **CAREERS** Donisha Adams, Rachel Bernstein(Editor) **COPY EDITORS** Julia Cole, Dorie Chevlen, Jennifer Levin (Chief) **ADMINISTRATIVE SUPPORT** Jessica Williams

Executive Publisher Rush D. Holt
Interim Publisher Bill Moran **Chief Digital Media Officer** Rob Covey

BUSINESS OPERATIONS AND PORTFOLIO MANAGEMENT DIRECTOR Sarah Whalen **PRODUCT DEVELOPMENT DIRECTOR** Will Schweitzer **PRODUCT DEVELOPMENT ASSOCIATE** Hal Moore **BUSINESS SYSTEMS AND FINANCIAL ANALYSIS DIRECTOR** Randy Yi **MANAGER OF FULFILLMENT SYSTEMS** Neal Hawkins **SYSTEMS ANALYST** Nicole Mehmedovich **ASSISTANT DIRECTOR, BUSINESS OPERATIONS** Eric Knott **MANAGER, BUSINESS OPERATIONS** Jessica Tierney **BUSINESS ANALYST** Cory Lipman **FINANCIAL ANALYST** Robert Clark **RIGHTS AND PERMISSIONS ASSISTANT DIRECTOR** Emilie David **PERMISSIONS ASSOCIATE** Elizabeth Sandler **RIGHTS, CONTRACTS, AND LICENSING ASSOCIATE** Lili Kiser

MARKETING DIRECTOR Elise Swinehart **ASSOCIATE DIRECTOR OF ACQUISITION AND RETENTION** Julianne Wielga **MARKETING ASSOCIATE** Elizabeth Sattler **SR. MARKETING EXECUTIVE** Jennifer Reeves **ASSOCIATE DIRECTOR, CREATIVE SERVICES** Tzeitel Sorrosa **ART ASSOCIATE** Seil Lee **JR. ART ASSOCIATE** Kim Huynh **ASSISTANT COMMERCIAL EDITOR** Selby Frame **MARKETING PROJECT MANAGER** Angelissa McArthur **PROGRAM DIRECTOR, AAAS MEMBER CENTRAL** Peggy Mihelich **FULFILLMENT SYSTEMS AND OPERATIONS** membership@aaas.org **MANAGER, MEMBER SERVICES** Pat Butler **SPECIALISTS** Terrance Morrison, Latasha Russell **MANAGER, DATA ENTRY** Mickie Napoleoni **DATA ENTRY SPECIALISTS** Brenden Aquilino, Fiona Giblin

INTERIM DIRECTOR, SITE LICENSING Will Schweitzer **PUBLISHER RELATIONS MANAGER** Catherine Holland **PUBLISHER RELATIONS, EASTERN REGION** Keith Layson **PUBLISHER RELATIONS, WESTERN REGION** Ryan Rexroth **SALES RESEARCH COORDINATOR** Aiesha Marshall **MANAGER, SITE LICENSE OPERATIONS** Iquo Edim **SENIOR PRODUCTION SPECIALIST** Robert Koepke **SENIOR OPERATIONS ANALYST** Lana Guz **FULFILLMENT ANALYST** Judy Lillibridge **ASSOCIATE DIRECTOR, MARKETING** Christina Schlecht **MARKETING ASSOCIATES** Thomas Landreth, Isa Sesay-Bah

WEB TECHNOLOGIES SR. DEVELOPER Chris Coleman **DEVELOPERS** Dan Berger, Jimmy Marks, Ryan Jensen **SR. PROJECT MANAGER** Trista Smith **PROJECT MANAGER** Nick Fletcher

DIGITAL MEDIA DIRECTOR OF ANALYTICS Enrique Gonzales **DIGITAL REPORTING ANALYST** Eric Hossinger **SR. WEB PRODUCER** Sarah Crespi **WEB PRODUCER** Alison Crawford **VIDEO PRODUCER** Nguyen Nguyen **SOCIAL MEDIA PRODUCER** Brice Russ

DIRECTOR OF OPERATIONS PRINT AND ONLINE Lizabeth Harman **DIGITAL/PRINT STRATEGY MANAGER** Jason Hillman **QUALITY TECHNICAL MANAGER** Marcus Spiegler **PROJECT ACCOUNT MANAGER** Tara Kelly **DIGITAL PRODUCTION MANAGER** Lisa Stanford **ASSISTANT MANAGER DIGITAL/PRINT** Rebecca Doshi **SENIOR CONTENT SPECIALISTS** Steve Forrester, Antoinette Hodal, Lori Murphy, Anthony Rosen **CONTENT SPECIALISTS** Jacob Hedrick, Kimberley Oster

DESIGN DIRECTOR Beth Rakouskas **DESIGN EDITOR** Marcy Atarod **SENIOR DESIGNER** Garvin Grullón **DESIGNER** Chrystal Smith **GRAPHICS MANAGING EDITOR** Alberto Cuadra **SENIOR SCIENTIFIC ILLUSTRATORS** Chris Bickel, Katharine Sutliff **SCIENTIFIC ILLUSTRATOR** Valerie Altounian **SENIOR ART ASSOCIATES** Holly Bishop, Nathalie Cary, Preston Huey **PHOTOGRAPHY MANAGING EDITOR** William Douthitt **PHOTO EDITORS** Leslie Blizard, Christy Steele

DIRECTOR, GLOBAL COLLABORATION, CUSTOM PUBLICATIONS, ADVERTISING Bill Moran **EDITOR, CUSTOM PUBLISHING** Sean Sanders: 202-326-6430 **ASSISTANT EDITOR, CUSTOM PUBLISHING** Tianna Hicklin: 202-326-6463 **ADVERTISING MARKETING MANAGER** Justin Sawyers: 202-326-7061 science_advertising@aaas.org **ADVERTISING SUPPORT MANAGER** Karen Foote: 202-326-6740 **ADVERTISING PRODUCTION OPERATIONS MANAGER** Deborah Tompkins **SR. PRODUCTION SPECIALIST/GRAPHIC DESIGNER** Amy Hardcastle **SR. TRAFFIC ASSOCIATE** Christine Hall **SALES COORDINATOR** Shirley Young **ASSOCIATE DIRECTOR, COLLABORATION, CUSTOM PUBLICATIONS/CHINA/TAIWAN/KOREA/SINGAPORE** Ruolei Wu: +86-186 0082 9345, rwu@aaas.org **COLLABORATION/CUSTOM PUBLICATIONS/JAPAN** Adarsh Sandhu + 81532-81-5142 asandhu@aaas.org **EAST COAST/E. CANADA** Laurie Faraday: 508-747-9395, FAX 617-507-8189 **WEST COAST/W. CANADA** Lynne Stickrod: 415-931-9782, FAX 415-520-6940 **MIDWEST** Jeffrey Dembski: 847-498-4520 x3005, Steven Loerch: 847-498-4520 x3006 **UK EUROPE/ASIA** Roger Goncalves: TEL/FAX +41 43 243 1358 **JAPAN** Katsuyoshi Fukamizu(Tokyo): +81-3-3219-5777 kfukamizu@aaas.org **CHINA/TAIWAN** Ruolei Wu: +86-186 0082 9345, rwu@aaas.org

WORLDWIDE ASSOCIATE DIRECTOR OF SCIENCE CAREERS Tracy Holmes: +44 (0) 1223 326525, FAX +44 (0) 1223 326532 tholmes@science-int.co.uk **CLASSIFIED** advertise@sciencecareers.org **U.S. SALES** Tina Burks: 202-326-6577, Nancy Toema: 202-326-6578 **EUROPE/ROW SALES** Sarah Lelarge **SALES ASSISTANT** Kelly Grace **JAPAN** Hiroyuki Mashiki(Kyoto): +81-75-823-1109 hmashiki@aaas.org **CHINA/TAIWAN** Ruolei Wu: +86-186 0082 9345 rwu@aaas.org **MARKETING MANAGER** Allison Pritchard **MARKETING ASSOCIATE** Aimee Aponte

AAAS BOARD OF DIRECTORS RETIRING PRESIDENT, CHAIR Gerald R. Fink **PRESIDENT** Geraldine (Geri) Richmond **PRESIDENT-ELECT** Barbara A. Schaal **TREASURER** David Evans Shaw **CHIEF EXECUTIVE OFFICER** Rush D. Holt **BOARD** Bonnie L. Bassler, May R. Berenbaum, Carlos J. Bustamante, Stephen P.A. Fodor, Claire M. Fraser, Michael S. Gazzaniga, Laura H. Greene, Elizabeth Loftus, Mercedes Pascual

SUBSCRIPTION SERVICES For change of address, missing issues, new orders and renewals, and payment questions: 866-434-AAAS (2227) or 202-326-6417, FAX 202-842-1065. Mailing addresses: AAAS, P.O. Box 96178, Washington, DC 20090-6178 or AAAS Member Services, 1200 New York Avenue, NW, Washington, DC 20005

INSTITUTIONAL SITE LICENSES 202-326-6730 **REPRINTS:** Author Inquiries 800-635-7181 **COMMERCIAL INQUIRIES** 803-359-4578 **PERMISSIONS** 202-326-6765, permissions@aaas.org **AAAS Member Services** 202-326-6417 or http://membercentral.aaas.org/discounts

Science serves as a forum for discussion of important issues related to the advancement of science by publishing material on which a consensus has been reached as well as including the presentation of minority of conflicting points of view. Accordingly, all articles published in *Science*—including editorials, news and comment, and books reviews—are signed and reflect the individual views of the authors and not official points of view adopted by AAAS or the institutions with which the authors are affiliated.

INFORMATION FOR AUTHORS See pages 678 and 679 of the 6 February 2015 issue or access www.sciencemag.org/about/authors

SENIOR EDITORIAL BOARD

Gary King, *Harvard University,* **Susan M. Rosenberg,** *Baylor College of Medicine,*
Ali Shilatifard, *Northwestern University Feinberg School of Medicine*

BOARD OF REVIEWING EDITORS (Statistics board members indicated with **(S)**)

Adriano Aguzzi, *U. Hospital Zürich*
Takuzo Aida, *U. of Tokyo*
Leslie Aiello, *Wenner-Gren Foundation*
Judith Allen, *U. of Edinburgh*
Sonia Altizer, *U. of Georgia*
Sebastian Amigorena, *Institut Curie*
Kathryn Anderson, *Memorial Sloan-Kettering Cancer Center*
Meinrat O. Andreae, *Max-Planck Inst. Mainz*
Paola Arlotta, *Harvard U.*
Johan Auwerx, *EPFL*
David Awschalom, *U. of Chicago*
Clare Baker, *University of Cambridge*
Jordi Bascompte, *University of Zurich*
Facundo Batista, *London Research Inst.*
Ray H. Baughman, *U. of Texas, Dallas*
David Baum, *U. of Wisconsin*
Carlo Beenakker, *Leiden U.*
Kamran Behnia, *ESPCI-ParisTech*
Yasmine Belkaid, *NIAID, NIH*
Philip Benfey, *Duke U.*
May Berenbaum, *U. of Illinois*
Gabriele Bergers, *U. of California, San Francisco*
Bradley Bernstein, *Massachusettes General Hospital*
Peer Bork, *EMBL*
Bernard Bourdon, *Ecole Normale Supérieure de Lyon*
Chris Bowler, *École Normale Supérieure*
Ian Boyd, *U. of St. Andrews*
Emily Brodsky, *U. of California, Santa Cruz*
Ron Brookmeyer, *U. of California Los Angeles* **(S)**
Christian Büchel, *U. Hamburg-Eppendorf*
Joseph A. Burns, *Cornell U.*
Carter Tribley Butts, *U. of California, Irvine*
Gyorgy Buzsaki, *New York U. School of Medicine*
Blanche Capel, *Duke U.*
Mats Carlsson, *U. of Oslo*
Ib Chorkendorff, *U. of Denmark*
David Clapham, *Children's Hospital Boston*
Joel Cohen, *Rockefeller U., Columbia U.*
James J. Collins, *MIT*
Robert Cook-Deegan, *Duke U.*
Lisa Coussens, *Oregon Health & Science U.*
Alan Cowman, *Walter & Eliza Hall Inst.*
Robert H. Crabtree, *Yale U.*
Roberta Croce, *Vrije Universiteit*
Janet Currie, *Princeton U.*
Jeff L. Dangl, *U. of North Carolina*
Tom Daniel, *U. of Washington*
Frans de Waal, *Emory U.*
Stanislas Dehaene, *Collège de France*
Robert Desimone, *MIT*
Claude Desplan, *New York U.*
Dennis Discher, *U. of Pennsylvania*
Gerald W. Dorn II, *Washington U. School of Medicine*
Jennifer A. Doudna, *U. of California, Berkeley*
Bruce Dunn, *U. of California, Los Angeles*
William Dunphy, *Caltech*
Christopher Dye, *WHO*
Todd Ehlers, *U. of Tuebingen*
David Ehrhardt, *Carnegie Inst. of Washington*
Tim Elston, *U. of North Carolina at Chapel Hill*
Gerhard Ertl, *Fritz-Haber-Institut, Berlin*
Barry Everitt, *U. of Cambridge*
Ernst Fehr, *U. of Zurich*
Anne C. Ferguson-Smith, *U. of Cambridge*
Michael Feuer, *The George Washington U.*
Toren Finkel, *NHLBI, NIH*
Kate Fitzgerald, *U. of Massachusetts*
Peter Fratzl, *Max-Planck Inst.*
Elaine Fuchs, *Rockefeller U.*
Daniel Geschwind, *UCLA*
Karl-Heinz Glassmeier, *TU Braunschweig*
Ramon Gonzalez, *Rice U.*
Julia R. Greer, *Caltech*
Elizabeth Grove, *U. of Chicago*
Nicolas Gruber, *ETH Zurich*
Kip Guy, *St. Jude's Children's Research Hospital*
Taekjip Ha, *U. of Illinois at Urbana-Champaign*
Christian Haass, *Ludwig Maximilians U.*
Michael Hasselmo, *Boston U.*
Martin Heimann, *Max-Planck Inst. Jena*
Yka Helariutta, *U. of Cambridge*
James A. Hendler, *Rensselaer Polytechnic Inst.*
Janet G. Hering, *Swiss Fed. Inst. of Aquatic Science & Technology*
Kai-Uwe Hinrichs, *U. of Bremen*
David Hodell, *U. of Cambridge*
David Holden, *Imperial College*
Lora Hooper, *UT Southwestern Medical Ctr. at Dallas*
Tamas Horvath, *Yale University*
Raymond Huey, *U. of Washington*
Auke Ijspeert, *EPFL Lausanne*
Steven Jacobsen, *U. of California, Los Angeles*
Stephen Jackson, *U. of Arizona*
Kai Johnsson, *EPFL Lausanne*
Peter Jonas, *Inst. of Science & Technology (IST) Austria*
Matt Kaeberlein, *U. of Washington*
William Kaelin Jr., *Dana-Farber Cancer Inst.*
Daniel Kahne, *Harvard U.*
Daniel Kammen, *U. of California, Berkeley*
Masashi Kawasaki, *U. of Tokyo*
V. Narry Kim, *Seoul National U.*
Joel Kingsolver, *U. of North Carolina at Chapel Hill*
Robert Kingston, *Harvard Medical School*
Etienne Koechlin, *Ecole Normale Suprieure*
Alexander Kolodkin, *Johns Hopkins U.*
Thomas Langer, *U. of Cologne*
Mitchell A. Lazar, *U. of Pennsylvania*
David Lazer, *Harvard U.*
Thomas Lecuit, *IBDM*
Virginia Lee, *U. of Pennsylvania*
Stanley Lemon, *U. of North Carolina at Chapel Hill*
Ottoline Leyser, *Cambridge U.*
Wendell Lim, *U.C. San Francisco*
Marcia C. Linn, *U. of California, Berkeley*
Jianguo Liu, *Michigan State U.*
Luis Liz-Marzan, *CIC biomaGUNE*
Jonathan Losos, *Harvard U.*
Ke Lu, *Chinese Acad. of Sciences*
Christian Lüscher, *U. of Geneva*
Laura Machesky, *CRUK Beatson Inst. for Cancer Research*
Anne Magurran, *U. of St. Andrews*
Oscar Marin, *CSIC & U. Miguel Hernández*
Charles Marshall, *U. of California, Berkeley*
C. Robertson McClung, *Dartmouth College*
Graham Medley, *U. of Warwick*
Tom Misteli, *NCI*
Yasushi Miyashita, *U. of Tokyo*
Mary Ann Moran, *U. of Georgia*
Richard Morris, *U. of Edinburgh*
Alison Motsinger-Reif, *NC State U.* **(S)**
Thomas Murray, *The Hastings Center*
Daniel Neumark, *U. of California, Berkeley*
Kitty Nijmeijer, *U. of Twente*
Pär Nordlund, *Karolinska Inst.*
Helga Nowotny, *European Research Advisory Board*
Ben Olken, *MIT*
Joe Orenstein, *U. of California Berkeley & Lawrence Berkeley National Lab*
Harry Orr, *U. of Minnesota*
Andrew Oswald, *U. of Warwick*
Steve Palumbi, *Stanford U.*
Jane Parker, *Max-Planck Inst. of Plant Breeding Research*
Giovanni Parmigiani, *Dana-Farber Cancer Inst.* **(S)**
John H. J. Petrini, *Memorial Sloan-Kettering Cancer Center*
Samuel Pfaff, *Salk Institute for Biological Studies*
Joshua Plotkin, *U. of Pennsylvania*
Albert Polman, *FOM Institute AMOLF*
Philippe Poulin, *CNRS*
Jonathan Pritchard, *Stanford U.*
David Randall, *Colorado State U.*
Felix Rey, *Institut Pasteur*
Trevor Robbins, *U. of Cambridge*
Jim Roberts, *Fred Hutchinson Cancer Research Ctr.*
Barbara A. Romanowicz, *U. of California,Berkeley*
Amy Rosenzweig, *Northwestern University*
Mike Ryan, *U. of Texas, Austin*
Mitinori Saitou, *Kyoto U.*
Shimon Sakaguchi, *Kyoto U.*
Miquel Salmeron, *Lawrence Berkeley National Lab*
Jürgen Sandkühler, *Medical U. of Vienna*
Alexander Schier, *Harvard U.*
Vladimir Shalaev, *Purdue U.*
Robert Siliciano, *Johns Hopkins School of Medicine*
Denis Simon, *Arizona State U.*
Uri Simonsohn, *U. of Pennsylvania*
Alison Smith, *John Innes Centre*
Richard Smith, *U. of North Carolina* **(S)**
John Speakman, *U. of Aberdeen*
Allan C. Spradling, *Carnegie Institution of Washington*
Jonathan Sprent, *Garvan Inst. of Medical Research*
Eric Steig, *U. of Washington*
Paula Stephan, *Georgia State U. and National Bureau of Economic Research*
Molly Stevens, *Imperial College London*
V. S. Subrahmanian, *U. of Maryland*
Ira Tabas, *Columbia U.*
Sarah Teichmann, *Cambridge U.*
John Thomas, *North Carolina State U.*
Shubha Tole, *Tata Institute of Fundamental Research*
Christopher Tyler-Smith, *The Wellcome Trust Sanger Inst.*
Herbert Virgin, *Washington U.*
Bert Vogelstein, *Johns Hopkins U.*
Cynthia Volkert, *U. of Göttingen*
Douglas Wallace, *Dalhousie U.*
David Wallach, *Weizmann Inst. of Science*
Ian Walmsley, *U. of Oxford*
Jane-Ling Wang, *U. of California, Davis* **(S)**
David A. Wardle, *Swedish U. of Agric. Sciences*
David Waxman, *Fudan U.*
Jonathan Weissman, *U. of California, San Francisco*
Chris Wikle, *U. of Missouri* **(S)**
Ian A. Wilson, *The Scripps Res. Inst.* **(S)**
Timothy D. Wilson, *U. of Virginia*
Rosemary Wyse, *Johns Hopkins U.*
Jan Zaanen, *Leiden U.*
Kenneth Zaret, *U. of Pennsylvania School of Medicine*
Jonathan Zehr, *U. of California, Santa Cruz*
Len Zon, *Children's Hospital Boston*
Maria Zuber, *MIT*

BOOK REVIEW BOARD

David Bloom, *Harvard U.,* **Samuel Bowring,** *MIT,* **Angela Creager,** *Princeton U.,*
Richard Shweder, *U. of Chicago,* **Ed Wasserman,** *DuPont*

EDITORIAL

Global science engagement

In rural Laos, more than 50% of newborns will be stunted by age 2 due to chronic malnourishment. Worldwide, 161 million children under the age of 5, many of them in Africa and Asia, suffered irreversible stunting as of 2013. The developed world is not immune. As recently as 2010, stunting affected 8 to 9% of babies enrolled in U.S. federal food-subsidy programs. Next week in Washington, DC, the American Association for the Advancement of Science (AAAS is the publisher of *Science*) will convene its annual meeting (11 to 15 February), where world leaders will discuss food security and other major challenges that lie ahead in both the science and international policy arenas.

Ensuring a sustainable world in the face of climate change and a world population of 9 billion demands a major shift in how nations seek ingenious ways to coexist with ever-expanding needs for energy, food, water, and a healthy environment—situations that are complex and interconnected. Solutions demand innovative international research partnerships and policies that include talents and perspectives from both the developed and developing worlds. This collaboration will be the focus of the AAAS meeting, under the theme "Global Science Engagement." The meeting will provide an opportunity to hear about the latest new approaches and creative thinking from around the world.



"...diversity in opinions, ideas, and experiences fuels creativity and innovation."

Amid budget constraints and current isolationist views, many policy-makers, including those in the United States, may understandably see international initiatives as less important than domestic ones. Such research isolation is unwise. Water security is a good example. The United States spends billions of dollars making water potable and then flushes an estimated 90% of that water down the toilet or drain. There is much to learn from countries such as Namibia, the most arid country in southern Africa, where people have been drinking recycled water since 1969 with no health consequences, or Singapore, which has no natural aquifers and a small landmass. International research collaborations can save money in the long run.

To solve complex global problems, the world's technical workforce must include countries at all economic levels. No segment can be ignored or overlooked in the talent search, because diversity in opinions, ideas, and experiences fuels creativity and innovation. We can no longer afford to lose talented young women around the globe who were science stars in their early schooling and career preparation, yet later were lost from the technical talent pool—lost to factors that are not beyond control but require a strong global commitment to resolve.

In my work with developing countries in Africa, Asia, and Latin America, I continue to be impressed by the talent and creativity of scientists there: male and female, abled and disabled, young and old. We need their ideas and perspectives as much as those from countries with advanced science and technology infrastructures. But their ability to connect with scientists in the more developed research mainstream is fraught with difficulties, including international cultural biases that also make it difficult for them to get access to, or publish in, respected journals. Equally, I see scientists and engineers, especially the younger generation in the United States, who are passionate about global research engagement but do not know how to connect with potential partners in the developing world. I applaud organizations that have a history of success in facilitating such connections.

AAAS has a long history of international engagement activities, as have other scientific societies, but we all can do more to facilitate international research networking, collaborations, and journal access. Through the upcoming AAAS Annual Meeting and beyond, I hope that countries can commit to strengthening these connections. It is imperative for the sustainability of the planet and those malnourished babies in Laos and around the world, whose lives we cannot afford to waste or lose.

– Geraldine Richmond



Geraldine Richmond is president of AAAS and Presidential Chair in Science and professor in the Department of Chemistry and Biochemistry at the University of Oregon, Eugene, OR. E-mail: richmond@oregon.edu

Downloaded from on January 31, 2016

PHOTOS: (TOP) UNIVERSITY OF OREGON; (INSET) © REBECCA COLES/ALAMY STOCK PHOTO

10.1126/science.aaf2869

Published by AAAS

8 Speed, in kilometers per hour, of a *Tyrannosaurus rex* that strode along a shoreline 66 million years ago—a brisk but not outrunnable pace, say researchers who analyzed the spacing and arrangement of a set of fossilized footprints (*Cretaceous Research*). **http://scim.ag/Trexwalk**

IN BRIEF

Spanish missions triggered crash of Pueblo population



Spanish missions, like San Jose de los Jemez (shown), may have helped spread disease among the Pueblo.

When European explorers first arrived at Jemez province in New Mexico in 1541, its ponderosa pine forests were home to between 5000 and 8000 Pueblo people. Some time afterward, the population had plummeted by 87%, probably because of a series of devastating epidemics, but the timing of this has been unclear. Now, a new study suggests that the downfall occurred about a century after the first contact with Europeans—corresponding with the establishment of Spanish missions in the region, which likely helped spread disease. By counting the rings of trees now growing in the ruins of Jemez villages, researchers determined that many of them sprouted in the 1630s and 1640s, suggesting that the sites were abandoned soon after the missions arrived. The population crash also triggered ecological changes, the researchers report this week in the *Proceedings of the National Academy of Sciences*. Without the Pueblo people clearing underbrush for firewood and cutting down trees for construction, the region was primed for forest fires, which became more frequent in the decades following the population collapse. **http://scim.ag/Pueblomission**

AROUND THE WORLD

Data sharing stance sparks debate

BOSTON | Support for data sharing is trending among scientists, but it has proven difficult to implement in clinical trials. Last week, *The New England Journal of Medicine* (*NEJM*) published two editorials, one of which sparked a backlash on social media. In the first, *NEJM* joined 13 other medical journals in proposing to require authors to agree to share anonymized patient data within 6 months of an article's publication. That proposal is now accepting comments at www.icmje.org. In the second, *NEJM* editors focused on *how* clinical trial data should be shared; the writers noted concerns that data might be nabbed by "research parasites" who would use them for their own ends or to disprove the original hypothesis. This outraged many scientists, some of whom coined a Twitter hashtag—#IAmAResearchParasite. *NEJM* Editor-in-Chief Jeffrey Drazen defended the editorial's stance to *Science*, noting that collaborating with the group that produced data is "what we think is the preferred way to [proceed], not necessarily the only way."

New ocean health monitoring plan

TOKYO | Marine scientists are developing new sensors they plan to deploy in a global monitoring system to better observe changes occurring in the world's



Tracking rapid ocean changes requires new data.

PHOTOS: (LEFT TO RIGHT) © WITOLD SKRYPCZAK/ALAMY STOCK PHOTO; ARGO PROGRAM, GERMANY/IFREMER

Downloaded from on January 31, 2016

Published by AAAS

oceans. The Partnership for Observation of the Global Oceans (POGO), a consortium of 40 oceanographic institutions, announced the new strategy at a press conference 25 January, ahead of the partnership's annual meeting. POGO has previously coordinated the worldwide deployment of 20,000 autonomous probes known as Argo (shown) floats that gather ocean data including temperature and salinity. But POGO researchers say that scientists will need much more data to keep pace with rapid changes in the oceans, such as measurements of temperatures at depths below 2 kilometers (the depth limit of Argo sensors) as well as biological activity throughout the water column. The goal is to have the new global monitoring system in place by 2030. http://scim.ag/POGOplan

Chinese scientists indicted

PHILADELPHIA, PENNSYLVANIA | In the latest of a series of cases against Chinese or Chinese-American scientists, two GlaxoSmithKline (GSK) scientists were accused last week of transferring trade secrets to China. On 20 January, federal prosecutors in Philadelphia announced the indictment of Yu Xue and Lucy Xi and three associates for trade secrets theft, wire fraud, and other charges. The scientists stand accused of emailing and downloading proprietary data about GSK products and sending it to contacts working for the Chinese start-up Renopharma; the indictment alleges that Xue was financially involved in Renopharma and hoped to profit off the transfer of information. But experts are urging caution in interpreting the case, noting that it bears similarities to two other recent cases involving Chinese American or Chinese defendants in which prosecutors abruptly dropped charges because of improper analysis or insufficient evidence. http://scim.ag/GSKsecrets

FINDINGS

Cats domesticated twice?

Cats may have been domesticated more than once. That's the intriguing possibility raised by a new analysis of feline bones from three ancient farming villages in China. The bones—dated to about 5000 years ago—all belong to the leopard cat (*Prionailurus bengalensis*), researchers report this month in *PLOS ONE*. That's a different species than the Near Eastern wildcat (*Felis silvestris lybica)*, the ancestor of today's house cat, which was domesticated in the Middle East about 10,000 years ago. Some of the bones show signs that the villagers cared for these animals, suggesting they may have been on the road to domestication. But the process hit a dead end at some point. Still, leopard cats survive in house cats in the Bengal breed, a hybrid of the two created in the 1960s. http://scim.ag/catsdom



Analyses of the microbes in these tire imprints added science to an art project.

PHOTO: WOLFGANG BURTSCHER

Cycling artist maps soil microbes across Eurasia

Art, science, and dirt collided during Wolfgang Burtscher's cross-continent bicycle trip from Austria to Laos. In anticipation of the International Year of Soils in 2015, Burtscher, an artist, stopped each day during his 11-month trek in 2012 to make a "tripmark"—a tire-track imprint—and to collect soil. Teaming up with artist and microbial ecology graduate student Magdalena Nagler of the University of Innsbruck in Austria, he turned the art project into a scientific study. Nagler sequenced the soils' DNA to identify which fungi and soil bacteria, called actinobacteria, were present. It was a rare opportunity to cover such a broad geographic area, she says, and to confirm that microbes really follow a century-old rule: "Everything is everywhere, but the environment selects." Many microbes were ubiquitous across Eurasia, she and her colleagues report in the March issue of *Applied Soil Ecology*—but how similar two microbial communities are is determined more by the similarity of the soils and local climates than by their actual proximity. "For me it was surprising that [the result] was so nicely fitting our hypothesis," Nagler says. "You are not always so lucky."

NEWSMAKERS

Three Q's

On 22 January, neuroscientist **Ian Chubb** stepped down after 5 years as Australia's chief scientist. He held the position during a turbulent time. Under former Prime Minister Tony Abbott, who led the country from September 2013 to September 2015, funding for scientific research fell to a 30-year low and the government failed to appoint a science minister for more than a year. *Science* spoke with Chubb about his experiences.

Q: You've said that Australia should not rely on "voodoo economics." Why?
A: [Some] members of the commentariat believe in the omnipotence of the market. So when governments say we ... have to make choices [for science funding], they are criticised as "picking winners." In contrast, there are ample examples of sensible government interventions which can harness the nation's educational and scientific strengths. We must put our faith in evidence-based policy, not uninformed ideology.

Q: What would you like to say to Australian scientists as you leave the job?
A: Be patient, and persistent. We need the science. [The public] needs reassurance that what you do is important to their future.

Q: What advice do you have for your successor, neuroscientist Alan Finkel?
A: My only comments are: Don't flinch, and don't forget the importance of the public.

Published by AAAS



CLIMATE POLICY

Can Germany engineer a coal exit?

Debate grows over whether nation could eliminate a key but dirty fuel by 2040

By **Christopher Schrader**

On a recent frigid day, towering plumes of steam rose from the cooling towers of Germany's Jänschwalde generating station, a huge coal-fired power plant near the nation's border with Poland. The carbon dioxide–spewing plant is a jarring sight in the land of the Energiewende, Germany's ambitious plan to transform its energy system and cut national greenhouse gas emissions by 80% to 95% by 2050. But Jänschwalde is just one of about 40 coal-burning plants that, together, are Germany's top source of electricity.

Now, in the wake of the Paris climate pact, Germans are debating whether and when to close Jänschwalde and other coal plants. "Germany can't be the Energiewende country and remain a coal country," says Patrick Graichen, head of Agora Energiewende, a Berlin think tank. It released a report this month concluding that Germany could abandon coal by 2040 by shifting to cleaner alternatives. Last week, Germany's environment minister, Barbara Hendricks, said that she soon will unveil a plan for reaching the 2050 emissions goal. Many observers expect it to include a coal exit timeline.

But German Vice Chancellor Sigmar Gabriel is pushing back, along with major labor and industry groups that fear job losses and energy market disruptions. They also argue that Europe's emissions trading market means that a German coal exit would lead to rising emissions in other countries. "We are convinced the problem should be solved on the European level," Gabriel said last week.

Germany's energy system is already undergoing a dramatic transformation. The nation plans to close its seven remaining nuclear power plants by 2022 and has been investing heavily in wind, solar, and other renewable sources of power. Renewables are now Germany's second leading source of electricity, providing about one-third of the total. Officials want to boost that share to at least 80% by 2050, as part of the plan to "decarbonize" Germany's economy.

> ***"Germany can't be the Energiewende country and remain a coal country."***
>
> **Patrick Graichen**, Agora Energiewende

But relatively cheap coal remains a top power source. In 2015, coal plants produced 43% of Germany's electricity. That's down from 50% in 2000, but coal is still Germany's leading source of carbon emissions—producing 40% of the total—and the nation is Europe's champion emitter, releasing 800 million tons of CO_2 in 2014.

Particularly problematic is Germany's reliance on its massive reserves of lignite, a soft brown coal that burns inefficiently, producing roughly one-fourth more carbon dioxide than hard coal and almost three times as much as natural gas. Overall, lignite-fueled plants such as Jänschwalde, which gets its coal from huge open pits nearby, produce about one-fourth of Germany's power. (Plants fueled with hard coal produce about one-fifth.)

To curb emissions, Germany is already planning to pay utilities to mothball eight lignite plants—including two of Jänschwalde's six units—by 2020. But analysts argue much more will be needed. "Ultimately, there is no alternative to phasing out … coal power if Germany is to fulfill its climate goals," Agora Energiewende concluded in its 11 January report, which lays out a wide-ranging plan for a coal exit by 2040.

The plan calls on the government to immediately bar the construction of new power plants and lignite mines and, beginning in 2018, for utilities to start abandoning older coal-fired plants. It envisions reducing Germany's 49 gigawatts of coal generating capacity by 3 gigawatts per year, or the equivalent of closing three to six big plants annually. Germany can replace coal plants with cleaner natural gas generators and existing renewable technologies without causing a spike in power prices, the group says: It calculates a 2040 coal exit would increase power prices by just €0.03 to €0.05 per kilowatt hour, compared with a slower business-as-usual scenario that envisions coal use tailing off after 2050.

PHOTO: PATRICK PLEUL/PICTURE-ALLIANCE/DPA/AP IMAGES

Downloaded from on January 31, 2016

Published by AAAS

Fueled by lignite, the Jänschwalde plant is one of Germany's largest carbon dioxide emitters.

Agora Energiewende also calls on the government to quickly convene a "round table" of key players—including unions, energy firms, and environmentalists—which would develop a coal exit schedule by the end of 2016. That idea has been endorsed by Hendricks, the environment minister, who aims to deliver a national climate plan to Chancellor Angela Merkel's cabinet this summer. Hendricks has said she'd like to see Germany's last lignite-fueled plant close by 2050.

Gabriel, the energy and economics minister, also backs the idea of talks, but says he is skeptical of developing a "master plan." And industry and union groups have raised numerous concerns about a rapid coal exit, noting that some 60,000 jobs are at stake.

Some of the critics argue that Germany doesn't need new rules to reach its 2050 goals, because existing domestic and Europe-wide climate policies—including the E.U. emissions permit trading system—will be sufficient to reduce Germany's reliance on coal. Others predict that a hurried phase-out will disrupt electricity markets, especially if it forces many larger, older lignite plants to close in the early 2020s, just as nuclear plants are disconnected, too. Analysts also worry that, by acting alone, Germany could end up unintentionally boosting emissions elsewhere, as power producers in other nations purchase cheap emissions permits that German utilities no longer need. "The CO_2 will only be released in other countries," predicts Uwe Maaßen of the Bundesverband Braunkohle in Cologne, which represents the lignite industry.

To prevent displaced emissions, the Agora Energiewende report says Germany must push for reforms to Europe's emissions trading scheme, so that it doesn't undermine aggressive national policies. It also recommends that Germany create programs aimed at softening the blow of job losses.

The coal exit discussion is coming "at the right time and is the next logical step in the Energiewende debate," says Marcus Ferdinand, an analyst at Thomson Reuters in Oslo. But the politics are perilous. Last year, fierce opposition forced Gabriel to abandon a proposal to heavily tax the most polluting lignite plants. Instead, he opted for the less onerous—and costlier—plan to pay owners to mothball some plants. But Agora Energiewende warns that the cost of expanding such a buyout scheme to Germany's whole coal sector would be exorbitant. ■

Christopher Schrader is a writer in Hamburg, Germany.

PHOTO: DR. KAREN YOUNG

GEOCHEMISTRY

Rare isotopes offer clues to the chemistry of the planet

New lab tools bring exotic isotopic signatures into view

By **Eric Hand**

To learn about some of the grandest processes on Earth, from plant growth to climate change, researchers are weighing molecules on ever more sensitive scales. Molecules containing an unexpected isotope—carbon-13 in place of carbon-12 in carbon dioxide (CO_2), say—weigh a hair more or less than their commoner counterparts and carry a wealth of information about biological or chemical processes. Those carbon isotopes, for example, are a gauge of plant productivity, because photosynthesis prefers to take up carbon-12 over its heavier cousin.

For decades, geochemists had to be content to measure one isotope at a time. Now, however, formidable new lab instruments are enabling them to detect some of the rarest isotopic variants in nature: molecules containing two or more rare isotopes at once. The quantities are minuscule, and the targets are almost indistinguishable from other forms of the molecule. But already, the lab results on small molecules including methane and nitrogen are starting to offer tantalizing clues to paleoclimate, nutrient cycling, energy exploration, and Earth's deep biosphere.

"We are all realizing that these new instruments just open up so many possibilities, we don't know where to start," says Laurence Yeung, a geochemist at Rice University in Houston, Texas. "Every stone you look under, there will be something new and interesting. It's a sea change in how we engage with isotope geochemistry."

One group, led by John Eiler of the California Institute of Technology in Pasadena, is going even further: looking at large molecules from living things, such as amino acids and sugars. Because of their size, each compound can come in millions of isotopic flavors, all of them clues to biological processes. "Every one of those isotopic forms is in some sense unique and encodes something about the molecule," Eiler says. As scientists hone their ability to detect and measure these flavors, isotopic analysis of biomolecules could benefit drug development and personalized medicine, says Eiler, who has started a company that will seek commercial applications.

Eiler began the trend a decade ago by pointing out the scientific benefits of studying so-called clumped isotopes. A molecule like CO_2 comes not only in flavors with single-isotope substitutions—such as $^{13}C^{16}O^{16}O$ (in which carbon-13 replaces carbon-12), or $^{12}C^{18}O^{16}O$—but also in rarer, doubly substituted forms, such as $^{13}C^{18}O^{16}O$.



At the University of California, Los Angeles, the world's largest gas-fed mass spectrometer, Panorama, will probe methane origins.

The prevalence of this rare molecule, or isotopologue, offers clues to the temperature at which it formed. CO_2 made at high temperatures contains just 44 parts per million of $^{13}C^{18}O^{16}O$, the proportion that would be expected by chance alone. But at lower temperatures, nature has a small tendency to assemble more of these special molecules, because the heavier atoms bond slightly more stably. Eiler realized that mass spectrometers—a kind of molecular scale—could measure that slight preference for "clumping" of the two heavy atoms, and that scientists could harness that bias as

Downloaded from on January 31, 2016

Published by AAAS

a geothermometer. Sure enough, he found progressively more clumping as he sampled CO_2 made at lower and lower temperatures of formation: car exhaust (200°C), human respiration (37°C), and urban air (20°C).

Since Eiler proposed the idea in 2004, a few dozen labs have run with it, focusing on one paleoclimate application in particular: measuring clumped isotopes in CO_2 extracted from carbonate rocks, such as limestone, that precipitated out of ancient seawater. Previously, paleoclimatologists estimated ancient temperatures by measuring single isotopes in limestone—but they couldn't tell whether an unusual mixture of isotopes in the original seawater might be skewing their calculations. "We don't have the water from the past, so we're missing a key component to making a temperature determination," says Albert Colman, a geochemist at the University of Chicago in Illinois. By contrast, the clumped-isotope effect is independent of seawater composition. It is frozen in the limestone at the time of its precipitation, as the ions jostle for the most stable thermodynamic arrangement for a given temperature.

Now, a few labs are using new tools to branch out of carbonates and into new molecules that require finer mass measurements. Shuhei Ono, at the Massachusetts Institute of Technology in Cambridge, is using infrared spectroscopy to study isotopologues of methane in order to understand its origin. Different isotopic forms of the gas absorb different frequencies of infrared light; by tuning lasers to those absorption frequencies, he can measure how abundant the isotopes are. The laser spectrometer fits in a box less than a meter across—"You can put it in your Dodge Caravan," Ono says—and the pace of laser development keeps costs dropping as capabilities grow, he says.

Ed Young, a geochemist at the University of California, Los Angeles, is also analyzing clumped isotopes in methane, seeking clues to its origins, but he's betting on a different technology: bulked-up mass spectrometers. Mass spectrometers take streams of ionized molecules and use a magnet to guide them on a curving path into a detector. Lighter molecules swerve more in flight than heavier ones do, so they strike the detector in different places. A bigger magnet gives the finer mass resolution needed for rarer isotopologues. Young's spectrometer, called Panorama, contains the largest magnet ever used in a spectrometer of its kind, and the machine fills an entire room. (This week in *Science* [p. 493], Young and colleagues publish the first results from Panorama, measurements of single oxygen isotopes that have implications for the formation of the moon but nothing to do with clumping.)

Young aims to use Panorama to measure two doubly substituted flavors of methane: one with two deuteriums in place of hydrogens, and one with a single deuterium and a carbon-13 instead of carbon-12. Measuring both at once, he hopes, will enable him to distinguish methane made by microbes—as most is thought to be—from "abiotic" methane made from mineral reactions at high pressures and temperatures deep in Earth.

The energy industry, which has long wondered whether accessible sources of abiotic methane lurk underground, will be eager for more such clues, Young says. Colman adds that clumped isotope analysis of methane could also help biologists spot signs of organisms in the depths of Earth's crust and measure the temperatures they endure, a clue to how far down the "deep biosphere" extends. The methane fingerprint "could be used as a fingerprint for life in the deep subsurface," he says.

Yeung, a former postdoc of Young's, is using Panorama to explore another key biogeochemical process: the denitrification in Earth's oceans that returns nitrogen to the atmosphere after it has cycled through living things as "fixed nitrogen," bound in proteins and other biomolecules. Biologists know of two main pathways by which microbes remove fixed nitrogen, each with its own enzyme, but they have no idea which pathway is more important or how climate change might be affecting them. Yeung suspects that the two pathways clump doubly substituted nitrogen molecules—N_2 with two nitrogen-15 atoms in place of nitrogen-14—to different degrees. "There's no tracer of this type of process globally," he says. "We're trying to figure out [the clumped effect] now."

The mass-spectrometry-on-steroids approach of Panorama comes at a cost: The machine cost about $2 million dollars, and it took years to assemble and bring up to speed. A smaller but roughly comparable machine in Eiler's laboratory cost about $1.5 million.

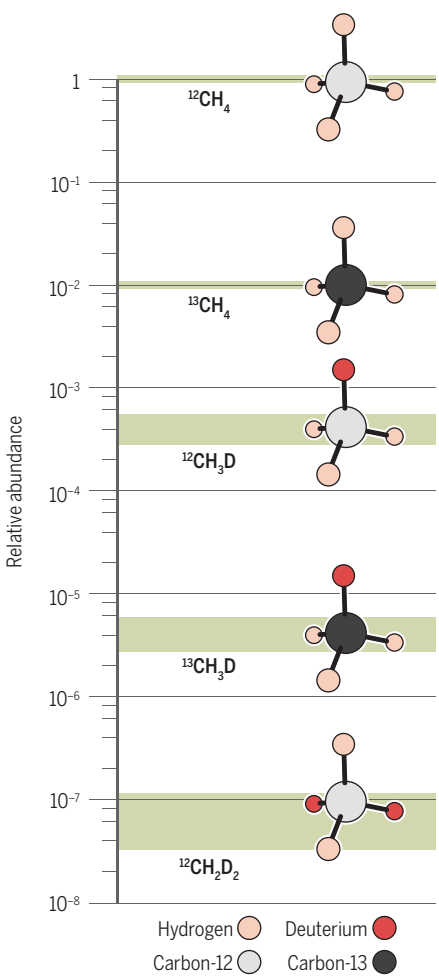
Eiler, however, is already looking ahead to the next tool: the Fourier transform mass spectrometer, which traps ions in a small resonating chamber and determines their masses from their oscillation frequencies. With some tweaking, Eiler says, the instrument can not only identify the many isotopologues of different large biomolecules but also measure their abundances. He is first targeting simple sugars and amino acids, but he eventually hopes to detect isotopic signatures in drug metabolites. They could yield clues to how the body is processing the drug and how well it is working.

Colman thinks clumped-isotope analysis could also lead to new diagnostics, based on differences in the isotopic signatures of molecules found in diseased cells versus healthy ones. "If things like that materialize, this will be huge, and you will see not just [National Science Foundation] money put in but also NIH money," he says.

Researchers agree, however, that a lot of spadework will be necessary first. Gwyneth Gordon, a geochemist at Arizona State University, Tempe, says that, for now, geochemists need to concentrate on the unexplored, basic science: which isotopologues can be measured, what signals there are, if any—and what the signals mean. "In some ways I think the technology is getting ahead of the science," she says. "It's in the descriptive phase." ■

Rare flavors

The methane molecule comes in a handful of ever-more-rare isotopic flavors. By measuring the abundance of these subspecies in a sample—and how those amounts differ from normal—scientists can learn about the methane's temperature of formation and mixing history.



* Bars show the ranges of naturally occurring abundances.

GRAPHIC: P. HUEY/*SCIENCE*

Published by AAAS



Some annual killifish embryos can shut down and survive months with no oxygen.

PHOTO: JASON PODRABSKY AND CLAIRE RIGGS

PHYSIOLOGY

A fish back from the dead

Understanding how killifish survive months without oxygen could help stroke victims

By **Elizabeth Pennisi**, *in Portland, Oregon*

Deprive a human of oxygen for 5 minutes or more and she will turn blue, pass out, and may die. Suffocate the embryo of a Venezuelan annual killifish, however, and it survives for months, emerging unscathed to complete its development. Pinkie-sized and nondescript, the killifish is "a champion of anoxia tolerance among vertebrates," says Daniel Warren, a comparative physiologist at St. Louis University in Missouri.

At the annual meeting of the Society for Integrative and Comparative Biology here last month, Jason Podrabsky offered a look at the killifish's bag of tricks. The comparative physiologist from Portland State University in Oregon and his students are studying the fish to explore the extremes of vertebrate physiology—and to find clues to treating stroke, heart attack, or trauma, which can starve tissues of oxygen. "If we can figure out the mechanisms that animals naturally use to keep them tolerant of anoxia, the potential is there to adopt and use them in a surgical or trauma setting," says W. Wesley Dowd, a comparative physiologist at Loyola Marymount University in Los Angeles, California.

Researchers have identified two other vertebrates, Europe's crucian carp and North America's Western painted turtle, that can live without oxygen just as long as the killifish. But those organisms experience anoxia when the lakes they live in freeze, and the cold helps them survive by slowing their metabolism. In contrast, killifish survive anoxia at tropical temperatures, a much harder task.

The killifish inhabit temporary pools that form during the rainy season and often vanish before the fish can complete their life cycle. Their eggs may be marooned in the clay-laden mud, sealed off from oxygen, for weeks or months until the rains return. Podrabsky's studies revealed that changes in temperature help trigger the embryos to enter "diapause," or dormancy. Rainy seasons, when the ponds fill and killifish thrive, are warm. But when Podrabsky cooled the embryos to 25°C, they stopped developing and entered diapause. At that point, he reported, the fish's heart stopped in a matter of hours, mitochondria—the cell's power plants—reduced their production of the energy molecule ATP, and metabolism shut down.

Over the past several years, Podrabsky and his students have searched for the genetic basis of this shutdown by sequencing the killifish genome and isolating RNAs it produces. Graduate student Amie Romney, for example, has followed both the protein-coding RNA packaged by the mother in her eggs and small pieces of RNA produced by the embryo. The two types of RNA appear to tussle for control over diapause, she reported. The maternal RNA carries the instructions for initiating diapause, but high temperatures—meaning wet conditions—seem to stimulate the embryo's production of small noncoding RNAs that may counter those instructions. One such small RNA, mir430, is known to inactivate maternal RNA in the embryos of another fish, the zebrafish. In killifish embryos that skip diapause, mir430 increases in abundance and stays plentiful, Romney reported.

Many other RNAs seem to help the fish deal with low or no oxygen, graduate student Claire Riggs found. She reported that some RNAs isolated from killifish embryos resemble small RNAs seen in mammal cells temporarily deprived of oxygen, and many are concentrated in the brain, an organ especially sensitive to hypoxia. Even so, Dowd says researchers can map "only 10% [of RNAs] … to a genomic sequence that we know something about."

Riggs and others are also comparing the killifish's adaptations with those of other anoxia-tolerant champions. Unlike killifish, anoxic turtles continue making ATP, Warren has found; the turtles rely on an anaerobic pathway, like a human sprinter outrunning her oxygen supply. That causes extreme lactic acid buildup, which the turtles buffer with carbonate taken from their shell and other bones. They also slow down their heart. The crucian carp, in contrast, keeps its heart beating strongly, even after 5 days without oxygen, Göran Nilsson, a physiologist at the University of Oslo, has found. The carp also generates energy anaerobically, but it produces alcohol instead of lactic acid. And it continues to glean oxygen from its environment by increasing the surface area of its gills sevenfold.

The three anoxia champions do have some common strategies. Over the past few decades, Nilsson has shown that levels of GABA, a chemical that inhibits nerve activity in humans, increases in the brains of carp and painted turtles during anoxia, perhaps slowing brain energy consumption. Podrabsky also found that GABA increases in his killifish—to concentrations "far beyond any vertebrate that's been looked at," he says. Killifish embryos die if they can't build up GABA when they are deprived of oxygen.

Now Riggs, with the help of other anoxia researchers, is examining small RNAs from all three species, to see whether they share the same rapid cellular switches that seem to shut down metabolism. If so, Dowd says, "that would be a remarkable example of convergent evolution"—and a hint that similar switches could protect other organisms from hypoxia, perhaps even us. ■

Downloaded from on January 31, 2016

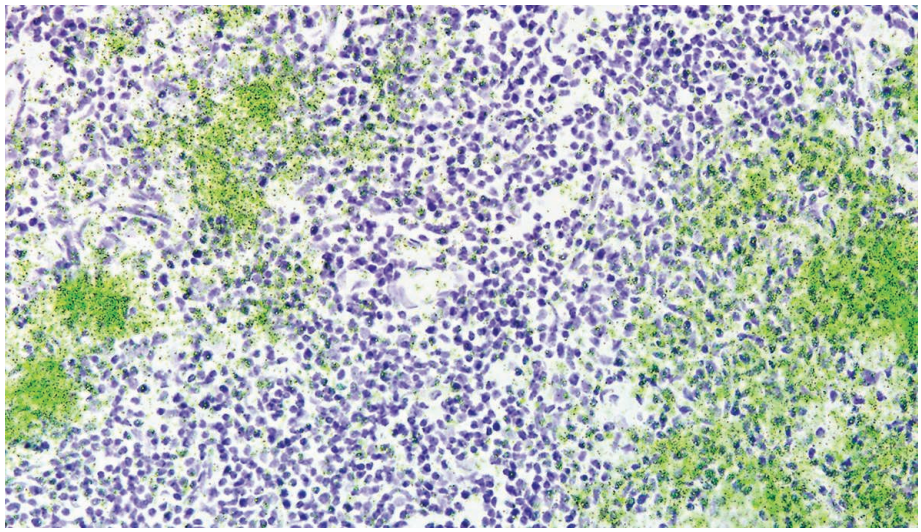
Published by AAAS

INFECTIOUS DISEASE

Researchers claim to find HIV sanctuaries

The most powerful antiretrovirals may not reach virus lurking in some tissues

By **Jon Cohen**



Antiretroviral drugs reduced HIV levels in this man's blood to minuscule levels, but his lymph node cells (purple) still produced detectable viral RNA (green).

PHOTO: STEPHEN WIETGREFE, UNIVERSITY OF MINNESOTA

For all the progress made in HIV treatment, a depressing fact stands in the way of a cure. Even after powerful antiretroviral drugs (ARVs) have driven the virus down to undetectable levels in the blood, it isn't gone. It lurks in "reservoirs," out of reach of treatment, and if drugs are stopped it almost always rebounds. But exactly how these reservoirs stick around for a person's entire life is contentious.

A new study supports a controversial proposal about why HIV persists in spite of aggressive treatment. The standard view is that the virus lies dormant inside of human chromosomes, out of reach of treatment because it is not replicating. The new study, published online in the 27 January issue of *Nature* by a prominent group of HIV/AIDS researchers, suggests instead that despite the barrage of drugs, HIV continues to replicate, sheltered in the lymph nodes, which ARVs have trouble reaching.

"The debate is over: There is ongoing replication" in people on ARVs who have no detectable virus in their blood, contends the *Nature* study's lead author, virologist Steven Wolinsky of Northwestern University Feinberg School of Medicine in Chicago, Illinois. If he's right, the current best hope of curing HIV infection—"kicking" latently infected cells to produce virus, which would lead to their destruction—will need rethinking. Instead, a cure might also have to up the dose of existing ARVs or develop others that better target tissues like the lymph nodes.

The debate is actually far from over. Daria Hazuda, who heads antiviral research at Merck in West Point, Pennsylvania, calls the new data "intriguing and compelling" and says the study is "very consistent with other pieces of data that have been percolating for a decade." But other HIV experts say the data don't support the study's bold conclusions. "It's quite upsetting," says virologist John Mellors of the University of Pittsburgh in Pennsylvania. "The authors should be much more cautious." The study "just doesn't agree with results that we have," says John Coffin, a retrovirologist at Tufts University in Boston.

More than 4 years ago, two of the *Nature* paper's co-authors reported that concentration of ARVs in lymph nodes and other tissues may be far lower than in blood—not high enough to stop all viral replication (*Science*, 23 December 2011, p. 1614). To test that possibility, the team analyzed HIV genetic sequences in difficult-to-obtain samples of lymph nodes taken over 6 months in three patients. All had started ARVs and fully suppressed the virus on standard blood tests. HIV mutates each time it copies itself, so if the virus were replicating in the lymph nodes, the sequences should show signs of evolution. The researchers found just that: sequence changes showing that HIV had evolved in the lymph node of each patient. A slow trickle of new virus was apparently being produced.

Coffin counters that he and others have seen no signs of evolution in several studies that examined virus found in the blood of patients who take powerful ARVs for longer than a decade. He and Mellors fault the machine Wolinsky and his colleagues relied on—a Roche 454 DNA Sequencer—which is no longer used by most labs. "The reason it's obsolete is it had unacceptably high error rates," Mellors says.

"He's categorically wrong," Wolinsky counters. "As long as you know the errors introduced by the technique, you can control for it." He points out the group analyzed each sample twice and obtained the same results. What's more, Wolinsky says the viral family trees created from sequences in each person match the mutation rates that would be expected if new viruses were made. "I think the data are real," says Douglas Richman, a virologist at the University of California, San Diego, who has long been in Coffin and Mellors's camp. Richman adds that the study's authors are "the best in the world" at analyzing HIV in tissues and viral evolution.

Wolinsky and his co-authors enlisted leading viral evolutionary biologist and modeler Andrew Rambaut from the United Kingdom's University of Oxford to address another argument made by those who contend ARVs stop all new virus production: If replication is occurring because of insufficient concentrations of the drugs in the tissues, then drug-resistant mutants should emerge. Rambaut's model suggests that when ARV concentrations are low, wild-type virus isn't hampered much and handily "outcompetes" resistant variants.

"You can use a model to support anything you want, but you can prove nothing," Mellors says. "You can model that the sun orbits the Earth."

Sharon Lewin, an HIV cure researcher at the University of Melbourne in Australia, isn't totally convinced, either. She says she'd like to see data from more than three people and also from those suppressed for longer than 6 months. But she adds that "the work raises lots of new questions and avenues for research."

Wolinsky and co-authors agree. They hope their study will spark clinical experiments that attempt to increase ARV concentration in lymph nodes and then assess the impact on HIV reservoirs. "It's a spectacular debate," Wolinsky says. "And if indeed we have ongoing replication in these drug sanctuaries, we now have a new path to a cure." ■

Downloaded from on January 31, 2016

Published by AAAS

ARCHAEOLOGY

Ancient Babylonians took first steps to calculus

Math whizzes left precocious geometric calculations on clay tablets by 50 B.C.E.

By **Ron Cowen**

Tracking and recording the motion of the sun, the moon, and the planets as they paraded across the desert sky, ancient Babylonian astronomers used simple arithmetic to predict the positions of celestial bodies. Now, new evidence reported on p. 482 reveals that these astronomers, working several centuries B.C.E., also employed sophisticated geometric methods that foreshadow the development of calculus. Historians had thought such techniques did not emerge until more than 1400 years later, in 14th century Europe.

The study "is an extremely important contribution to the history of Babylonian astronomy, and more generally to the history of science," says astronomy historian John Steele of Brown University, who was not part of the work.

Astroarchaeologist Mathieu Ossendrijver of Humboldt University in Berlin bases his findings on a reexamination of clay tablets, one of them unknown until recently, dating from 350 B.C.E. to 50 B.C.E. One week each year for the past 14 years, Ossendrijver has made a pilgrimage to the British Museum's vast collection of tablets inscribed in the Babylonian cuneiform script. He was trying to solve a puzzle posed by two tablets dealing with astronomical calculations: They also contained instructions for constructing a trapezoidal figure that seemed unrelated to anything astronomical.

Between 2002 and 2008, Ossendrijver, an astrophysicist turned historian, studied two other tablets that also prescribed the drawing of a trapezoid, and in these he thought he could make out a reference to Jupiter. The giant planet was a favorite among the Babylonians, who equated the orb with their main god, Marduk, patron deity of the city of Babylon. But the Jupiter link was tentative.

Then, late in 2014, retired Assyriologist Hermann Hunger of the University of Vienna visited Ossendrijver, bringing photos taken decades ago of an uncatalogued Babylonian tablet from the British Museum that described some kind of astronomical computation. Alone in his office a few months later, Ossendrijver perused the photos. The images were blurry and the inscriptions slanted, making them hard to read, but he realized the numbers were identical to those in the trapezoid inscriptions he had been scrutinizing. By comparing the photos with fragments of other Babylonian texts, he discovered that the computations described the motion of Jupiter.

Examining all of the tablets at the British Museum, Ossendrijver figured out that the trapezoid calculations were a tool for calculating Jupiter's displacement each day along the ecliptic, the path that the sun appears to trace through the stars. The computations recorded on the tablets covered a period of 60 days, beginning on a day when the giant planet first appeared in the night sky just before dawn.



Marduk, the patron god of Babylon, was equated with Jupiter, so ancient astronomers charted the planet's path across the heavens with care.

During that interval, Jupiter's motion across the sky appears to slow. (Such erratic apparent motion stems from the complex combination of Earth's own orbit around the sun with that of Jupiter.) A graph of Jupiter's apparent velocity against time slopes downward, so that the area under the curve forms a trapezoid. The area of the trapezoid in turn gives the distance that Jupiter has moved along the ecliptic during the 60 days. Calculating the area under a curve to determine a numerical value is a basic operation, known as the integral between two points, in calculus. Discovering that the Babylonians understood this "was the real 'aha!' moment," Ossendrijver says.

Although elated, Ossendrijver wasn't ready to publish, because a second part of the trapezoid prescription remained unclear. By delving into older, purely mathematical Babylonian texts written between 1800 B.C.E. and 1600 B.C.E., which also described computations with a trapezoid, he realized that the astronomers who made the tablets had gone a step further. To compute the time at which Jupiter would have moved halfway along its ecliptic path, the astronomers divided the 60-day trapezoid into two smaller ones of equal area. The vertical line dividing the two trapezoids marked the halfway time; because of the different shapes of the trapezoids, it indicated not 30 days but slightly fewer.

The Babylonians had developed "abstract mathematical, geometrical ideas about the connection between motion, position and time that are so common to any modern physicist or mathematician," Ossendrijver says.

Indeed, compared with the complex geometry embraced by the ancient Greeks a few centuries later, with its cycles and epicycles, the inscriptions reflect "a more abstract and profound conception of a geometrical object in which one dimension represents time," says historian Alexander Jones of New York University in New York City. "Such concepts have not been found earlier than in 14th century European texts on moving bodies," he adds. "Their presence … testifies to the revolutionary brilliance of the unknown Mesopotamian scholars who constructed Babylonian mathematical astronomy."

After cuneiform died out around 100 C.E., Babylonian astronomy was thought to have been virtually forgotten, he notes. It was left to French and English philosophers and mathematicians in the late Middle Ages to reinvent what the Babylonians had developed.

The new discovery may hint that Babylonian geometry did not die out completely after all. Either way, Jones says, learning how the Babylonians astronomers acquired their geometric acumen "would tell us something about why human beings do science in the first place, and from time to time do it very well indeed." ■

Ron Cowen is a freelance writer in Silver Spring, Maryland.

PHOTO: © AS400 DB/CORBIS

Downloaded from on January 31, 2016

Published by AAAS



The Guliya ice cap in northwest Tibet, China, may hold the best record of midlatitude climate during the last ice age.

Downloaded from on January 31, 2016

TIBET'S PRIMEVAL ICE

The quest for the world's oldest ice could yield a Rosetta Stone for how Asia responds to a changing climate

By **Jane Qiu**, *on Guliya ice cap, China*

The team is running out of time. Bureaucratic hassles, the challenge of lugging 7 tons of equipment onto an ice cap that crests 6700 meters above sea level, and, now, in the waning days of September 2015, fierce winds have delayed drilling by weeks. High on the western edge of the Tibetan Plateau, the hunt for what may be the oldest ice on the planet has become a race against the elements.

But with winter fast approaching, the drilling in the western Kunlun Mountains has at last begun. On 26 September 2015, Stanislav Kutuzov, a glaciologist with the Institute of Geography of the Russian Academy of Sciences in Moscow, pulls a canister out of the barrel of the 1.5-meter-long corer. Wind-blown ice crystals sting his face as he dashes into a nearby tent, huffing in the thin air. He slides an 11-centimeter-thick ice cylinder out of the canister and onto a metal stand. Expedition leaders Yao Tandong, director of the Institute of Tibetan Plateau Research (ITP) at the Chinese Academy of Sciences in Beijing, and Lonnie Thompson of Ohio State University, Columbus, coo over the sample as if it were a newborn. In faint layers of dust and gas bubbles and subtle variations in chemicals within the ice, the glistening cylinder holds part of a record of ancient climate on the Tibetan Plateau that could stretch back nearly a million years.

This is not their first delivery at the Guliya ice cap. In the early 1990s, Yao and Thompson made an astounding find here: ice surviving from before the last ice age. Until then, the only ice so ancient had come from Antarctica or Greenland. But the ice cap, a white cape draped over 200 square kilometers of the remote Kunlun range that in spots is hundreds of meters thick, offered a record extending 130,000 years into the past. The deepest ice—too old to be reliably dated at that time—seemed to be at least half-a-million years older, potentially older than any other on the planet.

Since then, Guliya's allure has only grown. Ice cores collected from every other site on the Tibetan Plateau over the past 2 decades date back no earlier than the Holocene: the epoch since the end of the last ice age that spans the last 11,000 years or so. About 8000 years ago in the early Holocene, when temperatures were even warmer than today, the plateau seems to have been largely ice-free. Guliya likely retained its white pate during the Holocene warm-up because the Westerlies—the same winds that keep Siberia, Russia, an icebox—blow through the Kunlun Mountains. Other areas in Tibet are dominated by a different weather system, the Indian monsoon.

That accident of preservation may make Guliya—which lies at the same latitude as Durham, North Carolina, and Memphis, Tennessee—the best record of midlatitude climate during the last ice age. It also may hold insights into past and future conditions on the Tibetan Plateau. The Guliya ice, Thompson says, "may well turn out to be the Rosetta Stone we've been looking for to understand"

PHOTO: JANE QIU

Published by AAAS

how Asia responds to a changing climate.

The stakes are enormous. Also known as the Third Pole, the Tibetan Plateau contains the largest stock of ice outside the Arctic and the Antarctic: all told, some 46,000 glaciers. The lofty plateau is the engine that drives the Indian monsoon and gives rise to major rivers like the Indus, the Mekong, and the Brahmaputra that are the lifeblood of more than 1.4 billion people. "Yet we know less about the Third Pole region than any other place on Earth," Thompson says. A supreme challenge of climatology is integrating the plateau's profound effects on Asia into global models. "Figuring out the role of this massive place and how it's linked to the global picture is critical to understanding our climate system," says Kenichi Ueno, a climate scientist at University of Tsukuba in Japan.

China has made the Third Pole a top science priority. In 2012, the government set aside $47 million over 5 years for a Tibetan Plateau research program led by Yao. That support plus Thompson's backing from the U.S. National Science Foundation's Paleoclimate Program gave the duo a chance for one more audacious push into Guliya's deep past. Last fall, the two battle-scarred veterans of glaciology led a 60-person team that retrieved five cores from the ice cap. In December 2015, at the American Geophysical Union meeting in San Francisco, California, Thompson unveiled preliminary results. At Guliya's summit, the ice is thin; the layers near bedrock from three cores there are 8000 years old and laced with a "tremendous" amount of dust, Thompson says. But 10 kilometers away, the team extracted a core 310 meters long. New dating techniques not available in the early 1990s will soon reveal whether the lowest layer is the oldest ice ever retrieved on Earth.

If so, says Ted Scambos, a glaciologist at the U.S. National Snow and Ice Data Center in Boulder, Colorado, the ice could transport climatologists back to another world. It "would be hugely significant," he says. "That would tell us what climate was really like before there were major ice ages, when the [carbon dioxide] level in the atmosphere was high and the ice cover not nearly as extensive."

WITH AN AREA of 5 million square kilometers—half the size of the United States—and an average elevation of 4000 meters above sea level, the "roof of the world" is geographically unique. Sunlight beating down through the thin air turns the Tibetan Plateau into a gigantic hot plate, which causes the air above it to rise, powering the Indian monsoon. Air rushes in from across India, drawing water vapor from the tropics and bringing precipitation to the eastern Himalayas and southern and eastern Tibet. On the plateau's western edge, precipitation is swept in by the westerlies, the prevailing midlatitude winds driven by Earth's rotation.

Precession—the slow wobbling of Earth's rotational axis—alters the monsoon over thousands of years. Over each 21,000-year wobble, the Tibetan Plateau's position relative to the sun shifts, varying how far north moisture-laden air penetrates the plateau. From 45,000 to 30,000 years ago, the monsoonal rains reached all the way to Siberia. "There was a lot of water moving into the midlatitudes," Thompson says. That turned the plateau into grassland dotted with lakes. Other climate cycles lasting even longer—41,000 years and 100,000 years—also shape the monsoon and other features of midlatitude climate. Such midlatitude perturbations don't show up in ice cores from the poles. To study them, glaciologists have looked to Tibet.

Thompson and Yao began their glacial partnership in 1984, when they met on a 3-month expedition to scope out drilling sites in China's Tian Shan Mountains. Although China and the United States had recently restored diplomatic relations, "there was still a lot of suspicion on both sides," says Yao, then a Ph.D. student. But the two bonded while talking shop during long hikes.

Yao had never intended to study ice. In 1974, after working on a farm during the Cultural Revolution, he won a place at the prestigious Peking University in Beijing studying physics. But the authorities sent him instead to study glaciology at Lanzhou University in western China. Bitter at first, Yao became mesmerized by the beauty of ice and the notion that glaciers are a time capsule for lost worlds. When he visited a glacier for the first time in the Qilan Mountains in 1975, he says, "it was love at first sight."

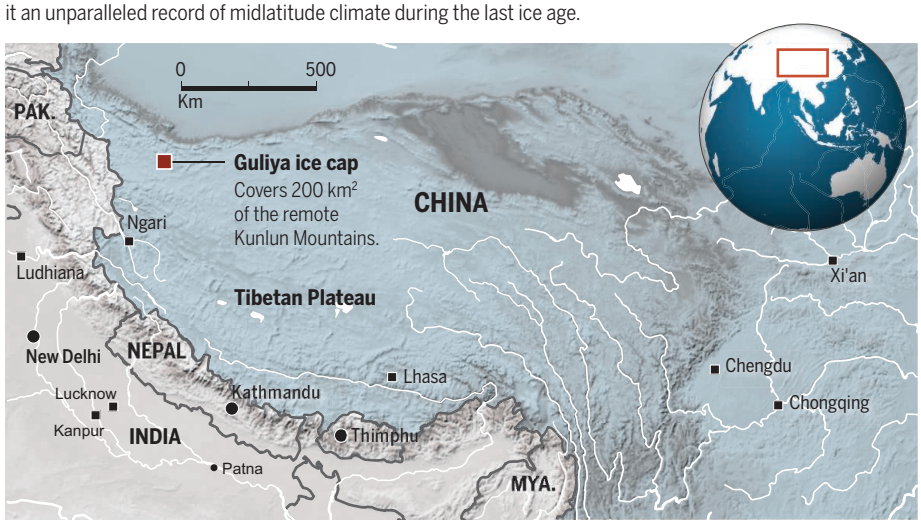
Yao's first trip to Guliya nearly cost him his life. Scoping out the ice cap for drilling sites in 1991, he was driving a snowmobile across the ice field on a foggy day when he suddenly had a strange feeling. He stopped the snowmobile and jumped off: "Just in time," he says. A massive patch of ice collapsed into a crevasse right in front of him. Caught in a crevasse field, Yao had to gingerly pick his way back to camp. Undaunted, he went on to lead 18 expeditions in Tibet and insists he's happiest and feels most at home on the lofty plateau, when he's "at the mercy of nature."

The year after his near-death experience, Yao returned to Guliya with Thompson and a drilling team. "It's a wild part of the world now, but it was much wilder back then," Thompson says. It took nearly a week driving on a dirt road across Tibet to reach the ice field. The team's modest goal, he says, was "to see if we could get a frozen ice core from that part of the world."

They were richly rewarded for the effort: The team recovered a 308-meter core, all the way to bedrock, at 6200 meters above sea level. They reliably dated the top 266 meters of the core to a period spanning 130,000 years, correlating fluctuations in oxygen-18, methane, and other chemicals to well-dated events in cores from Greenland and Vostok, a Russian site in Antarctica. Other features of the record were unique. It showed, for example, that from about 34,000 to 23,000 years ago, average temperatures in Tibet whip-

The Third Pole's icebox

Located on the western edge of the Tibetan Plateau in China, the Guliya ice cap's oldest ice may date from several hundred thousand years ago—far older than any other glacier sampled in the region. That would make it an unparalleled record of midlatitude climate during the last ice age.



GRAPHIC: A. CUADRA/*SCIENCE*

Published by AAAS



Yao Tandong and Lonnie Thompson, éminences grises of glaciology, log a section of Guliya's core. At left, dust speckles the bottom of a core from the glacier's summit.

sawed up or down by several degrees Celsius in roughly 200-year cycles, likely corresponding to a 205-year cycle of solar activity. Why ice-age temperatures responded so strongly to the solar cycle is still a mystery, Thompson says. The core also recorded warm periods corresponding to 21,000-year methane cycles driven by tropical wetlands, which have been observed in polar ice cores.

The final 40 meters or so of the core were old beyond reckoning. "The bottom ice was chlorine-36 dead," Thompson says. The radioactive isotope—at the time, one of the few markers for the age of ice older than 100,000 years—has a half-life of 300,000 years. The dearth of chlorine-36 meant that the ice "had to be over 750,000 years old," Thompson says. That's within range of the oldest ice sample ever, the 800,000-year-old bottom layer of an Antarctic core from Dome Concordia. (Antarctica's ice sheets formed millions of years ago, but pressure and geothermal heat melt away the oldest layers, near the bedrock.)

Over the last quarter-century, new dating techniques using argon isotopes have made it feasible to accurately date ice that's a million years old, or older. That capability got Yao and Thompson contemplating another assault on Guliya.

THESE DAYS A MODERN HIGHWAY connects western Tibet and the capital, Lhasa. But getting into Tibet is a sterner challenge than ever. Ethnic Tibetan protests against Chinese rule in recent years have drawn periodic crackdowns that restrict research and largely bar foreign researchers from the restive region. Yao is lobbying to make Tibet "a special scientific zone" for international collaboration. So far, that's been a non-starter. The western Kunlun are normally off limits even to Chinese tourists. But as a measure of ITP's sway with the authorities, Thompson and nine other researchers from three other countries were permitted to take part in last year's Guliya expedition.

For Thompson, the challenge was also personal: He had a heart transplant in 2012. The highest altitude a heart transplant recipient had ever reached was 6100 meters, "and that was a much younger guy." At Guliya's 6700-meter summit, he says, "the heart worked fine. My 67-year-old body was a different story."

Mounting the ice cap was a supreme challenge. Three mountaineers operated a pulley system that laboriously hoisted the drill rig, equipment such as snowmobiles, and supplies onto the ice sheet. The first core the team drilled was a bust: At 72 meters' depth, they hit a crevasse. They moved the drill rig a few hundred meters and on their second try reached bedrock, 310 meters down. At the summit, they drilled three more cores, each of which hit bedrock at about 50 meters. To keep the cores cold and shield them from the elements—especially the sun's melting rays—the team stored them in covered trenches they built near the drilling sites. Tibetan porters then carried sections of core to the base camp for storage in freezers. The freezers were trucked to ITP's branch in Lhasa, where the cores were cut in half for analyses in Beijing and in Columbus.

Back in the labs, the team will analyze oxygen isotopes preserved in the ice as a proxy for temperatures and monsoon rainfall in Tibet over many millennia. They will also measure ammonia and nitrate and probe for remnants of pollen and bacteria to reconstruct ancient ecosystems. "Ice is a wonderful recorder of anything that falls into it," Thompson says. And they will date the ice to see just how far back their record really goes.

They will also address a more recent puzzle, one that has cropped up consistently across the plateau: What happened to other glaciers at the beginning of the Holocene? At the time, "there was a lot more energy coming in" to the plateau, Thompson says. His theory is that windy, warm, and dry conditions led to sublimation on an epic scale: Most of Tibet's glaciers simply evaporated away. A clue may lie in the dust trapped in the bottom layers of the summit cores, which appear to have formed soon after the sublimation event. "We need to explain all this dust," Thompson says.

The ancient glaciers' disappearance raises an unsettling question: How quickly might glaciers vanish a second time as the climate of Tibet warms past its Holocene maximum? Yao and Thompson have already gleaned from the new cores that since 1992, Guliya's ice has become more enriched in oxygen's heaviest isotope (oxygen-18), indicating rapid warming. That's consistent with observations that the Tibetan Plateau is warming faster than the lowlands, and that the warming at higher elevations is more pronounced. It would also explain why the majority of glaciers in the Tibetan Plateau and the Himalayas—the water tower of Asia—are receding.

As midlatitude glaciers disappear, they will take with them a vital water source—and insights into past climates that could help us forecast the future. "A century from now, it will be the histories that we were able to capture at the turn of the 21st century that will be remembered," Thompson says. Guliya may turn out to be the most fascinating paleo history of them all. ■

PHOTOS: (LEFT TO RIGHT) LONNIE G. THOMPSON; JANE QIU

Published by AAAS



Downloaded from on January 31, 2016

A CANCER LEGACY

Once viewed as tragic anomalies, many childhood cancers may have their roots in inherited mutations

By **Jennifer Couzin-Frankel** *Photography by* **Jeff Haller** *and* **Meggan Haller**

Two cancers in a young family: It was either horribly bad luck or the tip-off to a deeper connection. The story unfolded when Michael Walsh, a young pediatric oncologist, was caring for a boy undergoing a bone marrow transplant at St. Jude Children's Research Hospital in Memphis, Tennessee. The child wasn't responding as expected to standard therapies, suggesting something curious about the rare form of leukemia from which he suffered. Suspicious, Walsh inquired about the family's health history—and was startled to learn that the boy's father had died of brain cancer a couple years earlier, at age 31.

Walsh took a skin biopsy from the child and reached out to MD Anderson Cancer Center in Houston, Texas, where the father had been hospitalized. There he tracked down a stored sample of noncancerous tissue from the man's brain. Sequencing DNA in father and son's normal cells revealed a defective gene, *P53*, passed from one to the other. Crucial for DNA repair, *P53* is a familiar villain in cancer. Mutations in it cause Li-Fraumeni syndrome,

Published by AAAS

After 8-year-old Claudia was diagnosed with a soft tissue cancer, her mother Amanda Seymour learned that the disease and a family history of thyroid problems were tied to a gene mutation.

which predisposes people to many pediatric and adult cancers. The boy's form of leukemia, however, was not on that list. "Was this driving the cancer the boy had?" Walsh, now at Memorial Sloan Kettering Cancer Center in New York City, remembers wondering. "It certainly smelled like it … [but] we didn't really know what to think."

Hospitals increasingly experiment with broad DNA sequencing of tumor cells, a fishing expedition of sorts to try to pinpoint a cancer's genetic flaws and guide treatment. Until recently, however, they rarely did the same for DNA in other tissues, such as the boy's skin cells, which might reveal cancer-causing mutations that the patient was born with. There were a few reasons: Those mutations are exceedingly rare, the thinking went, and it would be easy to identify patients whom sequencing might help based on their form of cancer.

Those suppositions are slowly being called into question—at least when it comes to children. In the last several years more than 2000 youngsters with cancer, from infants to young adults, have had the DNA in their noncancerous cells run through sequencing machines. The readouts are casting tantalizing clues across the pediatric cancer world, and changing how doctors think of the disease.

Unlike an adult, who may have spent decades accumulating genetic abnormalities and suffering the effects of poor diet, smoking, and other environmental factors, a 3-year-old with cancer presents a conundrum. "Up until 5 or 6 years ago, many, many people thought [such cancers] were just mistakes of nature," says John Maris, a pediatric oncologist at The Children's Hospital of Philadelphia (CHOP) in Pennsylvania. Yet others, including Maris, had long suspected that inherited mutations might play a considerable role. Changes in a handful of genes, such as *P53* and *RB*, which is linked to the eye cancer retinoblastoma, have long been considered culprits in rare childhood cancers. But for most affected kids, "we just didn't know" which genes might be at work, says Will Parsons, who treats brain tumors at Texas Children's Hospital in Houston.

A deeper dive into the DNA of young cancer patients is now turning up evidence that a sizable subset of childhood cancers might be rooted in inherited genes, or mutations so soon after conception that they pervade every cell—rather than in freak genetic events that accumulate after birth and turn cells malignant. And the suspect genes are not necessarily the expected ones. A gene mutation that predisposes men to prostate cancer has shown up in a child with a kidney tumor; defective genes previously associated with breast cancer are appearing in children with the nerve tissue cancer neuroblastoma. These cases and many others suggest that the silos into which cancer genes have been neatly organized may not be so clear-cut.

"We've been taught as pediatric oncologists never to test these genes in children because they only predispose" to adult cancers, something that's potentially wrong, says Kim Nichols, a pediatric oncologist who was recruited from CHOP to St. Jude a year ago to lead the hospital's new cancer predisposition clinic. The findings engender hope that some cancers, either in children who survive their first bout with the disease or in their siblings and parents, could be prevented or caught early. But they also raise complicated questions: about what to communicate to families in the midst of a health crisis, whether to screen other family members for certain mutations, and what to do if those relatives share them.



Recuperating at home after cancer treatment, Claudia works on some homework while surrounded by craft supplies. She will turn 9 next month, and her younger brothers are being tested for the gene mutation she shares with her mother.

ADVANCES IN PEDIATRIC SURVIVAL are justly hailed as a shining success in the wider "War on Cancer," but most of the gains involve the commonest form of childhood leukemia and solid tumors that haven't spread. Across many pediatric cancers, survival rates have plateaued. "We really need to use new technology and new biological insight to improve the cure rate," says Rajen Mody, a pediatric oncologist at the University of Michigan (UM) and C.S. Mott Children's Hospital in Ann Arbor, who often works with families whose children are out of options. Like many shifts in medicine, Mody says, the desire to sequence normal tissue was born "out of frustration, or necessity."

There was reason to hope this DNA might hold some answers. Anecdotally, doctors often see cancer's tentacles stretching through families with affected children. "You recognize it," says David Malkin of The Hospital for Sick Children in Toronto, Canada. Malkin guesses that about 40% of children in the hospital's cancer clinic have a family history suggesting a faulty, inherited gene. A study done in the cancer survivor clinic at Cincinnati Children's Hospital Medical Center in Ohio supports that estimate. Detailed family histories of 370 youngsters suggested that 29% of them might have cancers with an inherited genetic component. "And I think that's a gross underestimate," says pediatric oncologist Joshua Schiffman, who himself survived Hodgkin's lymphoma as a teenager and now works at the University of Utah in

Published by AAAS

Salt Lake City. Many children who inherited the most aggressive gene mutations, he says, likely died and went uncounted in this sample of survivors.

Mody was among the first to embark on a serious hunt for inborn mutations. In 2011 he met Arul Chinnaiyan, a UM pathologist who was exploring a new approach to sequencing in adult cancer patients. Sequencing the tumor—itself a relatively new strategy, though an increasingly popular one—can't always unveil which mutations the patient was born with, because cancer transforms a genome into something unrecognizable, overflowing with abnormal DNA. Instead, Chinnaiyan combined sequencing tumor DNA with reading the DNA of normal cells in men with prostate cancer, to see whether he could learn more about their disease. Mody wanted to do the same for his young patients. "This would be the time," he told Chinnaiyan. "Let's try this."

They recruited 102 youngsters, most of them fitting the profile Mody typically sees: children and teenagers whose cancer has spread and whose disease isn't responding to standard therapy. On average they were ten-and-a-half years old. At a cost of about $5000 per patient, the team sequenced and analyzed the "exome," the DNA that produces proteins, in both tumors and healthy cells.

Ten percent of the young participants had been born with a mutation in a cancer gene—but sometimes one linked to cancers very different from the child's disease, Mody, Chinnaiyan, and their colleagues reported in the *Journal of the American Medical Association* (*JAMA*) in September 2015. A 4-year-old with neuroblastoma had healthy cells harboring a mutated version of *BARD1*, a gene associated with breast cancer; a child with an abdominal mass had an abnormal version of *MITF*, which predisposes to melanoma and renal cancer in adults. Despite significant uncertainty about whether these faulty genes were driving the children's cancers, families were referred for genetic counseling and additional testing, if they chose.

A similar crisscrossing of cancer genes is showing up in older patients. In November 2015, a group from Sloan Kettering reported in *JAMA Oncology* that 12% to 15% of 1566 adult patients with advanced cancer had cancer gene mutations in healthy cells. Patients with stomach cancer, a neuroendocrine tumor, and a sarcoma had mutated versions of the breast cancer genes *BRCA1* or *BRCA2*. An individual with colon cancer had a pervasive *RET* mutation, which is normally found in those predisposed to thyroid tumors. "There were adults with cancer with mutations in genes that would never have been reported and tested" under normal circumstances, Nichols says.

What these unexpected mutations actually mean can be unclear. They could be flukes, entirely unrelated to the cancer at hand. And then there are the children whose normal cells have variants of unknown significance in known cancer genes, which may or may not have anything to do with their disease. "What are we going to say to patients about this?" says Stephen Chanock, a pediatric oncologist at the National Cancer Institute (NCI) in Bethesda, Maryland, who is sequencing 6000 exomes from childhood cancer survivors. One way to learn more is by heading back to the lab and testing, in a petri dish or a mouse, whether a particular mutation makes cells more vulnerable to the patient's particular cancer.

> ***"We've been taught as pediatric oncologists never to test these genes in children because they only predispose" to adult cancers.***
>
> **Kim Nichols**, St. Jude Children's Research Hospital

Another is to accumulate more examples in patients. Because pediatric cancer is relatively rare, that can be difficult—but it also means that just a few cases can signal a link. At CHOP, Maris has found mutated versions of *BARD1* in several children with neuroblastoma, two of whom he reported in a recent paper. Neuroblastoma is diagnosed in only about 700 children in the United States each year. "You see this [mutation] in four, five, six neuroblastoma patients," Maris says. Especially when it doesn't turn up in children without cancer, it's hard to deny a connection. "Yeah, I'm pretty convinced."

FOR FAMILIES, the knowledge that an inherited mutation could have contributed to a child's cancer can be unnerving. "Initially I was like, this is stress I don't need, there's a feeling of guilt, you start thinking 'I gave this to my child,'" says Amanda Seymour, an attorney in Biloxi, Mississippi. Last spring, while she was trying to wrap her mind around her 8-year-old daughter Claudia's diagnosis of rhabdomyosarcoma, a soft tissue cancer, Seymour found herself sitting opposite a genetic counselor at St. Jude. Her own family had a history of thyroid problems stretching back generations—a pattern so striking that they were the subject of a scientific paper in the 1980s. Seymour herself had had benign thyroid growths removed, as had two other siblings, and her older sister, now 44, was diagnosed with thyroid cancer at age 3. When combined with a cousin's rare kidney disorder in early childhood, this left the genetic counselor certain of what should happen next: Claudia needed to be tested for mutations in *DICER1*, which can predispose to specific types of benign and malignant tumors. Claudia's test came back positive, and so, not surprisingly, did Seymour's.

Yet a seemingly inherited mutation in a child with cancer isn't always accompanied by an arresting family history. In November 2015, St. Jude reported on a cohort of more than 1100 children whose tumor and noncancerous cell DNA were sequenced. In DNA from their normal cells, 8.5% of children had potentially harmful mutations in cancer genes. Yet among those children, only 40% of those for whom a family history was available had relatives with cancer. How was that possible?

One explanation is that the mutation might be new, having popped up spontaneously when the child was conceived. Schiffman suggests another: Doctors "do a lousy, lousy job of collecting family history" and may be deaf to alarm bells in an extended family. A "ringing message" of the new wave of sequencing, Schiffman says, is that every single child with cancer needs a detailed history taken at diagnosis.

But family history is also fluid: Over time, a sunny family history can flip. "This just happened to one of my own patients," says Malkin of Toronto's Hospital for Sick Children. He treated a teenager with adrenal carcinoma, a disease often caused in children by inherited mutations. When genetic testing came back clean, doctors concluded this youngster was an exception. Then, 4 years later, the boy's mother developed breast cancer. "She's young enough that one has to believe there's a connection," Malkin says. DNA diggers were likely looking in the wrong place.

Ultimately, even an impeccable family history doesn't rule out cancer mutations lurking in the genome and later causing disease. Families are far smaller than they used to be, says Sharon Plon, a medical geneticist at Texas Children's, which means that a mutation with, say, a 30% chance of causing cancer might never have a chance to bare its teeth twice in a single family.

ABOUT 3 YEARS AGO, Plon teamed up with Parsons, the brain cancer physician, and they began reaching out to Texas Children's families 2 months after their children were diagnosed with a solid tumor. As part of a research study called BASIC3, each child was offered sequencing of both tumor and

Published by AAAS

nontumor DNA. Then Plon and Parsons went a step further: In addition to studying the patients and families, they enrolled their doctors, probing how the oncologists felt about returning sometimes confusing or difficult genetic results.

The doctors and genetic counselors are sharing not only cancer-predisposing mutations that might or might not have fueled that child's illness. They are also offering up genetic findings unrelated to cancer if treatment or monitoring can help—for example, mutations that cause the life-threatening heart condition long QT syndrome or familial hypercholesterolemia. (They do not return results when there is no way to act on them. No 8-year-old is finding out whether she's at elevated risk of Alzheimer's disease, for example.) Families also learn whether their child has so-called "variants of unknown significance" in cancer genes, as most do.

Parsons was struck by how easy it was to recruit the participants, who now include roughly 250 patients. "Our families will agree to just about anything," he says. That sometimes worries him, as he wants to be sure these parents, already facing a devastating blow, grasp what might come next for the affected son or daughter and the rest of the family. The findings can mean recommending genetic testing on siblings, full-body MRIs for parents, or a lifetime of surveillance of the ailing child, because those who survive one cancer may have a high chance of developing another.

Yet parents whose child has cancer may view genetic information through an altogether different lens than would a healthy—and potentially wary—adult. "Yeah, sure, you're going to have some anxiety, and yeah, sure, you're going to learn some things that you may not really want to know," one parent shared, in a paper the group published in September 2015 on the ethics of whole-exome sequencing in these children. "But I just—I couldn't live with myself if we were in the same situation in 2 years and I had a chance to at least know about it."

In the disorienting time after Claudia's diagnosis of rhabdomyosarcoma, Seymour's emotions mirrored those of the families in the Houston study. With her rising third-grader enduring major surgery and months of chemotherapy, "my counselor would tell you I literally ran from her," she says. Genetic counseling, with any abstract future worries it might highlight, sank to the bottom of her priority list.

But as weeks passed, Seymour's mindset evolved. Claudia completed treatment in November 2015. She continues to recuperate at home, where she is a "craft maniac," making soaps, snow globes, lip balm, and lava lamps thanks to YouTube instructional videos. Seymour, meanwhile, says she decided to "stop thinking of it as, 'There's nothing they can do.'" She is waiting on *DICER1* results for her two younger children, 6- and 1-year-old boys. If one or both test positive, St. Jude would recommend regular screening, including chest x-rays and kidney and thyroid ultrasounds that might catch tumors early.

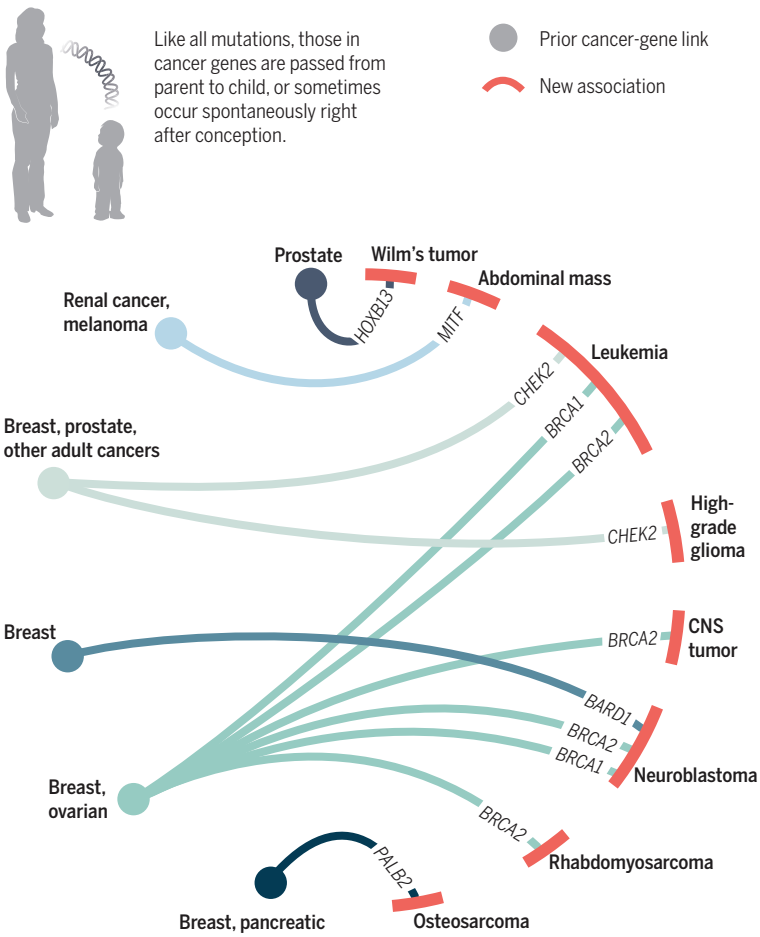
Right now many inherited mutations in pediatric cancer patients are identified because of a suspicious family history like Claudia's, or as part of broader research efforts like Plon's. Plon, for one, isn't quite ready to go beyond that and offer full DNA sequencing of noncancerous tissue to every child with cancer who walks into her hospital, but other centers are moving in that direction to varying degrees. They include St. Jude, UM, The Hospital for Sick Children, and Intermountain Primary Children's Hospital in Salt Lake City, where Schiffman, the lymphoma survivor, works. He had his own genome sequenced as part of a research study; many variants of unknown significance cropped up, but nothing to suggest known cancer predisposition for his three children or himself.

Oncologists hope that at least some new findings about the inborn risks of cancer will eventually lead to better treatments: Already one drug is approved for women with advanced ovarian cancer who carry *BRCA* mutations. To try to speed the science along, an NCI-funded study called Pediatric MATCH plans to start rolling out across more than 190 U.S. centers. It will offer tumor and nontumor DNA sequencing to children with cancer, aiming to identify molecularly guided therapies, and potentially families who might benefit from genetic testing and surveillance.

Right now, however, the new biology can generate electrifying connections and inform a family, but without saving the life that helped spawn that knowledge. The link Walsh discovered between a *P53* mutation and his young patient's leukemia advanced understanding of that disease but didn't help the child. The boy died when he was 11 years old. His two siblings tested negative for mutations in *P53*. ■

Crisscross biology

Genetic sequencing is showing that the normal cells of some kids with cancer harbor gene mutations with known links to different adult cancers. Scientists are trying to understand whether these gene changes could explain the kids' cancers or are largely or entirely unrelated to a child's disease.



GRAPHIC: V. ALTOUNIAN/*SCIENCE*; (DATA) J. ZHANG *ET AL.*, *THE NEW ENGLAND JOURNAL OF MEDICINE* (28 NOVEMEBER 2015), R. J. MODY *ET AL.*, *JOURNAL OF THE AMERICAN MEDICAL ASSOCIATION* **314**, 9 (1 SEPTEMBER 2015), SHARON PLON/BAYLOR COLLEGE OF MEDICINE/TEXAS CHILDREN'S HOSPITAL

Published by AAAS



Downloaded from on January 31, 2016

DISPLACED POPULATIONS

Life on the edge

Stories of hardship and resilience take center stage in a probing portrait of the world's largest refugee camp

By **Michaela Hynie**

Millions of refugees have fled the conflict in Syria since 2010. But the urgency of the situation only captured the full attention of the media, governments, and the public once refugees began entering Europe in large numbers in 2015. Yet, even as our attention finally shifts to refugees fleeing Syria, it shifts further away from the hundreds of thousands who continue to struggle for existence in semipermanent encampments around the world. Our apparent indifference toward the suffering of those displaced by global political actions is a core theme of *City of Thorns*, Ben Rawlence's book about the Dadaab refugee camps in Kenya, the world's largest and oldest refugee settlement.

Established in 1991–1992 in response to the civil war in Somalia, the Dadaab refugee complex was designed to temporarily house 90,000 people. But starvation and violence drove thousands more into the camps. The officially registered population in Dadaab—now five camps—is approximately 350,000 (*1*), although Rawlence notes counts of over 600,000. While new residents continue to arrive, people born in the camps are now having children of their own, producing a third generation of refugees raised by parents who have known no other life and have nowhere else to go.

The central government of Somalia fell in a civil war in 1991. The subsequent years saw intense fighting between clans, followed by a brief respite with the rise of the Islamic Courts Union (ICU), a group of Sharia courts that united for the purpose of restoring order to the country. In 2007, the Ethiopian army overthrew the ICU and installed the Transitional Federal Government, backed by the United Nations, the African Union, and the United States.

Al-Shabaab—the most extreme faction within the ICU—emerged from this conflict. Today, al-Shabaab continues fighting against African Union peacekeeping forces in Somalia, supporting itself with grain and livestock taken as taxes and with young men and boys taken as soldiers. The years following 2007 were marked not only by violence but also by recurrent drought, which made al-Shabaab more desperate in its actions.

Rawlence, a journalist and a former Human Rights Watch researcher, spent 3 years working in Dadaab, building relationships with the residents. In *City of Thorns*, he skillfully describes camp life, as well as the underlying history and politics, through the interwoven stories of individual residents. In doing so, he succeeds in making the uncertainty, poverty, hunger, and powerlessness experienced by the refugees concrete,

The reviewer is affiliated with the Refugee Research Network, York University, Toronto, Ontario M3J 1P3, Canada. E-mail: mhynie@yorku.ca

PHOTO: © PER-ANDERS PETTERSSON/CORBIS

Published by AAAS



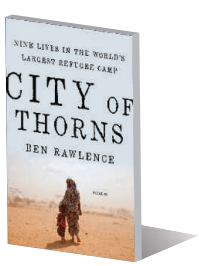


Hundreds of thousands of people now reside in the Dadaab refugee camps, which were founded in 1992 as a temporary encampment for individuals fleeing Somalia's civil war. More arrive each day, displaced by continued violence that has been exacerbated by prolonged drought in the surrounding regions.

PHOTO: © PER-ANDERS PETTERSSON/CORBIS

immediate, and moving. The men's stories are perhaps richer, as would be expected given limits on cross-gender interactions in the camp setting, but Rawlence makes an effort to include the voices of women as well.

Although refugees cannot legally work in Kenya, the camps have a robust informal economy. There is a dense and busy market, with work for a lucky few. Nisho, a young man born en route to Dadaab in 1991, labors as a porter distributing food but sees his income dwindle with the fluctuating price of sugar. Hunger is a constant concern. Some residents—like Professor White Eyes, who came to the camp with his grandmother at the age of 4 or 5—manage to establish successful businesses. Others, like Kheyro, a young woman who arrived at the age of 2, find jobs as "incentive workers" with aid organizations, where they are paid a fraction of the salaries made by their Kenyan co-workers.



City of Thorns
Nine Lives in the World's Largest Refugee Camp
Ben Rawlence
Picador, 2016.
400 pp.

Those adept at navigating the world of nongovernmental organizations find leadership opportunities, especially as responsibility for camp activities shifts to residents with the withdrawal of aid workers. A handful are offered permanent resettlement, with priority to those who are most vulnerable. Muna and Monday, a Somali-Sudanese couple whose mixed-ethnicity marriage enrages Muna's Somali relatives to the point of violence, are among these lucky few.

Over the course of the book, the violence both within and outside the camps escalates. Al-Shabaab's attacks within Dadaab lead to the withdrawal of aid agencies and a devastating loss of medical services. Attacks elsewhere in Kenya lead to arrests and harassment of Somali residents in Nairobi. The Kenyan government declares its intention to close the Dadaab camps because of fears that they are a site of recruitment for al-Shabaab. Food rations within the camp steadily decrease, linked to scandals associated with the World Food Program. Corruption surrounding the trade and transportation of sugar destroys the economy within the camps.

What dominates *City of Thorns* is how little control residents have over their circumstances, how few options are open to them, and how vulnerable they are to the actions of others. Rawlence is scathing in describing corrupt systems that prey on vulnerable people, and the indifference of aid agencies and workers and world leaders who fail to intervene, except to protect their own interests.

In the end, Rawlence succeeds in clearly describing the complex geopolitical factors that created and sustain the Dadaab camps and in bringing our attention back to those whose lives have seemed not to matter.

REFERENCES

1. United Nations High Commissioner for Refugees (UNHCR), Refugees in the Horn of Africa: Somali displacement crisis. Information sharing portal: Kenya: Dadaab (2015); http://data.unhcr.org/horn-of-africa/region.php?id=3&country=110.

10.1126/science.aad8525

Published by AAAS



PHOTO: © WINFRIED WISNIEWSKI/MINDEN PICTURES/CORBIS

Downloaded from on January 31, 2016

EVOLUTION

Avian supergenes

Genetic data reveal how two complex bird mating systems evolved

By **Scott Taylor**[1,2] *and* **Leonardo Campagna**[1,2]

As the extravagant displays of birds of paradise remind us, many birds go to great lengths to pass their genes on to the next generation. Recent papers explore the genetic basis of the reproductive strategies in two bird species: the ruff (*Philomachus pugnax*) (*1*, *2*) and the white-throated sparrow (*Zonotrichia albicollis*) (*3*). In each species, striking variation in both plumage and behavior is controlled in concert via the inheritance of coadapted gene complexes (supergenes) in large chromosomal inversions. The similar ways in which these independently evolved supergenes influence morphology and behavior elucidate how complex phenotypes evolve and are maintained.

Supergenes are two or more linked genes that are inherited together. They can play an important role in generating biological diversity in taxa ranging from plants to humans. The mimetic wing patterns of butterflies are a particularly well-documented example of how supergenes can underlie complex adaptations (*4*). However, knowledge of the genetic architecture of supergenes remains limited, and the molecular mechanisms by which they can generate complex phenotypes are unclear. The recent studies of the ruff (*1*, *2*) and the white-throated sparrow (*3*) provide critical advances to our understanding of these aspects of supergenes.

Reduced recombination within supergenes is central to their evolution, allowing multiple genes to be inherited as a single linked unit and setting the stage for their coevolution. Inversions, chromosomal rearrangements where large portions of the DNA molecule are flipped, suppress local recombination (*5*). Perhaps not surprisingly, inversions harbor supergene complexes (*4*) in groups that now include the ruff and the white-throated sparrow (*1*–*3*). In each of these bird species, individuals can exhibit strikingly different plumage and behavior that we can now link to genomic variation.

The ruff is a lek-breeding wading bird in wetlands of northern Eurasia (*6*). Male ruffs occur as one of three morphs, each with a distinct breeding strategy and appearance (see the photo). Independent males (80 to 95% of the population) are dominant holders of display sites, with diverse patterns of ornamented dark plumage. Satellite males (5 to 20%) are also ornamented, but with white plumage. They do not defend display sites, but rather visit the leks of independent males, where they assist with female attraction and attempt to "steal" copulations. Faeder males (<1%) mimic females in their plumage and smaller size and also steal copulations.

Lekking ruffs. From left to right, a female, an independent male, and a satellite male ruff. A third type of male ruff closely resembles the female. Recent research has shed light on the genetic underpinnings of the ruff's complex reproductive strategies (*1*, *2*).

As Küpper *et al.* (*1*) and Lamichhaney *et al.* (*2*) now show, these three reproductive behaviors and associated phenotypes are determined by a ~4.5 Mb inversion located on an autosome (see the figure). Independent males carry two copies of the ancestral, noninverted chromosome: They do not possess either ruff supergene. Satellites and faeders have different supergenes: They each carry one ancestral haplotype and one morph-specific version of the supergene. Females carrying either version of the supergene can also be identified by size or from their behavioral response to testosterone implantation (*1*).

The white-throated sparrow is a common North American bird with two equally abundant color morphs: white-striped and tan-striped. White males invest in securing mates at the expense of parental care, whereas tan males are monogamous and help to look after their young (*7*). A similar trade-off is also seen in females. The two morphs are controlled by the presence of an inversion that harbors a large, ~100 Mb supergene, roughly 10% of the genome (*3*, *8*, *9*), and Tuttle *et al.* (*3*) have disentangled its evolutionary origin. White birds carry one copy of the supergene and one noninverted form, whereas tan birds only carry the non-

[1]*Fuller Evolutionary Biology Program, Cornell Lab of Ornithology, Cornell University, Ithaca, NY, USA.* [2]*Department of Ecology and Evolutionary Biology, Cornell University, Ithaca, NY, USA. E-mail: sat235@cornell.edu*

Published by AAAS

inverted form (see the figure). White birds of either sex nearly always mate with tan birds of the opposite sex.

Although the supergenes of white-throated sparrows and ruffs are both ancient, they have different origins. The ruff supergenes arose from rearrangements in the ruff genome. The faeder supergene appears to have arisen ~3.8 million years ago via an inversion of the ancestral chromosome. The satellite supergene may be a product of rare recombination between the ancestral ruff chromosome and the faeder supergene that took place ~0.5 million years ago (*2*). In contrast, in white-throated sparrows, Tuttle *et al*.'s phylogenomic analyses indicate that the supergene predates the existence of that species and may be the product of introgression via hybridization with a now extinct relative (*3*).

In other taxa, supergenes and their potentially adaptive gene complexes have spread via hybridization (*4*), but the relative importance of hybridization versus intraspecific chromosomal rearrangements for the generation of supergenes is not known. The recent studies (*1*–*3*) show that supergenes with similarly complex influences on morphology and behavior can arise in both ways. It remains to be shown whether supergenes tend to be the product of within-species processes, or are more often co-opted from other species via introgressive hybridization.

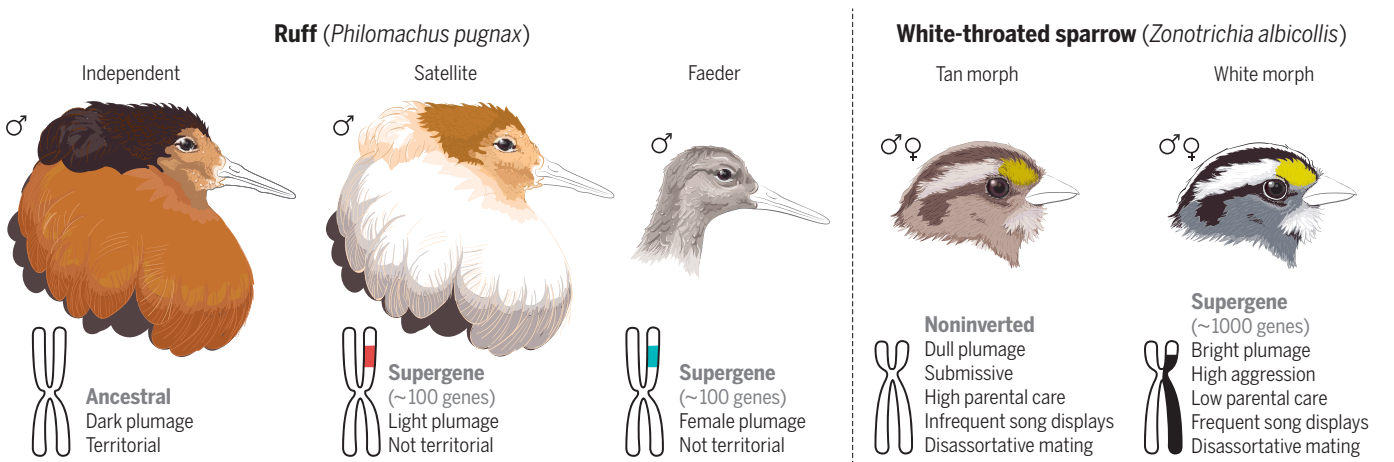
In both birds, there are fitness consequences associated with possessing the supergene, yet the polymorphisms appear demographically stable. The ruff supergenes are lethal when either sex has a copy on each chromosome (*1*), whereas the sparrow supergene only appears to be lethal when males have a copy on each chromosome (*3*). In ruffs, the inversion interrupts a gene essential for mitosis (*1*, *2*); in sparrows, the precise mechanism remains unknown (*3*). Why do the supergenes persist despite these fitness costs? The answer is that each mating system allows alternative reproductive strategies to coexist as balanced polymorphisms. Satellite and faeder ruffs are hypothesized to have fitness advantages that maintain these morphs at low frequencies (*1*, *2*). Polymorphism in sparrows persists via their mating pattern (white nearly always mates with tan, producing both tan and white offspring) and similar fitness benefits to either mating strategy (*3*).

Although the ruff and sparrow supergene variants can each be unambiguously linked to morph-specific traits, moving past this general association will be challenging. Each supergene region contains from 100 (ruff) to over 1000 (white-throated sparrow) genes, all of which are highly differentiated from their respective noninverted haplotypes (*1*–*3*). The divergent alleles on the supergenes could drive differentiation between morphs, yet there is evidence that the supergenes are degrading (*1*–*3*), as is the case for the mammalian Y and avian W sex chromosomes (*10*).

Typically, experimental crosses can be used to tease apart regions of the genome involved in generating a trait. However, the lack of recombination within supergenes makes this an unfeasible approach. Now that the genes within the ruff and white-throated sparrow supergenes are known and the genomic resources for these nonmodel organisms have been generated, the relative influence of different genes in each supergene can be explored with targeted gene expression analyses and genome-editing technology.

The broad overlap in the function of the genes within the ruff and sparrow supergenes provides a hint as to how their complex phenotypes could be generated. In both cases, loci involved in the response to sex hormones and plumage pigmentation exist in the supergene and likely act in concert to produce the alternative mating strategies and their associated behaviors and morphologies. In two closely related crow species, another putative inversion-generated supergene also contains genes involved in pigmentation and hormonal regulation (*11*). This mechanism is different from that seen in the rhinoceros beetle (*Trypoxylus dichotomus*), where differential sensitivity to growth hormones based on a single signaling gene has been proposed as a molecular mechanism by which ornaments and weapons can grow to exaggerated proportions (*12*).

Considered in concert, the findings in ruff and white-throated sparrow highlight the importance of supergenes in the generation of complex phenotypes. They provide insight into the varied ways in which supergenes can be generated and maintained and begin to expose their genetic architecture. These recent studies provide a link between genotype and phenotype, a long-standing goal in evolutionary biology research. Supergenes may have an underappreciated role in the generation of biodiversity, one that we are now poised to more fully appreciate and understand. ■



The genetic architecture of two avian mating systems. The presence of inversion-generated supergenes determines morphological and behavioral traits in ruffs and white-throated sparrows. The ruff supergenes harbor close to 100 genes; the white-throated sparrow supergene is much larger, with over 1000 genes.

ILLUSTRATION: K. SUTLIFF/*SCIENCE*

REFERENCES

1. C. Küpper *et al*., *Nat. Genet.* 10.1038/ng.3443 (2016).
2. S. Lamichhaney *et al*., *Nat. Genet.* 10.1038/ng.3430 (2016).
3. E. M. Tuttle *et al*., *Curr. Biol.* 10.1126/j.cub.2015.11.069 (2016).
4. T. Schwander *et al*., *Curr. Biol.* **24**, R288 (2014).
5. L. H. Rieseberg, *Trends Ecol. Evol.* **16**, 351 (2001).
6. J. G. van Rhijn, *The Ruff* (Poyser, London, 1991).
7. E. M. Tuttle, *Behav. Ecol.* **14**, 425 (2003).
8. J. W. Thomas *et al*., *Genetics* **179**, 1455 (2008).
9. H. B. Throneycroft, *Evolution* **29**, 611 (1975).
10. D. Bachtrog, *Curr. Biol.* **16**, 1694 (2006).
11. J. W. Poelstra *et al*., *Science* **344**, 1410 (2014).
12. D. J. Emlen *et al*., *Science* **337**, 860 (2012).

10.1126/science.aae0389

Published by AAAS



Downloaded from on January 31, 2016

ECOLOGY

How ecosystems change

Conservation planning must accommodate changes in ecosystem composition to protect biodiversity

By **Anne E. Magurran**

Human impacts on the planet, including anthropogenic climate change, are reshaping ecosystems in unprecedented ways. To meet the challenge of conserving biodiversity in this rapidly changing world, we must understand how ecological assemblages respond to novel conditions (*1*). However, species in ecosystems are not fixed entities, even without human-induced change. All ecosystems experience natural turnover in species presence and abundance. Taking account of this baseline turnover in conservation planning could play an important role in protecting biodiversity.

More than 150 years ago, Darwin observed that taxa "favoured by any slight change of climate" will increase in numbers, whereas other, less-favored species "must decrease" (*2*). In these few words, Darwin touches on two ideas key to understanding the fate of ecosystems. On the one hand, he suggests that the number of individuals and species in an ecosystem will tend toward some equilibrium level. On the other, there is constant turnover in the identities and abundances of species in any locality. Darwin's views were probably shaped by personal experience: In Western Europe, the 1850s were unusually cold. But they provide a context for understanding the fate of ecological communities at a time when climate change is remodeling the natural world at a pace that exceeds historical levels.

Darwin's proposition that ecological communities track fluctuations in climate is supported by time series collected over decades to reveal how rapidly ecosystems change. For instance, Barceló *et al.* recently reported that the fish species now present in the near-shore assemblage of the Skagerrak to the south of Norway differ from those caught during a colder period in the 1960s and 1970s (*3*). The current community composition is more similar to that seen during a warmer phase in the 1930s and 1940s. These community shifts arise because species adjust their ranges in response to temperature (*4*), with cold-favoring fish moving south in colder years and warm-favoring ones extending north in warmer years. Total species richness increases in the Skagerrak during warmer phases and declines during cooler ones. Barceló *et al.* saw no systematic trend over the duration of the eight-decade time series (*2*). However, the recent appearance of previously unrecorded species such as the European anchovy (*Engraulis encrasicolus*), European pilchard (*Sardina pilchardus*), and tub gurnard (*Trigla lucerna*) reinforces the idea that even if the species richness of an assemblage does not change, its composition can shift markedly (see the figure).

Great strides have been made in modeling vulnerability to climate change on a species-by-species basis (*5*), but it is also important to understand how entire communities respond to novel conditions (*6*). Ecological communities reorganize over time as a result of changes in both α diversity (such as a change in species richness) and β diversity (change, or turnover, in species composition). Human actions in the form of land use change and pollution can drive down the number of species in local assemblages (*7*). However, in many communities, such as the Skagerrak, average species richness has remained constant over recent decades (*3*, *8*–*10*). Indeed, as Darwin suggested (*2*), ecological processes may help to regulate local α diversity (*11*), and seemingly unvarying richness can mask substantial change in community structure (*12*). Temporal α diversity is thus not always an informative gauge of the severity of human impacts on the natural world (see the figure).

In contrast, investigations of temporal β diversity suggest that community reorganization is occurring at rates that exceed historical baseline turnover (*1*, *8*). For instance, the 66 freshwater fish found in the rivers of

Centre for Biological Diversity, School of Biology, University of St. Andrews, St. Andrews, Scotland, UK. E-mail: aem1@st-andrews.ac.uk

PHOTO: © JOHN DE LA BASTIDE/ALAMY STOCK PHOTO

Published by AAAS



Beyond baseline turnover. The Caroni River system in Trinidad supports a rich fish fauna, including the introduced tetra, *Copella arnoldi* (*13*). Today's species turnover rate in the rivers of Trinidad and Tobago is roughly double that seen historically.

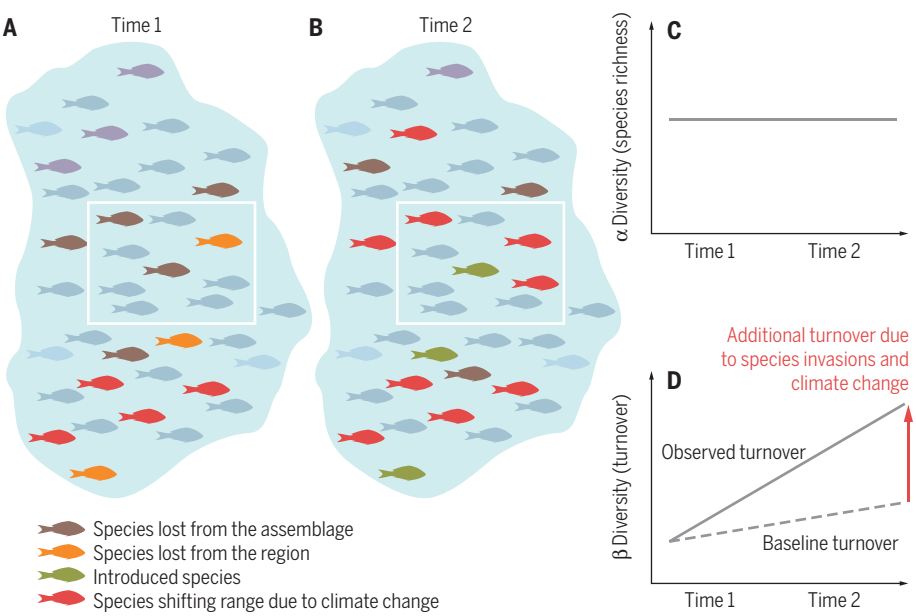
the islands of Trinidad and Tobago (see the photo) include six introduced species (*13*). Local extinctions offset these gains, but the presence of exotic species alongside natural colonists means that the contemporary turnover rate has approximately doubled relative to the historical level.

Invasive species are a prominent feature of many assemblages and have contributed to greater biotic homogenization at both local and regional scales. Communities are increasingly dominated by the same cosmopolitan species, rather as shopping districts around the world have become populated by familiar brands. For example, the common carp (*Cyprinus carpio*) and goldfish (*Carassius auratus*), species that originated in Asia, now inhabit freshwaters in 48 and 42 U.S. states, respectively (*14*). Further, groundfish assemblages of the Northeast Atlantic have become progressively more similar in species composition over the past three decades (*12*). Thus, biotic homogenization may also be linked to climate change. The homogenization of Northeast Atlantic fish communities parallels an evening-out of water temperature (a consequence of ocean warming) over the same period.

Conservation is sometimes regarded as synonymous with preservation. Yet paradoxically, to protect biodiversity, conservation managers will increasingly need to accommodate species turnover in their planning. A first step is to report changes both in abundance of individual species and in species composition. Identifying which taxa are native to a locality or biome and which are new to it will be crucial information, both to support native taxa and to ameliorate the impact of invasive ones. More data on contemporary rates of turnover, relative to baseline rates, would be invaluable.

Scale is also important. Day-to-day conservation management often occurs at a local scale, but conservation strategy needs to be enacted at an appropriate scale to accommodate changes in species distributions. Further, managed change can support conservation. In Europe, rewilding takes advantage of farmland abandonment and is contributing to the recovery of megafauna (*15*).

Finally, we have little understanding of how changes in composition will affect ecosystem function (*1*). However, new insights into how different species respond to warming will help to provide early warning of accelerated turnover in ecosystems (*6*). It will also be important to investigate evolutionary change alongside ecological change (*2*). ■



Toward managing biodiversity change. (**A** and **B**) A regional assemblage at two time points. The taxa observed in the sampled assemblage (white rectangle) change over time as a result of local and regional species loss. These losses may be offset by gains due to range shifts and introductions of exotic species. In this example, there is no change in α diversity (such as species richness) (**C**), even though there are substantial changes in assemblage composition (**D**). A major challenge in conservation planning is managing turnover that exceeds baseline turnover, arising from human impacts such as invasive species and climate change.

ILLUSTRATION: P. HUEY/*SCIENCE*

REFERENCES

1. J. M. Pandolfi, C. E. Lovelock, *Science* **344**, 266 (2014).
2. C. Darwin, *On the Origin of Species by Means of Natural Selection, or the Preservation of Favoured Races in the Struggle for Life* (John Murray, 1859).
3. C. Barceló, L. Ciannelli, E. M. Olsen, T. Johannessen, H. Knutsen, *Global Change Biol.* 10.1111/gcb.13047 (2015).
4. I.-C. Chen, J. K. Hill, R. Ohlemüller, D. B. Roy, C. D. Thomas, *Science* **333**, 1024 (2011).
5. E. S. Poloczanska *et al.*, *Nat. Clim. Change* **3**, 919 (2013).
6. R. D. Stuart-Smith, G. J. Edgar, N. S. Barrett, S. J. Kininmonth, A. E. Bates, *Nature* 10.1038/nature16144 (2015).
7. T. Newbold *et al.*, *Nature* **520**, 45 (2015).
8. M. Dornelas *et al.*, *Science* **344**, 296 (2014).
9. M. Vellend *et al.*, *Proc. Natl. Acad. Sci. U.S.A.* **110**, 19456 (2013).
10. S. R. Supp, S. K. M. Ernest, *Ecology* **95**, 1717 (2014).
11. S. K. M. Ernest, J. H. Brown, K. M. Thibault, E. P. White, J. R. Goheen, *Am. Nat.* **172**, E257 (2008).
12. A. E. Magurran, M. Dornelas, F. Moyes, N. J. Gotelli, B. McGill, *Nat. Commun.* **6**, 10.1038/ncomms9405 (2015).
13. D. A. T. Phillip *et al.*, *Zootaxa* **3711**, 1 (2013).
14. F. J. Rahel, *Science* **288**, 854 (2000).
15. S. Ceauşu *et al.*, *Conserv. Biol.* **29**, 1017 (2015).

10.1126/science.aad6758

Published by AAAS



A herder with sheep, cattle, and donkeys in the Spiti Valley in India. Village communities have spared land for snow leopards, while improving livestock yields.

PHOTO: MILAN MOUDGILL

CONSERVATION ECOLOGY

How can higher-yield farming help to spare nature?

Mechanisms to link yield increases with conservation

By **Ben Phalan,[1]* Rhys E. Green,[1,2] Lynn V. Dicks,[1] Graziela Dotta,[3] Claire Feniuk,[1] Anthony Lamb,[1] Bernardo B. N. Strassburg,[4,5] David R. Williams,[1] Erasmus K. H. J. zu Ermgassen,[1] Andrew Balmford[1]**

Expansion of land area used for agriculture is a leading cause of biodiversity loss and greenhouse gas emissions, particularly in the tropics. One potential way to reduce these impacts is to increase food production per unit area (yield) on existing farmland, so as to minimize farmland area and to spare land for habitat conservation or restoration. There is now widespread evidence that such a strategy could benefit a large proportion of wild species, provided that spared land is conserved as natural habitat (*1*). However, the scope for yield growth to spare land by lowering food prices and, hence, incentives for clearance ("passive" land sparing) can be undermined if lower prices stimulate demand and if higher yields raise profits, encouraging agricultural expansion and increasing the opportunity cost of conservation (*2*, *3*). We offer a first description of four categories of "active" land-sparing mechanisms that could overcome these rebound effects by linking yield increases with habitat protection or restoration (table S1). The effectiveness, limitations, and potential for unintended consequences of these mechanisms have yet to be systematically tested, but in each case, we describe real-world interventions that illustrate how intentional links between yield increases and land sparing might be developed.

POLICY

FOUR LINKING MECHANISMS. *Land-use zoning.* Zoning some land for conservation and some for agriculture limits agricultural expansion, provides security to landholders investing in agricultural productivity, and can incentivize yield increases to compensate for the scarcity of available land ["Boserupian innovation" (*4*)]. However, zoning does not drive yield increases in agricultural zones directly. Hence, there is a risk of its leading to displacement of production outside the regions subject to zoning. Such "leakage" might be less likely where zoning restrictions are placed on the expansion of export commodities for which demand shows high price elasticity, rather than on staple foods (*2*).

In Costa Rica, after the government zoned forests as off-limits for agricultural expansion, the rate of clearance of mature forests halved (*5*). Export-oriented agriculture shifted from cattle pasture toward high-yielding pineapple and banana crop, (for fuller information and references for this and other case studies, see supplementary materials (SM). Beef production declined, albeit temporarily, whereas production of pineapples and other crops has continued to increase. The risk of leakage could be reduced by prioritizing less-productive land for conservation to minimize loss of production and by combining zoning with other interventions (*6*).

Economic instruments, such as payments, land taxes, and subsidies. In principle, these can be tailored to stimulate yield increases, discourage habitat conversion, and make receipt of benefits conditional on habitat conservation. Incentive programs often involve contracts, and difficulties can arise through hidden actions and information asymmetries. For example, recipients might conceal breaches of contract or accept money for actions they would have carried out anyway. These risks can be reduced by building trust, understanding the people and places where interventions occur, developing cost-effective monitoring, and enforcing contracts.

An incentive program that has successfully spared land has been implemented in the Spiti Valley of Himalayan India (*7*). In exchange for designating land set-asides for the recovery of snow leopard prey, herders receive payments and technical assistance to reduce livestock losses to snow leopards (improving yield) and to organize insurance against losses. The program, which was developed collaboratively with herders and local government to ensure that it addresses local priorities, reduced snow leopard predation of livestock by two-thirds in its first 4 years and eliminated snow leopard killings.

Spatially strategic deployment of technology, infrastructure, or agronomic knowledge. Land sparing can be encouraged if yield-enhancing measures (such as technical advice on soil, nutrient, or water management; improved germplasm; multiple cropping; integrated pest and disease control; and improved access to roads or irrigation) are intentionally directed toward certain areas and

[1]*Conservation Science Group, Department of Zoology, University of Cambridge, Cambridge CB2 3EJ, UK.* [2]*RSPB Centre for Conservation Science, Royal Society for the Protection of Birds, Sandy SG19 2DL, UK.* [3]*Laboratório de Ornitologia, Museu de Ciências e Tecnologia, PUC-RS, 6681, Porto Alegre, Brazil.* [4]*International Institute for Sustainability, 22460-320 Rio de Janeiro, Brazil.* [5]*Rio Conservation and Sustainability Science Centre, Department of Geography and the Environment, Pontifícia Universidade Católica, 22453-900 Rio de Janeiro, Brazil. *Corresponding author. E-mail: btp22@cam.ac.uk*

Downloaded from on January 31, 2016

Published by AAAS

not others. Such interventions could enhance yields and reduce postharvest losses in established farmlands, while avoiding the risks involved in stimulating agriculture in areas of extensive natural habitat (*8*). Increasing yields of staple crops, for which demand is inelastic to price changes, appears more likely to support land sparing than increasing yields of luxury or export crops (*2*). A limitation of strategic deployment is that it encourages yield increases directly but only protects natural habitats indirectly, by reducing pressure for conversion. It will often be necessary to combine this mechanism with others, especially land-use zoning. A key challenge is to ensure that benefits and costs are not unfairly distributed.

In the Philippine province of Palawan, introduction of irrigation helped lowland rice farmers produce two crops per year rather than one (*9*). They met their higher labor demands by employing upland farmers, who used part of their new-found income to invest in fertilizers, which improved their own yields and reduced their need to clear forests. Deforestation rates in the uplands halved. Larger and poorer households were those most likely to benefit. Nevertheless, addressing social justice remains practically and ethically complex, is often hampered by unequal power relations and may often require additional measures, such as increasing nonagricultural job opportunities for marginalized groups.

"...efforts to reduce habitat loss must do so while safeguarding the interests of smallholders...."

Standards and certification. Voluntary standards could link yield growth to conservation by requiring habitat protection, defining sustainable yield-increasing practices, monitoring compliance, and rewarding good performance with market access and price premiums. Sparing or restoring natural habitats at farm scale can be more beneficial for biodiversity than certifying lower-yielding "wildlife-friendly" practices (*10*). To maximize their contribution to landscape-level conservation, certification schemes should widen their focus from individual farms to coordinated actions by groups of farmers in places where potential conservation gains are greatest.

Participating farmers in the Ibis rice scheme in northern Cambodia receive technical assistance and a price premium, which makes it easier to afford simple technology and additional labor (*11*). At the same time, they agree to a village-level land-use plan that protects habitats. These agreements are maintained in part by social pressure: A major infraction would put everyone's benefits at risk. Together with other initiatives, the scheme has reduced deforestation and increased rice harvests. It illustrates one way of making landscape conservation relevant and feasible for individual farmers.

CONDITIONS AND SYNERGIES. Some conditions make successful implementation of land-sparing mechanisms more likely. Labor- and capital-intensive technologies and practices are those most likely to be conducive to land sparing (*8*). Knowledge networks can also help improve implementation of sustainability standards or payment schemes (*12*). For example, thousands of Landcare groups in Australia share knowledge on accessing funds, conserving habitats, and improving agricultural techniques. Landcare participants are more likely to protect and restore native vegetation and to adopt practices that sustain agricultural yields (*13*). Markets also matter. For commodities with globalized markets and elastic demand, limiting rebound effects through demand-side measures and restrictions on land use will be crucial. In the case of staples grown by smallholders, supporting them to increase their yields (and thereby, limit leakage) might be more appropriate.

Each mechanism is most likely to be effective if implemented in synergy with others, so that strong protection is provided to habitats and adequate support is provided to farmers to increase their yields. Command-and-control zoning policies will more likely be accepted as legitimate if accompanied by incentives, improved access to technology and infrastructure, and knowledge-sharing (*14*). Because of the risk of rebound effects, strategic deployment will often have to be integrated with mechanisms, such as zoning, that apply over large areas. Environmental and agricultural policies need to be coordinated to work in synergy rather than in conflict.

Brazil provides an example of how multiple policy interventions can work together. Natural habitats are conserved through several instruments including protected areas, indigenous reserves, and Forest Code requirements on private lands (*15*). Government-subsidized loans are provided to farmers to increase productivity on degraded pastureland. Partly due to these initiatives, and despite widespread noncompliance with the Forest Code, deforestation in the Brazilian Amazon declined steeply after 2004, whereas agricultural production continued to grow.

Whether these trends can be sustained and replicated elsewhere will depend largely on the political will to deliver strong environmental governance. There is a risk that environmental regulations will be corrupted or diluted by powerful special interests, as happened in Europe with the Common Agricultural Policy (*16*). Further efforts to reduce habitat loss must do so while safeguarding the interests of smallholders, as agricultural credit programs in Brazil seek to do by supporting family farms. In many parts of the world, higher yields have eroded not only on-farm biodiversity but also water, soil, and air quality. Much remains to be done to reduce these impacts by applying improved agronomic and agroecological knowledge (*17*).

Harnessing the potential of higher-yield farming to make space for nature at scales that matter will not be straightforward, but the examples described here illustrate that it can be done. The challenge is to move on from thinking about higher yields simply as a means to produce more food and to use them to free up land for conserving biodiversity and ecosystem services. Reconciling agriculture and conservation is one of this century's greatest challenges. We hope that by describing some promising solutions, we can stimulate the proposal, testing, and application of many more. ■

REFERENCES AND NOTES

1. A. Balmford, R. Green, B. Phalan, *Daedalus* **144**, 57 (2015).
2. E. F. Lambin, P. Meyfroidt, *Proc. Natl. Acad. Sci. U.S.A.* **108**, 3465 (2011).
3. D. Byerlee *et al.*, *Glob. Food Secur.* **3**, 92 (2014).
4. E. Boserup, *The Conditions of Agricultural Growth: The Economics of Agrarian Change under Population Pressure* (Allen & Unwin, London, 1965).
5. M. E. Fagan *et al.*, *Environ. Res. Lett.* **8**, 034017 (2013).
6. A. E. Latawiec, B. B. Strassburg, P. H. Brancalion, R. R. Rodrigues, T. Gardner, *Front. Ecol. Environ* **13**, 211 (2015).
7. R. M. Jackson, C. Mishra, T. M. McCarthy, S. B. Ale, in *The Biology and Conservation of Wild Felids* (Oxford Univ. Press, Oxford, 2010), pp. 417–430.
8. A. Angelsen, *Proc. Natl. Acad. Sci. U.S.A.* **107**, 19639 (2010).
9. G. Shively, S. Pagiola, *Environ. Dev. Econ.* **9**, 241 (2004).
10. R. B. Chandler *et al.*, *Conserv. Biol.* **27**, 785 (2013).
11. T. Clements, E. J. Milner-Gulland, *Conserv. Biol.* **29**, 78 (2015).
12. J. R. Franks, S. B. Emery, *Land Use Policy* **30**, 847 (2013).
13. A. Curtis, D. Lucas, M. Nurse, M. Skeen, "Achieving NRM outcomes through voluntary action: lessons from landcare" (Charles Sturt Univ. and Department of Sustainability and Environment, Melbourne, Australia, 2008).
14. E. F. Lambin *et al.*, *Glob. Environ. Change* **28**, 129 (2014).
15. D. Nepstad *et al.*, *Science* **344**, 1118 (2014).
16. G. Pe'er *et al.*, *Science* **344**, 1090 (2014).
17. R. Bommarco, D. Kleijn, S. G. Potts, *Trends Ecol. Evol.* **28**, 230 (2013).

ACKNOWLEDGMENTS

We thank T. Gardner, M. Fagan, A. John, A. Mould, G. Shively, E. Beauchamp, C. Mishra, T. Clements, N. Selva, and three anonymous reviewers for comments. Funding: Zukerman fellowship, King's College, Cambridge (B.P.); Natural Environment Research Council NE/K015419/1 (L.V.D.); Gordon and Betty Moore Foundation and Norwegian Agency for Development Cooperation (B.B.N.S.); Biotechnology and Biological Sciences Research Council BB/J014540/1 (E.K.H.J.z.E.).

SUPPLEMENTARY MATERIALS

www.sciencemag/content/351/6272/450/suppl/DC1

10.1126/science.aad0055

Published by AAAS

MICROBIOME

Prescription drugs obscure microbiome analyses

Patient populations should be stratified for medications when looking for gut microbial signatures of disease

By **Suzanne Devkota**

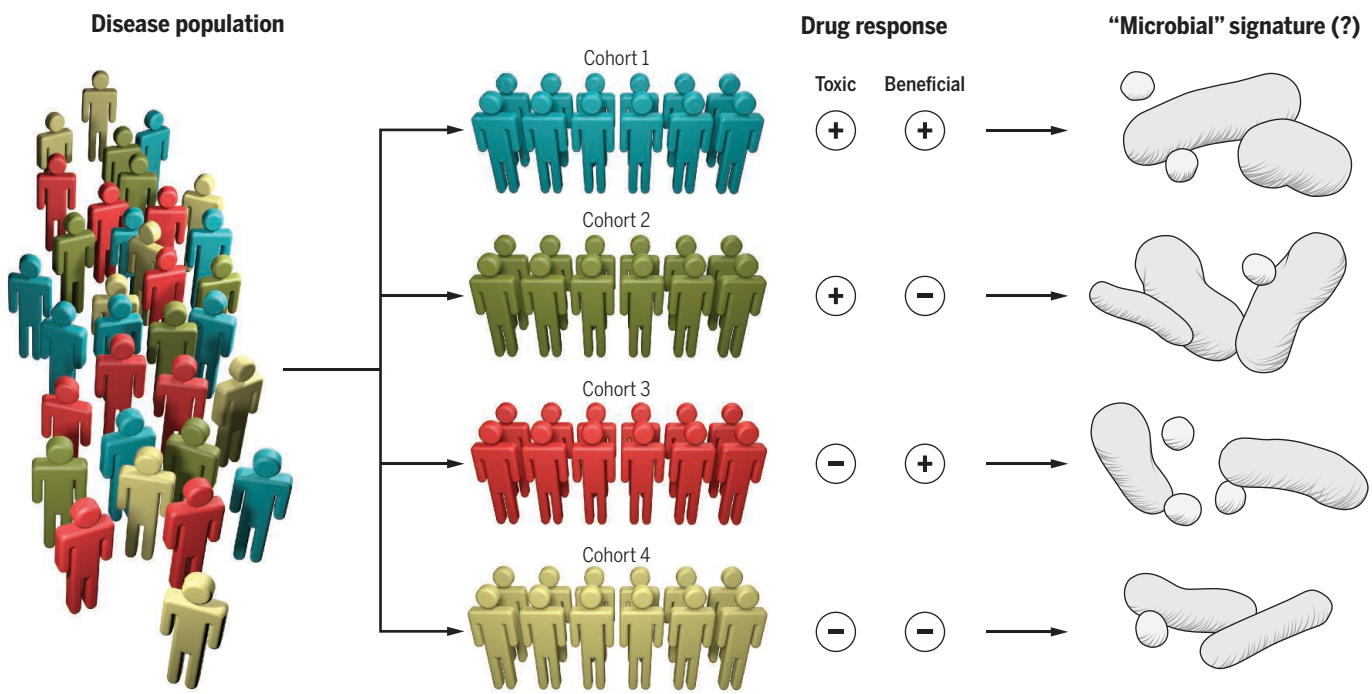
Although observations linking members of the gut microbiome to human disease have been plentiful, some are fraught with complex and confounding variables, emphasizing the need for vetting such associations with greater computational and mechanistic rigor. A recent study by Forslund *et al.* (*1*) adds another dimension for consideration by illustrating how medications may adversely affect the microbiome—an interaction often overlooked in post hoc analyses of disease-microbe relationships.

Focusing on type 2 diabetes, Forslund *et al.* used new and existing gut metagenomic data sets from 199 patients with type 2 diabetes and 554 nondiabetic controls from Danish (*2*), Swedish (*3*), and Chinese cohorts (*4*) to examine whether stratifying for metformin treatment, the most commonly prescribed antidiabetic drug, affected whether microbial signatures of disease were still apparent. The studies from which most of these data sets were derived could distinguish diabetic from nondiabetic patients based on such microbial signatures. However, Forslund *et al.* cite the lack of drug stratification as a potential confounder. When the patients with type 2 diabetes were stratified based on whether they were taking metformin or not, the microbial signatures between untreated patients with type 2 diabetes and nondiabetic controls were diminished, whereas the metformin-treated patients could be reliably predicted. These results suggest that either metformin treatment may be a bigger driver of the observed microbial differences than type 2 diabetes status itself, or that those individuals whose disease is adequately controlled by metformin alone define a unique subset of type 2 diabetes—an idea yet unexplored.

Indeed, there is increasing evidence that medications can profoundly affect microbial gene expression (*5*), and likewise, that the microbiota can transform drugs, affecting their bioavailability (*6*). In this context, however, metformin is intriguing because its mode of action—suppression of liver glucose production—is known, yet the mechanism by which this is carried out is unclear and open to testing. Studies in mice suggest microbial mediation of the drug's antihyperglycemic effects (*7*). However, the drug is excreted largely intact in the urine with no known metabolites, essentially excluding the possibility of transformation of the drug by the bacteria.

Although Forslund *et al.* do not examine the mechanism by which metformin appears to affect the microbiome, they do make a testable observation that untreated patients with type 2 diabetes have a decrease in beneficial butyrate-producing bacteria, which is reversed with metformin treatment. This is consistent with their findings that metformin increases the functional potential for short-chain fatty acid production, specifically butyrate and propionate. The authors, in turn, hypothesize that short-chain fatty acids alter intestinal glucose production, previously shown in rats (*8*), which may favorably affect liver glucose production and overall glycemic regulation. When controlling for gender, body mass index, and fasting blood glucose or insulin concentration, metformin treatment was further associated with increases in *Escherichia* spp. (except in the Chinese cohort) and a decrease in *Intestinibacter*. Although the relevance of this interplay is unclear, this may be a case of competitive exclusion whereby metformin is somehow creating a favorable environment for the *Escherichia*

F. Widjaja Foundation Inflammatory Bowel and Immunobiology Research Institute, Cedars-Sinai Medical Center, Los Angeles, CA, USA. E-mail: suzanne.devkota@cshs.org



Microbial signatures. For a disease such as type 2 diabetes, patients should be stratified based on medications to reveal drug-microbe interactions.

ILLUSTRATION: P. HUEY/*SCIENCE*

Downloaded from on January 31, 2016

Published by AAAS

spp. to thrive where *Intestinibacter* cannot, or by directly compromising the integrity of the microbe. Evidence for the latter can be found in a pharmaco-materials study whereby metformin attached to gold nanoparticles had the highest antibacterial and bactericidal activity against pathogens by compromising the cell wall when compared to other nonantibiotic drugs (*9*).

Interestingly, a cohort that was missing from the Forslund *et al.* study, and that would lend insight into the above observations, is the 30% of patients with type 2 diabetes who cannot tolerate metformin due to gastrointestinal distress. This common side effect often prevents patients from taking what is otherwise a relatively safe, effective, and inexpensive drug. Understanding whether these individuals have a distinct microbiome signature of their own that predisposes them to the unpleasant side effects creates an opportunity to alter the offending microbes through diet or other means, such that metformin becomes a viable treatment option. Within the existing metformin-treated cohort in the Forslund *et al.* study, the authors suggest that microbial genes encoding virulence factors and involved in gas production are enriched. However, the associations are unclear, as the implication for inclusion in this cohort is that these individuals are tolerant to the drug. Furthermore, metformin is often prescribed in combination with another antidiabetic drug, and it remains unclear whether the stratification also accounted for combination therapy.

Overall, Forslund *et al.* make a strong case for the importance of stratifying for any ubiquitously prescribed drug in a disease of interest when looking for microbial signatures (see the figure). For prospective studies, exclusion criteria aim to identify such confounding factors and exclude them in the first place. However, for most diseases, it is rare to find enough patients who have not undergone treatment to sufficiently power a study; nor is it ethical to take a patient off a drug that is controlling a disease for the purpose of a study. Therefore, we are left with the less than ideal option of keeping careful patient records and stratifying post hoc. However, what this study truly underscores is the need for more investigation into drug-microbiome interactions and the mechanisms therein. ■

REFERENCES

1. K. Forslund *et al.*, *Nature* **528**, 262 (2015).
2. E. Le Chatlier *et al.*, *Nature* **500**, 541 (2013).
3. F. H. Karlsson *et al.*, *Nature* **498**, 99 (2013).
4. J. Qin *et al.*, *Nature* **490**, 55 (2013).
5. C. F. Maurice *et al.*, *Cell* **152**, 39 (2013).
6. H. J. Haiser *et al.*, *Science* **341**, 295 (2013).
7. N. Shin *et al.*, *Gut* **63**, 727 (2014).
8. M. Croset *et al.*, *Diabetes* **50**, 740 (2001).
9. Y. Zhao *et al.*, *J. Am. Chem. Soc.* **135**, 12940 (2013).

10.1126/science.aaf1353

CANCER

Tracking the origins of tumorigenesis

A zebrafish model allows visualization of embryonic reprogramming during melanoma initiation

By **Soufiane Boumahdi**[1] *and* **Cédric Blanpain**[1,2]

Cancer arises through mutations that transform normal cells into cells that proliferate in an uncontrolled manner, form a tumor, invade the underlying tissue, and then metastasize to distant organs (*1*). Although the genetic events required to induce tumor formation are relatively well known (*2*), the additional early downstream molecular events that are required to reprogram normal cells into cancer cells are still poorly understood. On page 464 of this issue, Kaufman *et al.* report the development of an elegant transgenic reporter system that allows the early steps of tumor initiation to be tracked in situ. They find that oncogene-expressing melanocytes are reprogrammed into neural crest–like progenitors before progressing into invasive tumors (*3*).

Melanomas arise from the transformation of melanocytes, pigment-producing cells, which are derived from neural crest progenitors (NCPs) during embryonic development (*4*). Melanoma formation is associated with mutations in *BRAF*, N-*RAS*, and other oncogenes or tumor suppressor genes (*5*). In zebrafish, melanocytes are responsible for the pigmented stripes located on the scales of the fish. Transgenic overexpression in fish melanocytes of a mutated form of *BRAF* [with the mutation $Val^{600} \rightarrow$ Glu (V600E), the most frequent driver mutation in human melanoma] induced the formation of benign nevi, mole-like features; the concomitant deletion of *p53* promoted the progression of these nevi into malignant melanomas (*6*). Even though all melanocytes expressed the $BRAF^{V600E}$ oncogene and were deficient for *p53*, very few eventually formed melanomas, indicating that other mechanisms besides $BRAF^{V600E}$ and *p53* loss of function are needed for tumor initiation.

To better elucidate these mechanisms, Kaufman *et al.* generated transgenic zebrafish to visualize and characterize the early steps of melanoma formation in situ. They engineered fish expressing a crestin-GFP (green fluorescent protein) reporter gene, which faithfully recapitulates crestin expression during embryogenesis and in melanomas (*7*). Crestin-GFP is invariably expressed, prior to the malignant transition, in all lesions that will eventually progress into invasive tumors; this suggests that crestin-GFP marks a point of no return during tumorigenesis and represents one of the earliest molecular states associated with tumor initiation. The survival and propagation of crestin-GFP–expressing cells after transplantation in the scales of $BRAF^{V600E}/p53^{-/-}$ fish further supports the idea that these early crestin-GFP^{+} patches are already tumorigenic. The reexpression of markers of embryonic NCP cells during melanoma initiation supports the notion that oncogene-expressing cells progressing into invasive tumors are reprogrammed into a state that resembles their embryonic progenitor counterpart. The embryonic reprogramming of adult stem cells during tumor initiation was previously reported during initiation of basal cell carcinoma, the most frequent cancer in humans (*8*).

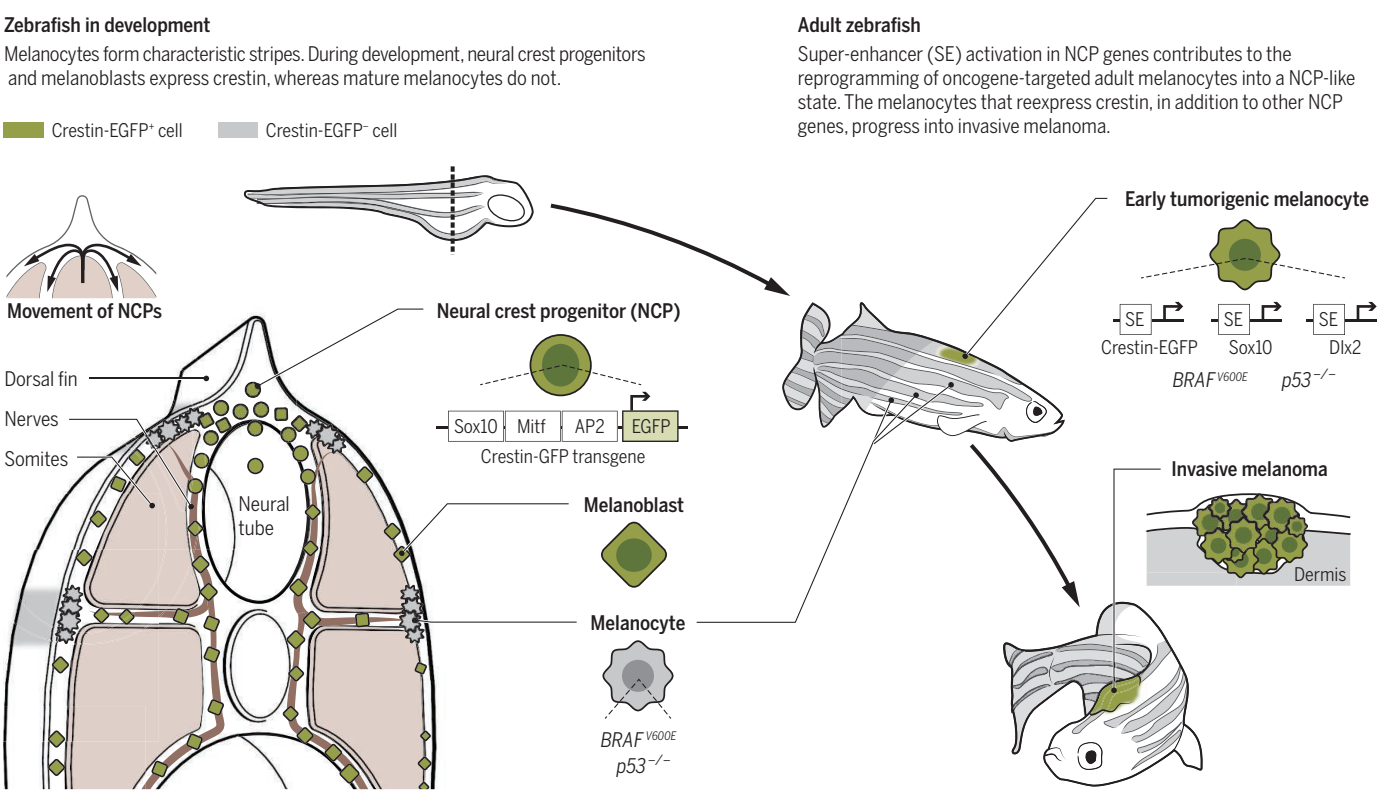
> ***"...crestin-GFP marks a point of no return during tumorigenesis..."***

The authors identified a 296–base pair minimal promoter/enhancer element that regulates crestin-GFP transgene expression during embryonic development and melanoma formation. This element contains binding sites for multiple transcription factors, including Sox10, Pax3, Mitf, and Tfap2, that regulate NCP specification and differentiation (*9*). Mutations in these transcription factor binding sites decreased the specificity of crestin-GFP transgene expression during embryogenesis, supporting the notion that Sox10 together with Mitf and Tfap2 control crestin-GFP expression during melanocyte development. It will be important to assess

[1]*Université Libre de Bruxelles, Institut de Recherche Interdisciplinaire en Biologie Humaine et Moléculaire, Brussels B-1070, Belgium.* [2]*WELBIO, Université Libre de Bruxelles, Brussels B-1070, Belgium. E-mail: cedric.blanpain@ulb.ac.be*

Downloaded from on January 31, 2016

Published by AAAS



Reprogrammed to be transformed. During zebrafish embryonic development, NCPs express crestin, marked by crestin-GFP (green), which is regulated by specific transcription factors; NCPs then migrate and give rise to melanocytes (gray), which down-regulate crestin expression. In the *BRAF*^{V600E}*/p53* zebrafish, among the oncogene-expressing melanocytes, only a few reexpress crestin-GFP and will invariably progress to invasive melanoma. Super-enhancers (SE) associated with key neural crest genes are activated during the reprogramming of oncogene-targeted melanocytes into a NCP-like state.

whether the same set of transcription factors and enhancer regions controls crestin-GFP during melanoma initiation. Microarray analysis of early crestin-GFP$^+$ patches, compared to adjacent crestin-GFP$^-$ scales, showed an enrichment for NCPs (Mitf, Sox10) and melanoma-expressed genes. Bioinformatic analysis of the genes overexpressed in crestin-GFP$^+$ cells during melanoma initiation revealed a positive correlation with zebrafish and human neural crest gene signatures, strengthening the notion that key elements of the NCP state reemerge at the time of melanoma initiation.

Sox10 is a transcription factor essential for melanocyte development (*4*) and a key regulator of melanoma formation (*10*, *11*). Kaufman *et al.* showed that Sox10 overexpression in melanocytes increased crestin-GFP reporter expression and accelerated melanoma onset, suggesting that Sox10 overexpression promotes the establishment of a NCP state and melanoma formation. In contrast, mutating Sox10 by means of CRISPR/Cas9 gene editing resulted in a delay in tumor onset. Moreover, in the tumors that developed, Sox10-targeted alleles were strongly enriched for noninactivating mutations, suggesting that Sox10 activity is necessary for melanoma initiation. By combining transcriptional, chromatin, and epigenetic profiling, the authors propose that super-enhancer elements associated with neural crest genes, including crestin and Sox10, are active in crestin-GFP–marked preneoplastic lesions and are likely to contribute to the reprogramming of oncogene-targeted melanocytes into a NCP fate during melanoma formation.

Defining more precisely the early steps of tumor initiation and why only some oncogene-targeted cells eventually progress into invasive cancer, whereas others do not, is critical for our basic understanding of tumorigenesis and for cancer prevention and treatment. The reprogramming of oncogene-targeted cells into embryonic-like progenitors is potentially amenable to drug targeting. For example, blocking Wnt signaling during basal cell carcinoma initiation completely prevents embryonic reprogramming and skin tumorigenesis (*8*). Genetic, transcriptional, and epigenetic profiling of tumor cells isolated by fluorescence-activated cell sorting at different stages of tumor initiation will be important to define more precisely how oncogene-targeted melanocytes develop into invasive tumors. For example, tumor-initiating cells may need to accumulate further somatic mutations or other chromosomal abnormalities to progress. Because Sox10 is already expressed in melanocytes and benign nevi, although at lower levels (*12*), it will be important to define the other transcription factors, epigenetic regulators, or signaling pathways that are essential for tumor initiation. The competence of melanocytes to be reprogrammed and to initiate tumorigenesis could either be a stochastic process or be predefined by the fate of the cells initially targeted. Indeed, stem cells might be more easily reprogrammed than progenitors or differentiated cells. We also need to know whether the underlying microenvironment of the oncogene-targeted cells influences tumor initiation. Crestin is unique to zebrafish, raising the question of whether there is an equivalent marker of NCP and early melanoma-initiating cells in mice and humans. ■

REFERENCES

1. D. Hanahan, R. A. Weinberg, *Cell* **144**, 646 (2011).
2. B. Vogelstein *et al.*, *Science* **339**, 1546 (2013).
3. C. K. Kaufman *et al.*, *Science* **351**, aad2197 (2016).
4. R. L. Mort, I. J. Jackson, E. E. Patton, *Development* **142**, 620 (2015).
5. J. A. Lo, D. E. Fisher, *Science* **346**, 945 (2014).
6. E. E. Patton *et al.*, *Curr. Biol.* **15**, 249 (2005).
7. R. M. White *et al.*, *Nature* **471**, 518 (2011).
8. K. K. Youssef *et al.*, *Nat. Cell Biol.* **14**, 1282 (2012).
9. W. J. Pavan, D. W. Raible, *Dev. Biol.* **366**, 55 (2012).
10. O. Shakhova *et al.*, *Nat. Cell Biol.* **14**, 882 (2012).
11. J. C. Cronin *et al.*, *Cancer Res.* **73**, 5709 (2013).
12. D. Talantov *et al.*, *Clin. Cancer Res.* **11**, 7234 (2005).

10.1126/science.aad9670

ILLUSTRATION: V. ALTOUNIAN/*SCIENCE*

Published by AAAS

EXTENDED PDF FORMAT
SPONSORED BY


www.rndsystems.com



Tracking the origins of tumorigenesis

Soufiane Boumahdi and Cédric Blanpain

Science **351**, 453 (2016);
DOI: 10.1126/science.aad9670

This copy is for your personal, non-commercial use only.

If you wish to distribute this article to others, you can order high-quality copies for your colleagues, clients, or customers by clicking here.

Permission to republish or repurpose articles or portions of articles can be obtained by following the guidelines here.

The following resources related to this article are available online at www.sciencemag.org (this information is current as of January 30, 2016):

Updated information and services, including high-resolution figures, can be found in the online version of this article at:
/content/351/6272/453.full.html

A list of selected additional articles on the Science Web sites **related to this article** can be found at:
/content/351/6272/453.full.html#related

This article **cites 12 articles**, 6 of which can be accessed free:
/content/351/6272/453.full.html#ref-list-1

This article appears in the following **subject collections:**
Cell Biology
/cgi/collection/cell_biol

Downloaded from on January 31, 2016

Science (print ISSN 0036-8075; online ISSN 1095-9203) is published weekly, except the last week in December, by the American Association for the Advancement of Science, 1200 New York Avenue NW, Washington, DC 20005. Copyright 2016 by the American Association for the Advancement of Science; all rights reserved. The title *Science* is a registered trademark of AAAS.

LETTERS

Edited by **Jennifer Sills**

A necrogenomic registry's potential

THE REDUCED COST and increased capacity of next-generation sequencing technologies have substantially increased the numbers of DNA variants identified per test. However, many of these variants are of unknown significance or are incidental findings (*1*). The lack of an evidence base hinders the translation of genetic findings into disease prevention and rational treatment choice. Furthermore, many population groups have not been adequately assessed genetically, which means that normal genetic variation within these groups is unknown, especially with respect to disease manifestation and drug metabolism.

We advocate the creation of a nationwide necrogenomic registry, recording the genomic sequences of all Danish citizens and residents at the time of their death. Danish law would allow these data to be linked to the Danish Civil Registration System, which registers medical history as well as socioeconomic information for all citizens and residents (*2*). The clinical and genomic data of 50,000 Danes (*3*) could be linked each year. With the combined data records, researchers could assess the phenotype/genotype association for many diseases that commonly affect the Danish population, enabling large genetic epidemiological studies.

Studies based on the necrogenomics database could provide strong evidence of genetic association, identify potential drug targets, and inform treatment modalities. The database would also provide the evidence necessary to adequately evaluate the clinical risk associated with incidental findings. Furthermore, a family physician, with the consent of the treated or advised patient, could request genetic findings found in deceased family members. This information could enable the patient to choose early and preventative treatment, thus avoiding premature death, serious disability, or adverse drug reactions. The release of such findings should follow the recommendations of the American College of Medical Genetics to ensure that the information provided is actionable (*4*).

There would be many ethical challenges. To address consent, an "opt-out" possibility similar to organ donation procedures in Denmark might allow individuals with reservations to exclude themselves from sampling upon their death. Anonymization, access, protection of minors and others who cannot decide for themselves would also be crucial. Defining the cultural, legal, and ethical framework of the necrogenomics registry will require public debate and detailed discussions in ethics committees and the political arena. Only once strict legal and ethical standards are in place can the advantages of necrogenomics be fully realized. In Denmark, a necrogenomics registry can be handled within the framework of our laws on biobanking, but laws in other countries may differ. If properly administered, necrogenomics will provide the predictive power necessary to offset the current lack of evidence that plagues genetic testing for many disorders.

Paula L. Hedley[1]* and Michael Christiansen[1,2]

[1]Department for Congenital Disorders, Statens Serum Institut, 2300, Copenhagen, Denmark. [2]Department of Biomedical Sciences, University of Copenhagen, 1165, Copenhagen, Denmark.

*Corresponding author. E-mail: phy@ssi.dk

REFERENCES

1. R. D. Aatre, S. M. Day, *Circ. Cardiovasc. Genet.* **4**, 81 (2011).
2. C. B. Pedersen, H. Gotzsche, J. O. Moller, P. B. Mortensen, *Dan. Med. Bull.* **53**, 441 (2006).
3. Statistics Denmark, *Deaths and Life Expectancy* (Statistics Denmark, 2015), vol. 2015.
4. R. C. Green *et al.*, *Genet. Med.* **15**, 565 (2013).



Construction on the Belo Monte dam in Brazil.

PHOTO: © PHIL CLARKE HILL/IN PICTURES/CORBIS

Tropical dams: To build or not to build?

IN THEIR POLICY Forum "Balancing hydropower and biodiversity in the Amazon, Congo, and Mekong" (8 January, p. 128), K. O. Winemiller and colleagues present a much-needed window on biodiversity impacts of tropical dams. They conclude that "without more careful planning," impacts will include species extinctions and losses of fisheries and ecosystem services. It needs to be made clear that the most important change required is a fundamental reform of how decisions are made on whether or not to build dams, not the planning of how dams are designed, sited, or managed.

"[V]alidation of technologies intended to mitigate environmental impacts" or improved "design parameters" from better environmental impact assessments (EIAs) pale in comparison with the initial decision: to build or not to build a dam. No amount of adjustment would prevent enormous impacts from a dam like Belo Monte in Brazil—impacts that far exceed what was considered in the EIA, let alone what was considered when the decision to build the dam was made long before the EIA existed (*1*).

Winemiller *et al.* state that the dam projects they discuss "address important energy needs" and that their suggestions for better dam planning would "ensure that societal objectives for energy production are met." The assumption that these dams are needed is questionable from the standpoint of societies in the three cases presented: the Congo, Mekong, and Amazon basins. The Democratic Republic of Congo's Grand Inga Dam is primarily to export electricity to South Africa (*2*, *3*); mainstream Mekong dams will destroy livelihoods in Laos and Cambodia to export electricity to Thailand and Vietnam (*4*); and Amazon dams will feed Brazil's "National Interconnected System," which has many lower-impact options for providing the benefits of electric power. Brazilian society's interests are poorly served by exporting electricity in the form of aluminum, because smelting consumes vast amounts of energy while creating little employment: The environmental and social impacts of the dams that power the smelters stay in Brazil, whereas the benefits are exported (*5*). Brazil has massive potential to reduce inefficiencies in electricity transmission, distribution, and use and to tap wind and solar sources (*6*).

Weinmiller *et al.* state that "at least 334 new Amazon dams have been proposed."

Downloaded from on January 31, 2016

Published by AAAS

One cannot simply treat this as inevitable and limit suggestions to a better choice of sites to locate these dams and to improving their design and management. It is essential to face the issue of whether such a massive dam-building plan should exist in the first place.

Philip M. Fearnside

National Institute for Research in Amazonia (INPA), Manaus, Amazonas, 69067-375, Brazil.
E-mail: pmfearn@inpa.gov.br

REFERENCES

1. P. M. Fearnside, *GWF Discussion Paper 1210*, Global Water Forum, Canberra, Australia (2012); www.globalwaterforum.org/wp-content/uploads/2012/04/Belo-Monte-Dam-A-spearhead-for-Brazils-dam-building-attack-on-Amazonia_-GWF-1210.pdf.
2. F. Misser, *La Saga d'Inga: L'Histoire des Barrages du Fleuve Congo* (Éditions L'Harmattan, Paris, 2013).
3. R. Sanyanga, "Will Congo's poor benefit from world's largest dam project?" International Rivers (2013); www.internationalrivers.org/blogs/266/will-congo%E2%80%99s-poor-benefit-from-world%E2%80%99s-largest-dam-project.
4. G. Ziv, E. Baran, S. Nam, I. Rodríguez-Iturbe, S. A. Levin, *Proc. Natl. Acad. Sci. U.S.A.* **109**, 5609 (2012).
5. P. M. Fearnside, *World Dev.* **77**, 48 (2016).
6. P. F. Moreira, Ed., *O Setor Elétrico Brasileiro e a Sustentabilidade no Século 21: Oportunidade e Desafios* (Rios Internacionais, Brasília, ed. 2, 2012); www.internationalrivers.org/node/7525.

TECHNICAL COMMENT ABSTRACTS

Comment on "Worldwide evidence of a unimodal relationship between productivity and plant species richness"

Andrew T. Tredennick, Peter B. Adler, James B. Grace, W. Stanley Harpole, Elizabeth T. Borer, Eric W. Seabloom, T. Michael Anderson, Jonathan D. Bakker, Lori A. Biederman, Cynthia S. Brown, Yvonne M. Buckley, Chengjin Chu, Scott L. Collins, Michael J. Crawley, Philip A. Fay, Jennifer Firn, Daniel S. Gruner, Nicole Hagenah, Yann Hautier, Andy Hector, Helmut Hillebrand, Kevin Kirkman, Johannes M. H. Knops, Ramesh Laungani, Eric M. Lind, Andrew S. MacDougall, Rebecca L. McCulley, Charles E. Mitchell, Joslin L Moore, John W. Morgan, John L. Orrock, Pablo L. Peri, Suzanne M. Prober, Anita C. Risch, Martin Schütz, Karina L. Speziale, Rachel J. Standish, Lauren L. Sullivan, Glenda M. Wardle, Ryan J. Williams, Louie H. Yang

Fraser *et al.* (Reports, 17 July 2015, p. 302) report a unimodal relationship between productivity and species richness at regional and global scales, which they contrast with the results of Adler *et al.* (Reports, 23 September 2011, p. 1750). However, both data sets, when analyzed correctly, show clearly and consistently that productivity is a poor predictor of local species richness.

Full text at http://dx.doi.org/10.1126/science.aad6236

Response to Comment on "Worldwide evidence of a unimodal relationship between productivity and plant species richness"

Jason Pither, Lauchlan H. Fraser, Anke Jentsch, Marcelo Sternberg, Martin Zobel, James Cahill, Carl Beierkuhnlein, Sándor Bartha, Jonathan A. Bennett, Bazartseren Boldgiv, Leslie R. Brown, Marcelo Cabido, Giandiego Campetella, Cameron N. Carlyle, Stefano Chelli, Anna Mária Csergő, Sandra Diaz, Lucas Enrico, David Ensing, Alessandra Fidelis, Heath W. Garris, Hugh A. L. Henry, Maria Höhn, John Klironomos, Kadri Koorem, Rachael Lawrence-Lodge, Peter Manning, Randall J. Mitchell, Mari Moora, Valério D. Pillar, Gisela C. Stotz, Shu-ichi Sugiyama, Szilárd Szentes, Radnaakhand Tungalag, Sainbileg Undrakhbold, Camilla Wellstein, Talita Zupo

Tredennick *et al.* criticize one of our statistical analyses and emphasize the low explanatory power of models relating productivity to diversity. These criticisms do not detract from our key findings, including evidence consistent with the unimodal constraint relationship predicted by the humped-back model and evidence of scale sensitivities in the form and strength of the relationship.

Full text at http://dx.doi.org/10.1126/science.aad8019

ONLINE BUZZ

Tenure's tenure

In her 11 December 2015 Editorial, "Whither (wither?) tenure?" (p. 1295), Editor-in-Chief Marcia McNutt questions whether tenure is still relevant and proposes replacing it with a 10-year rolling contract system, which she suggests would benefit women and discourage unproductive faculty. Excerpts of your comments are below. Read the full comments at http://comments.sciencemag.org/content/10.1126/science.aad9966.

A selection of your thoughts:

...[A]djunct teaching faculty are most widely used at cash-strapped public universities and colleges.... Eliminating tenure will have little impact on the financial constraints faced by universities....

Roger Albin

Tenure is very important in my field.... Academic freedom that only tenure can provide is critical for the protection of scientists....

George Leikauf

...Without tenure, professors would be under enormous pressure to make pedagogical and assessment/grading decisions that "keep the students happy." This would...erode the quality of our educational systems....

Loren Byrne

...Ten-year contracts do not increase family security or promote women employment.... The true problem is the large number of newly minted Ph.D.s....

John Smith

...Tenure can become a burden to [large research] universities...required to support faculty who have no real purpose if they don't have grant funding. That is not the case for...nonscience disciplines....

David Martin

...Wouldn't it be better to argue that we need to consider how tenure is awarded so all can profit from the freedom it brings...?

Toby Walsh

I'm partial to the idea of a "rolling" contract that is renewed every year for some span of time (say 10 years) unless the institution decides not to renew. ...That way tenure does not turn into employment for life doing anything an individual desires, but the individual's predilections are not at the mercy of the short-term whims of administrators....

Warren Gallin

Published by AAAS

TECHNICAL COMMENT

PLANT ECOLOGY

Comment on "Worldwide evidence of a unimodal relationship between productivity and plant species richness"

Andrew T. Tredennick,[1]*† Peter B. Adler,[1]† James B. Grace,[2]† W. Stanley Harpole,[3]† Elizabeth T. Borer,[4]† Eric W. Seabloom,[4]† T. Michael Anderson,[5] Jonathan D. Bakker,[6] Lori A. Biederman,[7] Cynthia S. Brown,[8] Yvonne M. Buckley,[9] Chengjin Chu,[10] Scott L. Collins,[11] Michael J. Crawley,[12] Philip A. Fay,[13] Jennifer Firn,[14] Daniel S. Gruner,[15] Nicole Hagenah,[16] Yann Hautier,[17] Andy Hector,[18] Helmut Hillebrand,[19] Kevin Kirkman,[16] Johannes M. H. Knops,[20] Ramesh Laungani,[21] Eric M. Lind,[4] Andrew S. MacDougall,[22] Rebecca L. McCulley,[23] Charles E. Mitchell,[24] Joslin L Moore,[25] John W. Morgan,[26] John L. Orrock,[27] Pablo L. Peri,[28] Suzanne M. Prober,[29] Anita C. Risch,[30] Martin Schütz,[30] Karina L. Speziale,[31] Rachel J. Standish,[32] Lauren L. Sullivan,[4] Glenda M. Wardle,[33] Ryan J. Williams,[34] Louie H. Yang[35]

Fraser *et al*. (Reports, 17 July 2015, p. 302) report a unimodal relationship between productivity and species richness at regional and global scales, which they contrast with the results of Adler *et al*. (Reports, 23 September 2011, p. 1750). However, both data sets, when analyzed correctly, show clearly and consistently that productivity is a poor predictor of local species richness.

Fraser *et al*. (*1*) collected a worldwide data set to examine the relationship between productivity and species richness at global and local scales. They present their results as a direct contrast with the results of Adler *et al*. (*2*). However, their presentation obscures substantial areas of agreement, and where results between the two studies do differ, problems in Fraser *et al*.'s statistical analysis amplify the apparent differences.

The most important area of agreement is the low explanatory power of the "humped-back model" (HBM), in which species richness peaks at intermediate productivity and declines at low and high productivity. Fraser *et al*. fit a bivariate relationship between productivity and diversity that accounts for less than 1% of the observed variation in species richness in their data (Table 1, marginal R^2s for the Fraser *et al*. data set). The same is true for an analysis of the Adler *et al*. data set using a generalized linear mixed model (GLMM) with a block nested within-site random-effects structure (Table 1, marginal R^2s for the Adler *et al*. data set). Thus, the analyses in both Adler *et al*. and Fraser *et al*. demonstrate that productivity is an uninformative predictor of richness for most grasslands. A combined analysis using both data sets yields similar results (Table 1).

A second point of agreement is the difficulty of inferring process from bivariate patterns. The HBM can arise through a wide array of mechanisms (*3*, *4*), meaning that the detection of a unimodal pattern does not provide evidence for any particular mechanism.

Adler *et al*. argued, "[e]cologists should focus on fresh, mechanistic approaches to understanding the multivariate links between productivity and richness" (*2*). Fraser *et al*. also concluded "more work is needed to determine the underlying causal mechanisms that drive the unimodal pattern" and called for "additional efforts to understand the multivariate drivers of species richness."

The key disagreement between Fraser *et al*. and Adler *et al*. concerns the statistical significance of the quadratic term that determines the downward concavity of the richness productivity relationship. Adler *et al*. found little evidence for a concave-down relationship at the site scale (2% of 48 sites) [figure 2 in (*2*)] and at the global scale reported a significant effect but noted that it was sensitive to choices about which sites to include in the analysis [figure 3 in (*2*)]. In contrast, Fraser *et al*. found that 68% of 28 site-level relationships were significantly concave-down [figure 2A in (*1*)], and in a global extent regression, across all sites, the negative quadratic term had a significant, and robust, *P* value. However, their analysis at the site level is flawed, and the presentation of the global regression in their main figure is misleading.

The site-level regressions reported by Fraser *et al*. and displayed in their figure 2A do not include the proper random-effects structure. An important feature of the Fraser *et al*. design was explicitly selecting areas (i.e., grids) to sample across productivity gradients within sites, whereas Adler *et al*. located blocks of plots randomly with respect to local productivity gradients. To properly reflect their sampling design, in which each "grid" of quadrats was located at one point along the within-site productivity gradient, each site-level

[1]Department of Wildland Resources and the Ecology Center, Utah State University, 5230 Old Main, Logan, UT 84322, USA. [2]U.S. Geological Survey, Wetland and Aquatic Research Center, 700 Cajundome Boulevard, Lafayette, LA 70506, USA. [3]Department of Physiological Diversity, Helmholtz Center for Environmental Research – UFZ, Permoserstrasse 15, 04318 Leipzig, Germany. [4]Department of Ecology, Evolution, and Behavior, University of Minnesota, St. Paul, MN 55108, USA. [5]Department of Biology, Wake Forest University, Box 7325 Reynolda Station, Winston-Salem, NC 27109, USA. [6]School of Environmental and Forest Sciences, University of Washington, 3501 NE 41st Street, Box 354115, Seattle, WA 98195, USA. [7]Ecology, Evolution and Organismal Biology, Iowa State University, 251 Bessey Hall, Ames, IA 50010, USA. [8]Department of Bioagricultural Sciences and Pest Management, Colorado State University, 307 University Avenue, Fort Collins, CO 80523, USA. [9]School of Natural Sciences, Trinity College Dublin, University of Dublin, Zoology, Dublin 2, Ireland. [10]School of Life Sciences, Sun Yat-sen University, Xingang Xi Road 135, Guangzhou, 510275, China. [11]Department of Biology, University of New Mexico, Albuquerque, NM 87131, USA. [12]Department of Biology, Imperial College London, Silwood Park, Ascot, SL5 7PY, UK. [13]Grassland, Soil, and Water Research Laboratory, USDA-ARS, 808 East Blackland Road, Temple, TX 76502, USA. [14]School of Earth, Environmental and Biological 42 Sciences, Queensland University of Technology (QUT), Gardens Point, Brisbane, Queensland, Australia, 4001. [15]Department of Entomology, University of Maryland, 4112 Plant Sciences, College Park, MD 20742, USA. [16]School of Life Sciences, University of KwaZulu-Natal, 1 Carbis Road, Pietermaritzburg, 3201, South Africa. [17]Department of Biology, Ecology and Biodiversity group, Utrecht University, Padualaan 8, 3584 CH Utrecht, Netherlands. [18]Department of Plant Sciences, University of Oxford, South Parks Road, Oxford, OX1 3RB, UK. [19]Institute for Chemistry and Biology of the Marine Environment, Carl-von-Ossietzky University Oldenburg, Schleusenstrasse 1, 26382 Wihlhemshaven, Germany. [20]School of Biological Sciences, University of Nebraska, 211 Manter Hall, Lincoln, NE 68588, USA. [21]Biology Department, Doane College, 1014 Boswell Avenue, Crete, NE 68333, USA. [22]Department of Integrative Biology, University of Guelph, 50 Stone Road, Guelph, Ontario, Canada N1G 2W1. [23]Department of Plant and Soil Science, University of Kentucky, N-222D Ag Science North, Lexington, KY 40546-0091, USA. [24]Department of Biology, University of North Carolina at Chapel Hill, CB#3280, Chapel Hill, NC 27599, USA. [25]School of Biological Sciences, Monash University, Clayton Campus, Wellington Road, Clayton 3800, Victoria, Australia. [26]Department of Ecology, Environment and Evolution, La Trobe University, Kingsbury Drive, Bundoora 3086, Victoria, Australia. [27]Department of Zoology, University of Wisconsin, 430 Lincoln Drive, Madison, WI 53706, USA. [28]Department of Forestry, Agriculture and Water, Southern Patagonia National University-INTA-CONICET, CC 332 (CP 9400), Río Gallegos, Santa Cruz, Patagonia, Argentina. [29]Commonwealth Scientific and Industrial Research Organisation Land and Water, Private Bag 5, Wembley, WA 6913, Australia. [30]Community Ecology, Swiss Federal Institute for Forest, Snow and Landscape Research, Zuercherstrasse 111, 8903 Birmensdorf, Switzerland. [31]Department of Ecology, INIBIOMA (CONICET-UNCO), Quintral 1250, Bariloche (8400), Rio Negro, Argentina. [32]School of Veterinary and Life Sciences, Murdoch University, Perth, Western Australia, 90 South Street, Murdoch, Western Australia 6150. [33]School of Biological Sciences, University of Sydney, Heydon-Laurence Building, A08, University of Sydney, Sydney, NSW, 2006, Australia. [34]Agricultural and Biosystems Engineering, Iowa State University, Ames, IA, USA. [35]Department of Entomology and Nematology, University of California, Davis, One Shields Avenue, Davis, CA 95616, USA.

***Corresponding author. E-mail: atredenn@gmail.com** †Core authors that led the analysis and wrote the paper. All other authors, listed alphabetically, are Nutrient Network members and/or coauthors of Adler *et al*. (2011) who sign our Comment in support to show consensus among the Nutrient Network.

Downloaded from on January 31, 2016

Table 1. Results from global-extent GLMMs for both data sets. Results from regressions with and without a quadratic effect of productivity on species richness across all sites. Both models include a random-effects structure of grid nested within site (Fraser *et al*.) or block nested within site (Adler *et al*.). Marginal and conditional R^2 values estimated using (*7*, *8*). For the combined analysis, we use the same grid (or block) nested within-site random-effects structure and also include a "study" random effect.

Data set	Model type	Marginal R^2 (variance explained by fixed effects)	Conditional R^2 (variance explained by fixed + random effects)	Root mean square error (in units of species number)
Fraser *et al*.	Linear	0.00007	0.84	8.5
Fraser *et al*.	Quadratic	0.009	0.84	8.3
Adler *et al*.	Linear	0.0007	0.79	7.7
Adler *et al*.	Quadratic	0.001	0.78	7.7
Combined	Linear	0.00005	0.82	8.4
Combined	Quadratic	0.003	0.82	8.3

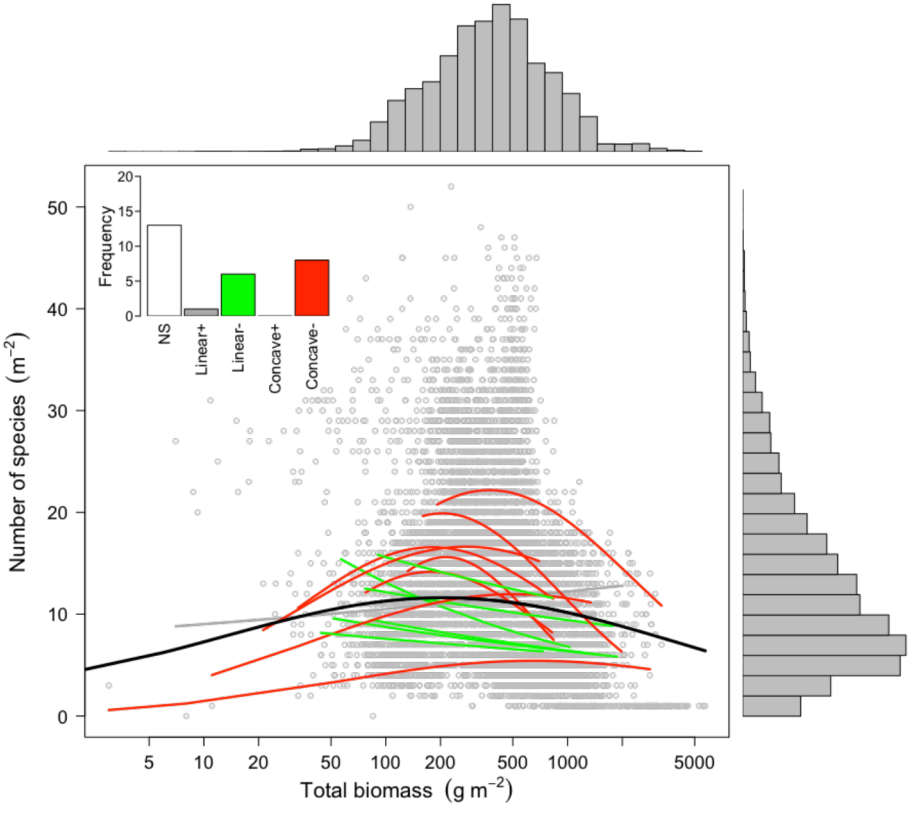


Fig. 1. Species richness as a function of biomass production at the site level (colored lines) and at the global extent (heavy black line). These regressions are the same as presented by Fraser *et al*. except that we included a grid random effect for the site-level regressions, and we show the proper global extent regression line from a GLMM with grid nested within site. Nonsignificant regression fits are not plotted.

regression requires a random effect of "grid" to account for the inherent correlation among plots nested within a sampling grid. We reran the analysis of Fraser *et al*. with the grid random effect included (*5*), except for one site (*6*). When the proper statistical model is used, we find that only 29% of 28 site-level regressions are significantly concave-down (Fig. 1).

Fraser *et al*. correctly account for their sampling design at the global extent by using a GLMM with grid nested within site, as reported in their table 1. However, in their figure 2A, they plot the much more compelling fit from the statistical model without the random effects. Although still significant ($P < 0.0001$), the valid relationship is much weaker than the relationship presented by Fraser *et al*. (Fig. 1, heavy black line, and Table 1).

Despite Fraser *et al*.'s assertion that their results are diametrically opposed to those presented in Adler *et al*., the degree of concordance is impressive. In both data sets, the variance explained by the addition of a quadratic term is virtually indistinguishable from that of a linear model (Table 1). In fact, in both data sets the random effects of site and grid (block for Adler *et al*.) explain much more of the variation in species richness than productivity, the supposed mechanistic driver of species richness (Table 1). Furthermore, with the appropriate statistical treatment, the main difference in our results—the strength of evidence for a significant quadratic term—appears smaller.

A continued focus on this bivariate relationship hinders progress toward understanding the underlying multivariate causal relationship (*4*) and the development of truly predictive models. It is time to focus on effect sizes and variance explained rather than just *P* values. The title of Adler *et al*.'s paper, "Productivity is a poor predictor of plant species richness," would be a perfectly appropriate title for the Fraser *et al*. paper, too.

REFERENCES AND NOTES

1. L. H. Fraser *et al*., *Science* **349**, 302–305 (2015).
2. P. B. Adler *et al*., *Science* **333**, 1750–1753 (2011).
3. J. B. Grace *et al*., *Science* **335**, 6075 (2012).
4. J. B. Grace *et al*., *Nature* **529**, 10.1038/nature16524 (2016).
5. We used the "lme4" package in the statistical programming environment R to fit the GLMMs at the site and global extents. Some models struggled to converge on coefficient estimates, a well-known issue with mixed-effects models. We conducted the analyses using different optimizers to make sure that our results are robust (they are), and we did our own checks of model diagnostics to make sure that the warnings could be ignored (they could). Lastly, we fit a hierarchical mixed-effects model using a Bayesian approach to make sure we obtained consistent results (we did). All of our analyses and results can be found on GitHub at http://github.com/atredennick/prodDiv and as release v0.1, https://github.com/atredennick/prodDiv/tag/v0.1
6. There are four sites, out of 28, that have only two grids. In only one case did this result in inadequate fits of the GLMM model with a "grid" random effect. We therefore fit that one site with a generalized linear model with no random effects.
7. S. Nakagawa, H. Schielzeth, *Methods Ecol. Evol.* **4**, 133–142 (2013).
8. J. Lefcheck, R-squared for generalized linear mixed-effects models (2014); https://github.com/jslefche/rsquared.glmm

ACKNOWLEDGMENTS

We thank L. Fraser and colleagues for making their analyses and data openly available. D. Johnson, USGS, provided comments on an earlier version of the manuscript. J.B.G. was supported by the USGS Ecosystems and Climate and Land Use Change Programs. The use of trade, firm, or product names is for descriptive purposes only and does not imply endorsement by the U.S. Government. USDA is an equal opportunity employer. We also acknowledge support from the National Science Foundation Research Coordination Network (NSF-DEB-1042132) and Long Term Ecological Research (NSF-DEB-1234162 to Cedar Creek LTER) programs, and the Institute on the Environment (DG-0001-13).

16 October 2015; accepted 17 December 2015
10.1126/science.aad6236

TECHNICAL RESPONSE

PLANT ECOLOGY

Response to Comment on "Worldwide evidence of a unimodal relationship between productivity and plant species richness"

Jason Pither,[1]* Lauchlan H. Fraser,[2] Anke Jentsch,[3] Marcelo Sternberg,[4] Martin Zobel,[5] James Cahill,[6] Carl Beierkuhnlein,[7] Sándor Bartha,[8,9] Jonathan A. Bennett,[5,6] Bazartseren Boldgiv,[10] Leslie R. Brown,[11] Marcelo Cabido,[12] Giandiego Campetella,[13] Cameron N. Carlyle,[14] Stefano Chelli,[13] Anna Mária Csergő,[15] Sandra Diaz,[16] Lucas Enrico,[16] David Ensing,[17] Alessandra Fidelis,[18] Heath W. Garris,[2] Hugh A. L. Henry,[19] Maria Höhn,[20] John Klironomos,[1] Kadri Koorem,[5] Rachael Lawrence-Lodge,[21] Peter Manning,[22] Randall J. Mitchell,[23] Mari Moora,[5] Valério D. Pillar,[24] Gisela C. Stotz,[6] Shu-ichi Sugiyama,[25] Szilárd Szentes,[26] Radnaakhand Tungalag,[10] Sainbileg Undrakhbold, Camilla Wellstein,[27] Talita Zupo[18]

Tredennick *et al*. criticize one of our statistical analyses and emphasize the low explanatory power of models relating productivity to diversity. These criticisms do not detract from our key findings, including evidence consistent with the unimodal constraint relationship predicted by the humped-back model and evidence of scale sensitivities in the form and strength of the relationship.

Tredennick *et al.* (*1*), among them many contributors to the original Adler *et al.* study (*2*), argue that our findings (*3*) align closely with those of Adler *et al.* once their criticisms (described below) are addressed. This is not the case. Tredennick *et al.* fail to acknowledge key findings of ours that remain at odds with those of Adler *et al.*, including (i) a significantly concave-down, global-extent relationship between productivity and richness; (ii) a significantly concave-down, global-extent quantile regression, consistent with the constraint prediction of the humped-back model (HBM); and (iii) our finding that patterns consistent with the HBM appear more evident when a broad range of productivity is sampled.

Tredennick *et al.* present three main criticisms of our study: (i) the analyses of the within-site productivity-diversity relationship should have included sample "grid" as a random effect, thereby accounting for our nested sampling design; (ii) our analyses focused too much on the significance of the quadratic term and not enough on the limited explanatory power of the models; and (iii) our figure 2A (*3*) was "misleading" and should have included a line representing the mixed-effects model for the global-extent relationship. We address each of these in turn.

(i) We agree that including "grid" as a random effect within mixed-effects models would be a reasonable approach. In our within-site analyses, we intentionally replicated the within-site analyses of Adler *et al.*, who did not accommodate the nestedness inherent to their sampling design. In hindsight, we regret not including the results of mixed-effects models for our within-site analyses in the supplementary materials, as we did for all other analyses. We made our data publicly available, which enabled Tredennick *et al.* to conduct analyses of their own, finding that 8 (29%) rather than 19 (69%) of the 28 within-site analyses yielded a significant concave-down relationship when "grid" is included as a random effect. Crucially, these revised analyses by Tredennick *et al.* have no effect on the global models we presented that form the main conclusion of the study. Also, thanks to Tredennick *et al.* making their data and analyses publicly available, we found that the 8 sites that did exhibit a significantly concave-down relationship in their analyses encompassed a significantly larger range of productivity (on the $\log_{10}$ scale) than the 13 sites where no association was found (permutation test on the difference in mean productivity; 9999 permutations; Z score = 2.09; P = 0.039). Moreover, the probability of detecting a concave-down relationship (i.e., significant quadratic term) over no relationship using the mixed-effects modeling approach tended to increase with increasing biomass range (logistic regression; residual deviance = 22.6 on 19 df; P = 0.078).

(ii) We recognize that regressions modeling the mean trend between productivity and richness yield limited explanatory power, and stated so in our Report (*3*). We suggest that Tredennick *et al.*'s focus on the mean trend is misplaced because, provided one samples a sufficiently broad range of productivity, the HBM predicts a constraint relationship, whereby richness is constrained to low levels at very low and very high productivity. Our study provided evidence of this, in the form of a significantly concave-down, global-extent quantile regression (both with and without random effects included). Adler *et al.* also tested for such a constraint relationship (without random effects) but failed to detect it, possibly because of limits to their sampling (*3*). For our analyses of mean trends, we focused on the form of the relationship, and hence the significance of the quadratic term, because this—not explanatory power—lies at the heart of the debate surrounding the HBM (*4*, *5*). Our sampling design and sampling scope allowed us to test the sensitivity of the form of the relationship to varying sampling grains and extents.

(iii) We formatted our figure 2A (*3*) with the objective of making it directly comparable to the results presented by Adler *et al.* (*2*), specifically their figure 2, and their global-extent regression, which was displayed in their figure 3. Adler *et al.* did not account for nested sampling structure in any of their analyses (i.e., using mixed-effects models), including within their global-extent analysis that yielded a significantly concave-down

[1]Department of Biology, University of British Columbia, Okanagan Campus, Kelowna, BC, Canada. [2]Department of Natural Resource Sciences, Thompson Rivers University, Kamloops, BC, Canada. [3]Department of Disturbance Ecology, BayCEER, University of Bayreuth, Bayreuth, Germany. [4]Department of Molecular Biology and Ecology of Plants, Tel Aviv University, Tel-Aviv, Israel. [5]Department of Botany, Institute of Ecology and Earth Sciences, University of Tartu, Tartu, Estonia. [6]Department of Biological Sciences, University of Alberta, Edmonton, Alberta, Canada. [7]Department of Biogeography, Bayreuth Center of Ecology and Environmental Research (BayCEER), University of Bayreuth, Bayreuth, Germany. [8]Hungarian Academy of Sciences Centre for Ecological Research, Institute of Ecology and Botany, Vácrátót, Hungary. [9]School of Plant Biology, University of Western Australia, Crawley, Australia. [10]Ecology Group, Department of Biology, National University of Mongolia, Ulaanbaatar, Mongolia. [11]Department of Environmental Sciences, University of South Africa, Florida, South Africa. [12]Facultad de Ciencias Exactas, Físicas y Naturales, Universidad Nacional de Córdoba, Córdoba, Argentina. [13]School of Biosciences and Veterinary Medicine, Plant Diversity and Ecosystems Management Unit, University of Camerino, Camerino, Italy. [14]Department of Agricultural, Food and Nutritional Science, University of Alberta, Edmonton, Canada. [15]School of Natural Sciences, Trinity College Dublin, The University of Dublin, Dublin, Ireland. [16]Instituto Multidisciplinario de Biología Vegetal (IMBIV), National Scientific and Technical Research Council and Facultad de Ciencias Exactas, Físicas y Naturales, Universidad Nacional de Córdoba, Córdoba, Argentina. [17]Department of Biology, Queen's University, Kingston, Ontario, Canada. [18]Departamento de Botânica, UNESP – Universidade Estadual Paulista, Rio Claro, SP, Brazil. [19]Department of Biology, University of Western Ontario, London, Ontario, Canada. [20]Department of Botany, Faculty of Horticultural Science, Corvinus University of Budapest, Hungary. [21]Department of Botany, University of Otago, Dunedin, New Zealand. [22]Biodiversity and Climate Research Centre, Senckenberg Gesellschaft für Naturforschung, Germany. [23]Department of Biology, University of Akron, Akron, OH, USA. [24]Department of Ecology, Federal University of Rio Grande do Sul, Porto Alegre, Brazil. [25]Faculty of Agriculture and Life Science, Hirosaki University, Aomori, Japan. [26]Institute of Plant Production, Szent István University, Gödöllő, Hungary. [27]Faculty of Science and Technology, Free University of Bozen-Bolzano, Bolzano, Italy.
*Corresponding author. E-mail: jason.pither@ubc.ca

Downloaded from on January 31, 2016

relationship. We therefore opted to show our analogous regression results in figure 2A (*3*). We showed the results of our mixed-effects model for the global relationship in figure S1 (*3*).

We encourage future research to (i) explore why low species richness (per unit area) is found at the extreme ends of the productivity gradient and (ii) determine the processes that suppress species richness below its potential at intermediate levels of productivity.

REFERENCES

1. A. T. Tredennick *et al.*, *Science* **351**, 457 (2016).
2. P. B. Adler *et al.*, *Science* **333**, 1750–1753 (2011).
3. L. H. Fraser *et al.*, *Science* **349**, 302–305 (2015).
4. J. P. Grime, *J. Environ. Manage.* **1**, 151–167 (1973).
5. L. H. Fraser, A. Jentsch, M. Sternberg, *J. Veg. Sci.* **25**, 1160–1166 (2014).

16 November 2015; accepted 17 December 2015
10.1126/science.aad8019



The delegations gathered at CNEURO's new Havana headquarters, completed in 2014.

U.S. and Cuban researchers begin neuroscience collaborations

The projects reflect a decades-long commitment by AAAS to foster partnerships with Cuban scientists

By **Becky Ham**

Guided by a historic 2014 agreement, scientists from the United States and Cuba have identified three areas of neuroscience as the focus of new research collaborations between the two countries.

The focus areas include magnetic resonance imaging technology and neuroinformatics, neurodevelopment, and a plan to establish an international nonhuman primate research center in Cuba. At their 11 to 13 December 2015 meeting in Havana, participants also discussed a biomedical research fellows exchange program for early and midcareer scientists in both countries.

One part of the exchange program, administered by the AAAS Center for Science Diplomacy and supported with a grant from the Lounsbery Foundation, may bring Cuban scientists to the United States as early as May, said Marga Gual Soler, project director at the AAAS center. She said the center is also working to identify funds to bring U.S.-based scientists to Cuba. "We hope this will be a very horizontal collaboration, where we can eventually place many scientists in top labs in both countries."

The December meeting, organized by AAAS and the Cuban Neurosciences Center (CNEURO), fulfills part of the 2014 agreement by AAAS and the Cuban Academy of Sciences. In their memorandum of understanding, the two organizations pledged to advance scientific cooperation between the United States and Cuba in areas of mutual interest.

The United States delegation included participants from the academic, industry, policy, and foundation sectors, who met with their Cuban counterparts to discuss the latest research advances in neurodegenerative and psychiatric disorders, brain mapping techniques, and therapeutics. The delegation also visited the Drug Regulatory Authority (CECMED), the National Clinical Trials Coordinating Center (CENCEC), and the Center for Molecular Immunology (CIM).

The research topics identified "are already part of the Cuban strength in working full-cycle from the lab to primary health, with a demonstrated impact on health indicators in Cuba and other countries," said Pedro Valdés Sosa, CNEURO's general vice-director for research and leader of the Cuban delegation. "And for areas in which we have strengths, such as neuroinformatics and translational neuroscience, I hope the introduction of these results in primary health would be of benefit to the U.S."

CNEURO is outfitted with equipment like a powerful, high-resolution 3 Tesla MRI system that keeps its researchers at the forefront of medical imaging technology, Valdés Sosa said. He now hopes for "intensive exchange that will allow Cuban neuroscientists to assimilate cutting-edge technologies and knowledge to be integrated into our current research programs."

Mark Rasenick, a professor of physiology and psychiatry at the University of Illinois at Chicago and a fellow of both AAAS and the Cuban Academy, is among a handful of U.S. scientists who have seen for themselves the dynamic and productive pace of Cuban science during 20 years' worth of visits. The re-establishment of diplomatic ties between the two countries in 2015 seems to have invigorated the Cuban scientific community, said Rasenick. "I was there last year, and the changes are remarkable in just a year. You can see a vibrancy, you can see money being put into research and buildings."

Even during difficult economic times for the country, when the government lost much outside financial support after the

PHOTO: MARGA GUAL SOLER

Downloaded from on January 31, 2016

Published by AAAS

collapse of the Soviet Union in 1991, "there was always a resolve to try and do science," Rasenick continued. "But now that there are beginning to be more resources available, there is an enthusiasm, especially among younger people working there, and a feeling that things are going to be better for scientists."

U.S. scientists want to work with Cuban researchers in areas where the neuroscience community there has made tremendous strides, he said, including sophisticated imaging techniques. Pharmaceutical companies are also eager to collaborate with Cuban scientists on clinical trials, given the island's diverse population and extensive health care records.

Rasenick said that the U.S.-Cuba economic embargo still is a significant barrier to sharing technology and equipment between labs in the two countries, and could keep large numbers of U.S. scientists from working in Cuba. "The embargo is as much of a relic as those late 1950s cars that are so popular on the island," he said. "We still have a number of impediments to research, and in order to fix them, we need to end the embargo."

Valdés Sosa noted that scientists in the United States and Cuba have a long history of working together. One of the founding fathers of CNEURO, he pointed out, was renowned New York University neuroscientist Erwin Roy John, who collaborated with Valdés Sosa and other Cuban researchers on a 1977 *Science* paper.

The groundwork laid in the past two decades by the Cuban Academy and AAAS "have led to specific suggestions that make the most of the current, more positive situation of U.S.-Cuba relations, and help us plan for a more open future," said Valdés Sosa. ■

Call for nomination of 2016 fellows

Fellows who are current members of AAAS are invited to nominate members for election as Fellows. A member whose efforts on behalf of the advancement of science or its applications are scientifically or socially distinguished, and who has been a continuous member for the 4-year period leading up to the year of nomination, may by virtue of such meritorious contribution be elected a Fellow by the AAAS Council.

A nomination must be sponsored by three previously elected AAAS Fellows (who are current in their membership), two of whom must have no affiliation with the nominee's institution.

Nominations undergo review by the steering groups of the Association's sections (the chair, chair-elect, retiring chair, secretary, and four members-at-large of each section). Each steering group reviews only those nominations designated for its section. Names of Fellow nominees who are approved by the steering groups are presented to the Council in the fall for election.

Nominations with complete documentation must be received by 20 April 2016. Nominations received after that date or nominations that are incomplete as of the deadline will not move forward. Complete instructions and a copy of the nomination form are available at www.aaas.org/current-nomination-cycle. Questions may be directed to fellownomination@aaas.org.

Results of the 2015 election of AAAS officers

Following are the results of the 2015 election. Terms begin on 16 February 2016.

GENERAL ELECTION

President-Elect: Susan Hockfield, Massachusetts Institute of Technology

Board of Directors: Cynthia M. Beall, Case Western Reserve Univ.; May R. Berenbaum, Univ. of Illinois at Urbana-Champaign

Committee on Nominations: Alice M. Clark, Univ. of Mississippi; Susan L. Graham, Univ. of California, Berkeley; William H. Press, Univ. of Texas at Austin; Peter H. Raven, Missouri Botanical Garden

SECTION ELECTIONS

Agriculture, Food, and Renewable Resources

Chair Elect: Lisa Ainsworth, USDA-ARS/Univ. of Illinois at Urbana-Champaign

Member-at-Large of the Section Committee: Mel Oliver, Univ. of Missouri

Electorate Nominating Committee: C. Robin Buell, Michigan State Univ.; Neelima Roy Sinha, Univ. of California, Davis

Anthropology

Chair Elect: Carol V. Ward, Univ. of Missouri School of Medicine

Member-at-Large of the Section Committee: Steven R. Leigh, Univ. of Colorado Boulder

Electorate Nominating Committee: J. Josh Snodgrass, Univ. of Oregon; Deborah Winslow, National Science Foundation

Council Delegate: Clark Spencer Larsen, Ohio State Univ.

Astronomy

Chair Elect: Kathryn Flanagan, Space Telescope Science Institute

Member-at-Large of the Section Committee: Steven D. Kawaler, Iowa State Univ.

Electorate Nominating Committee: Tom Abel, Stanford Univ./SLAC National Accelerator Laboratory; David R. Soderblom, Space Telescope Science Institute

Council Delegate: Chryssa Kouveliotou, George Washington Univ.

Atmospheric and Hydrospheric Sciences

Chair Elect: Joan Kleypas, National Center for Atmospheric Research

Member-at-Large of the Section Committee: Drew T. Shindell, Duke Univ.

Electorate Nominating Committee: Rob Jackson, Stanford Univ.; Jean Lynch-Stieglitz, Georgia Institute of Technology

Biological Sciences

Chair Elect: Elizabeth (Toby) Kellogg, Donald Danforth Plant Center

Member-at-Large of the Section Committee: Marisa S. Bartolomei, Univ. of Pennsylvania Perelman School of Medicine

Electorate Nominating Committee: Marnie E. Halpern, Carnegie Institution for Science; Mary Ann Moran, Univ. of Georgia

Council Delegate (1-year term): James R. Broach, Pennsylvania State Univ. College of Medicine; Jessica Gurevitch, Stony Brook Univ.

Council Delegate (2-year term): Jennifer Jane Loros, Dartmouth College; Ann K. Sakai, Univ. of California, Irvine

Published by AAAS

Council Delegate (3-year term): Carol Dieckmann, Univ. of Arizona; Susan M. Rosenberg, Baylor College of Medicine; Susan R. Ross, Univ. of Illinois at Chicago

Chemistry

Chair Elect: Karen I. Goldberg, Univ. of Washington

Member-at-Large of the Section Committee: Judith N. Burstyn, Univ. of Wisconsin-Madison

Electorate Nominating Committee: Michelle Chang, Univ. of California, Berkeley/Lawrence Berkeley National Laboratory; Mercouri G. Kanatzidis, Northwestern Univ./Argonne National Laboratory

Council Delegate (1-year term): Nancy E. Levinger, Colorado State Univ.

Council Delegate (2-year term): Seth M. Cohen, Univ. of California, San Diego

Council Delegate (3-year term): Melissa A. Hines, Cornell Univ.

Dentistry and Oral Health Sciences

Chair Elect: Janet Moradian-Oldak, Univ. of Southern California

Member-at-Large of the Section Committee: Thomas E. Van Dyke, Forsyth Institute/Harvard Univ.

Electorate Nominating Committee: Renny T. Franceschi, Univ. of Michigan; Mary MacDougall, Univ. of Alabama at Birmingham

Education

Chair Elect: Muriel E. Poston, Pitzer College

Member-at-Large of the Section Committee: Ann Reid, National Center for Science Education

Electorate Nominating Committee: John R. Jungck, Univ. of Delaware; Dennis Schatz, Pacific Science Center

Engineering

Chair Elect: Linda P. B. Katehi, Univ. of California, Davis

Member-at-Large of the Section Committee: Nadine Aubry, Northeastern Univ.

Electorate Nominating Committee: Nancy Jackson, Sandia National Laboratories; Robert M. Kelly, North Carolina State Univ.

General Interest in Science and Engineering

Chair Elect: Bruce V. Lewenstein, Cornell Univ.

Member-at-Large of the Section Committee: Erica Goldman, COMPASS

Electorate Nominating Committee: Barbara Gastel, Texas A&M Univ.; Erika C. Shugart, American Society for Microbiology

Geology and Geography

Chair Elect: Bruce H. Corliss, Univ. of Rhode Island

Member-at-Large of the Section Committee: Paul A. Baker, Duke Univ.

Electorate Nominating Committee: Laurie C. Anderson, South Dakota School of Mines and Technology; Frank W. Davis, Univ. of California, Santa Barbara

Council Delegate: Louis A. Derry, Cornell Univ.

History and Philosophy of Science

Chair Elect: Nancy J. Nersessian, Georgia Institute of Technology

Member-at-Large of the Section Committee: Alan C. Love, Univ. of Minnesota

Electorate Nominating Committee: Marsha L. Richmond, Wayne State Univ.; Rose-Mary Sargent, Merrimack College

Industrial Science and Technology

Chair Elect: Enrique J. Lavernia, Univ. of California, Irvine

Member-at-Large of the Section Committee: Thomas Zacharia, Oak Ridge National Laboratory/UT-Batelle, LLC

Electorate Nominating Committee: Stephen P. Long, Univ. of Illinois at Urbana-Champaign; Stuart Parkin, Martin Luther Univ. of Halle-Wittenberg/Max Planck Institute of Microstructure Physics (Germany)

Information, Computing, and Communication

Chair Elect: Henry Kautz, Univ. of Rochester

Member-at-Large of the Section Committee: Carla E. Brodley, Northeastern Univ.

Electorate Nominating Committee: Vasant G. Honavar, Pennsylvania State Univ.; Adele F. Howe, Colorado State Univ.

Linguistics and Language Science

Chair Elect: Joan A. Sereno, Univ. of Kansas

Member-at-Large of the Section Committee: Colin Phillips, Univ. of Maryland, College Park

Electorate Nominating Committee: Danny Fox, Massachusetts Institute of Technology; Louise McNally, Pompeu Fabra Univ. (Spain)

Mathematics

Chair Elect: Linda Petzold, Univ. of California, Santa Barbara

Member-at-Large of the Section Committee: Carlos Castillo-Chavez, Arizona State Univ.

Electorate Nominating Committee: Charles L. Epstein, Univ. of Pennsylvania; Ilse Ipsen, North Carolina State Univ.

Council Delegate: Juan C. Meza, Univ. of California, Merced

Medical Sciences

Chair Elect: Gregory A. Petsko, Weill Cornell Medical College

Member-at-Large of the Section Committee: Arlene H. Sharpe, Harvard Medical School/Brigham and Women's Hospital

Electorate Nominating Committee: Paul A. Insel, Univ. of California, San Diego; Juanita L. Merchant, Univ. of Michigan Medical School

Council Delegate: Mary C. Dinauer, Washington Univ. School of Medicine in St. Louis

Neuroscience

Chair Elect: Edwin (Ted) Abel, Univ. of Pennsylvania

Member-at-Large of the Section Committee: Vivian Budnik, Univ. of Massachusetts Medical School

Electorate Nominating Committee: Kristen M. Harris, Univ. of Texas at Austin; John H. Morrison, Univ. of California, Davis

Council Delegate: Ronald L. Davis, Scripps Research Institute

Pharmaceutical Sciences

Chair Elect: Lynn Wecker, Univ. of South Florida Morsani College of Medicine

Member-at-Large of the Section Committee: John S. Lazo, Univ. of Virginia

Electorate Nominating Committee: Catherine E. Peishoff, GlaxoSmithKline; Rick G. Schnellmann, Medical Univ. of South Carolina

Physics

Chair Elect: Barbara A. Jones, IBM Almaden Research Center

Member-at-Large of the Section Committee: Andrew Millis, Columbia Univ.

Electorate Nominating Committee: Sally Dawson, Brookhaven National Laboratory; P. Chris Hammel, Ohio State Univ.

Council Delegate (2-year term): Nora Berrah, Univ. of Connecticut

Council Delegate (3-year term): E. Dan Dahlberg, Univ. of Minnesota

Psychology

Chair Elect: Nora S. Newcombe, Temple Univ.

Member-at-Large of the Section Committee: Patricia K. Kuhl, Univ. of Washington

Electorate Nominating Committee: Susan C. Levine, Univ. of Chicago; Jeffrey M. Zacks, Washington Univ. in St. Louis

Social, Economic, and Political Sciences

Chair Elect: Julia Lane, New York Univ.

Member-at-Large of the Section Committee: Ronald D. Lee, Univ. of California, Berkeley

Electorate Nominating Committee: Virginia S. Cain, National Center for Health Statistics/Center for Disease Control & Prevention; Phyllis Moen, Univ. of Minnesota

Societal Impacts of Science and Engineering

Chair Elect: Norine E. Noonan, Univ. of South Florida St. Petersburg

Member-at-Large of the Section Committee: David Goldston, Natural Resources Defense Council

Electorate Nominating Committee: Kathie L. Olsen, ScienceWorks International, LLC; Paula J. Olsiewski, Alfred P. Sloan Foundation

Statistics

Chair Elect: Kathryn Roeder, Carnegie Mellon Univ.

Member-at-Large of the Section Committee: Arlene S. Ash, Univ. of Massachusetts Medical School

Electorate Nominating Committee: Kim-Anh Do, Univ. of Texas MD Anderson Cancer Center; Katherine Bennett Ensor, Rice Univ./StatAnalyticsIDD

Published by AAAS

RESEARCH ARTICLE SUMMARY

MELANOMA INITIATION

A zebrafish melanoma model reveals emergence of neural crest identity during melanoma initiation

Charles K. Kaufman, Christian Mosimann, Zi Peng Fan, Song Yang, Andrew J. Thomas, Julien Ablain, Justin L. Tan, Rachel D. Fogley, Ellen van Rooijen, Elliott J. Hagedorn, Christie Ciarlo, Richard M. White, Dominick A. Matos, Ann-Christin Puller, Cristina Santoriello, Eric C. Liao, Richard A. Young, Leonard I. Zon*

INTRODUCTION: The "cancerized field" concept posits that cells in a given tissue sharing an oncogenic mutation are cancer-prone, yet only discreet clones within the field initiate tumors. Studying the process of cancer initiation has remained challenging because of (i) the rarity of these events, (ii) the difficulty of visiualizing initiating clones in living organisms, and (iii) the transient nature of a newly transformed clone emerging before it expands to form an early tumor. A more complete understanding of the molecular processes that regulate cancer initiation could provide important prognostic information about which precancerous lesions are most prone to becoming cancer and also implicate druggable molecular pathways that, when inhibited, may prevent the cancer from ever starting.

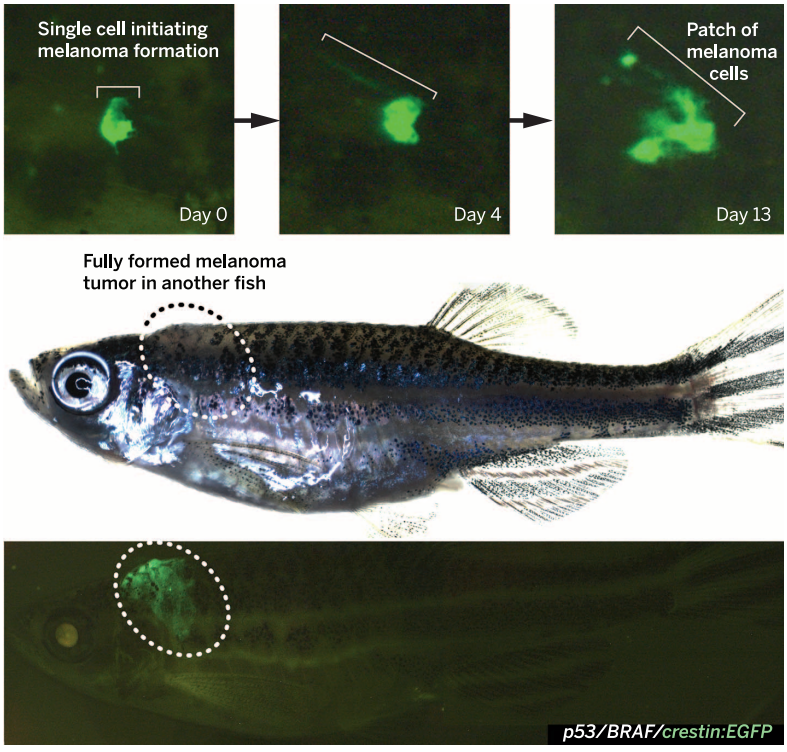
RATIONALE: The majority of benign nevi carry oncogenic *BRAF*^{V600E} mutations and can be considered a cancerized field of melanocytes, but they only rarely convert to melanoma. In an effort to define events that initiate cancer, we used a melanoma model in the zebrafish in which the human *BRAF*^{V600E} oncogene is driven by the melanocyte-specific *mitfa* promoter. When bred into a *p53* mutant background, these fish develop melanoma tumors over the course of many months. The zebrafish *crestin* gene is expressed embryonically in neural crest progenitors (NCPs) and is specifically reexpressed only in melanoma tumors, making it an ideal candidate for tracking melanoma from initiation onward.

RESULTS: We developed a *crestin:EGFP* reporter that recapitulates the embryonic neural crest expression pattern of *crestin* and its expression in melanoma tumors. We show through live imaging of transgenic zebrafish *crestin* reporters that within a cancerized field (*BRAF*^{V600E}-mutant; *p53*-deficient), a single melanocyte reactivates the NCP state, and this establishes that a fate change occurs at melanoma initiation in this model. Early *crestin*$^{+}$ patches of cells expand and are transplantable in a manner consistent with their possessing tumorigenic activity, and they exhibit a gene expression pattern consistent with the NCP identity readout by the *crestin* reporter. The *crestin* element is regulated by NCP transcription factors, including *sox10*. Forced *sox10* overexpression in melanocytes accelerated melanoma formation, whereas CRISPR/Cas9 targeting of *sox10* delayed melanoma onset. We show activation of super-enhancers at NCP genes in both zebrafish and human melanomas, identifying an epigenetic mechanism for control of this NCP signature leading to melanoma.

ON OUR WEB SITE

Read the full article at http://dx.doi.org/10.1126/science.aad2197

CONCLUSION: This work using our zebrafish melanoma model and in vivo reporter of NCP identity allows us to see cancer from its birth as a single cell and shows the importance of NCP-state reemergence as a key event in melanoma initiation from a field of cancer-prone melanocytes. Thus, in addition to the typical fixed genetic alterations in oncogenes and tumor supressors that are required for cancer development, the reemergence of progenitor identity may be an additional rate-limiting step in the formation of melanoma. Preventing NCP reemergence in a field of cancer-prone melanocytes may thus prove therapeutically useful, and the association of NCP genes with super-enhancer regulatory elements implicates the associated druggable epigenetic machinery in this process. ■



Neural crest reporter expression in melanoma. The *crestin:EGFP* transgene is specifically expressed in melanoma in *BRAF*^{V600E}/*p53* mutant melanoma-prone zebrafish. (Top) A single cell expressing *crestin:EGFP* expands into a small patch of cells over the course of 2 weeks, capturing the initiation of melanoma formation (bracket). (Bottom) A fully formed melanoma specifically expresses *crestin:EGFP*, whereas the rest of the fish remains *EGFP*-negative.

The list of author affiliations is available in the full article online.
*Corresponding author. E-mail: zon@enders.tch.harvard.edu
Cite this article as C. K. Kaufman *et al.*, *Science* **351**, aad2197 (2016). DOI: 10.1126/science.aad2197

Downloaded from on January 31, 2016

RESEARCH ARTICLE

MELANOMA INITIATION

A zebrafish melanoma model reveals emergence of neural crest identity during melanoma initiation

Charles K. Kaufman,[1,2,3,4] Christian Mosimann,[5] Zi Peng Fan,[6,7] Song Yang,[1,2] Andrew J. Thomas,[1] Julien Ablain,[1,2,4] Justin L. Tan,[1] Rachel D. Fogley,[1] Ellen van Rooijen,[1,2,4] Elliott J. Hagedorn,[1,2,4] Christie Ciarlo,[1,4] Richard M. White,[8] Dominick A. Matos,[9] Ann-Christin Puller,[10] Cristina Santoriello,[1,11] Eric C. Liao,[2,4,12] Richard A. Young,[6,13] Leonard I. Zon[1,2,3,4,11]*

The "cancerized field" concept posits that cancer-prone cells in a given tissue share an oncogenic mutation, but only discreet clones within the field initiate tumors. Most benign nevi carry oncogenic *BRAF*^{V600E} mutations but rarely become melanoma. The zebrafish *crestin* gene is expressed embryonically in neural crest progenitors (NCPs) and specifically reexpressed in melanoma. Live imaging of transgenic zebrafish *crestin* reporters shows that within a cancerized field (*BRAF*^{V600E}-mutant; *p53*-deficient), a single melanocyte reactivates the NCP state, revealing a fate change at melanoma initiation in this model. NCP transcription factors, including *sox10*, regulate *crestin* expression. Forced *sox10* overexpression in melanocytes accelerated melanoma formation, which is consistent with activation of NCP genes and super-enhancers leading to melanoma. Our work highlights NCP state reemergence as a key event in melanoma initiation.

Understanding the earliest events in cancer formation remains an incompletely fulfilled goal in biology, with important implications for human health. In cancer initiation, an activated oncogene or inactivated tumor suppressor can trigger tumor formation. However, it is unclear as to why only sporadic cells with these genetic alterations complete the conversion to a malignant state when they are present in a large group of cancer-prone cells, sometimes described as a "cancerized field" (*1*). Better characterizing initiating events would help identify targets for early therapeutic interventions and also provide prognostic information about which precancerous lesions are most likely to progress to cancer.

Melanoma is a cancer of transformed melanocytes, which are pigment-producing cells derived from the embryonic neural crest lineage. It is frequently driven by *BRAF* or *RAS* mutations (~80% of cases) (*2*, *3*). Melanoma is treatable and curable when it is localized and resected completely but remains largely incurable once it has spread, even when treated with new kinase- and immune checkpoint–targeted therapies (*4*). Our laboratory previously developed an animal model of a *BRAF*^{V600E}-driven cancer by placing the human *BRAF*^{V600E} gene under the control of the melanocyte-specific *mitfa*-promoter in transgenic zebrafish (*5*). When crossed into a *p53* mutant loss-of-function background, these zebrafish (referred to here as *p53/BRAF*) invariably develop nevi and, after several months, invasive melanoma (*5*). Despite creating this extensive "cancerized field" in which all melanocytes harbor both oncogenic *BRAF*^{V600E} and *p53* loss throughout their life span, these *p53/BRAF* melanoma–prone zebrafish all develop one to three melanoma tumors after several months of age, indicating that other molecular alterations are important for tumor initiation.

crestin transgenics mark neural crest

To investigate the dynamics and mechanism of sporadic melanoma formation, we visualized and characterized melanoma lesion initiation. The functionally uncharacterized zebrafish *crestin* gene marks the neural crest during embryonic development, becomes undetectable by ~72 hours after fertilization (*6*, *7*), and is specifically reexpressed in melanoma tumors in adult zebrafish (*8*). We reasoned that a *crestin*-based reporter transgene would allow us to track embryonic neural crest cells as well as melanoma tumors in vivo, potentially from their earliest onset. We amplified by means of polyermase chain reaction (PCR) a 4.5-kb upstream region common to multiple *crestin* insertions in the zebrafish genome and cloned this element upstream of an *enhanced green fluorescent protein* (*EGFP*) reporter (Fig. 1A, *crestin:EGFP*). In stable transgenic zebrafish embryos, this construct reproduced *crestin* mRNA expression through EGFP fluorescence (Fig. 1, B and C, and fig. S1A), and time-lapse videos demonstrated the dorsal emergence and wide migration of these *crestin*-expressing putative neural crest progenitor cells (movies S1 and S2). Neural crest expression was reproducible in multiple independent lines and with additional reporter genes (*creERT2* and *mCherry*) (Fig. 1, D to G, and fig. S5, A to C). As with endogenous *crestin* expression, transgenic *crestin:EGFP* expression was not detectable after 3 days after fertilization and did not come back on in wild-type juvenile or adult zebrafish.

To confirm that the *crestin* transgenes target neural crest progenitors, we also generated transgenics for *crestin:creERT2* to genetically mark *crestin*-expressing embryonic cells using a Cre/*lox*–dependent *EGFP*-to-*mCherry* switching line ("*ubi:switch*") (*9*) and genetically labeled neural crest-derived cells, including melanocytes/pigment cells (Fig. 1, D and E, red cells), jaw cartilage (Fig. 1F), and lateral line glia (Fig. 1G). Because the *crestin* gene is specific to zebrafish, we wanted to ensure that *crestin* reporter embryonic expression is consistent with another conserved early neural crest marker, the transcription factor *sox10*. Confocal analysis of double-transgenic *Tg(crestin_1kb:EGFP)* and *Tg(sox10:mCh)* (*10*) zebrafish embryos showed a high degree of overlap in reporter gene expression (Fig. 1H), with any differences matching published in situ hybridization (ISH) data (*11*). Thus, our *crestin* transgenic lines recapitulate *crestin* expression and specifically mark the embryonic neural crest stem/progenitor cell population.

crestin transgenics visualize melanoma initiation

We next determined whether *crestin:EGFP* is reexpressed in melanoma tumors, as noted previously by ISH (*8*). We found *crestin:EGFP* is expressed in tumors arising on triple transgenic *p53/BRAF/crestin:EGFP* adult zebrafish but is absent in the remainder of the animal, highlighting its specificity to the tumor (Fig. 2A). We next followed developing zebrafish in order to observe the onset of *crestin:EGFP*$^{+}$ expression. Before *EGFP*-expressing patches of cells formed raised melanoma lesions on a given fish (Fig. 2B), we were able to detect single isolated *EGFP*$^{+}$ cells in *p53/BRAF/crestin:EGFP* zebrafish (Fig. 2C). We could track their persistence and enlargement (fig. S2, A and B). Small patches of *EGFP*$^{+}$ cells, containing <50 cells, are readily tractable as they enlarge (fig. S2C). Analysis of single scales with

[1]Stem Cell Program and Division of Hematology/Oncology, Children's Hospital Boston, Howard Hughes Medical Institute, Boston, MA 02115, USA. [2]Harvard Stem Cell Institute, Boston, MA 02115, USA. [3]Department of Medical Oncology, Dana-Farber Cancer Institute, Boston, MA 02215, USA. [4]Harvard Medical School, Boston, MA 02115, USA. [5]Institute of Molecular Life Sciences, University of Zürich, 8057 Zürich, Switzerland. [6]Whitehead Institute for Biomedical Research, 9 Cambridge Center, Cambridge, MA 02142, USA. [7]Computational and Systems Biology Program, Massachusetts Institute of Technology, Cambridge, MA 02139, USA. [8]Memorial Sloan Kettering Cancer Center, Weill Cornell Medical College, New York, NY 10075, USA. [9]Massachusetts General Hospital Cancer Center, Harvard Medical School, Charlestown, MA 02129, USA. [10]Research Institute Children's Cancer Center Hamburg and Department of Pediatric Hematology and Oncology, University Medical Center Hamburg-Eppendorf, 20246 Hamburg, Germany. [11]Department of Stem Cell and Regenerative Biology, Harvard University, Cambridge, MA 02138, USA. [12]Center for Regenerative Medicine, Massachusetts General Hospital, Boston, MA 02114, USA. [13]Department of Biology, Massachusetts Institute of Technology, Cambridge, MA 02139, USA.
*Corresponding author. E-mail: zon@enders.tch.harvard.edu

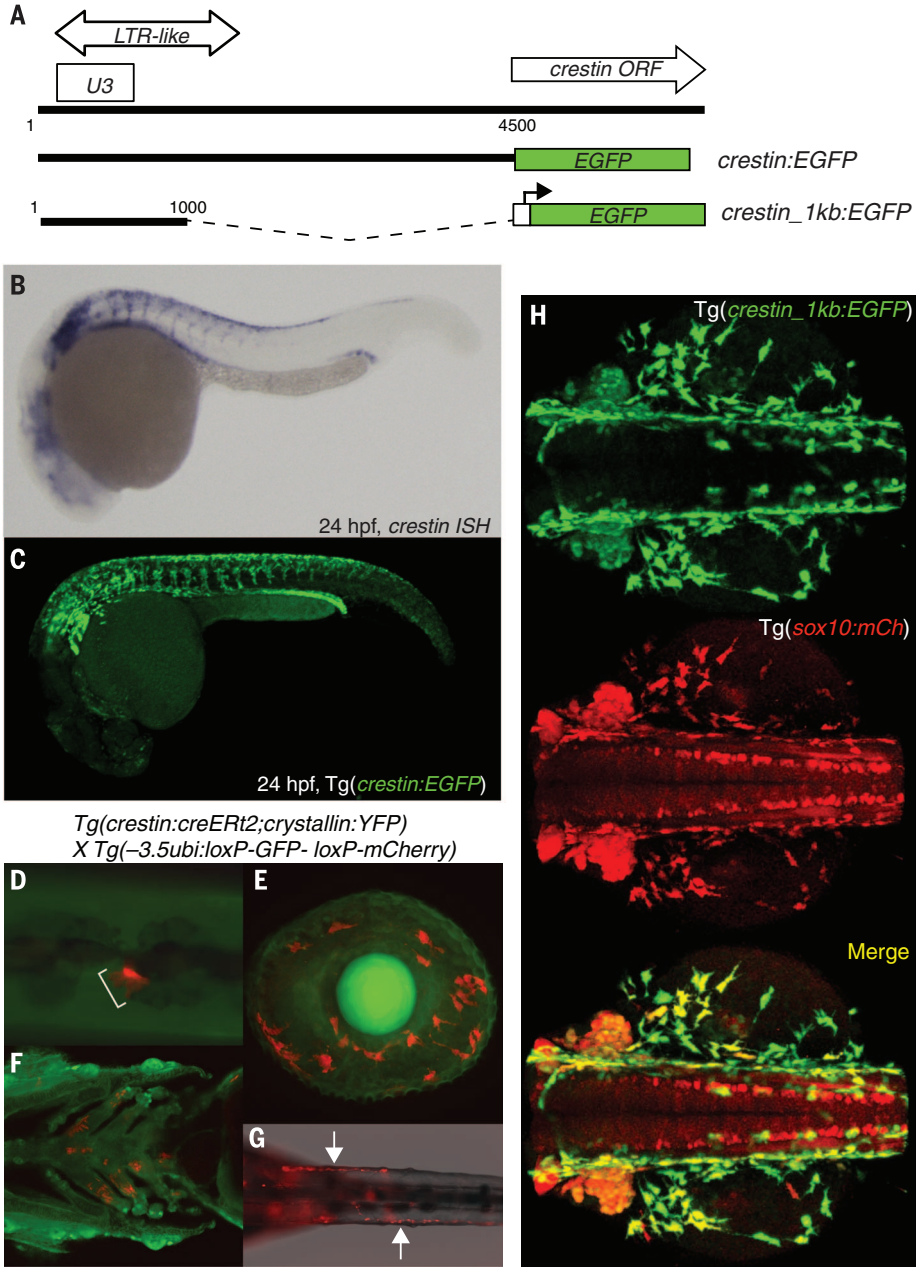


Fig. 1. The *crestin* promoter/enhancer drives neural crest-specific gene expression. (**A**) Prototypical *crestin* retrotransposon locus with predicted ORF, LTR-like, and U3-like promoter regions. Shown are locations of 4.5- and 1-kb segments used for *crestin:EGFP* constructs (white box/promoter arrow indicate β-globin gene minimal promoter). (**B**) Endogenous expression pattern of *crestin* transcript by means of ISH (purple staining) at 24 hours after fertilization marks developing and migrating neural crest cells. (**C**) This expression pattern (green) is recapitulated by a stable *Tg(crestin:EGFP)* embryo at 24 hours after fertilization. (**D** to **G**) Genetic lineage tracing of cells that express *crestin* [*Tg(crestin:creERt2;crystallin:YFP)* X *Tg(–3.5ubi:loxP-GFP-loxP-mCherry)*] marks multiple neural crest lineages (red cells), including melanocytes (bracket) on (D) the dorsum and (E) the eye (72 hours after fertilization), (F) jaw cartilage (ventral view, 5 days after fertilization), and (G) glial cells of the lateral line (arrows, dorsal view posterior to the yolk, 72 hours after fertilization). (**H**) *Tg(crestin:EGFP)* expression overlaps substantially with a *sox10:mCh* transgene (confocal image, dorsal view over yolk, 24 hours after fertilization).

discrete *crestin:EGFP*$^+$ patches demonstrated that transgene expression detectable with fluorescence microscopy overlaps with *crestin* mRNA detected with ISH (Fig. 2D). Together, these observations reveal that after pan-neural crest expression confined to the embryo, our *crestin* reporter expresses specifically and reproducibly in melanoma tumors, thus providing an in vivo genetic label for melanoma cells that is earlier than with previous detection methods (*5*, *12*).

We next addressed the dynamics of reemerging *crestin* expression in cohorts of *p53/BRAF/crestin:EGFP* zebrafish. At the population level, *crestin:EGFP*$^+$ patches of cells (fig. S1, B and C) were visible before the appearance of grossly raised melanoma lesions (Fig. 2E, fig. S1D, and movie S3). The *crestin:EGFP* expression is undetectable in the *p53/BRAF* fish from 3 to >21 days after fertilization, which is again consistent with previous in situ analyses for endogenous *crestin*. We tracked individual small patches of *crestin:EGFP*$^+$ cells over time as they progressed into fully formed raised melanoma lesions (Fig. 2E) and found that all melanomas tracked in this manner initiated from *crestin:EGFP*$^+$ patches of cells (30 out of 30). Thus, if a patch is seen in the *p53/BRAF* background, it will become an overt melanoma. These data demonstrate that reemergence of *crestin:EGFP* expression, and a neural crest progenitor state, correlates with melanoma initiation in an in vivo model of de novo melanoma formation.

To establish that pretumor patches of *crestin:EGFP*$^+$ cells are tumorigenic and can autonomously expand locally after transplant, we performed scale auto-transplants on *p53/BRAF/crestin:EGFP* zebrafish (*13*). After transplant, patches of *crestin:EGFP*$^+$ cells survive and expand at the new site. The *EGFP*$^+$ cells persist and further expand when later removing the transplanted scale, suggesting that the cells have invaded the hypodermis (Fig. 2G, representative example). We achieved similar results with isolated scales placed in tissue culture but on a shorter time scale (figs. S3A, and S4, A and B) and with allotransplants to sublethally irradiated recipient zebrafish (fig. S3B) (*8*). Thus, early patches of *crestin:EGFP*–expressing cells are transplantable in a manner suggesting that they are already tumorigenic.

Transcriptional regulators of *crestin* expression

As the *crestin* element proved to be a highly specific and distinct tool for monitoring neural crest and melanoma development, we aimed to identify (i) a minimal element within the 4.5-kb *crestin* promoter/enhancer that could drive this expression pattern and (ii) key transcriptional regulators within the element. Sequence analysis of the *crestin* locus, which is replicated throughout the zebrafish genome >40 times, is similar to another retroelement called *bhikari* that is expressed in early mesendoderm (fig. S6A) (*6*, *7*, *14*). Both a 1-kb segment from the putative retroelement promoter region and a smaller 296–base pair (bp) subregion fully reproduced the neural crest- and melanoma-specfic expression pattern of the full 4.5-kb *crestin* element (Fig. 1H and fig. S5, A to G), with slightly weaker expression for the 296-bp element. Hence, key neural crest regulatory elements are contained in this 296-bp of DNA, although additional contributory binding sites may also be functional in the context of the larger *crestin* element.

Database searches identified multiple predicted transcription factor binding sites for important neural crest developmental regulators within the 296-bp segment, including two *sox10*, one *pax3*,

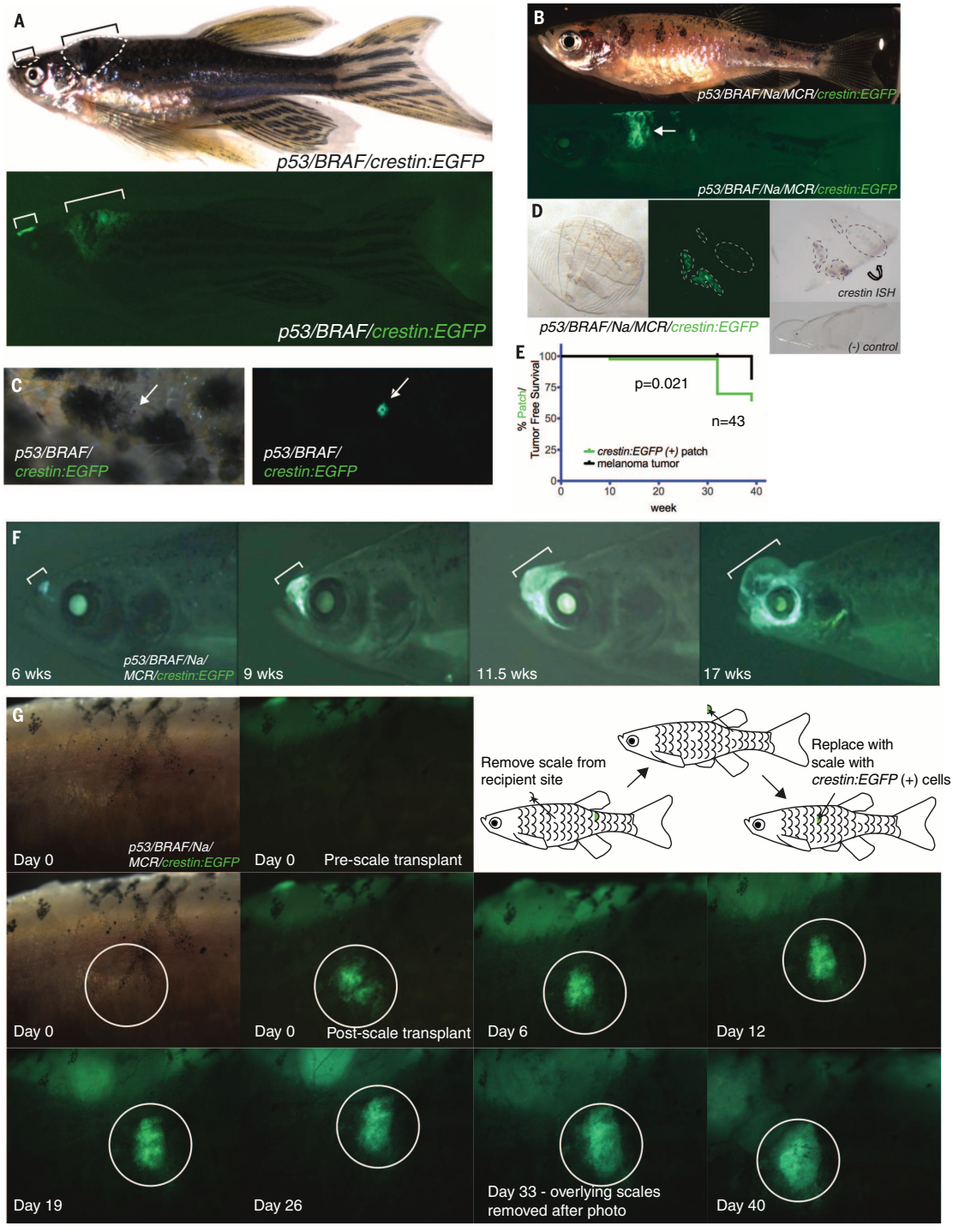


Fig. 2. *Tg(crestin:EGFP)* specifically marks melanoma tumors and precursor lesions. (**A**) Spontaneously arising tumors (outlined) in *p53/BRAF/crestin:EGFP* zebrafish express *EGFP* (brackets), whereas the remainder of the animal is negative. (**B**) *crestin:EGFP* expression is also visible in precursor, nonraised lesions. (**C**) Example of a single *crestin:EGFP*$^+$ cell in *p53/BRAF* background. (**D**) Scales expressing *crestin:EGFP* from precursor, nonraised regions [(B), bottom, arrow] were plucked, photographed [(D), left and middle], and subjected to ISH for *crestin* transcript [(D), right]. There is a concordance of *EGFP* (green) and *crestin* transcript (purple, dotted outlines, scales curl during ISH procedure, indicated by the curved arrow, observed in 5 of 5 scales). (Bottom right) *crestin:EGFP*$^-$ scales are negative for *crestin* ISH staining (observed in 7 of 7 tested scales). (**E**) Cohorts of *p53/BRAF/crestin:EGFP* zebrafish were tracked over time for the appearance of *crestin:EGFP*$^+$ patches and tumors, with *crestin:EGFP*$^+$ cells/patches (green line) identifiable before raised melanoma tumors (black line). (**F**) Example of an *EGFP*$^+$ preclinical patch tracked over time (6, 9, 11.5, and 17 weeks) as it expands into a clinically apparent melanoma tumor. (**G**) Scale autotransplant and expansion of *crestin:EGFP*$^+$ patch of cells. At day 0, the recipient site is free of *crestin:EGFP*$^+$ cells (pre–scale transplant), but immediately after transplant of a single scale (post–scale transplant), the patch of *EGFP*$^+$ cells is apparent (white circle). This patch expands outward, and even upon removal of the original transplanted scale after the day 33 photograph, *EGFP*$^+$ cells remain in place and continue to expand. The magnification and size of white circle is the same in each image.

one *E-box* (*myc* or *mitf*-binding site), and one *tfap2* site (Fig. 3A and table S1) (*15*). To determine which sites are functionally required for *crestin* transgene expression, we individually mutated the core consensus for each site (Fig. 3A and fig. S6B) and tested expression at 24 hours after fertilization in F0 embryos injected with the different *crestin_296bp:EGFP* constructs at the one-cell stage, examining >80 successfully injected F0 embryos per construct. Whereas mutation of the predicted *pax3* site left the expression pattern largely unchanged from that of the wild type (~55% of embryos with neural crest predominant expression in both), mutation of either *sox10* site drastically reduced neural crest expression (≤20%), as did mutation of the *tfap2* site or the *E-box* site (<10% and none, respectively) (Fig. 3A and fig. S6, C and D). These functional transcription factor binding sites provide an explanation for the neural crest specificity of *crestin* transgene expression, which integrates regulatory signals of multiple neural crest transcription factors, including *sox10*.

Neural crest signature in melanoma initiation

To test whether early precursor melanoma lesions express other melanoma and neural crest progenitor markers in addition to *crestin*, we isolated individual scales from *p53/BRAF/Na/MiniCoopR/crestin:EGFP* zebrafish with early *crestin:EGFP*$^+$ patches and compared them with adjacent individual scales without *crestin:EGFP* expression (Fig. 3, B and C) and performed Affymetrix microarrays (*12*). Such scales appear well-matched in their cell make-up, particularly in regards to melanocytes, as shown through *mitf:mCh* co-expression (marking melanocytes), and *crestin:EGFP* (fig. S7). *Crestin:EGFP*$^+$ scale-enriched genes include neural crest– (such as *crestin*, *mitf*, and *dlx2a)* and melanoma-expressed [such as *mia* and *mt* (metallothionein)] genes (table S2) (*16*–*18*). We confirmed enrichment by means of quantitative reverse transcription PCR (RT-PCR) on independent *crestin:EGFP*$^+$ and *crestin:EGFP*$^-$ scales (including *crestin*, *dlx2a*, and *mia*) (Fig. 3D). We also found *sox10* expression enriched in the *crestin:EGFP*$^+$ samples (Fig. 3D). *Sox10* is a known marker and key regulator of neural crest identity (Fig. 1H) (*19*) and, from our data, of *crestin* expression (Fig. 3A); it is also sufficient to direct reprogramming of human fibroblasts to induced neural crest cells (*20*) and can be highly express in melanoma, where it is involved in growth control (*21*–*23*). We used gene set enrichment analysis (GSEA) to query a rank-ordered list of the *crestin:EGFP*$^+$ scale enriched genes for an association with all neural crest–expressed genes in the Zebrafish Information Network (ZFIN) database, and we found a significant correlation [false discovery rate (FDR) Q = 0.019, and familywise error rate (FWER) P = 0.019] (Fig. 3E, left, and table S6). Similarly, we used GSEA to compare a rank-ordered list of genes enriched in embryonic stem (ES)–derived human neural crest cells (*24*) with genes enriched ≥2-fold in *crestin:EGFP*$^+$ scales, and we found a positive correlation, detectable even across species (FDR Q = 0.089, FWER P = 0.089) (Fig. 3E, right, and table S6). These data collectively support the concept that key aspects of NCP state reemerge at the time of melanoma initiation, as read out by the *crestin:EGFP* reporter.

Neural crest progenitor identity and melanomagenesis

On the basis of our analysis of *crestin* expression, which provides an in vivo readout of NCP identity at the time of melanoma initiation, we reasoned that favoring entry into or inappropriately maintaining the NCP state in a cancerized field of melanocytes would accelerate the onset of melanoma formation (Fig. 3F). The neural crest master transcription factor *sox10* has been shown to increase *crestin* mRNA in embryos when overexpressed (*25*), and we found similar results for our *crestin:EGFP* reporter (fig. S8). Misexpression of *SOX10* in postnatal fibroblasts also generates multipotent neural crest cells in culture (*20*). We therefore overexpressed *sox10* in melanocytes using the transgenic *MiniCoopR* system (*12*) and found that *sox10* overexpression in melanocytes accelerated melanoma onset significantly versus controls (Fig. 3G). To examine the consequence of *sox10* inactivation, we used a melanocyte-specific CRISPR/Cas9 system to target *sox10* in the *p53/BRAF/Na* background (fig. S9A). As compared with controls in which *p53* is redundantly targeted (already mutated in our system) using an analogous vector, we found a significant slowing of median tumor onset in the *sox10* CRISPR/Cas9 setting [133 days (*p53*) versus 180 days (*sox10*), P < 0.0001] (fig. S9B). When melanomas developed in the *sox10*-targeted background, the *sox10* target genomic locus exhibited a propensity for mutations that preserve predicted *sox10* function (for example, point mutations or in-frame deletions, ~60% of sequenced genomes) as opposed to inactivating mutations (for example, frame-shifts, ~40% of sequenced genomes), suggesting a selective pressure for retention of *sox10* function (fig. S9, C and D). These gain- and loss-of-function results together strongly support our hypothesis that reemergence of NCP state is an important event in melanoma tumor initiation.

Neural crest super-enhancers and melanoma

In order to understand how the expression of neural crest genes such as *sox10* may be regulated in zebrafish and human melanoma, we used a combination of chromatin immunoprecipitation sequencing (ChIP-seq) and assay for transposase-accessible chromatin using sequencing (ATAC-seq). Chromatin regions with high levels of H3K27Ac histone marks have been referred to as super-enhancers (SEs), or stretch-enhancers (*26*, *27*), and have been identified as key transcriptional regulatory elements that modulate cell type–specific and cancer-related gene expression (*26*–*29*). We used ChIP-seq to identify H3K27Ac-enriched regions in a zebrafish *crestin:EGFP*$^+$ melanoma cell line (zcrest1) that we derived from *p53/BRAF/Na/MiniCoopR/crestin:EGFP* zebrafish and noted substantial regions of H3K27Ac enrichment at *crestin* loci, identified as SEs (representative locus shown in Fig. 4A, red bar indicates SE). We also identified Sox10 binding by means of ChIP-seq across the *crestin* locus (Fig. 4A, bottom track), which is consistent with our promoter analysis linking *sox10* to *crestin* transcriptional regulation (Fig. 3A). We examined the *sox10* locus in the zcrest 1 zebrafish melanoma cell line and also identified H3K27Ac SE marks (Fig. 4B). These SEs were similarly found at *sox10* and *crestin* via H3K27Ac ChIP-seq performed on a freshly isolated *primary* zebrafish melanoma tumor (fig. S10, A and B, red bars), supporting our findings on the cell lines as being representative of the in vivo landscape. ATAC-seq identified open and accessible chromatin corresponding to the SEs at *crestin* and *sox10* (Fig. 4, A and B) and other SE-associated loci in two zebrafish melanoma cell lines (fig. S10, E and F) (*30*). These data suggest a molecular basis for the epigenetic state readout by *crestin* of NCP identity in initiating melanoma cells.

To compare our fish studies with human melanoma, for which SE analysis is limited, we examined the Cancer Cell Line Encyclopedia (CCLE) database (*31*) and found that most human melanoma lines (51 of 60) express *SOX10* according to Affymetrix microarray data (fig. S11A). As with zebrafish melanomas, ChIP-seq showed enriched H3K27Ac marks near the *SOX10* locus in six *SOX10*-expressing human melanoma lines tested but not in a rare *SOX10*-negative human melanoma cell line (LOXIMVI) (Fig. 4, C and E, and fig. S11A). The *SOX10* SE's were ranked 3 and 6 out of 842 SEs from ~15,000 total enhancers in the A375 line (fig. S11B and table S3). Clustering based on the SE landscape yielded two distinct groups of *SOX10*-expressing lines that correlated with the presence or absence of expression of melanocyte differentiation markers, *TYR* and *DCT* (fig. S11, C and D). H3K4me1, a histone modification typically at active enhancers, was also enriched at *SOX10* in the representative A375 melanoma line (Fig. 4C). Remarkably, these *SOX10* SE peaks were also found in published H3K27Ac data from human ES-derived neural crest cells (hNCCs) (Fig. 4, C and E) (*32*). Examining multiple normal and cancer cell types (66 and 18 types, respectively), the enrichment of H3K27Ac signal at *SOX10* was evident and specific to melanoma cells, hNCCs, and brain tissue, which contains *SOX10*-expressing oligodendrocytes (Fig. 4E) (*26*). Beyond *SOX10*, a similar SE epigenetic signature was shared for the neural crest transcription factor *DLX2* among melanomas across species and was enriched in melanomas and hNCCs (Fig. 4, D and E, and fig. S10, C and E). *DLX2* expression is enriched in sorted *crestin*$^+$ embryonic neural crest cells (table S4), in *crestin*$^+$ precursor melanoma patches (Fig. 3D), and in the less differentiated, *TYR/DCT*$^-$ melanomas relative to cultured normal human melanocytes (fig. S11, C, D, and F; and table S5). SEs were

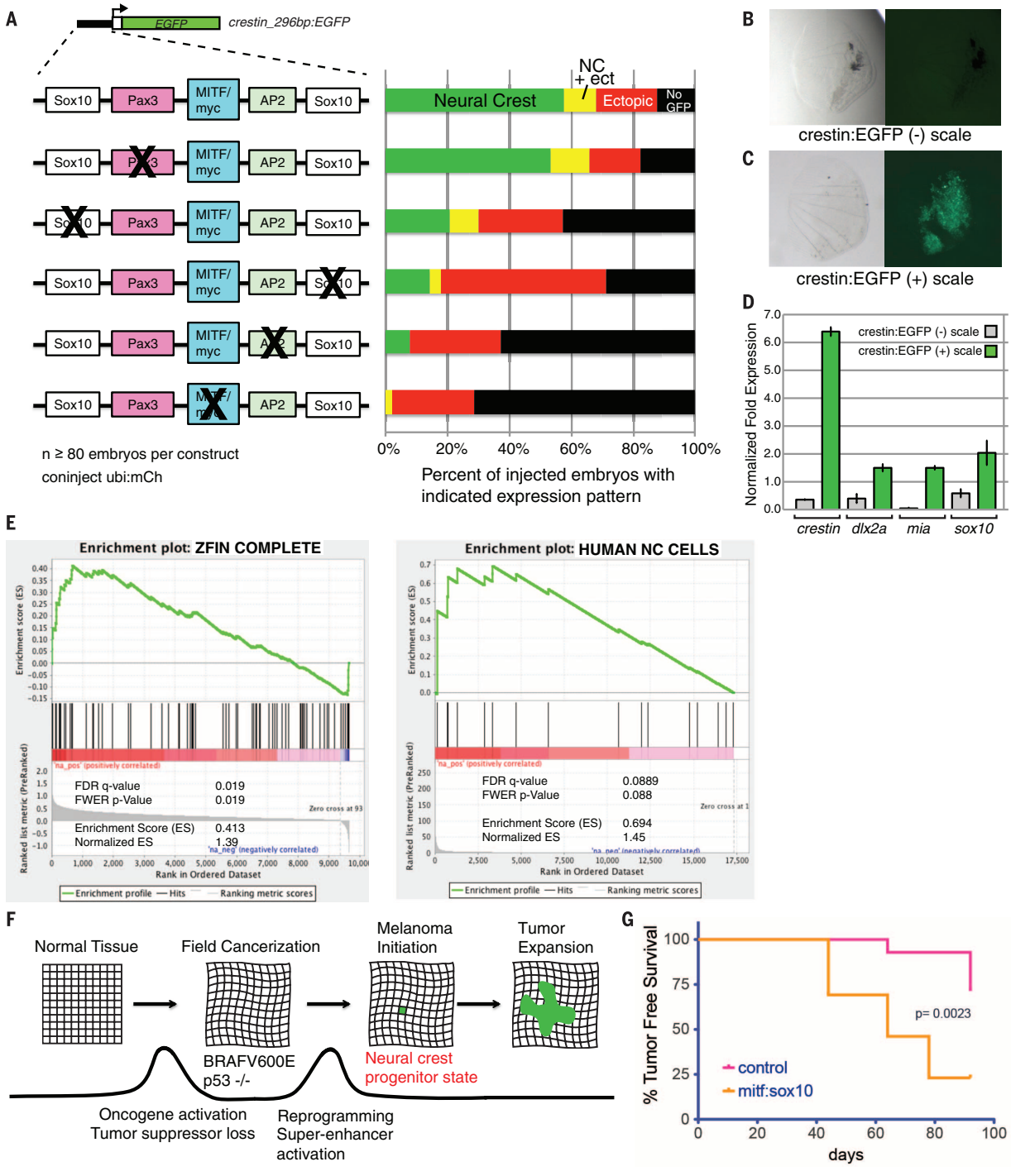


Fig. 3. Reemergence of neural crest progenitor identity in melanoma initiation. (**A**) Mutation of key neural crest transcription factor binding sites in the 296-bp *crestin* element, including *sox10*, *tfap2*, and an E-box for *myc* or *mitf*, substantially reduces neural crest *EGFP* expression at 24 hours after fertilization, whereas mutation of the predicted *pax3* site does not alter expression. Coinjection of a ubiquitous *ubi:mCh* transgene confirmed successful injection for the >80 independently injected F0 embryos analyzed for each construct. Scales from *p53/BRAF/Na/MiniCoopR/crestin:EGFP* adult zebrafish (**B**) with and (**C**) without $EGFP^+$ cells were collected, and total RNA was isolated for microarray analysis. (**D**) Quantitative RT-PCR of $crestin:EGFP^+$ versus $crestin:EGFP^-$ scales reveals enrichment of neural crest (*crestin*, *dlx2a*, *sox10*) and melanoma marker expression (*crestin*, *mia*, *sox10*). (**E**) GSEA analysis shows a positive association between $crestin:EGFP^+$ patch-enriched genes and neural crest–expressed genes in zebrafish (left) and in human ES–derived neural crest cells (right). (**F**) Model for the importance of reemergence of NCP state through SE activation as an essential step in melanoma initiation. The acquisition of genetic lesions in normal tissue leads to oncogene activation ($BRAF^{V600E}$) and tumor suppressor loss ($p53^{-/-}$) and represents an initial barrier that generates a cancerized field from which rare clones (green) overcome the additional barrier of achieving a NCP state to initiate melanoma formation and then tumor expansion. Favoring reemergence of the neural crest progenitor state would then increase melanoma formation, and strengthening this barrier to inhibit adoption of the $crestin^+$ NCP state would block melanoma initiation. (**G**) Misexpression of the NCP transcription factor *sox10* accelerates melanoma onset as compared with controls in *p53/BRAF/Na* zebrafish rescued with the *MiniCoopR* construct.

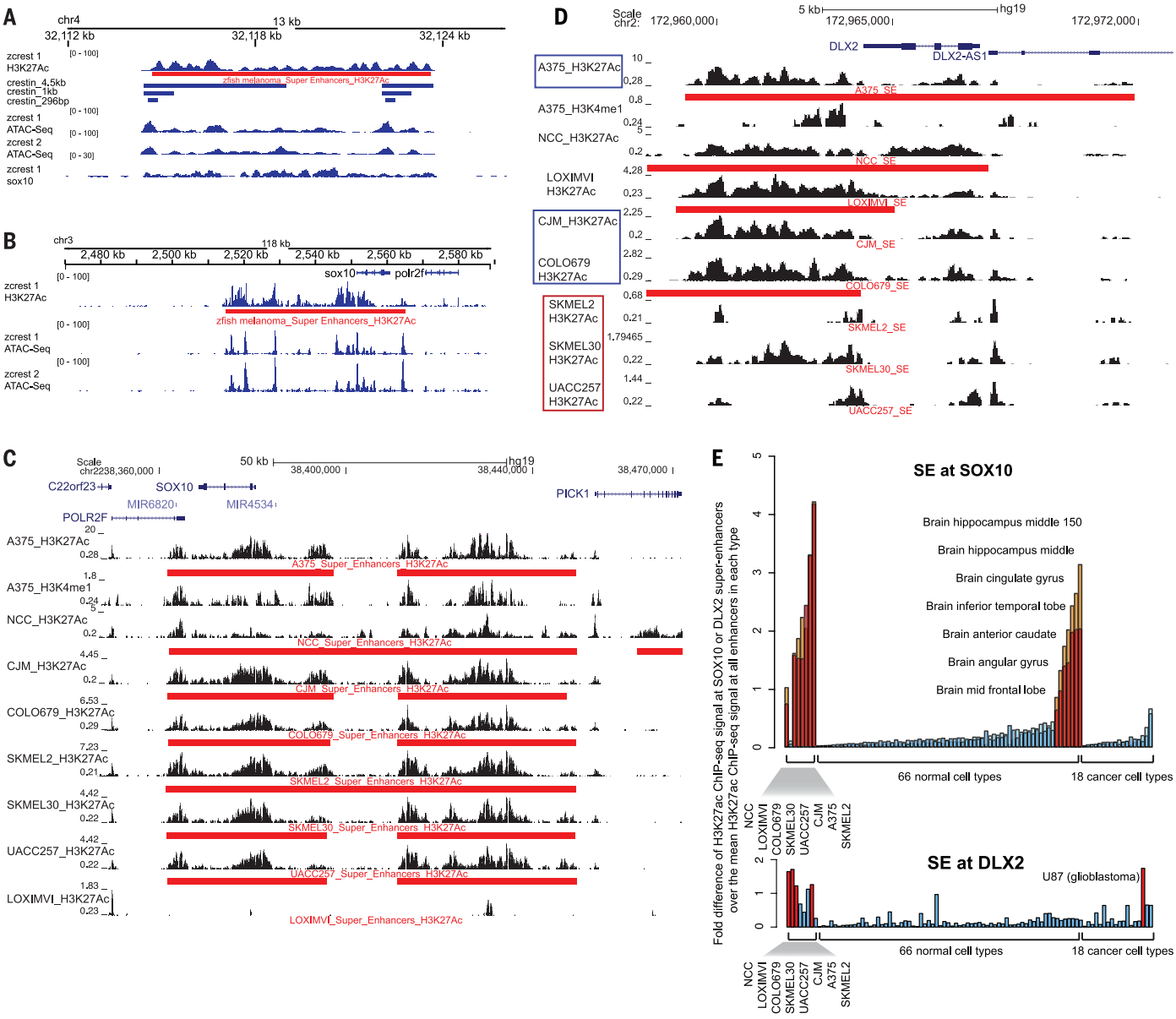


Fig. 4. A SE signature in zebrafish and human melanoma. (**A**) ChIP-seq for the H3K27Ac histone mark (top row) in a *crestin:EGFP*$^{+}$ zebrafish melanoma cell line (zcrest 1) reveals enriched peaks, identified as a SE (red bar), at a representative *crestin* locus. Sequences of *crestin_4.5kb*, *crestin_1kb*, and *crestin_296bp* shown with blue horizontal bars. ATAC-seq on two zebrafish melanoma lines (zcrest 1 and zcrest 2) identifies open chromatin coincident with the H3K27Ac marks at *crestin* loci. ChIP-seq for Sox10 shows enrichment across the *crestin* locus (bottom row) in zcrest 1 cells. (**B**) ChIP-seq for the H3K27Ac histone mark (top row) on the zcrest 1 line identifies robust enrichment and a SE at *sox10* (red bar). ATAC-seq identifies corresponding regions of open chromatin (rows 2 and 3). (**C**) ChIP-seq for the H3K27Ac mark on multiple *SOX10*-expressing melanoma lines (A375, CJM, COLO679, SKMEL2, SKMEL30, and UACC257) and a rare *SOX10*-negative melanoma line (LOXIMVI). Robust peaks corresponding to SEs (red bars) are identified in all lines, except the *SOX10*-negative LOXIMVI line. Published H3K27Ac ChIP-seq data from hNCCs reveal a similar SE pattern. ChIP-seq for H3K4Me1, an enhancer mark, on a representative melanoma line, A375 (row 2), identifies regions corresponding to the H3K27Ac marks. (**D**) H3K27Ac signal is robust at the *DLX2* locus in melanoma cell lines not expressing the melanocyte differentiation genes *TYR* and *DCT* (blue box), in hNCCs, and in the *SOX10*-negative LOXIMVI melanoma line. Human genomic track images were generated at http://genome.ucsc.edu. (**E**) High relative H3K27Ac signal at *SOX10* (top) and *DLX2* (bottom) identifies SEs (presence = red/orange bar, absence = blue bars) and is largely enriched in melanomas and hNCCs compared with 66 normal and 18 cancer cell types.

also found at *TFAP2* family members, whose functional binding site was identified in the 296-bp *crestin* element (Fig. 3A), in A375 human melanoma (*TFAP2C*) (fig. S12A), and in the zebrafish melanoma cell line and primary melanoma (*tfap2a*) (fig. S10, D and F). Such SEs are also found near other *crestin*$^{+}$ cell-enriched genes *MIA* and *MT2A* (metallothionein genes) in A375 melanoma cells (fig. S12, B and C).

Discussion

This work shows that melanoma precursor cells reinitiate an embryonic neural crest signature and activate a melanoma gene program. Although the expression of stem cell factors or embryonic genes has been noted previously in advanced malignancies including melanoma (*8*, *23*), it remained uncertain whether this was simply due to aberrant misexpression of these genes or whether these genes were present from tumor outset (Fig. 3F). Our data support a model in which the stem/progenitor

cell gene programs are an integral part of cancer initiation and not reacquired later (Fig. 3F). Analogously, this theme was also recently described in basal cell carcinoma (BCC), a cancer arising from a different cell lineage, in which careful analysis of gene expression from tissue collected during early BCC formation in a mouse model of the disease exhibited an embryonic hair follicle progenitor signature, indicating that this may be a general feature of cancer initiation (*33*). There also is a conceptual similarity between the reprogramming-induced pluripotent stem process and the tumorigenic reemergence of NCP state seen in our system as melanocytes with the required, but insufficient, *p53/BRAF* genetic mutations stochastically reenter a NCP state (as read out by *crestin* expression) early at the initiation of melanoma. As the initiating stages of more cancers are analyzed, stem cell/progenitor phenotype reacquisition may be a generally observed phenomenon in most cancers (*33*).

Our work establishes a method to live-image cancer development when a tumor starts, potentially as a single cell, providing a singular view of the initiating events. NCP identity arises, and is likely a necessary step, early in tumor development. In our *p53/BRAF/crestin:EGFP* model, all $EGFP^{+}$ patches of *crestin:EGFP* cells that we track go on to enlarge and form tumors; given the rarity of capturing single cells in this background, we cannot rule out that clones may rarely fail to progress to patches. The *crestin* gene has the distinct characteristic of being expressed in neural crest cells in embryos, but not being expressed in adult tissues except when melanoma arises. Super-enhancers shared between melanoma and neural crest are specifically activated. The neural crest signature encompasses a combinatorial code including *SOX10*, *DLX2*, and the *TFAP2* family. It is unlikely that any one of these genes is sufficient for the reprogramming event, but it is the combination of multiple transcription factors that participate. In contrast to *SOX10*, *DLX2* expression is characteristic of genes that are expressed by neural crest and melanoma, but not expressed in melanocytes. As such, this gene set may have diagnostic importance in the initiating cancer cell. A reevaluation of published expression data for nevi, primary melanoma, and metastatic melanoma does reveal increased *SOX10* expression in malignant melanomas (*34*). Nevi show a wide range and consistently lower amount of *SOX10* expression than that of melanoma, raising the possibility that the histologically defined category of nevus is capturing a range of melanoma-initiating capacity (those nevi expressing higher *SOX10* levels may have initiated or may be more prone to initiating melanoma).

Several major questions remain about an initiating cancer cell that may now be more accessible with our live visualization tool. The niche environment must participate in the process of initiation, perhaps through the activation of neural crest signaling pathways akin to the development of the normal neural crest or by stress pathways related to irradiation or oxidative damage. Further genetic mutations, as opposed to isolated epigenetic changes, may be required for tumor initiation from the cancerized field; however, the absence of identifiable functionally relevant exomic mutations in a study of 53 zebrafish melanoma tumors to which we contributed would tend to favor that the key genetic drivers ($BRAF^{V600E}$ and mutant *p53*) are already present in our model (*35*). Work on this question will provide information on how cancer initiates. The reprogramming event appears to occur in one melanocyte or progenitor in a cancerized field, and defining why the process initiates in that single cell rather than an adjacent cell will provide an understanding of protective mechanisms in cancer formation.

Materials and methods

Cloning of crestin *promoter/enhancer*

The transcript for *crestin*, originally described as AF195881, was used with Basic Local Alignment Search Tool (BLAST) on the zebrafish genome and, as has been previously noted, identified many partial or complete highly similar (>90% identical) sequences spread throughout the genome (*6*, *7*). Multiple insertions are present on chromosome 4, and a ~4.5-kb sequence located upstream of the predicted *crestin* open reading frame (ORF) was noted to be present in multiple instances. Reasoning that this segment may contain the relevant regulatory elements of *crestin*, primers were designed to amplify via PCR upstream sequences of the *crestin* locus (LOC796814) on chromosome 4 in the TU background (primers 299 and 302; primers supplemental table). The 1-kb fragment and 296-bp fragment were isolated by using PCR primers 302/340 and 517/516, respectively. Fragments were cloned into pENTR5′ (Life Technologies, Grand Island, NY) per manufacturers instructions. Expression vectors were derived by using Multisite Gateway technology per manufacturer's specifications and the Tol2 Kit (*36*) [*EGFP*, vector 383; *mCh*, vector 386; SV40 poly A, vector 302; *EGFP* with mouse minimal ß-globin promoter (*37*); destination vectors, vector 394 alone and modified with addition of *crystallin:YFP* marker; *zmitfa* middle entry vector, gift of Craig Ceol; MiniCoopR from (*15*)].

Production of transgenic zebrafish and lineage tracing

One-cell-stage embryos from the AB strain grown under standard, Institutional Animal Care and Use Committee (IACUC)–approved conditions were injected with the given DNA construct at 25 ng/μl with Tol2 mRNA at 20 ng/μl (*36*). Embryos were screened at 24 hours after fertilization for neural crest expression of *EGFP* or *mCh*, or in the case of *Tg(crestin:CreERt2;crystallin:YFP)*, screened for yellow fluorescent protein (YFP)–positive lenses at 4 days after fertilization. These were grown to adulthood and outcrossed so as to identify founders that gave germline transmission. For each DNA construct, ≥2 independent lines were generated to confirm the expression pattern. For lineage tracing of *crestin*-expressing cells, a stable transgenic line of *Tg(crestin:creERt2;crystalline:YFP)* was crossed to the *Tg(-3.5ubi:loxP-GFP-loxP-mCherry)* line (*ubi:Switch*) (*9*); embryos were collected and treated with 10 μM 4-hydroxytamoxifen (4-OHT) at 50% epiboly and 24 hours after fertilization while grown at 28°C in E3 medium, as per standard protocol.

Embryo and adult imaging

Transmitted light and fluorescence images of adult and nonconfocal images of embryos were collected on a Zeiss Discovery V.8 Stereoscope with an Axiocam HRc. Static confocal images were collected on a Nikon C2si Laser Scanning Confocal using 25× objective on embryos mounted in 1% low melt agarose. Maximum intensity projections of Z stacks or three-dimensional reconstructions are presented here. Movies of developing embryos were collected on a Nikon Eclipse Ti Spinning Disk Confocal with a 10× objective, with tiled images collected every 6 to 7 min. Images were processed by using Photoshop, ImageJ, or Imaris. Multiple tiled images of adult zebrafish were stitched together by using the automated Photomerge function in Photoshop or manually aligned.

Melanoma model and MiniCoopR *system*

Experiments were performed as outlined in (*15*). Briefly, *p53/BRAF/Na* embryos were injected with equal amounts of *MiniCoopR* alone or *MiniCoopR; mitf:sox10* and selected for melanocyte rescue at 48 hours. Equal numbers of melanocyte-rescued embryos were grown to adulthood (n = 14 for control and n = 13 for mitf:sox10) and scored for the emergence of raised melanoma lesions as per (*15*). Survival curves and statistics were generated in Prism.

Quantitative PCR, microarray, and in situ hybridization

Adult *p53/BRAF/Na/MiniCoopR/crestin:EGFP* fish were anesthetized with Tricaine, viewed under the fluorescent dissecting scope, and precursor patches of *crestin:*$EGFP^{+}$ cells were identified and associated single scales removed. These fish contained stable (germ-line transmitted) alleles of *crestin:EGFP* and control *MiniCoopR* (no test gene). Neighboring *crestin:EGFP*–negative scales from the same zebrafish were selected for controls. Scales were immediately placed in Trizol, and total RNA was purified following the manufacturer's instructions, with the additional use of Sigma GenElute LPA carrier. RNA was analyzed on a BioAnalyzer, and high-quality samples were chosen for microarray libraries generated by using the Ovation Pico WTA System V2 and Encore Biotin labeling system for hybridization on the Zebrafish Gene 1.0 ST Affymetrix Array or used for cDNA preparation using SuperScript III. RMA-normalized Affymetrix Array results were sorted for maximum fold (log2) increase in gene expression in GFP-positive samples versus negative samples. Quantitative PCR reactions were run on triplicate biological samples with triplicate technical replicates and normalized to β-actin expression, with representative results presented.

For in situ hybridizations, we used the methods of (*38*) and the *crestin* probe from (*7*).

ChIP-seq and SE analysis

Human melanoma cells were grown to confluence in Dulbecco's Modified Eagle medium (DMEM) + 10% fetal calf serum (FCS), and ~ 1×10^8 cells were formaldehyde cross-linked and collected. ChIP was performed by using the methods of (*30*, *39*) with antibodies against H3K27Ac (ab4729) (Abcam), H3K4Me1 (ab8895) (Abcam), and SOX10 [Santa Cruz Biotechnology (Dallas, TX), sc-17342x]. Libraries were prepared by using the NEBNext Multiplex Oligos for Illumina kit (NEB) and run on an Illumina HiSeq 2000. Data analysis, including enhancer and SE calling, was performed as described in (*26*). Genomic track images were generated by using the IGV package (*40*) and the University of California, Santa Cruz Browser (*41*).

All human ChIP-seq data sets were aligned to build version NCBI37/HG19 of the human genome using Bowtie (version 0.12.9) (*42*) with the following parameters: –n2, –e70, –m2, –k2, –best. We used the MACS version 1.4.1 (Model based analysis of ChIP-seq) (*43*) peak finding algorithm to identify regions of ChIP-seq enrichment over background. A P value threshold of enrichment of 1×10^{-9} was used for all data sets. Wiggle files for gene tracks were created by using MACS with options –w –S –space = 50 to count reads in 50-bp bins. They were normalized to the total number (in millions) of mapped reads producing the final tracks in units of reads per million mapped reads per base pair (rpm/bp).

Identifying SEs

The identification of SEs has previously been described in detail (*26*). Briefly, H3K27Ac peaks were used to identify constituent enhancers. These were stitched if within 12.5 kb, and peaks fully contained within ±2kb from a TSS were excluded from stitching. H3K27Ac signal (less input control) was used to rank enhancers by their enrichment. Super-enhancers were assigned to active genes by using the ROSE software package (younglab.wi.mit.edu/super_enhancer_code.html).

ATAC-seq

Zebrafish melanoma cell lines were grown to 80% confluence, trypsinized, and counted, and 50,000 cells were lysed and subjected to "tagmentation" reaction and library construction as described in (*30*). Libraries were run on an Illumina HiSeq 2000. All zebrafish ATAC-seq data sets were aligned to build version Zv9 of the zebrafish genome by using Bowtie2 (version 2.2.1) (*42*) with the following parameters: –end-to-end, –N0, –L20. We used the MACS2 version 2.1.0 (*43*) peak-finding algorithm to identify regions of ATAC-seq peaks, with the following parameter–nomodel–shift –100–extsize 200. A Q value threshold of enrichment of 0.05 was used for all data sets.

Scale transplants

Adult *p53/BRAF/Na/MiniCoopR/crestin:EGFP* were anesthetized, viewed under the fluorescent dissecting scope; precursor patches of *crestin:EGFP*$^+$ cells were identified (not from raised melanoma lesions); and single associated scales were removed and placed in 50-µl drops of E3 buffer on a petri dish lid. Anesthetized recipient zebrafish (in the case of allotransplants) or the same zebrafish (in the case of autotransplants) were gently placed on a wet sponge and a recipient site selected (free of *crestin:EGFP*–expressing cells). One scale was removed at the donor site, and the previously selected donor scale from the drop of E3 was placed on the zebrafish and slid posterior to anterior into place by using surrounding scales to hold it in place. Recipients were quickly placed in fresh zebrafish water and monitored for recovery from anesthesia. Transplants were monitored frequently with some loss of transplanted scales (~20%) occurring quickly within 1 day because of simple dislodgement. Once in place for ~4 days, scales were firmly incorporated and could be monitored over time and photographed at the same magnification under the dissecting scope after mild Tricaine anesthesia of the recipient zebrafish. In single-scale autotransplants in a representative cohort of 10 fish, three scales were lost in the first week (we consider a technical failure with the scales falling out), five showed expansion of the *crestin:EGFP* cells, and three showed no change or loss of *crestin:EGFP* cells. In single-scale allotransplants onto sublethally irradiated *casper* recipient fish, eight *EGFP*$^+$ scales were transplanted onto different recipients with one scale lost in the first week, five scales showing expansion of the *crestin:EGFP* cells for ≥2.5 weeks, and two showing stable appearance for ≥ 2 weeks. Six of six *EGFP*$^-$ scales showed loss of pigmented cells in this time frame.

Promoter analysis

Transcription factor binding sites were predicted by using JASPAR (*14*). We used the Q5 Site-Directed Mutagenesis Kit from NEB to introduce mutations to destroy the chosen transcription factor binding site (primers supplemental table). To analyze expression in vivo, equal volumes of a mixture of the *crestin_296bp:EGFP* construct variant at 20 ng/µl mixed with 5 ng/µl of *ubi:mCh* (*9*, *36*) (for an injection control) were injected with 20 ng/µl of Tol2 mRNA into single-cell AB embryos. At 24 hours after fertilization, embryos were fixed in paraformaldehyde (PFA), washed and stored in phosphate-buffered saline (PBS), and scored for *mCh* expression to identify successfully injected embryos and for *EGFP* to bin based on the predominant expression pattern. More than 80 transgenic F0 embryos for each construct were scored.

Investigating SOX10 and DLX2 SEs in healthy normal cells and melanoma cells

To investigate whether the two SOX10-asscociated SEs identified in A375 cells are also present in other cell types, they were compared with the SEs identified in other melanoma cell types, neural crest cells, and 84 additional cell types from normal or cancer cells described in (*26*).

First, the SOX10-asscociated SEs were operationally called "present" in a cell type if the SEs identified in the cell-type overlap with the SOX10 SEs in A375 cells by at least 1 bp. Second, the H3K27Ac signal density of the SOX10-asscociated SEs identified in A375 cells was compared with the mean H3K27Ac signal density of all enhancer clusters in each cell type. For each cell type, the average H3K27Ac ChIP-seq read density was calculated in rpm/bp for the two SOX10 SEs identified in A375 cells as well as all enhancers clusters identified by using the ROSE software package in the cell type (younglab.wi.mit.edu/super_enhancer_code.html). The fold difference of H3K27Ac ChIP-seq signal at SOX10 SEs over the mean H3K27Ac ChIP-seq signal at all enhancers in each cell type was plotted in Fig. 4E. The same process was undertaken for the SEs at the *DLX2* locus.

Pairwise comparison of SEs between different melanoma cell lines and neural crest cells

The set of SE regions in each cell type (SKMEL2, SKMEL30, UACC257, LOXIMVI, A375, CJM, COLO679, and neural crest cells) were merged together if overlapping by 1 bp, resulting in a total of 3407 merged SE regions. The neural crest cell data were previously published in (*32*). The average H3K27Ac ChIP-seq read density was calculated in rpm/bp for each of the merged regions. The pair-wise comparisons by Pearson correlation were performed on all data sets by using the average read density at the merged regions. The average linkage hierarchical clustering of the Pearson correlation was shown in the heatmap (fig. S11C).

Zebrafish melanoma cell lines and in vitro scale imaging

A single *EGFP*$^+$ melanoma tumor arising in a *p53/BRAF/Na* fish injected with *MiniCoopR* plasmid and *crestin:EGFP* plasmid (zcrest 1 line) or a *p53/BRAF/Na/crestin:EGFP* fish injected with MiniCoopR plasmid (zcrest 2 line) was removed after killing the adult fish. Briefly, tumors were dissociated with a razor blade and trypsin, filtered, and plated on a fibronectin-coated well and grown in rich media supplemented with FBS and zebrafish embryo extract as described (*44*). After several passages, the zcrest 1 line was sorted for *EGFP*$^+$ cells, which were continued as the line. For the zcrest 2 line, after several passages, most if not all cells remaining were *EGFP*$^+$. Both lines continue to be *EGFP*$^+$ and have been grown for >50 passages on plastic in standard DMEM + 10% FBS with 1X GlutaMAX supplement and penicillin/streptomycin antibiotics.

Scales from *p53/BRAF/Na/crestin:EGFP/MiniCoopR* and *p53/BRAF/crestin:EGFP* fish with and without *EGFP*$^+$ patches of cells were placed in zebrafish melanoma growth medium in fibronectin coated wells in 384-well format, flat-bottomed plates and imaged daily on a Yokogawa

CV7000 confocal imager with brightfield and z-stack image projections collected.

GSEA analysis

Using our microarrays comparing *crestin:EGFP*$^{+}$ versus *crestin:EGFP*$^{-}$ scale gene expression, zebrafish genes were rank-ordered (10,705 genes) from high to low for enrichment (crestin scales rank.rnk). We generated a gene list of all neural-crest–expressed genes in the ZFIN database (317 genes, zfincomp.gmt) (*45*) and used the preranked GSEA analysis tool. Using a list of genes with ≥2-fold enrichment in *crestin:EGFP*$^{+}$ scales by means of microarray (Crestin Scales.gmt), we queried a list of 17,575 genes rank-ordered for their enrichment in human neural crest cells versus parental ES cells from (*32*) (Rada Ranked.rnk), also using the preranked GSEA analysis tool (*46*).

RNA-seq analysis

Multiple human melanoma cell lines and adult human epidermal melanocytes (purchased from Life Technologies) were grown to near confluence, and total RNA was isolated by using the standard Trizol protocol. Illumina libraries were prepared by using Ribo-Zero Magnetic Gold Kit (epicenter) and NEBNext Ultra RNA Library Prep Kit (NEB) and run on a HiSeq 2500, reads aligned by using Tophat 2.0, and fragments per kilobase of exon per million fragments mapped values determined by using Cufflinks. For sorted *crestin*$^{+}$ cells, transgenic *crestin_1kb:EGFP* adults were mated, and embryos collected and grown to the 15-somite stage. These were homogenized, filtered, and sorted by using fluorescence-activated cell sorting into PBS, collecting ~5500 *EGFP*$^{+}$ cells and 100K *EGFP*$^{-}$ cells. Total RNA was again collected by using Trizol and GenElute LPA carrier per manufacturer instructions. Libraries were prepared by using Ribogone kit (Clontech) and the SMARTer Universal Low RNA Kit (Clontech) and sequenced on the Illumina HiSeq 2500, with post-analysis performed as above with the zebrafish genome.

CRISPR/Cas9 experiment

Cas9 mRNA was produced by means of in vitro transcription from a pCS2 *Cas9* vector (*47*) by using mMESSAGE mMACHINE SP6 kit (Invitrogen). Guide RNAs (gRNAs) were generated by following established methods (*48*). The *Sox10* target sequence was GGCCGCGCGCAGGAAACTGG. Six hundred picograms of *Cas9* mRNA and 25 pg of gRNA were injected into embryos of the AB strain. After microinjection, embryos were raised in E3 medium at 28.5°C. The T7E1 assay was performed as reported (*49*). Briefly, genomic DNA was extracted from 2-day-old embryos by using the hotSHOT method (*50*). A fragment of 434 bp was amplified from genomic DNA by using the following primers: GAAGTCCGACGAGGAAGAT and CTTGACTGAGTAAATAGTGCGT. The PCR amplicons were then purified on a 1% agarose gel. Two hundred nanograms of purified DNA were denatured at 95°C for 5 min and slowly reannealed before digestion with 10 units of T7E1 enzyme (NEB) for 1 hour at 37°C. The digestion product was finally run on a 2.5% agarose gel.

CRISPR/Cas9 tumor-free survival curves

In order to inactivate *sox10* specifically in the melanocytes of our zebrafish melanoma model, the *MiniCoopR* vector was engineered to express Cas9 under the control of the melanocyte-specific *mitfa* promoter and a gRNA efficiently mutating *sox10*, described above, off a *U6* promoter. A gRNA against *p53* was used as a negative control (*51*). The two vectors were injected into one-cell stage, Tg (*mitfa:BRAF*^{V600E}), *p53*$^{-/-}$, *mitfa*$^{-/-}$ embryos, and tumor formation was monitored.

To sequence genomic DNA from tumors, tumor tissue was dissected carefully, digested in buffer with proteinase K (*52*), and after inactivation of proteinase K, PCR was performed by using the primers described above as for the T7E1 reaction. PCR fragments were cloned by using TopoTA cloning per manufacturer instructions, and colony PCR was performed on resulting individual clones and submitted for Sanger sequencing for fig. S9C. For next-generation sequencing in fig. S9D, nested PCR (primer sequences TGAACGGGTACGACTGGACGCT and TGTTGTAGCAGTGCGTTTA, yielding a 238-bp amplicon) was performed on the initially amplified genomic locus so as to bring the amplicon ends closer to the CRISPR target sequence in order to allow for coverage by using a MiSeq-based 150-bp paired-end Illumina run with pooled and barcoded samples at the MGH DNA Core. Both Sanger and compiled next-generation sequences were aligned to the wild-type locus by using Lasergene Seqman in order to identify changes at the CRISPR target sequence. Wild-type *sox10* reads, although potentially from nontargeted *sox10* loci in melanocytes and not necessarily from other tissue types in the sample, were excluded from the calculations of fractions of allele types. If included, these would only increase the fraction of active *sox10* alleles and would further favor our interpretation of the results. When determining the fractions of alleles in fig. S9D, each tumor was weighted equally so as to avoid skewing from more reads from a given tumor.

Injection of sox10 mRNA

The *sox10* cDNA from zebrafish was cloned into pENTR/D-TOPO and transferred into pCSDest (*53*) by using Gateway cloning, all per manufacturer instructions. mRNA was generated by using SP6 mMessage mMachine Kit (Ambion) per manufacturer, and 1 nl mRNA mix was injected into single-cell *p53/BRAF/crestin:EGFP* embryos at multiple concentrations, with 20 pg being the highest tolerated dose without substantial toxicity. Embryos were imaged on a Zeiss Discovery V.8 Stereoscope and scored for EGFP expression.

REFERENCES AND NOTES

1. D. P. Slaughter, H. W. Southwick, W. Smejkal, Field cancerization in oral stratified squamous epithelium; clinical implications of multicentric origin. *Cancer* **6**, 963–968 (1953). doi: 10.1002/1097-0142(195309)6:5<963::AID-CNCR2820060515>3.0.CO;2-Q; pmid: 13094644
2. R. L. Mort, I. J. Jackson, E. E. Patton, The melanocyte lineage in development and disease. *Development* **142**, 620–632 (2015). doi: 10.1242/dev.106567; pmid: 25670789
3. The Cancer Genome Atlas Research Network, Comprehensive molecular profiling of lung adenocarcinoma. *Nature* **511**, 543–550 (2014). pmid: 25079552
4. J. A. Lo, D. E. Fisher, The melanoma revolution: From UV carcinogenesis to a new era in therapeutics. *Science* **346**, 945–949 (2014). doi: 10.1126/science.1253735; pmid: 25414302
5. E. E. Patton *et al*., BRAF mutations are sufficient to promote nevi formation and cooperate with p53 in the genesis of melanoma. *Curr. Biol.* **15**, 249–254 (2005). doi: 10.1016/j.cub.2005.01.031; pmid: 15694309
6. R. Luo, M. An, B. L. Arduini, P. D. Henion, Specific pan-neural crest expression of zebrafish Crestin throughout embryonic development. *Dev. Dyn.* **220**, 169–174 (2001). pmid: 11169850
7. A. L. Rubinstein, D. Lee, R. Luo, P. D. Henion, M. E. Halpern, Genes dependent on zebrafish *cyclops* function identified by AFLP differential gene expression screen. *Genesis* **26**, 86–97 (2000). doi: 10.1002/(SICI)1526-968X(200001)26:1<86::AID-GENE11>3.0.CO;2-Q; pmid: 10660676
8. R. M. White *et al*., DHODH modulates transcriptional elongation in the neural crest and melanoma. *Nature* **471**, 518–522 (2011). doi: 10.1038/nature09882; pmid: 21430780
9. C. Mosimann *et al*., Ubiquitous transgene expression and Cre-based recombination driven by the *ubiquitin* promoter in zebrafish. *Development* **138**, 169–177 (2011). doi: 10.1242/dev.059345; pmid: 21138979
10. Y. Kong *et al*., Neural crest development and craniofacial morphogenesis is coordinated by nitric oxide and histone acetylation. *Chem. Biol.* **21**, 488–501 (2014). pmid: 24684905
11. M. Grzmil *et al*., The *INT6* cancer gene and MEK signaling pathways converge during zebrafish development. *PLOS ONE* **2**, e959 (2007). doi: 10.1371/journal.pone.0000959; pmid: 17895999
12. C. J. Ceol *et al*., The histone methyltransferase SETDB1 is recurrently amplified in melanoma and accelerates its onset. *Nature* **471**, 513–517 (2011). pmid: 21430779
13. W. H. Hildemann, Tissue transplantation immunity in goldfish. *Immunology* **1**, 46–54 (1958). pmid: 13513141
14. A. M. Vogel, T. Gerster, Promoter activity of the zebrafish *bhikhari* retroelement requires an intact activin signaling pathway. *Mech. Dev.* **85**, 133–146 (1999). doi: 10.1016/S0925-4773(99)00104-5; pmid: 10415354
15. A. Sandelin, W. Alkema, P. Engström, W. W. Wasserman, B. Lenhard, JASPAR: An open-access database for eukaryotic transcription factor binding profiles. *Nucleic Acids Res.* **32**, D91–D94 (2004). doi: 10.1093/nar/gkh012; pmid: 14681366
16. M. Uhlén *et al*., A human protein atlas for normal and cancer tissues based on antibody proteomics. *Mol. Cell. Proteomics* **4**, 1920–1932 (2005). doi: 10.1074/mcp.M500279-MCP200; pmid: 16127175
17. A. K. Bosserhoff, Melanoma inhibitory activity (MIA): An important molecule in melanoma development and progression. *Pigment Cell Res.* **18**, 411–416 (2005). pmid: 16280006
18. G. Weinlich *et al*., Metallothionein—Overexpression as a highly significant prognostic factor in melanoma: A prospective study on 1270 patients. *Br. J. Cancer* **94**, 835–841 (2006). doi: 10.1038/sj.bjc.6603028; pmid: 16508630
19. R. N. Kelsh, Sorting out *Sox10* functions in neural crest development. *BioEssays* **28**, 788–798 (2006). doi: 10.1002/bies.20445; pmid: 16927299
20. Y. J. Kim *et al*., Generation of multipotent induced neural crest by direct reprogramming of human postnatal fibroblasts with a single transcription factor. *Cell Stem Cell* **15**, 497–506 (2014). doi: 10.1016/j.stem.2014.07.013; pmid: 25158936
21. J. C. Cronin *et al*., SOX10 ablation arrests cell cycle, induces senescence, and suppresses melanomagenesis. *Cancer Res.* **73**, 5709–5718 (2013). pmid: 23913827
22. S. A. Graf, C. Busch, A. K. Bosserhoff, R. Besch, C. Berking, SOX10 promotes melanoma cell invasion by regulating melanoma inhibitory activity (MIA). *J. Investig. Dermatol.* **134**, 2212–2220 (2014). doi: 10.1038/jid.2014.128
23. O. Shakhova *et al*., Sox10 promotes the formation and maintenance of giant congenital naevi and melanoma. *Nat. Cell Biol.* **14**, 882–890 (2012). pmid: 22772081
24. A. Rada-Iglesias *et al*., Epigenomic annotation of enhancers predicts transcriptional regulators of human neural crest. *Cell Stem Cell* **11**, 633–648 (2012). doi: 10.1016/j.stem.2012.07.006; pmid: 22981823
25. E. Olesnicky, L. Hernandez-Lagunas, K. B. Artinger, *prdm1a* Regulates *sox10* and *islet1* in the development of neural crest

and Rohon-Beard sensory neurons. *Genesis* **48**, 656–666 (2010). doi: 10.1002/dvg.20673; pmid: 20836130
26. D. Hnisz *et al*., Super-enhancers in the control of cell identity and disease. *Cell* **155**, 934–947 (2013). doi: 10.1016/j.cell.2013.09.053; pmid: 24119843
27. S. C. J. Parker *et al*., NISC Comparative Sequencing Program, National Institutes of Health Intramural Sequencing Center Comparative Sequencing Program Authors, NISC Comparative Sequencing Program Authors, Chromatin stretch enhancer states drive cell-specific gene regulation and harbor human disease risk variants. *Proc. Natl. Acad. Sci. U.S.A.* **110**, 17921–17926 (2013). pmid: 24127591
28. W. A. Whyte *et al*., Master transcription factors and mediator establish super-enhancers at key cell identity genes. *Cell* **153**, 307–319 (2013). doi: 10.1016/j.cell.2013.03.035; pmid: 23582322
29. J. Lovén *et al*., Selective inhibition of tumor oncogenes by disruption of super-enhancers. *Cell* **153**, 320–334 (2013). doi: 10.1016/j.cell.2013.03.036; pmid: 23582323
30. J. D. Buenrostro, P. G. Giresi, L. C. Zaba, H. Y. Chang, W. J. Greenleaf, Transposition of native chromatin for fast and sensitive epigenomic profiling of open chromatin, DNA-binding proteins and nucleosome position. *Nat. Methods* **10**, 1213–1218 (2013). doi: 10.1038/nmeth.2688; pmid: 24097267
31. J. Barretina *et al*., The Cancer Cell Line Encyclopedia enables predictive modelling of anticancer drug sensitivity. *Nature* **483**, 603–607 (2012). doi: 10.1038/nature11003; pmid: 22460905
32. A. Rada-Iglesias *et al*., A unique chromatin signature uncovers early developmental enhancers in humans. *Nature* **470**, 279–283 (2011). doi: 10.1038/nature09692; pmid: 21160473
33. K. K. Youssef *et al*., Adult interfollicular tumour-initiating cells are reprogrammed into an embryonic hair follicle progenitor-like fate during basal cell carcinoma initiation. *Nat. Cell Biol.* **14**, 1282–1294 (2012). doi: 10.1038/ncb2628; pmid: 23178882
34. L. Rönnstrand, B. Phung, Enhanced SOX10 and KIT expression in cutaneous melanoma. *Med. Oncol.* **30**, 648 (2013). doi: 10.1007/s12032-013-0648-y; pmid: 23801280
35. J. Yen *et al*., The genetic heterogeneity and mutational burden of engineered melanomas in zebrafish models. *Genome Biol.* **14**, R113 (2013). doi: 10.1186/gb-2013-14-10-r113; pmid: 24148783
36. K. M. Kwan *et al*., The Tol2kit: A multisite gateway-based construction kit for *Tol2* transposon transgenesis constructs. *Dev. Dyn.* **236**, 3088–3099 (2007). doi: 10.1002/dvdy.21343; pmid: 17937395
37. O. J. Tamplin, B. J. Cox, J. Rossant, Integrated microarray and ChIP analysis identifies multiple Foxa2 dependent target genes in the notochord. *Dev. Biol.* **360**, 415–425 (2011). doi: 10.1016/j.ydbio.2011.10.002; pmid: 22008794
38. C. Thisse, B. Thisse, High-resolution in situ hybridization to whole-mount zebrafish embryos. *Nat. Protoc.* **3**, 59–69 (2008). doi: 10.1038/nprot.2007.514; pmid: 18193022
39. T. I. Lee, S. E. Johnstone, R. A. Young, Chromatin immunoprecipitation and microarray-based analysis of protein location. *Nat. Protoc.* **1**, 729–748 (2006). doi: 10.1038/nprot.2006.98; pmid: 17406303
40. J. T. Robinson *et al*., Integrative genomics viewer. *Nat. Biotechnol.* **29**, 24–26 (2011). doi: 10.1038/nbt.1754; pmid: 21221095
41. W. J. Kent *et al*., The human genome browser at UCSC. *Genome Res.* **12**, 996–1006 (2002). doi: 10.1101/gr.229102; pmid: 12045153
42. B. Langmead, S. L. Salzberg, Fast gapped-read alignment with Bowtie 2. *Nat. Methods* **9**, 357–359 (2012). doi: 10.1038/nmeth.1923; pmid: 22388286
43. Y. Zhang *et al*., Model-based analysis of ChIP-Seq (MACS). *Genome Biol.* **9**, R137 (2008). doi: 10.1186/gb-2008-9-9-r137; pmid: 18798982
44. S. Heilmann *et al*., A quantitative system for studying metastasis using transparent zebrafish. *Cancer Res.* **75**, 4272–4282 (2015). doi: 10.1158/0008-5472.CAN-14-3319; pmid: 26282170
45. D. G. Howe *et al*., ZFIN, the Zebrafish Model Organism Database: Increased support for mutants and transgenics. *Nucleic Acids Res.* **41** (D1), D854–D860 (2013). doi: 10.1093/nar/gks938; pmid: 23074187
46. A. Subramanian *et al*., Gene set enrichment analysis: A knowledge-based approach for interpreting genome-wide expression profiles. *Proc. Natl. Acad. Sci. U.S.A.* **102**, 15545–15550 (2005). doi: 10.1073/pnas.0506580102; pmid: 16199517
47. L.-E. Jao, S. R. Wente, W. Chen, Efficient multiplex biallelic zebrafish genome editing using a CRISPR nuclease system. *Proc. Natl. Acad. Sci. U.S.A.* **110**, 13904–13909 (2013). doi: 10.1073/pnas.1308335110; pmid: 23918387
48. J. A. Gagnon *et al*., Efficient mutagenesis by Cas9 protein-mediated oligonucleotide insertion and large-scale assessment of single-guide RNAs. *PLOS ONE* **9**, e98186 (2014). doi: 10.1371/journal.pone.0098186; pmid: 24873830
49. H. J. Kim, H. J. Lee, H. Kim, S. W. Cho, J.-S. Kim, Targeted genome editing in human cells with zinc finger nucleases constructed via modular assembly. *Genome Res.* **19**, 1279–1288 (2009). doi: 10.1101/gr.089417.108; pmid: 19470664
50. G. E. Truett *et al*., Preparation of PCR-quality mouse genomic DNA with hot sodium hydroxide and tris (HotSHOT). *BioTechniques* **29**, 52–54 (2000).
51. J. Ablain, E. M. Durand, S. Yang, Y. Zhou, L. I. Zon, A CRISPR/Cas9 vector system for tissue-specific gene disruption in zebrafish. *Dev. Cell* **32**, 756–764 (2015). doi: 10.1016/j.devcel.2015.01.032; pmid: 25752963
52. E. Wienholds *et al*., Efficient target-selected mutagenesis in zebrafish. *Genome Res.* **13**, 2700–2707 (2003). doi: 10.1101/gr.1725103; pmid: 14613981
53. J. A. Villefranc, J. Amigo, N. D. Lawson, Gateway compatible vectors for analysis of gene function in the zebrafish. *Dev. Dyn.* **236**, 3077–3087 (2007). doi: 10.1002/dvdy.21354; pmid: 17948311

ACKNOWLEDGMENTS

C.K.K. and research reported here is supported by the National Institute of Arthritis and Musculoskeletal and Skin Diseases of the National Institutes of Health under award K08 AR061071. C.M. received support from a European Molecular Biology Organization long-term fellowship, a Human Frontier Science Program long-term fellowship, and a Swiss National Science Foundation advanced postdoctoral fellowship. L.I.Z. is supported by R01 CA103846, the Ellison Foundation, the V Foundation, and the Melanoma Research Alliance and is a Howard Hughes Medical Institute Investigator. R.A.Y. is supported by NIH HG002668. Z.P.F. was supported by NIH HG002668. E.J.H. is a Howard Hughes Medical Institute Fellow of the Helen Hay Whitney Foundation. L.I.Z. is a founder and stock holder of Fate, Inc. and Scholar Rock. R.A.Y. is a founder of Syros Pharmaceuticals. The content is solely the responsibility of the authors and does not necessarily represent the official views of the National Institutes of Health. We thank the Massachusetts General Hospital DNA Core for providing technical assistance with deep sequencing. We thank J. Ablain for critical review of the manuscript, C. Ceol for the gift of the zebrafish *mitfa* middle entry clone, and G. Musso for helpful discussions on microarray data and GSEA. All microarray, Chip-seq, and RNA-seq are deposited at Gene Expression Omnibus, ID GSE75356.

SUPPLEMENTARY MATERIALS

www.sciencemag.org/content/351/6272/aad2197/suppl/DC1
Figs. S1 to S12
Tables S1 to S6
Movies S1 to S3

11 August 2015; accepted 22 December 2015
10.1126/science.aad2197

RESEARCH ARTICLE SUMMARY

STRESS RESPONSE

Translation from the 5′ untranslated region shapes the integrated stress response

Shelley R. Starck,* Jordan C. Tsai, Keling Chen, Michael Shodiya, Lei Wang, Kinnosuke Yahiro, Manuela Martins-Green, Nilabh Shastri,* Peter Walter*

INTRODUCTION: Protein synthesis is controlled by a plethora of developmental and environmental conditions. One intracellular signaling network, the integrated stress response (ISR), activates one of four kinases in response to a variety of distinct stress stimuli: the endoplasmic reticulum (ER)–resident kinase (PERK), the interferon-induced double-stranded RNA–dependent eIF2α kinase (PKR), the general control nonderepressible 2 (GCN2), or the heme-regulated inhibitor kinase (HRI). These four kinases recognize a central target and phosphorylate a single residue, Ser51, on the α subunit of the eukaryotic initiation factor 2 (eIF2α), which is a component of the trimeric initiation factor eIF2 that catalyzes translation initiation at AUG start codons. Phosphorylation of eIF2α down-regulates eIF2-dependent protein synthesis, which is important in development and immunity but also is implicated in neurodegeneration, cancer, and autoimmunity. However, protein synthesis does not cease on all mRNAs during the ISR. Rather, eIF2α phosphorylation is required for expression of select mRNAs, such as ATF4 and CHOP, that harbor small upstream open reading frames (uORFs) in their 5′ untranslated regions (5′ UTRs). Still other mRNAs sustain translation despite ISR activation. We developed tracing translation by T cells (3T) as an exquisitely sensitive technique to probe the translational dynamics of uORFs directly during the ISR. With 3T, we measured the peptide products of uORFs present in the 5′ UTR of the essential ER-resident chaperone, binding immunoglobulin protein (BiP), also known as heat shock protein family A member 5 (HSPA5), and characterized their requirement for BiP expression during the ISR.

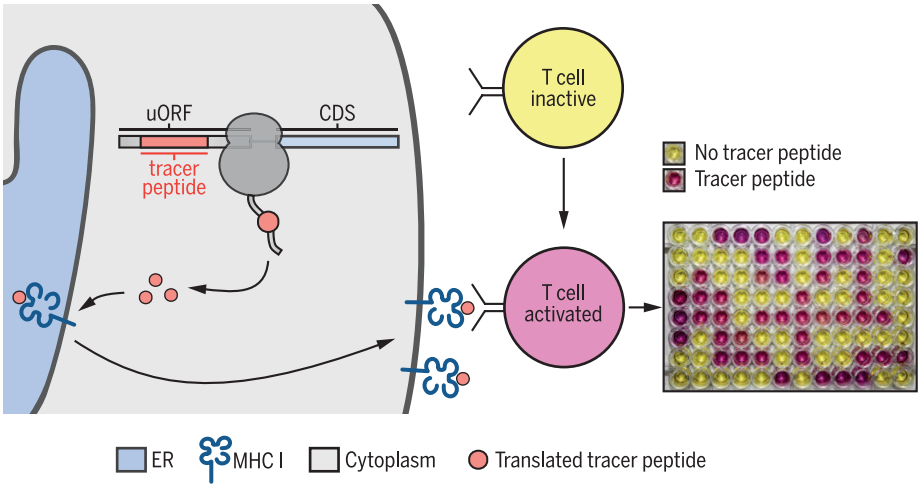
RATIONALE: We repurposed the sensitivity and specificity of T cells to interrogate the translational capacity of RNA outside of annotated protein coding sequences (CDSs). 3T relies on insertion of a tracer peptide coding sequence into a candidate DNA sequence. The resulting mRNAs harboring the nested tracer peptide coding sequence are translated to produce tracer peptides. These translation products are processed and loaded onto major histocompatibility complex class I (MHC I) molecules in the ER and transit to the cell surface, where they can be detected by specific T cell hybridomas that are activated and quantified using a colorimetric reagent. 3T provides an approach to interrogate the thousands of predicted uORFs in mammalian genomes, characterize the importance of uORF biology for regulation, and generate fundamental insights into uORF mutation-based diseases.

RESULTS: 3T proved to be a sensitive and robust indicator of uORF expression. We measured uORF expression in the 5′ UTR of mRNAs at multiple distinct regions, while simultaneously detecting expression of the CDS. We directly measured uORF peptide expression from ATF4 mRNA and showed that its translation persisted during the ISR. We applied 3T to study BiP expression, an ER chaperone stably synthesized during the ISR. We showed that the BiP 5′ UTR harbors uORFs that are exclusively initiated by UUG and CUG start codons. BiP uORF expression bypassed a requirement for eIF2 and was dependent on the alternative initiation factor eIF2A. Both translation of the UUG-initiated uORF and eIF2A were necessary for BiP expression during the ISR. Unexpectedly, the products of uORF translation are predicted to generate MHC I peptides active in adaptive immunity. We propose that this phenomenon presents an extracellular signature during the ISR.

ON OUR WEB SITE

Read the full article at http://dx.doi.org/10.1126/science.aad3867

CONCLUSION: Our findings introduce the notion that cells harbor a distinct translation initiation pathway to respond to a variety of environmental conditions and cellular dysfunction. We showed that cells utilize a distinct, eIF2A-mediated initiation pathway, which includes uORF translation, to sustain expression of particular proteins during the ISR. 3T offers a valuable method to characterize the thousands of predicted translation events in 5′ UTRs and other noncoding RNAs and, expanded to a genome-wide scale, can complement ribosome profiling and mass spectrometry in uORF and short ORF discovery. Our observations underscore the importance of translation outside of annotated CDSs and challenge the very definition of the U in 5′ UTR. ■



3T reveals the translational landscape of the genome outside of annotated coding sequences. Tracer peptide coding sequences are inserted into regions outside the annotated CDS, such as uORFs. When translated, they generate peptides that are transported into the ER, are loaded onto MHC I, and transit to the cell surface. T cell hybridomas that recognize the specific tracer peptide–MHC I complex become activated, which is detected using a colorimetric substrate.

The list of author affiliations is available in the full article online.
*Corresponding authors. E-mail: shelley@walterlab.ucsf.edu (S.R.S.); nshastri@berkeley.edu (N.S.); peter@walterlab.ucsf.edu (P.W.) Cite this article as S. R. Starck *et al.*, *Science* 351, aad3867 (2016). DOI: 10.1126/science.aad3867

Downloaded from on January 31, 2016

RESEARCH ARTICLE SUMMARY

STRESS RESPONSE

Translation from the 5′ untranslated region shapes the integrated stress response

Shelley R. Starck,* Jordan C. Tsai, Keling Chen, Michael Shodiya, Lei Wang, Kinnosuke Yahiro, Manuela Martins-Green, Nilabh Shastri,* Peter Walter*

INTRODUCTION: Protein synthesis is controlled by a plethora of developmental and environmental conditions. One intracellular signaling network, the integrated stress response (ISR), activates one of four kinases in response to a variety of distinct stress stimuli: the endoplasmic reticulum (ER)–resident kinase (PERK), the interferon-induced double-stranded RNA–dependent eIF2α kinase (PKR), the general control nonderepressible 2 (GCN2), or the heme-regulated inhibitor kinase (HRI). These four kinases recognize a central target and phosphorylate a single residue, Ser51, on the α subunit of the eukaryotic initiation factor 2 (eIF2α), which is a component of the trimeric initiation factor eIF2 that catalyzes translation initiation at AUG start codons. Phosphorylation of eIF2α down-regulates eIF2-dependent protein synthesis, which is important in development and immunity but also is implicated in neurodegeneration, cancer, and autoimmunity. However, protein synthesis does not cease on all mRNAs during the ISR. Rather, eIF2α phosphorylation is required for expression of select mRNAs, such as ATF4 and CHOP, that harbor small upstream open reading frames (uORFs) in their 5′ untranslated regions (5′ UTRs). Still other mRNAs sustain translation despite ISR activation. We developed tracing translation by T cells (3T) as an exquisitely sensitive technique to probe the translational dynamics of uORFs directly during the ISR. With 3T, we measured the peptide products of uORFs present in the 5′ UTR of the essential ER-resident chaperone, binding immunoglobulin protein (BiP), also known as heat shock protein family A member 5 (HSPA5), and characterized their requirement for BiP expression during the ISR.

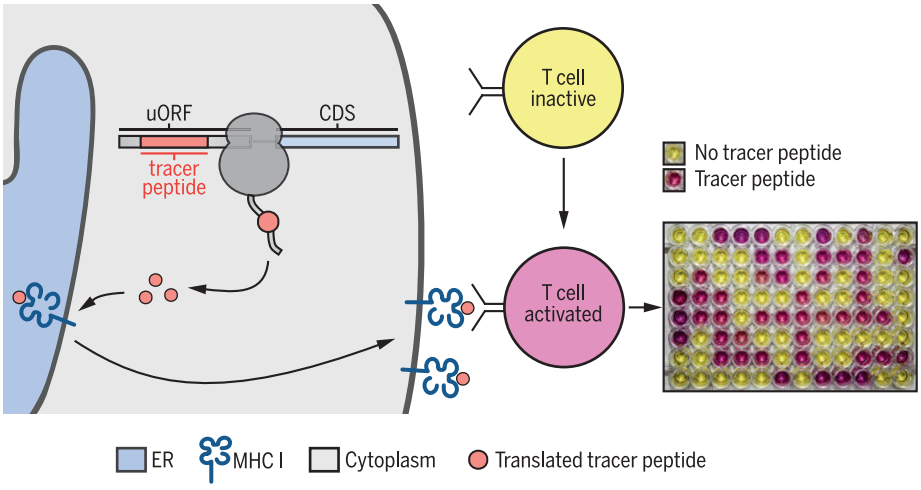
RATIONALE: We repurposed the sensitivity and specificity of T cells to interrogate the translational capacity of RNA outside of annotated protein coding sequences (CDSs). 3T relies on insertion of a tracer peptide coding sequence into a candidate DNA sequence. The resulting mRNAs harboring the nested tracer peptide coding sequence are translated to produce tracer peptides. These translation products are processed and loaded onto major histocompatibility complex class I (MHC I) molecules in the ER and transit to the cell surface, where they can be detected by specific T cell hybridomas that are activated and quantified using a colorimetric reagent. 3T provides an approach to interrogate the thousands of predicted uORFs in mammalian genomes, characterize the importance of uORF biology for regulation, and generate fundamental insights into uORF mutation-based diseases.

RESULTS: 3T proved to be a sensitive and robust indicator of uORF expression. We measured uORF expression in the 5′ UTR of mRNAs at multiple distinct regions, while simultaneously detecting expression of the CDS. We directly measured uORF peptide expression from ATF4 mRNA and showed that its translation persisted during the ISR. We applied 3T to study BiP expression, an ER chaperone stably synthesized during the ISR. We showed that the BiP 5′ UTR harbors uORFs that are exclusively initiated by UUG and CUG start codons. BiP uORF expression bypassed a requirement for eIF2 and was dependent on the alternative initiation factor eIF2A. Both translation of the UUG-initiated uORF and eIF2A were necessary for BiP expression during the ISR. Unexpectedly, the products of uORF translation are predicted to generate MHC I peptides active in adaptive immunity. We propose that this phenomenon presents an extracellular signature during the ISR.

ON OUR WEB SITE

Read the full article at http://dx.doi.org/10.1126/science.aad3867

CONCLUSION: Our findings introduce the notion that cells harbor a distinct translation initiation pathway to respond to a variety of environmental conditions and cellular dysfunction. We showed that cells utilize a distinct, eIF2A-mediated initiation pathway, which includes uORF translation, to sustain expression of particular proteins during the ISR. 3T offers a valuable method to characterize the thousands of predicted translation events in 5′ UTRs and other noncoding RNAs and, expanded to a genome-wide scale, can complement ribosome profiling and mass spectrometry in uORF and short ORF discovery. Our observations underscore the importance of translation outside of annotated CDSs and challenge the very definition of the U in 5′ UTR. ■



3T reveals the translational landscape of the genome outside of annotated coding sequences. Tracer peptide coding sequences are inserted into regions outside the annotated CDS, such as uORFs. When translated, they generate peptides that are transported into the ER, are loaded onto MHC I, and transit to the cell surface. T cell hybridomas that recognize the specific tracer peptide–MHC I complex become activated, which is detected using a colorimetric substrate.

The list of author affiliations is available in the full article online.
*Corresponding authors. E-mail: shelley@walterlab.ucsf.edu (S.R.S.); nshastri@berkeley.edu (N.S.); peter@walterlab.ucsf.edu (P.W.) Cite this article as S. R. Starck *et al.*, *Science* 351, aad3867 (2016). DOI: 10.1126/science.aad3867

RESEARCH ARTICLE

STRESS RESPONSE

Translation from the 5′ untranslated region shapes the integrated stress response

Shelley R. Starck,[1,2]† Jordan C. Tsai,[1] Keling Chen,[2] Michael Shodiya,[2] Lei Wang,[3] Kinnosuke Yahiro,[4] Manuela Martins-Green,[3] Nilabh Shastri,[2]*† Peter Walter[1]*†

Translated regions distinct from annotated coding sequences have emerged as essential elements of the proteome. This includes upstream open reading frames (uORFs) present in mRNAs controlled by the integrated stress response (ISR) that show "privileged" translation despite inhibited eukaryotic initiation factor 2–guanosine triphosphate–initiator methionyl transfer RNA (eIF2·GTP·Met-tRNA$_i^{Met}$). We developed tracing translation by T cells to directly measure the translation products of uORFs during the ISR. We identified signature translation events from uORFs in the 5′ untranslated region of binding immunoglobulin protein (BiP) mRNA (also called heat shock 70-kilodalton protein 5 mRNA) that were not initiated at the start codon AUG. BiP expression during the ISR required both the alternative initiation factor eIF2A and non–AUG-initiated uORFs. We propose that persistent uORF translation, for a variety of chaperones, shelters select mRNAs from the ISR, while simultaneously generating peptides that could serve as major histocompatibility complex class I ligands, marking cells for recognition by the adaptive immune system.

Homeostatic mechanisms facilitate adaptation to a variety of environmental conditions and cellular dysfunction. The integrated stress response (ISR) is one such mechanism, triggered when cells encounter an array of stress stimuli. These stimuli include misfolded proteins, which elicit the unfolded protein response (UPR) and thereby activate the endoplasmic reticulum (ER)–resident kinase (PERK) (*1*–*3*). In addition, three related kinases are activated by other stimuli, such as the interferon-induced double-stranded RNA (dsRNA)–dependent eIF2α kinase (PKR) (by viral infection) (*4*, *5*); the general control nonderepressible 2 (GCN2) (by amino acid deprivation) (*6*); and the heme-regulated inhibitor kinase (HRI) (by heme deficiency, oxidative stress, heat shock, or osmotic shock) (*7*). Each of these conserved kinases initiate the ISR by phosphorylating the same single residue (Ser51) on the α subunit of eukaryotic initiation factor 2α (eIF2α) and down-regulate translation initiation at AUG start codons by the eukaryotic initiation factor 2–guanosine triphosphate (GTP)–initiator methionyl transfer RNA (tRNA) (eIF2·GTP·Met-tRNA$_i^{Met}$) ternary complex. Phosphorylation of eIF2α (eIF2α-P) inhibits exchange of guanosine diphosphate for GTP by eIF2B, the dedicated eIF2 guanine nucleotide exchange factor, which causes inhibition of total protein synthesis (*8*). The blockade in translation is important for cell survival and the eventual switch into apoptosis if homeostasis cannot be reestablished.

Although eIF2α-P limits global translation, it is required for the regulated expression of several proteins, such as activating transcription factor 4 (ATF4 or CREB-2) (*9*–*11*) and C/EBP homologous protein (*12*, *13*), that finely tune cell survival (*14*). These ISR-induced proteins are translated from mRNAs and harbor a series of upstream open reading frames (uORFs) in the 5′ untranslated region (5′ UTR) that limit ribosome access to the main coding sequence (CDS), as first characterized in the budding yeast *Saccharomyces cerevisiae* (*15*). According to the prevailing model, under normal growth conditions, ribosome initiation occurs predominantly at uORFs, which prevents access to the downstream CDS. By contrast, when the ISR is induced and eIF2α-P levels rise, stochastic ribosome bypass of the uORFs allows access to the downstream CDS AUG start codon.

Another subset of mRNAs remains efficiently translated during the ISR. These include mRNAs encoding heat shock and UPR proteins (*1*, *16*–*18*) and a variety of inflammatory cytokines in response to viral (*19*, *20*) and bacterial (*21*) pathogens. In the context of the UPR, for example, translation of mRNAs encoding ER chaperones is imperative to alleviate ER stress. BiP [immunoglobulin heavy chain–binding protein, also known as heat shock 70 kD protein (HSP70), heat shock protein family A member 5 (HSPA5), or glucose-regulated protein 78] is an essential HSP70-type chaperone in the ER and is expressed persistently during ER stress (*22*–*24*). It plays a role in cancer progression (*25*) and is a therapeutic target for a variety of diseases (*26*, *27*). Yet, it has remained a mystery how BiP and other stress-response mRNAs escape translational down-regulation imposed by the ISR. Elements in the 5′ UTRs, including internal ribosome entry sites (IRESs), uORFs, and nucleotide modifications, have all been suggested to confer translational privilege to these mRNAs (*28*, *29*).

Recent genome-wide approaches predict that nearly half of all mammalian mRNAs harbor uORFs in their 5′ UTRs, and many are initiated with non-AUG start codons (*30*–*34*). The presence of uORFs in 5′ UTRs may reflect a general mechanism to regulate downstream CDS expression, such as proto-oncogenes and growth factors (*30*), as well as other disease-causing proteins (*35*), including hereditary thrombocythemia (*36*–*38*). Given the abundance of uORFs and their potential for regulatory roles, as well as the emerging plethora of short open reading frames (sORFs) (*39*–*41*) with bioactive properties (*42*), we developed a method to measure translation from RNA regions outside of annotated CDSs systematically.

Development of tracing translation by T cells (3T) to measure translation outside of annotated coding sequences

Ribosome-profiling experiments reveal that mRNAs encoding stress-response proteins harbor a particularly high abundance of uORFs (*43*, *44*). Yet, despite the thousands of peptides predicted by ribosome profiling to be translated from uORFs, very few uORF peptides have been identified by mass spectrometry (*45*). Currently, there is considerable effort to improve proteomic approaches for the detection of peptides from uORFs and other sORFs (*39*). Here, we exploited the exquisite sensitivity and specificity of T cells to detect such translation products.

We developed an approach, termed 3T, where cells are supplied with DNA vectors containing noncoding RNA elements, such as 5′ UTRs, harboring sequences that encode tracer peptides (Fig. 1A). If the resulting RNA is translated, cells proteolytically process the translated polypeptides. The resulting peptides are then transported by the transporter associated with antigen processing (TAP) into the ER. In the ER, the peptides (also called antigens) are loaded onto major histocompatibility complex class I (MHC I) molecules and displayed on the cell surface. We assessed presentation of the translated tracer peptide by MHC I by addition of a peptide–MHC I–cognate T cell hybridoma, engineered to express *LacZ* from the interleukin 2 (IL-2) promoter under control of the *N-FAT* enhancer (*46*). Engagement with tracer peptide–loaded MHC I

[1]Department of Biochemistry and Biophysics, Howard Hughes Medical Institute, University of California, San Francisco, CA 94143, USA. [2]Division of Immunology and Pathogenesis, Department of Molecular and Cell Biology, University of California, Berkeley, CA 94720, USA. [3]Department of Cell Biology and Neuroscience, University of California, Riverside, CA 92521, USA. [4]Departments of Molecular Infectiology, Graduate School of Medicine, Chiba University, Chiba, Japan.
*These authors contributed equally to this work. †Corresponding authors. E-mail: shelley@walterlab.ucsf.edu (S.R.S.); nshastri@berkeley.edu (N.S.); peter@walterlab.ucsf.edu (P.W.)

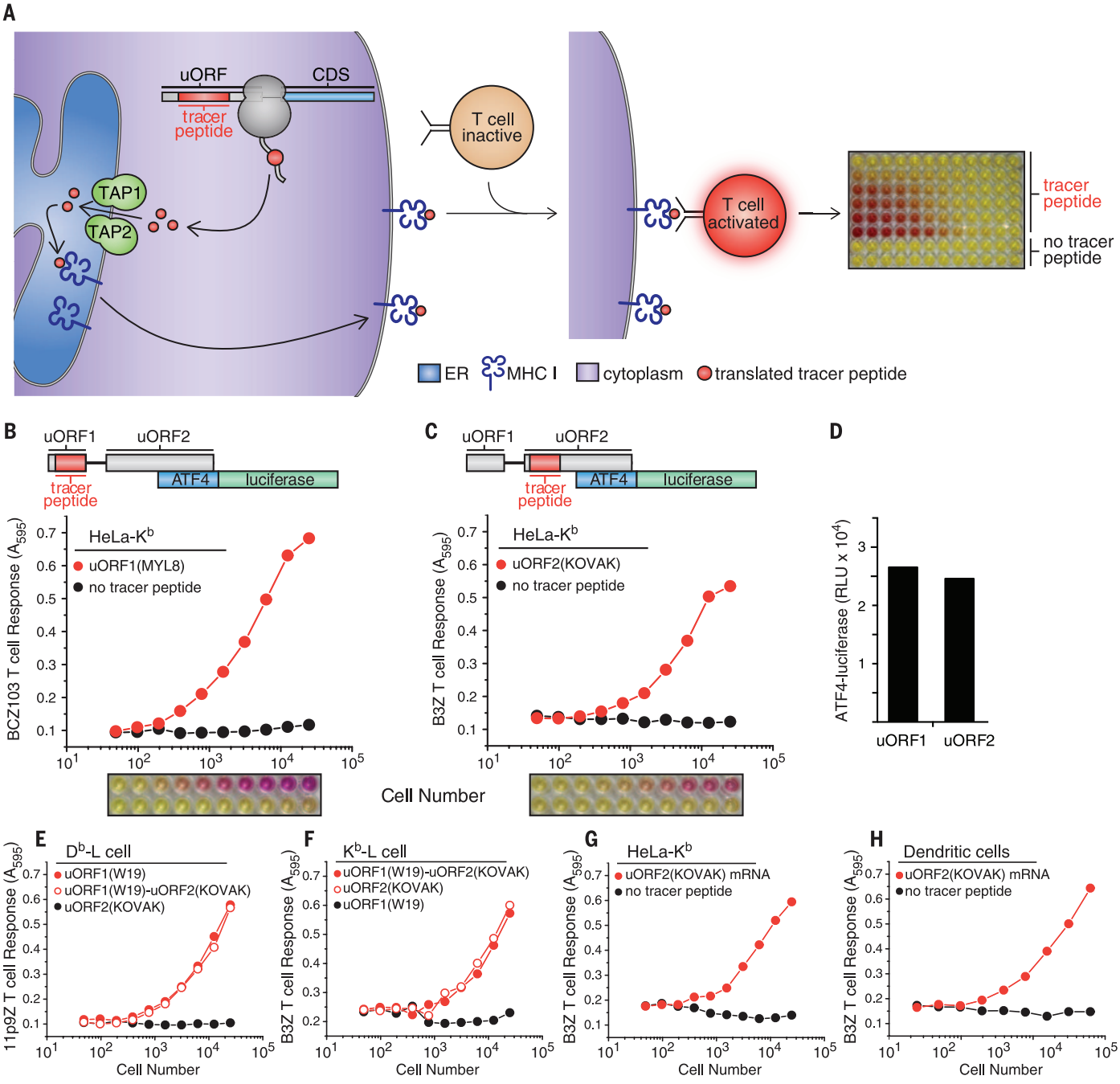


Fig. 1. 3T reveals the translational capacity of uORFs in 5′ UTRs. (**A**) Schematic of 3T: A tracer peptide inserted into noncoding regions of the 5′ UTR, such as uORFs, followed by translation, peptide processing, and transport by TAP into the ER for loading onto MHC I molecules. The tracer peptide–MHC I complex transits to the cell surface and is recognized by a T cell hybridoma. Recognition of the tracer peptide–MHC I complex on the cell surface activates the T cell hybridoma, which is measured by a colorimetric assay and indicates the presence of a uORF translation product. Schematics of the ATF4 5′ UTR with nested tracer peptides. Plotted T cell responses and colorimetric readout of the 3T assay from tracer peptides generated from transfection of HeLa-K^b cells with (**B**) uORF1(MYL8)–ATF4-luciferase detected with the BCZ103 T cell hybridoma and (**C**) uORF2(KOVAK)–ATF4-luciferase detected with the B3Z T cell hybridoma with simultaneous detection of ATF4-luciferase expression (**D**). T cell responses from tracer peptides generated from uORF1(WI9)–ATF4-luciferase, uORF1(WI9)-uORF2(KOVAK)–ATF4-luciferase, or uORF2(KOVAK)–ATF4-luciferase transfected (**E**) D^b-L cells detected with the 11p9Z T cell hybridoma or (**F**) K^b-L cells detected with the B3Z T cell hybridoma. 3T responses from uORF2(KOVAK)–ATF4-luciferase (detected with the B3Z T cell hybridoma) generated from mRNA transfection of HeLa-K^b cells (**G**) and primary bone marrow–derived dendritic cells (**H**). T cell responses are representative of $n \geq 3$. A_{595}, absorption at 595 nm.

cells triggered *LacZ* expression, which resulted in production of its translation product, β-galactosidase. We detected β-galactosidase using its substrate, chlorophenol red–β-D-galactopyranoside (CPRG), which yielded a red cleavage product. In the absence of tracer peptide, the T cell hybridoma did not engage cells, and *LacZ* was transcriptionally inactive (Fig. 1A) (*47*).

To validate 3T, we tested the coding capacity of the activating transcription factor 4 (ATF4) 5′ UTR, which contains well-characterized uORFs (fig. S1). To this end, we inserted tracer peptides

into two highly conserved uORFs that were previously shown to regulate ATF4 expression in response to eIF2α phosphorylation (*11*, *48*) (Fig. 1, B and C, and fig. S1). To assess the levels of uORF translation, we transfected cells harboring the appropriate MHC I with uORF (tracer peptide)–ATF4–luciferase constructs. We first nested the coding sequence for the peptide MTFNYRNL (MYL8) (fig. S1) into uORF1 of ATF4-luciferase and the peptide KSIINFEHLK (KOVAK) (fig. S1) into uORF2. Both tracer peptides are presented by MHC I H-2K^b (K^b MHC I). We then added, as a titration of increasing cell numbers, an equal number of T cell hybridomas specific for the tracer peptides displayed [BCZ103 for uORF1(MYL8) or B3Z for uORF2(KOVAK)], followed by CPRG. As expected, T cell responses were only observed when the tracer peptide was present in either uORF (Fig. 1, B and C).

The tracer peptide constructs allowed robust detection of translation from multiple different regions of the mRNA. For example, we measured ATF4-luciferase activity resulting from CDS translation (Fig. 1D) from cells expressing tracer peptides from either uORF1 or uORF2 (Fig. 1, B and C, and fig. S2). Similarly, using the tracer peptide WMHHNMDLI (WI9), presented by MHC I H-2D^b (D^b MHC I) and detected by a different T cell hybridoma, we measured uORF1 expression from either the uORF1(WI9) or the uORF1(WI9)-uORF2(KOVAK) constructs (Fig. 1E). As expected, uORF2(KOVAK) generated a peptide that was only detected by the appropriate T cell hybridoma (compare Fig. 1, E and F). Similarly, the KOVAK tracer peptide was detected independently of its placement in uORF1 or uORF2 (Fig. 1F).

3T can be adapted for detection of tracer peptides from mRNAs directly transfected into cells. In particular, we observed uORF2 tracer peptide expression from uORF2(KOVAK)–ATF4-luciferase mRNA (Fig. 1G). Furthermore, we readily observed tracer peptide expression from uORF2 from primary bone marrow–derived dendritic cells after only a 3-hour mRNA transfection (Fig. 1H). These observations underscore the possibility that any mRNA and a diverse range of cell types can be used to measure uORF expression, as long as the MHC I peptide presentation pathway is constitutively expressed in these cells.

For 3T to reflect expression from distinct regions of the mRNA reliably, tracer peptide placement should not deregulate the expression of the main CDS during steady-state and stress conditions. Therefore, we tested CDS expression (ATF4-luciferase activity) from constructs bearing various uORF tracer peptide insertions. Indeed, insertion of tracer peptides into either uORF1 or uORF2 or simultaneously into both uORFs did not substantially impair the inhibitory function of the uORFs, as assessed by luciferase activity compared with wild type–ATF4-luciferase

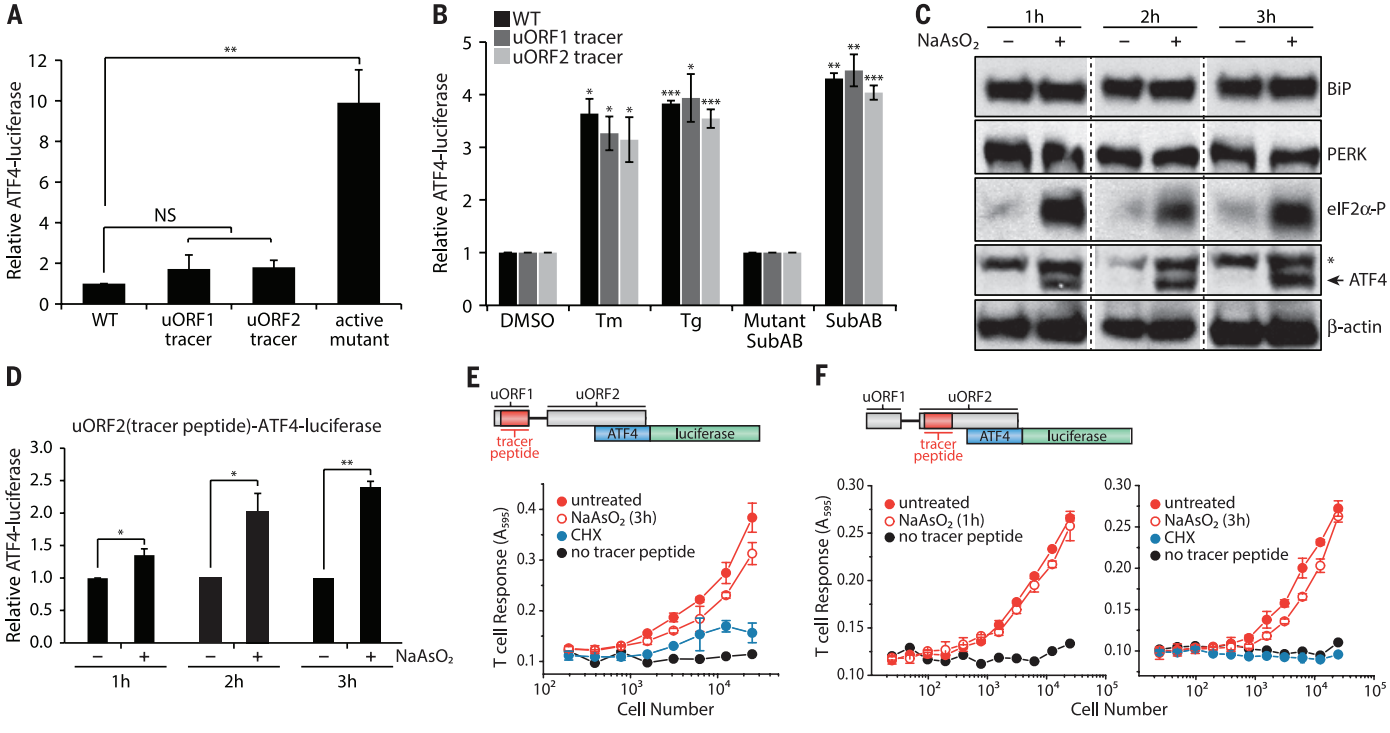


Fig. 2. uORFs are expressed during stress-induced expression of ATF4. (**A**) ATF4-luciferase levels during normal growth conditions were measured from HeLa-K^b cells transfected with wild type–ATF4-luciferase, ATF4-luciferase constructs with tracer peptide insertions [uORF1(MYL8) or uORF2(KOVAK) tracer peptides], or a constitutively active ATF4-luciferase variant (means ± SEM; n = 3 to 4). (**B**) Stress-induced ATF4-luciferase levels were measured from HeLa-K^b cells transfected with wild type–ATF4-luciferase and ATF4-luciferase constructs with tracer peptide insertions [uORF1(MYL8) or uORF2(KOVAK) tracer peptides] and after treatments with tunicamycin (Tm) (1 μg/ml), Tg (1 μM), or Mutant SubAB or SubAB (0.2 μg/ml) for 6 hours (means ± SEM; n = 3 to 4). HeLa-K^b cells from independent tracer peptide DNA transfections were treated with $NaAsO_2$ (10 μM) for 1 to 3 hours and analyzed by immunoblot (n = 3; *nonspecific ATF4-specific antibody signal) (**C**) or for luciferase expression from uORF2(KOVAK)–ATF4-luciferase–transfected cells (means ± SD; n = 3 to 4) (**D**). Tracer peptide expression was measured from HeLa-K^b cells transfected with either uORF1(MYL8)–ATF4 luciferase (**E**) or uORF2(KOVAK)–ATF4 luciferase (**F**) after treatment with $NaAsO_2$ (10 μM) (means ± SD from two biological replicates are representative of n = 3). Stable uORF2(KOVAK)–ATF4-luciferase HeLa-K^b cells were treated for 3 hours with $NaAsO_2$ (10 μM) and assayed for uORF2(KOVAK) tracer peptide expression (**G**) (means ± SD from two biological replicates are representative of n = 3) or for ATF4-luciferase expression (**H**) (means ± SEM; n = 3). Statistical significance was evaluated with the unpaired t test (NS, not significant; *P < 0.05; **P < 0.01; ***P < 0.001).

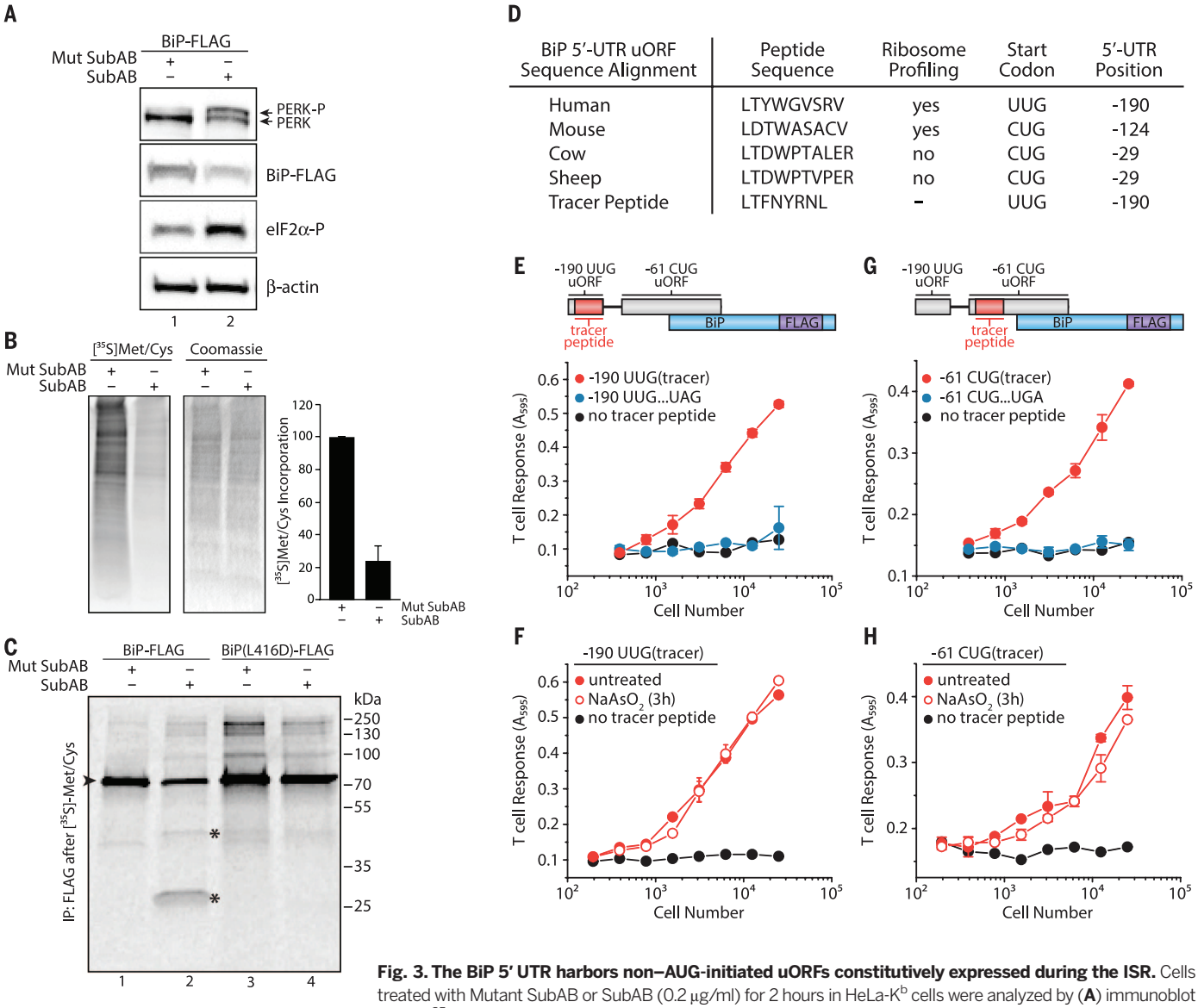


Fig. 3. The BiP 5′ UTR harbors non–AUG-initiated uORFs constitutively expressed during the ISR. Cells treated with Mutant SubAB or SubAB (0.2 μg/ml) for 2 hours in HeLa-K^b cells were analyzed by (**A**) immunoblot or (**B**) [^{35}S]Met-Cys pulse-labeled to measure total protein synthesis (means ± SEM; $n = 4$). (**C**) SubAB-treated HeLa-K^b cells (1 hour) followed by [^{35}S]Met-Cys pulse-labeling (1 hour) and BiP-FLAG immunoprecipitation (▸is full-length BiP and * indicates BiP cleavage products; data representative of $n = 2$). (**D**) Amino acid sequence alignment of the BiP 5′ UTR –190 uORF with non-AUG start codons. (**E**) Schematic of the BiP 5′ UTR with the tracer peptide LYL8 at the –190 UUG uORF. Translation of the –190 UUG uORF was measured from –190 UUG uORF tracer peptide BiP-FLAG–transfected HeLa-K^b cells detected with the BCZ103 T cell hybridoma and compared with cells transfected with an identical construct containing an in-frame UAG stop codon inserted in the middle of the tracer peptide (see fig. S9) or transfected with a no-tracer peptide construct (BiP-FLAG) and (**F**) after treatment with $NaAsO_2$ (10 μM) for 3 hours (means ± SD from two biological replicates and are representative of $n = 3$). (**G**) Schematic of the BiP 5′ UTR with the nested tracer peptide KOVAK in the –61 CUG uORF. Translation of the –61 CUG uORF was measured from –61 CUG uORF tracer peptide BiP-FLAG–transfected HeLa-K^b cells detected with the B3Z T cell hybridoma and compared with cells transfected with an identical construct containing an in-frame UGA stop codon inserted after the –61 CUG uORF start codon but before the tracer peptide (see fig. S9) or transfected with a no-tracer peptide construct (BiP-FLAG) and (**H**) after treatment with $NaAsO_2$ (10 μM) for 3 hours (data are presented as means ± SD of two biological replicates and are representative of $n = 3$).

and a constitutively active variant of ATF4-luciferase (*49*) (Fig. 2A and fig. S3).

To test whether control of ATF4 induction by the ISR was likewise intact in the reporter cell lines bearing the tracer peptide insertions, we exposed cells to subtilase cytotoxin (SubAB), a bacterial AB toxin that is endocytosed by cells and retrotransported to the ER lumen, where it destroys BiP by proteolysis (*50*). BiP destruction induced protein misfolding in the ER and PERK-catalyzed phosphorylation of eIF2α, which inhibited cellular translation (fig. S4A). The translation block was readily reversed by ISRIB, a small molecule that overcomes the effects of eIF2α phosphorylation (*51*–*53*) (fig. S4A). SubAB triggered PERK activation, expression of endogenous ATF4, eIF2α phosphorylation (fig. S4B), and up-regulation of the plasmid-borne ATF4-luciferase reporter (fig. S4C). ISRIB inhibited endogenous ATF4 expression and ATF4-luciferase expression, which indicated that the ATF4 transgene behaved like endogenous ATF4 (fig. S4). Furthermore, multiple UPR inducers stimulated ATF4-luciferase expression equivalently from constructs harboring either a uORF1 or uORF2 tracer peptide (Fig. 2B). These results indicate that tracer peptide placement does not compromise the control of ATF4 expression during ER stress.

3T relies on proper processing of tracer peptides, including import into the ER and loading

onto MHC I molecules. To induce eIF2α phosphorylation without disturbing the normal processes in the ER lumen, such as protein folding (compromised by SubAB cleavage of BiP), or N-linked glycosylation (inhibited by tunicamycin), or directly activating the T cell hybridomas [calcium fluxes with thapsigargin (Tg)], we treated cells with $NaAsO_2$, an inducer of oxidative stress, which rapidly induces eIF2α phosphorylation and ATF4 induction by activating cytosolic HRI (*54*). We observed rapid and robust expression of endogenous ATF4 without activation of PERK or altered expression of BiP (Fig. 2C and fig. S5). Pertinent to the utility of 3T, ATF4-luciferase harboring a nested uORF2 tracer peptide showed the expected induction with $NaAsO_2$ treatment (Fig. 2D). Peptide expression from uORF1 (Fig. 2E) and uORF2 (Fig. 2, F to H, and fig. S6) largely persisted when ATF4-luciferase was induced, a finding that differs from studies with yeast *GCN4* (*55*). However, the pervasive uORF2 peptide expression measured here is consistent with recent ribosome-profiling studies on *ATF4* mRNA upon ISR induction (*43*, *44*). These results validate 3T as a sensitive and robust indicator of uORF expression. As such, we next applied this method to ask whether uORF translation is a general strategy that cells use to ensure privileged protein expression during the ISR.

3T reveals a novel regulatory element in the 5′ UTR of BiP mRNA

BiP synthesis, which is initiated at a standard AUG start codon (fig. S7), persists during ER stress, when the ISR is induced (*56*). To explore this phenomenon, we treated cells with SubAB, resulting in PERK activation, eIF2α phosphorylation, and a massive reduction in protein synthesis (Fig. 3, A and B). As expected, treatment with a catalytically inactive form of SubAB (Mut SubAB) did not result in ISR induction (Fig. 3, A and B, and fig. S8). To assess directly whether BiP is synthesized after onset of the ISR, we transfected cells with DNA encoding FLAG-tagged BiP [or BiP(L416D)-FLAG, a SubAB-resistant mutant] and treated them with Mut SubAB or SubAB. We next pulse-labeled cells with [^{35}S] Met-Cys to label newly synthesized proteins, followed by immunoprecipitation of BiP. In agreement with previous results, BiP from both constructs was readily synthesized despite ISR induction (Fig. 3C). Thus, elements other than conventional initiation at the annotated BiP AUG start codon or its CDS may be required to ensure privileged expression during the UPR.

Recent ribosome profiling measurements indicate that BiP mRNA shows substantial levels of ribosome occupancy in the 5′ UTR (*33*). The most prominent ribosome initiation signal was detected at an UUG codon at position −190 (relative to BiP coding sequence +1 AUG), encoding a putative nine–amino acid peptide (Fig. 3D and fig. S9A). To test whether this predicted uORF is translated, we nested a tracer peptide [LTFNYRNL (LYL8)] in the −190 UUG uORF (Fig. 3D), which did not alter the expression of BiP during basal conditions or its targeting to the ER as assayed by SubAB sensitivity (fig. S10A). When assessed by 3T, we readily detected the −190 UUG leucine codon–initiated expression of the tracer peptide (Fig. 3E). Translation of the −190 UUG uORF persisted upon eIF2α phosphorylation induced by $NaAsO_2$ treatment (Fig. 3F). Given that an UUG codon codes for leucine and that leucine initiation is resistant to $NaAsO_2$ treatment and reduced eIF2·GTP·Met-tRNA$_i^{Met}$ levels (*57*, *58*), a noncanonical UUG or CUG initiation mechanism may function in the BiP 5′ UTR.

We similarly tested expression of the nested KOVAK tracer peptide in the predicted −61 leucine CUG-initiated uORF in the BiP 5′ UTR (*33*) (Fig. 3G and fig. S9B). This uORF is out of frame with the BiP AUG-initiated CDS. Indeed, the −61 CUG-initiated uORF supports expression of a peptide in cells when present out of frame (Fig. 3G) or in frame with the BiP coding sequence (fig. S10, A and B). Expression of the −61 CUG uORF was not markedly reduced in the presence of $NaAsO_2$ (Fig. 3H), which suggests that multiple noncanonical initiation events are involved in sustaining BiP expression during stress.

BiP uORF expression is regulated by eIF2A

The alternative initiation factor eIF2A, a monomeric protein structurally and functionally distinct from the trimeric eIF2, coordinates noncanonical leucine (CUG) initiation (*58*) and expression of a CUG leucine–initiated phosphatase and tensin homolog deleted on chromosome 10 isoform (*59*). Given these findings, we examined the consequences of eIF2A depletion on −190 UUG uORF and BiP expression. Although when eIF2A is depleted (eIF2A knockdown) with small interfering RNA (siRNA), this did not measurably impair global protein synthesis (fig. S11), and it substantially impaired expression of the −190 UUG uORF (Fig. 4A and fig. S12), which required nearly 40% more tracer-expressing cells to stimulate T cells to a half-maximal response (Fig. 4B). This observation is consistent with a requirement for eIF2A-dependent initiation of the BiP −190 UUG uORF, which may regulate the levels of BiP.

Indeed, siRNA knockdown of eIF2A (Fig. 4C) measurably compromised expression of BiP-FLAG, during induction of the ISR with Tg, an ER stress inducer (Fig. 4D, lane 4, and 4E); deregulated the steady-state levels of endogenous BiP; and compromised its expression during the ISR (fig. S13). Notably, deletion of the −190 UUG uORF concurrently with eIF2A siRNA knockdown dramatically impaired the expression of BiP in ER-stressed cells (Fig. 4F, lane 4, and 4G). Moreover, the expression of eIF2A was induced by SubAB in our cell model (Fig. 4, H and I) and in primary mouse dendritic cells in response to a variety of other stresses (Fig. 4J). In these cells, eIF2A was induced by poly(I:C) and lipopolysaccharide (LPS) (which are activators of PKR) and the small molecule NSC119893 that blocks Met-tRNA$_i^{Met}$ binding to eIF2 and compromises canonical AUG-dependent, but not noncanonical, initiation (*58*, *60*). eIF2A up-regulation during acute loss of eIF2·GTP·Met-tRNA$_i^{Met}$ ternary complex caused by NSC119893 and dependence on eIF2A for −190 UUG uORF expression are consistent with a requirement for eIF2A in order for BiP to be expressed during cellular stress (Fig. 4K).

uORFs harbor predicted HLA epitopes

In addition to regulating BiP levels during stress, the peptide translated from the −190 UUG uORF is predicted (*61*) to be a potent human leukocyte antigen (HLA)–presented epitope (human MHC I–peptide) recognized by human T cells (Fig. 5A and fig. S14), as is a peptide potentially generated by translation and processing of the −61 CUG uORF (fig. S14). Peptide expression from these uORFs, during basal and/or ISR conditions, suggested that there may be widespread peptide expression that could serve a variety of extracellular regulatory roles, such as HLA presentation, yet escape detection by currently available techniques, as these peptides are smaller than 10 kD.

To begin to assess the prevalence of these translation events, we measured the presence of peptides under conditions of limiting ternary complex using a global readout of their abundance. To this end, we measured diffusion of green fluorescent protein (GFP)–labeled TAP after photobleaching (TAP-FRAP) (*62*) (Fig. 5B). TAP is an ER-resident adenosine triphosphate–binding cassette transporter that consists of two subunits, TAP1 and TAP2. Antigenic precursor peptides are transported from the cytosol into the ER lumen by TAP (*63*) and loaded onto MHC I molecules with the aid of ER-resident chaperones (*64*). Note that the mobility of TAP in the ER membrane depends on peptide abundance. When peptides are lacking, TAP mobility in the ER membrane is measurably enhanced, which is indicative of peptide engagement and, hence, provides a robust readout for peptide abundance (*62*). We treated cells with NSC119893 to induce the ISR and block eIF2-mediated initiation or with cycloheximide (CHX) to globally inhibit translation (Fig. 5C). As expected, BiP expression was not inhibited by NSC119893 but was by other translation inhibitors (Fig. 5D and fig. S15). In the TAP-FRAP assay, untreated cells showed baseline levels of TAP diffusion, indicative of high peptide availability and TAP engagement, as shown by dimethyl sulfoxide (DMSO) (Fig. 5E). As previously shown (*62*), CHX inhibited peptide supply and, therefore, enhanced TAP diffusion (Fig. 5E). By contrast, treatment with NSC119893 showed only a modest increase in TAP diffusion (Fig. 5E), which was substantially less than that observed with CHX, despite an equivalent reduction of full-length protein synthesis as assayed by [^{35}S]Met-Cys incorporation (Fig. 5C). These results provide independent evidence for the ubiquitous presence of newly synthesized peptides during normal growth and ISR conditions.

Stress-resistant expression is a common feature of chaperones and heat shock proteins (*65*), with the 5′ UTR often necessary and sufficient to reconstitute expression during stress (*66*, *67*). We examined ribosome profiling data (*33*) for a

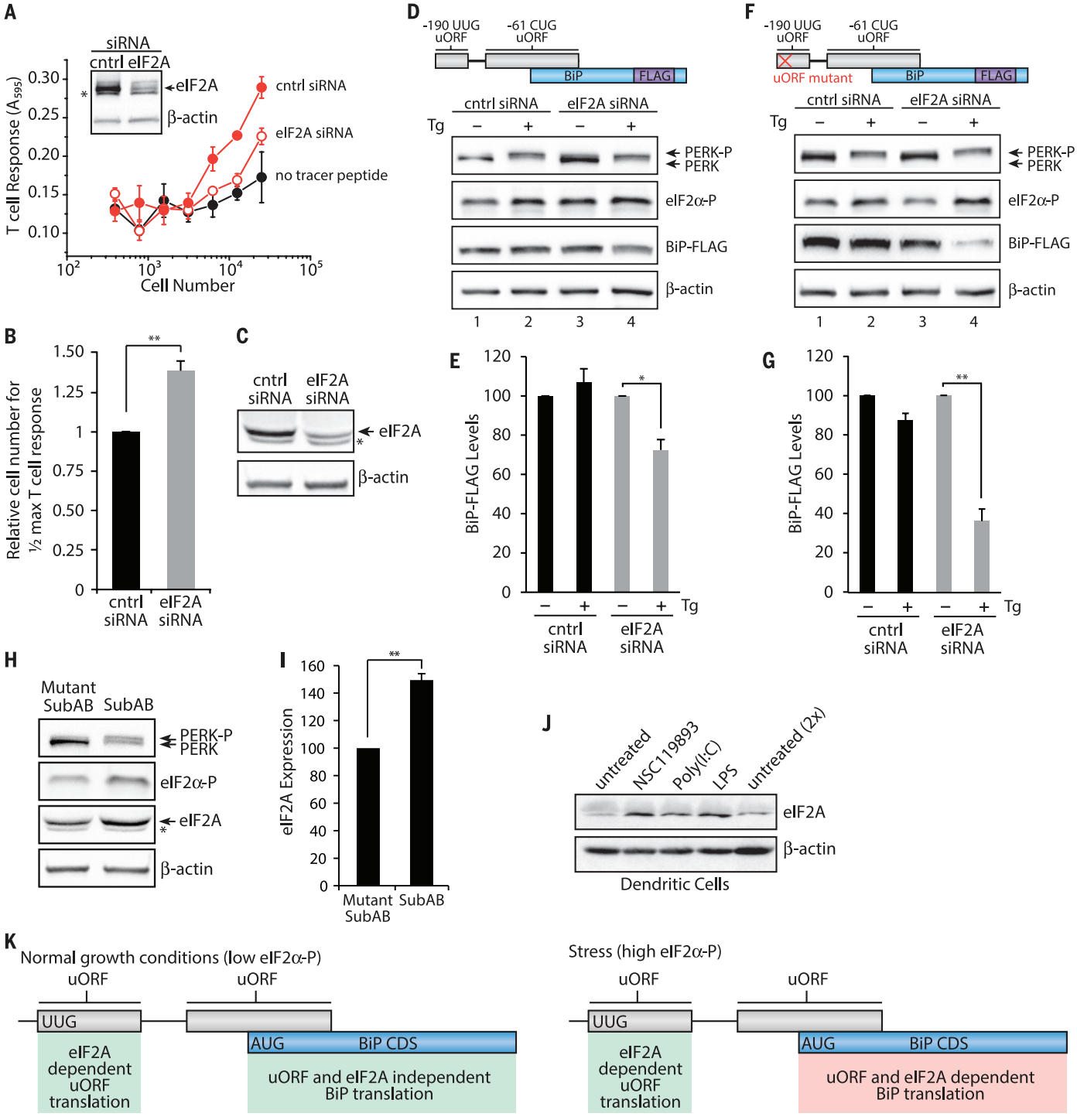
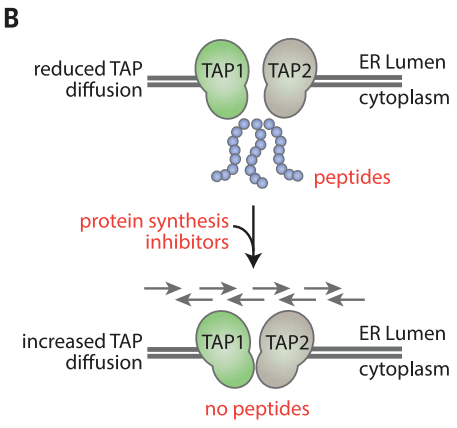
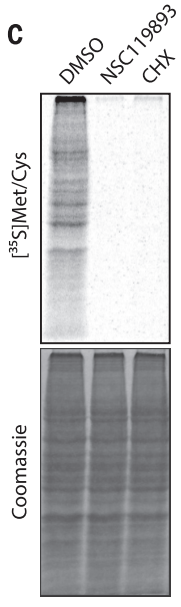


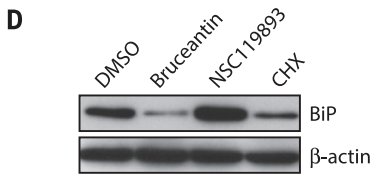
Fig. 4. eIF2A and 5′ UTR uORFs are required for sustained BiP expression during the ISR. (**A**) Translation of the –190 UUG uORF from –190 UUG uORF tracer peptide (LYL8) BiP-FLAG–transfected HeLa-K^b cells after 48 hours siRNA knockdown detected with the BCZ103 T cell hybridoma and compared with cells transfected with a no-tracer peptide construct (data are presented as means ± SD of two biological replicates and are representative of $n = 4$). Inset shows an immunoblot for eIF2A knockdown and a β-actin loading control. (**B**) Relative number of cells required to achieve half-maximal T cell response for –190 UUG uORF expression with eIF2A siRNA knockdown (mean ± SEM; $n = 4$). Expression of BiP-FLAG analyzed by immunoblot from BiP-FLAG (**D** and **E**) or uORF mutant BiP-FLAG (**F** and **G**) transfected HeLa-K^b cells after 48 hours of siRNA knockdown (**C**) and treatment with DMSO or Tg (1 μM) for 3 hours ($n = 3$). BiP levels are presented relative to untreated for each siRNA. (**H** and **I**) HeLa-K^b cells treated with Mut SubAB or SubAB (0.2 μg/ml) for 2 hours and analyzed by immunoblot for eIF2A expression (*nonspecific anti-eIF2A antibody signal) (means ± SEM; $n = 3$). (**J**) Primary bone marrow–derived dendritic cells analyzed by immunoblot for eIF2A expression after treatment with NSC119893 (50 μM), poly(I:C) (1 μg/ml), or LPS (1 μg/ml) for 3 hours ($n = 2$). (**K**) Working model for uORF translation regulation of BiP CDS expression. During normal growth conditions, BiP CDS expression is not dependent on uORF translation and eIF2A. Stress up-regulates eIF2α-P levels, leads to elevated eIF2A levels, and leads to constitutive uORF translation, which positively regulates BiP CDS expression. Statistical significance was evaluated with the unpaired t test (*$P < 0.05$; **$P < 0.01$)

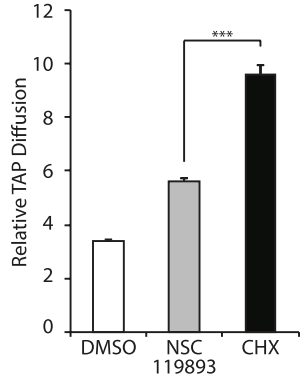
A

BiP 5′ UTR -190 uORF peptide	Predicted HLA	Predicted affinity (nM)
LTYWGVSRV	HLA-A*02:01	276
MTYWGVSRV	HLA-A*02:01	44









F

Chaperone 5′ UTR uORFs predicted by ribosome profiling	uORF initiation codon	Peptide sequence	Predicted HLA	Predicted affinity (nM)
HSPA1B (NM_005346.4)	-127 CUG	LLSRIPSAV	HLA-A*02:01	74
HSPA1B (NM_005346.4)	-127 CUG	FPAFRRTEL	HLA-B*07:02	9
HSPA8 (NM_153201.3)	-47 AUU	VLILAPPTL	HLA-A*02:01	41
HSP90B1 (NM_003299.2)	-23 UUG	LRLTGRTP	—	—
HSP90AB1 (NM_007355.3)	-71 UUG	RRWRLLPFR	HLA-B*27:05	9
CCT3 (NM_001008800.2)	-47 CUG	VPPALGTRL	HLA-B*07:02	155
CCT3 (NM_001008800.2)	-29 CUG	LGTRLCIASP	—	—

Fig. 5. Peptides translated from uORFs and other RNAs during the ISR are predicted to be MHC I peptides. (**A**) HLA epitope (human MHC I) prediction from translation of the BiP 5′ UTR –190 UUG uORF using the immune epitope database (IEDB) analysis resource consensus tool (*94*). (**B**) Schematic for TAP diffusion [TAP1(GFP)-TAP2 complex] in the ER in the presence or absence of peptides. (**C**) Meljuso cells stably expressing TAP1-GFP (*62*) treated for 1 hour with NSC119893 (25 μM) or CHX (50 μg/ml) or (**D**) HeLa-K^b cells treated for 8 hours with bruceantin (100 nM); NSC119893 (50 μM, replenished every 2 hours); or CHX 100 μg/ml were labeled with [^{35}S] Met-Cys (n = 3). (**E**) Meljuso cells stably expressing TAP1-GFP were treated with either NSC119893 or CHX and imaged using fluorescence confocal microscopy for lateral mobility of TAP with treatment (means ± SEM; n = 4 to 7). (**F**) uORFs predicted from ribosome profiling of chaperone mRNAs (*33*) generate peptides predicted to be HLA epitopes using the IEDB resource consensus tool (*94*). Statistical significance was evaluated with the unpaired t test (***P < 0.001).

variety of chaperones to identify non-AUG uORFs in their 5′ UTRs. This analysis revealed that UUG- and CUG-initiated uORFs are present in the 5′ UTR of a variety of human chaperones (Fig. 5F). Furthermore, several of these uORFs encode peptides, which, after cellular processing, are predicted to be bound by HLA with strong affinity (Fig. 5F). Taken together, our results suggest that the HLA peptide repertoire is larger than previously predicted and includes peptides derived from 5′ UTR uORFs that may be selectively translated under stress conditions.

Discussion

Here, we exploited the sensitivity and specificity of T cells to assess whether translation occurs outside of the standard protein CDS using 3T. The basis for 3T is the insertion of a tracer peptide coding sequence, known to be presented by MHC I to T cells, into a predefined DNA sequence, which is transcribed into mRNA and translated by ribosomes. The translated tracer peptides, whether nested in a polypeptide or translated from their own ORFs, are efficiently processed and loaded onto MHC I molecules in the ER and travel to the cell surface, where the peptide–MHC I complex is detected by exquisitely specific and sensitive T cell hybridomas. This candidate approach allows customized insertion of tracer peptides into any region of the genome and is amenable to genome tiling of tracer peptides for large-scale discovery and validation of translated uORFs, sORFs, protein isoforms, and "noncoding" RNAs, such as introns, long noncoding RNAs, and 3′ UTRs.

We validated 3T by detecting translated peptides from the uORFs of ATF4, a transcription factor only expressed during the ISR. We measured a high degree of peptide expression from both ATF4 uORF1 and uORF2 during both normal growth and stress conditions, a finding recently predicted from ribosome profiling measurements (*43*, *44*). The high degree of uORF expression during stress, however, was not predicted on the basis of the current reinitiation model for ATF4 expression (*11*) or the related yeast homolog GCN4 during stress (*55*). In this model, the small ribosomal subunit is expected to remain mRNA bound and scans past uORF2 and acquires eIF2·GTP·Met-$tRNA_i^{Met}$ and the large ribosomal subunit in time for initiation at the conventional AUG start codon of the CDS. Our measurements indicate either that reinitiation commences after only a few ribosomes skip uORF2 or that translation of the ATF4 CDS is a combination of reinitiation and scanning past the uORFs ("leaky scanning"), two events that

are technically challenging to distinguish (*45*). Our finding that uORFs are constitutively expressed during stress and limiting eIF2·GTP·Met-tRNA$_i^{Met}$ levels prompts us to speculate that uORF translation might serve an additional role during the ISR, which provides an explanation for the high level of ribosome occupancy within the 5′ UTRs of mRNAs expressed during stress (*43*). Constitutive uORF expression could thus protect mRNAs from translational down-regulation during stress and thereby serve to control gene expression.

Using *3T*, we showed that BiP harbors uORFs that are constitutively translated during stress. By contrast to the AUG-initiated uORFs of ATF4, BiP 5′ UTR uORFs are exclusively initiated by the non-AUG leucine codons UUG and CUG. Expression of the –190 UUG uORF from the BiP 5′ UTR requires the alternative initiation factor eIF2A. By contrast to initiation with the conventional eIF2·GTP·Met-tRNA$_i^{Met}$ ternary complex, eIF2A is a monomer and does not bind GTP (*68*). In addition to initiation at CUG start codons (*58*, *59*), eIF2A is required for initiation at the AUG start codon of a hepatitis C virus internal ribosome entry site (IRES) reporter (*69*) and viral proteins from the Sindbis alphavirus (*70*), during stress conditions and high levels of eIF2α phosphorylation. Stress-induced eIF2A could substitute for eIF2 during initiation at the BiP AUG start codon. Our data support a model where eIF2A and a combination of uORFs maintain the levels of BiP synergistically during translational attenuation accompanying cellular stress. We propose that elevated levels of eIF2A, as we observed upon ISR induction, protect BiP mRNA from translational shutdown upon eIF2α phosphorylation.

It was suggested previously that BiP mRNA harbors an IRES in its 5′ UTR, required for BiP expression during continuous heat shock (*71*, *72*). Our data reveal an added level of regulation within the BiP 5′ UTR wherein persistent, noncanonical uORF translation and eIF2A function as a cis-acting regulatory element necessary for privileged BiP expression during stress. The role for eIF2A and noncanonical initiation in the 5′ UTR during ribosome scanning of cellular mRNAs is an emerging property of translational regulation (*59*), which highlights a new translational mechanism used during the integrated stress response. These findings add to a growing list of alternative initiation events, such as initiation from structured 5′ UTRs with DEAD/DExH-box proteins (*73*, *74*) or eIF2-independent recruitment of Met-tRNA$_i^{Met}$ on viral mRNAs by Ligatin and MCT-1 or DENR (*75*). The observation that other chaperones, also stably expressed during stress, harbor non–AUG-initiated uORFs in the 5′ UTR indicates that uORF expression may be a general mechanism used to regulate the synthesis of proteins necessary during the ISR. Thus, substantial evidence now suggests that uORFs are required for regulation of CDSs and that uORF mutations are linked to a number of diseases [reviewed in (*45*)].

The notion that some uORF peptides fall outside the detectable range of mass spectrometry analysis because of their short length or selective proteolysis (*76*) presents an advantage for *3T*. The TAP channel readily transports short peptides into the ER for the peptide-loading complex, which is poised to efficiently facilitate loading onto MHC I molecules. Therefore, the detection of translated products from very short uORFs, such as ATF4 uORF1 (three amino acids), is ideal for *3T*, because the entirety of the translated uORF serves to generate the mature peptide for MHC I loading and subsequent detection by T cells. Additionally, the uORF products with short half-lives that are efficiently processed serve to enhance the sensitivity of *3T*, because proteolysis is required before TAP transport and MHC I loading. Last, the *3T* assay is exquisitely sensitive because of the inherent sensitivity of T cells that can detect even a few copies of the peptide–MHC I and trigger the *LacZ* response (*46*, *77*).

The apparent disconnect between the number of translated uORFs predicted by ribosome profiling (*32*, *33*) and the number of translated uORFs identified by mass spectrometry is likely explained by the challenges encountered by extensive mass spectrometry analysis of HLA-bound peptides over the years (*78*, *79*). These HLA-associated peptide analyses have revealed that mass spectrometry analysis is unlikely to capture all the different peptides presented by MHC I molecules for a variety of reasons. Early analyses predicted that 10,000 to 20,000 different peptides are presented on the cell surface by both MHC I and MHC II molecules, although recent estimates suggest that MHC I alone could display between 30,000 and 120,000 peptides on each cell surface (*80*). An analogous disconnect is observed between the 42,271 human sORFs (40 to 100 amino acids long) predicted by ribosome profiling (*41*) and the 1259 alternative proteins detected by mass spectrometry (*81*). Absolute peptide abundance may limit the recovery of some peptides if they are present at low copy numbers, such as 1 to 1000 molecules per cell (*39*, *78*, *82*). Furthermore, assignment of peptides from low-molecular-weight precursors (less than 100 amino acids) by mass spectrometry is limited by the presence of many unidentified ion peaks and the lack of comprehensive low-molecular-weight reference databases (*83*), which is currently being addressed (*81*, *83*). In addition, standard assignment of recovered HLA-bound peptides is typically performed by alignment with the CDS of the mRNA (*78*, *79*) not to regions outside the annotated open reading frames. Examples of MHC I peptides generated from translation of noncoding RNA—such as 5′ UTRs, introns, and intron-exon junctions (*84*)—highlight the need to explore regions outside of the CDS for sources of MHC I peptides and other bioactive peptides. The recent reports of non-AUG start codon initiation (*58*, *59*, *67*) suggest that standard peptide alignments should also include ORFs initiated with CUG, UUG, and other non-AUG start codons, whether inside or outside of the annotated CDS (*81*).

Discovery of uORF translation from the 5′ UTR of BiP and prediction of uORF translation in other stress-related chaperones could generate a pool of peptides that serve a variety of biological functions. For example, uORF peptides may shape the immune response as self-antigens during cancer progression and autoimmune disease (*80*). Indeed, nonmutant tumor antigens generate physiologically relevant immune responses for cancer immunotherapy (*85*). Therefore, a reexamination of HLA-associated peptide libraries (*78*) promises to uncover peptides that are generated from translation outside of annotated CDS, such as uORFs initiated with non-AUG start codons. Translated uORFs could also generate bioactive peptides that directly or indirectly regulate expression of the main CDS, as seen with the peptide translated from the uORF in *S*-adenosylmethionine decarboxylase mRNA (*86*), or function in signaling pathways, such as Toddler—a short, secreted peptide essential for embryogenesis (*42*).

3T offers a robust approach for characterization of the numerous predicted translation events in 5′ UTRs and other noncoding RNA (*32*, *33*). These results emphasize the importance of translated regulatory features in 5′ UTRs, which regulate translational control of the downstream CDS, as indicated by a variety of disease-causing 5′ UTR uORF mutations (*35*). We propose that this phenomenon presents an extracellular signature during the ISR to modulate T cell immune responses (*84*).

REFERENCES AND NOTES

1. P. Walter, D. Ron, The unfolded protein response: From stress pathway to homeostatic regulation. *Science* **334**, 1081–1086 (2011). doi: 10.1126/science.1209038; pmid: 22116877
2. Y. Shi *et al*., Identification and characterization of pancreatic eukaryotic initiation factor 2 alpha-subunit kinase, PEK, involved in translational control. *Mol. Cell. Biol.* **18**, 7499–7509 (1998). doi: 10.1128/MCB.18.12.7499; pmid: 9819435
3. H. P. Harding, Y. Zhang, D. Ron, Protein translation and folding are coupled by an endoplasmic-reticulum-resident kinase. *Nature* **397**, 271–274 (1999). doi: 10.1038/16729; pmid: 9930704
4. J. Galabru, M. G. Katze, N. Robert, A. G. Hovanessian, The binding of double-stranded RNA and adenovirus VAI RNA to the interferon-induced protein kinase. *Eur. J. Biochem.* **178**, 581–589 (1989). doi: 10.1111/j.1432-1033.1989.tb14485.x; pmid: 2912723
5. E. Meurs *et al*., Molecular cloning and characterization of the human double-stranded RNA-activated protein kinase induced by interferon. *Cell* **62**, 379–390 (1990). doi: 10.1016/0092-8674(90)90374-N; pmid: 1695551
6. J. J. Berlanga, J. Santoyo, C. De Haro, Characterization of a mammalian homolog of the GCN2 eukaryotic initiation factor 2alpha kinase. *Eur. J. Biochem.* **265**, 754–762 (1999). doi: 10.1046/j.1432-1327.1999.00780.x; pmid: 10504407
7. L. Lu, A. P. Han, J. J. Chen, Translation initiation control by heme-regulated eukaryotic initiation factor 2alpha kinase in erythroid cells under cytoplasmic stresses. *Mol. Cell. Biol.* **21**, 7971–7980 (2001). doi: 10.1128/MCB.21.23.7971-7980.2001; pmid: 11689689
8. R. J. Jackson, C. U. Hellen, T. V. Pestova, The mechanism of eukaryotic translation initiation and principles of its regulation. *Nat. Rev. Mol. Cell Biol.* **11**, 113–127 (2010). doi: 10.1038/nrm2838; pmid: 20094052
9. T. W. Hai, F. Liu, W. J. Coukos, M. R. Green, Transcription factor ATF cDNA clones: An extensive family of leucine zipper proteins able to selectively form DNA-binding heterodimers. *Genes Dev.* **3** (12B), 2083–2090 (1989). doi: 10.1101/gad.3.12b.2083; pmid: 2516827
10. P. D. Lu, H. P. Harding, D. Ron, Translation reinitiation at alternative open reading frames regulates gene expression in an integrated stress response. *J. Cell Biol.* **167**, 27–33 (2004). doi: 10.1083/jcb.200408003; pmid: 15479734

11. K. M. Vattem, R. C. Wek, Reinitiation involving upstream ORFs regulates ATF4 mRNA translation in mammalian cells. *Proc. Natl. Acad. Sci. U.S.A.* **101**, 11269–11274 (2004). doi: 10.1073/pnas.0400541101; pmid: 15277680
12. A. J. Fornace Jr., I. Alamo Jr., M. C. Hollander, DNA damage-inducible transcripts in mammalian cells. *Proc. Natl. Acad. Sci. U.S.A.* **85**, 8800–8804 (1988). doi: 10.1073/pnas.85.23.8800; pmid: 3194391
13. D. Ron, J. F. Habener, CHOP, a novel developmentally regulated nuclear protein that dimerizes with transcription factors C/EBP and LAP and functions as a dominant-negative inhibitor of gene transcription. *Genes Dev.* **6**, 439–453 (1992). doi: 10.1101/gad.6.3.439; pmid: 1547942
14. J. Han *et al*., ER-stress-induced transcriptional regulation increases protein synthesis leading to cell death. *Nat. Cell Biol.* **15**, 481–490 (2013). doi: 10.1038/ncb2738; pmid: 23624402
15. A. G. Hinnebusch, The scanning mechanism of eukaryotic translation initiation. *Annu. Rev. Biochem.* **83**, 779–812 (2014). doi: 10.1146/annurev-biochem-060713-035802; pmid: 24499181
16. G. Joslin, W. Hafeez, D. H. Perlmutter, Expression of stress proteins in human mononuclear phagocytes. *J. Immunol.* **147**, 1614–1620 (1991). pmid: 1880418
17. R. Panniers, Translational control during heat shock. *Biochimie* **76**, 737–747 (1994). doi: 10.1016/0300-9084(94)90078-7; pmid: 7893824
18. K. Richter, M. Haslbeck, J. Buchner, The heat shock response: Life on the verge of death. *Mol. Cell* **40**, 253–266 (2010). doi: 10.1016/j.molcel.2010.10.006; pmid: 20965420
19. S. D. Der, A. S. Lau, Involvement of the double-stranded-RNA-dependent kinase PKR in interferon expression and interferon-mediated antiviral activity. *Proc. Natl. Acad. Sci. U.S.A.* **92**, 8841–8845 (1995). doi: 10.1073/pnas.92.19.8841; pmid: 7568028
20. F. D. Gilfoy, P. W. Mason, West Nile virus-induced interferon production is mediated by the double-stranded RNA-dependent protein kinase PKR. *J. Virol.* **81**, 11148–11158 (2007). doi: 10.1128/JVI.00446-07; pmid: 17686861
21. L.-C. Hsu *et al*., The protein kinase PKR is required for macrophage apoptosis after activation of Toll-like receptor 4. *Nature* **428**, 341–345 (2004). doi: 10.1038/nature02405; pmid: 15029200
22. R. P. Shiu, J. Pouyssegur, I. Pastan, Glucose depletion accounts for the induction of two transformation-sensitive membrane proteins[ ]in Rous sarcoma virus-transformed chick embryo fibroblasts. *Proc. Natl. Acad. Sci. U.S.A.* **74**, 3840–3844 (1977). doi: 10.1073/pnas.74.9.3840; pmid: 198809
23. I. G. Haas, M. Wabl, Immunoglobulin heavy chain binding protein. *Nature* **306**, 387–389 (1983). doi: 10.1038/306387a0; pmid: 6417546
24. S. Munro, H. R. Pelham, An Hsp70-like protein in the ER: Identity with the 78 kd glucose-regulated protein and immunoglobulin heavy chain binding protein. *Cell* **46**, 291–300 (1986). doi: 10.1016/0092-8674(86)90746-4; pmid: 3087629
25. J. Li, A. S. Lee, Stress induction of GRP78/BiP and its role in cancer. *Curr. Mol. Med.* **6**, 45–54 (2006). doi: 10.2174/156652406775574523; pmid: 16472112
26. M. S. Gorbatyuk, O. S. Gorbatyuk, The molecular chaperone GRP78/BiP as a therapeutic target for neurodegenerative disorders: A mini review. *J. Genet. Syndr. Gene Ther.* **4**, 128 (2013). doi: 10.4172/2157-7412.1000128; pmid: 23750325
27. L. Booth *et al*., GRP78/BiP/HSPA5/Dna K is a universal therapeutic target for human disease. *J. Cell. Physiol.* **230**, 1661–1676 (2015). doi: 10.1002/jcp.24919; pmid: 25546329
28. C. U. Hellen, P. Sarnow, Internal ribosome entry sites in eukaryotic mRNA molecules. *Genes Dev.* **15**, 1593–1612 (2001). doi: 10.1101/gad.891101; pmid: 11445534
29. J. Zhou *et al*., Dynamic m(6)A mRNA methylation directs translational control of heat shock response. *Nature* **526**, 591–594 (2015). doi: 10.1038/nature15377; pmid: 26458103
30. S. E. Calvo, D. J. Pagliarini, V. K. Mootha, Upstream open reading frames cause widespread reduction of protein expression and are polymorphic among humans. *Proc. Natl. Acad. Sci. U.S.A.* **106**, 7507–7512 (2009). doi: 10.1073/pnas.0810916106; pmid: 19372376
31. A. M. Resch, A. Y. Ogurtsov, I. B. Rogozin, S. A. Shabalina, E. V. Koonin, Evolution of alternative and constitutive regions of mammalian 5′UTRs. *BMC Genomics* **10**, 162 (2009). doi: 10.1186/1471-2164-10-162; pmid: 19371439
32. N. T. Ingolia, L. F. Lareau, J. S. Weissman, Ribosome profiling of mouse embryonic stem cells reveals the complexity and dynamics of mammalian proteomes. *Cell* **147**, 789–802 (2011). doi: 10.1016/j.cell.2011.10.002; pmid: 22056041
33. S. Lee *et al*., Global mapping of translation initiation sites in mammalian cells at single-nucleotide resolution. *Proc. Natl. Acad. Sci. U.S.A.* **109**, E2424–E2432 (2012). doi: 10.1073/pnas.1207846109; pmid: 22927429
34. N. T. Ingolia *et al*., Ribosome profiling reveals pervasive translation outside of annotated protein-coding genes. *Cell Reports* **8**, 1365–1379 (2014). doi: 10.1016/j.celrep.2014.07.045; pmid: 25159147
35. M. Cazzola, R. C. Skoda, Translational pathophysiology: A novel molecular mechanism of human disease. *Blood* **95**, 3280–3288 (2000).pmid: 10828006
36. T. Kondo *et al*., Familial essential thrombocythemia associated with one-base deletion in the 5′-untranslated region of the thrombopoietin gene. *Blood* **92**, 1091–1096 (1998). pmid: 9694695
37. A. Wiestner, R. J. Schlemper, A. P. van der Maas, R. C. Skoda, An activating splice donor mutation in the thrombopoietin gene causes hereditary thrombocythaemia. *Nat. Genet.* **18**, 49–52 (1998). doi: 10.1038/ng0198-49; pmid: 9425899
38. N. Ghilardi, R. C. Skoda, A single-base deletion in the thrombopoietin (TPO) gene causes familial essential thrombocythemia through a mechanism of more efficient translation of TPO mRNA. *Blood* **94**, 1480–1482 (1999). pmid: 10484635
39. S. A. Slavoff *et al*., Peptidomic discovery of short open reading frame-encoded peptides in human cells. *Nat. Chem. Biol.* **9**, 59–64 (2013). doi: 10.1038/nchembio.1120; pmid: 23160002
40. S. J. Andrews, J. A. Rothnagel, Emerging evidence for functional peptides encoded by short open reading frames. *Nat. Rev. Genet.* **15**, 193–204 (2014). doi: 10.1038/nrg3520; pmid: 24514441
41. V. Olexiouk *et al*., sORFs.org: A repository of small ORFs identified by ribosome profiling. *Nucleic Acids Res.* gkv1175 (2015). doi: 10.1093/nar/gkv1175; pmid: 26527729
42. A. Pauli *et al*., Toddler: An embryonic signal that promotes cell movement via Apelin receptors. *Science* **343**, 1248636 (2014). doi: 10.1126/science.1248636; pmid: 24407481
43. D. E. Andreev *et al*., Translation of 5′ leaders is pervasive in genes resistant to eIF2 repression. *eLife* **4**, e03971 (2015). doi: 10.7554/eLife.03971; pmid: 25621764
44. C. Sidrauski, A. M. McGeachy, N. T. Ingolia, P. Walter, The small molecule ISRIB reverses the effects of eIF2α phosphorylation on translation and stress granule assembly. *eLife* **4**, (2015). doi: 10.7554/eLife.05033; pmid: 25719440
45. J. Somers, T. Pöyry, A. E. Willis, A perspective on mammalian upstream open reading frame function. *Int. J. Biochem. Cell Biol.* **45**, 1690–1700 (2013). doi: 10.1016/j.biocel.2013.04.020; pmid: 23624144
46. J. Karttunen, S. Sanderson, N. Shastri, Detection of rare antigen-presenting cells by the lacZ T-cell activation assay suggests an expression cloning strategy for T-cell antigens. *Proc. Natl. Acad. Sci. U.S.A.* **89**, 6020–6024 (1992). doi: 10.1073/pnas.89.13.6020; pmid: 1378619
47. Materials and methods are available as supplementary materials on *Science* Online.
48. H. P. Harding *et al*., An integrated stress response regulates amino acid metabolism and resistance to oxidative stress. *Mol. Cell* **11**, 619–633 (2003). doi: 10.1016/S1097-2765(03)00105-9; pmid: 12667446
49. L. M. Mielnicki, R. G. Hughes, P. M. Chevray, S. C. Pruitt, Mutated Atf4 suppresses c-Ha-ras oncogene transcript levels and cellular transformation in NIH3T3 fibroblasts. *Biochem. Biophys. Res. Commun.* **228**, 586–595 (1996). doi: 10.1006/bbrc.1996.1702; pmid: 8920955
50. A. W. Paton *et al*., AB5 subtilase cytotoxin inactivates the endoplasmic reticulum chaperone BiP. *Nature* **443**, 548–552 (2006). doi: 10.1038/nature05124; pmid: 17024087
51. C. Sidrauski *et al*., Pharmacological brake-release of mRNA translation enhances cognitive memory. *eLife* **2**, e00498 (2013). doi: 10.7554/eLife.00498; pmid: 23741617
52. C. Sidrauski *et al*., Pharmacological dimerization and activation of the exchange factor eIF2B antagonizes the integrated stress response. *eLife* **4**, e07314 (2015). doi: 10.7554/eLife.07314; pmid: 25875391
53. Y. Sekine *et al*., Mutations in a translation initiation factor identify the target of a memory-enhancing compound. *Science* **348**, 1027–1030 (2015). doi: 10.1126/science.aaa6986; pmid: 25858979
54. K. Zhan *et al*., Phosphorylation of eukaryotic initiation factor 2 by heme-regulated inhibitor kinase-related protein kinases in *Schizosaccharomyces pombe* is important for resistance to environmental stresses. *Mol. Cell. Biol.* **22**, 7134–7146 (2002). doi: 10.1128/MCB.22.20.7134-7146.2002; pmid: 12242291
55. J. P. Abastado, P. F. Miller, B. M. Jackson, A. G. Hinnebusch, Suppression of ribosomal reinitiation at upstream open reading frames in amino acid-starved cells forms the basis for GCN4 translational control. *Mol. Cell. Biol.* **11**, 486–496 (1991). pmid: 1986242
56. K. Gülow, D. Bienert, I. G. Haas, BiP is feed-back regulated by control of protein translation efficiency. *J. Cell Sci.* **115**, 2443–2452 (2002). pmid: 12006628
57. S. R. Schwab, J. A. Shugart, T. Horng, S. Malarkannan, N. Shastri, Unanticipated antigens: Translation initiation at CUG with leucine. *PLOS Biol.* **2**, e366 (2004). doi: 10.1371/journal.pbio.0020366; pmid: 15510226
58. S. R. Starck *et al*., Leucine-tRNA initiates at CUG start codons for protein synthesis and presentation by MHC class I. *Science* **336**, 1719–1723 (2012). doi: 10.1126/science.1220270; pmid: 22745432
59. H. Liang *et al*., PTENα, a PTEN isoform translated through alternative initiation, regulates mitochondrial function and energy metabolism. *Cell Metab.* **19**, 836–848 (2014). pmid: 24768297
60. F. Robert *et al*., Initiation of protein synthesis by hepatitis C virus is refractory to reduced eIF2·GTP·Met-tRNA$_i^{Met}$ ternary complex availability. *Mol. Biol. Cell* **17**, 4632–4644 (2006). doi: 10.1091/mbc.E06-06-0478; pmid: 16928960
61. H. Rammensee, J. Bachmann, N. P. Emmerich, O. A. Bachor, S. Stevanović, SYFPEITHI: Database for MHC ligands and peptide motifs. *Immunogenetics* **50**, 213–219 (1999). doi: 10.1007/s002510050595; pmid: 10602881
62. E. A. Reits, J. C. Vos, M. Grommé, J. Neefjes, The major substrates for TAP in vivo are derived from newly synthesized proteins. *Nature* **404**, 774–778 (2000). doi: 10.1038/35008103; pmid: 10783892
63. M. J. Androlewicz, P. Cresswell, How selective is the transporter associated with antigen processing? *Immunity* **5**, 1–5 (1996). doi: 10.1016/S1074-7613(00)80304-0; pmid: 8758889
64. G. E. Hammer, T. Kanaseki, N. Shastri, The final touches make perfect the peptide-MHC class I repertoire. *Immunity* **26**, 397–406 (2007). doi: 10.1016/j.immuni.2007.04.003; pmid: 17459809
65. K. R. Brandvold, R. I. Morimoto, The chemical biology of molecular chaperones—Implications for modulation of proteostasis. *J. Mol. Biol.* **427**, 2931–2947 (2015). doi: 10.1016/j.jmb.2015.05.010; pmid: 26003923
66. B. Wu, C. Hunt, R. Morimoto, Structure and expression of the human gene encoding major heat shock protein HSP70. *Mol. Cell. Biol.* **5**, 330–341 (1985). doi: 10.1128/MCB.5.2.330; pmid: 2858050
67. X. Zhang *et al*., Translational control of the cytosolic stress response by mitochondrial ribosomal protein L18. *Nat. Struct. Mol. Biol.* **22**, 404–410 (2015). pmid: 25866880
68. W. L. Zoll, L. E. Horton, A. A. Komar, J. O. Hensold, W. C. Merrick, Characterization of mammalian eIF2A and identification of the yeast homolog. *J. Biol. Chem.* **277**, 37079–37087 (2002). doi: 10.1074/jbc.M207109200; pmid: 12133843
69. J. H. Kim, S. M. Park, J. H. Park, S. J. Keum, S. K. Jang, eIF2A mediates translation of hepatitis C viral mRNA under stress conditions. *EMBO J.* **30**, 2454–2464 (2011). doi: 10.1038/emboj.2011.146; pmid: 21556050
70. I. Ventoso *et al*., Translational resistance of late alphavirus mRNA to eIF2alpha phosphorylation: A strategy to overcome the antiviral effect of protein kinase PKR. *Genes Dev.* **20**, 87–100 (2006). doi: 10.1101/gad.357006; pmid: 16391235
71. D. G. Macejak, P. Sarnow, Internal initiation of translation mediated by the 5′ leader of a cellular mRNA. *Nature* **353**, 90–94 (1991). doi: 10.1038/353090a0; pmid: 1652694
72. Y. K. Kim, S. K. Jang, Continuous heat shock enhances translational initiation directed by internal ribosomal entry site. *Biochem. Biophys. Res. Commun.* **297**, 224–231 (2002). doi: 10.1016/S0006-291X(02)02154-X; pmid: 12237106
73. M. C. Lai, Y. H. Lee, W. Y. Tarn, The DEAD-box RNA helicase DDX3 associates with export messenger ribonucleoproteins as well as tip-associated protein and participates in translational control. *Mol. Biol. Cell* **19**, 3847–3858 (2008). doi: 10.1091/mbc.E07-12-1264; pmid: 18596238
74. V. P. Pisareva, A. V. Pisarev, A. A. Komar, C. U. Hellen, T. V. Pestova, Translation initiation on mammalian mRNAs with structured 5′UTRs requires DExH-box protein DHX29. *Cell* **135**, 1237–1250 (2008). doi: 10.1016/j.cell.2008.10.037; pmid: 19109895
75. M. A. Skabkin *et al*., Activities of Ligatin and MCT-1/DENR in eukaryotic translation initiation and ribosomal recycling. *Genes*

Dev. **24**, 1787–1801 (2010). doi: 10.1101/gad.1957510; pmid: 20713520
76. M. Oyama *et al*., Analysis of small human proteins reveals the translation of upstream open reading frames of mRNAs. *Genome Res.* **14** (10B), 2048–2052 (2004). doi: 10.1101/gr.2384604; pmid: 15489325
77. M. A. Purbhoo, D. J. Irvine, J. B. Huppa, M. M. Davis, T cell killing does not require the formation of a stable mature immunological synapse. *Nat. Immunol.* **5**, 524–530 (2004). doi: 10.1038/ni1058; pmid: 15048111
78. D. F. Hunt *et al*., Characterization of peptides bound to the class I MHC molecule HLA-A2.1 by mass spectrometry. *Science* **255**, 1261–1263 (1992). doi: 10.1126/science.1546328; pmid: 1546328
79. H. Escobar *et al*., Large scale mass spectrometric profiling of peptides eluted from HLA molecules reveals N-terminal-extended peptide motifs. *J. Immunol.* **181**, 4874–4882 (2008). doi: 10.4049/jimmunol.181.7.4874; pmid: 18802091
80. V. H. Engelhard, The contributions of mass spectrometry to understanding of immune recognition by T lymphocytes. *Int. J. Mass Spectrom.* **259**, 32–39 (2007). doi: 10.1016/j.ijms.2006.08.009; pmid: 18167512
81. B. Vanderperre *et al*., Direct detection of alternative open reading frames translation products in human significantly expands the proteome. *PLOS ONE* **8**, e70698 (2013). doi: 10.1371/journal.pone.0070698; pmid: 23950983
82. V. L. Crotzer *et al*., Immunodominance among EBV-derived epitopes restricted by HLA-B27 does not correlate with epitope abundance in EBV-transformed B-lymphoblastoid cell lines. *J. Immunol.* **164**, 6120–6129 (2000). doi: 10.4049/jimmunol.164.12.6120; pmid: 10843661
83. G. Lubec, L. Afjehi-Sadat, Limitations and pitfalls in protein identification by mass spectrometry. *Chem. Rev.* **107**, 3568–3584 (2007). doi: 10.1021/cr068213f; pmid: 17645314
84. S. R. Starck, N. Shastri, Non-conventional sources of peptides presented by MHC class I. *Cell. Mol. Life Sci.* **68**, 1471–1479 (2011). doi: 10.1007/s00018-011-0655-0; pmid: 21390547
85. D. J. Kowalewski *et al*., HLA ligandome analysis identifies the underlying specificities of spontaneous antileukemia immune responses in chronic lymphocytic leukemia (CLL). *Proc. Natl. Acad. Sci. U.S.A.* **112**, E166–E175 (2015). pmid: 25548167
86. G. L. Law, A. Raney, C. Heusner, D. R. Morris, Polyamine regulation of ribosome pausing at the upstream open reading frame of *S*-adenosylmethionine decarboxylase. *J. Biol. Chem.* **276**, 38036–38043 (2001). pmid: 11489903

ACKNOWLEDGMENTS

We are grateful for technical help from K. Banta and S. J. Yang (University of California, Berkeley) and K. Crotty (University of California, San Francisco). We thank M. Elvekrog, E. Costa, M. Lam, and W. Merrick for critical reading of the manuscript and C. Sidrauski, S. Ramundo, H. Tran, N. Ingolia, and J. Weissman for helpful discussions and advice. The human retinal pigment epithelial cell line (RPE-19) was a gift from X. Gong (School of Optometry, University of California, Berkeley). This research was supported by grants from the NIH to N.S. and P.W. P.W. is an Investigator of the Howard Hughes Medical Institute.

SUPPLEMENTARY MATERIALS

www.sciencemag.org/content/351/6272/aad3867/suppl/DC1
Material and Methods
Figs. S1 to S15
References (*87*–*98*)

5 September 2015; accepted 3 December 2015
10.1126/science.aad3867

RESEARCH ARTICLE

STRUCTURAL BIOLOGY

The 3.8 Å structure of the U4/U6.U5 tri-snRNP: Insights into spliceosome assembly and catalysis

Ruixue Wan,[1]* Chuangye Yan,[1]* Rui Bai,[1] Lin Wang,[1] Min Huang,[2] Catherine C. L. Wong,[2] Yigong Shi[1]†

Splicing of precursor messenger RNA is accomplished by a dynamic megacomplex known as the spliceosome. Assembly of a functional spliceosome requires a preassembled U4/U6.U5 tri-snRNP complex, which comprises the U5 small nuclear ribonucleoprotein (snRNP), the U4 and U6 small nuclear RNA (snRNA) duplex, and a number of protein factors. Here we report the three-dimensional structure of a *Saccharomyces cerevisiae* U4/U6.U5 tri-snRNP at an overall resolution of 3.8 angstroms by single-particle electron cryomicroscopy. The local resolution for the core regions of the tri-snRNP reaches 3.0 to 3.5 angstroms, allowing construction of a refined atomic model. Our structure contains U5 snRNA, the extensively base-paired U4/U6 snRNA, and 30 proteins including Prp8 and Snu114, which amount to 8495 amino acids and 263 nucleotides with a combined molecular mass of ~1 megadalton. The catalytic nucleotide U80 from U6 snRNA exists in an inactive conformation, stabilized by its base-pairing interactions with U4 snRNA and protected by Prp3. Pre-messenger RNA is bound in the tri-snRNP through base-pairing interactions with U6 snRNA and loop I of U5 snRNA. This structure, together with that of the spliceosome, reveals the molecular choreography of the snRNAs in the activation process of the spliceosomal ribozyme.

In the precursor mRNA (pre-mRNA) of eukaryotes, the protein-coding sequences, termed exons, are interrupted by noncoding sequences known as introns (*1*, *2*). Pre-mRNA splicing, involving the removal of introns and the ligation of neighboring exons, is carried out by a dynamic, multi-megadalton ribonucleoprotein (RNP) complex known as the spliceosome (*3*). Each splicing cycle entails two sequential transesterification reactions, with the first producing a free 5′-exon and an intron lariat-3′-exon and the second resulting in a freed intron lariat and a joined 5′-exon-3′-exon (*4*). The spliceosome responsible for these two reactions consists of U2 and U5 small nuclear RNPs (snRNPs), U6 small nuclear RNA (snRNA), and a large number of additional proteins (*5*, *6*). Assembly of the catalytically active spliceosome, however, requires a series of concerted steps, with the U4/U6.U5 tri-snRNP playing an indispensable role (*7*–*9*).

According to the prevailing model, U1 snRNP recognizes the 5′ splice site (5′SS) of an intron, and U2 snRNP binds to the branch point sequence and 3′ splice site (3′SS) of the same intron, forming the prespliceosomal complex (the A complex) (*7*). The preassembled tri-snRNP comprises U5 snRNA, the base-paired U4/U6 snRNAs, and more than 30 proteins, including the key factors Prp8 (Spp42 in *Schizosaccharomyces pombe*), Brr2, and Snu114 (Cwf10 in *S. pombe*). Binding of the U4/U6.U5 tri-snRNP to the A complex results in the formation of the precatalytic B complex. Subsequent RNP rearrangement leads to dissociation of the U1 and U4 snRNPs and the recruitment of many additional proteins, producing the activated B complex (B^{act}) and then the catalytically competent B* complex. During this process, the U4/U6 duplex is unwound, allowing U6 snRNA to extensively base-pair with U2 snRNA. The B* complex catalyzes the first transesterification reaction, ending with the C complex, which contains a free 5′-exon and an intron lariat-3′-exon (*7*). The C complex carries out the second transesterification reaction, resulting in the ligation of two exons and formation of the postcatalytic P complex. Release of the ligated exon generates the intron-lariat spliceosomal complex. In the last step, the intron lariat is released, and the protein and RNA components are recycled, a sizable fraction of which reassemble into the U4/U6.U5 tri-snRNP (*7*).

The spliceosome was thought to be a protein-directed metalloenzyme (*10*–*12*), with two catalytic magnesium (Mg^{2+}) ions coordinated by conserved nucleotides in the intramolecular stem loop (ISL) of U6 snRNA (*13*, *14*). These predicted features are observed in the recent electron cryomicroscopy (cryo-EM) structure of a yeast spliceosome at 3.6 Å resolution (*15*, *16*). The spliceosomal catalytic center comprises helix I of the U2/U6 snRNA duplex, ISL of U6 snRNA, loop I of U5 snRNA, and Mg^{2+} ions, all of which are located in a positively charged surface cavity in Prp8 (*15*, *16*). In the U4/U6.U5 tri-snRNP, however, U6 snRNA is thought to exist in an inactive conformation through extensive base-pairing interactions with U4 snRNA (*7*, *17*). Elucidation of the tri-snRNP structure is essential for a mechanistic understanding of spliceosomal assembly and U6 snRNA activation.

The dynamic nature and large size of the spliceosomal complexes have made detailed structural investigation a daunting challenge (*8*). Earlier EM studies of the human and yeast tri-snRNPs, at resolutions of 21 Å or lower, revealed the overall shape and global features (*18*, *19*). More recently, the cryo-EM structure of a U4/U6.U5 tri-snRNP from *Saccharomyces cerevisiae*, determined at 5.9 Å resolution, has allowed positional identification of many proteins and the snRNA components; secondary structural elements are also discernible for many protein components in the tri-snRNP (*20*). Despite these encouraging advances, the relatively low resolution revealed few features of amino acid side chains or nucleotides (*20*), precluding the generation of an atomic model for the tri-snRNP.

Isolation and characterization of the U4/U6.U5 tri-snRNP

Six protein components of the U4/U6.U5 tri-snRNP, each tagged with protein A and calmodulin binding peptide at the C terminus, were individually introduced into *S. cerevisiae* to enable screening of protein expression and pulling down of endogenous tri-snRNP. The best outcome obtained was for Prp6, a protein required for accumulation of the tri-snRNP (*21*). We purified ~260 μg of spliceosomal U4/U6.U5 tri-snRNP from 36 liters of *S. cerevisiae* culture (see the supplementary materials; fig. S1A). The purified tri-snRNP was eluted from gel filtration as a single peak (fig. S1B) and contained three major RNA species (fig. S1C). The lengths of these RNA molecules are consistent with those of U4, U5, and U6 snRNAs from *S. cerevisiae*. The purified tri-snRNP included a large number of proteins (fig. S1D), and the negatively stained sample appeared in EM to contain mostly homogeneous particles (fig. S1E). The EM sample was confirmed by mass spectrometry to include all core components of the U4/U6.U5 tri-snRNP (figs. S1F and S2) (*22*).

The presence of U4, U5, and U6 snRNAs in the purified tri-snRNP sample was confirmed by Northern blots using specific DNA probes (fig. S3). Increasing the exposure time by 50 times also revealed U2 and U1 snRNAs, suggesting the presence of a very small amount of other contaminating complexes. The tri-snRNP particles were disassembled upon incubation with ATP (adenosine triphosphate) but not with ADP (adenosine diphosphate) or the nonhydrolyzable analog

[1]Ministry of Education Key Laboratory of Protein Science, Tsinghua-Peking Joint Center for Life Sciences, Beijing Advanced Innovation Center for Structural Biology, School of Life Sciences, Tsinghua University, Beijing 100084, China. [2]National Center for Protein Science Shanghai, Institute of Biochemistry and Cell Biology, Shanghai Institutes of Biological Sciences, Chinese Academy of Sciences, Shanghai 200031, China.
*These authors contributed equally to this work.
†Corresponding author. E-mail: shi-lab@tsinghua.edu.cn

Downloaded from on January 31, 2016

AMPPNP (adenosine 5′-(β,γ-imido)triphosphate) (fig. S4). These results suggest a role of ATP hydrolysis–dependent unwinding of the U4/U6 duplex by the ATPase (adenosine triphosphatase)/helicase Brr2. The presence of GDP (guanosine diphosphate), which is known to inhibit the Brr2-activating function of Snu114 (*23*), appears to inhibit the disassembly of tri-snRNP in the presence of ATP (fig. S4A). These findings confirm that the vast majority of the particles observed by means of EM belong to tri-snRNP. To facilitate future structural assignment, we chemically cross-linked the tri-snRNP and performed mass spectrometry analysis on the resulting complex. This analysis uncovered 104 pairs of intermolecular interactions among the protein components of the tri-snRNP (fig. S5).

EM analysis of the U4/U6.U5 tri-snRNP

The U4/U6.U5 tri-snRNP sample was imaged under cryogenic conditions with a K2 direct electron detector mounted on a Titan Krios microscope operating at 300 kV. A total of 3141 micrographs were collected (Fig. 1A and table S1); 635,850 semi-autopicked particles were subjected to particle sorting, reference-free two-dimensional (2D) classification, and 3D classification (Fig. 1B and fig. S6). Using a published protocol (*15*), we manually picked more particles. After two rounds of 3D classification, 207,238 particles were used to produce a cryo-EM map at an average resolution of 4.5 Å (fig. S6). After particle polishing and an additional round of 3D classification, 172,134 particles gave a final reconstruction at an average resolution of 3.8 Å on the basis of the gold-standard Fourier shell correlation (FSC) criterion (Fig. 1, C and D, and fig. S7). Application of soft masks improved the resolutions of local maps to 3.4 to 3.8 Å, with the central regions of the tri-snRNP reaching 3.0 to 3.5 Å (figs. S8 and S9). Throughout the tri-snRNP, most secondary structural elements in the protein components are visible, and ~70% of all amino acids in the core regions of tri-snRNP exhibit discernible side chain features (figs. S10 to S12). Both U4/U6 snRNA duplex and U5 snRNA are well resolved in cryo-EM maps, which, together with prior knowledge of specific base-pairing interactions, allows sequence assignment (fig. S13).

Using a combination of homologous structure docking and de novo assignment, we generated an atomic model for the spliceosomal U4/U6.U5 tri-snRNP that includes most known components (Fig. 2, A and B). The final refined model of the tri-snRNP contains 8495 amino acids from 30 proteins and three snRNA molecules (Fig. 2B and tables S1 to S3), with a combined molecular mass just exceeding 1.0 MD. The full-length U4/U6 and U5 snRNAs contain a total of 486 nucleotides (nt), of which 243 have been tentatively assigned in our structure. Some very weak cryo-EM maps, probably reflecting dynamic components of the tri-snRNP, remain unassigned. Our atomic model includes 18 protein components of U4/U6 snRNP, all 11 core proteins of U5 snRNP, and the tri-snRNP–specific protein Prp6.

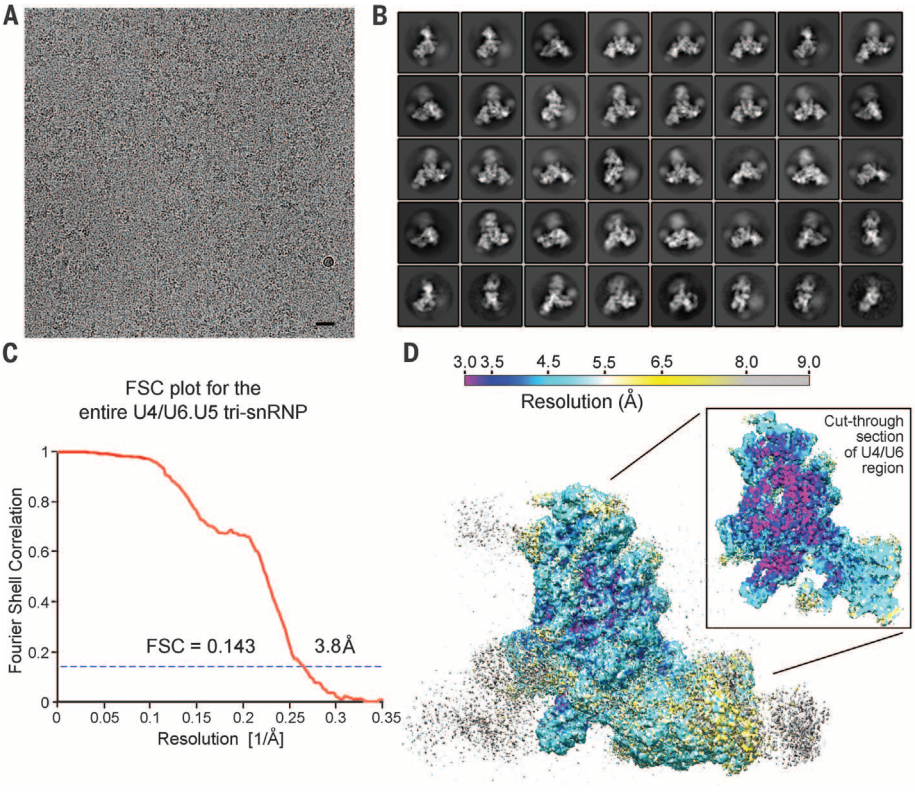


Fig. 1. Cryo-EM analysis of the spliceosomal U4/U6.U5 tri-snRNP from *S. cerevisiae*. (**A**) A representative cryo-EM micrograph of the yeast spliceosomal U4/U6.U5 tri-snRNP. The low image contrast made it challenging to manually pick particles. An entire micrograph is shown. Scale bar, 30 nm. (**B**) Representative 2D class averages of the yeast spliceosomal U4/U6.U5 tri-snRNP. (**C**) The overall resolution is estimated to be 3.81 Å on the basis of the FSC criterion of 0.143. (**D**) An overall view of the cryo-EM maps for the yeast spliceosomal U4/U6.U5 tri-snRNP. The resolution is color-coded for different regions of the complex. A cross section of the tri-snRNP surface view is shown in the inset. The resolution reaches to 3.0 to 3.5 Å for the core regions of the U4/U6.U5 tri-snRNP, including but not limited to the U4/U6 snRNA duplex, protein components of U4 snRNP, much of U5 snRNA, the bulk of Prp8, and Snu114.

Overall structure of U4/U6.U5 tri-snRNP

The spliceosomal U4/U6.U5 tri-snRNP complex has a triangular appearance, with U5 snRNP constituting both the center and two corners of the triangle and spanning the longest dimension of ~315 Å (Fig. 2 and fig. S14). One end of U5 snRNP, comprising Snu114 and the U5 Sm ring, is resolved in the overall cryo-EM maps (Fig. 1D) and exhibits well-defined structural features in the improved local map (figs. S8 and S11). The other end of U5 snRNP, however, appears to be highly flexible (Fig. 1D); this end contains the helicase/ATPase Brr2 and the U4 Sm ring and is linked to the center of tri-snRNP mainly through the Jab1/MPN domain of Prp8 (Fig. 2). This region has a relatively low resolution of 7.9 Å even after the application of a local mask (fig. S8). Relative to its longest side, the tri-snRNP has a height of 210 Å and a thickness of about 150 Å (Fig. 2A). The third corner of the triangle is well resolved in cryo-EM maps (Fig. 1D) and is occupied by the U4/U6 snRNA duplex and its associated proteins (Fig. 2A). Located in close proximity to this corner, the heptameric Sm-like (Lsm) ring and the bound 3′-end of U6 snRNA are poorly resolved in cryo-EM maps, and the intervening components between the Lsm ring and U4/U6 snRNP remain to be structurally identified. Because of their low resolutions, the cryo-EM maps for the Brr2 region and the Lsm ring disallow assignment of side chains or specific interactions; proteins in these regions were fitted into the cryo-EM maps in a rigid-body mode using previously determined crystal structures.

The core of Prp8, comprising residues 749 to 1830, is located at the center of the U4/U6.U5 tri-snRNP (Fig. 2B). The U4/U6 snRNP closely associates with the core of Prp8 through the ferredoxin-like protein Prp3 (*24*) and the Nop domain containing protein Prp31 (*25*). The N-terminal domain (N domain) of Prp8 is mainly responsible for binding U5 snRNA and the only GTPase (guanosine triphosphatase), Snu114, whereas the C-terminal Jab1/MPN domain of Prp8 binds Brr2, and the RNaseH-like domain of Prp8 interacts with Prp3 and the tri-snRNP–specific protein Prp6 (Fig. 2B). The U4-associated Sm ring contacts Brr2 on the opposite side relative to the Jab1/MPN domain of Prp8. The U5 snRNP component Dib1, which has a thioredoxin-like fold (*26*), interacts with an extended loop of Prp31 and bridges the core and the N domain of Prp8.

The U5-associated Sm ring encircles a stretch of U5 snRNA sequence and binds Snu114.

Despite its close proximity to the core of Prp8, the U4/U6 snRNA duplex has few direct interactions with Prp8. The U4/U6 snRNA duplex is surrounded and directly recognized by four proteins: Prp3, Prp6, Prp31, and the globular RNA-binding protein Snu13 (Fig. 2B and fig. S15) (*27*). These interactions are stabilized by the core of Prp8 at the bottom and the β-propeller protein Prp4 at the top; Prp4 directly contacts Prp3, Snu13, and Prp6. Together, these proteins help maintain the inactive conformation of the U4/U6 snRNA duplex in the tri-snRNP; during catalytic activation of the spliceosome, these proteins must be stripped as the U4/U6 snRNA duplex is unwound by the RNA-dependent ATPase Brr2.

Structure of the U4/U6 snRNA duplex

The U4/U6 snRNA duplex and the 5′-stem loop of U4 snRNA both have excellent cryo-EM maps (fig. S13, A to D). The U4/U6 snRNA duplex consists of stem I, which is base-paired by nucleotides 56 to 62 of U6 snRNA and 57 to 63 of U4 snRNA, and stem II between nucleotides 64 and 81 of U6 snRNA and 18 nucleotides at the 5′-end of U4 snRNA (Fig. 3, A and B). Stems I and II are interrupted by the 5′-stem loop of U4 snRNA, which forms a bulged duplex. The catalytic uridine nucleotide 80 (U80) of U6 snRNA (*13*) is sequestered in an inactive conformation in the U4/U6 snRNA duplex by at least two mechanisms. First, U80 of U6 snRNA pairs with A1 of U4 snRNA at the tip of stem II, where the fully extended conformation of the phosphodiester

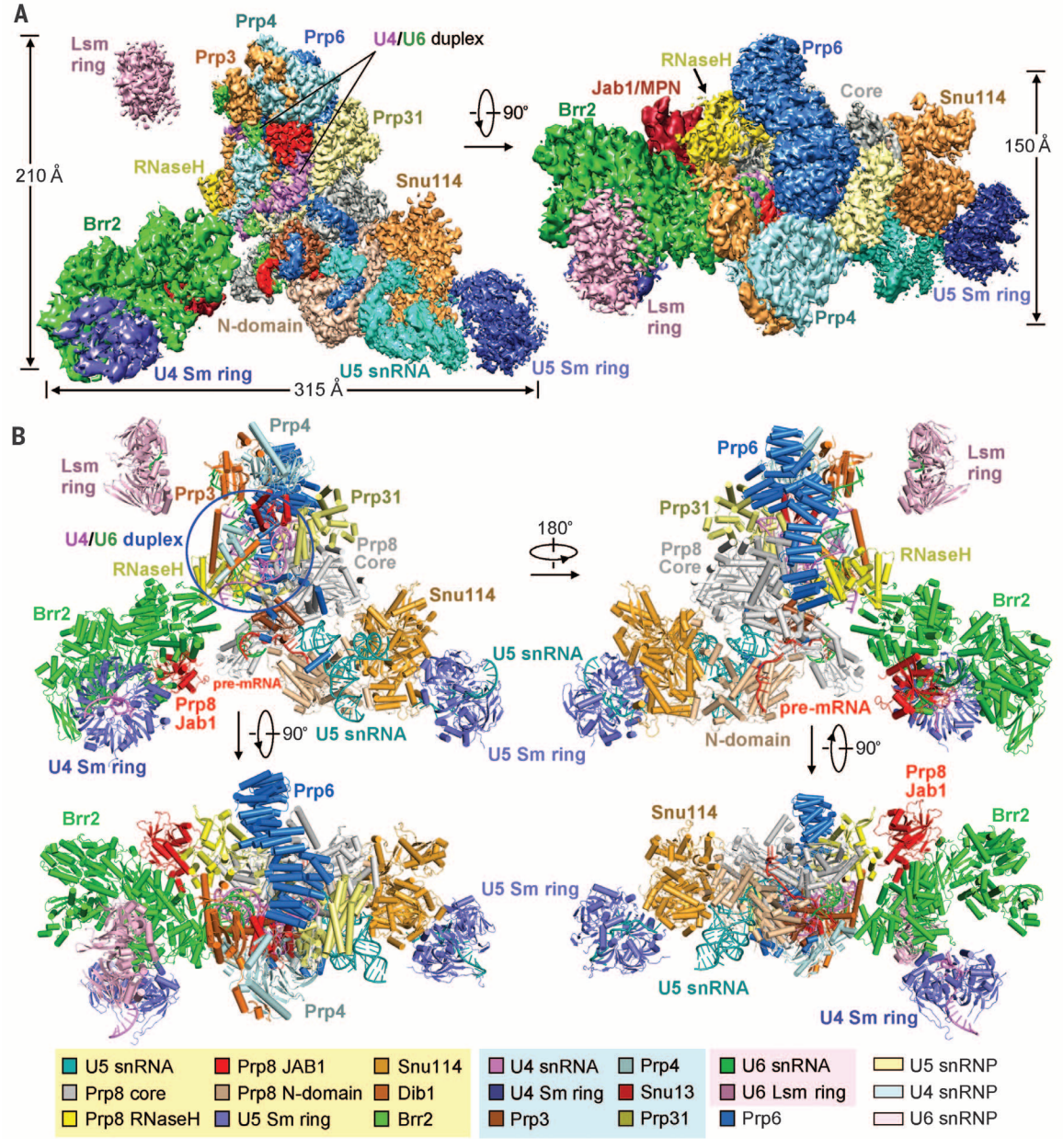


Fig. 2. Structure of the spliceosomal U4/U6.U5 tri-snRNP from *S. cerevisiae*. (**A**) The cryo-EM maps of the yeast U4/U6.U5 tri-snRNP at an overall resolution of 3.81 Å. The cryo-EM maps were generated by Chimera (*54*) and carved using the atomic coordinates. To display cryo-EM maps for all regions of the tri-snRNP, varying contour levels were applied to different regions, with low contour levels for the Brr2 region and the Lsm ring. (**B**) A cartoon of the yeast U4/U6.U5 tri-snRNP complex. The protein and RNA components are color-coded. Four views are shown. This structure includes 30 proteins, three snRNA molecules, and a pre-mRNA molecule, with a combined molecular weight of ~1 MD. The atomic model includes 8495 amino acids; 243 nucleotides from U4, U5, and U6 snRNAs; and 20 nucleotides from pre-mRNA.

backbone no longer allows coordination of two catalytic Mg^{2+} ions (Fig. 3A, inset). Second, this part of the U4/U6 duplex is bound by Prp3, with the phosphate group of U80 probably forming hydrogen (H) bonds with the side chain of Arg^{399} from Prp3 (fig. S15A).

Although only 41 nucleotides of U6 snRNA in the U4/U6.U5 tri-snRNP were clearly assigned, they contain most of the catalytically important sequences and are highly conserved from yeast to humans (Fig. 3C). These corresponding nucleotides in U6 snRNA form helix I in the U2/U6 snRNA duplex and the ISL in the activated *S. pombe* spliceosome (Fig. 3, D and E). Superposition of the core of Prp8 with that of Spp42 allows assessment of the relative positioning of U6 snRNA in the tri-snRNP and the *S. pombe* spliceosome. The nucleotides in U6 snRNA of the tri-snRNP are located up to 100 Å away from their corresponding positions in the active *S. pombe* spliceosome (Fig. 3D), with the 5′-stem loop of U4 snRNA placed in between (Fig. 3E). Thus, during Brr2-mediated activation of the spliceosome, U6 snRNA must undergo a dramatic structural rearrangement to arrive at its active conformation.

Recognition of U4 and U6 snRNA

The core of the U4/U6 snRNP is a closely associated complex that consists of U4/U6 snRNA, Prp3, Prp4, Snu13, and Prp31 (Fig. 4A). This complex interacts intimately with the core of Prp8 and the tri-snRNP–specific protein Prp6, forming a compact structure that stands out from the rest of the U4/U6.U5 tri-snRNP (Figs. 2B and 4A). Within this structure, Prp3 only recognizes the U4/U6 duplex, whereas Snu13 and Prp6 mostly bind to the 5′-stem loop of U4 snRNA (Fig. 4B). Prp31, in an extended conformation, interacts with both U4 snRNA and the minor groove in stem I of the U4/U6 snRNA duplex. The U4/U6 snRNA duplex is specifically recognized through a large number of H bonds by amino acids from Prp3, Snu13, Prp31, and Prp6.

Prp3 plays a major role in the recognition of the U4/U6 snRNA duplex (Fig. 4B and fig. S15A). Two extended α-helices in the N-terminal half of Prp3 bind to the major groove and the axial side, respectively, of stem II in the U4/U6 snRNA duplex. In the first helix (residues 238 to 262), six Arg and three Lys residues may donate up to nine direct and water-mediated H bonds to the phosphate backbone in the major groove of stem II (Fig. 4C and fig. S16A). In the second helix (residues 291 to 326), His^{308}, Asn^{312}, and Arg^{315} recognize A11 of U4 snRNA, G71 of U6 snRNA, and C10 of U4 snRNA, respectively, in the minor groove of stem II (fig. S15A, top middle panel). A C-terminal domain of Prp3 directly interacts with the 5′-end of U4 snRNA and the phosphodiester backbone of U6 snRNA around the nucleotide U80 (fig. S15A, top right panel). The doubly methylated 2′-amino group of the 5′-m_3G cap from U4 snRNA may make hydrophobic contacts with the side chains of Glu^{362}, Leu^{363}, and Phe^{391}, whereas Arg^{399} may donate two H bonds to the phosphate group of U80.

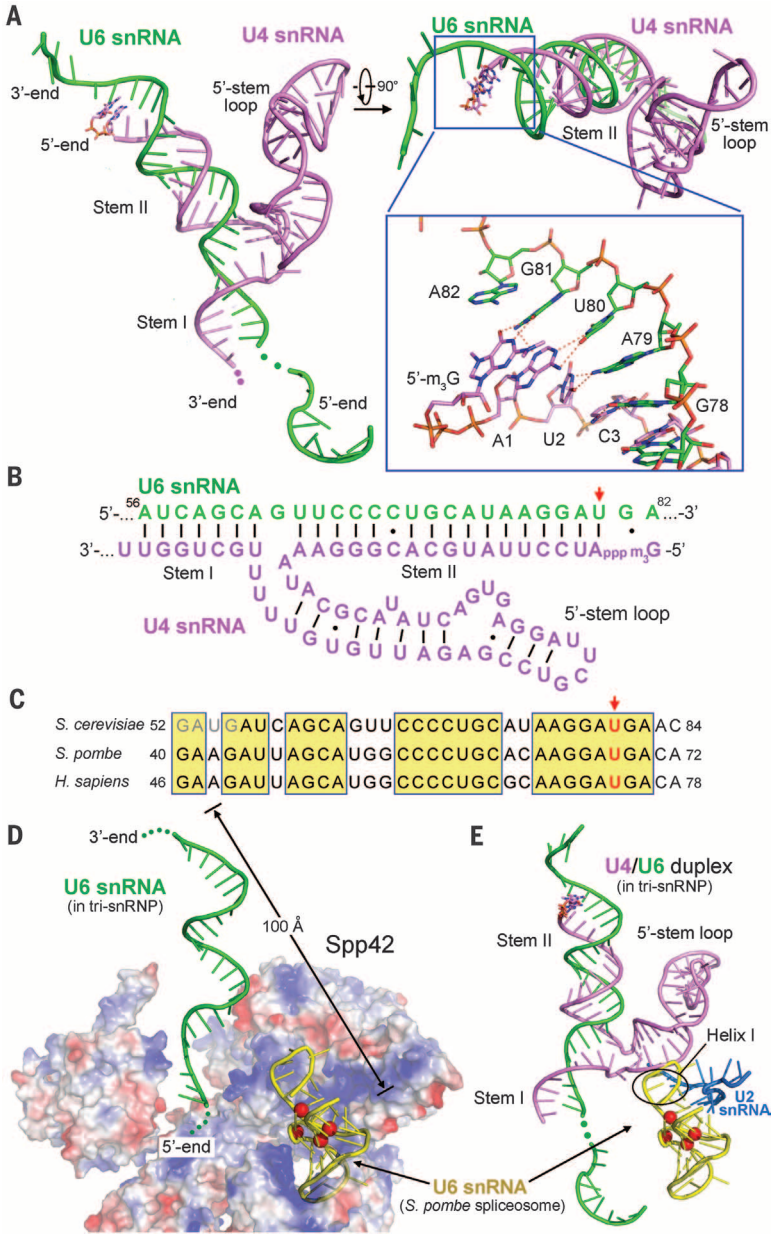


Fig. 3. Structure of the U4 and U6 snRNAs in the spliceosomal U4/U6.U5 tri-snRNP. (**A**) Structure of the U4/U6 snRNA duplex. U4 snRNA (colored violet) and U6 snRNA (green) extensively base-pair with each other to form two stretches of duplexes termed stem I and stem II, which are interrupted by the 5′-stem loop of the U4 snRNA. Base-pairing interactions between four nucleotides at the 5′-end of U4 snRNA and nucleotides G78 to A81 of U6 snRNA are highlighted in the close-up view. (**B**) A schematic diagram of the base-pairing interactions in the U4/U6 snRNA duplex. (**C**) Sequence alignment of U6 snRNA from *S. cerevisiae*, *S. pombe*, and *Homo sapiens*. Only 33 nucleotides are shown from each U6 snRNA. Twenty-nine of these nucleotides have been assigned for U6 snRNA in the cryo-EM maps of tri-snRNP. The catalytic uridine nucleotide (U80 in *S. cerevisiae* and U68 in *S. pombe*) is identified by a red arrow in (B) and (C). (**D**) U6 snRNA undergoes a dramatic conformational switch and a translocation of up to 100 Å during the assembly of a functional spliceosome. The *S. cerevisiae* U4/U6.U5 tri-snRNP is aligned to the *S. pombe* spliceosome on the basis of the core domains of Prp8 and Spp42. The resulting U6 snRNA (green) from U4/U6.U5 tri-snRNP is shown in relation to U6 snRNA (yellow) from the *S. pombe* spliceosome. For visual clarity, only Prp8 is shown by its surface electrostatic potential (red indicates high and blue indicates low surface electrostatic potential). Red spheres indicate the catalytic magnesium ions. (**E**) A close-up view on the U4/U6 snRNA duplex of the tri-snRNP in relation to the activated U6 snRNA in the *S. pombe* spliceosome. A small portion of U2 snRNA (colored marine) from the *S. pombe* spliceosome is shown.

The globular protein Snu13 is wedged between stem II and the 5′-stem loop of the U4/U6 duplex but mainly interacts with the 5′-stem loop (Fig. 4B and fig. S15B). The side chains of Glu[39], Lys[42], and Arg[46] contact both the phosphate backbone and specific bases in the 5′-stem loop (Fig. 4D and fig. S16B). Similar to Prp3, Prp31 also adopts an extended conformation. An α-helical domain at the N-terminal half of Prp31 interacts with the tip of the 5′-stem loop of U4 snRNA (Fig. 4B and fig. S15C). A protracted loop (residues 346 to 438) follows the ridge of the 5′-stem loop, goes into the major groove of stem I, and comes out in an extended conformation. In the major groove of stem I, at least two bases of U4 and U6 snRNAs are recognized by the positively charged residues Arg[367] and Lys[371] from Prp31 (Fig. 4E and fig. S16C). The extended conformation of Prp31 is sustained through close interactions with other proteins, particularly Prp8 (Fig. 4A).

In our atomic structure, the superhelical protein Prp6 consists of 44 α-helices, of which 36 are organized into 18 tetratricopeptide repeats. Only helices α6 preceding the tetratricopeptide repeats and α39 at the C terminus bind to the stem and tip, respectively, of the 5′-stem loop of U4 snRNA (Fig. 4B and fig. S15D). Arg[136] and Gln[140] of α6 may make specific H bonds to U51 and A20/U54, respectively, whereas Lys[133] and Arg[143] contact the phosphate backbone (Fig. 4F and fig. S16D). The overall appearance of Prp6 resembles a cup handle, with the N-terminal helices of Prp6 contacting the RNaseH-like domain and the core of Prp8 and the C-terminal domain interacting with Prp4, Snu13, and Prp31 (Fig. 4A).

Structure of U5 snRNP

U5 snRNP adopts an elongated and flexible conformation, with most components assigned in our atomic model (Fig. 5A). One end of U5 snRNP contains a heptameric Sm ring, which is bound to the 3′-end sequences of U5 snRNA. The other end of U5 snRNP is capped by a second Sm ring, which associates with the 3′-end sequences of U4 snRNA. U5 snRNP constitutes two corners of the triangular-shaped U4/U6.U5 tri-snRNP. One corner, consisting of U5 snRNA, Snu114, and the N domain of Prp8, has a well-defined conformation and is connected to the centrally located Prp8 core through multiple interfaces, including that mediated by Dib1. The other corner, comprising mostly Brr2 and the bound Jab1/MPN domain of Prp8, is flexibly attached to the rest of the tri-snRNP and exhibits a dynamic conformation.

U5 snRNA from *S. cerevisiae* has two forms, of which the long form (214 nt) contains 35 extra nucleotides beyond the 3′-end of the short form (179 nt). Nucleotides 28 to 53, 62 to 127,

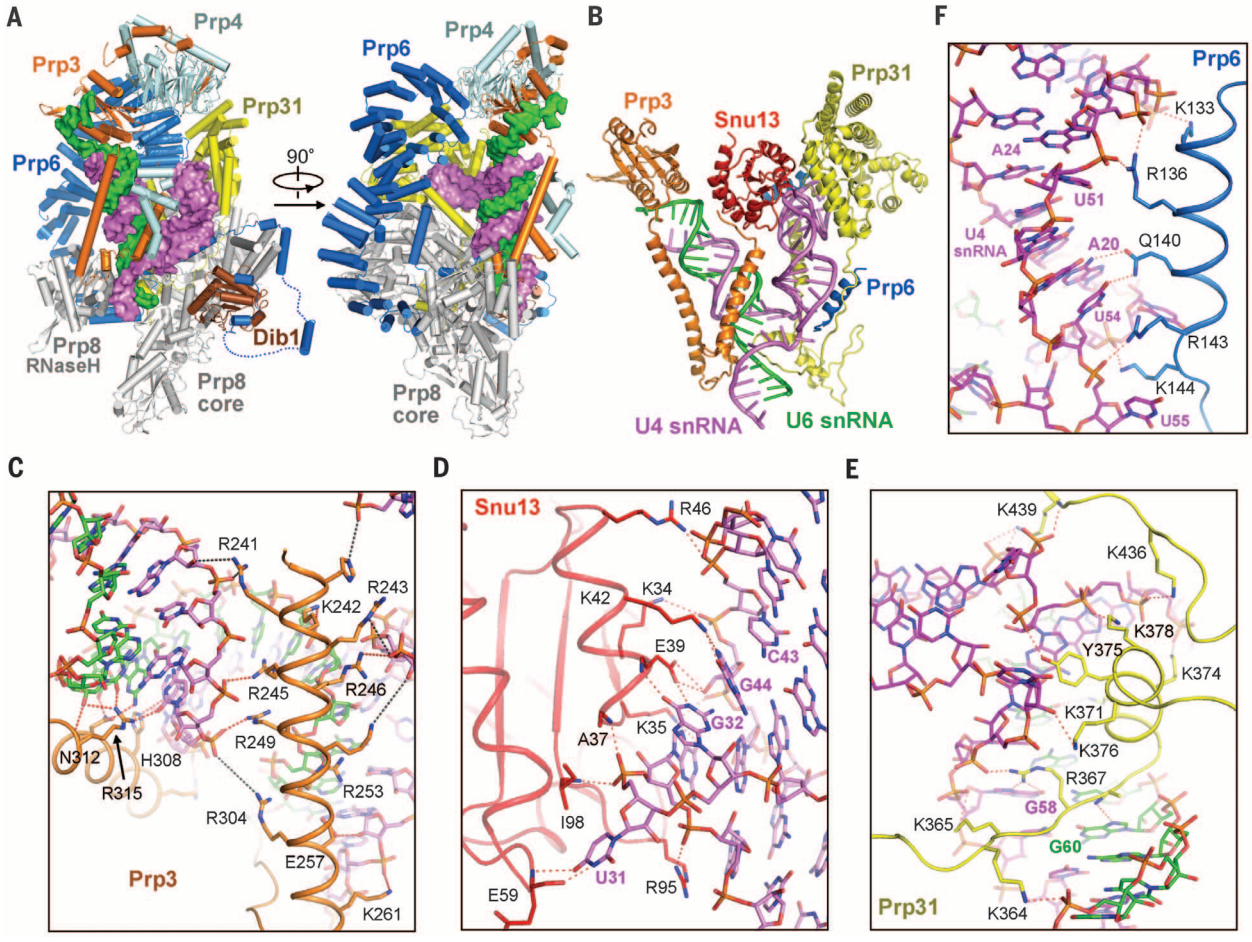


Fig. 4. Recognition of the U4/U6 snRNA duplex by spliceosomal proteins. (**A**) Overall structure of the U4/U6 snRNP core. The U4/U6 snRNA duplex and the intervening 5′-stem loop of U4 snRNA are surrounded by Prp3 (orange), Prp4 (light cyan), Prp6 (marine), Prp8 core (gray), Snu13 (red), Prp31 (yellow), and Dib1 (brown). (**B**) The U4/U6 snRNA duplex is mainly recognized by four proteins: Prp3, Prp6, Snu13, and Prp31. Prp3 interacts only with the U4/U6 snRNA duplex, whereas Prp6 uses two α-helices to contact the 5′-stem loop of U4 snRNA. Both Snu13 and Prp31 mainly associate with U4 snRNA. (**C**) An α-helix from Prp3 binds the major groove of stem II in the U4/U6 snRNA duplex. A few Arg and Lys residues may donate H bonds to the backbone phosphates of RNA duplex. The red and black dashed lines represent direct and water-mediated H bonds, respectively. (**D**) Positively charged amino acids from Snu13 may directly H-bond with backbone phosphates and the bases of U4 snRNA. (**E**) An extended loop from Prp31 interacts with the minor groove of stem I in the U4/U6 snRNA duplex. Arg[367] may directly recognize the base G58 of U4 snRNA, whereas Lys[371] probably H-bonds to G63 of U6 snRNA. (**F**) A close-up view of the interactions of an α-helix from Prp6 and the 5′-stem loop of U4 snRNA.

and 163 to 183 are distinguishable in cryo-EM maps (fig. S13) and were explicitly modeled in our structure (Fig. 5B). The U5 snRNA structure consists of loop 1, stem I, stem II, a variable stem loop, and extended sequences at the 3′-end. The core regions of U5 snRNA from *S. cerevisiae* and from *S. pombe* have a very similar structure with respect to both loop I and stems I and II (Fig. 5C). Loop II of the U5 snRNA from *S. pombe* is replaced by a much longer variable stem loop in *S. cerevisiae* (Fig. 5C). Loop III of the U5 snRNA from *S. pombe* is replaced by a predicted internal loop II in U5 snRNA from *S. cerevisiae*. Both internal loop II and stem III of U5 snRNA in our tri-snRNP structure are disordered.

Conformational changes in Prp8

Prp8 in *S. cerevisiae* (Spp42 in *S. pombe*) is a central component of the spliceosome and the splicing reaction. In the U4/U6.U5 tri-snRNP, Prp8 is divided into four distinct structural regions: the N domain (residues 130 to 736), the core (residues 747 to 1830), the RNaseH-like domain (residues 1831 to 2078), and the Jab1/MPN domain (residues 2148 to 2396). The core, also known as the large domain (*28*), consists of the reverse transcriptase palm/finger, thumb/X, linker, and endonuclease-like subdomains. Each of these four regions is able to undergo pronounced rigid-body movement relative to neighboring regions, exemplified by the RNaseH-like domain. The core of Prp8 from the tri-snRNP can be superimposed onto that of Spp42 from the *S. pombe* spliceosome with a root mean square deviation (RMSD) of 3.06 Å between 1099 pairs of aligned Cα atoms (Fig. 6A). With the cores of Prp8 and Spp42 aligned, their RNaseH-like domains adopt different positions and are related to each other by a pseudo–two-fold rotational axis (fig. S17A), yet these two domains can be aligned with an RMSD of 1.24 Å for 225 Cα atoms (Fig. 6B). Similarly, the position of the RNaseH-like domain relative to the core of Spp42 in the *S. pombe* spliceosome is different from that in Prp8 bound to Aar2 (*15*, *28*). The C-terminal Jab1/MPN domain moves freely of the rest of Prp8 and mainly functions to regulate the activity of the ATPase/helicase Brr2 through physical association (*29*).

As with the RNaseH-like domain, the relative position of the Prp8 N domain is different from that of the Spp42 N domain (fig. S17B), yet these two domains can be perfectly aligned with a RMSD of 0.94 Å for 486 Cα atoms (Fig. 6C). Because the catalytic cavity of the *S. pombe* spliceosome is formed between the N domain and the core of Spp42/Prp8 (*15*, *16*), the relative movement between these two domains leads to a misaligned catalytic cavity in Prp8 of the U4/U6.U5 tri-snRNP (Fig. 6D). Such structural distortion generates misalignment of the U5 snRNA between the tri-snRNP and the *S. pombe* spliceosome (Fig. 6E, upper panel). The U5 snRNA in the tri-snRNP can be brought into registry with that in the *S. pombe* spliceosome by a rotation of ~30° (Fig. 6E, lower panel). The N domain of Prp8 associates with the GTPase Snu114 through a highly conserved interface, and alignment of the N domains between Prp8 and Spp42 only produced a slight misalignment between Snu114 and Cwf10 (fig. S18A) that

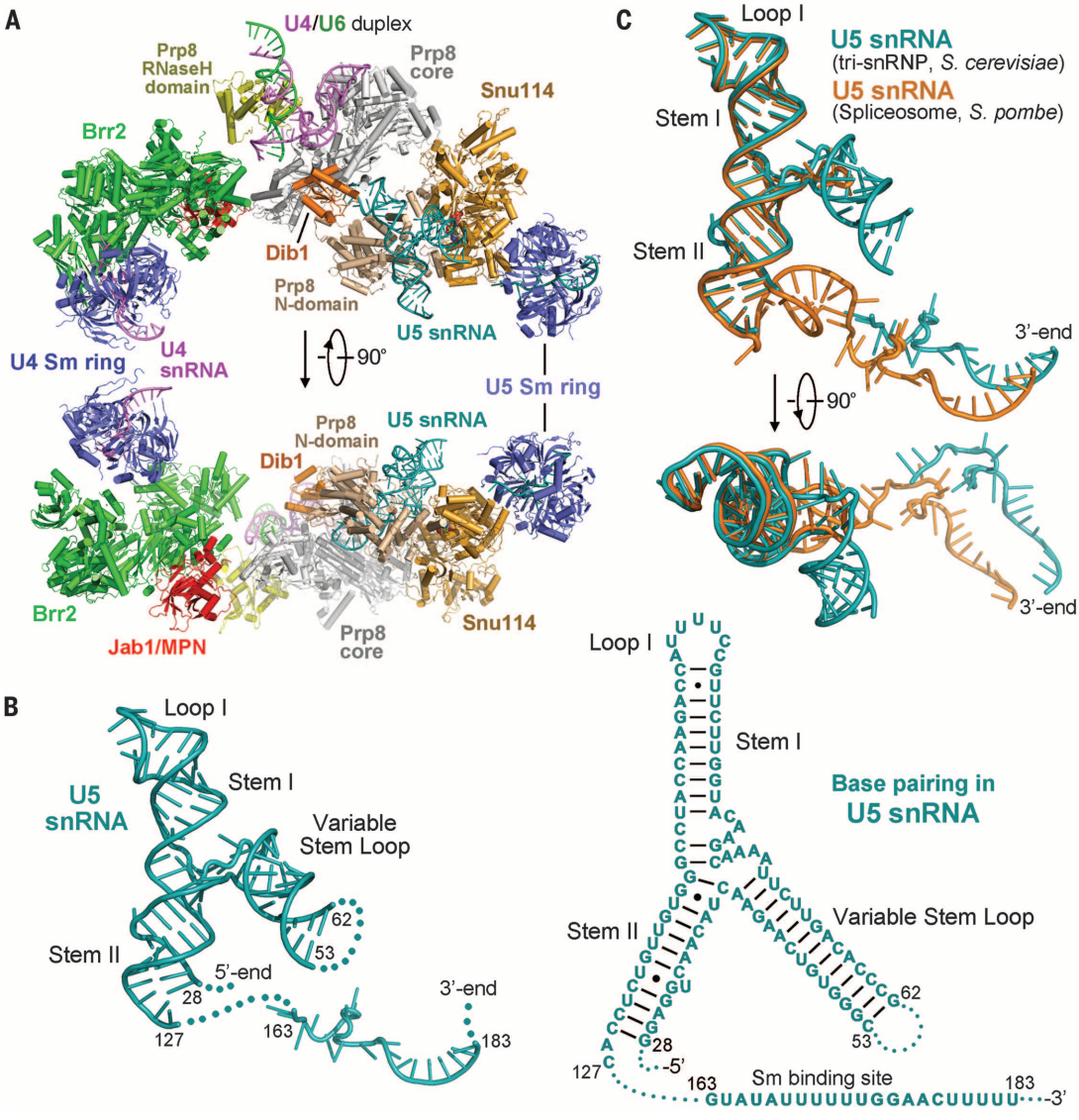


Fig. 5. Structures of U5 snRNP and U5 snRNA in the U4/U6.U5 tri-snRNP. (**A**) Overall structure of the U5 snRNP. The U4/U6 snRNA duplex and the U4 Sm ring are also shown for reference. The centrally located Prp8 is displayed in four colors: tan for the N domain, gray for the core, yellow for the RNaseH-like domain, and red for the Jab1/MPN domain. (**B**) Structure of U5 snRNA. A schematic representation of base-pairing interactions in U5 snRNA is shown in the right panel. (**C**) Structural comparison of U5 snRNAs from the *S. cerevisiae* tri-snRNP and *S. pombe* spliceosome. The two U5 snRNA molecules from U4/U6.U5 tri-snRNP and the *S. pombe* spliceosome are colored cyan and gold, respectively. Two perpendicular views are shown.

could be mitigated by minor rigid-body adjustment (fig. S18B). Compared with the GDP-bound Cwf10, binding of GTP (guanosine triphosphate) in Snu114 appears to induce no apparent conformational changes (fig. S18C).

Recognition of pre-mRNA by tri-snRNP

At the beginning of atomic modeling, we recognized a stretch of cryo-EM density close to Prp8 and loop I of U5 snRNA. The density is characteristic of RNA but cannot be assigned to U4, U5, or U6 snRNA because of topological considerations, suggesting the presence of pre-mRNA. After most components of the U4/U6.U5 tri-snRNP had been assigned, features of this density became clear, with some bulges projecting out from the linear-shaped density (fig. S13, G and H). Consideration of snRNA directionality and local density features only allowed one possible assignment for the pre-mRNA (Fig. 7A). The 5′SS of the intron is base-paired with the ACAGA box of U6 snRNA, whereas three consecutive nucleotides in the preceding 5′-exon sequences are recognized by loop I of U5 snRNA through base-pairing interactions (Fig. 7, B and C, and fig. S19).

Immediately after the 3′-end nucleotide of the 5′-exon, the first two bases of the 5′SS, guanine and uracil, protrude away from the extended pre-mRNA phosphodiester backbone (Fig. 7C and fig. S13H). The distinct configuration of the guanine base is maintained through five candidate H bonds with the side-chain amino group of Lys^{1378} and the main-chain groups of Gly^{1636} and Phe^{1623} in Prp8 (Fig. 7D). The extended conformation of the pre-mRNA sequence is probably a prerequisite for the first-step transesterification reaction involving an adenine nucleotide from the branch point sequence of the intron and two Mg^{2+} ions coordinated by U6 snRNA. The assignment of pre-mRNA also identifies Dib1 as a critical player in the U4/U6.U5 tri-snRNP, because it interacts simultaneously with Prp31, the N domain of Prp8, loop I of U5 snRNA, and 5′SS of pre-mRNA (Fig. 7E). Dib1 also directly contacts residues 1585 to 1598 of Prp8, hereafter termed the 1585 loop, which were found to play an important role in pre-mRNA splicing (*17*).

Implication for pre-mRNA splicing

The structure of pre-mRNA, characterized by its base-pairing interactions with both loop I of U5 snRNA and the ACAGA box of U6 snRNA, is indicative of a productive conformation that is poised for an impending transesterification reaction. To further examine this scenario, we aligned the N domains between Spp42 and Prp8, which brought U5 snRNA from the *S. pombe* spliceosome into registry with that in the tri-snRNP (Fig. 8A). If such an alignment matrix was applied to the entire *S. pombe* spliceosome, it would bring the catalytic Mg^{2+} ions and their coordinating nucleotides into close proximity with the guanine nucleotide at the 5′-end of 5′SS (Fig. 8A, inset). The catalytic metal 1 (M1) (*14*), which is known to stabilize the 3′-OH group of the 3′-end nucleotide of the 5′-exon, is positioned only about 2 Å away from the oxygen atom of the 3′-OH. In addition, the 1585 loop of Prp8 is positioned next to the guanine nucleotide and the catalytic metals. These observations suggest that the conformation of the pre-mRNA bound to tri-snRNP is ready for the first-step transesterification reaction. Our analysis also indicates that at least part of the tri-snRNP, which may include the N domain of Prp8/Spp42, Snu114/Cwf10, and U5 snRNA, already adopts a productive conformation for the splicing reaction. This conclusion is supported by the near-perfect alignment between these corresponding regions from *S. cerevisiae* tri-snRNP and *S. pombe* spliceosome (Fig. 8, B to D).

Discussion

X-ray crystallography on individual components or subcomplexes of the spliceosome has yielded

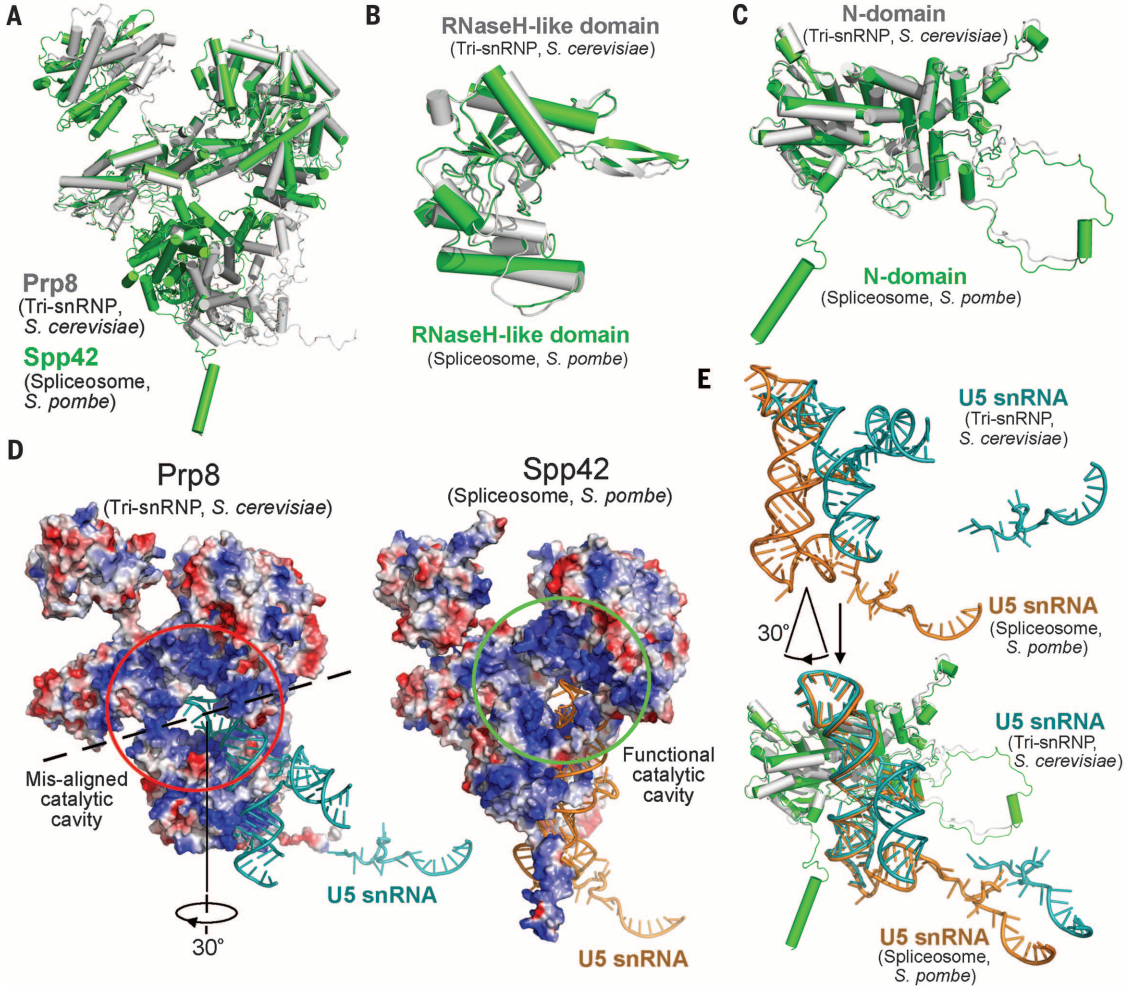


Fig. 6. Structure of Prp8 from tri-snRNP and its comparison with Spp42 from the *S. pombe* spliceosome. (**A**) The structure of Prp8 (gray) is aligned to that of Spp42 (green) on their respective core domains. In contrast to the near-perfect alignment of the core domains, the N and RNaseH-like domains are positioned differently. (**B**) The RNaseH-like and (**C**) N domains from Prp8 and Spp42 exhibit a similar conformation and can be aligned to each other. (**D**) Because of the rotation of the N domain relative to the core, Prp8 has a mis-aligned catalytic cavity (left panel) relative to Spp42 (right panel). (**E**) U5 snRNA of tri-snRNP can be aligned to U5 snRNA of the spliceosome by a rotation of ~30°.

structural information about U1 snRNP (*30*–*32*), U2 snRNP (*33*–*36*), U4 snRNP (*37*), U6 snRNP (*38*, *39*), Prp8 (*28*), and Brr2 (*29*, *40*). EM, on the other hand, has been used to probe the structure of both the human and yeast spliceosomes at various stages of the splicing reaction (*41*–*51*). These structures, mostly at moderate resolutions, have led to identification of global features of the spliceosome. The cryo-EM structure of the *S. cerevisiae* U4/U6.U5 tri-snRNP, at a resolution of 5.9 Å (*20*), allowed assignment of the components and identification of some secondary structural elements but not generation of an atomic model. Recently, we reported the first atomic structure of an intact spliceosome from *S. pombe* at 3.6 Å resolution, which reveals the fine-scale features of the pre-mRNA splicing machinery (*15*). In this study, we report the cryo-EM structure of the *S. cerevisiae* U4/U6.U5 tri-snRNP at an overall resolution of 3.8 Å and present an atomic model for this complex.

Spliceosomal complexes are notorious for their conformational and compositional heterogeneity, which underlies unsuccessful crystallization attempts. Compared to x-ray crystallography, single-particle cryo-EM analysis has the distinctive advantage of 2D and 3D classifications to effectively identify a subgroup of particles that share a similar conformation. In the case of U4/U6.U5 tri-snRNP, conformational heterogeneity is particularly severe, with flexible linkages between the Brr2 region and the tri-snRNP core. In the previous tri-snRNP structure (*20*), about 48% of the 347,241 total particles were used to generate the final cryo-EM map. In our current study, about 57% of the 299,993 total particles were used to generate the final cryo-EM map.

Although the global features of the cryo-EM maps from this study and the previous one (*20*) are similar, our cryo-EM maps reveal atomic details of the U4/U6.U5 tri-snRNP. The "head," "foot," and "arm" described in that report correspond to the three corners in our structure, with the foot including Snu114, U5 snRNA, the U5 Sm ring, and the N domain of Prp8. Because no atomic coordinates were reported for the previous tri-snRNP structure (*20*), we are unable to make a detailed comparison. In this study, we built protein components through either homology modeling or de novo building with most side chains assigned. The U4/U6 snRNA duplex is specifically assigned, and its interactions with surrounding proteins are elucidated.

Similar to the spliceosome (*15*, *16*), the structure of the U4/U6.U5 tri-snRNP reveals rich structural and mechanistic information. For example, Dib1 in *S. cerevisiae* (Dim1 in *S. pombe* and U5-15K in *H. sapiens*) plays an important role in pre-mRNA splicing, indicated by both its central location in the tri-snRNP and its association with U5 snRNA, pre-mRNA, Prp31, and the N domain and 1585 loop of Prp8 (Fig. 7E). Yet the function of Dib1 remains to be determined. This is echoed by Cwf19 in *S. pombe*, which is centrally located in the *S. pombe* spliceosome and interacts with U2 snRNA, U6 snRNA, and the RNaseH-like domain and the core of Spp42 (*15*, *16*), yet its function remains largely unknown. The enigmatic cases of Dib1 and Cwf19 apply to a number of other functionally unknown or uncertain spliceosomal proteins. The structural information provides a framework for functional and biochemical investigations.

An initially unexpected result in this study is the identification of pre-mRNA in the U4/U6.U5 tri-snRNP. The pre-mRNA–loaded tri-snRNP may represent an intermediate that recognizes pre-mRNA but still contains the extensively base-paired U4/U6 duplex. Consistent with this finding, analysis by reverse transcription polymerase chain reaction revealed the presence of *TUB3* pre-mRNA in the cryo-EM sample (fig. S20). Consideration of the tri-snRNP structural features in fact makes this finding unsurprising. First, the ACAGA box of U6 snRNA is exposed in the tri-snRNP and free to recognize the 5′SS of an intron in the pre-mRNA. Second, loop I of U5 snRNA is available in the tri-snRNP to interact with the 3′-end sequences of the 5′-exon in the pre-mRNA. Third, the linker domain of Prp8 is available to bind the

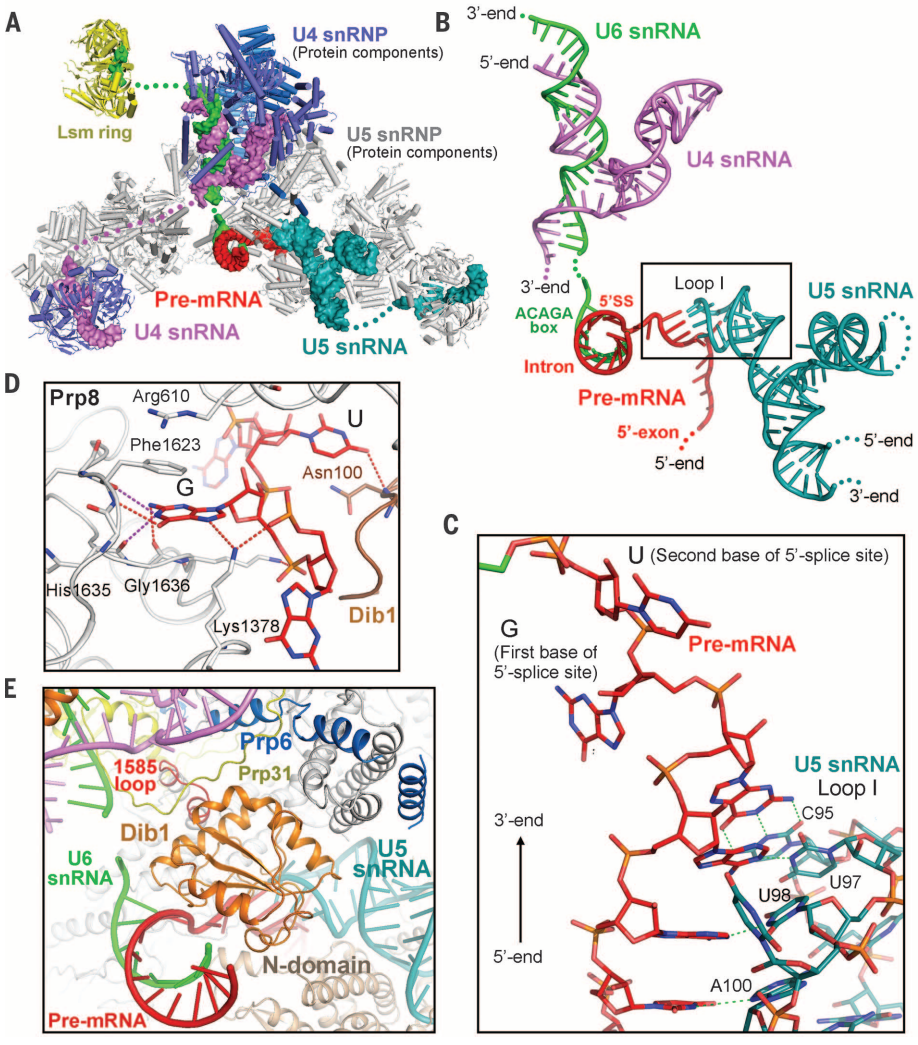


Fig. 7. Pre-mRNA is recognized by U6 snRNA and loop I of U5 snRNA in the U4/U6.U5 tri-snRNP. (**A**) Structure of the U4/U6.U5 tri-snRNP with pre-mRNA bound. All RNA components are shown in surface representation, with U4, U5, and U6 snRNAs colored violet, teal, and green, respectively. Pre-mRNA is highlighted in red. (**B**) The pre-mRNA is located in the center of tri-snRNP and forms duplexes with both U6 snRNA and U5 snRNA. For visual clarity, all protein components are stripped and only the RNA components in the center of tri-snRNA are displayed. The 5′SS of pre-mRNA is base-paired with the ACAGA box of U6 snRNA, whereas the 3′-end sequences of the 5′-exon are recognized by loop I of U5 snRNA. (**C**) A close-up view on the base-pairing interactions between the exon sequences and loop I of U5 snRNA. For base complementarity, the three consecutive nucleotides at the 3′-end of the 5′-exon were modeled as A-A-G (*55*), and they form a duplex with C95-U97-U98 of U5 snRNA. The first two bases of the 5′SS, guanine and uracil, are shown. (**D**) The guanine base of the first nucleotide in the 5′SS is specifically coordinated by amino acids in Prp8. The guanine base is recognized by the side chain of Lys^{1378} and the main chain groups of Phe^{1623} and Gly^{1636} through five putative H bonds. (**E**) Dib1 directly interacts with pre-mRNA, U5 snRNA, and the protein components Prp8 and Prp31. In particular, the N domain and the 1585 loop of Prp8 bind to Dib1.

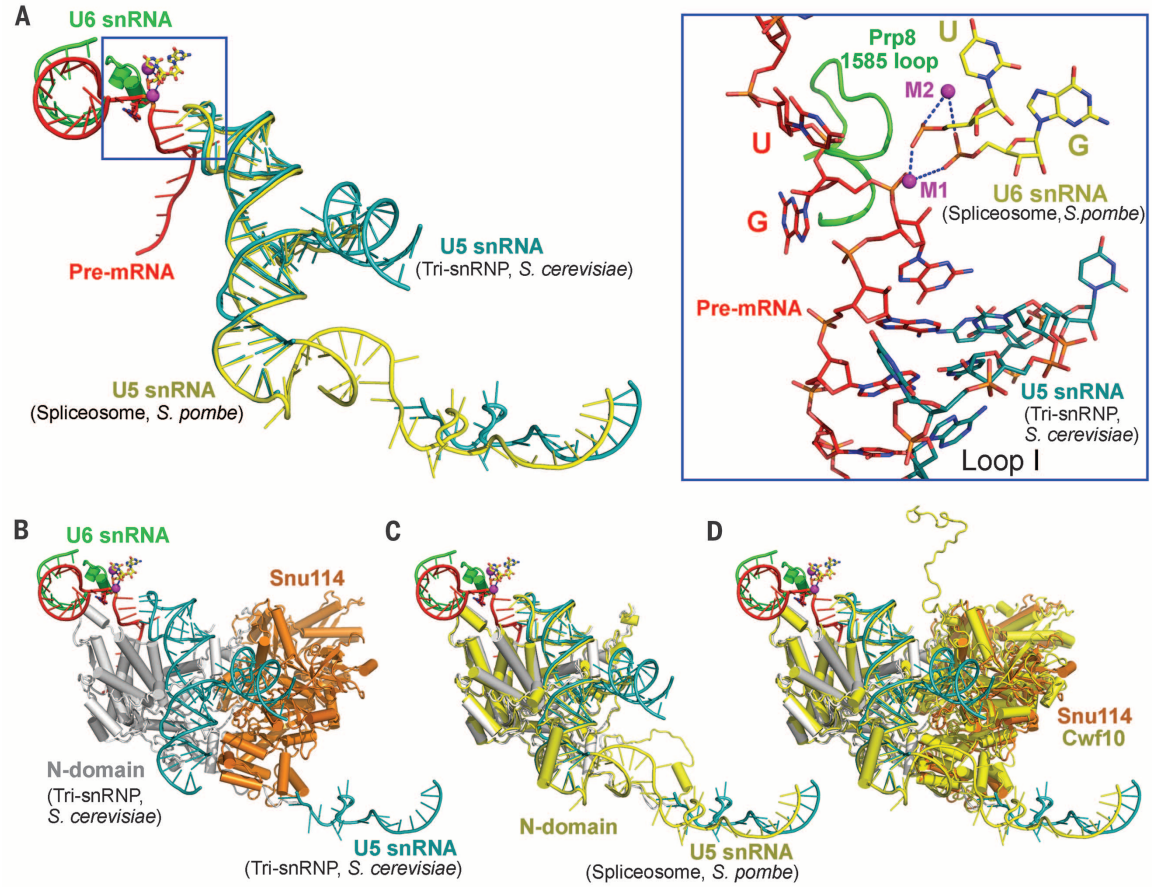


Fig. 8. Pre-mRNA in the U4/U6.U5 tri-snRNP is poised for the splicing reaction. (**A**) Superposition of the U4/U6.U5 tri-snRNP and the *S. pombe* spliceosome brings pre-mRNA in the tri-snRNP into close proximity to the Mg^{2+} ions in the catalytic center of the *S. pombe* spliceosome (*15*). The superposition matrix is the same as that between the N domains of Spp42 and Prp8. This alignment brings the catalytic Mg^{2+} ion (M1) to a distance of about 2 Å from the 3′-OH group of the ribose in the last nucleotide of the 5′-exon (close-up view). (**B**) A subcomplex comprising U5 snRNA, Prp8 N domain, and Snu114 probably constitutes the scaffold for the two-step splicing reaction. An overall structure of this subcomplex is shown here, together with those of pre-mRNA and a short stretch of U6 snRNA. The superimposed Mg^{2+} ions and their coordinating nucleotides from U6 snRNA in the *S. pombe* spliceosome are also shown for reference. (**C**) Superposition of the N domains of Prp8 and Spp42 brings the two U5 snRNA molecules in tri-snRNP and *S. pombe* spliceosome into registry. (**D**) Superposition of the N domains of Prp8 and Spp42 brings Snu114 from tri-snRNP and Cwf10 from *S. pombe* spliceosome into registry.

5′-nucleotide of the 5′SS. Fourth and last, the back side of Prp8 is strongly positively charged (fig. S21A), so it may bind and orient the 5′-exon sequences. Some of the cryo-EM density located in this region appears to be connected to the 5′-end of the pre-mRNA (fig. S21B). Nevertheless, although unlikely, we cannot rule out the possibility that the pre-mRNA–loaded tri-snRNP may represent part of the B complex.

The current understanding of spliceosomal assembly suggests that the spliceosomal A complex, which contains pre-mRNA loaded with U1 and U2 snRNPs, associates with U4/U6.U5 tri-snRNP to form the spliceosomal B complex (fig. S22, red arrows). According to this model, the U4/U6.U5 tri-snRNP is free of pre-mRNA and exists as an inhibitory complex by keeping U6 snRNA in an inactive conformation. Our structural finding suggests additional possibilities (fig. S22, black arrows). In the tri-snRNP, the ACAGA box of U6 snRNA and loop I of U5 snRNA are both free to engage pre-mRNA, and they do so through base-pairing interactions with both the 5′SS of an intron and the 3′-end sequences of the 5′-exon. Thus the U4/U6.U5 tri-snRNP may freely recruit pre-mRNA, independently of U1 snRNP (fig. S22). Our speculative model further predicts that the tri-snRNP loaded with pre-mRNA may directly associate with U2 snRNP and proceed to form a catalytically competent spliceosome (fig. S22). Consistent with this prediction, most protein components of U2 snRNP were identified by mass spectrometry in our sample and exhibited relatively high peptide-spectrum match values, suggesting a reasonable abundance (fig. S23). In contrast, the protein components of U1 snRNP were present with considerably less abundance (fig. S23). Supporting our model, direct recognition of the 5′SS in the pre-mRNA by the U4/U6.U5 tri-snRNP has been previously reported (*52*).

Despite these clues and analyses, our model awaits experimental scrutiny. This speculative model may be inconsistent with some of the reported biochemical data. For example, using an in vitro purification method, inactivation of pre-mRNA binding by U1 snRNP was shown to nearly cripple pre-mRNA binding by all other snRNPs (*53*). However, such studies were performed under highly specific settings and stringent analysis conditions, such as those for detection of snRNA species in stalled splicing reactions, and thus may not fully capture the complex situations in cells.

The molecular choreography of many different components, exemplified by that of Prp8 and Spp42 (Fig. 6) and U6 snRNA (fig. S24), serves to execute the splicing reactions for tens of thousands of distinct pre-mRNA molecules. The near-atomic structures of the *S. pombe* spliceosome (*15*) and the *S. cerevisiae* tri-snRNP provide a principal framework for ultimately elucidating the underlying molecular mechanisms of pre-mRNA splicing.

REFERENCES AND NOTES

1. S. M. Berget, C. Moore, P. A. Sharp, *Proc. Natl. Acad. Sci. U.S.A.* **74**, 3171–3175 (1977).
2. L. T. Chow, R. E. Gelinas, T. R. Broker, R. J. Roberts, *Cell* **12**, 1–8 (1977).

3. C. B. Burge, T. Tuschl, P. A. Sharp, "Splicing of precursors to mRNAs by the spliceosomes," in *The RNA World, Second Edition: The Nature of Modern RNA Suggests a Prebiotic RNA World*, R. F. Gesteland, T. R. Cech, J. F. Atkins, Eds. (Cold Spring Harbor Monograph vol. 37, Cold Spring Harbor Laboratory Press, 1999).
4. M. J. Moore, C. C. Query, P. A. Sharp, "Splicing of precursors to mRNA by the spliceosome," in *The RNA World*, R. F. Gesteland, J. F. Atkins, Eds. (Cold Spring Harbor Monograph vol. 24, Cold Spring Harbor Laboratory Press, 1993).
5. D. A. Wassarman, J. A. Steitz, *Science* **257**, 1918–1925 (1992).
6. C. L. Will, R. Lührmann, *Cold Spring Harbor Perspect. Biol.* **3**, a003707 (2011).
7. M. C. Wahl, C. L. Will, R. Lührmann, *Cell* **136**, 701–718 (2009).
8. W. Chen, M. J. Moore, *Curr. Opin. Struct. Biol.* **24**, 141–149 (2014).
9. A. Hegele *et al.*, *Mol. Cell* **45**, 567–580 (2012).
10. T. A. Steitz, J. A. Steitz, *Proc. Natl. Acad. Sci. U.S.A.* **90**, 6498–6502 (1993).
11. E. J. Sontheimer, S. Sun, J. A. Piccirilli, *Nature* **388**, 801–805 (1997).
12. P. M. Gordon, E. J. Sontheimer, J. A. Piccirilli, *RNA* **6**, 199–205 (2000).
13. S. L. Yean, G. Wuenschell, J. Termini, R. J. Lin, *Nature* **408**, 881–884 (2000).
14. S. M. Fica *et al.*, *Nature* **503**, 229–234 (2013).
15. C. Yan *et al.*, *Science* **349**, 1182–1191 (2015).
16. J. Hang, R. Wan, C. Yan, Y. Shi, *Science* **349**, 1191–1198 (2015).
17. W. P. Galej, T. H. Nguyen, A. J. Newman, K. Nagai, *Curr. Opin. Struct. Biol.* **25**, 57–66 (2014).
18. B. Sander *et al.*, *Mol. Cell* **24**, 267–278 (2006).
19. I. Häcker *et al.*, *Nat. Struct. Mol. Biol.* **15**, 1206–1212 (2008).
20. T. H. Nguyen *et al.*, *Nature* **523**, 47–52 (2015).
21. F. Galisson, P. Legrain, *Nucleic Acids Res.* **21**, 1555–1562 (1993).
22. A. Gottschalk *et al.*, *EMBO J.* **18**, 4535–4548 (1999).
23. E. C. Small, S. R. Leggett, A. A. Winans, J. P. Staley, *Mol. Cell* **23**, 389–399 (2006).
24. S. Liu *et al.*, *eLife* **4**, e07320 (2015).
25. S. Liu *et al.*, *Science* **316**, 115–120 (2007).
26. K. Reuter, S. Nottrott, P. Fabrizio, R. Lührmann, R. Ficner, *J. Mol. Biol.* **294**, 515–525 (1999).
27. H. C. Dobbyn *et al.*, *Biochem. Biophys. Res. Commun.* **360**, 857–862 (2007).
28. W. P. Galej, C. Oubridge, A. J. Newman, K. Nagai, *Nature* **493**, 638–643 (2013).
29. S. Mozaffari-Jovin *et al.*, *Science* **341**, 80–84 (2013).
30. G. Weber, S. Trowitzsch, B. Kastner, R. Lührmann, M. C. Wahl, *EMBO J.* **29**, 4172–4184 (2010).
31. D. A. Pomeranz Krummel, C. Oubridge, A. K. Leung, J. Li, K. Nagai, *Nature* **458**, 475–480 (2009).
32. Y. Kondo, C. Oubridge, A. M. van Roon, K. Nagai, *eLife* **4**, e04986 (2015).
33. S. R. Price, P. R. Evans, K. Nagai, *Nature* **394**, 645–650 (1998).
34. E. A. Sickmier *et al.*, *Mol. Cell* **23**, 49–59 (2006).
35. P. C. Lin, R. M. Xu, *EMBO J.* **31**, 1579–1590 (2012).
36. J. L. Jenkins, A. A. Agrawal, A. Gupta, M. R. Green, C. L. Kielkopf, *Nucleic Acids Res.* **41**, 3859–3873 (2013).
37. A. K. Leung, K. Nagai, J. Li, *Nature* **473**, 536–539 (2011).
38. L. Zhou *et al.*, *Nature* **506**, 116–120 (2014).
39. E. J. Montemayor *et al.*, *Nat. Struct. Mol. Biol.* **21**, 544–551 (2014).
40. T. H. Nguyen *et al.*, *Structure* **21**, 910–919 (2013).
41. N. Behzadnia *et al.*, *EMBO J.* **26**, 1737–1748 (2007).
42. D. Boehringer *et al.*, *Nat. Struct. Mol. Biol.* **11**, 463–468 (2004).
43. E. Wolf *et al.*, *EMBO J.* **28**, 2283–2292 (2009).
44. J. Deckert *et al.*, *Mol. Cell. Biol.* **26**, 5528–5543 (2006).
45. S. Bessonov *et al.*, *RNA* **16**, 2384–2403 (2010).
46. M. M. Golas *et al.*, *Mol. Cell* **40**, 927–938 (2010).
47. M. S. Jurica, D. Sousa, M. J. Moore, N. Grigorieff, *Nat. Struct. Mol. Biol.* **11**, 265–269 (2004).
48. J. O. Ilagan, R. J. Chalkley, A. L. Burlingame, M. S. Jurica, *RNA* **19**, 400–412 (2013).
49. P. Fabrizio *et al.*, *Mol. Cell* **36**, 593–608 (2009).
50. M. D. Ohi, L. Ren, J. S. Wall, K. L. Gould, T. Walz, *Proc. Natl. Acad. Sci. U.S.A.* **104**, 3195–3200 (2007).
51. W. Chen *et al.*, *RNA* **20**, 308–320 (2014).
52. P. A. Maroney, C. M. Romfo, T. W. Nilsen, *Mol. Cell* **6**, 317–328 (2000).
53. S. W. Ruby, J. Abelson, *Science* **242**, 1028–1035 (1988).
54. E. F. Pettersen *et al.*, *J. Comput. Chem.* **25**, 1605–1612 (2004).
55. E. Bon *et al.*, *Nucleic Acids Res.* **31**, 1121–1135 (2003).

ACKNOWLEDGMENTS

We thank X. Fang for technical assistance and the Tsinghua University Branch of the China National Center for Protein Sciences (Beijing) for access to the EM facility. We also thank the Explorer 100 cluster system of the Tsinghua National Laboratory for Information Science and Technology, the Computing Platform of the China National Center for Protein Sciences, and Lenovo for providing high-performance computing. This work was supported by funds from the Ministry of Science and Technology (grant 2014ZX09507003006) and the National Natural Science Foundation of China (grants 31430020 and 31321062). The atomic coordinates have been deposited in the Protein Data Bank under the accession code 3JCM. The cryo-EM maps have been deposited in the Electron Microscopy Data Bank with the accession codes EMD-6561 for the overall map and EMD-6562 to EMD-6573 for the 12 local maps. The authors declare no competing financial interests.

SUPPLEMENTARY MATERIALS

www.sciencemag.org/content/351/6272/466/suppl/DC1
Figs. S1 to S25
Tables S1 to S3
References (*56–80*)

15 October 2015; accepted 24 December 2015
Published online 7 January 2016
10.1126/science.aad6466

REPORTS

SURFACE SCIENCE

Activation of Cu(111) surface by decomposition into nanoclusters driven by CO adsorption

Baran Eren,[1]* Danylo Zherebetskyy,[1]* Laerte L. Patera,[1,2,3] Cheng Hao Wu,[1,4] Hendrik Bluhm,[5] Cristina Africh,[2] Lin-Wang Wang,[1] Gabor A. Somorjai,[1,4] Miquel Salmeron[1,6]†

The (111) surface of copper (Cu), its most compact and lowest energy surface, became unstable when exposed to carbon monoxide (CO) gas. Scanning tunneling microscopy revealed that at room temperature in the pressure range 0.1 to 100 Torr, the surface decomposed into clusters decorated by CO molecules attached to edge atoms. Between 0.2 and a few Torr CO, the clusters became mobile in the scale of minutes. Density functional theory showed that the energy gain from CO binding to low-coordinated Cu atoms and the weakening of binding of Cu to neighboring atoms help drive this process. Particularly for softer metals, the optimal balance of these two effects occurs near reaction conditions. Cluster formation activated the surface for water dissociation, an important step in the water-gas shift reaction.

An extensive array of surface-sensitive characterization techniques that provide structural (e.g., electron and x-ray diffraction and scanning probe microscopy) and spectroscopic (e.g., Auger electron, x-ray photoelectron, infrared, and Raman) information (*1*, *2*) have revealed the structure of many crystal surfaces in their pristine clean state. Most of these studies are carried out in ultrahigh vacuum (UHV), which makes it possible to control sample composition and cleanliness to better than 0.1% of a monolayer (ML). Under realistic ambient conditions, however, our knowledge is far less extensive, because the most sensitive techniques using electrons cannot operate in the presence of gases at pressures above ~10^{-6} Torr. Of particular interest is the structure of surfaces in dynamic equilibrium with gases at near-ambient pressure and temperature (*1*). Under these conditions, weakly bound adsorbates can be present in considerable densities, a situation that can also be achieved under vacuum, but only at cryogenic temperatures. The surface structures obtained in such rarefied conditions often represent kinetically frozen states and may not be representative of the structure under practical operating conditions. Here, we overcome this difficulty using high-pressure scanning tunneling microscopy (HPSTM) (*3–8*) and ambient pressure x-ray photoelectron spectroscopy (APXPS) (*9*, *10*), which make possible the study of surfaces in the presence of gases at or near atmospheric pressures at room temperature and above.

Copper-based heterogeneous catalysts are used in reactions such as water gas-shift (WGS), methanol oxidation, methanol synthesis, and others (*11–17*). The weaker cohesive energy of Cu

[1]Materials Sciences Division, Lawrence Berkeley National Laboratory, 1 Cyclotron Road, Berkeley, CA 94720, USA. [2]CNR-IOM, Laboratorio TASC, Strada Statale 14, Km. 163.5, I-34149 Trieste, Italy. [3]Physics Department and CENMAT, University of Trieste, via A. Valerio 2, I-34127 Trieste, Italy. [4]Department of Chemistry, University of California, Berkeley, CA, USA. [5]Chemical Sciences Division, Lawrence Berkeley National Laboratory, 1 Cyclotron Road, Berkeley, CA 94720, USA. [6]Department of Materials Science and Engineering, University of California, Berkeley, CA, USA.
*These authors contributed equally to this work. **†Corresponding author. E-mail: mbsalmeron@lbl.gov**

Downloaded from on January 31, 2016

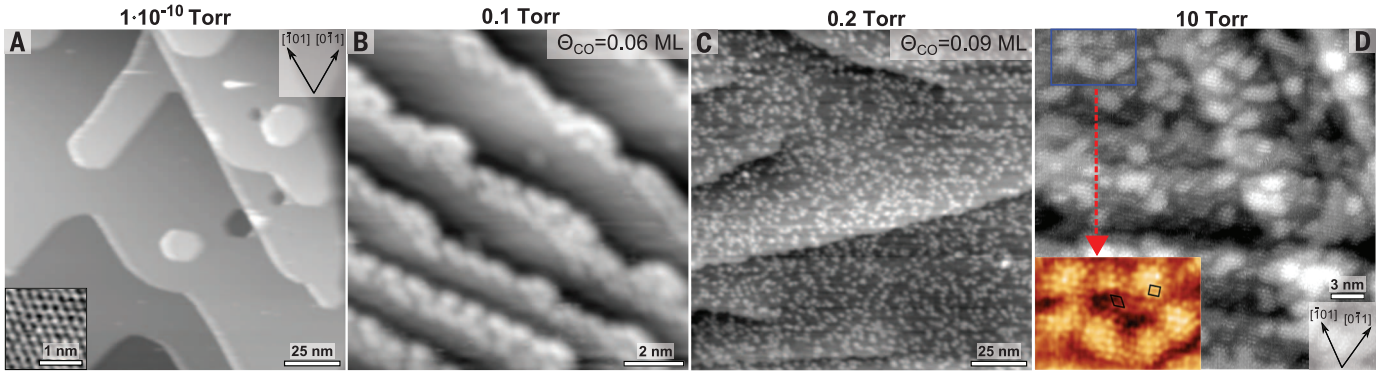


Fig. 1. STM images of Cu(111) showing clusters filling the terraces as a function of ambient CO pressure. (**A**) In UHV [V_b = −2.4 V; I_t = 0.1 nA]. (Bottom inset) Atomically resolved image [V_b = 0.2 V; I_t = 1 nA]. (**B**) Under 0.1 Torr of CO clusters form at step edges [V_b = −2.5 V; I_t = 0.2 nA]. (**C**) Under 0.2 Torr of CO clusters form on the terraces [V_b = 1.85 V; I_t = 0.5 nA]. CO coverages in (B) and (C) are shown in the insets, as determined from the APXPS peak intensities. (**D**) Under 10 Torr of CO [V_b = 0.15 V; I_t = 0.8 nA]. A high density of clusters with adsorbed CO molecules (expanded in the inset) completely covers the surface. The bright spots, due to CO on top sites, form (2×2)-3CO and c(4×2) unit cells. Scale bars are 25 nm for (A) and (C), 2 nm for (B), and 3 nm for (D).

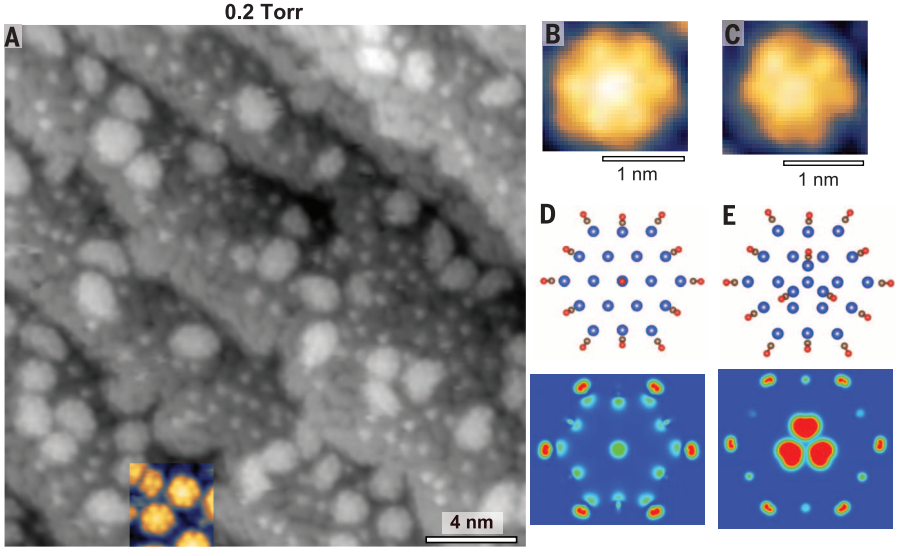


Fig. 2. STM images, ball models, and simulated contrast images of Cu clusters at 0.2 Torr with hexagonal and trigonal symmetries. (**A**) STM image [bias voltage (V_b) = −1.5 V; tunneling current (I_t) = 0.2 nA]. (**B**) and (**C**) are images of the two types of clusters with C_6 or C_3 symmetry colored in (A). The bright center of the cluster in (B) is due to a CO molecule and to a cluster of three Cu atoms decorated by CO in (C). (**D**) A 19-atom cluster model from DFT calculations and simulated STM image (V_b = −2.7 V) of the cluster in (B). (**E**) DFT-optimized model and simulated STM image (V_b = −2.7 V) of the cluster in (C). Images are simulated with a CO-terminated tip and using a higher bias (in absolute values) than the experimental value because of the +U correction, used to match the experimental CO-binding energy on the flat surface.

compared with other metals, such as Pt (3.50 versus 5.84 eV), is an important factor that influences (*18*, *19*) its response to CO adsorption, as we will show here. Because of its high cohesive energy, Pt(111) is stable under CO at pressures of up to at least one atmosphere (*20*, *21*), although stepped surfaces restructure under CO due to the increased binding strength of CO at step edges (*22*). For Cu(111), the densest and lowest energy surface, the adsorption of CO (weaker in energy than on Pt by a factor of ~1.7) causes a much larger restructuring in the form of metal clusters formed by detachment of atoms from the steps. These clusters are mobile and adopt particularly stable sizes and shapes, including 3 and 19 atoms. With the help of density functional theory (DFT) calculations, we explain the findings as resulting from the increased adsorption energy of CO at low-coordinated Cu atoms, together with the lowering of the binding energy of the metal atoms bound to CO [experimental details of sample preparation, HPSTM imaging, and methodology used in DFT calculations are explained in detail in the supplementary materials (*23*)]. The cluster-covered surface is stable at room temperature (in the scale of hours) after desorption of CO when the gas phase is evacuated, and this surface is extremely active in the dissociation of water, an important step in the WGS reaction.

An image of the clean Cu(111) surface under UHV (Fig. 1A) shows micrometer-scale terraces, atomic steps, and a few screw dislocations are visible. After introduction of 0.1 Torr of CO in the chamber, a new structure was observed along the step edges, while the rest of the terrace remained atomically flat (Fig. 1B). At 0.2 Torr, the terraces became covered with nanoclusters (Fig. 1C) that increased in density with CO pressure until the clusters filled the surface (Fig. 1D and fig. S3) (*23*). The CO coverage, evaluated from APXPS measurements in a different chamber under identical conditions, increased from 0.06 ML at 0.1 Torr to 0.09 ML at 0.2 Torr and to 0.16 ML at 0.5 Torr of CO (*24*).

The structure of the clusters formed at 0.2 Torr of CO is shown in Fig. 2A. A roughly bimodal size distribution is apparent, with small clusters ~0.5 nm in diameter with poorly resolved triangular shape and larger hexagonal shape clusters ~1.5 nm in diameter. We associate the first with three Cu atom clusters with an apparent height about half that of a monatomic step, similar to the case in UHV studies (*25*). The larger ones we assign to 19 atom clusters forming hexagonal closed-shell structures (typically with an apparent height corresponding to a monatomic step). The 19-atom closed-shell structures ("magic number" clusters) are reported to be the building blocks for the homoepitaxial Cu growth on Cu(111) (*26*). Sometimes the clusters contain a few more atoms (fig. S1) (*23*) or come in contact with each other, forming aggregates that separate again later as a result of thermal mobility, which causes the clusters to evolve spatially in the scale of minutes, as illustrated in fig. S2 (*23*). Time-lapse images show the clusters forming by splitting from step edges and growing by coalescence and accretion of smaller clusters. At 1 Torr, the clusters increased further in size and density (fig. S3) (*23*). These clusters are not aggregates of CO molecules, because their height is close to that of the steps, whereas CO produces a contrast of only a fraction of an angstrom (*27*).

High-resolution images (Fig. 2, B and C) showed that the perimeters of the clusters contain bright maxima arranged in hexagonal (C_6) or trigonal (C_3) symmetries, which we attribute to CO molecules. The presence of CO bound to Cu edge atoms can

be rationalized by the energy gain obtained by CO adsorption on low-coordinated Cu atoms. As discussed below, DFT predicts that 12 CO molecules, one for each atom in the periphery of the 19 atom cluster, are necessary for energetic stability, and only the molecules bound to corner Cu atoms appear bright. The three-atom clusters require three CO molecules for stability. From the known CO coverage (from APXPS) and from simple cluster counting in the STM images, we conclude that all the adsorbed CO molecules are bound to the cluster edges, leaving the rest of the surface with a negligible CO coverage below 0.01 ML.

At pressures between 10 and 100 Torr, the surface was completely covered with clusters that were larger and closer to each other, making estimation of their individual sizes difficult because of finite tip-size effects. Figure 1D shows an example of the topography of the surface under 10 Torr of CO, with clusters densely covering adjacent terraces separated by monatomic steps. Unlike the case for pressure below a few Torr, the clusters are now completely covered by CO molecules, imaged as bright spots separated by distances of $\sqrt{3}$ and 2 times the Cu atomic periodicity and aligned in directions forming 60° and 90° between them. A similar surface was also observed at 100 Torr of CO (fig. S4). We interpret the observed STM contrast as arising from atop site CO molecules in local (2×2)-3CO and c(4×2) geometries with coverages of 0.75 and 0.5 ML, respectively. In mixed top and bridge or hollow CO sites, the STM contrast is large only for the top sites (*21*, *28*). The (4×4) superstructure reported at cryogenic temperatures (*29*) was not observed here.

The CO-promoted formation of metal clusters on Cu(111) contrasts with the case of Pt(111), where no clustering is observed, and with the stepped Pt(332) and Pt(557) surfaces, where clusters form and entirely occupy the terraces (*22*). The CO adsorption energy on Pt is > 1 eV, but on Cu(111), this energy is only ~0.5 eV. However, Cu has a much lower cohesive energy of 3.50 eV compared with the 5.84 eV of Pt (*18*, *19*). The low cohesive energy of Cu has many manifestations, such as the frizzled appearance of the steps of the clean surface at room temperature caused by kink atom diffusion (*30*), which was not observed on Pt.

On the Cu(111) surface, we calculated the formation energy of a Cu adatom by detachment from kink sites as 0.83 eV, indicating that on a clean surface the formation of clusters is energetically unfavorable. However, the adsorption of CO on a kink site reduces the detachment energy of CO+Cu molecule-adatom couples to 0.63 eV because of the difference in CO adsorption energy on a kink site and on a Cu adatom, which we calculated as −0.77 eV and −0.96 eV, respectively. The mobility of the Cu adatoms on (111) terraces can be predicted from the calculated potential energy surface that shows a diffusion barrier of 0.14 eV (fig. S5) (*23*). This barrier decreases to 0.10 eV for the Cu+CO couple. The lowering of the binding energy of metal atoms by adsorbed CO, leading to their detachment from the steps and their higher mobility on the terrace, is known as the "harpooning" effect (*31*). The higher density

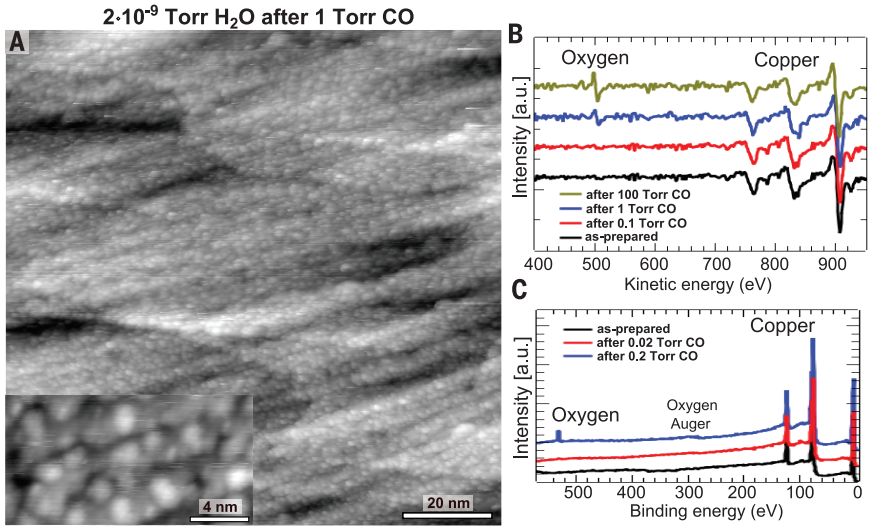
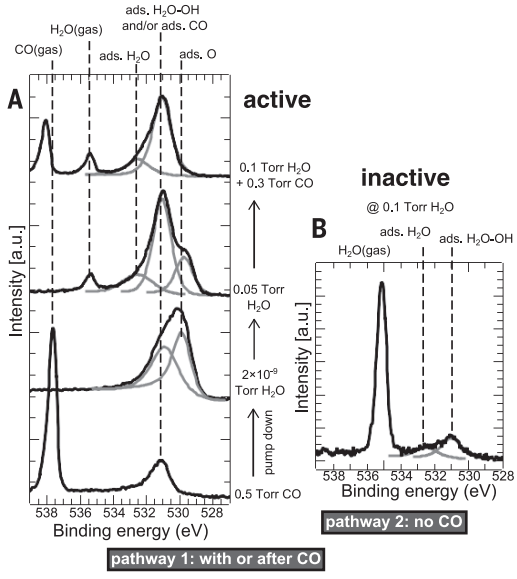


Fig. 3. STM images and AES spectra taken after evacuation of the CO gas phase. (**A**) STM images show that the Cu clusters remain on the surface in the presence of 2×10^{-9} Torr of water 0.5 hours after evacuation [V_b = 0.5 V; I_t = 0.5 nA]. Expanded image in inset [V_b = 1.5 V; I_t = 0.2 nA]. (**B**) AES after evacuation of the gas-phase CO from different initial pressures. The dissociative adsorption of H_2O on the cluster-covered surface is evident from the increasing intensity of the O peak. (**C**) Similar observation using XPS in the Synchrotron chamber.

Fig. 4. APXPS experiments of H_2O adsorption on Cu(111), with and without pre-adsorption of CO. (**A**) H_2O adsorption after CO-induced morphological changes. From bottom: under 0.5 Torr of CO; after pump down to 2×10^{-9} Torr, mostly containing water [mass spectra shown in fig. S8 (*23*)]; under 0.05 Torr of water; and (top) under 0.4 Torr of a 3:1 gas mixture of CO and H_2O. Water dissociation is activated by the large increase of low-coordinated sites produced by the CO-induced nanocluster formation. In the presence of both water and CO (top), only OH and H_2O species are observed because of the efficient reaction of CO with atomic O (*24*). (**B**) APXPS of a pristine Cu(111) (i.e., not exposed to CO) in the presence of 0.1 Torr of H_2O. The weak adsorption peaks of H_2O and OH [compare with top two spectra in (A)] probably arise from adsorption on the defect sites.



and diffusion rate of Cu+CO couples on the surface is the reason for their coalescence into clusters.

A detailed look at the Cu clusters, colored in Fig. 2A, shows that two types of CO decoration motifs exist, with C_6 and C_3 symmetry (Fig. 2, B and C). To explain the formation, stability, and structure of these clusters, we start by placing six CO molecules on the six corner Cu atoms of a 19-atom hexagon, plus one additional CO on the top site of the center atom. The DFT calculation for this cluster provides a CO adsorption energy of 0.83 eV on the low-coordinated corner sites, much greater than the 0.47-eV adsorption energy on the flat terrace. The adsorption energy of CO in the cluster's center is 0.47 eV, similar to the flat surface. The total energy gain from the six corner CO molecules (2.16 eV) is not enough to overcome the formation energy of a 19-atom cluster, which we calculated to be 3.61 eV (table S2) (*23*). Adsorption of CO molecules to each Cu periphery atom (i.e., including those in the middle of each side), however, results in an energy gain averaging 0.82 eV per CO. Hence, the formation of the 19-atom cluster with 13 CO molecules is −0.59 eV (Fig. 2B), meaning that it is energetically favorable (table S2) (*23*). The CO molecules on this cluster have different adsorption geometries with tilt angles of 0°, 26°, and 37° with respect to the surface normal for the central, edge, and corner CO molecules, respectively.

The observation of only six bright spots at the periphery (plus the central spot) is related to the

electronic structure and tunneling probability of the different CO molecules. We illustrate this by calculating the tunneling current probability using the standard Bardeen approximation [equations 2 and 3 in (*23*)] and the calculated partial density of states (DOS) for CO molecules on the cluster and on the tip (fig. S6) (*23*). The calculation reveals that the CO molecules on the corners indeed have greater tunneling contributions than the CO molecules on the edges, qualitatively explaining the experimentally observed contrast of the STM images with the six bright spots plus one in the center, as shown in Fig. 2, B and D. We could explain the threefold symmetry of some of the 19 atom clusters by adding three Cu atoms at the center of the 19 atoms. These three low-coordinated Cu atoms, producing the bright center of the cluster images, can bind three additional CO molecules and distort the tilt angles of the peripheral CO molecules, as shown in Fig. 2, C and E [(details are shown in (*23*)].

Finally, we investigated the effect of clustering on surface reactivity for the WGS reaction (i.e., $CO+H_2O \leftrightarrow CO_2+H_2$), which Cu catalyzes. Water does not adsorb on the Cu(111) surface at room temperature (Fig. 4B) (*32*), whereas it dissociatively adsorbs on the more active Cu(110) surface (*32*). Once the gas phase CO at 1 Torr was pumped away, the STM images revealed that the Cu clusters were still present, although atomic resolution could not be achieved, likely because of the absence of CO molecules adsorbed on the tip in high vacuum (Fig. 3A). In the presence of 2×10^{-9} Torr of H_2O, the cluster-covered surface was very active in dissociating water, as shown by the increasing oxygen peak in both the Auger electron spectra (AES) shown in Fig. 3B, and in the XPS spectra shown in Fig. 3C. The APXPS spectrum indicates that the O peak is a result of the dissociative adsorption of H_2O (Fig. 4A) and that no such peak appears after experiments at 0.1 Torr of CO because clustering of the Cu did not occur at lower CO pressures (Figs. 1B and 3B). A similar effect was also observed during exposure to $CO+H_2O$ mixtures, as shown in Fig. 4A. The pristine Cu(111) surface, on the other hand, not pre-exposed to CO, is inactive (Fig. 4B).

Our findings open the possibility that other soft materials (e.g., Ag, Au, and Zn) can similarly undergo large reconstructions at sufficiently high pressures of CO (or other molecules). We have also demonstrated that the inactive (111) face of Cu for water dissociation, a key step in the water-gas shift reaction, becomes highly activated as a result of the CO-induced clustering. The need for this type of study to extend our understanding of the working of catalysts under operating conditions is clear.

REFERENCES AND NOTES

1. G. A. Somorjai, *Introduction to Surface Chemistry and Catalysis* (Wiley-VCH, 1999).
2. G. Ertl, *Angew. Chem. Int. Ed.* **47**, 3524–3535 (2008).
3. B. J. McIntyre, M. Salmeron, G. A. Somorjai, *Rev. Sci. Instrum.* **64**, 687–691 (1993).
4. L. Österlund *et al.*, *Phys. Rev. Lett.* **86**, 460–463 (2001).
5. E. Laegsgaard *et al.*, *Rev. Sci. Instrum.* **72**, 3537–3542 (2001).
6. F. Tao, D. Tang, M. Salmeron, G. A. Somorjai, *Rev. Sci. Instrum.* **79**, 084101 (2008).
7. F. Besenbacher, P. Thostrup, M. Salmeron, *MRS Bull.* **37**, 677–681 (2012).
8. C. T. Herbschleb *et al.*, *Rev. Sci. Instrum.* **85**, 083703 (2014).
9. M. Salmeron, R. Schlögl, *Surf. Sci. Rep.* **63**, 169–199 (2008).
10. M. Salmeron, *MRS Bull.* **38**, 650–657 (2013).
11. K. Klier, in *Advances in Catalysis, Vol. 31*, D. D. Eley, H. Pines, P. B. Weisz, Eds. (Academic Press, 1982), pp. 243–313.
12. D. S. Newsome, *Catal. Rev.* **21**, 275–318 (1980).
13. J. Szanyi, D. W. Goodman, *Catal. Lett.* **10**, 383–390 (1991).
14. J. Yoshihara, C. T. Campbell, *J. Catal.* **161**, 776–782 (1996).
15. M. Behrens *et al.*, *Science* **336**, 893–897 (2012).
16. G. A. Olah, *Angew. Chem. Int. Ed.* **52**, 104–107 (2013).
17. M. Behrens, *Angew. Chem. Int. Ed.* **53**, 12022–12024 (2014).
18. K. Kambe, *Phys. Rev.* **99**, 419–422 (1955).
19. C. Kittel, *Introduction to Solid State Physics, 8th Edition* (Wiley, 2005).
20. S. R. Longwitz *et al.*, *J. Phys. Chem. B* **108**, 14497–14502 (2004).
21. D. Tang, K. S. Hwang, M. Salmeron, G. A. Somorjai, *J. Phys. Chem. B* **108**, 13300–13306 (2004).
22. F. Tao *et al.*, *Science* **327**, 850–853 (2010).
23. See supplementary materials on *Science* Online
24. B. Eren *et al.*, *J. Phys. Chem. C* **119**, 14669–14674 (2015).
25. J. Lagoute, X. Liu, S. Fölsch, *Phys. Rev. Lett.* **95**, 136801 (2005).
26. O. V. Lysenko, V. S. Stepanyuk, W. Hergert, J. Kirschner, *Phys. Rev. Lett.* **89**, 126102 (2002).
27. M. Mehlhorn, H. Gawronski, K. Morgenstern, *Phys. Rev. Lett.* **104**, 076101 (2010).
28. H. J. Yang, T. Minato, M. Kawai, Y. Kim, *J. Phys. Chem. C* **117**, 16429–16437 (2013).
29. L. Bartels, D. Meyer, K. H. Rieder, *Surf. Sci. Lett.* **432**, L621–L626 (1999).
30. M. Poensgen, J. F. Wolf, J. Frohn, M. Giesen, H. Ibach, *Surf. Sci.* **274**, 430–440 (1992).
31. M. M. Waldrop, *Science* **234**, 673–674 (1986).
32. S. Yamamoto *et al.*, *J. Phys. Chem. C* **111**, 7848–7850 (2007).

ACKNOWLEDGMENTS

This work was supported by the Office of Basic Energy Sciences (BES), Division of Materials Sciences and Engineering, of the U.S. Department of Energy (DOE) under contract no. DE-AC02-05CH11231, through the Chemical and Mechanical Properties of Surfaces, Interfaces and Nanostructures program (FWP KC3101). It used resources of the National Energy Research Scientific Computing Center and the Advanced Light Source, which are supported by the Office of Science of the U.S. DOE. The computation used resources from the Oak Ridge Leadership Computing Facility (OLCF), with time allocated by the Innovative and Novel Computational Impact on Theory and Experiment (INCITE) project.

SUPPLEMENTARY MATERIALS

www.sciencemag.org/content/351/6272/475/suppl/DC1
Materials and Methods
Supplementary Text
Figs. S1 to S8
Tables S1 to S3
References (*33*–*41*)

16 November 2015; accepted 14 December 2015
10.1126/science.aad8868

OCEANOGRAPHY

Enhanced East Pacific Rise hydrothermal activity during the last two glacial terminations

D. C. Lund,[1]* P. D. Asimow,[2] K. A. Farley,[2] T. O. Rooney,[3] E. Seeley,[1] E. W. Jackson,[4] Z. M. Durham[4]

Mid-ocean ridge magmatism is driven by seafloor spreading and decompression melting of the upper mantle. Melt production is apparently modulated by glacial-interglacial changes in sea level, raising the possibility that magmatic flux acts as a negative feedback on ice-sheet size. The timing of melt variability is poorly constrained, however, precluding a clear link between ridge magmatism and Pleistocene climate transitions. Here we present well-dated sedimentary records from the East Pacific Rise that show evidence of enhanced hydrothermal activity during the last two glacial terminations. We suggest that glacial maxima and lowering of sea level caused anomalous melting in the upper mantle and that the subsequent magmatic anomalies promoted deglaciation through the release of mantle heat and carbon at mid-ocean ridges.

Sea level–driven pressure variations due to the growth and decay of ice sheets likely modulate melt production in the upper mantle on Milankovitch time scales (*1*, *2*). Model simulations suggest that the magnitude of the resulting signal at mid-ocean ridges depends on the plate spreading rate, the melt extraction velocity, and the thermal properties of the lithosphere (*1*, *3*). Because of the slow rate of melt migration in the upper mantle, the magmatic signal at ridges probably lags changes in sea level by thousands of years (*1*). Surveys of ridge bathymetry reveal Milankovitch-scale frequencies in abyssal-hill spacing, consistent with the sea-level hypothesis (*3*, *4*). Bathymetry records are subject to geological damping effects and

[1]Deptartment of Marine Sciences, University of Connecticut, Groton, CT 06340, USA. [2]Division of Geological and Planetary Sciences, California Institute of Technology, Pasadena, CA 91125, USA. [3]Department of Geological Sciences, Michigan State University, East Lansing, MI 48824, USA. [4]Department of Earth and Environmental Sciences, University of Michigan, Ann Arbor, MI 48109, USA.
***Corresponding author. E-mail: david.lund@uconn.edu**

Downloaded from on January 31, 2016

substantial age uncertainties, however, and they therefore require validation with other proxies. Because hydrothermal activity along ridge sections is ultimately driven by magmatic heat, sedimentary records of hydrothermal output can be used to assess the sea-level hypothesis and determine the timing of magmatic anomalies relative to key Pleistocene climate transitions.

The southern East Pacific Rise (SEPR) has the fastest spreading rate and the highest magmatic budget of any ridge in the global mid-ocean ridge system (*5*). Due to its elevated magmatism, the SEPR has over 50 known active vent sites from 5°S to 37°S (*6*), consistent with the global trend in plume incidence versus magmatic budget for ridges spanning a range of spreading rates (*5*, *7*). Intense hydrothermal venting and topographically steered flow of plumes along the SEPR create a spatially integrated pattern of metalliferous sediments near the ridge crest (*8*–*10*). Compared with slower ridges, SEPR sediments have anomalously high metal concentrations (*8*, *11*), suggesting that magmatism is the primary factor governing hydrothermal input to these sedimentary archives on geologic time scales. Hydrothermal plume particles are highly enriched in elements that are derived directly from vents and scavenged from seawater. Variations in the flux of these elements to ridge-flank sediments should therefore reflect long-term changes in hydrothermal activity.

We used a multiproxy geochemical strategy to reconstruct SEPR hydrothermal activity during the last glacial cycle. We analyzed a total of seven ridge-crest cores from 6°S and 11°S, where the half-spreading rate averages 75 mm/year (Fig. 1). Together with two published records from near the East Pacific Rise (EPR)–Dietz volcanic-ridge triple junction at 1°N (*12*), the locations span a range of spreading rates, sedimentary environments, and surface-ocean productivity regimes. To control for spatial heterogeneity in plume incidence versus magmatic budget (*7*), the sampling locations span three separate EPR segments. At each segment, we analyzed cores from both sides of the ridge axis to address potential biases due to horizontal sediment focusing, bioturbation, and spatial variability in hydrothermal-plume direction. Radiocarbon and oxygen isotopic analyses of planktonic foraminifera provided age control for each core (*13*). Major and trace element concentrations were determined using x-ray fluorescence (XRF) and inductively coupled plasma mass spectrometry (ICP-MS). The fluxes of hydrothermal components were estimated using both mass accumulation rates and the ^{3}He normalization method (*13*). Given that plume particles primarily consist of Fe oxyhydroxides and Mn oxides (*14*), we used sedimentary Fe and Mn to track hydrothermal inputs. To cross-check the Fe and Mn results, we also measured arsenic, which is scavenged from seawater by Fe oxyhydroxides and varies coherently with Fe in hydrothermal-plume particles (*15*) and SEPR sediments (*16*).

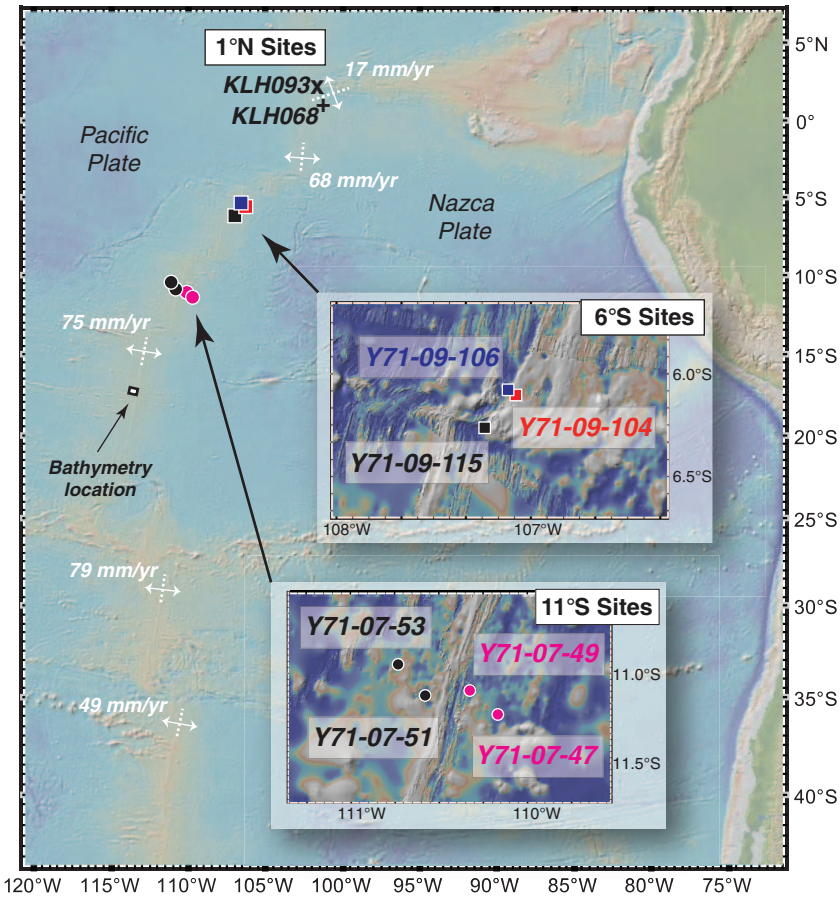


Fig. 1. Map of sampling sites near the EPR. Core locations include 1°N (cores KLH068 and KLH093) (*12*), 6°S (core Y71-09-104 in blue, Y71-09-106 in red, and Y71-09-115 in black), and 11°S (cores Y71-07-47 and Y71-07-49 in magenta and Y71-07-51 and Y71-07-53 in black). Also shown is the location of the bathymetry record at 17°S (*4*). Half-spreading rates are shown in white (www.ldeo.columbia.edu/~menke/plates.html). The half-spreading rate at 1°N (17 mm/year measured at Dietz volcanic ridge) is from (*29*). The map was generated using GeoMapApp (www.geomapapp.org).

Oxygen stable isotope records from 1°N, 6°S, and 11°S outline marine isotope stages 1, 2, and 3, indicating that there has been minimal stratigraphic disturbance of the cores due to sediment winnowing or downslope transport (Fig. 2). The flux of Fe in all nine records peaks between 10 and 20 thousand years before the present (ky B.P.). Manganese fluxes to EPR sediments follow a similar pattern, with maximum values centered at ~15 ky B.P. Arsenic fluxes at 6°S and 11°S reach a maximum between 10 and 20 ky B.P., supporting the Fe and Mn results. Offsets between time series are generally 5 ky or less (Fig. 2), similar to the age uncertainty associated with the mass accumulation rate method (*13*). Results from the ^{3}He normalization technique, which yields fluxes that are insensitive to age-model uncertainty, show that positive shifts in metal fluxes at 11°S and 6°S occurred within 2 ky of one another (fig. S1). Thus, the overall pattern for the past 50 ky is one of coherent variations in hydrothermal sedimentation along 1300 km of the EPR, with maximum metal inputs coinciding with the last deglaciation (Termination I).

Two cores at 11°S span the penultimate deglaciation (Termination II), including core Y71-07-53 on the western flank of the SEPR and core Y71-07-47 on the eastern flank (Fig. 3). Metal fluxes are higher in the western-flank core, consistent with the east-west contrast in the shorter records (Fig. 2) and the spatial pattern in metal concentrations of late Holocene sediments (*8*). In the western-flank core, the flux of each metal increases markedly at ~140 ky B.P., reaches a maximum by 130 ky B.P., and then returns to background levels by 120 ky B.P. (Fig. 3). A similar pattern occurs in the eastern-flank core. The contemporaneous signal at these locations indicates that hydrothermal inputs on each side of the ridge crest varied in phase. The records also show that the maximum flux of hydrothermal metals coincided with Termination II, similar to the pattern for Termination I.

Diagenetic overprinting, horizontal sediment focusing, and dilution with nonhydrothermal components can complicate the interpretation of hydrothermal proxies. Diagenetic remobilization should influence Fe oxyhydroxides and MnO_2 differently, given the large offset in their redox potentials (*17*), yet we observed coherent down-core variations in Fe, Mn, and As, regardless of location. Furthermore, down-core Fe/Mn ratios generally fall within the expected range for hydrothermal input (*8*). Anomalously high

Fe/Mn ratios at 1°N are probably due to suboxic diagenesis and Mn remobilization (*13*). At the 1°N locations, near-zero Mn levels before 20 ky BP are likely driven by MnO_2 reduction and upward migration of dissolved Mn^{2+}. Nevertheless, the overall coherent pattern in Fe records from the high-productivity equatorial Pacific (1°N) to the northern edge of the subtropical gyre (11°S) indicates that the organic carbon flux to the sediments is not a first-order control on down-core metal variability. Sediment focusing is an equally unlikely explanation, given the similar pattern in multiple cores from a range of sedimentary environments. Focusing factors estimated using ^{3}He also show no evidence for anomalous horizontal sediment transport during Termination I (fig. S3). Lastly, the ^{3}He-based metal fluxes are consistent with the mass accumulation rate results, indicating that carbonate dilution was not a primary driver of the down-core signal. Taken together, these lines of evidence indicate that the metal fluxes primarily reflect the input of hydrothermal-plume particles to ridge-crest sediments.

The temporal variability in metal fluxes is similar to that in seafloor bathymetry at 17°S on the SEPR, implying that both have a common driver (Fig. 4). A lowering of sea level due to ice-sheet expansion would promote decompression melting in the upper mantle. The resulting increase in melt delivery to the ridge crest should result in shoaling of the bathymetry and greater hydrothermal activity (*1*, *3*). Ice-sheet retreat and rising sea level would have the opposite effect. Shallower bathymetry on the SEPR generally corresponds to elevated hydrothermal fluxes, consistent with the expected pattern (Fig. 4). The bathymetry record lags the hydrothermal proxies by ~10 ky, however (fig. S4). The offset is most likely due to age uncertainty in the bathymetry time series, where the age model is based on a half-spreading rate that optimizes the match between the bathymetry and atmospheric CO_2 records (*4*). More generally, age constraints for late Pleistocene oceanic crust are limited to two control points, an assumed zero age at the ridge crest and the Brunhes-Matuyama boundary at 780 ky B.P. Even if reliable absolute ages were available for individual abyssal hills, it is unlikely that their bathymetry would reflect only the melt delivery that occurred when that oceanic crust was at the ridge crest, because of the confounding influences of lower crustal accretion, surface

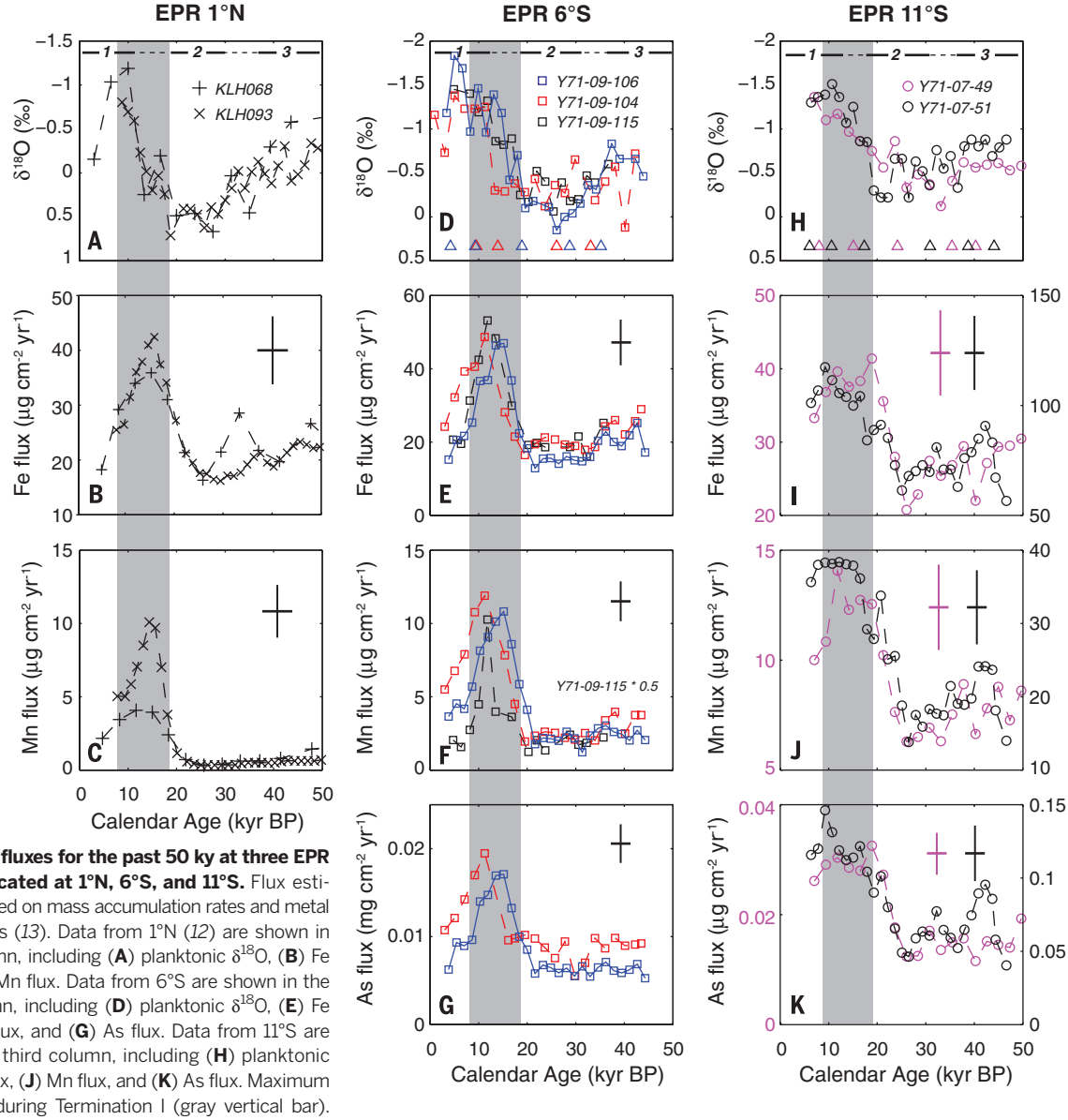


Fig. 2. Metal fluxes for the past 50 ky at three EPR segments located at 1°N, 6°S, and 11°S. Flux estimates are based on mass accumulation rates and metal concentrations (*13*). Data from 1°N (*12*) are shown in the first column, including (**A**) planktonic $\delta^{18}O$, (**B**) Fe flux, and (**C**) Mn flux. Data from 6°S are shown in the second column, including (**D**) planktonic $\delta^{18}O$, (**E**) Fe flux, (**F**) Mn flux, and (**G**) As flux. Data from 11°S are shown in the third column, including (**H**) planktonic $\delta^{18}O$, (**I**) Fe flux, (**J**) Mn flux, and (**K**) As flux. Maximum fluxes occur during Termination I (gray vertical bar). Typical errors for each record (crosses in each panel) represent the uncertainty of the flux estimates (vertical line) and age model error (horizontal line). Calendar-corrected radiocarbon ages are shown as triangles. Approximate time intervals for marine isotope stages 1 to 3 are indicated in the top row of panels. Arsenic results are not available for cores collected at 1°N because these cores were analyzed using XRF rather than ICP-MS (*12*).

lava flows, and vertical and horizontal offsets of crustal blocks by faulting (*3*, *4*, *18*, *19*). Although bathymetric time series are useful for identifying Milankovitch frequencies, the absolute timing of events is poorly constrained by these records. Hydrothermal proxies, on the other hand, can be accurately dated using radiocarbon and oxygen isotope stratigraphy. As a result, we are able to infer that intervals of intense hydrothermal activity on the EPR occurred during the last two glacial terminations.

The coincidence in timing between hydrothermal maxima and glacial terminations implies that there may be a direct causal relationship between sea-level rise and hydrothermal activity. Our understanding of the physical mechanisms of decompression melting and melt migration to the ridge axis suggests a more complex relationship, however. Proxies of magmatic flux should lag sea-level changes by thousands of years, because of the slow rate of melt migration from the magma source region to the ridge axis (*1*). During the Last Glacial Maximum, the maximum rate of sea-level decrease (and hence of pressure release in the melting regime) occurred between 30 and 25 ky B.P. (*20*), or 15 ± 5 ky before the inferred maximum in EPR hydrothermal activity (Fig. 2). We observed a similar lag between the maximum rate of sea-level rise at ~15 ky B.P. (*20*) and the late Holocene minimum in metal flux. Assuming an average melt origin depth of 50 km (*21*), the implied melt extraction velocities range from 2.5 to 5 m/year, which is consistent with the rate of >1 m/year implied by U/Th disequilibrium in zero-age mid-ocean ridge basalts (*22*) but much lower than the estimates of >50 m/year based on the time lag between deglaciation and volcanism in Iceland (*23*). Our estimate is independent of previous methods and provides a range of constraints for refining models of melt extraction at fast spreading centers.

Our results support the hypothesis that enhanced ridge magmatism, hydrothermal output, and perhaps mantle CO_2 flux act as a negative feedback on ice-sheet size (*1*, *4*). Although the modern carbon output from ridges is small (0.02 to 0.2 Pg C/year) (*24*), the flux probably increased as a result of sea-level modulation. Carbon sources at off-axis locations, backarc basins, and island arcs may also amplify the mid-ocean ridge signal (*2*). The long melt-migration times for carbon-rich melts may lead to considerable differences in timing between hydrothermal and carbon-flux variations, however (*25*). Another mechanism whereby magmatic variations may influence climate is the hydrothermal heat flux itself. Enhanced geothermal heat flux should warm and destabilize the deep ocean (*26*), with excess heat emerging along isopycnals into the surface Southern Ocean (*26*, *27*). Temperatures in the deep

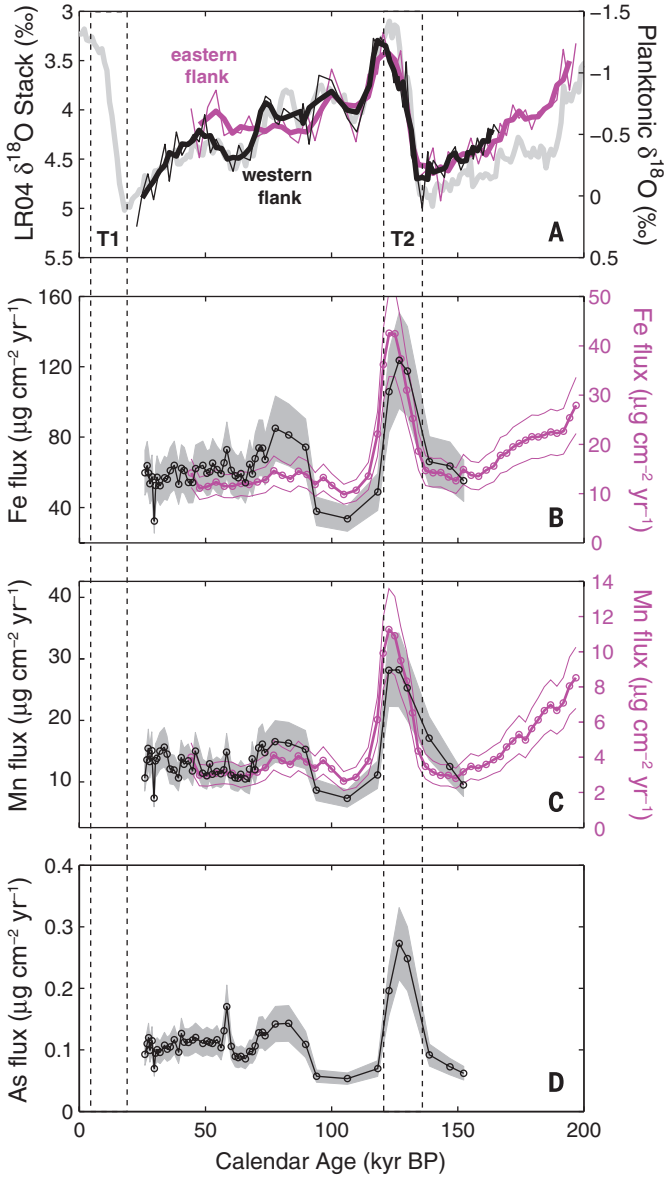


Fig. 3. Planktonic $\delta^{18}O$ and metal fluxes spanning Termination II at 11°S. The time series are from the eastern (core Y71-07-47; magenta) and western (core Y71-07-53; black) flanks of the EPR. (**A**) Planktonic $\delta^{18}O$ results superimposed on a global benthic $\delta^{18}O$ stack [LR04 (*30*)] (gray line), (**B**) Fe flux, (**C**) Mn flux, and (**D**) As flux. In (A), thin lines indicate data from discrete samples, and thick lines indicate time series smoothed with a three-point running mean. In (B) to (D), flux estimates are based on mass accumulation rates and metal concentrations. Glacial terminations are indicated by dashed vertical lines. Hydrothermal metal fluxes peaked during Termination II (T2). Error bars for the western flank (gray shaded area) and eastern flank (thin magenta lines) reflect the uncertainty of the flux estimates in (B) to (D) (*13*). Metal data for core Y71-07-53 (*16*) were assigned ages based on the $\delta^{18}O$ stratigraphy generated for this work. Arsenic data are not available for core Y71-07-47 because it was analyzed using XRF rather than ICP-MS.

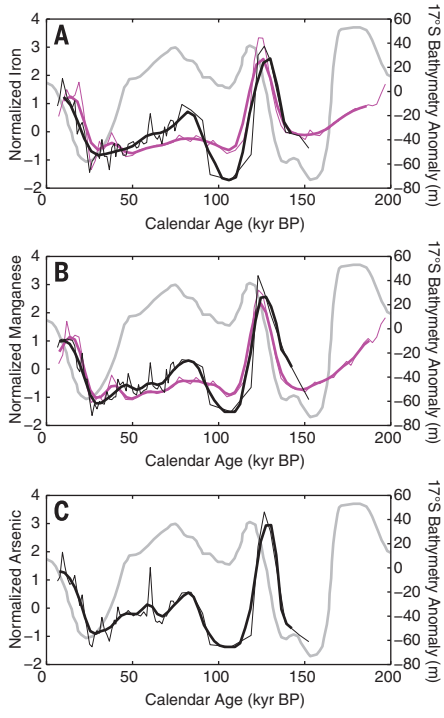


Fig. 4. Normalized metal fluxes at 11°S compared with EPR bathymetry. The hydrothermal time series are from the eastern (magenta) and western (black) flanks of the EPR and include (**A**) Fe flux, (**B**) Mn flux, and (**C**) As flux. We normalized each record by subtracting the mean and dividing by the standard deviation of each time series to facilitate comparison between cores with different mean metal concentrations. The results include both discrete samples (thin lines) and time series smoothed with a 20-ky-wide Gaussian window (thick lines) to approximate the resolution of the bathymetry compilation at 17°S (gray lines) (*4*). Fluxes from 0 to 40 ky are based on the results from Fig. 2; the interval from 40 to 200 ky B.P. is based on results shown in Fig. 3.

eastern tropical Pacific and Antarctica peaked during each of the last two glacial terminations (*28*), consistent with the timing of enhanced EPR hydrothermal activity.

Isolating a mechanistic linkage between ridge magmatism and glacial terminations will require a suite of detailed proxy records from multiple ridges that are sensitive to mantle carbon and geothermal inputs, as well as modeling studies of their influence in the ocean interior. The EPR results establish the timing of hydrothermal anomalies, an essential prerequisite for determining whether ridge magmatism can act as a negative feedback on ice-sheet size. The data presented here demonstrate that EPR hydrothermal output increased after the two largest glacial maxima of the past 200,000 years, implicating mid-ocean ridge magmatism in glacial terminations.

REFERENCES AND NOTES

1. D. C. Lund, P. D. Asimow, *Geochem. Geophys. Geosyst.* **12**, Q12009 (2011).
2. P. Huybers, C. Langmuir, *Earth Planet. Sci. Lett.* **286**, 479–491 (2009).
3. J. W. Crowley, R. F. Katz, P. Huybers, C. H. Langmuir, S. H. Park, *Science* **347**, 1237–1240 (2015).
4. M. Tolstoy, *Geophys. Res. Lett.* **42**, 1346–1351 (2015).
5. E. T. Baker, G. R. German, in *Mid-Ocean Ridges: Hydrothermal Interactions Between the Lithosphere and Oceans*, C. R. German, J. Lin, L. M. Parson, Eds. (Geophysical Monograph Series vol. 148, American Geophysical Union, 2004), pp. 245–266.
6. S. E. Beaulieu, E. T. Baker, C. R. German, A. Maffei, *Geochem. Geophys. Geosyst.* **14**, 4892–4905 (2013).
7. E. T. Baker, *Geochem. Geophys. Geosyst.* **10**, Q06009 (2009).
8. J. Dymond, *Geol. Soc. Am.* **154**, 133–174 (1981).
9. G. B. Shimmield, N. B. Price, *Geochim. Cosmochim. Acta* **52**, 669–677 (1988).
10. K. G. Speer, M. E. Maltrud, A. M. Thurnherr, in *Energy and Mass Transfer in Hydrothermal Systems*, P. E. Halbach, V. Tunnicliffe, J. R. Hein, Eds. (Dahlem University Press, 2003), pp. 287–302.
11. K. Boström, M. N. Peterson, O. Joensuu, D. E. Fisher, *J. Geophys. Res.* **74**, 3261–3270 (1969).
12. M. Frank *et al.*, *Paleoceanography* **9**, 559–578 (1994).
13. Material and methods are available as supplemental materials on *Science* Online.
14. C. R. German, S. Colley, M. R. Palmer, A. Khripounoff, G. P. Klinkhammer, *Deep Sea Res. Part I Oceanogr. Res. Pap.* **49**, 1921–1940 (2002).
15. R. R. Cave, C. R. German, J. Thomson, R. W. Nesbitt, *Geochim. Cosmochim. Acta* **66**, 1905–1923 (2002).
16. T. Schaller, J. Morford, S. R. Emerson, R. A. Feely, *Geochim. Cosmochim. Acta* **64**, 2243–2254 (2000).
17. S. Emerson, J. I. Hedges, in *Treatise on Geochemistry*, K. K. Turekian, H. D. Holland, Eds. (Elsevier, vol. 6, 2004), pp. 293–319.
18. J. A. Goff, *Science* **349**, 1065 (2015).
19. J. A. Olive *et al.*, *Science* **350**, 310–313 (2015).
20. P. U. Clark *et al.*, *Science* **325**, 710–714 (2009).
21. K. Key, S. Constable, L. Liu, A. Pommier, *Nature* **495**, 499–502 (2013).
22. P. B. Kelemen, G. Hirth, N. Shimizu, M. Spiegelman, H. J. B. Dick, *Philos. Trans. R. Soc. Lond. A* **355**, 283–318 (1997).
23. J. Maclennan, M. Jull, D. McKenzie, L. Slater, K. Gronvold, *Geochem. Geophys. Geosyst.* **3**, 1–25 (2002).
24. P. Cartigny, F. Pineau, C. Aubaud, M. Javoy, *Earth Planet. Sci. Lett.* **265**, 672–685 (2008).
25. J. M. A. Burley, R. F. Katz, *Earth Planet. Sci. Lett.* **426**, 246–258 (2015).
26. M. Hofmann, M. A. Morales Maqueda, *Geophys. Res. Lett.* **36**, L03603 (2009).
27. J. Emile-Geay, G. Madec, *Ocean Sci.* **5**, 203–217 (2009).
28. P. Martin, D. Archer, D. W. Lea, *Paleoceanography* **20**, PA2015 (2005).
29. D. K. Smith, H. Schouten, L. Montési, W. Zhu, *Earth Planet. Sci. Lett.* **371–372**, 6–15 (2013).
30. L. E. Lisiecki, M. E. Raymo, *Paleoceanography* **20**, PA1003 (2005).

ACKNOWLEDGMENTS

We dedicate this paper to J. Dymond, whose 1981 treatise on Nazca plate sediments made this work possible. We are also indebted to the Oregon State University Core Repository for carefully preserving the EPR sediment cores since they were collected in the early 1970s. We are grateful to L. Wingate at the University of Michigan and M. Cote at the University of Connecticut for technical support. This work has benefited from discussions with J. Granger, P. Vlahos, B. Fitzgerald, and M. Lyle. Data presented here are available on the National Oceanic and Atmospheric Administration's Paleoclimatology Data website (www.ncdc.noaa.gov/data-access/paleoclimatology-data). Funding was provided by the University of Michigan and the University of Connecticut.

SUPPLEMENTARY MATERIALS

www.sciencemag.org/content/351/6272/478/suppl/DC1
Materials and Methods
Supplementary Text
Figs. S1 to S11
Tables S1 to S5
References (*31*–*45*)

14 September 2015; accepted 6 January 2016
10.1126/science.aad4296

HISTORY OF SCIENCE

Ancient Babylonian astronomers calculated Jupiter's position from the area under a time-velocity graph

Mathieu Ossendrijver*

The idea of computing a body's displacement as an area in time-velocity space is usually traced back to 14th-century Europe. I show that in four ancient Babylonian cuneiform tablets, Jupiter's displacement along the ecliptic is computed as the area of a trapezoidal figure obtained by drawing its daily displacement against time. This interpretation is prompted by a newly discovered tablet on which the same computation is presented in an equivalent arithmetical formulation. The tablets date from 350 to 50 BCE. The trapezoid procedures offer the first evidence for the use of geometrical methods in Babylonian mathematical astronomy, which was thus far viewed as operating exclusively with arithmetical concepts.

The so-called trapezoid procedures examined in this paper have long puzzled historians of Babylonian astronomy. They belong to the corpus of Babylonian mathematical astronomy, which comprises about 450 tablets from Babylon and Uruk dating between 400 and 50 BCE. Approximately 340 of these tablets are tables with computed planetary or lunar data arranged in rows and columns (*1*). The remaining 110 tablets are procedure texts with computational instructions (*2*), mostly aimed at computing or verifying the tables. In all of these texts the zodiac, invented in Babylonia near the end of the fifth century BCE (*3*), is used as a coordinate system for computing celestial positions. The underlying algorithms are structured as branching chains of arithmetical operations (additions, subtractions, and multiplications) that can be represented as flow charts (*2*). Geometrical concepts are conspicuously absent from these texts, whereas they are very common in the Babylonian mathematical corpus (*4*–*7*). Currently four tablets, most likely written in Babylon between 350 and 50 BCE, are known to preserve portions of a trapezoid procedure (*8*). Of the four procedures, here labeled B to E (figs. S1 to S4), one (B) preserves a mention of Jupiter and three (B, C, E) are embedded in compendia of procedures dealing exclusively with Jupiter. The previously unpublished text D probably belongs to a similar compendium for Jupiter. In spite of these indications of a connection with Jupiter, their astronomical significance was previously not acknowledged or understood (*1*, *2*, *6*).

A recently discovered tablet containing an unpublished procedure text, here labeled text A (Fig. 1), sheds new light on the trapezoid procedures. Text A most likely originates from the same period and location (Babylon) as texts B to E (*8*). It contains a nearly complete set of instructions for Jupiter's motion along the ecliptic in accordance with the so-called scheme $X.S_1$ (*2*). Before the discovery of text A, this scheme was too fragmentarily known for identifying its connection with the trapezoid procedures. Covering one complete synodic cycle, scheme $X.S_1$ begins with Jupiter's heliacal rising (first visible rising at dawn), continuing with its first station (beginning of apparent retrograde motion), acronychal rising (last visible rising at dusk), second station (end of retrograde motion), and heliacal setting (last visible setting at dusk) (*2*). Scheme $X.S_1$ and the four trapezoid procedures are here shown to contain or imply mathematically equivalent descriptions of Jupiter's motion during the first 60 days after its first appearance. Whereas scheme $X.S_1$ employs a purely arithmetical terminology, the trapezoid procedures operate with geometrical entities.

Excellence Cluster TOPOI–Institute of Philosophy, Humboldt University, Berlin, Germany.
***Corresponding author. E-mail: mathieu.ossendrijver@hu-berlin.de**

Downloaded from on January 31, 2016

In text A, Jupiter's motion along the ecliptic is described in terms of its daily displacement (modern symbol: v) expressed in °/d (degrees/day) and its total displacement (S) expressed in degrees. A crucial new insight about scheme X.S$_1$ provided by text A concerns its use of piecewise linearly changing values for v. Although not formulated explicitly, this linear dependence on time is clearly implied (*8*). Jupiter's motion along the ecliptic is described for two consecutive intervals of 60 days between its first appearance and its first station. For each interval, initial and final values of v are provided. Note that Babylonian astronomy employs a sexagesimal; i.e., base-60 place-value system in which numbers are represented as sequences of digits between 0 and 59, each associated with a power of 60 that decreases in the right direction. In the commonly used modern notation for these numbers, all digits are separated by commas, except for the digit pertaining to 60°, which is separated from the next one pertaining to 60^{-1} by a semicolon (;), the analog of our decimal point. For the first interval of 60 days, v_0 = 0;12°/d (=12/60) and v_{60} = 0;9,30°/d (=9/60 + 30/60^2). Their sum is multiplied by 0;30 (=1/2), resulting in a mean value $(v_0 + v_{60})/2$ = 0;10,45°/d, which is multiplied by 1,0 (=60) days, resulting in a total displacement S = 1,0•$(v_0 + v_{60})/2$ = 10;45°. For the second interval, v_{60} = 0;9,30°/d and v_{120} = 0;1,30°/d (=1/60 + 30/60^2), leading to $(v_{60} + v_{120})/2$ = 0;5,30°/d and S = 5;30°. The sum of the total displacements, 10;45° + 5;30° = 16;15°, is declared to be the total distance by which Jupiter proceeds along the ecliptic in 120 days. In other words, the ecliptic longitude of Jupiter after 60 and 120 days is computed as $\lambda_{60} = \lambda_0$ + 10;45° and $\lambda_{120} = \lambda_0$ + 16;15°, respectively.

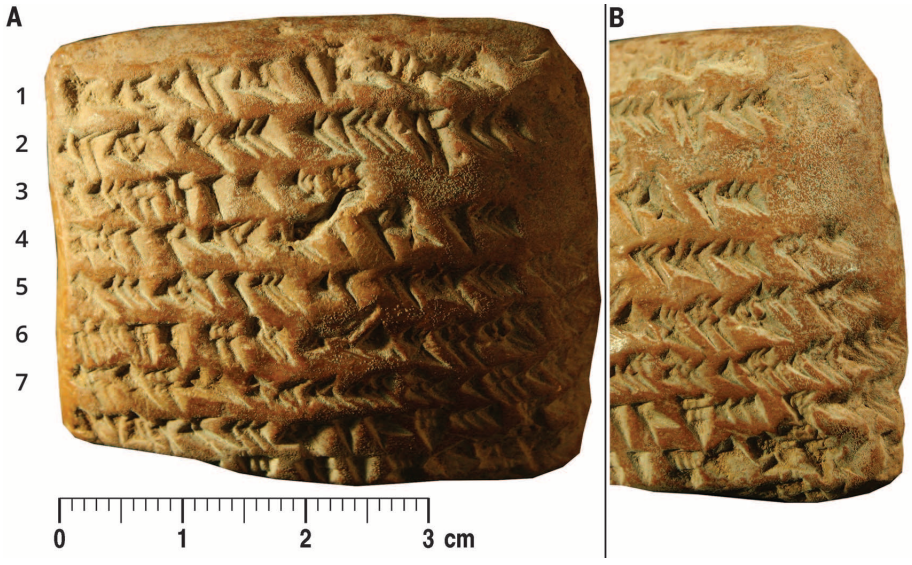


Fig. 1. Photograph of text A (lines 1 to 7). (**A**) Full image. (**B**) Partial image of the right side taken under different lighting conditions.

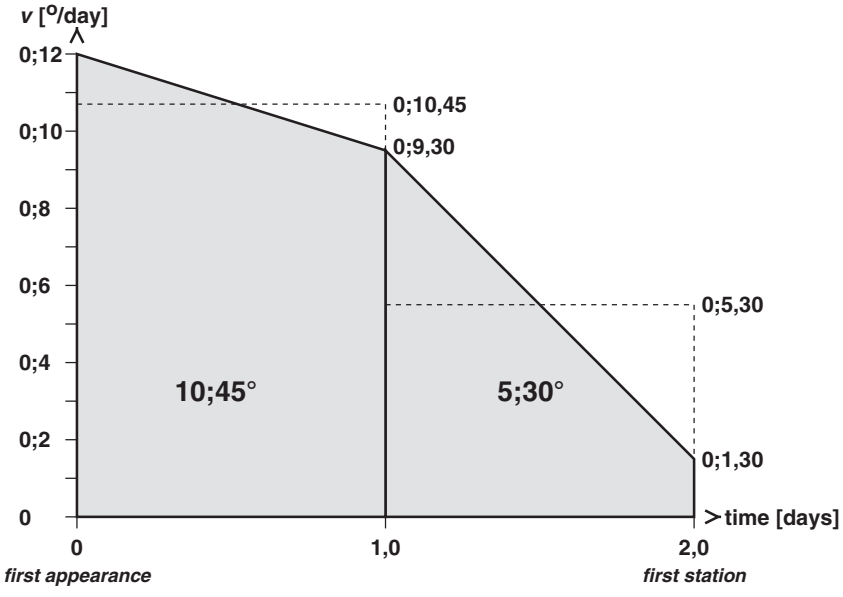


Fig. 2. Time-velocity graph of Jupiter's motion. Daily displacement along the ecliptic (v) between Jupiter's first appearance (day 0) and its first station (day 120) as a function of time according to scheme X.S$_1$ as inferred from text A. All numbers and axis labels are in sexagesimal place-value notation. The areas of the trapezoids, 10;45° and 5;30°, each represent Jupiter's total displacement during one interval of 60 days.

Text A does not describe how v varies from day to day, but of the three forms of time dependence of v that are attested in Babylonian planetary texts—piecewise constant, linear, or quadratic in each time interval (*2*, *9*)—only the linear one comes into question. If v were piecewise constant, then S should equal 60•v for each interval. If v were piecewise quadratic, then S = 60•$(v_0 + v_{60})/2$ can only be some rough approximation. That would be unexpected, since other tablets imply that some Babylonian scholars in this period were familiar with the exact algorithm for summing a quadratic series (*9*, *10*). By contrast, the values of S computed in text A are exact if one assumes that v changes linearly in each interval. It follows that in scheme X.S$_1$, v decreases linearly from 0;12°/d to 0;9,30°/d between day 0 and day 60, and from 0;9,30°/d to 0;1,30°/d between day 60 and day 120.

This new reconstruction of the first 120 days of scheme X.S$_1$ results in trapezoidal figures if v is plotted against time in a modern fashion (Fig. 2). It is important to note that text A itself does not contain or imply a geometrical representation. However, it turns out to be explicitly formulated in the trapezoid procedures, texts B to E (figs. S1 to S4). Although their formulation differs in details, at least three of them (B to D) consist of the same two parts, I and II.

In part I, Jupiter's total displacement for the first 60 days of scheme X.S$_1$ is computed. A corresponding introductory statement mentioning Jupiter and the measures of the trapezoid is partly preserved in texts B and C, and perhaps in text E (*8*). The number 10;45, referred to as the "area" of the trapezoid (B, C), is then added to the "position of appearance" (B, C, D), the technical term for Jupiter's ecliptical longitude at first appearance, i.e., $\lambda_{60} = \lambda_0$ + 10;45°. Texts B and C partly preserve the computation of 10;45 as the area of the trapezoid through a series of steps equivalent to the computations in text A. Its "large side" and "small side," v_0 = 0;12°/d and v_{60} = 0;9,30°/d, are averaged, $(v_0 + v_{60})/2$ = 0;10,45°/d, which is then multiplied by 60 days, the width of the trapezoid, resulting in 10;45°. The latter operation is partly preserved in text C and can be restored in text B.

Part II, partly preserved in texts B, D, and E, is concerned with the time in which Jupiter reaches a position referred to by a term tentatively translated as the "crossing" (*8*). It is now clear that this denotes a point on the ecliptic, say λ_c, located halfway between λ_0 and λ_{60}, i.e., $\lambda_c = \lambda_0$ + 10;45°/2. This interpretation is consistent with a statement, preserved only in text B, according to which the "crossing" is located in the middle of Jupiter's "path," readily interpreted as a reference to the ecliptical segment from λ_0 to λ_{60}. Texts B and D also preserve the following statement that

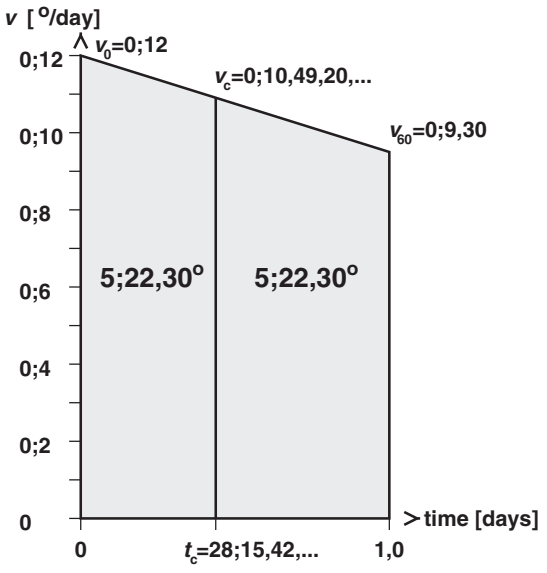


Fig. 3. Partitioning the trapezoid for days 0 to 60. The time at which Jupiter reaches the "crossing," t_c, where it has covered the distance 5;22,30° = 10;45°/2, is computed geometrically by dividing the trapezoid for days 0 to 60 into two smaller trapezoids of equal area. In text E, v_c is rounded to 0;10,50°/d, resulting in t_c = 28 d, S_1 = 5;19,40°, t_2 = 32 d, and S_2 = 5;25,20°.

precedes the solution procedure: "Concerning this 10;45, you see when it is halved." The time in which Jupiter reaches λ_c, say t_c, is then computed by the following geometrical method: The trapezoid for days 0 to 60 is divided into two smaller trapezoids of equal area (Fig. 3). In order to achieve this, the Babylonian astronomers applied a partition procedure that is well-attested in Old Babylonian (2000 to 1800 BCE) mathematics (*5*, *6*). In modern terms, it can be formulated as follows: If v_0 and v_{60} are the parallel sides of a trapezoid, then the intermediate parallel that divides it into two trapezoids of equal area has a height $v_c = [(v_0^2 + v_{60}^2)/2]^{1/2}$. In the present case, v_c denotes Jupiter's daily displacement when it is at the "crossing." This expression follows from equating the areas of the partial trapezoids, $S_1 = t_c \bullet (v_0 + v_c)/2 = S_2 = t_2 \bullet (v_c + v_{60})/2$, where t_c and t_2 are the widths of these trapezoids, and using $t_c = t \bullet (v_0 - v_c)/(v_0 - v_{60})$, where $t = t_c + t_2$ is the width of the original trapezoid (*6*, *10*). Inserting v_0 = 0;12°/d, v_{60} = 0;9,30°/d, and t = 1,0 d, we obtain $v_c = [(0;2,24 + 0;1,30,15)/2]^{1/2} = (0;1,57,7,30)^{1/2}$ = 0;10,49,20,44,58,...°/d, t_c = 28;15,42,0,48,...d, and t_2 = 31;44,17,59,12,...d. The computation of v_c is partly preserved in text D up to the addition 0;2,24 + 0;1,30,15 (*8*). In text B, the related quantity $u^2 = (v_0^2 - v_{60}^2)/2 = (0;2,24 - 0;1,30,15)/2$ = 0;0,26,52,30 is computed. This was most likely followed by another step in which v_c was computed using $v_c^2 = v_0^2 - u^2$. Whereas all known Old Babylonian examples of the partition algorithm concern trapezoids for which v_c, v_0, and v_{60} are terminating sexagesimal numbers (*6*), the present solution does not terminate in the sexagesimal system. Hence, texts B to E can only have offered rounded results for v_c and t_c. Nothing remains of this in texts B to D, but text E partly preserves a computation involving 0;10,50, which is, most plausibly, an approximation of v_c. This interpretation is confirmed by the fact that text E also mentions the value t_c = 28 d and, very likely, t_2 = 32 d, both in exact agreement with $t_c = 60 \bullet (v_0 - v_c)/(v_0 - v_{60})$ and $t_2 = 60 - t_c$ if one approximates v_c = 0;10,50°/d. By rounding v_c, only an approximately equal partition of the trapezoid is achieved.

Also partly preserved in text E is a computation of the area of the second partial trapezoid, using the same method as before, leading to $S_2 = t_2 \bullet (v_c + v_{60})/2$, where t_2 = 32 days, v_c = 0;10,50°/d, and v_{60} = 0;9,30°/d. The value of S_2 is broken away but can be restored as 5;25,20°. The probable purpose of this computation was to verify the solution for v_c, as is done in the Old Babylonian mathematical text UET 5, 858 (*5*, *11*). The analogous computation of the area of the first partial trapezoid, which can be reconstructed as $S_1 = t_c \bullet (v_0 + v_c)/2$ = 5;19,40°, is not preserved. Neither of these values equals 5;22,30° = $S/2$ as they ideally should (Fig. 3), a direct consequence of the rounding of v_c to 0;10,50°/d. At most two more lines are partly preserved in texts B, D, and E, but they are too fragmentary for an interpretation.

The evidence presented here demonstrates that Babylonian astronomers construed Jupiter's displacement along the ecliptic during the first 60 days after its first appearance as the area of a trapezoid in time-velocity space. Moreover, they computed the time when Jupiter covers half this distance by partitioning the trapezoid into two smaller ones of ideally equal area. These computations predate the use of similar techniques by medieval European scholars by at least 14 centuries. The "Oxford calculators" of the 14th century CE, who were centered at Merton College, Oxford, are credited with formulating the "Mertonian mean speed theorem" for the distance traveled by a uniformly accelerating body, corresponding to the modern formula $s = t \bullet (v_0 + v_1)/2$, where v_0 and v_1 are the initial and final velocities (*12*, *13*). In the same century Nicole Oresme, in Paris, devised graphical methods that enabled him to prove this relation by computing s as the area of a trapezoid of width t and heights v_0 and v_1 (*12*). Part I of the Babylonian trapezoid procedures can be viewed as a concrete example of the same computation. They also show that Babylonian astronomers did, at least occasionally, use geometrical methods for computing planetary positions. Ancient Greek astronomers such as Aristarchus of Samos, Hipparchus, and Claudius Ptolemy also used geometrical methods (*12*), while arithmetical methods are attested in the Antikythera mechanism (*14*) and in Greco-Roman astronomical papyri from Egypt (*15*). However, the Babylonian trapezoid procedures are geometrical in a different sense than the methods of the mentioned Greek astronomers, since the geometrical figures describe configurations not in physical space but in an abstract mathematical space defined by time and velocity (daily displacement).

REFERENCES AND NOTES

1. O. Neugebauer, *Astronomical Cuneiform Texts* (Lund Humphries, London, 1955).
2. M. Ossendrijver, *Babylonian Mathematical Astronomy: Procedure Texts* (Springer, New York, 2012).
3. J. P. Britton, *Arch. Hist. Exact Sci.* **64**, 617–663 (2010).
4. J. Høyrup, *Lengths, Widths, Surfaces. A Portrait of Old Babylonian Algebra and Its Kin* (Springer, New York, 2002).
5. A. A. Vaiman, *Shumero-Vavilonskaya matematika III-I tysyacheletiya do n. e.* (Izdatel'stvo Vostochnoy Literatury, Moscow, 1961).
6. J. Friberg, in *Reallexikon der Assyriologie*, D. O. Edzard, Ed. (De Gruyter, Berlin, 1990), vol. 7, pp. 561–563.
7. J. Friberg, *A Remarkable Collection of Babylonian Mathematical Texts. Manuscripts in the Schøyen Collection: Cuneiform Texts I* (Springer, New York, 2007).
8. Materials and methods are available as supplementary materials on *Science* Online.
9. P. J. Huber, *Z. Assyriol.* **52**, 265–303 (1957).
10. O. Neugebauer, *Mathematische Keilschrifttexte, I–III* (Springer, Berlin, 1935–1937).
11. J. Friberg, *Rev. Assyriol. Archeol. Orient.* **94**, 97–188 (2000).
12. O. Pedersen, *Early Physics and Astronomy. A Historical Introduction* (Cambridge Univ. Press, Cambridge, 1974).
13. E. D. Sylla, in *The Cambridge History of Later Medieval Philosophy*, N. Kretzmann, A. Kenny, J. Pinborg, Eds. (Cambridge Univ. Press, Cambridge, 1982), pp. 540–563.
14. T. Freeth, A. Jones, J. M. Steele, Y. Bitsakis, *Nature* **454**, 614–617 (2008).
15. A. Jones, *Astronomical Papyri from Oxyrhynchus* (American Philosophical Society, Philadelphia, 1999).

ACKNOWLEDGMENTS

The Trustees of the British Museum (London) are thanked for permission to photograph, study, and publish the tablets. Work was supported by the Excellence Cluster TOPOI, "The Formation and Transformation of Space and Knowledge in Ancient Cultures" (Deutsche Forschungsgemeinschaft grant EXC 264), Berlin. Photographs, transliterations, and translations of the relevant parts of the tablets are included in the supplementary materials. The tablets are accessible in the Middle Eastern Department of the British Museum under the registration numbers BM 40054 (text A), BM 36801, BM 41043, BM 34757 (text B), BM 34081+34622+34846+42816+45851+46135 (text C), BM 35915 (text D), and BM 82824+99697+99742 (text E). H. Hunger (Vienna) is acknowledged for providing an unpublished photograph of BM 40054.

SUPPLEMENTARY MATERIALS

www.sciencemag.org/content/351/6272/482/suppl/DC1
Materials and Methods
Figs. S1 to S4
References (*16*–*21*)

4 November 2015; accepted 23 December 2015
10.1126/science.aad8085

SUPERCONDUCTIVITY

Emergence of superconductivity in the canonical heavy-electron metal $YbRh_2Si_2$

Erwin Schuberth,[1,2]* Marc Tippmann,[1,3] Lucia Steinke,[1,2] Stefan Lausberg,[2] Alexander Steppke,[2] Manuel Brando,[2] Cornelius Krellner,[2,4] Christoph Geibel,[2] Rong Yu,[5,6] Qimiao Si,[7]* Frank Steglich[2,8,9]*

The smooth disappearance of antiferromagnetic order in strongly correlated metals commonly furnishes the development of unconventional superconductivity. The canonical heavy-electron compound $YbRh_2Si_2$ seems to represent an apparent exception from this quantum critical paradigm in that it is not a superconductor at temperature $T \geq 10$ millikelvin (mK). Here we report magnetic and calorimetric measurements on $YbRh_2Si_2$, down to temperatures as low as $T \approx 1$ mK. The data reveal the development of nuclear antiferromagnetic order slightly above 2 mK and of heavy-electron superconductivity almost concomitantly with this order. Our results demonstrate that superconductivity in the vicinity of quantum criticality is a general phenomenon.

Unconventional (i.e., nonphonon-mediated) superconductivity, which has been attracting much interest since the early 1980s, is often observed at the border of antiferromagnetic (AF) order (*1*). As exemplified by heavy-electron (or heavy-fermion) metals, the suppression of the AF order opens up a wide parameter regime where the physics is controlled by an underlying quantum critical point (QCP) (*2*, *3*). A central question, then, concerns the interplay between quantum criticality and unconventional superconductivity in strongly correlated electron systems such as heavy-electron metals. In many heavy-electron metals, superconductivity turns out to develop near such a QCP (*2*–*5*). However, the absence of superconductivity in the prototypical quantum critical material $YbRh_2Si_2$ (*6*) has raised the question as to whether the presence of an AF QCP necessarily gives rise to the occurrence of superconductivity. Because $YbRh_2Si_2$ exists in the form of high-quality single crystals, we are able to address this issue at very low temperatures without seriously encountering the limitations posed by disorder. $YbRh_2Si_2$ exhibits AF order below a Néel temperature T_{AF} = 70 mK. When applied within the basal plane of the tetragonal structure, a small magnetic field of B = 60 mT continuously suppresses the magnetic order and induces a QCP. Along with those of $CeRhIn_5$ (*7*–*9*) and $CeCu_{6-x}Au_x$ (*10*, *11*), the QCP in $YbRh_2Si_2$ has been exclusively demonstrated (*12*, *13*) to be of the unconventional type with Kondo breakdown (*14*–*16*). Electrical resistivity measurements down to 10 mK have failed to show any indications for superconductivity (*6*). Because a critical field of 60 mT is likely to destroy heavy-electron superconductivity with a superconducting transition temperature (T_c) of less than 10 mK, a different means of suppressing the antiferromagnetism is needed to eventually reveal any potential superconductivity at its border. We note that the application of pressure does not facilitate realization of a QCP in an AF Yb-based material, as increased pressure will strengthen the magnetic order—contrary to the case of Ce-based systems where magnetism usually becomes weakened by pressure. Compared to Ce, which does not exhibit a nuclear spin, two of the Yb isotopes have finite nuclear spin values [see below and section F of the supplementary materials (*17*)].

We have carried out magnetic and calorimetric measurements on high-quality $YbRh_2Si_2$ single crystals, using a nuclear-demagnetization cryostat with a base temperature of 400 μK (*17*). Figure 1, A and B, display the temperature dependence of the field-cooled (fc) dc magnetization $M(T)$, measured upon warming at various magnetic fields B ranging from 0.09 to 25 mT, applied within the basal plane of the $YbRh_2Si_2$ single crystals. The curves display peaks at 70 mK, which is the well-established Néel temperature for the AF order, as well as additional low-temperature anomalies. There is a second peak in $M(T)/B$ at $T_c \simeq 2$ mK, which indicates an almost-simultaneous onset of a nuclear-dominated AF order ("A phase") and the Meissner effect (see below). It is visible above 1 mK up to 23 mT and had already been observed previously (*18*). In addition, there is a shoulder around $T_B \approx 10$ mK, as defined in Fig. 1C. Below T_B, the results of the fc and zero-field-cooled (zfc) measurements become different. This divergence, which is ascribed to superconducting fluctuations [section F of (*17*)], can be followed as a function of the magnetic field, up to the limit of our setup (B = 0.5 mT) for measurements of the dc magnetization cooled at zero field.

At $T \simeq 2$ mK, the zfc dc $M(T)/B$ (0.012 mT) shows a sharp increase upon warming, starting from negative values (Fig. 1C). This indicates a substantial shielding signal due to superconductivity. Raising the temperature further, the zfc $M(T)/B$ slowly increases until it meets the fc curve at 10 mK. To verify this finding, we carried out measurements of the ac susceptibility, χ_{ac}, under nearly zero-field conditions [section D of (*17*)]. Its real part, $\chi'_{ac}(T)$, displays an even more pronounced diamagnetic signal (Fig. 1D), larger than what was found for the canonical heavy-electron superconductor $CeCu_2Si_2$ (*19*), again confirming the occurrence of superconducting shielding. In addition, the reduction of the fc magnetization upon cooling below 2 mK reflects flux expulsion from the sample (Meissner effect). The relatively small Meissner volume of ≈3% is most likely due to strong flux pinning [section C of (*17*)]. As shown in fig. S7, the superconducting phase transition is of first order. This suggests that superconductivity does not coexist on a microscopic basis with AF order, as previously observed for A/S-type $CeCu_2Si_2$ [compare with section D of (*17*)].

In Fig. 2A, the specific heat is displayed as $C(T)/T$ at B = 2.4 and 59.6 mT, respectively. As the electronic specific heat can be completely neglected below $T \approx 10$ mK (*20*), $C(T)$ denotes the nuclear contribution in this low-T regime. The solid lines show the calculated nuclear specific heats at various fields from (*20*), which include the quadrupolar as well as the Zeeman terms. At zero field, the nuclear specific heat is completely dominated by the nuclear quadrupole states, to which the Zeeman terms due to the nuclear spin states add at $B > 0$. In Fig. 2B, we display $\Delta C(T)/T$, where ΔC marks the difference between the specific heat measured at the lowest field B = 2.4 mT and the nuclear quadrupole contribution calculated for B = 0 (*20*). Our $\Delta C(T)/T$ results clearly reveal a peak at $T \approx 1.7$ mK. Assuming a continuous phase transition, the transition temperature can be obtained by replacing the high-T part of this peak by a sharp jump while keeping the entropy unchanged. This yields a jump height of ~1000 J/K² mol and $T_A \approx 2$ mK (B = 2.4 mT), almost coinciding with T_c (Fig. 1). Because the effect of the magnetic field on the quadrupole contribution to the nuclear specific heat is of higher order only, we can use the $\Delta C(T)/T$ data of Fig. 2B to estimate the nuclear spin entropy (at B = 2.4 mT), $S_I(T)$ [section F of (*17*)]. $S_{I,tot} \simeq 1.35\ R\ln 2$ (where R is the gas constant), the total nuclear spin entropy of $YbRh_2Si_2$ for B = 2.4 mT, is reached at $T \approx 10$ mK, where $\Delta C(T)$ vanishes within the experimental uncertainty (Fig. 2C). Upon cooling to $T = T_A$, $S_I(T)$ decreases to ~$0.94S_{I,tot}$—that is,

[1]Walther Meissner Institut für Tieftemperaturforschung der Bayerischen Akademie der Wissenschaften, 85748 Garching, Germany. [2]Max Planck Institute for Chemical Physics of Solids, 01187 Dresden, Germany. [3]Physikdepartment, Technische Universität München, 80333 München, Germany. [4]Physics Institute, University of Frankfurt, 60438 Frankfurt, Germany. [5]Department of Physics, Renmin University of China, Beijing 100872, China. [6]Department of Physics and Astronomy, Collaborative Innovation Center of Advanced Microstructures, Shanghai Jiaotong University, Shanghai 200240, China. [7]Department of Physics and Astronomy, Rice University, Houston, TX 77005, USA. [8]Center for Correlated Matter, Zhejiang University, Hangzhou, Zhejiang 310058, China. [9]Institute of Physics, Chinese Academy of Sciences, Beijing 100190, China.
*Corresponding author. E-mail: steglich@cpfs.mpg.de (F.S.); eschuber@ph.tum.de (E.S.); qmsi@rice.edu (Q.S.)

Downloaded from on January 31, 2016

most of this nuclear spin entropy must be released below the phase transition temperature T_A. The entropy of the ^{103}Rh and ^{29}Si spins is temperature independent at $T > 1$ mK, but the Yb-derived spin entropy $S_{Yb}(T)$ decreases by 26% upon cooling from 10 to 2 mK [compare with section F of (*17*)]. This indicates substantial short-range order, consistent with a second-order (antiferro)magnetic phase transition. We stress that this very large entropy at ultralow temperatures (Fig. 2C) can only be understood if the ordering transition at T_A involves the Yb-derived nuclear spins to a substantial degree.

To explore the role of the nuclear spins in the phase diagram [(*3*, *6*) and Fig. 3], we take

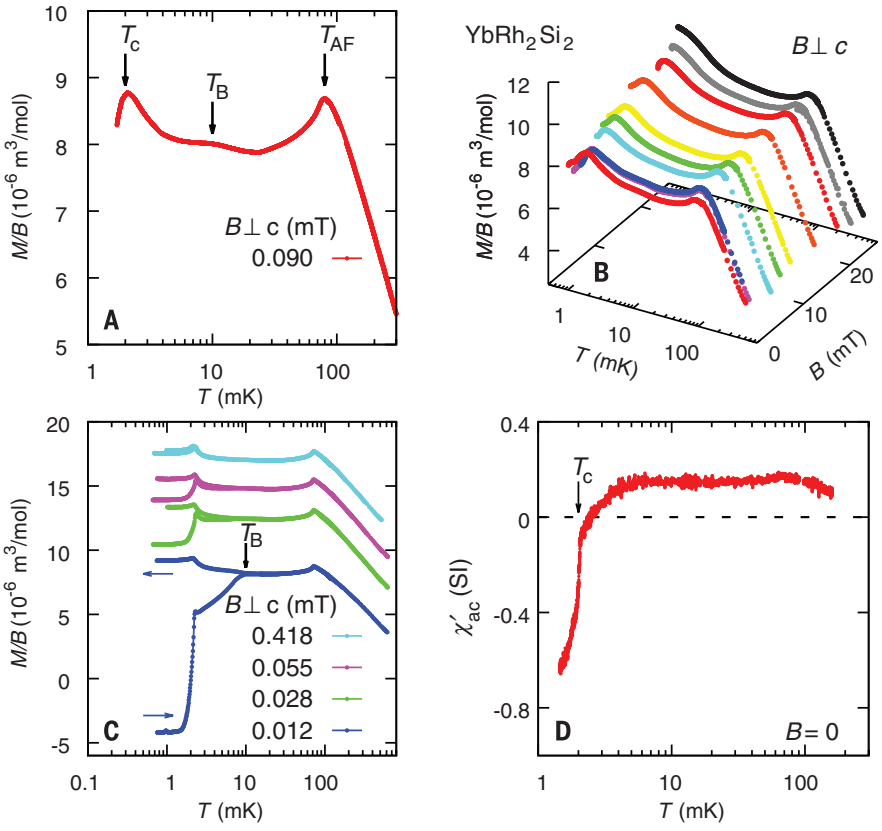


Fig. 1. Temperature dependence of the dc magnetization and ac susceptibility for $YbRh_2Si_2$. (**A**) Field-cooled (fc) dc magnetization curve of $YbRh_2Si_2$ taken at B = 0.09 mT applied within the basal plane. Three main features are clearly visible: the AF phase transition at T_{AF} = 70 mK, a shoulder in magnetization at $T_B \approx 10$ mK, and a sharp peak at T_c = 2 mK. (**B**) Series of fc magnetization data taken at fields of 0.10, 1.13, 1.13, 5.01, 7.48, 10.12, 15.01, 20.04, 22.42, and 25.02 mT. (**C**) Zero-field-cooled (zfc) and fc dc magnetization traces taken at selected small magnetic fields. The traces at 0.028, 0.055, and 0.418 mT were shifted upward for better visibility. For the smallest magnetic field of 0.012 mT, a sharp diamagnetic shielding signal is observed, suggesting a superconducting phase transition. (**D**) The ac susceptibility was measured using a superconducting quantum interference device magnetometer by modulating a primary coil around the pickup coils. Here we show the in-phase signal $\chi'_{ac}(T)$ (at 17 Hz), having compensated the Earth field. The features seen at T_{AF}, T_B, and T_c in the dc magnetization curve are also detected by the ac susceptibility. The large negative values of the zfc dc magnetization at B = 0.012 mT (Fig. 1C) and of $\chi'_{ac}(T)$ indicate superconducting shielding, whereas the low-temperature peak in the fc dc magnetization (Fig. 1, A to C) signals the onset of the Meissner effect. Measurements in (A) to (D) were performed on samples 1, 2, 3, and 4, respectively.

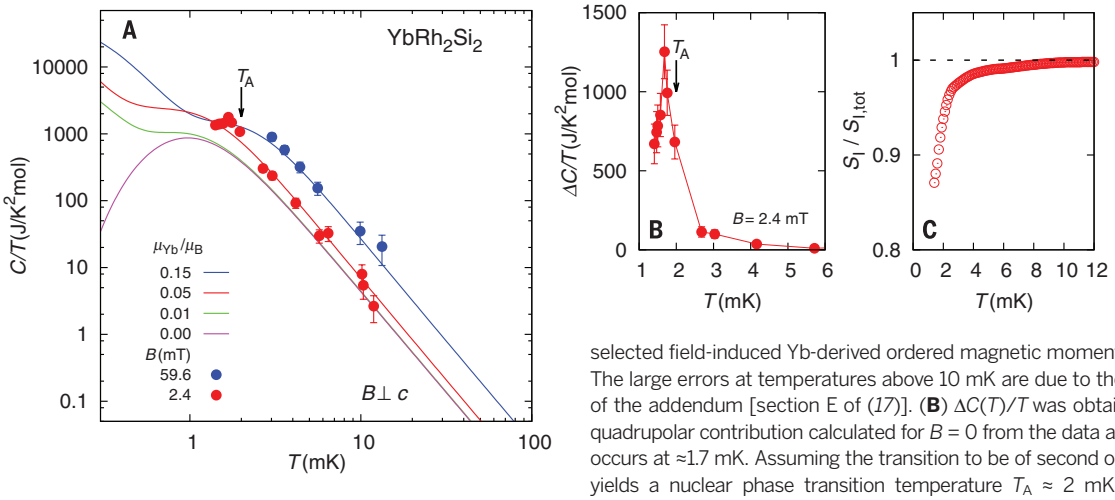


Fig. 2. Nuclear specific heat and entropy of $YbRh_2Si_2$. (**A**) The temperature dependence of the specific heat $C(T)$ of $YbRh_2Si_2$ divided by T is shown for B = 2.4 and 59.6 mT [section E of (*17*)]. The 2.4-mT data extend down to 1.4 mK. The solid lines denote the calculated nuclear specific heat from (*20*), which is the sum of the quadrupolar term and the Zeeman term with three selected field-induced Yb-derived ordered magnetic moments: 0.01, 0.05, and 0.15(μ_{Yb}/μ_B). The large errors at temperatures above 10 mK are due to the uncertainty in the subtraction of the addendum [section E of (*17*)]. (**B**) $\Delta C(T)/T$ was obtained by subtracting the nuclear quadrupolar contribution calculated for B = 0 from the data at B = 2.4 mT. A peak in $\Delta C(T)/T$ occurs at ≈1.7 mK. Assuming the transition to be of second order, an equal-area construction yields a nuclear phase transition temperature $T_A \approx 2$ mK. This coincides with the peak position found in the dc magnetization (compare with Fig. 1)—that is, the superconducting critical temperature T_c at 2.4 mT. The associated jump of $\Delta C(T)/T$ is on the order of 1000 J/K^2 mol. The error bars reflect the statistical error in the measurements of the specific heat by using a quasi-static heat-pulse technique, as well as the relaxation method. In the latter case, the error bar contains the statistical error in determining both the relaxation time and the heat conductivity of the weak link. In total, two runs have been performed for each field; therefore, four sets of data at the same temperature were used for determining the specific heat. Each data point was weighted by its reciprocal error. At the lowest temperatures, the error associated with the relaxation method is essentially smaller than that of the heat-pulse measurement. (**C**) From $\Delta C(T)/T$ (Fig. 1B), a rough estimate can be made for the nuclear spin entropy $S_I(T)$ at B = 2.4 mT (see text). We have normalized $S_I(T)$ to $S_{I,tot}$, the total nuclear spin entropy in $YbRh_2Si_2$ at B = 2.4 mT, reached at ~10 mK. By subtracting from $S_I(T)$ the contribution of the nuclear Si and Rh spins, which is temperature independent at $T \geq 1$ mK, we obtain the corresponding values $S_{Yb}(T)$ for the nuclear Yb spins. Measurements were performed on sample 3.

advantage of the early recognition that hyperfine coupling to nuclear spins can considerably influence the electronic spin properties near a quantum phase transition (*21*). Furthermore, measurements on $PrCu_2$ and related compounds have demonstrated a large coupling between the electronic and nuclear spins in rare-earth–based intermetallics at temperatures up to 50 mK (*22*, *23*). These considerations raise the possibility of using the presence of nuclear spins to weaken the electronic AF order, thereby enabling the formation of a superconducting state. We have written down a Landau theory of the interplay between the magnetic orders of the electronic and nuclear spins. Consider the electronic AF order, with an order parameter m_{AF} at the AF wave vector $\mathbf{Q}_{AF}$, as well as two bilinearly coupled order parameters, m_J and m_I, the staggered magnetizations of the electronic and nuclear spins at another finite wave vector $\mathbf{Q}_1 \neq \mathbf{Q}_{AF}$. The bilinear coupling arises from the hyperfine coupling between the two order parameters having the same wave vector. The Landau theory will then have the following free-energy functional

$$f = \frac{1}{2}r_{AF}\phi_{AF}^2 + \frac{1}{4}u_{AF}\phi_{AF}^4 + \frac{1}{2}r_J\phi_J^2 + \frac{1}{4}u_J\phi_J^4 + \frac{1}{2}r_I\phi_I^2 + \frac{1}{4}u_I\phi_I^4 - \lambda\phi_J\phi_I + \frac{1}{2}\varepsilon\phi_{AF}^2\phi_I^2 + \frac{1}{2}\eta\phi_J^2\phi_{AF}^2$$

where ϕ_{AF}, ϕ_J, and ϕ_I are, respectively, the normalized order parameters m_{AF}, m_J, and m_I; the r terms are quadratic couplings; the u terms as well as ε and η are the intracomponent as well as intercomponent quartic couplings; and λ is the bilinear hyperfine coupling between two normalized order parameters [section G of (*17*)].

Under suitable conditions (*17*), this can lead to two stages of phase transitions (Fig. 4). The phase transition at T_{AF} corresponds to the primary AF order setting in at ~70 mK and is not much affected by the nuclear spins. In a suitable parameter range of the Landau theory, the nuclear ϕ_I order dominates over the electronic ϕ_J order and, furthermore, suppresses the primary electronic ϕ_{AF} order. A second transition occurs at T_{hyb}, which represents a hybrid electronic-nuclear spin order. The component that is associated with the nuclear spins generates substantial entropy for the transition, which explains the large nuclear spin entropy that is experimentally observed (Fig. 2C) [section E of (*17*)]. In addition, the effective g-factor (g_{eff}) is on the order of $g_{el}\phi_J/\phi_I$ (where g_{el} is the electron g-factor), which is substantially smaller than the bare g-factor for the 4f electrons. This explains the $g_{eff} < 0.1$ observed in our experiment.

We thus conclude that the A phase forming at $T_A \simeq 2$ mK is an electronic-nuclear hybrid phase dominated by the Yb-derived nuclear spin ordering. We estimate that the small (1 to 2%) 4f electronic component contributes about one-third of the decrease in $M(T)$ below T_A [section C of (*17*)]. As the nuclear phase transition cannot be resolved because of the very small nuclear moment, the major part of this reduction of $M(T)$ (i.e., the other two-thirds) must be due to the Meissner effect [section C of (*17*)]. A measurement of the fc dc magnetization at very low fields reveals two separated phase transitions close to $T = 2$ mK: T_A and T_c (fig. S3B). Upon increasing the field to ~3 to 4 mT, however, T_A and T_c appear to merge within the experimental uncertainty (fig. S3C). As mentioned previously, this peak in the fc dc $M(T)$ curve remains visible (above 1 mK) up to $B \simeq 23$ mT (Fig. 1B). By analyzing magnetization data taken between 0.8 and 540 mK at a field of 10.1 mT (fig. S4), we conclude that superconductivity is likely to exist and coincide with the A phase at

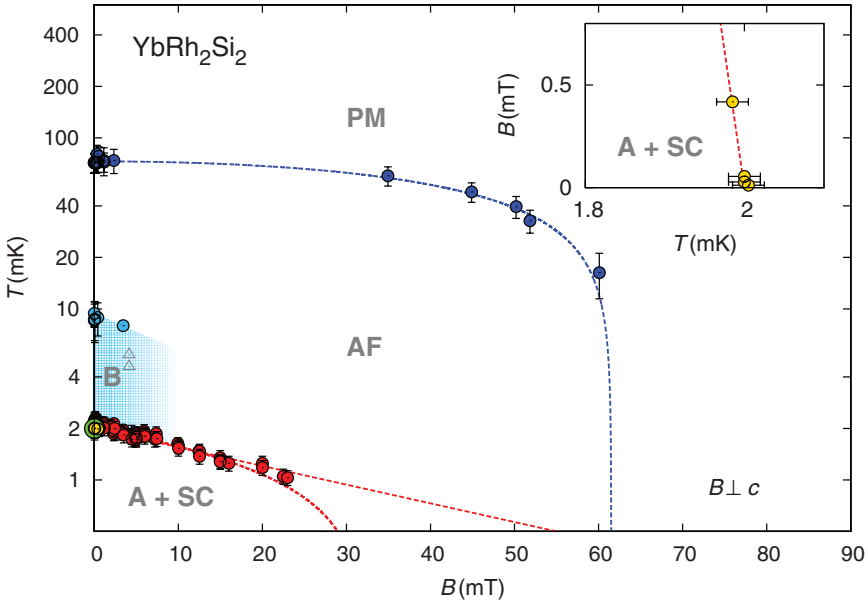


Fig. 3. Generic *T* versus *B* phase diagram of $YbRh_2Si_2$. This phase diagram (shown on semi-logarithmic scales) is obtained from dc magnetization and ac susceptibility measurements in several magnetic fields. Four samples were measured, and no sample dependence was found. AF indicates the electronic AF order ($T_{AF} = 70$ mK); PM indicates the paramagnetic state. All data points used to illustrate the AF-PM phase boundary $T_{AF}(B)$ were obtained in the present study. The hatched light-blue area indicates the onset of A-phase fluctuations, which give rise to a reduction of the staggered magnetization and a splitting of the zfc and fc dc magnetization curves (i.e., the beginning of shielding due to superconducting fluctuations) (Fig. 1C). The two data points (gray triangles) determined via field sweeps of the dc magnetization between 3.6 and 6.0 mK (fig. S4) are most likely not related to these A-phase fluctuations. The A + SC phase represents the concurring (dominantly) nuclear AF order and superconductivity, at least at fields below 3 to 4 mT. Only at $B = 0$ is nearly full shielding observed. The low-temperature limit of our experiment is ~800 μK; therefore, we cannot detect the fc dc $M(T)$ peaks above 23 mT. The two red dashed lines mark the range within which the A-phase boundary line may end. At low fields ($B < 4$ mT), the transition at ~2 mK is split into two parts (compare with fig. S3). The green circle indicates the superconducting transition temperature seen in the ac susceptibility at $B = 0$ (compare with Fig. 1D), whereas the yellow circles (partially covered by the green point) result from the shielding signals in the zfc dc magnetization (Fig. 1C). (**Inset**) These shielding transitions are shown separately on an enlarged scale. The superconducting phase boundary T_c versus B is extremely steep at low fields, with $-dB_{c2}/dT_{T_c} \approx 25$ T/K, consistent with results for the canonical heavy-electron superconductor $CeCu_2Si_2$ [section A of (*17*)]. If superconductivity exists at higher fields, $B_{c2}(T)$ extrapolates to 30 to 60 mT (at $T = 0$)—that is, close to the critical field of the primary electronic AF phase.

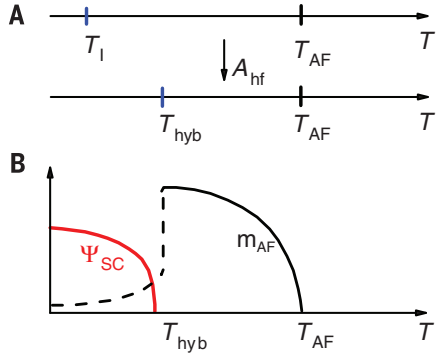


Fig. 4. Phase transitions at T_{AF} and T_{hyb}. (**A**) Sketch of the two phase transitions associated with electronic and nuclear spin orders. (Top line) Without any hyperfine coupling (A_{hf}), the electronic and nuclear spins are ordered at T_{AF} and T_I, respectively. (Bottom line) With a hyperfine coupling, T_{AF} is not affected, but a hybrid nuclear and electronic spin order is induced at $T_{hyb} \gg T_I$. (**B**) Temperature evolution of the primary electronic spin order parameter (m_{AF}) and the superconducting order parameter ϕ_{SC}. ϕ_{SC} is developed when m_{AF} is suppressed by the formation of hybrid nuclear and electronic spin order directly below T_{hyb}.

elevated fields, consistent with the evolution of the $M(T)$ peak as a function of field [section C of (*17*)].

Figure 4 describes a possible scenario for the two stages of transitions. Below T_{AF}, the Néel order develops. We speculate that the growth of the Néel order parameter m_{AF} is arrested as the temperature is lowered past T_{hyb}, due to the onset of the nuclear spin order. A diminished m_{AF} would place the electronic phase in the regime close to the QCP that underlies the pure electronic system in the absence of any hyperfine coupling. This quantum criticality effectively induced by the nuclear spin order at zero magnetic field would naturally lead to the development of a superconducting state [section I of (*17*)]. As inferred from the experimental results (Fig. 1C), fluctuations of the A phase are already set in near T_B and lead to a substantial reduction of the staggered magnetization and the emergence of superconducting fluctuations well above the A-phase ordering temperature [section I of (*17*)].

The large initial slope of the superconducting upper critical field $B_{c2}(T)$ at $T_c \simeq 25$ T/K, extracted from both shielding (Fig. 3, inset) and Meissner measurements (fig. S3C), corresponds to an effective charge-carrier mass of several hundred m_e (where m_e is the rest mass of the electron), which implies that the superconducting state is associated with the Yb-derived 4f electrons (heavy-electron superconductivity). Extrapolating the positions of the low-temperature fc $M(T)$ peak to zero temperature, the critical field of the A phase $B_A = B(T_A \rightarrow 0)$ is found to be 30 to 60 mT, which corresponds to $g_{eff} = k_B T_A(B = 0)/\mu_B B_A = 0.03$ to 0.06 (where k_B is the Boltzmann constant and μ_B is the Bohr magneton). This value of g_{eff} is much smaller than the in-plane electronic g-factor 3.5 (*24*) but is a factor of 20 to 40 larger than in case of a purely nuclear spin ordering transition. We can understand this g_{eff} if the ordered moment is a hybrid of the electronic and nuclear spins with, at most, 2% of the ordered moments being associated with the 4f electron–derived spins.

The very large entropy near $T_A \geq 2$ mK is one of the most pronounced features in our observation. An alternative possibility for this entropy is the involvement of a "nuclear Kondo effect"—that is, the formation of a singlet state between the nuclear and conduction electron spins. The resulting superheavy fermions may be assumed to form Cooper pairs and cause a superconducting transition at $T_c \approx 2$ mK that would be probed by the magnetic and specific-heat measurements. Though our estimates of the nuclear Kondo temperature and the quasi-particle effective mass reveal discrepancies with this picture [section E of (*17*)], further theoretical and experimental work is needed to investigate the possible role of the nuclear Kondo effect in generating superconductivity in $YbRh_2Si_2$.

It is likely that the coupling of electronic and nuclear spin orders, as well as the concomitant emergence of new physics, is not exclusive to $YbRh_2Si_2$ [section H of (*17*)]. Systematic studies of other heavy-electron antiferromagnets at ultralow temperatures are needed to find out whether a hybrid electronic-nuclear order is a more general phenomenon. In addition, a comparative study would be highly welcome to evaluate whether superconductivity is truly absent in isotopically enriched $YbRh_2Si_2$ without Yb-derived nuclear spins, similar to the compound studied in (*25*).

Our ultralow-temperature measurements on the unconventional quantum critical material $YbRh_2Si_2$ reveal heavy-electron superconductivity below $T_c = 2$ mK. This observation strongly supports the notion that superconductivity near an AF instability is a robust phenomenon.

REFERENCES AND NOTES

1. P. A. Lee, N. Nagaosa, X.-G. Wen, *Rev. Mod. Phys.* **78**, 17–85 (2006).
2. H. Löhneysen, A. Rosch, M. Vojta, P. Wölfle, *Rev. Mod. Phys.* **79**, 1015–1075 (2007).
3. P. Gegenwart, Q. Si, F. Steglich, *Nat. Phys.* **4**, 186–197 (2008).
4. N. D. Mathur *et al.*, *Nature* **394**, 39–43 (1998).
5. O. Stockert *et al.*, *Nat. Phys.* **7**, 119–124 (2011).
6. J. Custers *et al.*, *Nature* **424**, 524–527 (2003).
7. H. Shishido, R. Settai, H. Harima, Y. Ōnuki, *J. Phys. Soc. Jpn.* **74**, 1103–1106 (2005).
8. T. Park *et al.*, *Nature* **440**, 65–68 (2006).
9. G. Knebel, D. Aoki, J.-P. Brison, J. Flouquet, *J. Phys. Soc. Jpn.* **77**, 114704 (2008).
10. H. Löhneysen *et al.*, *Phys. Rev. Lett.* **72**, 3262–3265 (1994).
11. A. Schröder *et al.*, *Nature* **407**, 351–355 (2000).
12. S. Paschen *et al.*, *Nature* **432**, 881–885 (2004).
13. S. Friedemann *et al.*, *Proc. Natl. Acad. Sci. U.S.A.* **107**, 14547–14551 (2010).
14. Q. Si, S. Rabello, K. Ingersent, J.-L. Smith, *Nature* **413**, 804–808 (2001).
15. P. Coleman, C. Pépin, Q. Si, R. Ramazashvili, *J. Phys. Condens. Matter* **13**, R723–R738 (2001).
16. T. Senthil, M. Vojta, S. Sachdev, *Phys. Rev. B* **69**, 035111 (2004).
17. Supplementary materials are available on *Science* Online.
18. E. Schuberth, M. Tippmann, C. Krellner, F. Steglich, *Phys. Stat. Solidi B* **250**, 482–484 (2013).
19. F. Steglich *et al.*, *Phys. Rev. Lett.* **43**, 1892–1896 (1979).
20. A. Steppke *et al.*, *Phys. Stat. Solidi B* **247**, 737–739 (2010).
21. H. M. Rønnow *et al.*, *Science* **308**, 389–392 (2005).
22. K. Andres, E. Bucher, P. H. Schmidt, J. P. Maita, S. Darack, *Phys. Rev. B* **11**, 4364–4372 (1975).
23. L. Steinke *et al.*, *Phys. Rev. Lett.* **111**, 077202 (2013).
24. J. Sichelschmidt, V. A. Ivanshin, J. Ferstl, C. Geibel, F. Steglich, *Phys. Rev. Lett.* **91**, 156401 (2003).
25. G. Knebel *et al.*, *J. Phys. Soc. Jpn.* **75**, 114709 (2006).

ACKNOWLEDGMENTS

We thank K. Andres, P. Coleman, P. Gegenwart, S. Paschen, and S. Wirth for useful discussions. Part of the work at the Max Planck Institute for Chemical Physics of Solids was supported by the Deutsche Forschungsgemeinschaft Research Unit 960 "Quantum Phase Transitions." Q.S. was supported by NSF grant DMR-1309531 and Robert A. Welch Foundation grant C-1411. E.S., Q.S., and F.S. thank the Institute of Physics, Chinese Academy of Sciences, Beijing, for hospitality. Q.S. and F.S. acknowledge partial support from the NSF under grant 1066293 and the hospitality of the Aspen Center for Physics. We declare no competing financial interests.

SUPPLEMENTARY MATERIALS

www.sciencemag.org/content/351/6272/485/suppl/DC1
Materials and Methods
Supplementary Text
Figs. S1 to S9
References (*26*–*65*)

23 February 2015; accepted 16 December 2015
10.1126/science.aaa9733

Downloaded from on January 31, 2016

GEOPHYSICS

Periodic slow slip triggers megathrust zone earthquakes in northeastern Japan

Naoki Uchida,[1]* Takeshi Iinuma,[2]† Robert M. Nadeau,[3] Roland Bürgmann,[4] Ryota Hino[1]

Both aseismic and seismic slip accommodate relative motion across partially coupled plate-boundary faults. In northeastern Japan, aseismic slip occurs in the form of decelerating afterslip after large interplate earthquakes and as relatively steady slip on uncoupled areas of the subduction thrust. Here we report on a previously unrecognized quasi-periodic slow-slip behavior that is widespread in the megathrust zone. The repeat intervals of the slow slip range from 1 to 6 years and often coincide with or precede clusters of large [magnitude (*M*) ≥ 5] earthquakes, including the 2011 *M* 9 Tohoku-oki earthquake. These results suggest that inherently periodic slow-slip events result in periodic stress perturbations and modulate the occurrence time of larger earthquakes. The periodicity in the slow-slip rate has the potential to help refine time-dependent earthquake forecasts.

Slow (or aseismic) slip is a process by which faults displace rocks like earthquakes do, but much more slowly and without generating seismic waves (*1*, *2*). Slow fault-slip events increase stress in adjacent areas and may trigger damaging earthquakes (*3*). Foreshocks are sometimes related to precursory slow slip (*4*–*6*), and some slow-slip events revealed by geodetic measurements are accompanied by seismicity rate changes (*7*). However, the relationship between large earthquakes and aseismic slip is not well understood because of the poor

detectability of small slow-slip events with geodetic measurements and the rare occurrence of large earthquakes. We understand that repeating earthquakes involve the rupture of small asperities in the fault zone as seismic slips keep up with aseismic fault creep (slow slip) on the surrounding surface (*8*) (Fig. 1). Repeating earthquakes provide a remote measure of both localized seismic slip and the surrounding rate of aseismic slip on a fault that greatly improves the spatiotemporal resolution of slow slip (*4*, *9*, *10*). In this study, we refer to repeating earthquakes as "repeaters" and invoke them as a form of subsurface creep meter (Fig. 1). Here we consider repeater time series and global positioning system (GPS) measurements from the northeastern (NE) Japan subduction zone to detect small temporal changes in the slow-slip rate. Major earthquakes, including the great 2011 Tohoku-oki earthquake [magnitude (*M*) 9.0], also occur on the offshore plate interface between the subducting Pacific and continental plates (Fig. 2A) (*1*, *4*, *11*–*13*).

We examined the seismic moments and recurrence intervals of 6126 repeaters belonging to 1515 separate sequences to detect interplate slip-rate fluctuations for a period of up to 28 years (*14*) (table S1). In the offshore and near-shore Sanriku areas (Fig. 2), the slow-slip rates are estimated from 162 and 91 repeater sequences, respectively, using a 0.5-year moving time window, with the average rates plotted at the center of each time window (*14*) (Fig. 1). The variations in slip rate ranged from 0 to 290% of the long-term interplate slip rate (*15*) (7.4 ± 0.2 cm/year) and showed strong periodicity. The amplitude of the inferred slip rate depends on the length of the analysis window and the scaling relationship used to estimate the slip amount, but the periodicity is not affected by these conditions (*14*).

We estimated the dominant periods of slow slip, based on spectral analysis, to be 3.0 ± 0.1 SD years for the offshore Sanriku area (Fig. 2B and fig. S4I) and 2.7 ± 0.6 years for near-shore Sanriku area (Fig. 2C and figs. S4J and S5) (*14*). Two large slip-velocity peaks in 1990 and 1992 could bias the spectral estimate of period in the offshore Sanriku area (Fig. 2B), but analysis excluding data before 1992 also shows a similar dominant period (fig. S4I). We compared the timing of $M \geq 5$ events (Fig. 2, B and C) to the regional slip rate. The magnitude threshold was chosen to ensure a complete catalog for our analysis period and a big enough sample of larger events. Clustering of $M \geq 5$ earthquakes in the high slip-rate periods is evident, especially in the offshore area (Fig. 2B). We fitted simple sinusoidal curves to the slip-rate changes to define the phase of the periodicity, finding that 6.2 and 3.3 times as many 1984–2011 $M \geq 5$ earthquakes occurred during the positive period of the best-fit sinusoids for the offshore and near-shore Sanriku areas, respectively (Fig. 2, B and C; fig. S6, C and D; and table S2). We calculated the excess number of $M \geq 5$ earthquakes for a range of periods and found that they decay away ±0.15 years from the best-fit periods we established from the repeater data (fig. S6). We showed a concentration of $M \geq 5$ earthquakes near the inferred slip-rate peak (fig. S7), using histograms of earthquake occurrence with respect to phase of the best-fit sinusoids. We found a similar correlation between periodic slow-slip rates and large earthquakes for most of the eight offshore areas where we documented the distribution of repeaters and earthquakes (fig. S2 and table S2).

When we applied declustering to the earthquake catalog with a range of declustering parameters, the number of excess earthquakes in the positive period of the best-fit sinusoids decreased (tables S3 and S4). Although the excess ratios for the offshore Sanriku area range from 2.0 to 2.8, those for the near-shore Sanriku area are systematically reduced to 1.2, suggesting that clusters associated with large earthquakes influence the result.

A possible explanation for the correlated periodicity (Fig. 2 and fig. S7) is that periodically occurring $M \geq 5$ events and their afterslip trigger the smaller repeaters. However, close inspection of the repeater activity and inferred slip-rate changes for the major slip pulses in 1989–1990 and 1992 in the offshore Sanriku area (Fig. 3A) shows that the repeater-inferred slow slip begins accelerating a few days before the mainshocks associated with the slip pulses (*16*). The precursory repeater activity is a common feature before $M \geq 5$, $M \geq 6$, and $M \geq 7$ earthquakes (mainshocks) in the offshore Sanriku area and most of the other study areas (figs. S8 and S9). The precursory repeater accelerations concentrate close to mainshock epicenters (figs. S10 and S11), suggesting

[1]Graduate School of Science and International Research Institute of Disaster Science, Tohoku University, 6-6, Aramaki-aza-aoba, Aoba-ku, Sendai 980-8578, Japan. [2]International Research Institute of Disaster Science, Tohoku University, 468-1, Aramaki-aza-aoba, Aoba-ku, Sendai 980-0845, Japan. [3]Berkeley Seismological Laboratory and Berkeley Institute for Data Science, University of California, Berkeley, 211 McCone Hall, Berkeley, CA 94720-4767, USA. [4]Berkeley Seismological Laboratory and Department of Earth and Planetary Science, University of California, Berkeley, 389 McCone Hall, Berkeley, CA 94720-4767, USA.
***Corresponding author. E-mail: naoki.uchida.b6@tohoku.ac.jp**
†Present address: Japan Agency for Marine-Earth Science and Technology, Yokohama, 236-0001, Japan.

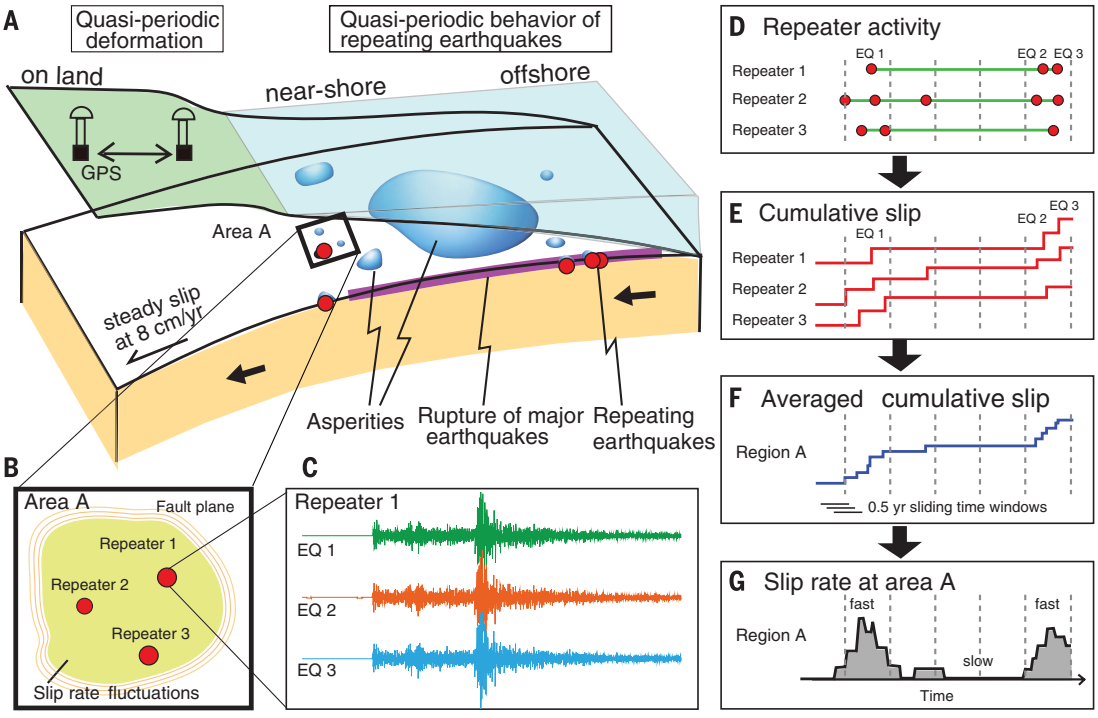


Fig. 1. Using repeaters to track slow plate-boundary slip. Schematic figure showing the tectonic setting (**A**), the activity of repeaters on the plate boundary (**B** and **C**), and steps to estimate the slip-rate time series from repeater data (**D** to **G**) (*14*). There are variably sized seismic patches on the plate boundary surrounded by aseismic slip areas (A). The small repeaters (C) represent repeated rupture of small patches that catch up with the creep in the surrounding areas (B). By calculating the slip of each earthquake, we obtain cumulative slip for each repeater sequence [(D) and (E)]. We average slip in each area (F) and obtain the temporal change of slip rate from the gradient of the averaged cumulative curve (G).

close interaction with the preceding repeater activity. Mainshocks are also generally followed by accelerated repeater activity (figs. S8 and S9), indicating rapid afterslip.

Marsan *et al.* (*17*) suggest occurrences of many slow-slip episodes in this subduction zone by discriminating normal from "abnormal" seismicity affected by transient loading. The activity of small repeaters indicates the involvement of spontaneous slow-slip events as the underlying aseismic loading process driving these episodic deformation transients. Observations from ocean-bottom pressure sensors of slow slip preceding M 6.1 and M 7.3 earthquakes occurring ~100 km south of this area in 2008 and 2011 (green stars in Fig. 2A) (*18*), respectively, are also consistent with this interpretation.

We tested the hypothesis of an ~3-year periodic slow slip promoting $M \geq 5$ earthquakes in the offshore Sanriku area by extrapolating the sinusoidal curve from the 1984 to 2011 slip-rate data back to 1930 (red curve in Fig. 3C). The positive phase of the sinusoidal curve (expected high–slip-rate periods) correlates with higher rates of $M \geq 5$ earthquakes back to around 1945 (Fig. 3C). The number of $M \geq 5$ earthquakes occurring during positive sinusoid amplitudes for the period 1956–1983 is about twice as high as the number of events occurring during negative sinusoid amplitudes (dashed curve in fig. S6C).

Our sinusoidal extrapolation of the slow slip assumes exact periodicity of the process, and slight shifts in the period result in large shifts in the timing of sinusoid peaks when extrapolating over many years. To address this, we examined the periodicity of the $M \geq 5$ declustered catalog using the Schuster spectrum (*19*). Our results show an ~3-year periodicity for the offshore Sanriku area (Fig. 3B) for all time spans considered, including the repeater analysis period. We do not find as strong a periodicity for the near-shore area (figs. S5A and S6D). Our

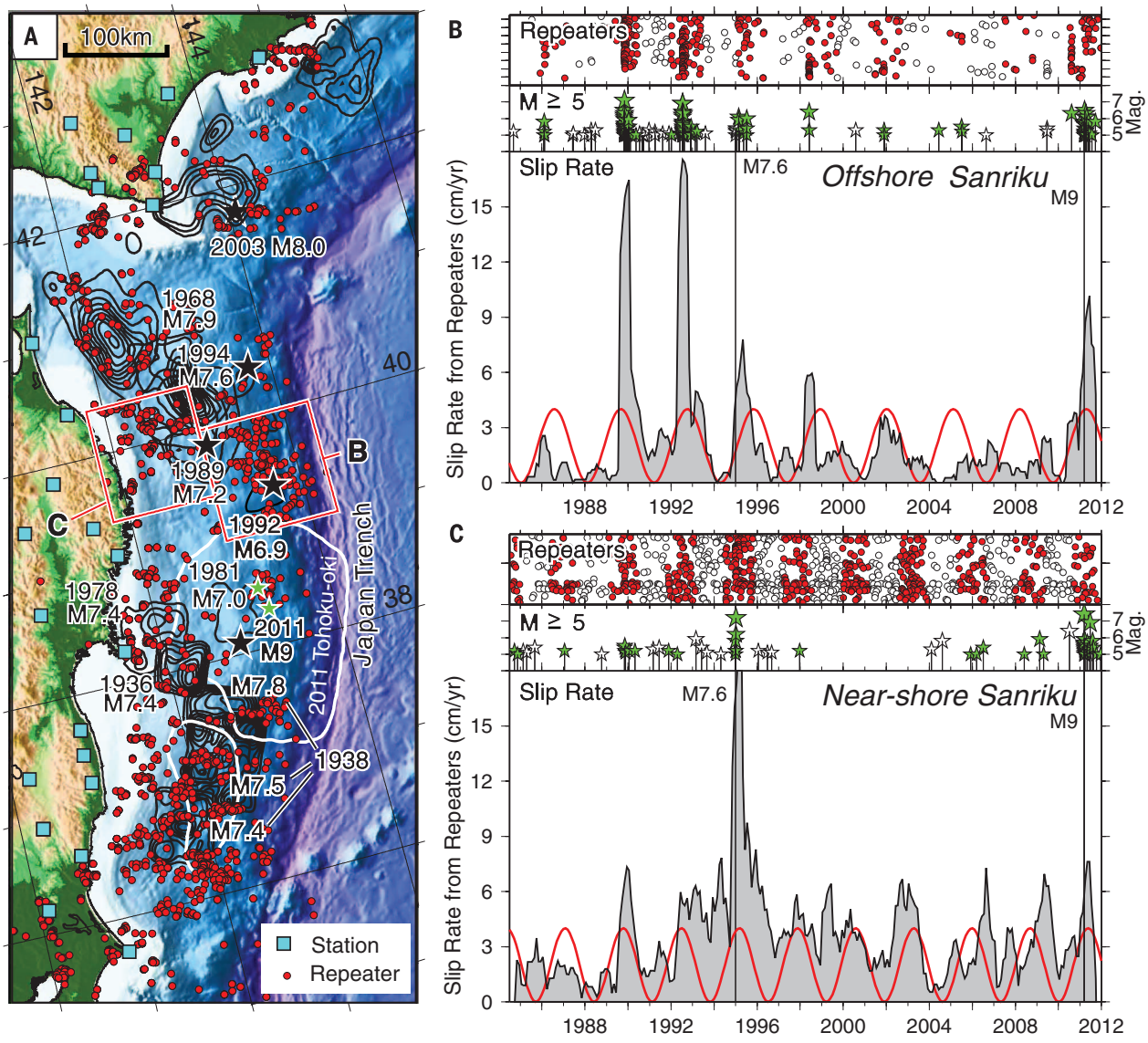


Fig. 2. Spatiotemporal distribution of repeaters and temporal variation of slow slip. (**A**) Distribution of repeater sequences (red circles) and slip areas of large earthquakes (black and white contours) (*11*–*13*, *29*, *30*). Cyan squares show seismic stations. Green stars show a M 6.1 earthquake in 2008 (north) and a M 7.3 earthquake in 2011 (south) that were preceded by slow slip (*18*). (**B** and **C**) Temporal distribution of repeaters near Sanriku aligned by latitude (top) (see fig. S1 for vertical enlargement), magnitude-time plot of $M \geq 5$ earthquakes (middle), and temporal change of slip rate inferred from repeaters (bottom) for offshore (B) and near-shore (C) areas off Sanriku shown in (A) (see fig. S3 for corresponding data for all other areas). Vertical lines show the times of the 1994 M 7.6 Sanriku-oki and the 2011 M 9 Tohoku-oki earthquakes. The number of $M \geq 5$ events in offshore and near-shore areas is 194 and 68, respectively. The red curves in (B) and (C) are best-fit sinusoidal functions fit to the slip-rate time series with 3.09- and 2.72-year periods, respectively. Repeaters and $M \geq 5$ events during the positive phase of the best-fitted sinusoid are shown by colored symbols, whereas those during the negative phase are shown by open symbols.

consideration of ~80 years of earthquakes offshore of Sanriku suggests that the periodicity of slow slip and associated larger earthquakes persists through time before the repeater analysis period.

Continuous GPS measurements across NE Japan provide complementary constraints on the time-variable coupling of the subduction thrust from the repeater data. The spatial gradient of observed displacement rates in the plate convergence direction reflects the strength of interplate locking and associated slip (*20*) (figs S12 and S13) (*14*), and its temporal variation may be a measure of the acceleration/deceleration of aseismic slip along the plate boundary. Although we infer that repeaters directly track slip on the subduction thrust, the on-land GPS data are only indirectly related to changing fault slip via elastic deformation. In order to stabilize the estimate of the time-dependent gradient of the displacement rate (the GPS gradient), we used a longer moving time window of 1 year. Periods of more negative GPS-gradient values, reflecting increased shortening, indicate times of stronger locking or lower slow-slip rates in the offshore area (fig. S12). The time series estimated from the observationally independent GPS gradient show similar fluctuations as those of the repeater slip rates (fig. S3).

We performed a moving spatial window analysis of the slip-rate spectrum to comprehensively examine the spatial distribution of the degree of periodicity and its dominant period along the NE Japan subduction zone. For each area, we determined the period of peak amplitude (short black vertical line in Fig. 3B) within the 1- to 9-year range and the degree of periodicity from the amplitude ratio of peak and average (red horizontal dashed line in Fig. 3B) amplitudes in the same period range. We used 0.4° (latitude) by 0.6° (longitude) spatial windows with 10 or more repeater sequences, showing widespread periodic behavior across the subduction zone (Fig. 4). The uncertainties of the estimated periodicities are generally on the order of 1 year (fig. S2B) (*14*). The dominant period has a heterogeneous distribution in both dip and strike directions (Fig. 4 and fig. S2A). Much of the subduction zone shows periods that range from 1 to 6 years and agrees with the periodicity of $M \geq 5$ earthquakes where strong slow-slip periodicity exists (fig. S2C). Around the slip areas of previous large earthquakes (*11*, *12*), including the 2011 Tohoku-oki earthquake (*13*), the aseismic slip rates are generally low and the periodicity is weak (light color in Fig. 4), with relatively long periods (>5 years). The relatively long period in the southern part of the coseismic slip area of the 2011 Tohoku earthquake (36.5° to 38°N) is consistent with a 5.9-year periodicity inferred from seismicity data for this area (*17*). The relatively weak periodicity near the large earthquakes may reflect the inhibition of periodic slip by strong interplate locking or indicate periods that are longer than the observation period.

The overall pattern of the offshore slip-rate periodicity from the repeater data correlates with the periods inferred from GPS gradients along profiles perpendicular to the margin (circles in Fig. 4 and fig. S13). A comprehensive evaluation of temporal slip-rate changes inferred from repeaters and GPS along the NE Japan subduction zone (figs. S2 to S4) shows correlations between the GPS gradients and near-shore repeater slip rates. The large variability in the correlations is probably due to the small-scale heterogeneities in periodic slow-slip behavior on the interplate fault in both along-dip and strike directions.

Periodic fault behavior may be driven by external forcing by tidal, atmospheric, and hydrologic cycles over a wide range of periods (*21*–*23*). However, we are unaware of forcing processes that recur at the most common periods we observe of 2 to 3 years (Fig. 4). Modeling

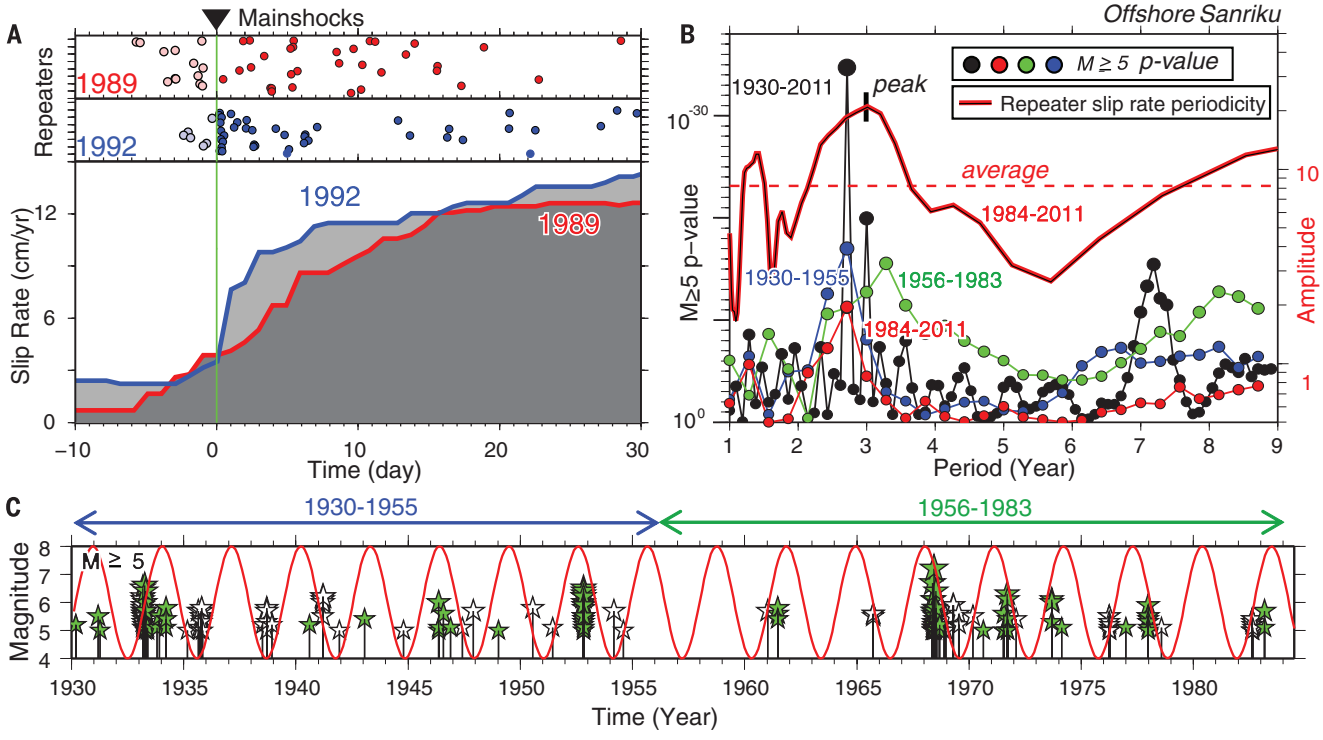


Fig. 3. Timing of repeaters, slow slip, and $M \geq 5$ earthquakes. (**A**) Times of the repeaters (top panels) and repeater-inferred slip rates (bottom panel) in the offshore Sanriku area (Fig. 2B) around the times of the 1989 M 7.2 (red) and 1992 M 6.9 (blue) mainshocks. Slip rates during 10 days before and 30 days after the mainshocks are plotted using a causal data window stepped every 1 day. Light and deep colors for the circles indicate repeaters before and after the mainshocks, respectively. (**B**) Amplitude spectrum of the slip rate for the offshore Sanriku area (red line; the original slip-rate time series is shown in Fig. 2B). The horizontal dashed red line shows the average of the amplitude in a 1- to 9-year period range. Black, red, green, and blue circles show Schuster spectra (*19*) for the $M \geq 5$ declustered earthquake catalogs for the time periods shown in the figure. The P values on the vertical axis give the probability of observing such a level of periodic variations in a catalog with a constant seismicity rate. (**C**) Magnitude-time plot of $M \geq 5$ earthquakes in the offshore Sanriku area before the repeater analysis period (i.e., 1930 to 1983). The red curve is the same sinusoidal function as in Fig. 2B, extrapolated from the fitting period. The green and white stars show events during times of positive and negative amplitude of the extrapolated sinusoid, respectively. Green and blue lines show the time period used in Fig. 3B. Plots similar to Fig. 3, B and C, but for the near-shore Sanriku area are shown in fig. S5, A and B, respectively.

studies suggest that slow-slip event periodicity may be governed by fault zone properties, including dilatancy, permeability, fluid pressure, and healing rates (*24*, *25*). Audet and Bürgmann (*26*) draw on the observed correlation of recurrence periods of deep slow-slip events in global subduction zones with seismic velocity variations to support a scenario of slow-slip event periodicity being governed by fault zone properties. The enduring nature of the periodic behavior we document suggests that fault zone constitutive properties could govern the recurrence of slow-slip events off northern Japan.

The 2011 Tohoku-oki earthquake occurred 0.7 years before the end of our analysis period. Slip rate peaks in the off-Sanriku areas before the 2011 Tohoku-oki earthquake, and the subsequent timing of the 2011 earthquake falls in the positive period of the sinusoidal slip-rate curve (Fig. 2, B and C), although the accelerations are not as obvious in the southern areas (fig. S3, E and F). Slow slip was detected in 2008 and 2011 from ocean-bottom pressure sensors (*18*) to the south of the off-Sanriku area. The slip episode appears to have triggered the largest foreshock (M 7.3) that occurred 2 days before the Tohoku-oki earthquake (*18*). Preseismic slow-slip migration toward the mainshock hypocenter occurred in February to March 2011 (*4*), but no significant preslip was detected on the megathrust fault immediately before the Tohoku-oki earthquake, from the analysis of seafloor vertical deformation data near the epicenter (*27*).

Large postseismic slip continues off Tohoku (*28*). If the inherent fault zone properties govern the periodicity of slow-slip transients, the periodicity may not change because of the Tohoku-oki earthquake. Previous examples support this scenario: The first slow-slip acceleration after the 1994 Sanriku-oki earthquake (M 7.6) that occurred just north of the Sanriku area (Fig. 2A) started somewhat earlier, but the period and phase did not change much for later slip accelerations in the offshore Sanriku area (Fig. 2B). In the case of the 2003 Tokachi-oki earthquake (M 8.0), the periodicity in the offshore area only became prominent after the earthquake (fig. S3C).

In most probabilistic earthquake forecasts based on recurrence intervals and time since the last event, a constant loading rate is implicitly assumed. The inherent periodicity of slow slip found in this study suggests that probabilistic forecasts of future earthquakes can be improved by explicitly considering cyclic loading-rate changes. The real-time monitoring of slow slip may also help improve the estimation of time-dependent earthquake hazards (*29*).

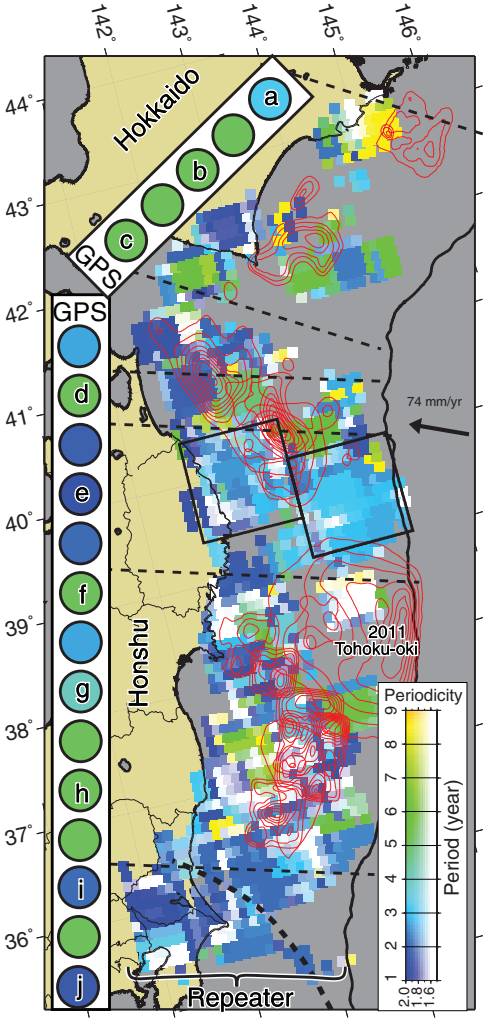


Fig. 4. Spatial distribution of degree of periodicity and dominant period estimated from the repeater data. The color intensity shows the degree of periodicity, and the colors show the dominant period for the periods from 1984 to 2011 (between 36.5° and 41.5°N) and from 1993 to 2011 (north of 41.5°N and south of 36.5°N). The periods indicated for each area represent the dominant peak in the amplitude spectrum of the slip-velocity variations inferred from repeaters for 0.4° (latitude) by 0.6° (longitude) spatial windows. Contours show slip areas for the 2011 Tohoku-oki earthquake (M 9.0) and other M 7 or larger earthquakes since 1930 (*11*–*13*, *30*). Colored circles show the dominant period of the on-land GPS gradient in plate motion parallel to the N105°E (Honshu) and N120°E (Hokkaido) directions (see fig. S13 for the spectrum of gradient time series in profile lines a to j that are used to compute the dominant periods).

REFERENCES AND NOTES

1. K. Heki, S. Miyazaki, H. Tsuji, *Nature* **386**, 595–598 (1997).
2. G. Dragert, K. Wang, T. S. James, *Science* **292**, 1525–1528 (2001).
3. P. Segall, A. M. Bradley, *Geophys. Res. Lett.* **39**, L18308 (2012).
4. A. Kato *et al.*, *Science* **335**, 705–708 (2012).
5. M. Bouchon, V. Durand, D. Marsan, H. Karabulut, J. Schmittbuhl, *Nat. Geosci.* **6**, 299–302 (2013).
6. S. Ruiz *et al.*, *Science* **345**, 1165–1169 (2014).
7. S. Ozawa, H. Suito, M. Tobita, *Earth Planets Space* **59**, 1241–1245 (2007).
8. R. M. Nadeau, T. V. McEvilly, *Science* **285**, 718–721 (1999).
9. R. M. Nadeau, T. V. McEvilly, *Science* **303**, 220–222 (2004).
10. N. Uchida, T. Matsuzawa, *Earth Planet. Sci. Lett.* **374**, 81–91 (2013).
11. Y. Yamanaka, M. Kikuchi, *Earth Planets Space* **55**, e21–e24 (2003).
12. Y. Yamanaka, M. Kikuchi, *J. Geophys. Res.* **109**, B07307 (2004).
13. T. Iinuma *et al.*, *J. Geophys. Res.* **117**, B07409 (2012).
14. Materials and methods are available as supplementary materials on *Science* Online.
15. G. F. Sella, T. H. Dixon, A. Mao, *J. Geophys. Res.* **107**, 2081 (2002).
16. N. Uchida, A. Hasegawa, T. Matsuzawa, T. Igarashi, *Tectonophysics* **385**, 1–15 (2004).
17. D. Marsan, T. Reverso, A. Helmstetter, B. Enescu, *J. Geophys. Res. Solid Earth* **118**, 4900–4909 (2013).
18. Y. Ito *et al.*, *Tectonophysics* **600**, 14–26 (2013).
19. T. J. Ader, J.-P. Avouac, *Earth Planet. Sci. Lett.* **377–378**, 97–105 (2013).
20. J. C. Savage, *J. Geophys. Res. Solid Earth* **88**, 4984–4996 (1983).
21. K. Heki, *Earth Planet. Sci. Lett.* **207**, 159–164 (2003).
22. Y. Tanaka, *Geophys. J. Int.* **196**, 760–787 (2014).
23. F. F. Pollitz, A. Wech, H. Kao, R. Bürgmann, *J. Geophys. Res. Solid Earth* **118**, 2445–2459 (2013).
24. Y. Liu, *Geophys. Res. Lett.* **40**, 1311–1316 (2013).
25. P. Segall, A. M. Rubin, A. M. Bradley, J. R. Rice, *J. Geophys. Res. Solid Earth* **115**, B12305 (2010).
26. P. Audet, R. Bürgmann, *Nature* **510**, 389–392 (2014).
27. R. Hino *et al.*, *Mar. Geophys. Res.* **35**, 181–190 (2014).
28. S. Ozawa *et al.*, *J. Geophys. Res.* **117**, B07404 (2012).
29. T. H. Jordan, L. M. Jones, *Seismol. Res. Lett.* **81**, 571–574 (2010).
30. T. Murotani, M. Kikuchi, Y. Yamanaka, "Rupture processes of large Fukushima-Oki earthquakes in 1938," paper S052-004, presented at the 2003 Japan Geoscience Union, Chiba, Japan, 2003.

ACKNOWLEDGMENTS

We thank Y. Yabe, T. Matsuzawa, W. Nakamura, R. C. Turner, S. Tanaka, C. W. Johnson, W. L. Ellsworth, Y. Ogata, and A. Hasegawa for fruitful discussion. The anonymous reviewers were helpful in greatly improving the manuscript. This work was supported in part by Japan Society for the Promotion of Science (JSPS) KAKENHI 23740328 and 15K05260 and the Ministry of Education, Culture, Sports, Science and Technology of Japan, under its Earthquake and Volcano Hazards Observation and Research Program. N.U. acknowledges support by Tohoku University under its Leading Young Researcher Overseas Visit Program. R.M.N. acknowledges support from the Berkeley Institute for Data Science, funded by the Moore-Sloan Data Science Environment Program. R.B. acknowledges support by U.S. NSF award EAR-1246850. R.H. acknowledges support by JSPS KAKENHI 26000002. The repeating earthquakes were selected based on the seismic waveforms from stations of Hokkaido University, Hirosaki University, Tohoku University, and the University of Tokyo. The repeating earthquake catalog is available as supplementary material on *Science* Online. The Japan Meteorological Agency (JMA) earthquake catalog used in this study is available at www.jma.go.jp, subject to the policies of the JMA. The GEONET F3 GPS solutions used in this study are available at www.gsi.go.jp, subject to the policies of the Geospatial Information Authority of Japan.

SUPPLEMENTARY MATERIALS

www.sciencemag.org/content/351/6272/488/suppl/DC1
Materials and Methods
Figs. S1 to S14
Tables S1 to S4
References (*31*–*42*)

26 August 2015; accepted 22 December 2015
10.1126/science.aad3108

LUNAR FORMATION

Oxygen isotopic evidence for vigorous mixing during the Moon-forming giant impact

Edward D. Young,[1]* Issaku E. Kohl,[1]* Paul H. Warren,[1] David C. Rubie,[2] Seth A. Jacobson,[2,3] Alessandro Morbidelli[3]

Earth and the Moon are shown here to have indistinguishable oxygen isotope ratios, with a difference in $\Delta'^{17}O$ of −1 ± 5 parts per million (2 standard error). On the basis of these data and our new planet formation simulations that include a realistic model for primordial oxygen isotopic reservoirs, our results favor vigorous mixing during the giant impact and therefore a high-energy, high-angular-momentum impact. The results indicate that the late veneer impactors had an average $\Delta'^{17}O$ within approximately 1 per mil of the terrestrial value, limiting possible sources for this late addition of mass to the Earth-Moon system.

The Moon is thought to be the consequence of a giant collision between the proto-Earth and a planetary embryo (named Theia, "mother of the Moon") ~10^8 years after the birth of the solar system (*1*, *2*). However, the distinct oxygen isotopic signatures of solar system bodies (*3*, *4*) has presented a problem for the impact hypothesis for the formation of the Moon (*5*, *6*). In order to create an iron-poor Moon and simultaneously reproduce the angular momentum of the Earth-Moon system, early models required a glancing blow by a Mars-sized impactor that resulted in the Moon being composed mainly of impactor material (*7*). Therefore, in the general case the Moon and Earth should not be identical in their oxygen isotopic compositions. Nonetheless, until recently the Moon and Earth have been found to be indistinguishable in their oxygen isotope ratios (*8*–*10*). Proposed higher-energy giant impacts offer potential solutions to this conundrum (*11*), although at the expense of the need to shed substantial angular momentum from the system via orbital resonances (*12*).

Oxygen reservoirs comprising rocky bodies of the solar system are characterized by distinct relative concentrations of oxygen isotopes. These relative concentrations are customarily represented by $\Delta^{17}O$, the departure in $^{17}O/^{16}O$ relative to a given $^{18}O/^{16}O$ under the assumption that these two isotope ratios covary as a consequence

[1]Department of Earth, Planetary, and Space Sciences, University of California Los Angeles, Los Angeles, CA, USA. [2]Bayerisches Geoinstitut, University of Bayreuth, D-95490 Bayreuth, Germany. [3]Laboratoire Lagrange, Université de Nice–Sophia Antipolis, Observatoire de la Cote d'Azur, CNRS, 06304 Nice, France.
*Corresponding author E-mail: eyoung@epss.ucla.edu (E.D.Y.); ikohl@epss.ucla.edu (I.E.K.)

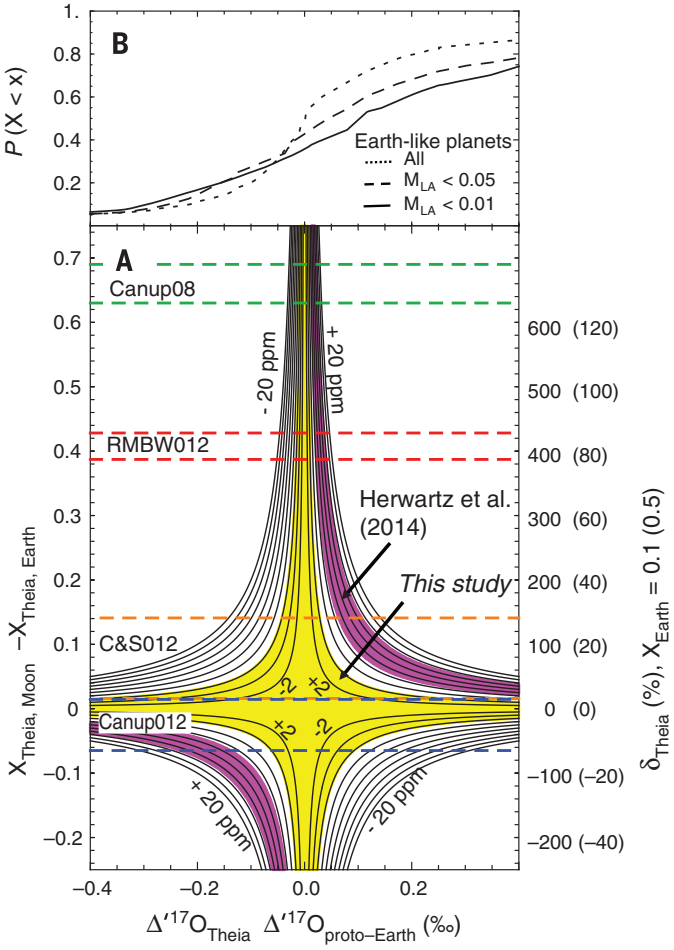


Fig. 1. Oxygen isotope mass balance diagram. (**A**) Contours of $\Delta'^{17}O_{Moon} - \Delta'^{17}O_{Earth}$ in parts per milliion versus fractional differences in Theia content of the bulk silicate Moon and Earth and $\Delta'^{17}O_{Theia} - \Delta'^{17}O_{proto\text{-}Earth}$. The contour interval is 2 ppm. The pink region indicates that the contour intervals are consistent with the $\Delta'^{17}O_{Moon} - \Delta'^{17}O_{Earth}$ reported by Herwartz *et al*. (*21*). The yellow region encompasses the contours consistent with our data ±2 SE. Corresponding values for δ_{Theia} are shown at right. One set of δ_{Theia} values applies if the fraction of the present-day bulk silicate Earth composed of Theia is 0.1, whereas the values in parentheses apply where the fraction of Theia in present-day Earth is 0.5. For comparison, the ranges in Theia contents of the Moon and Earth for four simulated Moon-forming impact scenarios are shown as dashed horizontal lines. The models include the "canonical" model requiring no subsequent angular momentum loss by Canup (2008; Canup08), the hit-and-run model of Reufer *et al*. (2012; RMBW012), and the high angular momentum scenarios, including Cuk & Stewart (2012; C&S012) and Canup (2012; Canup012). (**B**) The cumulative probability for $\Delta'^{17}O_{Theia} - \Delta'^{17}O_{proto\text{-}Earth}$ in per mil based on simulations in this study. Three cases are shown: those with late accreted mass to Earth <5%, those with late accreted mass <1%, and all simulations.

Downloaded from on January 31, 2016

of mass-dependent isotope fractionation. The small fractional differences in isotope ratios can be replaced with $\delta'^{17}O = 10^3\ln(^{17}R/^{17}R_o)$ and $\delta'^{18}O = 10^3\ln(^{18}R/^{18}R_o)$ (*13*) values, where ^{17}R is $^{17}O/^{16}O$, ^{18}R is $^{18}O/^{16}O$, and $^{17}R_o$ and $^{18}R_o$ refer to the initial isotope ratios (such as those characterizing bulk Earth) (*14*). These δ′ values are nearly equivalent to the fractional differences in per mil (‰) but are linearly related by the mass fractionation exponent β. The exact values for β depend on the processes involved in fractionation but are always near ½, as prescribed by oxygen isotope masses (*13*). With these definitions, $\Delta'^{17}O$ is written as

$$\Delta'^{17}O = \delta'^{17}O - \beta\delta'^{18}O \quad (1)$$

A positive $\Delta'^{17}O$ signifies that a reservoir is enriched in ^{17}O relative to Earth, whereas a negative value signifies that a reservoir is relatively depleted in ^{17}O compared with expectations from mass fractionation. At the scale of individual mineral grains, solar system materials exhibit variations in $\Delta'^{17}O$ spanning ~200‰ (*15*). The dispersion in $\Delta'^{17}O$ decreases drastically with mass. Differences in $\Delta'^{17}O$ among meteorite whole-rock samples are ~5 to 8‰ (*4*, *16*), representing parent asteroids with masses of ~10^{15} to 10^{17} kg. Differences between differentiated bodies with metal cores and silicate mantles are smaller still: Mars (6.4×10^{23} kg) has a $\Delta'^{17}O$ value of about +0.3‰, whereas Vesta (2.6×10^{20} kg) has a value of −0.25‰ (*17*, *18*). The reduced dispersion in $\Delta'^{17}O$ with mass evidently reflects averaging as smaller rocky bodies coalesced to form larger bodies in the solar system (*19*, *20*). Historically, the identical $\Delta'^{17}O$ values for Earth and the Moon have stood out against this backdrop of variability in the solar system.

However, some high-precision measurements on lunar samples indicated that the Moon has a greater $\Delta'^{17}O$ than that of Earth by 12 ± 3 parts per million (ppm) (*21*). The importance of this finding can be gauged by considering contours for $\Delta'^{17}O_{Moon} - \Delta'^{17}O_{Earth}$ plotted as functions of the difference in $\Delta'^{17}O$ between Theia and the proto-Earth and the difference in the fractions of the Moon and Earth inherited from Theia (Fig. 1A). The mass-balance equation plotted is

$$x_{Theia,Moon} - x_{Theia,Earth} = \frac{\Delta'^{17}O_{Moon} - \Delta'^{17}O_{Earth}}{\Delta'^{17}O_{Theia} - \Delta'^{17}O_{proto-Earth}} \quad (2)$$

where $x_{Theia,i}$ refers to the oxygen fraction of body *i* derived from Theia (essentially, mass fractions of the bulk silicate portions of the bodies). For convenience, we also use the fractional difference δ_{Theia} rather than the absolute difference in Eq. 2:

$$\delta_{Theia} = (x_{Theia,Moon} - x_{Theia,Earth})/x_{Theia,Earth} \quad (3)$$

The implications of a difference in oxygen isotopic composition between the Moon and Earth depend on the fraction of Theia contained within Earth (Eqs. 2 and 3). Four recent proposed giant impact scenarios (*5*, *11*, *12*, *22*) predict disparate differences in the Theia fractions in the Moon and Earth (Fig. 1A). If the difference in $\Delta'^{17}O$ between Theia and the proto-Earth was zero, there is no oxygen isotope constraint on δ_{Theia} (Fig. 1A). Similarly, if Earth and the Moon are composed of precisely the same concentrations of Theia, there is no constraint on differences in $\Delta'^{17}O$ between Theia and the proto-Earth.

A positive $\Delta'^{17}O$ of 12 ± 3 ppm for the Moon (*21*) requires a difference in the proportions of Moon and Earth composed of remnants of Theia because the contours representing this range of values (Fig. 1A, pink regions) do not include the center of the diagram (Fig. 1A). For a Mars-sized differentiated body with $\Delta'^{17}O$ ~ ± 0.3‰ (such as Mars or Vesta), the difference in Theia contents between the Moon and Earth is ± 50% or more (Fig. 1A). For the case of a proto-Earth–sized Theia, the result is a difference of ± 8% or more (Fig. 1A). Alternatively, assuming enstatite-chondrite–like material better represents the terrestrial planet-forming region (*23*, *24*), differences in oxygen isotope ratios between Theia and proto-Earth would have been smaller (~0.1‰) (*21*, *25*), and the lunar $\Delta'^{17}O$ of 12 ± 3 ppm (*21*) requires δ_{Theia} values of 150 and 30% for the Mars and proto-Earth–sized impactors, respectively (Fig. 1A). Such large δ_{Theia} values would effectively remove the constraint imposed by oxygen isotopes that the Earth-Moon system was well mixed.

We analyzed seven Apollo 12, 15, and 17 lunar samples and one lunar meteorite and compared their $^{17}O/^{16}O$ and $^{18}O/^{16}O$ isotope ratios with those for a suite of terrestrial igneous samples. The 1- to 4-mg lunar samples include high-Ti mare basalts, low-Ti Mg-rich olivine cumulate basalts, a quartz normative basalt, and a highland

Table 1. Summary of oxygen isotope data for lunar and terrestrial samples. Delta values are in logarithmic form as defined in the text.

Sample	$\delta'^{17}O$	$\delta'^{18}O$	$\Delta'^{17}O$
Lunar basalt			
Average (*n* = 8)	3.004	5.691	−0.001
Standard deviation	0.090	0.172	0.005
Standard error	0.032	0.061	0.002
Lunar basalt-fused beads			
Average (*n* = 4)	2.940	5.572	0.000
Standard deviation	0.133	0.245	0.006
Standard error	0.067	0.123	0.003
Lunar troctolite			
Average (*n* = 2)	3.178	6.050	−0.016
Standard deviation	0.009	0.026	0.005
Standard error	0.007	0.019	0.003
San Carlos olivine			
Average (*n* = 17)	2.711	5.134	0.000
Standard deviation	0.072	0.134	0.005
Standard error	0.017	0.033	0.001
Mauna Loa olivine			
Average (*n* = 4)	2.736	5.189	−0.004
Standard deviation	0.090	0.170	0.001
Standard error	0.045	0.085	0.001
Mauna Loa whole-rock samples			
Average (*n* = 5)	2.796	5.298	−0.002
Standard deviation	0.031	0.063	0.003
Standard error	0.014	0.028	0.001
San Carlos spinel			
Average (*n* = 2)	2.171	4.104	0.004
Standard deviation	0.135	0.285	0.015
Standard error	0.096	0.202	0.011
Bushveld anorthosite			
Average (*n* = 2)	3.522	6.694	−0.012
Standard deviation	0.002	0.002	0.001
Standard error	0.001	0.002	0.000
Gore Mountain garnet			
Average (*n* = 2)	3.174	6.020	−0.004
Standard deviation	0.017	0.026	0.003
Standard error	0.012	0.019	0.002

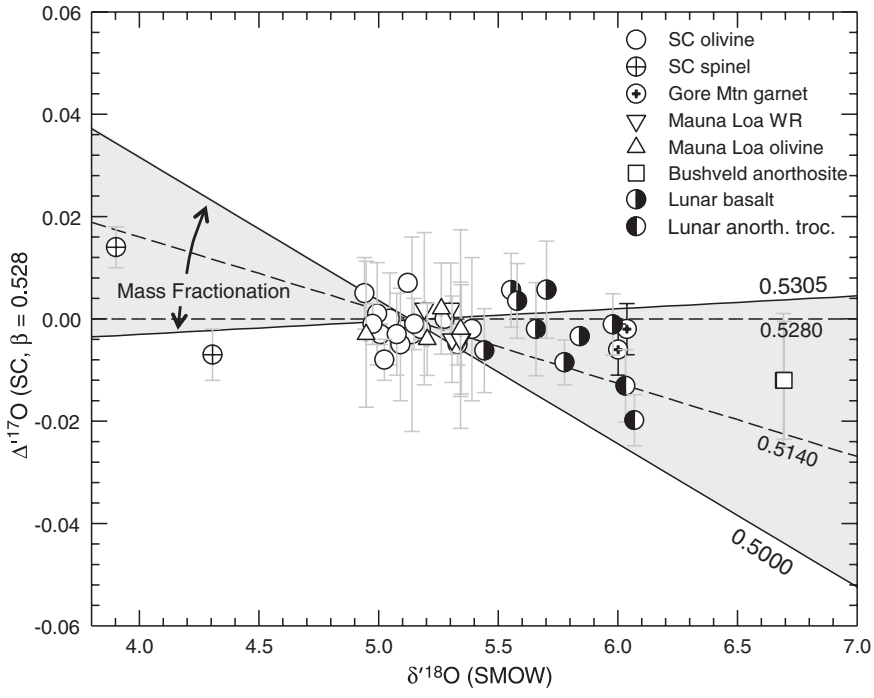


Fig. 2. Plot of $\Delta'^{17}O$ versus $\delta'^{18}O$ for lunar and terrestrial samples by using a fractionation line with β = 0.528 passing through San Carlos olivine as the reference. Only the powders of lunar samples are plotted. The gray region indicates the regions accessible through mass fractionation starting from SC olivine. Different fractionation laws are labeled with their defining β values. Error bars depict 2 SE for each measurement. Points lying inside of the gray region are consistent with simple one-stage, mass-dependent isotope fractionation relative to SC olivine, implying that they represent a single oxygen reservoir.

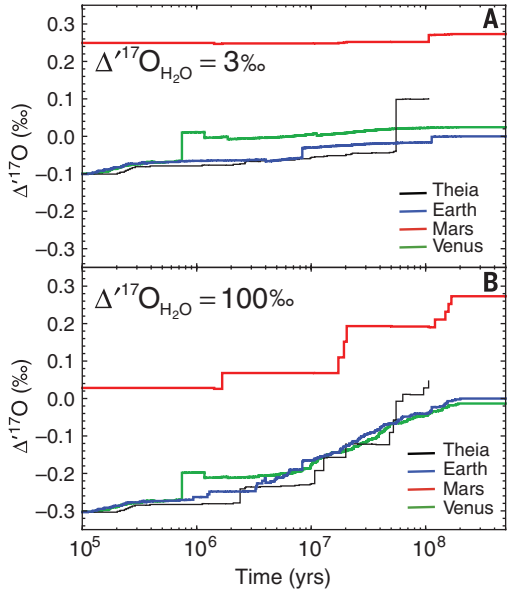


Fig. 3. A simulation of the oxygen isotopic evolution of the terrestrial planets and last giant (Moon-forming) impactor, Theia. The $\Delta'^{17}O$ values of the growing Venus-like (green), Earth-like (blue), and Mars-like (red) planets are shown as a function of time as well as the value for the Theia-like impactor (black). (**A**) The case in which the water oxygen reservoir has $\Delta'^{17}O$ = 3‰. (**B**) The case in which water $\Delta'^{17}O$ = 100‰.

anorthositic troctolite (table S1). The terrestrial samples include San Carlos mantle xenolith olivines, San Carlos mantle xenolith spinels, Mauna Loa basalt samples, Mauna Loa olivine separates, an anorthosite from the Bushveld complex, and a sample of Gore Mountain metamorphic garnet. We obtained our analyses (Table 1) using infrared laser heating (*26*) modified to include F_2 as the fluorinating agent and purification of the analyte O_2 gas for analysis of both $^{17}O/^{16}O$ and $^{18}O/^{16}O$ (*27*). We have improved our precision compared with many previous efforts by more thoroughly desiccating samples before analysis and by regular rebalancing of standard and sample ion beam intensities throughout the mass spectrometer analyses (*28*). We analyzed a range of lunar and terrestrial sample lithologies to account for the fact that β values vary with process (*13*, *29*, *30*). We use the traditional standard mean ocean water (SMOW) as the reference for $\delta'^{18}O$, but we use San Carlos (SC) olivine as the reference for $\Delta'^{17}O$ when characterizing oxygen isotope reservoirs of rocks (*28*). We adopt a typical igneous β of 0.528 passing through the mean value for San Carlos olivine as our reference fractionation line for calculating $\Delta'^{17}O$ (*28*).

Lunar basalts are relatively high in $\delta'^{18}O$ as compared with SC olivine and terrestrial basalts (Fig. 2). Nonetheless, the basalts show no clear deviation from the reference β of 0.528, allowing direct comparison of $\Delta'^{17}O$ values for these materials. No discernible difference exists in $\Delta'^{17}O$ between SC olivine and lunar basalts powders (−0.001 ± 0.002, 1 SE) or fused beads (0.000 ± 0.003, 1 SE). The mean for all mafic terrestrial samples, representing terrestrial mantle and its melt products, is 0.000 ± 0.001‰ (1 SE). Adding in quadrature, the analytical uncertainty in the SC olivine and the standard error for the lunar samples yields a difference between lunar basalt and SC olivine of −0.001 ± 0.0048‰ (−1 ± 4.8 ppm, 2 SE), which is indistinguishable from zero. Other mafic terrestrial whole rocks and olivines are within this uncertainty range (Table 1). We found no resolvable difference in $\Delta'^{17}O$ between lunar mantle melts represented by these basalts and terrestrial mantle and melts.

Our result does not agree with the conclusions of Herwartz *et al.* (*21*). Measurements on the one sample common to both studies (12018) agree within uncertainties when compared in the same reference frame (fig. S2) (*28*). It is therefore conceivable that an unfortunate difference in sample selection could be a plausible explanation for the difference between the studies.

The lunar highland sample has a significantly lower $\Delta'^{17}O$ value of −0.016 ± 0.003‰ (1 SE) (or −16 ± 3 ppm), which is similar to a previous study (*8*). However, the terrestrial anorthosite sample has a similarly low value (Table 1). The low $\Delta'^{17}O$ values for both the terrestrial and lunar highland anorthosites (anorthostic troctolite) imply a mass fractionation process related to formation of this rock type that results in low $\Delta'^{17}O$ values (Fig. 2). The low $\Delta'^{17}O$ value for the lunar highland rocks is not evidence for a distinction between the oxygen pools for the Moon and Earth because these samples are in the mass-fractionation envelope for Earth (Fig. 2), and low $\Delta'^{17}O$ values are found

in both terrestrial and lunar anorthosite-like rocks. One terrestrial mantle spinel sample also shows a measurable deviation from the $\beta = 0.528$ reference, implying a relatively low β value (Fig. 2).

Of course, in all cases invoking no difference in oxygen isotope ratios between Theia and proto-Earth results in no constraints on the relative Theia concentrations in the Moon and Earth. We can assess the purely statistical feasibility of two proto-planetary bodies having identical oxygen isotope ratios using the central limit theorem (*19*). Results suggest that a purely random sampling of asteroid-like materials would lead to variations in $\Delta'^{17}O$ among planetary embryos of ~3 ppm (*28*). However, the larger difference between Earth and Mars testifies to the fact that $\Delta'^{17}O$ was not distributed randomly in small bodies across the inner solar system.

Differences in $\Delta'^{17}O$ between Theia and the proto-Earth have expected values of 0.15‰ (*31*) or 0.05 ‰ (*32*) on the basis of two recent N-body simulations of standard terrestrial planet-formation scenarios with hypothesized gradients in $\Delta'^{17}O$ across the inner solar system. We used a planetary accretion model (*33*) that uses N-body accretion simulations based on the Grand Tack scenario (*34*). Our model differs from previous efforts in that we strictly limit our analysis to simulations that closely reproduce the current masses and locations of Earth and Mars and the oxidation state of Earth's mantle, we use a multi-reservoir model (composed of silicate, oxidized iron, and water) to describe the initial heliocentric distribution of oxygen isotopes, and we include the effects of mass accretion subsequent to the Moon-forming impact (*28*). An example simulation (Fig. 3) and others like it show that the $\Delta'^{17}O$ values of the colliding bodies rise together as the average $\Delta'^{17}O$ values increase during accretion. Incorporation of more material from greater distances from the Sun as accretion proceeds accounts for the rise. Large planets such as Earth and Venus reflect an average of many embryos and planetesimals and so exhibit similar $\Delta'^{17}O$ values with time, whereas stranded embryos averaging fewer components, such as Mars, show greater variation.

The cumulative distribution of $\Delta'^{17}O$ differences between Theia and proto-Earth is shown for 236 simulations of planet growth (*35*) (Fig. 1B). The median $\Delta'^{17}O_{Theia} - \Delta'^{17}O_{proto\text{-}Earth}$ is nearly 0 in these calculations for all simulations (Fig. 1B). However, our median predicted $\Delta'^{17}O_{Theia} - \Delta'^{17}O_{proto\text{-}Earth}$ is +0.1‰ if we restrict our analysis to those simulations consistent with adding ≤1% by mass of a "late veneer" (LV) of primitive material post Moon-forming giant impact, as required by geochemical constraints (*36*). This median value combined with our measurement of $\Delta'^{17}O_{Moon} - \Delta'^{17}O_{Earth}$ corresponds to δ_{Theia} of +20 to −60% for the Mars-sized impactor scenario and +8 to −12% in the proto-Earth–sized impactor scenarios. The corresponding values for δ_{Theia} using the previous 12 ± 3 ppm difference between Moon and Earth $\Delta'^{17}O$ values (*21*) are +80 to +180% and +16 to +36%, respectively (Fig. 1A). The new measurements presented here are consistent with Earth and the Moon having near-identical Theia contents. Indistinguishable $\Delta'^{17}O$ values of the Moon and Earth to the 5 ppm level of uncertainty suggests that the Moon-forming impact thoroughly mixed and homogenized the oxygen isotopes of Theia and proto-Earth.

Our interpretation has implications for the composition of the LV of primitive bodies that impacted the silicate Earth. A disproportionately larger flux of LV planetesimals is implied by a higher average $^{182}W/^{184}W$ for the Moon than for Earth and by previous estimates for the apparent differences in highly siderophile element (HSE) concentrations between the terrestrial and lunar mantles (*37*). The interpretation of these data is that the Moon and Earth began with the same W isotopic ratios, but that Earth inherited a greater fraction of low $^{182}W/^{184}W$ material in the form of chondritic planetesimals after the Moon-forming giant impact (*38*, *39*). If we adopt the conclusion from the W isotopes that the Earth-Moon system was well mixed as a result of the Moon-forming impact, then the nearly identical $\Delta'^{17}O$ values of Moon and Earth constrain the identity of the LV impactors by their oxygen isotope ratios. Estimates for the Earth/Moon ratio of the LV mass fluxes range from ~200 to 1200 (*37*, *40*, *41*). Using a late-veneer flux to Earth of 2×10^{22} kg (*37*) and a conservative maximum Earth/Moon flux ratio of 1200 (*41*), the difference in LV fractions comprising the silicate Earth and Moon is 0.00447. Combining this value with our measured value for $\Delta'^{17}O_{Moon} - \Delta'^{17}O_{Earth}$ of zero (28) requires that the LV impactors had average $\Delta'^{17}O$ values within ~0.2‰ or less of Earth, similar to enstatite chondrites (*25*). Alternatively, with our maximum permitted $\Delta'^{17}O_{Moon} - \Delta'^{17}O_{Earth}$ of ± ~5 ppm, the calculated $\Delta'^{17}O$ value for the LV is ±1.1‰. This value encompasses aqueously altered carbonaceous chondrites and some ordinary chondrites. For comparison, the same calculation using the 12 ppm difference between the Moon and Earth yields an LV $\Delta'^{17}O$ of −2.7‰, suggesting that the impactors were composed mainly of relatively unaltered and dry carbonaceous chondrites (*4*). Our result suggests that if the LV was composed mainly of carbonaceous chondrites, the parent bodies must have included substantial fractions of high-$\Delta'^{17}O$ water either in the form of aqueous alteration minerals or as water ice.

REFERENCES AND NOTES

1. W. K. Hartmann, D. R. Davis, *Icarus* **24**, 504–515 (1975).
2. S. A. Jacobson *et al*., *Nature* **508**, 84–87 (2014).
3. R. N. Clayton, *Annu. Rev. Earth Planet. Sci.* **21**, 115–149 (1993).
4. R. N. Clayton, N. Onuma, T. K. Mayeda, *Earth Planet. Sci. Lett.* **30**, 10–18 (1976).
5. R. M. Canup, *Icarus* **196**, 518–538 (2008).
6. K. Pahlevan, D. J. Stevenson, *Earth Planet. Sci. Lett.* **262**, 438–449 (2005).
7. R. M. Canup, E. Asphaug, *Nature* **412**, 708–712 (2001).
8. U. Wiechert *et al*., *Science* **294**, 345–348 (2001).
9. L. J. Hallis *et al*., *Geochim. Cosmochim. Acta* **74**, 6885–6899 (2010).
10. M. J. Spicuzza, J. M. D. Day, L. A. Taylor, J. W. Valley, *Earth Planet. Sci. Lett.* **253**, 254–265 (2007).
11. R. M. Canup, *Science* **338**, 1052–1055 (2012).
12. M. Ćuk, S. T. Stewart, *Science* **338**, 1047–1052 (2012).
13. E. D. Young, A. Galy, H. Nagahara, *Geochim. Cosmochim. Acta* **66**, 1095–1104 (2002).
14. C. R. McKinney, J. M. McCrea, S. Epstein, H. A. Allen, H. C. Urey, *Rev. Sci. Instrum.* **21**, 724–730 (1950).
15. N. Sakamoto *et al*., *Science* **317**, 231–233 (2007).
16. M. K. Weisberg *et al*., *Geochim. Cosmochim. Acta* **55**, 2657–2669 (1991).
17. I. A. Franchi, I. P. Wright, A. S. Sexton, C. T. Pillinger, *Meteorit. Planet. Sci.* **34**, 657–661 (1999).
18. R. N. Clayton, T. K. Mayeda, *Geochim. Cosmochim. Acta* **60**, 1999–2017 (1996).
19. J. A. Nuth III, H. G. M. Hill, *Meteorit. Planet. Sci.* **39**, 1957–1965 (2004).
20. V. S. Safronov, *Sov. Astron.* **9**, 987–991 (1966).
21. D. Herwartz, A. Pack, B. Friedrichs, A. Bischoff, *Science* **344**, 1146–1150 (2014).
22. A. Reufer, M. M. M. Meier, W. Benz, R. Wieler, *Icarus* **221**, 296–299 (2012).
23. S. B. Jacobsen, M. I. Petaev, S. Huang, paper presented at the American Geophysical Union Fall Meeting, San Francisco, CA, 2012.
24. L. R. Nittler *et al*., *Science* **333**, 1847–1850 (2011).
25. J. Newton, I. A. Franchi, C. T. Pillinger, *Meteorit. Planet. Sci.* **35**, 689–698 (2000).
26. Z. D. Sharp, *Geochim. Cosmochim. Acta* **54**, 1353–1357 (1990).
27. E. D. Young, H. Nagahara, B. O. Mysen, D. M. Audet, *Geochim. Cosmochim. Acta* **62**, 3109–3116 (1998).
28. Materials and methods are available as supplementary materials on *Science* Online.
29. X. Cao, Y. Liu, *Geochim. Cosmochim. Acta* **75**, 7435–7445 (2011).
30. J. Matsuhisa, J. R. Goldsmith, R. N. Clayton, *Geochim. Cosmochim. Acta* **42**, 173–182 (1978).
31. N. A. Kaib, N. B. Cowan, *Icarus* **252**, 161–174 (2015).
32. A. Mastrobuono-Battisti, H. B. Perets, S. N. Raymond, *Nature* **520**, 212–215 (2015).
33. D. C. Rubie *et al*., *Icarus* **248**, 89–108 (2015).
34. K. J. Walsh, A. Morbidelli, S. N. Raymond, D. P. O'Brien, A. M. Mandell, *Nature* **475**, 206–209 (2011).
35. S. A. Jacobson, A. Morbidelli, *Philos. Trans. A Math. Phys. Eng. Sci.* **372**, 20130174 (2014).
36. C.-L. Chou, *Proc. Lunar. Planet. Sci. Conf.* **9**, 219–230 (1978).
37. R. J. Walker *et al*., *Chem. Geol.* **411**, 125–142 (2015).
38. T. S. Kruijer, T. Kleine, M. Fischer-Gödde, P. Sprung, *Nature* **520**, 534–537 (2015).
39. M. Touboul, I. S. Puchtel, R. J. Walker, *Nature* **520**, 530–533 (2015).
40. H. E. Schlichting, P. H. Warren, Q.-Z. Yin, *Astrophys. J.* **752**, 8 (2012).
41. W. F. Bottke, R. J. Walker, J. M. D. Day, D. Nesvorny, L. Elkins-Tanton, *Science* **330**, 1527–1530 (2010).

ACKNOWLEDGMENTS

We are grateful to NASA Johnson Space Center for approving use of the Apollo samples for this study. E.D.Y. acknowledges support from a grant from the NASA Emerging Worlds program (NNX15AH43G). D.C.R., S.A.J., and A.M. acknowledge support from the European Research Council Advanced Grant "ACCRETE" (contract 290568). Development of the Panorama instrument was supported by the Deep Carbon Observatory (Sloan Foundation), NSF, U.S. Department of Energy, Shell, the Carnegie Institution of Washington, and the University of California, Los Angeles. The complete data table for this study can be found in the supplementary materials.

SUPPLEMENTARY MATERIALS

www.sciencemag.org/content/351/6272/493/suppl/DC1
Materials and Methods
SupplementaryText
Figs. S1 to S7
Tables S1 to S4
References (*42*–*67*)

18 July 2015; accepted 13 December 2015
10.1126/science.aad0525

POLYMERS

Simultaneous covalent and noncovalent hybrid polymerizations

Zhilin Yu,[1] Faifan Tantakitti,[2] Tao Yu,[1] Liam C. Palmer,[1,3] George C. Schatz,[1,4] Samuel I. Stupp[1,2,3,5,6]*

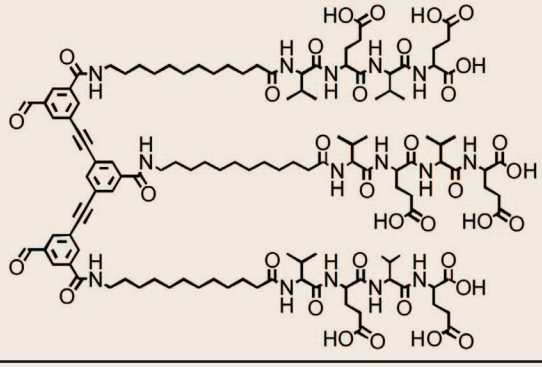
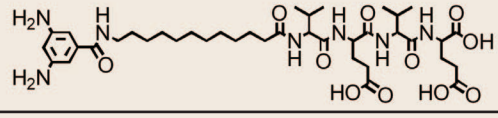
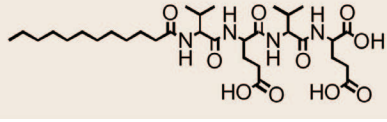
Covalent and supramolecular polymers are two distinct forms of soft matter, composed of long chains of covalently and noncovalently linked structural units, respectively. We report a hybrid system formed by simultaneous covalent and supramolecular polymerizations of monomers. The process yields cylindrical fibers of uniform diameter that contain covalent and supramolecular compartments, a morphology not observed when the two polymers are formed independently. The covalent polymer has a rigid aromatic imine backbone with helicoidal conformation, and its alkylated peptide side chains are structurally identical to the monomer molecules of supramolecular polymers. In the hybrid system, covalent chains grow to higher average molar mass relative to chains formed via the same polymerization in the absence of a supramolecular compartment. The supramolecular compartments can be reversibly removed and re-formed to reconstitute the hybrid structure, suggesting soft materials with novel delivery or repair functions.

Supramolecular soft matter encompasses organic materials in which structural units engage in strong and often complex noncovalent interactions to generate specific properties and functions. Structurally, these materials can be organized nanostructures (*1*) or supramolecular polymers (*2*). Supramolecular soft matter has obvious potential to create reversibly dynamic materials, given the finite lifetimes of interunit noncovalent bonds, and development of this area is clearly inspired by biological systems. In cytoskeleton fibers, for example, the monomers are covalent polymers, and it is their reversible noncovalent interactions into a supramolecular polymer that create their dynamic functions in cells (*3*, *4*). Variations in monomer structures (*5*, *6*), covalent templates (*7*), or catalysts (*8*) have facilitated great progress toward the design of supramolecular architectures in solution. However, the integration of covalent and supramolecular polymers into hybrid dynamic structures as a source of function has yet to be achieved.

Here we report the synthesis of polymeric systems based on the simultaneous covalent and noncovalent polymerization of structurally matched monomers. We aimed to explore the nature of hybrid structures that might form during this potentially synergistic process. The covalent polymer (C-Polymer) was designed to form by condensation reactions between an aromatic dialdehyde (monomer **1**) and an aromatic diamine (monomer **2**). These two monomers contained as side chains the amino acid sequence valine–glutamic acid–valine–glutamic acid, connected to the aromatic groups via a dodecyl linkage (Table 1). Monomer **3** of the supramolecular polymer (S-Polymer) (Table 1) is isostructural with the side chains of the C-Polymer and, on the basis of previous results, was expected to form ribbon-shaped supramolecular polymers (*9*). Consistent with previous work on foldamers (*10*–*12*), the C-Polymer was designed to have a sixfold helicoidal conformation, in this case promoted in polar media and stabilized by hydrogen bonds among the peptide segments, as well as π-π stacking interactions between aromatic groups.

To synthesize the C-Polymer, we mixed monomers **1** and **2** in a 1:1 molar ratio in aqueous solution at pH 5 to promote the condensation reaction between aldehydes and amines (*13*). The S-Polymer formed by simply dissolving monomer **3** in water, owing to its strong amphiphilic structure. Cryo–transmission electron microscopy (cryo-TEM) revealed the formation of a heterogeneous collection of one-dimensional (1D) structures in the C-Polymer (Fig. 1A and fig. S9), and the S-Polymer formed the expected ribbon-shaped flat assemblies (Fig. 1B). However, when we mixed solutions of monomers **1**, **2**, and **3** simultaneously in a molar ratio of 1:1:2 at pH 5, the flat assemblies of the S-Polymer did not form, and we instead observed 1D structures with precisely defined cylindrical shape with uniform diameter as the dominant morphology (in a few uncommon sites, thin ribbonlike

Table 1. Chemical structures of monomers 1, 2, and 3.

Monomers	Chemical structures
Monomer **1**	
Monomer **2**	
Monomer **3**	

[1]Department of Chemistry, Northwestern University, 2220 Campus Drive, Evanston, IL 60208, USA. [2]Department of Materials and Science and Engineering, Northwestern University, 2220 Campus Drive, Evanston, IL 60208, USA. [3]Simpson Querrey Institute for BioNanotechnology, Northwestern University, 303 East Superior Street, 11th floor, Chicago, IL 60611, USA. [4]Department of Chemical and Biological Engineering, Northwestern University, 2220 Campus Drive, Evanston, IL 60208, USA. [5]Department of Medicine, Northwestern University, 2220 Campus Drive, Evanston, IL 60208, USA. [6]Department of Biomedical Engineering, Northwestern University, 2220 Campus Drive, Evanston, IL 60208, USA.
*Corresponding author. E-mail: s-stupp@northwestern.edu

Downloaded from on January 31, 2016

defects can be observed) (Fig. 1C and fig. S10). These 1D structures appear well separated, which is possibly the result of the high charge density contributed by the integration of the S-Polymer in the hybrid structure.

We hypothesized that a covalent-noncovalent (CNC) hybrid system was formed by the simultaneous covalent and supramolecular polymerizations. More specifically, we considered that this CNC hybrid integrated distinct covalent and supramolecular compartments as a result of the structural match of their respective monomers (Fig. 1, D to H). In addition, we observed only a homogeneous cylindrical structure, suggesting thorough integration of both

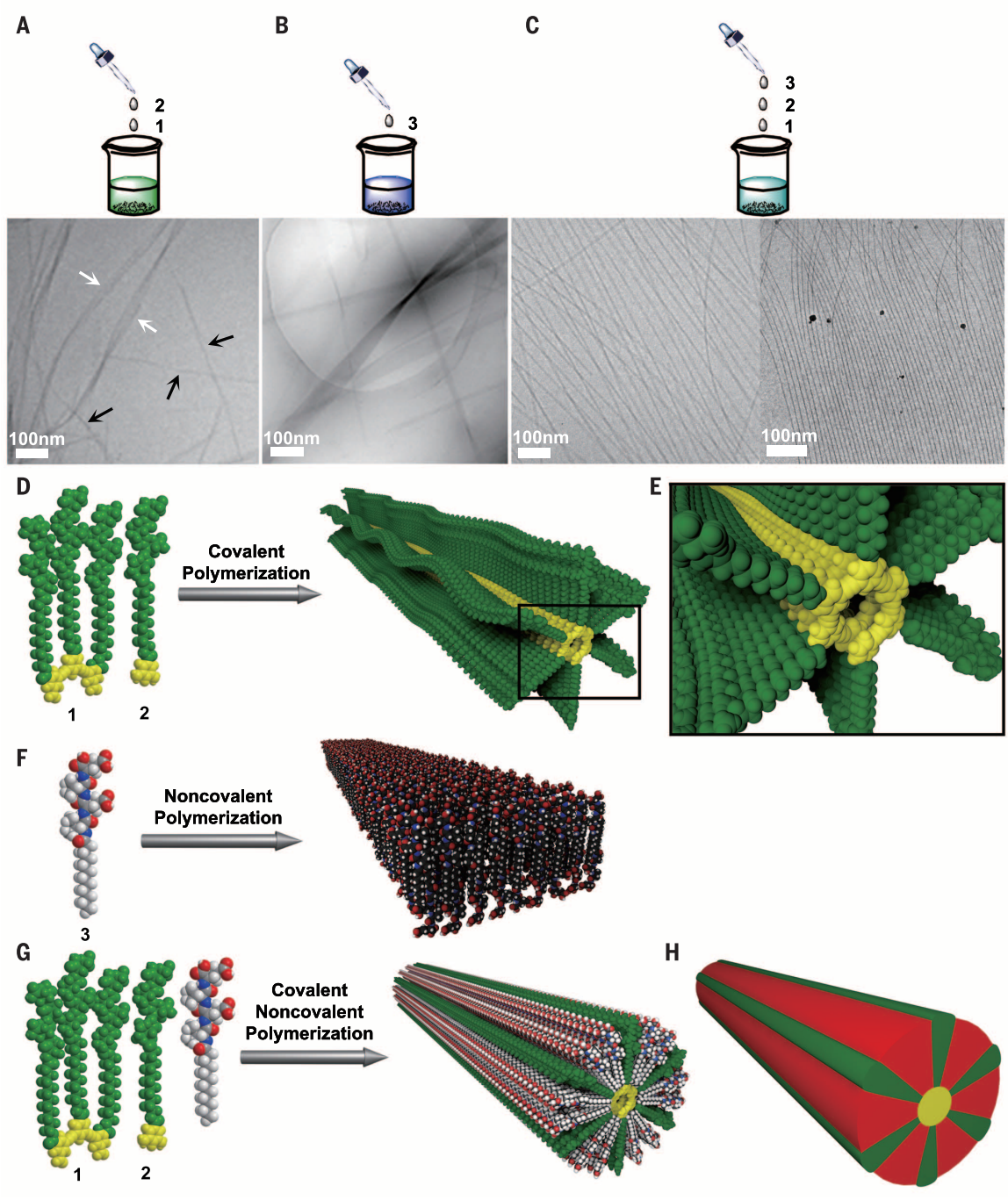


Fig. 1. Hybrid CNC polymers. (**A** to **C**) Cryo-TEM images for (A) the covalent polymer (C-Polymer) obtained by mixing monomers **1** and **2** in a 1:1 molar ratio at pH 5 (white arrows point to ribbonlike segments and black arrows to cylindrical ones), (B) the supramolecular polymer (S-Polymer) formed by monomer **3**, and (C) the CNC hybrid polymer obtained by simultaneously mixing monomers **1**, **2**, and **3** in a molar ratio of 1:1:2 at pH 5. (**D** to **G**) Molecular graphics illustrations of (D) the covalent polymerization of monomers **1** and **2** [including a magnified representation (E)], (F) the supramolecular polymerization of monomer **3**, and (G) the simultaneous covalent and supramolecular polymerizations that yield the hybrid polymer. Phenyl moieties in molecular graphics illustrations in (D), (E), and (G) are shown in yellow. (**H**) Schematic representation of the CNC hybrid polymer consisting of two distinct covalent (green and yellow) and supramolecular (red) compartments.

polymers. Mechanistically, the preference for helical conformation in the C-Polymer and common structural features in all three monomers could guide directional nucleation and growth of supramolecular compartments to create a cylindrical hybrid structure.

The morphologies of the C-Polymer and the CNC hybrid were also investigated using atomic force microscopy (AFM). In the hybrid samples, AFM experiments revealed the uniform, well-separated fibrils observed with cryo-TEM (fig. S12C), whereas the mixture of monomers **1** and **2** formed bundled fibrous structures (fig. S12B). We attribute the bundling (which was not observed with cryo-TEM) to drying effects as water is removed. This bundling was not observed with AFM when all three monomers (**1**, **2**, and ***3***) were mixed simultaneously, providing further evidence of the integration of monomer ***3*** in the hybrid, which should result in highly charged surfaces.

We first used optical spectroscopy to investigate the condensation between monomers **1** and **2** to form the C-Polymer. A 1:1 molar ratio of monomers **1** and **2** in a fresh solution at pH 5, which favors formation of imine bonds for polymerization, yielded a product revealing in its fluorescence spectrum the anticipated excimer emission appearing instantaneously at 430 nm, compared with 358 nm for monomer **1** (Fig. 2A). This shift indicates the existence of strong π-π stacking interactions in the folded backbone of the C-Polymer (*14*). Immediately upon mixing monomers **1**, **2**, and **3**, we observed substantial quenching of the excimer emission characteristic of the C-Polymer, which is expected with lengthening of the folded backbone (*14*). This observation and the absence of monomer emission at 358 nm suggest that the covalent polymerization of monomers **1** and **2** within the hybrid was facilitated by the simultaneous polymerizations (Fig. 2A).

The typical circular dichroism (CD) signals for β-sheet secondary structure in the peptide side chains were observed in the mixture of monomers **1** and **2** (Fig. 2B), whereas only CD signals corresponding to random coil conformation were observed for the individual monomers (fig. S6). These results indicate that attachment of the peptide to the C-Polymer

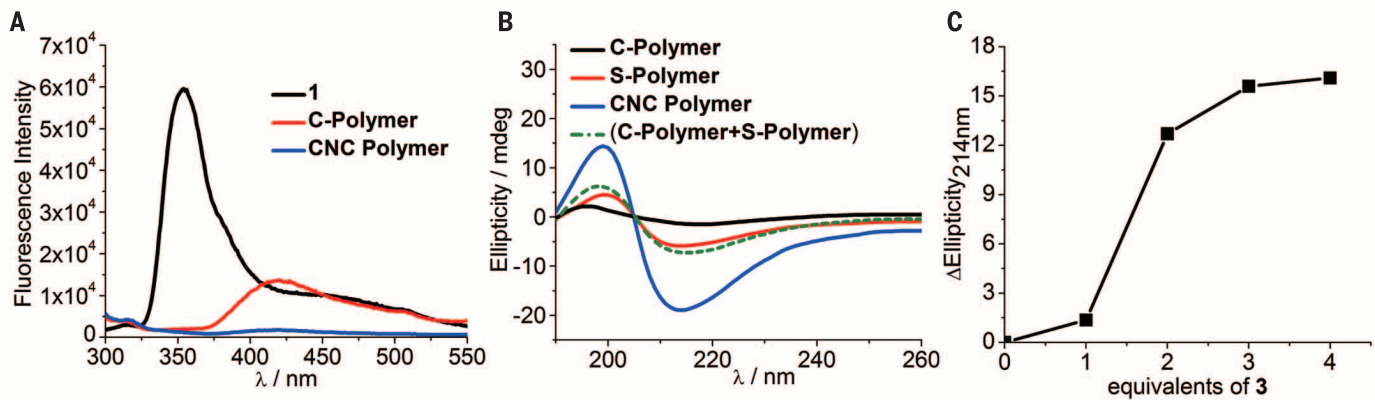


Fig. 2. Spectroscopic characterization. (**A**) Fluorescence spectra of monomer **1**, the C-Polymer, and the hybrid CNC polymer. Fluorescence is measured in units of counts. λ, wavelength. (**B**) CD spectra of the C-Polymer, the S-Polymer, the hybrid CNC polymer, and the sum of the spectra of the C-Polymer and S-Polymer. (**C**) Plot of the difference in CD signal intensity at 214 nm, corresponding to the mixture of all three monomers (**1**, **2**, and **3**) and that of monomer **3** [Δellipticity = CD intensity (mixture) – CD intensity (monomer **3**)], as a function of the added equivalents of monomer **3**. All samples were prepared at pH 5.

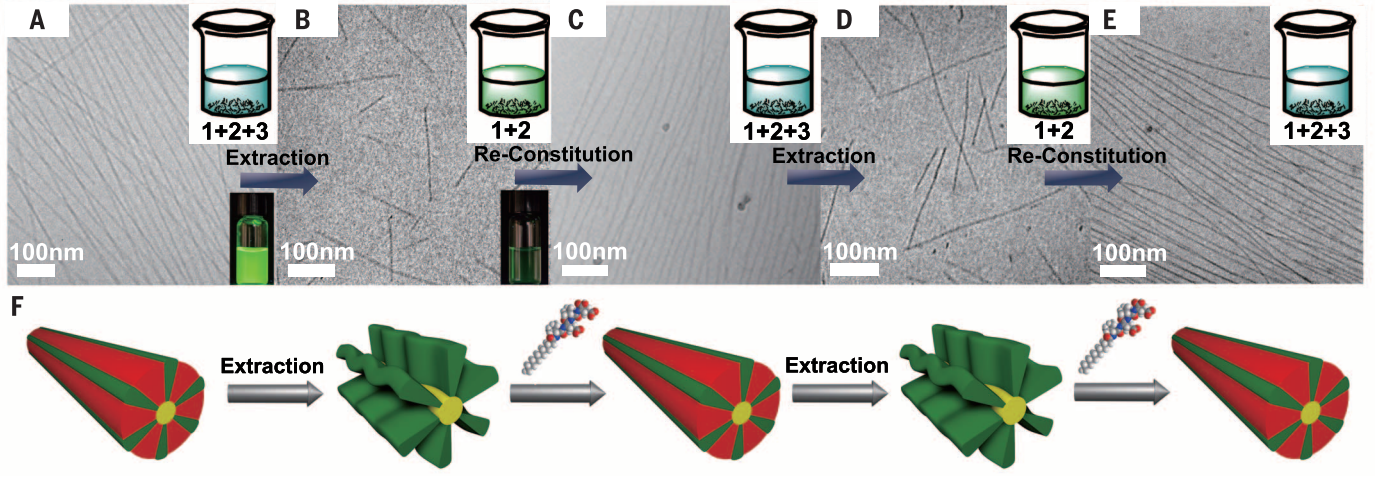


Fig. 3. Extraction and reconstitution. (**A** to **C**) Cryo-TEM image of (A) the CNC hybrid polymer, (B) the same material after extraction of the supramolecular compartments by dialysis, and (C) after reconstitution of the hybrid by adding a fresh solution of monomer **3**. (**D** and **E**) Images corresponding to samples exposed to a second cycle of extraction and reconstitution. (**F**) Schematic representation of the extraction of supramolecular compartments from CNC hybrid polymers and their reconstitution by adding monomer **3**.

backbone as a side chain enhanced formation of the β sheets. In turn, these hydrogen bonds can facilitate the growth of the folded backbone by preorganizing monomers. In addition, the absence of a CD signal in the absorption region of the folded backbone (~300 nm) indicates that the chiral centers in peptide segments are too distant or the dodecyl linkers are too flexible to bias the twist sense of the helical backbone (*15*). When solutions of monomers **1, 2**, and ***3*** were mixed simultaneously, the CD signal for β sheets increased relative to that of the C- or S-Polymer, and the signal intensity was even greater than the sum of both (Fig. 2B). This increase suggests the formation of a highly integrated hybrid structure in which peptide hydrogen bonding is enhanced through synergistic interactions among the three isostructural monomers. The increase in CD intensity depended on the relative concentrations of monomers **1** and **2** versus monomer ***3***, and the saturation of the signal was observed beyond the addition of two equivalents of monomer ***3*** (Fig. 2C). We also used cryo-TEM to examine samples resulting from mixtures of monomers **1**, **2**, and ***3*** with molar ratios of 1:1:1 and 1:1:4. In both mixtures, we observed a heterogeneous population of structures (fig. S11). Although adding one equivalent of monomer ***3*** into monomers **1** and **2** gives rise to formation of short cylindrical fibers and ribbons, the mixture containing four equivalents of monomer ***3*** forms long fibers and ribbons. These results indicate that there is not enough monomer ***3*** in the first case to form the highly defined structure of the CNC hybrid. However, an excess of monomer ***3*** in the second case leads to the formation of the CNC hybrid and a ribbon-shaped S-Polymer. On the basis of CD data and cryo-TEM images, we conclude that the supramolecular compartments are formed only by a finite number of monomer ***3*** molecules per unit length of hybrid structure (Fig. 1G). This is consistent with the well-defined shape and largely uniform diameter of hybrid fibrils.

We tested the possibility of removing the supramolecular compartment from the hybrid CNC polymer and subsequently reconstituting it. We synthesized a fluorescein-labeled version of monomer ***3*** (fl-***3***) to quantify this process. Cryo-TEM experiments showed that extraction of monomer ***3*** from the hybrid by dilution in pH 5 water and dialysis led to the appearance of short fibers (Fig. 3B). Upon addition of fresh monomer ***3*** to the extracted sample, the long cylindrical morphology of the CNC hybrid was recovered (Fig. 3, A to C), and when the extraction and reconstitution cycle was repeated, identical results were obtained (Fig. 3, D and E). Based on the fluorescence intensity of fl-***3*** in the polymer solution, 94% of monomer ***3*** was removed from the hybrid after dilution and dialysis (fig. S17).

To verify covalent polymerization in both the C-Polymer and the CNC hybrid, we used Fourier transform infrared (FTIR) spectroscopy, matrix-assisted laser desorption/ionization–time-of-flight (MALDI-TOF) mass spectrometry, and size exclusion chromatography with multiangle light scattering (SEC-MALS). The FTIR measurements provided evidence of imine bond formation in both the C-Polymer and the CNC hybrid (fig. S3), as well as the presence of hydrogen bonds in all samples (fig. S3). MALDI-TOF studies also confirmed the formation of covalent polymer upon mixing monomers **1** and **2** or monomers **1**, **2**, and ***3***, as indicated by an appropriate increase in molar mass in both cases (fig. S4). The average molecular weight when **1** and **2** were mixed was determined by SEC-MALS to be on the order of 14 kDa, but a much higher molecular weight of 250 kDa was measured by this technique for the covalent component of the CNC hybrid (fig. S5 and table S1). Based on the average molecular weight measured for the covalent polymer component of the hybrid and the cryo-TEM images, we conclude that cylindrical fibers contain multiple chains condensed by the synergistic secondary interactions among the three structural units. Overall, these results demonstrate the formation of a covalent polymer by mixing monomers **1** and **2** or within the hybrid structure. Furthermore, the results also strongly support the notion that formation of the supramolecular compartment in the hybrid effectively catalyzes covalent polymerization.

We analyzed the covalent component in the CNC hybrid after extraction of the supramolecular compartment using fluorescence and SEC-MALS experiments. Fluorescence spectra of the covalent component after removal of the supramolecular compartment revealed the recovery of quenched excimer emission over time (fig. S18). This result implies that, after removal of monomer ***3***, the covalent compartment is less stable and dissociates into short covalent chains. In addition, the average molecular weight of the covalent compartment aged for 10 days was determined by SEC-MALS to be ~16 kDa (fig. S18), a decrease of more than one order of magnitude relative to the original covalent component within the hybrid. Both results suggest that the CNC hybrid is more thermodynamically stable than the C-Polymer. Furthermore, CD data as a function of temperature showed that the signals for both the C-Polymer and the CNC hybrid decreased upon heating as a result of thermally induced depolymerization, as indicated by fluorescence results (fig. S7). However, in the CNC hybrid, depolymerization was found to start at a temperature 5°C higher than in the C-Polymer. Again, this finding provides evidence for the stability of the hybrid as a result of the synergistic secondary interactions among its three different structural units. The results also provide mechanistic insight into the CNC hybrid polymerization, strongly suggesting that the synergistic interactions are responsible for the enhanced levels of covalent polymerization in the CNC hybrid structure.

We used small-angle x-ray scattering (SAXS) experiments to further characterize the morphologies of the various supramolecular assemblies in solution. For monomers **2** and ***3***, the scattering signals showed a –2 slope in the low-q area (q, modulus of the momentum transfer vector), demonstrating the formation of flat structures in solution (Fig. 4A) (*16*, *17*). The C-Polymer exhibited a –1.3 slope, which suggests a heterogeneous mixture of morphologies, consistent with our cryo-TEM observations. In contrast, the CNC hybrid displayed a slope of nearly –1 (Fig. 4A), indicating the formation of highly 1D cylindrical structures without any evidence of the flat structures observed for monomers **2** and ***3*** (*17*, *18*). Additional geometrical information of the assemblies of the hybrid could be obtained by fitting the scattering curves to a core-shell cylinder model. The diameter for the hybrid was estimated to be 5.9 nm, which is comparable to our observations with cryo-TEM.

To gain insight into the mechanism for the formation of the hybrid CNC polymer, we monitored changes in the CD spectrum over time in different types of samples. As shown in Fig. 4B, a mixture of monomers **1** and **2** undergoing covalent polymerization revealed an increasing value of ellipticity that saturates after several hours. The CNC polymer formed by mixing all three monomers simultaneously exhibited a rapid rise in ellipticity, suggesting nucleation and growth of an ordered structure. At the same time, the invariant ellipticity of the S-Polymer formed by monomer ***3*** indicates that the increase in ellipticity of the CNC hybrid did not arise from independent supramolecular polymerization, but rather from the simultaneous supramolecular and covalent polymerizations. The faster kinetics associated with CNC hybrid formation compared with that of the C-Polymer strongly supports a distinctive mechanism involving simultaneous covalent and supramolecular reactions. These observations could explain why the average molecular weight measured for the covalent compartment of the CNC polymer is so much higher than that of the C-Polymer. In other words, the data are consistent with a synergistic enhancement of C-Polymer formation by supramolecular contacts with monomer ***3***.

We used CD spectroscopy to follow the interaction between a pre-formed C-Polymer and monomer ***3***. When different amounts of monomer ***3*** were added to the pre-formed C-Polymer, we observed only a small initial increase in CD signal intensity in the β-sheet region (Fig. 4C). However, when samples with an excess of monomer ***3*** aged for 2 days, the CD intensity increased and was comparable to that observed when the hybrid CNC polymers formed through the simultaneous mixing of monomers **1**, **2**, and ***3*** (Fig. 4C). Our SEC-MALS results indicate that the average molecular weight of the covalent component in solutions containing two equivalents of monomer ***3*** increased with time from 21.1 to 190 kDa (table S1). The fact that CD signatures of the ordered hybrid are not observed immediately upon mixing

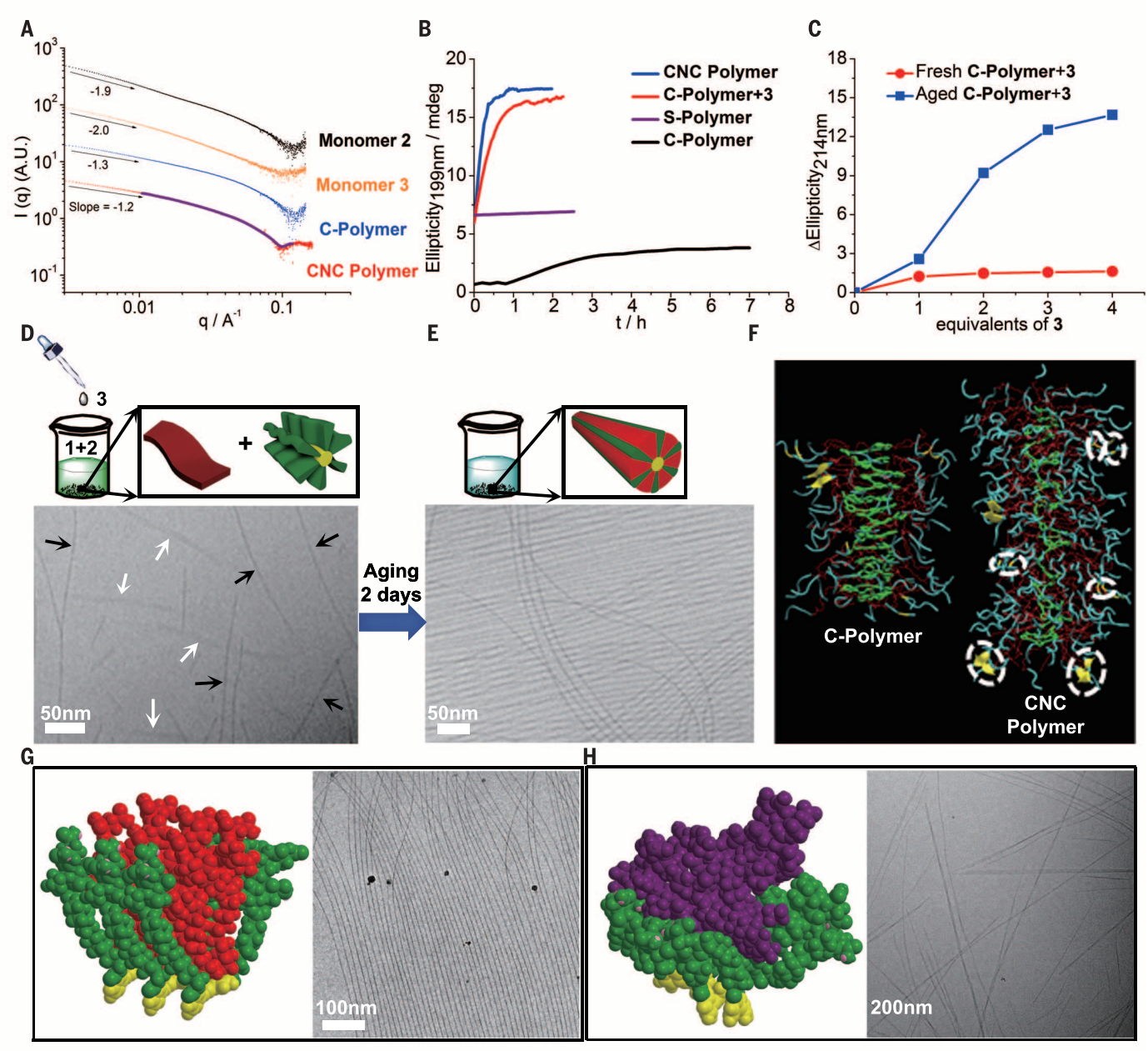


Fig. 4. Results of SAXS, cryo-TEM, and MD modeling experiments. (**A**) SAXS curves and their corresponding slopes in the linear region obtained from solutions of monomer **2**, monomer **3**, the C-Polymer, and the hybrid CNC polymer (scattering curves were offset for clarity). The fitting curve for the scattering data of the CNC hybrid is shown in purple. *q*, modulus of the momentum transfer vector; *I*, scattered intensity; A.U., arbitrary units. (**B**) Change in ellipticity at 199 nm as a function of time during formation of the C-Polymer, S-Polymer, and CNC hybrid polymer during simultaneous covalent and supramolecular polymerization (by mixing monomers **1**, **2**, and **3**), as well as the CNC hybrid polymer by adding monomer **3** to a pre-formed C-Polymer. *t*, time in hours. (**C**) Plot of the difference in CD signal intensity at 214 nm, corresponding to the mixture of **1** and **2** and that of monomer **3** [Δellipticity = CD intensity (mixture) – CD intensity (monomer **3**)], as a function of the added equivalents of monomer **3**. The plot shows one curve corresponding to a fresh sample of C-Polymer mixed with **3** and another corresponding to an aged sample. (**D** and **E**) Cryo-TEM images of a sample corresponding to a fresh mixture of a pre-formed C-Polymer and monomer **3** (D) and a sample of the same mixture aged for 2 days (E) (both samples contained two equivalents of monomer **3**). Black and white arrows in (D) indicate cylindrical fibers and ribbons, respectively. (**F**) Results from an atomistic MD modeling of the C-Polymer (left) and the CNC hybrid polymer (right) (green, folded aromatic backbone; red, flexible dodecyl linker; blue, the turn and random coil; yellow, β sheet). The white dashed ellipsoids indicate formation of hydrogen bonding between peptides in covalent and supramolecular compartments. (**G** and **H**) MM2 MD modeling (see supplementary materials) of the matched structures (monomers **1**, **2**, and **3**) next to the cryo-TEM image of the system prepared by mixing **1**, **2**, and **3** in a molar ratio of 1:1:2 at pH 5 (G) and, similarly, of the mismatched structures (monomers **1**, **2**, and **4**) with the corresponding cryo-TEM image (H) (red, monomer **3**; purple, monomer **4**; green, side chains of the covalent compartment; yellow, aromatic units of the covalent compartment).

could be explained by diffusional barriers within the system imposed by the pre-formed covalent polymer.

Both SAXS and cryo-TEM experiments supported our interpretation of the CD and molecular weight data. In SAXS experiments, the fresh mixture of pre-formed C-Polymer and monomer **3** revealed a slope of –1.4 in the low-q region, indicating a heterogeneous mixture of morphologies. In marked contrast, we measured a slope of approximately –1 for the aged sample, thus demonstrating the possibility of forming the well-defined cylindrical structure of the CNC hybrid by mixing monomer **3** with pre-formed covalent polymer. In addition, fitting the scattering data to a core-shell cylindrical model yields effectively the same diameter for structures in the aged sample and samples obtained by the simultaneous polymerization of monomers **1**, **2**, and **3** (fig. S19). Furthermore, cryo-TEM also reveals virtually identical morphologies in these two types of samples (Fig. 4, D and E).

We hypothesize that the structural match of the supramolecular monomer with the side chains of the covalent compartment plays a critical role in the integration of the two compartments and the catalytic effect of the supramolecular polymerization on covalent polycondensation. To test this hypothesis, we used a monomer (**4**; see supplementary materials) for the S-polymer that would not easily interact noncovalently with the side chains of the C-Polymer. This monomer was also a peptide amphiphile with the same general structural features as monomer **3**. However, the structural match in monomer **4** relative to the side chains is lost, both in the length of the hydrophobic region (four additional methylene groups) and its peptide sequence (a different sequence of two amino acids present in monomer *3*, valine and glutamic acid, plus two additional glycine residues). Cryo-TEM images of the mismatched system reveal a heterogeneous mixture of morphologies formed by combining monomers **1**, **2**, and **4** in the molar ratio of 1:1:2 (Fig. 4H and fig. S20). Additionally, in this system we observed only a slight difference in CD intensity after mixing monomers **1**, **2**, and **4** (fig. S21). These results demonstrate that the new supramolecular monomer does not integrate well with covalent compartments and does not form the distinct hybrid CNC polymer. The average molecular weight of the covalent compartments in the presence of monomer **4** was characterized by SEC-MALS to be ~18 kDa, more than an order magnitude lower than that of the matched system (fig. S21). We conclude from these results that the structural mismatch between monomer **4** and the side chains of the C-Polymer does not promote synergistic interactions responsible for stabilization of the C-Polymer by the S-Polymer, which in turn results in greater growth of the C-Polymer within the CNC hybrid.

In previous work (*19*–*22*), including our own (*23*–*25*), systems have been studied in which covalent polymerization is triggered after supramolecular self-assembly of monomers, leading to internally ordered covalent polymers. There is also another system in which an ordered covalent polymer was obtained after polymerization of the monomer in a solvent that does not promote formation of a supramolecular template (*26*). In our current work, a pathway is described to obtain hybrid polymers in which supramolecular and covalent polymers are integrated. The supramolecular compartment in these systems can be temporarily removed and reconstituted by simply adding its monomer again. Furthermore, we discovered that the supramolecular compartment within the hybrid catalyzes covalent polymerization.

We carried out atomistic molecular dynamics (MD) simulations on the C-Polymer and the hybrid CNC polymer (Fig. 4F). These MD simulations were performed for 24 molecules each of monomers **1** and **2** and 48 molecules of monomer **3** in the presence of water and sodium ions. Details of these simulations can be found in the supplementary materials and in a previous publication (*27*). The simulations yielded a hybrid CNC structure with a diameter equal to 7 nm, which is reasonably consistent with experimental results (fig. S23). The simulations showed also that β sheets formed among 15 peptide segments within the C-Polymer and 22 peptide segments in the hybrid CNC polymer (fig. S23). Most of the β sheets within the CNC hybrids formed between the supramolecular and covalent compartments (fig. S23 and MD simulations in the supplementary materials). We believe that the integration of the two distinct compartments into the CNC hybrids benefits from these secondary bonds, along with other noncovalent interactions. This integration among isostructural components in all three monomers was an important molecular design criterion.

These polymers self-organize to contain distinct covalent and supramolecular compartments that allow removal and re-formation of the supramolecular component, thus reconstituting the hybrid polymer. These structures could provide functional platforms for novel modes of molecular delivery or repair of structures, as hybrids are disassembled and re-formed by simple addition of small molecules. Our experimental results on these systems also suggest that supramolecular polymerizations can be used to catalyze the formation of covalent macromolecules.

REFERENCES AND NOTES

1. S. I. Stupp *et al*., *Science* **276**, 384–389 (1997).
2. T. Aida, E. W. Meijer, S. I. Stupp, *Science* **335**, 813–817 (2012).
3. A. J. Ridley, A. Hall, *Cell* **70**, 389–399 (1992).
4. C. G. Dos Remedios *et al*., *Physiol. Rev.* **83**, 433–473 (2003).
5. T. Jiang *et al*., *J. Am. Chem. Soc.* **136**, 4300–4308 (2014).
6. H. Cui, A. G. Cheetham, E. T. Pashuck, S. I. Stupp, *J. Am. Chem. Soc.* **136**, 12461–12468 (2014).
7. J. M. A. Carnall *et al*., *Science* **327**, 1502–1506 (2010).
8. A. R. Hirst *et al*., *Nat. Chem.* **2**, 1089–1094 (2010).
9. H. Cui, T. Muraoka, A. G. Cheetham, S. I. Stupp, *Nano Lett.* **9**, 945–951 (2009).
10. D. J. Hill, M. J. Mio, R. B. Prince, T. S. Hughes, J. S. Moore, *Chem. Rev.* **101**, 3893–4012 (2001).
11. G. Guichard, I. Huc, *Chem. Commun.* **47**, 5933–5941 (2011).
12. M. T. Stone, J. M. Heemstra, J. S. Moore, *Acc. Chem. Res.* **39**, 11–20 (2006).
13. C. Godoy-Alcántar, A. K. Yatsimirsky, J. M. Lehn, *J. Phys. Org. Chem.* **18**, 979–985 (2005).
14. R. B. Prince, J. G. Saven, P. G. Wolynes, J. S. Moore, *J. Am. Chem. Soc.* **121**, 3114–3121 (1999).
15. R. B. Prince, L. Brunsveld, E. W. Meijer, J. S. Moore, *Angew. Chem. Int. Ed.* **39**, 228–230 (2000).
16. J.-B. Guilbaud, A. Saiani, *Chem. Soc. Rev.* **40**, 1200–1210 (2011).
17. R.-J. Roe, *Methods of X-ray and Neutron Scattering in Polymer Science* (Oxford Univ. Press, 2000).
18. C. L. Pizzey *et al*., *J. Chem. Phys.* **129**, 095103 (2008).
19. K. Sada, M. Takeuchi, N. Fujita, M. Numata, S. Shinkai, *Chem. Soc. Rev.* **36**, 415–435 (2007).
20. D. Wu *et al*., *Chem. Rev.* **112**, 3959–4015 (2012).
21. T. Delclos *et al*., *Nano Lett.* **8**, 1929–1935 (2008).
22. J. Lee *et al*., *Nat. Chem.* **6**, 97–103 (2014).
23. S. I. Stupp, S. Son, H. C. Lin, L. S. Li, *Science* **259**, 59–63 (1993).
24. J. D. Hartgerink, E. Beniash, S. I. Stupp, *Science* **294**, 1684–1688 (2001).
25. L. Hsu, G. L. Cvetanovich, S. I. Stupp, *J. Am. Chem. Soc.* **130**, 3892–3899 (2008).
26. W. Jin *et al*., *J. Am. Chem. Soc.* **127**, 8284–8285 (2005).
27. O. S. Lee, S. I. Stupp, G. C. Schatz, *J. Am. Chem. Soc.* **133**, 3677–3683 (2011).

ACKNOWLEDGMENTS

The synthesis and structural characterization of this work was supported by the NSF under award no. DMR-1508731. Experimental work on SAXS was supported by the U.S. Department of Energy (DOE), Office of Science, Office of Basic Energy Sciences, under award no. DE-FG02-00ER45810. MD simulations were supported by the Center for Bio-Inspired Energy Science, an Energy Frontier Research Center funded by DOE, Office of Science, Basic Energy Sciences, under award no. DE-SC0000989 (T.Y. and G.C.S.). We thank A. Koltonow for help with AFM measurements and M. Seniw for help with the preparation of graphics. We also acknowledge S. Kewalramani for helpful discussions on the SAXS data. Use of the Advanced Photon Source (APS) was supported by DOE, Office of Science, Office of Basic Energy Sciences, under contract no. DE-AC02-06CH11357. SAXS experiments were performed at the DuPont–Northwestern–Dow Collaborative Access Team (DND-CAT) located at Sector 5 of APS. DND-CAT is supported by E. I. DuPont de Nemours and Co., The Dow Chemical Company, and Northwestern University. We thank the Biological Imaging Facility at Northwestern and the Electron Probe Instrumentation Center facilities of the Northwestern University Atomic and Nanoscale Characterization Experimental Center for the use of TEM. Nuclear magnetic resonance and MS equipment at the Integrated Molecular Structure Education and Research Center was supported by the NSF under grant no. CHE-9871268. We are also grateful to the Peptide Synthesis Core at the Simpson Querrey Institute for BioNanotechnology and Keck Biophysics Facility for instrument use.

SUPPLEMENTARY MATERIALS

www.sciencemag.org/content/351/6272/497/suppl/DC1
Materials and Methods
Supplementary Text
Schemes S1 to S3
Figs. S1 to S23
Table S1
References (*28*–*38*)

9 September 2015; accepted 31 December 2015
10.1126/science.aad4091

CYSTIC FIBROSIS

Airway acidification initiates host defense abnormalities in cystic fibrosis mice

Viral S. Shah,[1,2] David K. Meyerholz,[3] Xiao Xiao Tang,[1,4] Leah Reznikov,[1] Mahmoud Abou Alaiwa,[1] Sarah E. Ernst,[1,4] Philip H. Karp,[1,4] Christine L. Wohlford-Lenane,[5] Kristopher P. Heilmann,[6] Mariah R. Leidinger,[3] Patrick D. Allen,[1] Joseph Zabner,[1] Paul B. McCray Jr.,[5,6] Lynda S. Ostedgaard,[1] David A. Stoltz,[1,2,7] Christoph O. Randak,[5] Michael J. Welsh[1,2,4]*

Cystic fibrosis (CF) is caused by mutations in the gene that encodes the cystic fibrosis transmembrane conductance regulator (CFTR) anion channel. In humans and pigs, the loss of CFTR impairs respiratory host defenses, causing airway infection. But CF mice are spared. We found that in all three species, CFTR secreted bicarbonate into airway surface liquid. In humans and pigs lacking CFTR, unchecked H^+ secretion by the nongastric H^+/K^+ adenosine triphosphatase (ATP12A) acidified airway surface liquid, which impaired airway host defenses. In contrast, mouse airways expressed little ATP12A and secreted minimal H^+; consequently, airway surface liquid in CF and non-CF mice had similar pH. Inhibiting ATP12A reversed host defense abnormalities in human and pig airways. Conversely, expressing ATP12A in CF mouse airways acidified airway surface liquid, impaired defenses, and increased airway bacteria. These findings help explain why CF mice are protected from infection and nominate ATP12A as a potential therapeutic target for CF.

A thin layer of airway surface liquid (ASL) is the point of contact between an organism and potential pathogens from the environment. To maintain sterile lungs, ASL contains several innate defenses, including a complex mixture of antimicrobials that kill bacteria, mucociliary transport that carries pathogens out of the lung, and phagocytic cells (*1*–*3*). In the genetic disease cystic fibrosis (CF) (*4*, *5*), the loss of cystic fibrosis transmembrane conductance regulator (CFTR) impairs airway host defenses, initiating a cascade of bacterial airway infection, inflammation, and progressive destruction (*6*). After the discovery that mutations in the human *CFTR* gene cause CF, mice were produced with a disrupted *Cftr* gene (*7*, *8*). Unexpectedly, airways of CF mice cleared large bacterial inocula and did not develop the spontaneous bacterial infections typical of CF (*7*, *8*). Speculation about why CF mice fail to develop airway infections has relied on correlations. Compared with humans, mice have only a few submucosal glands, have different airway epithelial cell types, express other anion channels, and are smaller—features that correlate with absence of CF-related infections (*7*–*9*).

The recent finding that CF pigs develop airway disease that mirrors that of CF in humans (*10*, *11*) provided us with an opportunity to compare humans, pigs, and mice. We reasoned that a better understanding of why CF mice do not develop airway infections might offer new insights into the molecular basis of respiratory infections in humans with CF. A potential mechanism emerged with the discovery that a loss of CFTR-mediated HCO_3^- secretion and an acidic pH impair at least two airway host defense mechanisms. These defects inhibit the killing of bacteria in ASL (*12*, *13*) (fig. S1). They also alter ASL and mucus viscosity and impede mucociliary transport (*14*, *15*). In addition, they increase mucus viscoelasticity in other organs (*16*, *17*). We therefore explored whether differences between the pH of ASL in humans, pigs, and mice might account for differences in host defense properties. We found that the loss of CFTR reduced ASL pH in differentiated cultures of pig airway epithelia and in vivo, consistent with earlier findings (Fig. 1, A and B) (*12*). Loss of CFTR also reduced ASL pH in cultures of human airway epithelia (Fig. 1A) (*18*). In vivo studies of human CF neonates also found a reduced ASL pH (*19*), although studies of older people with CF yielded variable results (*19*–*21*). In contrast, in mice, the loss of CFTR did not reduce ASL pH either in vitro or in vivo (Fig. 1, A and B) (*22*).

Ca^{2+}-activated Cl^- channels might compensate for the loss of CFTR-mediated HCO_3^- secretion and prevent ASL acidification in CF mice; Ca^{2+}-activated Cl^- channels are abundant in mouse but not in human airways (*9*, *23*, *24*). Therefore, we predicted that pig airways would exhibit few Ca^{2+}-activated anion channels. We found transcripts for the Ca^{2+}-activated anion channel TMEM16A (anoctamin-1) in CF airway epithelia in a human:pig:mouse ratio of 1:9:18 (Fig. 1C). CF epithelia exhibited Ca^{2+}-stimulated anion secretion in a human:pig:mouse ratio of 1:5:10 (Fig. 1D). Adding carbachol, a Ca^{2+}-mediated secretagogue, elevated ASL pH by 0.02 ± 0.01 units in human, 0.11 ± 0.02 units in pig, and 0.09 ± 0.03 units in mouse epithelia (Fig. 1E). Thus, pig airway epithelia exhibit substantial Ca^{2+}-activated anion secretion, yet they develop airway infections. Although these data do not disprove the proposal that Ca^{2+}-activated anion channels prevent infection in CF mice, they suggest that other factors may be important.

We also reasoned that CF mice might not have an abnormally acidic ASL pH if there was little CFTR in non-CF mouse airways (*25*). To test CFTR activity, we applied forskolin and IBMX (3-isobutyl-1-methylxanthine) to elevate intracellular cyclic adenosine monophosphate (cAMP) and phosphorylate CFTR. Increasing cAMP stimulated HCO_3^- secretion in non-CF epithelia of all three species (Fig. 1F) (*18*, *26*, *27*). Moreover, stimulating HCO_3^- secretion elevated ASL pH in non-CF epithelia of all three species (Fig. 1G). These data suggest that the lack of CFTR alone does not explain CF–versus–non-CF differences in ASL pH among species. We expected that without CFTR, cAMP would merely fail to alkalinize ASL; unexpectedly, in CF pig and human epithelia, cAMP stimulation reduced ASL pH (Fig. 1H). In mice, the loss of CFTR prevented cAMP-induced alkalinization, but, in contrast to CF pigs and humans, it did not lower ASL pH.

These results suggest that pigs and humans have a mechanism that acidifies ASL and that this mechanism is absent or less efficient in mice. To focus selectively on H^+ secretion, we removed HCO_3^- and CO_2 from the basolateral solution and replaced ASL with a small amount of nonbuffered solution at pH 7. Non-CF pig and human epithelia rapidly acidified the apical solution, whereas non-CF mouse epithelia acidified at about one-sixth the rate (Fig. 2A). CF epithelia yielded similar results (Fig. 2B). Although several epithelial properties influence ASL pH, less H^+ secretion in mice is consistent with a higher ASL pH in CF mice than in CF pigs or humans (Fig. 1A).

To determine which transporters secrete H^+ in pig airways, we assessed several candidates (*28*–*30*). Of the transcripts evaluated, those for ATP12A [the α subunit of the nongastric H^+/K^+ adenosine triphosphatase (ATPase)] and the a1 and a2 subunits of V-type ATPase were the most abundant in airways, and levels were similar for CF and non-CF pigs (fig. S2). To test for function of H^+ secretory proteins, we applied pharmacological inhibitors to the apical surface

[1]Department of Medicine, University of Iowa, Iowa City, IA 52242, USA. [2]Department of Molecular Physiology and Biophysics, Pappajohn Biomedical Institute, Roy J. and Lucille A. Carver College of Medicine, University of Iowa, Iowa City, IA 52242, USA. [3]Department of Pathology, University of Iowa, Iowa City, IA 52242, USA. [4]Howard Hughes Medical Institute, University of Iowa, Iowa City, IA 52242, USA. [5]Department of Pediatrics University of Iowa, Iowa City, IA 52242, USA. [6]Department of Microbiology, University of Iowa, Iowa City, IA 52242, USA. [7]Department of Biomedical Engineering, College of Engineering, University of Iowa, Iowa City, IA 52242, USA.
*Corresponding author. E-mail: michael-welsh@uiowa.edu

Downloaded from on January 31, 2016

and found that ouabain, which inhibits ATP12A, increased ASL pH (Fig. 2C and figs. S3 and S4). ASL contains 20 to 40 mM K^+ (*12*), which would be required for ATP12A activity; removing apical K^+ prevented H^+ secretion (Fig. 2D). Inhibition of *ATP12A* by small interfering RNA (siRNA) also increased ASL pH, further supporting a role for ATP12A (Fig. 2E and fig. S5A). Previous reports indicate that elevating cAMP stimulates ATP12A activity (*31*). Consistent with that, apical ouabain and *ATP12A* siRNA inhibited cAMP-stimulated ASL acidification (fig. S5, B to D). Although ouabain also inhibits the basolateral Na^+/K^+ ATPase, these effects of apical ouabain did not arise from Na^+/K^+ ATPase inhibition (fig. S6).

On the basis of these results, we hypothesized that in the absence of CFTR, ATP12A acidifies ASL in pigs and humans, which impairs factors associated with airway defense, but that this process does not occur or is minimal in CF mice. Consistent with these ideas, mouse airways had only 1 to 10% as many *ATP12A* transcripts (Fig. 2F). Immunohistochemical staining revealed ATP12A at the apical surface of human and pig but not mouse airways (Fig. 2G). ATP12A associates with a β subunit, including the Na^+/K^+ ATPase β subunit (ATP1B1) (*28*). Pig and human epithelia showed apical ATP1B1 immunostaining in addition to basolateral staining, whereas in mouse airways, ATP1B1 immunostaining was primarily basolateral (fig. S8). Our hypotheses point to two predictions that can be tested experimentally. The first is that ATP12A is required for ASL acidification and host defense abnormalities in CF pigs. The second is that expressing ATP12A in CF mouse airways would be sufficient to reduce ASL pH and create host defense abnormalities.

To test the first prediction, we inhibited ATP12A with apical ouabain and found that it raised ASL pH in primary cultures of pig airway epithelia (Fig. 3A). We assayed antibacterial activity by briefly touching the ASL with a gold grid coated with *Staphylococcus aureus* and then determining the percentage of bacteria killed (*12*). Apical ouabain increased the killing of *S. aureus* (Fig. 3B). We also assayed ASL viscosity, which is increased in CF and may contribute to impaired mucociliary transport (*15*, *32*). We measured fluorescence recovery after photobleaching (*32*) and found that apical ouabain reduced viscosity (Fig. 3C). After we applied apical ouabain, the pH, antibacterial activity, and viscosity of CF ASL became similar to those of non-CF ASL.

To test the relevance of these findings in vivo, we studied pigs. We surgically created a small tracheal window and applied ouabain. As observed in vitro, ouabain increased ASL pH and the killing of *S. aureus* in CF pigs (Fig. 3, D and E). We also measured the effect of apical ouabain on the ASL pH of human epithelia; applying apical ouabain increased ASL pH (Fig. 3F). These data are consistent with a report implicating ATP12A in H^+ secretion in human cultures (*18*). The increase in ASL pH enhanced bacterial killing and reduced ASL viscosity (Fig. 3, G and H). These results suggest that inhibiting ATP12A would also elevate ASL pH in non-CF pigs and humans and improve host defense; supporting this idea, ouabain had similar effects in non-CF as in CF pigs and humans, both in vitro and in vivo (Fig. 3, A to H).

We next tested the second prediction—i.e., that expressing ATP12A in airways of CF mice would decrease ASL pH and generate host defense abnormalities. We treated cultured mouse airway epithelia with an adenovirus encoding *ATP12A* and found that it acidified ASL (Fig. 4A and figs. S13 to S15). Apical ouabain reversed the effect of ATP12A expression, increasing ASL pH (fig. S16), a result that further supports the conclusion that ATP12A acidifies ASL. ATP12A expression also impaired bacterial killing and increased ASL viscosity in CF mouse epithelia (Fig. 4, B and C).

To test the effects of ATP12A in vivo, we instilled adenovirus expressing *ATP12A* into the tracheae of CF mice. ATP12A reduced ASL pH

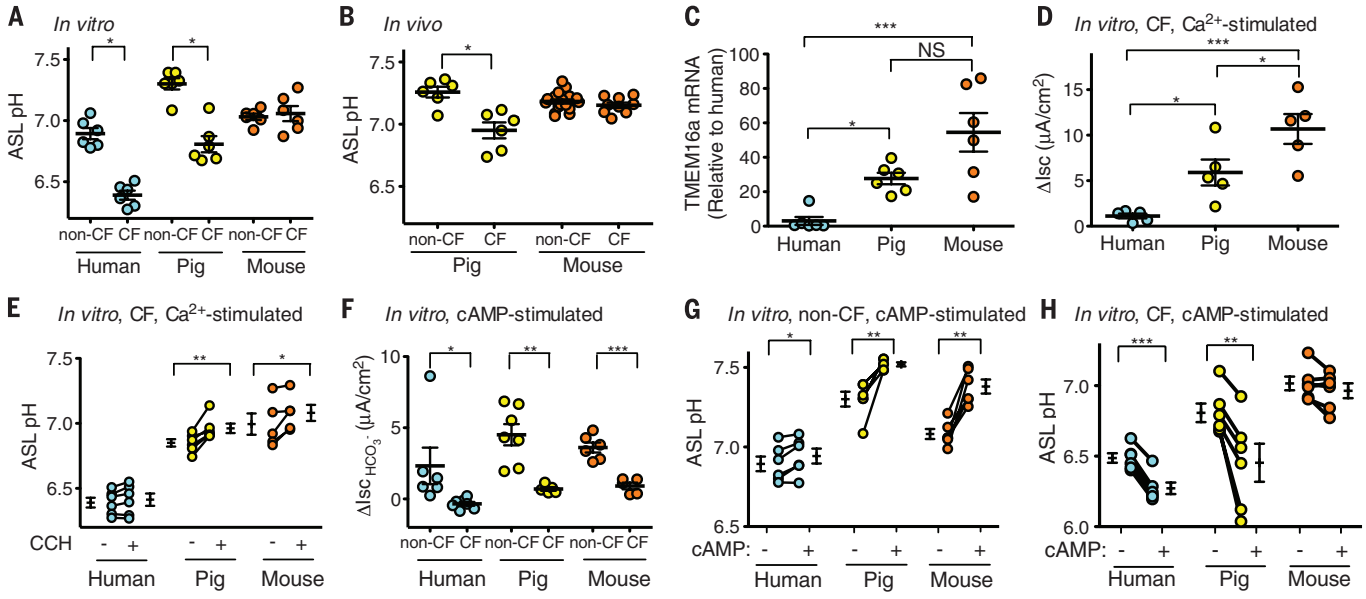


Fig. 1. ASL pH is abnormally acidic in CF pigs and humans, but not in CF mice. (**A**) ASL pH measured in differentiated primary airway epithelial cultures from humans, pigs, and mice using SNARF-dextran (n = 6). The basolateral solution contained 25 mM HCO_3^-, and the atmosphere contained 5% CO_2. (**B**) ASL pH measured in vivo on tracheal surfaces of newborn pigs and mature mice using a pH-sensitive optode (n = 6 for non-CF and CF pigs, 18 for non-CF mice, and 9 for CF mice). (**C**) *TMEM16a* mRNA expression in CF human, pig, and mouse cultured airway epithelia (n = 6). (**D**) Change in the short-circuit current (Δlsc) after adding 1 μM ionomycin basolaterally to cultured CF airway epithelia studied in Ussing chambers (n = 5). The solution contained 140 mM Cl^- bilaterally without HCO_3^- and CO_2. (**E**) ASL pH before and after adding the Ca^{2+}-mediated secretagogue carbachol (CCH, 200 μM) to basolateral surfaces of CF epithelia in the presence of HCO_3^- and CO_2 (n = 6 pigs and humans and 5 mice. (**F**) Δlsc induced by adding 10 μM forskolin and 100 μM IBMX to increase intracellular cAMP (n = 5 for CF pigs and mice, 6 for non-CF humans and mice, and 7 for non-CF pigs and CF humans). The solution was free of Cl^- and contained 25 mM HCO_3^- with a 5% CO_2 atmosphere. (**G** and **H**) ASL pH in non-CF and CF pig, human, and mouse cultured airway epithelia before and after basolateral addition of 10 μM forskolin and 100 μM IBMX to increase cAMP (n = 6). In all panels, each data point or pair of data points is from a different animal or human, and bars indicate means ± SEM. Analysis of variance (ANOVA) with Tukey's multiple comparison test [(C) and (D)] or paired [(E), (G), and (H)] or unpaired [(A), (B), and (F)] Student's t tests were used to assess statistical significance. *P < 0.05; **P < 0.01; ***P < 0.001; NS, not significant.

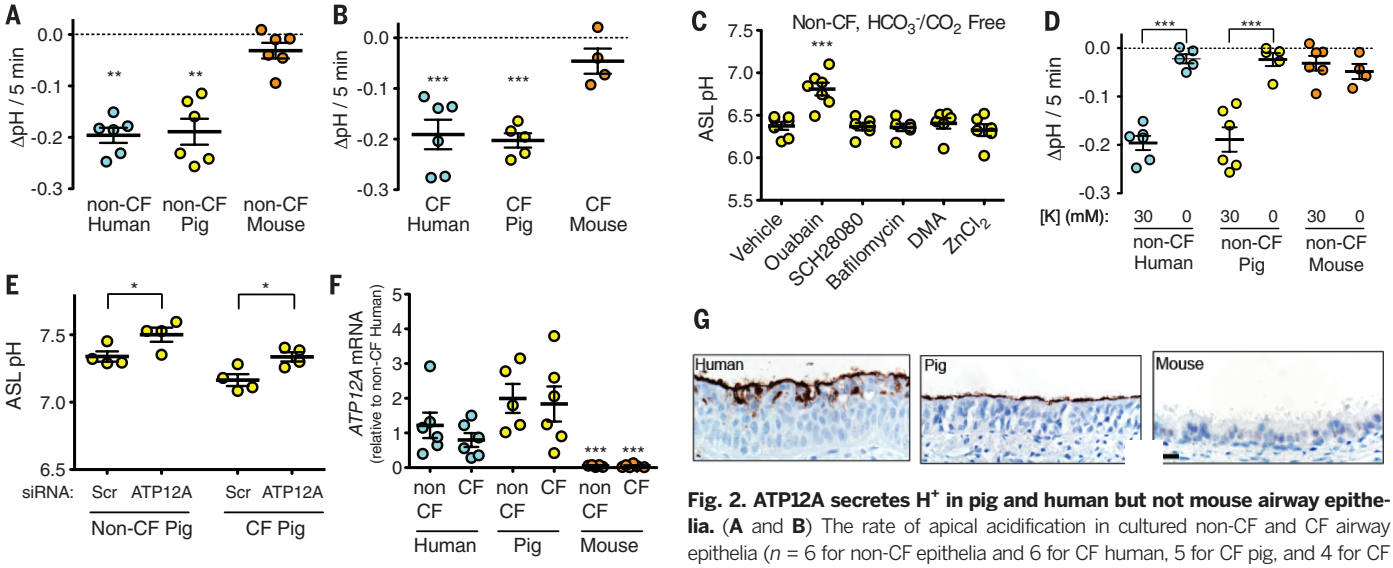


Fig. 2. ATP12A secretes H^+ in pig and human but not mouse airway epithelia. (**A** and **B**) The rate of apical acidification in cultured non-CF and CF airway epithelia (n = 6 for non-CF epithelia and 6 for CF human, 5 for CF pig, and 4 for CF mouse epithelia). 30 μl of a pH 7.0 unbuffered solution was placed on the apical surface, and pH was measured immediately and after 5 min. The basolateral solution was free of HCO_3^- and CO_2 and buffered with 25 mM Hepes. (**C**) ASL pH of non-CF and CF pig cultured airway epithelia in media free of HCO_3^- and CO_2 (n = 6 or 7). Epithelia were treated with the following agents dissolved in solvent and added apically in 20 μl of perfluorocarbon (target in parentheses): 10 μM ouabain (nongastric H^+/K^+ ATPase), 100 μM SCH28080 (gastric H^+/K^+ ATPase), 100 μM bafilomycin (V-type H^+-ATPase), 100 μM dimethyl amiloride, dimethylamine (NHE3), 1 mM $ZnCl_2$ (HVCN1), or dimethyl sulfoxide (DMSO) vehicle. (**D**) The rate of apical acidification in the presence and absence of K^+ (n = 4 to 6). 30 mM Na^+ replaced K^+. Conditions were same as described for (A) and (B). (**E**) Effect of siRNA directed against pig *ATP12A* or scrambled control (Scr) on ASL pH in cultured non-CF and CF airway epithelia (n = 4). Solutions contained HCO_3^- and CO_2. (**F**) *ATP12A* mRNA levels in non-CF and CF human, pig, and mouse airway epithelia (n = 5 for non-CF pig and non-CF mouse and 6 for all other epithelia). Values for mouse epithelia were less than for human and pig epithelia for both genotypes. (**G**) ATP12A immunostaining of human, pig, and mouse tracheal epithelium. The surface epithelium showed immunostaining along the apical surface in humans and pigs, but this was absent in mice. Scale bar, 18 μm. Figure S7 shows a positive control. In all panels, data points in each group are from epithelia from a different animal or human. Bars indicate means ± SEM. Data were analyzed using ANOVA with Tukey's multiple comparison test [(A) to (C) and (F)] or unpaired Student's t tests [(D) and (E)].

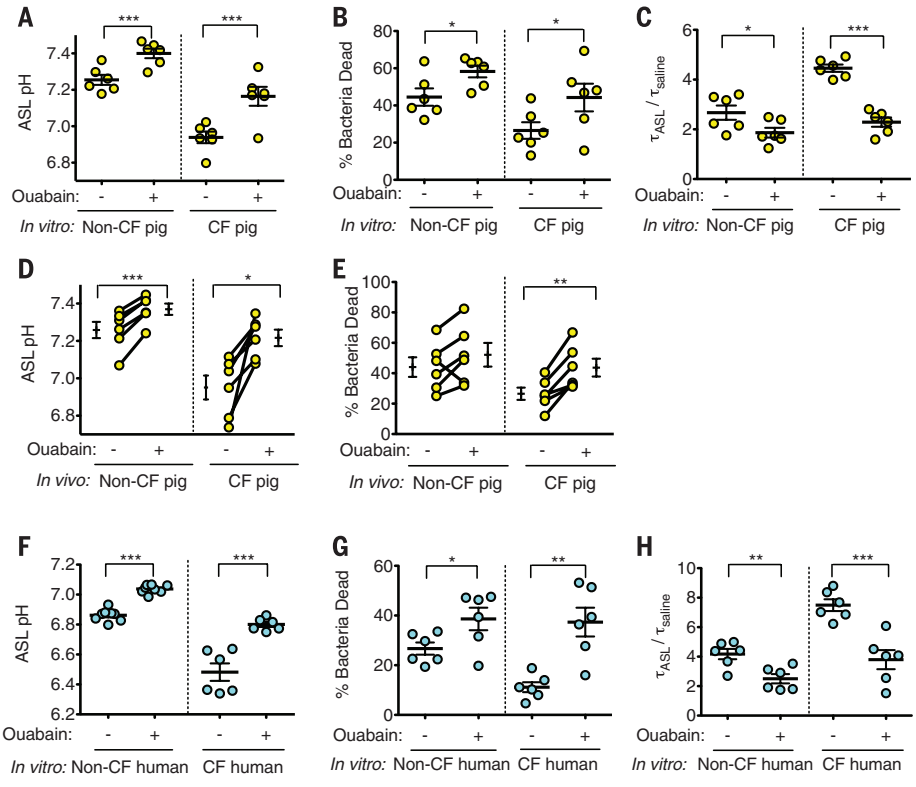


Fig. 3. Inhibiting ATP12A increases pig and human ASL pH and enhances host defense properties of ASL. (**A** to **C**) Non-CF and CF cultured pig airway epithelia were treated with 10 μM apical ouabain or DMSO vehicle for 2 hours (n = 6). The data shown are ASL pH (A), bacterial killing by ASL (B), and the time constant (τ) for fluorescence recovery after photobleaching of ASL relative to saline (C). For testing antibacterial activity, *S. aureus*–coated grids were placed on ASL for 1 min and then evaluated with a live/dead stain (fig. S9 shows a negative control). A higher τ_{ASL}/τ_{saline} indicates a greater viscosity (fig. S10 shows that ASL depth did not differ). (**D** and **E**) Effect of ouabain (dissolved in DMSO suspended in 100 μl of perfluorocarbon; estimated final concentration, 10 μM) applied to tracheal surfaces of non-CF and CF newborn pigs (n = 6). Thirty min later, we measured ASL pH (D) and bacterial killing [*S. aureus*-coated grids placed on the airway surface for 1 min (E)]. Figure S11 shows that aerosolized DMSO vehicle did not alter ASL pH, and fig. S12 shows a lack of histopathological changes after ouabain delivery. (**F** to **H**) Effect of 1 mM apical ouabain or vehicle on ASL pH (F), antibacterial activity (G), and ASL viscosity (H) in human non-CF and CF epithelia (n = 6 or 8). In all panels, each data point or pair of data points is from epithelia from a different pig [(A) to (E)] or human [(F) to (H)]. Bars indicate means ± SEM. Data were analyzed using unpaired [(A) to (C) and (F) to (H)] or paired [(D) and (E)] Student's t tests.

and impaired bacterial killing (Fig. 4, D and E). In parallel experiments, expressing *ATP12A* in non-CF mouse epithelia in vitro and in vivo did not significantly alter ASL pH, bacterial killing, or ASL viscosity (fig. S17, A to F). However, further increasing the amount of vector could reduce ASL pH (fig. S17G).

Finding acidic ASL in CF mice expressing *ATP12A* suggests that these mice would be predisposed to bacterial infection. The lungs of CF mice expressing *ATP12A* had 100 times as much bacteria as those of control mice (Fig. 4F). This result is similar to the spontaneous appearance of multiple different bacteria in the lungs of newborn CF pigs (fig. S18) (*11*, *33*). CF mice expressing *ATP12A* also developed evidence of inflammation; bronchoalveolar lavage revealed elevated numbers of myeloid cells (Fig. 4G and fig. S19). There were also positive correlations between *ATP12A* mRNA levels and numbers of bacteria and airway macrophages (Fig. 4, H to J).

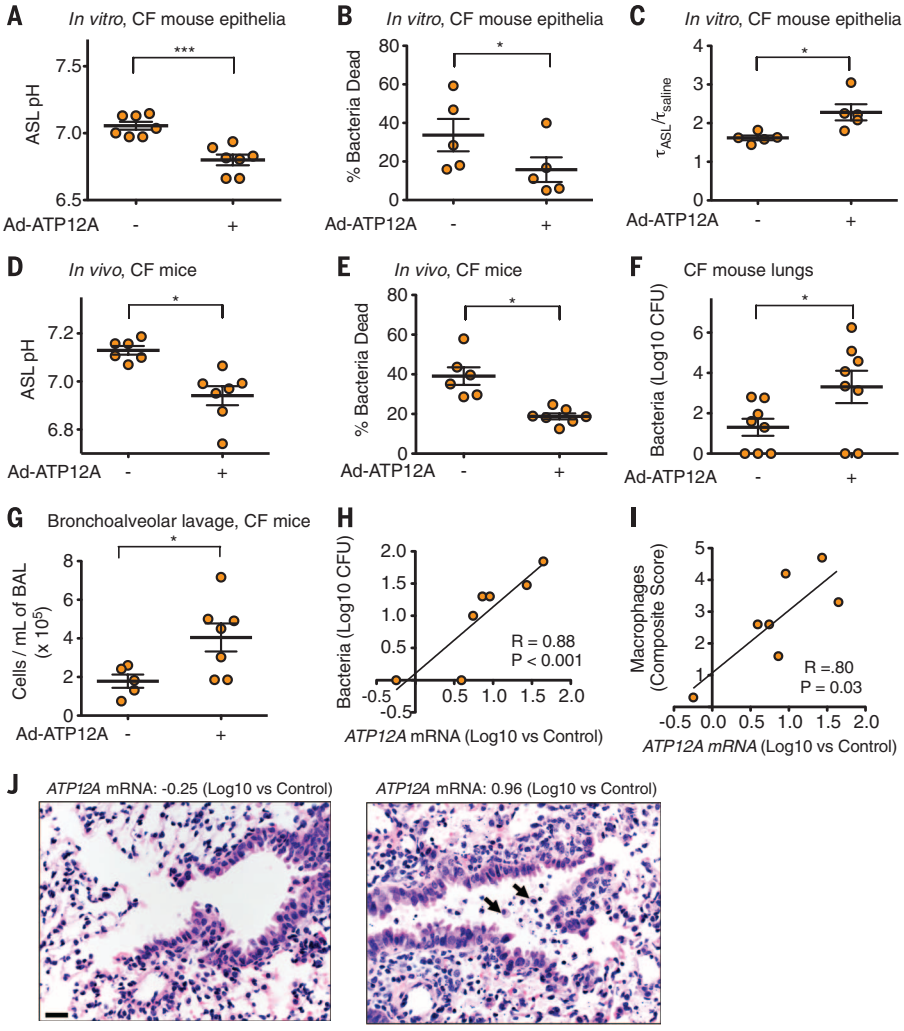


Fig. 4. Expressing ATP12A in CF mouse airways acidifies ASL, induces abnormalities in host defense processes, and increases the number of bacteria in lungs. (**A**) Effect of treating cultured mouse airway epithelia with adenovirus expressing *ATP12A* (Ad-ATP12A) or vehicle (control) on ASL pH, measured Three days later (n = 7). (**B** and **C**) Cultured mouse airway epithelia were treated with Ad-ATP12A or vehicle (control). Three days later, antimicrobial activity was measured by placing a *S. aureus*–coated grid on the apical surface for 1 min (B), and ASL viscosity was assessed by measuring the time constant (τ) for fluorescence recovery after photobleaching of ASL relative to saline (C) (n = 5). (**D** and **E**) Ad-ATP12A or Ad-GFP (control; GFP, green fluorescent protein) was administered to CF mice. ASL pH (D) and antimicrobial activity [*S. aureus*–coated grid placed on the apical surface for 1 min (E)] were measured in vivo 3 days later (n = 6 or 7). (**F**) Ad-ATP12A or Ad-GFP (control) were administered to CF mice. Three days later, lungs were removed, homogenized, and cultured. The data shown are colony-forming units (CFU) (n = 8; see also figs. S17H and S18). (**G**) Total cells/ml in bronchoalveolar lavage liquid from CF mice treated with Ad-ATP12A or Ad-GFP (control) 3 days earlier (n = 5 to 7). (**H** and **I**) Relationships between *ATP12A* mRNA and bacterial CFU from a partial lung homogenate (H) and composite macrophage score [foamy macrophage plus Iba1 (ionized calcium binding adapter molecule 1) staining (I)]. (**J**) Histopathological sections from CF mice 3 days after administering Ad-ATP12A. The left panel is from a mouse that had a low level of *ATP12A* mRNA, and the right panel is from a mouse with greater *ATP12A* mRNA (log10 relative to Ad-GFP control). Arrows identify macrophages admixed with cell debris and inflammation [see (I)]. In all panels, each data point or pair of data points is from a different mouse, and bars indicate means ± SEM. Data were analyzed using unpaired Student's t tests [(A) to (E) and (G)] Mann-Whitney U rank sum test (F), or linear correlation [(H) and (I)].

It has long been puzzling why mice with a disrupted *CFTR* gene have intact airway host defenses, and it has been hoped that understanding the reason might suggest a therapeutic strategy. Our data provide an explanation. In non-CF pigs and humans, CFTR mediates HCO_3^- secretion, and ATP12A mediates H^+ secretion. The balance between these two secretory processes influences ASL pH. In CF pigs and humans, the loss of CFTR leaves H^+ secretion unchecked by HCO_3^- secretion, ASL pH falls, and the acidic pH and/or the reduced HCO_3^- concentration impair at least two key ASL properties associated with host defense. Moreover, ASL antimicrobial activity and viscosity are very sensitive to small changes in pH. However, mouse airways express little *ATP12A* compared with those of pigs and humans. They use V-type ATPase for H^+ secretion, but the rate of H^+ secretion is low (Fig. 2, A and B, and fig. S20). As a result, the loss of CFTR has minimal effects on ASL pH, and two key ASL defense properties remain largely intact. Other differences between mice, humans, and pigs—such as Ca^{2+}-activated anion channels, the abundance of submucosal glands, and variations in cell types (*7*–*9*)—may also contribute to differences in host defense among these species.

Limited ASL acidification in CF mice provides an "experiment of nature" with implications for therapeutics. First, the knowledge that cAMP stimulates ATP12A-mediated H^+ secretion (*31*) and reduces ASL pH might have implications for CF treatments that elevate cAMP levels. For example, β-adrenergic agonists are often prescribed for people with CF to relax airway smooth muscle; although this approach can provide benefit, it seems possible that it might further impair respiratory host defenses. Second, inhibiting ATP12A might have therapeutic value in CF, regardless of *CFTR* genotype. The findings in mice and the results with apical ouabain in pigs and humans provide a proof of concept.

REFERENCES AND NOTES

1. A. M. Cole, P. Dewan, T. Ganz, *Infect. Immun.* **67**, 3267–3275 (1999).
2. J. J. Wine, N. S. Joo, *Proc. Am. Thorac. Soc.* **1**, 47–53 (2004).
3. T. S. Cohen, A. Prince, *Nat. Med.* **18**, 509–519 (2012).
4. P. M. Quinton, *Physiol. Rev.* **79**, S3–S22 (1999).
5. G. R. Cutting, *Nat. Rev. Genet.* **16**, 45–56 (2015).
6. D. A. Stoltz, D. K. Meyerholz, M. J. Welsh, *N. Engl. J. Med.* **372**, 351–362 (2015).

7. B. R. Grubb, R. C. Boucher, *Physiol. Rev.* **79**, S193–S214 (1999).
8. C. Guilbault, Z. Saeed, G. P. Downey, D. Radzioch, *Am. J. Respir. Cell Mol. Biol.* **36**, 1–7 (2007).
9. L. L. Clarke *et al.*, *Proc. Natl. Acad. Sci. U.S.A.* **91**, 479–483 (1994).
10. C. S. Rogers *et al.*, *Science* **321**, 1837–1841 (2008).
11. D. A. Stoltz *et al.*, *Sci. Transl. Med.* **2**, 29ra31 (2010).
12. A. A. Pezzulo *et al.*, *Nature* **487**, 109–113 (2012).
13. M. H. Abou Alaiwa *et al.*, *Proc. Natl. Acad. Sci. U.S.A.* **111**, 18703–18708 (2014).
14. M. J. Hoegger *et al.*, *Science* **345**, 818–822 (2014).
15. S. E. Birket *et al.*, *Am. J. Respir. Crit. Care Med.* **190**, 421–432 (2014).
16. P. M. Quinton, *Lancet* **372**, 415–417 (2008).
17. J. K. Gustafsson *et al.*, *J. Exp. Med.* **209**, 1263–1272 (2012).
18. R. D. Coakley *et al.*, *Proc. Natl. Acad. Sci. U.S.A.* **100**, 16083–16088 (2003).
19. M. H. Abou Alaiwa *et al.*, *J. Cyst. Fibros.* **13**, 373–377 (2014).
20. A. L. Garland *et al.*, *Proc. Natl. Acad. Sci. U.S.A.* **110**, 15973–15978 (2013).
21. D. McShane *et al.*, *Eur. Respir. J.* **21**, 37–42 (2003).
22. S. Jayaraman, Y. Song, L. Vetrivel, L. Shankar, A. S. Verkman, *J. Clin. Invest.* **107**, 317–324 (2001).
23. A. Caputo *et al.*, *Science* **322**, 590–594 (2008).
24. J. Jung *et al.*, *Proc. Natl. Acad. Sci. U.S.A.* **110**, 360–365 (2013).
25. B. R. Grubb, A. M. Paradiso, R. C. J. Boucher, *Am. J. Physiol.* **267**, C293–C300 (1994).
26. J.-H. Chen *et al.*, *Cell* **143**, 911–923 (2010).
27. J. J. Smith, M. J. Welsh, *J. Clin. Invest.* **89**, 1148–1153 (1992).
28. A. V. Grishin *et al.*, *Semin. Nephrol.* **19**, 421–430 (1999).
29. M. E. Krouse, J. F. Talbott, M. M. Lee, N. S. Joo, J. J. Wine, *Am. J. Physiol. Lung Cell. Mol. Physiol.* **287**, L1274–L1283 (2004).
30. H. Fischer, J. H. Widdicombe, *J. Membr. Biol.* **211**, 139–150 (2006).
31. N. Laroche-Joubert, S. Marsy, S. Michelet, M. Imbert-Teboul, A. Doucet, *J. Biol. Chem.* **277**, 18598–18604 (2002).
32. N. Derichs, B. J. Jin, Y. Song, W. E. Finkbeiner, A. S. Verkman, *FASEB J.* **25**, 2325–2332 (2011).
33. D. A. Stoltz *et al.*, *J. Clin. Invest.* **123**, 2685–2693 (2013).

ACKNOWLEDGMENTS

This work was funded by NIH (grants HL091842, HL51670, HL117744, F30HL123239, 5T32GM007337, DK054759, and K08HL097071), by the Cystic Fibrosis Foundation (University of Iowa Research Development Program, OSTEDG1410, and STOLTZ14XX0), and by the Roy J. Carver Charitable Trust. D.A.S. was funded by the Gilead Sciences Research Scholars Program in Cystic Fibrosis. M.J.W. is an investigator of the Howard Hughes Medical Institute. We thank J. Engelhardt for mice and D. Bouzek, J.-H. Chen, A. Cooney, N. Gansemer, J. Launspach, T. Mayhew, T. Moninger, C. Parker, S. Ramachandran, N. Sawin, P. Sinn, B. Stein, M. Strub, P. Taft, P. Tan, I. Thornell, L. Vargas, and S. Youtsey (Integrated DNA Technologies) for assistance, support, and advice. The CFTR inhibitor GlyH-101 was a generous gift from Cystic Fibrosis Foundation Therapeutics and R. Bridges. M.J.W. holds equity in Exemplar Genetics, which has licensed CF pigs from the University of Iowa.

SUPPLEMENTARY MATERIALS

www.sciencemag.org/content/351/6272/503/suppl/DC1
Materials and Methods
Figs. S1 to S20
References (*34*–*67*)

30 September 2015; accepted 16 December 2015
10.1126/science.aad5589

BIOCHEMISTRY

An unprecedented mechanism of nucleotide methylation in organisms containing *thyX*

Tatiana V. Mishanina,[1]* Liping Yu,[2] Kalani Karunaratne,[1] Dibyendu Mondal,[1] John M. Corcoran,[1] Michael A. Choi,[1] Amnon Kohen[1]†

In several human pathogens, *thyX*-encoded flavin-dependent thymidylate synthase (FDTS) catalyzes the last step in the biosynthesis of thymidylate, one of the four DNA nucleotides. *ThyX* is absent in humans, rendering FDTS an attractive antibiotic target; however, the lack of mechanistic understanding prohibits mechanism-based drug design. Here, we report trapping and characterization of two consecutive intermediates, which together with previous crystal structures indicate that the enzyme's reduced flavin relays a methylene from the folate carrier to the nucleotide acceptor. Furthermore, these results corroborate an unprecedented activation of the nucleotide that involves no covalent modification but only electrostatic polarization by the enzyme's active site. These findings indicate a mechanism that is very different from thymidylate biosynthesis in humans, underscoring the promise of FDTS as an antibiotic target.

Enzymes involved in DNA biosynthesis are primary targets of chemotherapeutic and antibiotic agents. One such enzyme is thymidylate synthase, or TSase [Enzyme Commission (EC) number 2.1.1.45]. Encoded by the *thyA* gene (*TYMS* in humans), TSase produces thymidylate (dTMP), a precursor of one of the DNA bases, thymine. TSase catalyzes the reductive methylation of the nucleotide deoxyuridine monophosphate (dUMP) with the folate derivative CH_2H_4fol (Fig. 1). The reaction also produces dihydrofolate (H_2fol), which is restored to tetrahydrofolate (H_4fol) for reuse in catalysis by dihydrofolate reductase (DHFR). TSase is successfully targeted by drugs such as 5-fluorouracil and raltitrexed, and DHFR is the target of methotrexate and trimethoprim.

However, in several human pathogens thymidylate formation is catalyzed by *thyX*-encoded flavin-dependent thymidylate synthase, or FDTS (EC 2.1.1.148), which carries out the functions of both TSase and DHFR (Fig. 1) (*1*, *2*). Many pathogens depend solely on *thyX* for thymine, including all *Rickettsia* (causing typhus, spotted fever, and other diseases). Pathogens containing both *thyX* and *thyA,* such as *Mycobacterium tuberculosis*, can synthesize thymidylate through either pathway and often develop multidrug resistance. As multi- and extreme-drug resistance in these pathogens becomes more common, the addition of an FDTS inhibitor to the cocktail could prove essential for treatment. Further information regarding the prevalence of *thyX* gene in human pathogens, and its potential as a drug target, is provided in the supplementary materials. Hitherto, no drugs are known to selectively inhibit FDTS, and the mechanistic intricacies necessary for the rational design of mechanism-based inhibitors are yet to be resolved. FDTS is genetically and structurally dissimilar not only from the canonical TSase and DHFR but from other flavoenzymes (*3*, *4*). The current report provides a road map to better understanding of FDTS catalysis and to rational design of inhibitory drugs.

To delineate the mechanism of FDTS catalysis, we report on the trapped reaction intermediates, that is, intermediate species that have been chemically modified by a reaction quencher (here, acid or base). Characterization of these trapped compounds suggested a unique nucleotide methylation path. Our previous report on rapid-quenching experiments with *Thermatoga maritima* FDTS (*Tm*FDTS) revealed a substantial accumulation of an acid-modified intermediate, identified as 5-hydroxymethyl-dUMP (*5*). In the current study, we used a basic quencher to stop enzymatic turnover and trap different derivatives of the intermediates. Indeed, with radiolabeled nucleotide, [2-^{14}C]-dUMP, we observed a previously unknown radioactive species, distinct from the acid-modified 5-hydroxymethyl-dUMP. The base-modified species was also observed with methylene-labeled folate, [11-^{14}C]-CH_2H_4fol, indicating that the nucleotide intermediate acquired the methylene before being trapped by the base (fig. S1).

The top panel in Fig. 2 shows the accumulation and decay of the base-trapped intermediate (blue) with [2-^{14}C]-dUMP as a substrate. Upon base addition, dTMP product (black) is formed even though the flavin is in a reduced state before the quencher's addition (green stopped-flow trace). A comparison of the time course of the acid- and base-modified intermediate derivatives (Fig. 2, bottom) suggests that at least two different reaction intermediates (I_1 and I_2) are

[1]Department of Chemistry, University of Iowa, Iowa City, IA 52242, USA. [2]Nuclear Magnetic Resonance (NMR) Core Facility and Department of Biochemistry, Carver College of Medicine, University of Iowa, Iowa City, IA 52242, USA. *Present address: Department of Biochemistry, University of Wisconsin-Madison, Madison, WI 53706, USA. **†Corresponding author. E-mail: amnon-kohen@uiowa.edu**

Downloaded from on January 31, 2016

trapped in acid as 5-hydroxymethyl-dUMP. In base, I_1 is trapped in a different chemical form than in acid, and I_2 is converted to dTMP (see further discussion of this phenomenon in the supplementary materials).

What is the base-modified intermediate? Its mass was determined to be $[M-H]^-$ 705.1212 daltons (fig. S2A). Tandem mass spectrometry (MS/MS) of the compound displayed a loss of 320 daltons, corresponding to CH_2-dUMP (fig. S2B), which accords with the ^{14}C found in this intermediate when using ^{14}C labeled dUMP or $^{14}CH_2H_4$fol. Hence the $[M-H]^-$ 385 ion, corresponding to the mass difference between the trapped species and CH_2-dUMP moiety (fig. S2B), must have belonged to an adduct covalently linked to the trapped nucleotide.

All FDTS mechanisms proposed heretofore (*6*–*9*) (e.g., fig. S3) postulate that the methylene is transferred directly from CH_2H_4fol to the nucleotide, as in the TSase reaction (*10*), and the absorbance spectrum of the trapped intermediate (fig. S4) accords with folate absorbance. Consequently, the most logical candidate for the adduct was the pterin moiety of CH_2H_4fol. However, when using CH_2H_4fol radiolabeled at pterin or benzoyl moieties, we found no radioactivity in the base-modified intermediate, ruling out folate as a component of the base-trapped intermediate. Furthermore, the MS/MS ion of 385 daltons in the base-trapped intermediate did not match any buffer or protein constituents.

The only remaining part of the quenched FDTS reaction that could have provided the mysterious adduct was a flavin adenine dinucleotide (FAD) derivative. To investigate, we turned to FDTS reconstituted with isotopically labeled FAD (*11*). FDTS reconstituted with FAD labeled at the adenine moiety yielded no labeled intermediate, but the reaction of [7a,8a-^{3}H]-FAD-FDTS produced a tritiated trapped intermediate (fig. S5B), indicating that the labeled dimethylbenzene portion of isoalloxazine (fig. S5A) was a part of the trapped species. Additionally, when we used FDTS containing FAD uniformly labeled with ^{13}C and

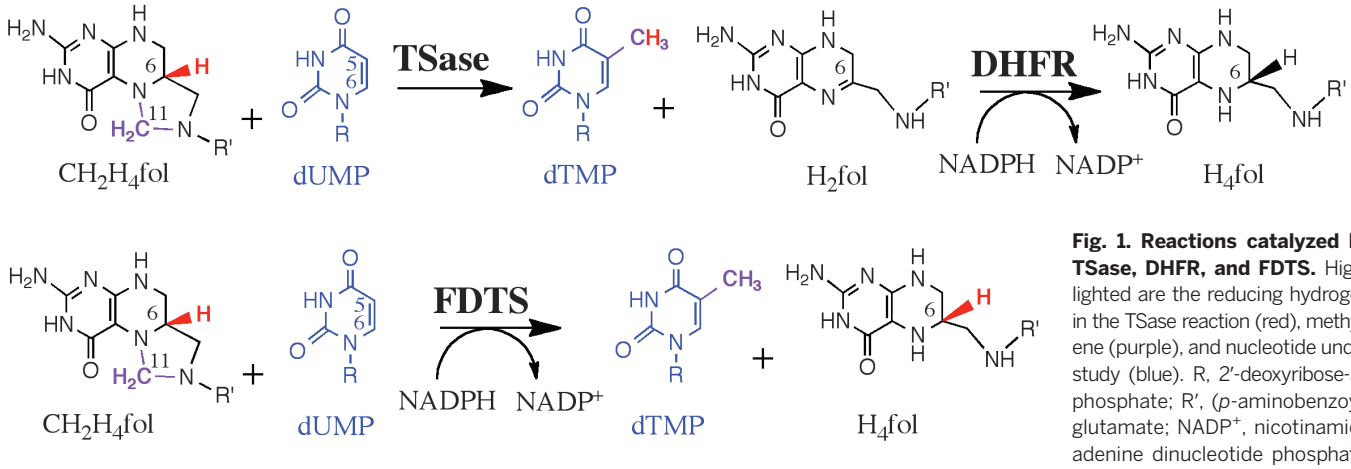


Fig. 1. Reactions catalyzed by TSase, DHFR, and FDTS. Highlighted are the reducing hydrogen in the TSase reaction (red), methylene (purple), and nucleotide under study (blue). R, 2′-deoxyribose-5′-phosphate; R′, (*p*-aminobenzoyl) glutamate; $NADP^+$, nicotinamide adenine dinucleotide phosphate; NADPH, reduced form of $NADP^+$.

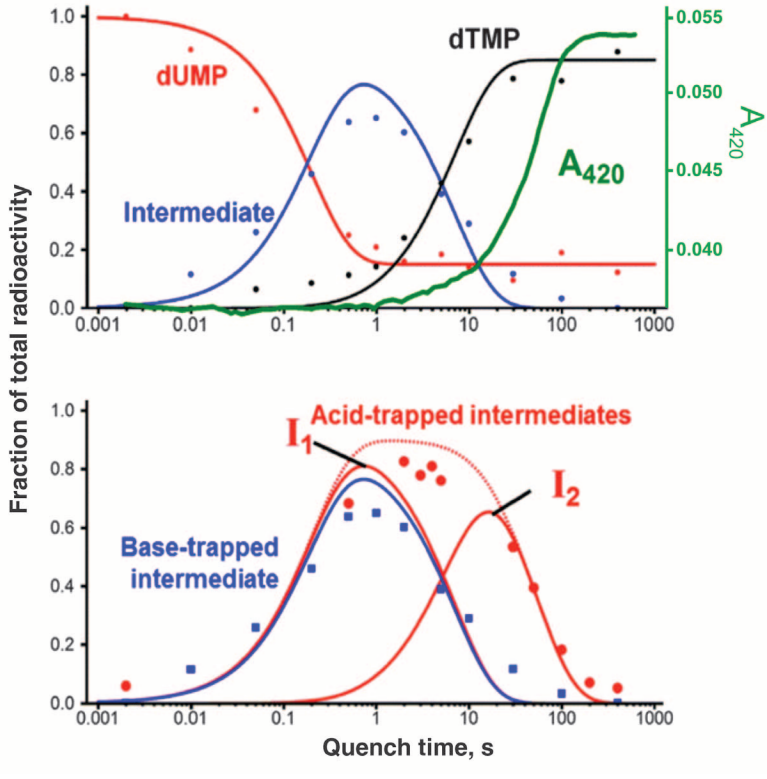


Fig. 2. Oxidative half-reaction kinetics of FDTS. (**Top**) Base-quenched data (dots) globally fitted to a single-intermediate model (lines), overlaid with stopped-flow traces at 420 nm (flavin absorbance, A_{420}, in green) (*6*). Each time point was obtained from a radiogram like that shown in fig. S1A, with dUMP in red, dTMP in black, and intermediate in blue. (**Bottom**) Base-trapped intermediate kinetics (blue) overlaid with acid-trapped intermediate data (red), globally fitted to a two-intermediate model (red curves). The sum of the two intermediates is shown as a dotted red curve.

^{15}N at its dioxopyrimidine (ring "C" in fig. S5), that is, 6 daltons heavier than unlabeled FAD, the mass of the isolated trapped intermediate was heavier by only 2 daltons than that produced by the unlabeled enzyme (fig. S2C). This finding suggests that only two labeled atoms of the dioxopyrimidine ring of the flavin are retained in the base-modified intermediate.

Several nuclear magnetic resonance (NMR) experiments were performed to determine the structure of the base-trapped intermediate (Fig. 3, figs. S6 and S7, and table S2). Critically, the methylene (U7) originating in the CH_2H_4fol had bonded to C5 of the dUMP moiety and coupled to FC5a and FC4a of the degraded flavin in the NMR heteronuclear multiple-bond correlation (HMBC) spectrum (Fig. 3). These results and others presented in the supplementary materials show that CH_2H_4fol-derived methylene bridges dUMP and degraded flavin, connecting C5 of dUMP and N5 of the decomposed isoalloxazine moiety. Other structural features of the base-trapped intermediate derivative are described in the supplementary materials.

The presence of a covalent methylene bridge between dUMP and flavin indicates a previously unconsidered mechanism substantially different from earlier mechanisms (*6*, *7*, *9*) (fig. S3). This mechanism, given in Fig. 4 and fig. S8, postulates that N5 of the reduced flavin accepts the activated methylene from the CH_2H_4fol Schiff base (step 1), and then passes it to C5 of the enzyme-polarized dUMP (steps 2 and 3). This mechanism agrees well with crystal structures of FDTS complexes with FAD, dUMP, and folates [Protein Data Bank identifications (PDB IDs): 4GT9, 4GTA, and 4GTB], in which the isoalloxazine moiety of FAD is sandwiched between the folate ring and uracil (*8*) (Fig. 4). Thus, whereas protein-bound flavins typically carry electrons from one side of the flavin ring to the other, the FAD of FDTS carries a methylene.

The proposed intermediates I_1 and I_2 are modified in base to the compound identified in Fig. 3 and product, respectively. However, both are converted to 5-hydroxymethyl-dUMP in acid. The mechanisms of their degradation are discussed in the supplementary materials and presented in fig. S10.

Why wasn't such a mechanism considered when the structure of FDTS complex with its substrates was solved in 2012 (*8*)? The reason lies in reports of activity of FDTS reconstituted with 5-deaza-5-carba-FAD (henceforth 5-deaza-FAD) (*7*, *9*). In 5-deaza-FAD, N5 of the flavin has been replaced with a carbon, which prohibits several chemical conversions proposed in Fig. 4. The identification of the base-modified intermediate prompted us to revisit this finding. We synthesized 5-deaza-FAD and incorporated it into apo-FDTS. In doing so, we found that the procedure used in the past for removing FAD from holo-*Tm*FDTS (salting out) (*4*, *9*) leaves behind variable amounts of FAD, producing the same level of (residual) activity in the salted-out "apoenzyme" as in 5-deaza-FAD–reconstituted FDTS. By denaturing the apoenzyme with 8 M urea after salting out, completely removing FAD, then refolding and reconstituting with either FAD or 5-deaza-FAD, we found no activity for the apoenzyme, fully recovered activity for FAD-reconstituted enzyme, and no activity for the enzyme reconstituted with 5-deaza-FAD (fig. S9). This indicates that 5-deaza-FAD-FDTS is actually not active at all ($<10^{-6}$ at the signal/noise limit, see supplementary materials), removing the conceptual barrier for the mechanism proposed in Fig. 4.

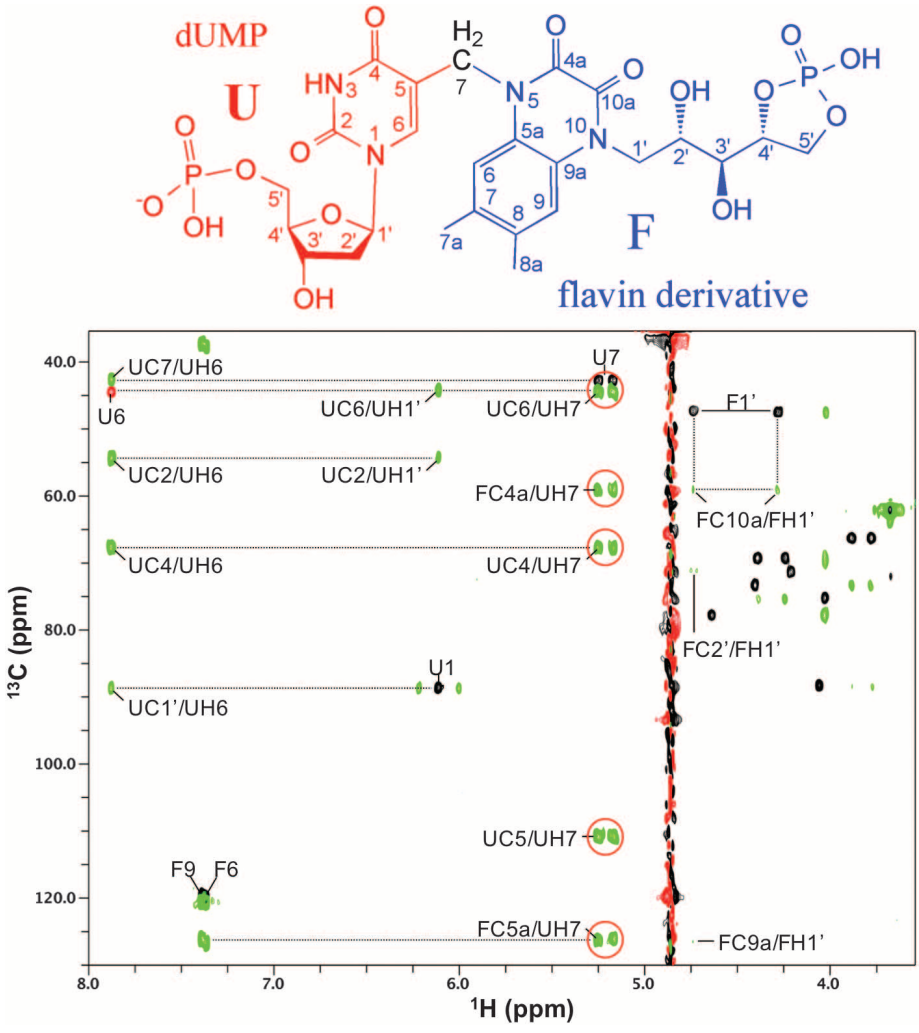


Fig. 3. Structure of the base-modified FDTS reaction intermediate. (**Top**) Structural components originating in dUMP (red) and CH_2H_4fol (black) are referred to as "U subunit" and the structural parts derived from FAD (blue) as "F subunit." Atomic numbering in F subunit follows convention adapted from the original FAD (fig. S5A). (**Bottom**) Overlay of ^{1}H/^{13}C heteronuclear multiple-quantum coherence (black; red marks folded cross-peaks) and HMBC (green) spectra. The cross-peaks are labeled with the first letter representing the subunit (U or F). The cross-peaks of the HMBC spectrum circled in red unambiguously establish that the CH_2H_4fol-drived methylene (U7) bridges dUMP and flavin derivative. ppm, parts per million.

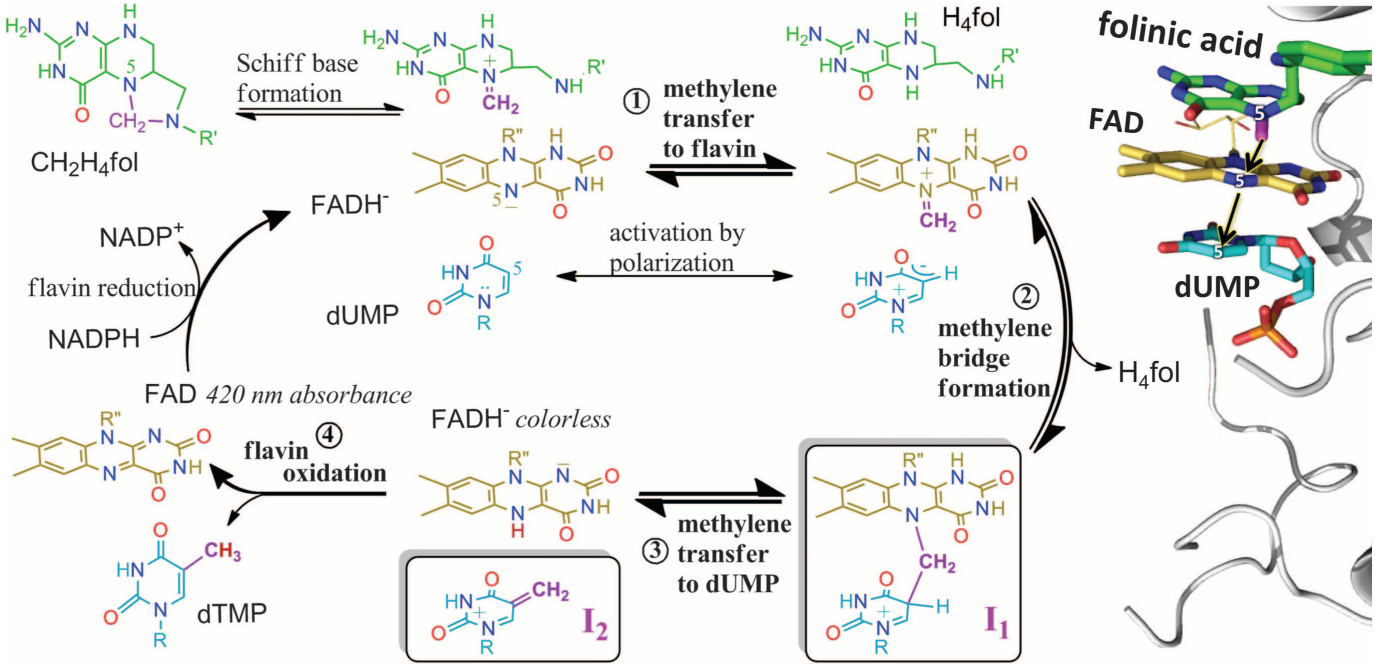


Fig. 4. Proposed chemical mechanism for FDTS. (**Left**) Methylene (CH_2, purple) is transferred from the N5 of H_4fol (green) via N5 of FAD cofactor (gold) to C5 of dUMP substrate (cyan). Oxygens are in red, nitrogens in blue, and the hydride transferred in step 4 in brown. The proposed steps of flavin oxidative half-reaction are numbered. I_1 (boxed) is the reaction intermediate that in base is converted to the compound presented in Fig. 3 and in acid undergoes water addition (fig. S10 and supplementary text). I_2 (boxed) refers to the intermediate that in base forms dTMP, and in acid reacts with water (fig. S10 and supplementary text). The "420 nm absorbance" versus "colorless" labels of flavins relate the 420-nm time trace (green line in Fig. 2) to the mechanistic model. A rigorous electron-pushing description of this mechanism is presented in fig. S8. R, 2′-deoxyribose-5′-phosphate; R′, (*p*-aminobenzoyl)glutamate; and R″, adenosine-5′-pyrophosphate–ribityl. (**Right**) Active site of FDTS [PDB ID 4GTA (*8*)] in complex with FAD, dUMP, and folinic acid, a stable analog of the activated CH_2H_4fol. For clarity, the carbonyl oxygen of folinic acid is not shown, and the structure is inversed to match the orientation of ligands in the left-hand structures. The formyl carbon (magenta) on folinic acid represents the methylene to be transferred. Black arrows mark the methylene-transfer trajectory from donor (N5 of folate) to proposed relay atom (N5 of flavin) and final acceptor (C5 of dUMP).

Flavin's N5-mediated methylene transfer might be rare, but it has been proposed for TrmFO tRNA methyltransferase (*12*). However, in TrmFO the uracil is activated via Michael addition of active-site cysteine to C6 of the pyrimidine ring, and a second cysteine activates and delivers the methylene to the flavin. In FDTSs, no such enzymatic nucleophile is available (*7*), and the cause of the uracil's initial activation has been a matter of uncertainty. One hypothesis posits that the N5 hydride of reduced FAD nucleophilically activates dUMP (*7*) (fig. S3A), whereas another suggests that the enzyme polarizes the pyrimidine ring of dUMP for an attack on the CH_2H_4fol methylene (*6*, *9*) without a Michael nucleophile (fig. S3B). The latter chemistry is unprecedented in nucleotide methylation, and the need for pyrimidine activation via Michael addition to its C6 has been emphasized in enzymatic and nonenzymatic systems (*6*). The only supporting pieces of evidence so far were the absence of deuterated trapped intermediates (*6*) and ultraviolet-visible features consistent with those of reduced flavin [Fig. 2, green trace, and (*5*, *9*)], but these observations can be rationalized by more conventional mechanisms (*6*). Such nucleotide activation was thus met with healthy skepticism.

The current findings provide the strongest supporting evidence so far for pyrimidine activation via polarization in the reduced enzyme's active center. Because the methylene-carrier role for flavin's N5 proposed here (Fig. 4) requires FAD to be reduced during carbon transfer to dUMP, flavin oxidation during substrate activation (fig. S3A) can be definitively ruled out. The mechanism proposed in Fig. 4 also agrees with the observation (*7*) that, when the *Tm*FDTS reaction is conducted in D_2O at near-physiological temperatures, a deuterium is incorporated at C7 of the dTMP product while some deuterium is found at C6 of the product at low temperature (fig. S8).

The data presented above dictate a thymidylate biosynthesis mechanism (Fig. 4) in *thyX*-dependent human pathogens that is fundamentally different from that found in humans, lending hope for development of mechanism-based FDTS inhibitors as a new class of nontoxic antibiotics (see supplementary materials).

REFERENCES AND NOTES

1. H. Myllykallio *et al.*, *Science* **297**, 105–107 (2002).
2. D. Leduc *et al.*, *Biochem. Soc. Trans.* **32**, 231–235 (2004).
3. S. A. Lesley *et al.*, *Proc. Natl. Acad. Sci. U.S.A.* **99**, 11664–11669 (2002).
4. I. I. Mathews *et al.*, *Structure* **11**, 677–690 (2003).
5. T. V. Mishanina *et al.*, *J. Am. Chem. Soc.* **134**, 4442–4448 (2012).
6. T. V. Mishanina, J. M. Corcoran, A. Kohen, *J. Am. Chem. Soc.* **136**, 10597–10600 (2014).
7. E. M. Koehn *et al.*, *Nature* **458**, 919–923 (2009).
8. E. M. Koehn *et al.*, *Proc. Natl. Acad. Sci. U.S.A.* **109**, 15722–15727 (2012).
9. J. A. Conrad, M. Ortiz-Maldonado, S. W. Hoppe, B. A. Palfey, *Biochemistry* **53**, 5199–5207 (2014).
10. C. W. Carreras, D. V. Santi, *Annu. Rev. Biochem.* **64**, 721–762 (1995).
11. T. V. Mishanina, A. Kohen, *J. Labelled Comp. Radiopharm.* **58**, 370–375 (2015).
12. D. Hamdane, M. Argentini, D. Cornu, B. Golinelli-Pimpaneau, M. Fontecave, *J. Am. Chem. Soc.* **134**, 19739–19745 (2012).

ACKNOWLEDGMENTS

We thank D. Roston for assistance with kinetic data fitting, and M. S. Hossain and F. W. Foss Jr. for assistance with preparation of 5-deaza-riboflavin. This work was funded by NIH R01 GM110775 to A.K. and a fellowship from the Iowa Center of Biocatalysis and Bioprocessing (NIH T32 GM008365) to T.V.M. and K.K.

SUPPLEMENTARY MATERIALS

www.sciencemag.org/content/351/6272/507/suppl/DC1
Materials and Methods
Supplementary Text
Figs. S1 to S10
Tables S1 and S2
References (*13*–*38*)

15 July 2015; accepted 17 December 2015
10.1126/science.aad0300

IMMUNOLOGY

Most microbe-specific naïve CD4$^+$ T cells produce memory cells during infection

Noah J. Tubo,[1] Brian T. Fife,[2] Antonio J. Pagan,[3] Dmitri I. Kotov,[4] Michael F. Goldberg,[4] Marc K. Jenkins[4]*

Infection elicits CD4$^+$ memory T lymphocytes that participate in protective immunity. Although memory cells are the progeny of naïve T cells, it is unclear that all naïve cells from a polyclonal repertoire have memory cell potential. Using a single-cell adoptive transfer and spleen biopsy method, we found that in mice, essentially all microbe-specific naïve cells produced memory cells during infection. Different clonal memory cell populations had different B cell or macrophage helper compositions that matched effector cell populations generated much earlier in the response. Thus, each microbe-specific naïve CD4$^+$ T cell produces a distinctive ratio of effector cell types early in the immune response that is maintained as some cells in the clonal population become memory cells.

Infection in vertebrates elicits CD4$^+$ memory T lymphocytes that participate in protective immunity (*1*, *2*). The process begins when major histocompatibility complex class II (MHC II)–bound microbial peptides are displayed on host cells and recognized by T cell receptors (TCRs) on a few naïve CD4$^+$ T cells from a vast repertoire. These cells proliferate and differentiate into distinct types of effector cells that help B cells or macrophages to eliminate the infection (*3*). About 90% of the cells then disappear, leaving a population of long-lived memory cells. Some naïve CD4$^+$ T cells have been reported to make terminally differentiated effector cells, while others—perhaps those with the most avid TCRs (*4*, *5*)—make memory cells (*6*). In contrast, other studies of one TCR showed that a single naïve cell can make both effector and memory cells (*7*, *8*). Thus, the contribution of all naïve T cells in a polyclonal repertoire to the memory cell pool is unclear.

We addressed this issue by determining the fates of many single cells from the repertoire of naïve CD4$^+$ T cells specific for an MHC II (I-A^b)–bound peptide (LLOp) from the listeriolysin O protein of *Listeria monocytogenes*. Using I-A^b tetramer–based cell enrichment and flow cytometry (*9*, *10*), we confirmed that uninfected C57BL/6 (B6) mice contained about 80 CD4$^+$ CD44^{low} LLOp:I-A^b tetramer–binding naïve cells (Fig. 1A) (*10*). Seven days after intravenous infection with the attenuated ActA-deficient *L. monocytogenes* strain (referred to hereafter as *L. monocytogenes*), these cells proliferated to produce about 200,000 CD44^{high} effector cells (Fig. 1A) consisting of CXCR5$^-$ PD-1^{low} T helper 1 (T_H1) macrophage helpers (*10*) and two kinds of B cell helpers: CXCR5$^+$ PD-1$^-$ T follicular helper (T_{FH}) cells and CXCR5^{++} PD-1$^+$ germinal center T_{FH} (GC-T_{FH}) cells (*11*) (Fig. 1B). The number of LLOp:I-A^b tetramer–binding cells then fell by about an order of magnitude 21 days after infection (*10*), and the surviving cells were CD44^{high} memory cells of two types: CXCR5$^-$ PD-1$^-$ T_H1 effector memory cells and CXCR5$^+$ PD-1$^-$ T_{FH}-like central memory cells (Fig. 1B) (*10*). Thus, acute systemic infection with *L. monocytogenes* caused a naïve T cell population to generate at least two long-lived memory cell populations that resemble earlier populations of effector cells.

A limiting dilution adoptive transfer strategy was then used to study the progeny of single naïve cells (*12*). CD4$^+$ T cells from eight different uninfected congenic strains expressing various combinations of CD45.1, CD45.2, CD90.1, or CD90.2 were transferred together into B6 mice (CD45.2/2 CD90.2/2) at a number expected to contain on average less than one LLOp:I-A^b tetramer–binding naïve T cell from each donor population. Recipient mice were then infected with *L. monocytogenes*, and 8 days later, LLOp:I-A^b tetramer–enriched cells were stained with fluorochrome-labeled CD45.1, CD45.2, CD90.1, and CD90.2 antibodies and analyzed by flow cytometry. Cells expressing CD45.1 and/or CD45.2 were identified in the LLOp:I-A^b tetramer–binding population (Fig. 1C), and cells expressing CD90.1 and/or CD90.2 were then identified in those populations (Fig. 1D).

This strategy identified nine different LLOp:I-A^b tetramer–binding effector cell populations (Fig. 1D), one derived from the naïve cells of the recipients (CD45.2/2 CD90.2/2) and eight others from single cells from one of the donor populations (Fig. 1D). Each of the eight donor cell–derived populations was detected in only 20 to 75% of the recipient mice and thus had an 83 to 98% chance of being derived from a single naïve cell (*13*). The earlier finding that all the cells from donor-derived populations like these had the identical *Tcrb-VDJ* sequence supports this contention (*12*).

The approach was then modified so that clonal effector and memory cells could be analyzed in the spleen from the same animal. This was accomplished by surgical removal of part of the spleen for analysis of effector cells, followed by the other part several months later for analysis of memory cells. This strategy was possible because more than 95% of secondary lymphoid organ–resident LLOp:I-A^b tetramer–binding CD4$^+$ effector and memory T cells were in the spleen on days 8 and 62 after infection (Fig. 1E). In addition, limiting dilution transfer experiments revealed that clonal populations were in both halves of the spleen on day 8 after infection (Fig. 1F) and the clonal cells in each half had similar T_H1, T_{FH}, and GC-T_{FH} ratios (Fig. 1G).

This strategy was then used to track the progeny of single naïve CD4$^+$ T cells. Examples for two different recipient mice, each containing two donor-derived clonal populations (CD45.1/2 and CD45.1/1 for mouse 1; CD90.1/2 and CD90.1/1 for mouse 2), are shown in Fig. 2A. All four of these clonal effector cell populations generated memory cells 60 days after infection. In this experiment, 73 different clonal effector cell populations ranging from 30 to 6000 cells and averaging about 500 cells were detected in 31 mice on day 8 after infection (Fig. 2B). Sixty-seven of these populations (92%) yielded detectable memory cells on day 60 to 62. All but one of the clonal memory cell populations were smaller than their effector cell predecessor populations and on average had the same 15% survival rate as polyclonal cells of recipient origin but were more variable in this regard (Fig. 2C). Although large effector cell populations tended to have lower survival rates, as suggested in other studies (*14*), this weak trend was not statistically significant (Fig. 2D). On the contrary, the six populations that did not produce detectable memory cells all contained fewer than 120 cells on day 8. Although this result may indicate that naïve cells that produce few effector cells are less likely to make memory cells, it is possible that memory cells were produced from these small populations but fell below the limit of detection of the assay. Essentially identical results were obtained in a second set of experiments in which 87% (41 of 47) of day 8 clonal effector cell populations produced memory cells on day 30 after infection (fig. S1). Thus, although clonal effector cell populations undergo contraction, almost all produce memory cells.

The phenotypes of clonal LLOp:I-A^b tetramer–binding T cell populations were also assessed. Different clonal populations had different numbers and percentages of CXCR5$^-$ T_H1, CXCR5$^+$ PD-1$^-$ T_{FH}, and CXCR5^{++} PD-1$^+$ GC-T_{FH} effector cells on day 8 (Fig. 3A and fig. S1), as previously described (*12*). The number of cells in each

[1]Immune Mediated Disease Therapy Group, Genzyme, a Sanofi Company, Framingham, MA 01701, USA. [2]Department of Medicine, Center for Immunology, University of Minnesota Medical School, Minneapolis, MN 55455, USA. [3]Department of Medicine, MRC Laboratory of Molecular Biology, Cambridge, UK. [4]Department of Microbiology and Immunology, Center for Immunology, University of Minnesota Medical School, Minneapolis, MN 55455, USA.
*Corresponding author. E-mail: jenki002@umn.edu

Downloaded from on January 31, 2016

population decreased by day 60 to 62, but the surviving memory populations had about the same percentages of CXCR5$^-$ and CXCR5$^+$ cells as the parent effector cell populations (Fig. 3, A to C). However, CXCR5^{++} PD-1$^+$ cells, which were present in many effector populations, were absent in memory cell populations, whereas CXCR5$^+$ PD-1$^-$ cells were found at elevated frequencies (Fig. 3, A, C, and D). Adoptive transfer experiments demonstrated that all tetramer-binding and most tetramer-negative CXCR5^{++} PD-1$^+$ effector cells become CXCR5$^+$ PD-1$^-$ memory cells

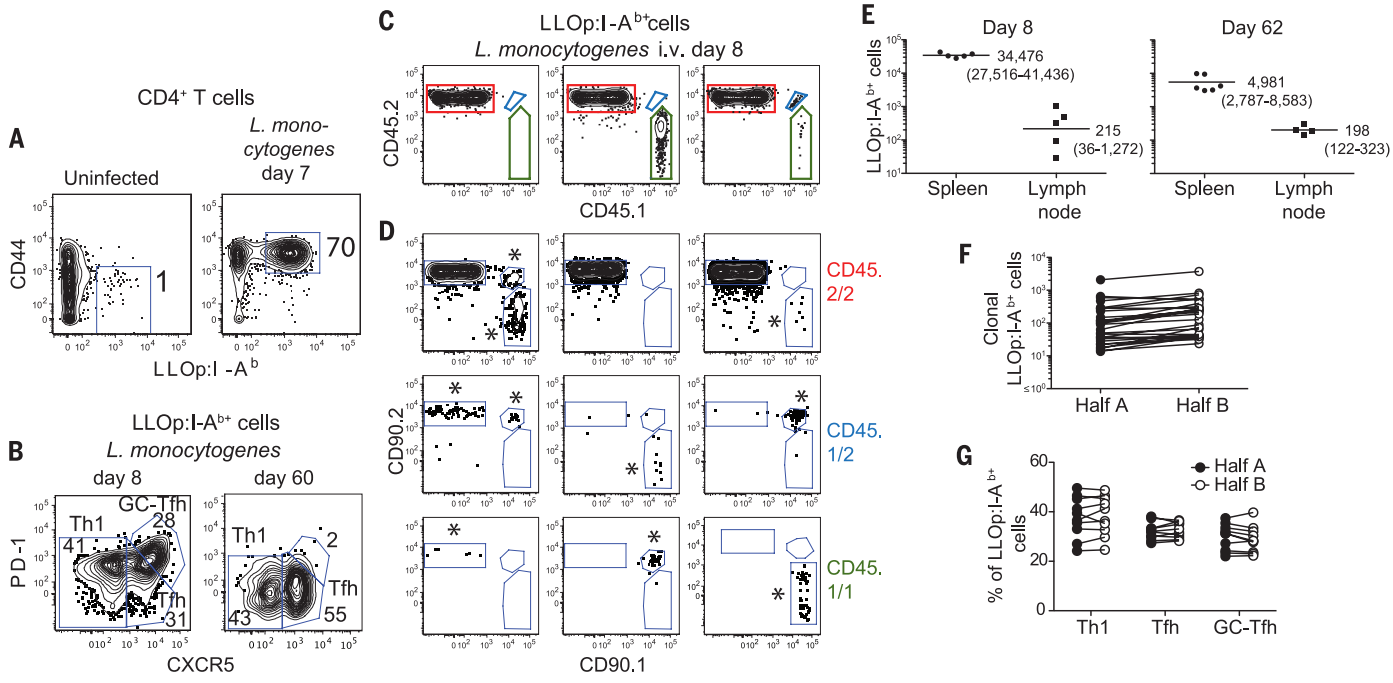


Fig. 1. Identification of clonal LLOp:I-A^b tetramer–binding T cells. (**A**) LLOp:I-A^b tetramer–enriched CD4$^+$ T cells from an uninfected mouse or a day 7 *L. monocytogenes*–infected B6 mouse with gates on CD44^{low} or CD44^{high} tetramer-binding cells. (**B**) Gates to identify LLOp:I-A^b tetramer–binding CXCR5$^-$ PD-1$^-$ T_H1, CXCR5$^+$ PD-1$^-$ T_{FH}, and CXCR5^{++} PD-1$^+$ GC-T_{FH} effector cells (left) or memory cells (right). (**C**) CD45.1 versus CD45.2 expression by LLOp:I-A^b tetramer–binding cells from day 8 *L. monocytogenes*–infected B6 mice that received 7 × 10^5 CD4$^+$ T cells from eight unique CD45 and CD90 congenic strains. (**D**) CD90.1 versus CD90.2 expression on cells expressing CD45.2/2 (red), CD45.1/2 (blue), or CD45.1/1 (green) identified as in (C) from nine different mice. Cells of recipient origin were CD45.2/2 CD90.2/2. Donor-derived populations considered to be genuine (at least five events) are indicated with asterisks. (**E**) LLOp:I-A^b tetramer–binding CD4$^+$ T cells in the spleens or lymph nodes of B6 mice after *L. monocytogenes* infection. Each dot is a value from a single mouse. Geometric mean values are shown with 95% confidence intervals in parentheses. (**F**) Number of donor-derived LLOp:I-A^b tetramer–binding cells derived from single naïve cells in each half of the spleen 7 days after *L. monocytogenes* infection. Lines connect values for the same clonal population. (**G**) Frequencies of T_H1, T_{FH}, and GC-T_{FH} cells [as defined in (B)] in clonal LLOp:I-A^b tetramer–binding cell populations in halves of the same spleens. In (F) and (G), lines connect populations derived from the same naïve cell. Representative data from single experiments are shown in (A) to (C). Pooled results from two independent experiments are shown in (E) to (G).

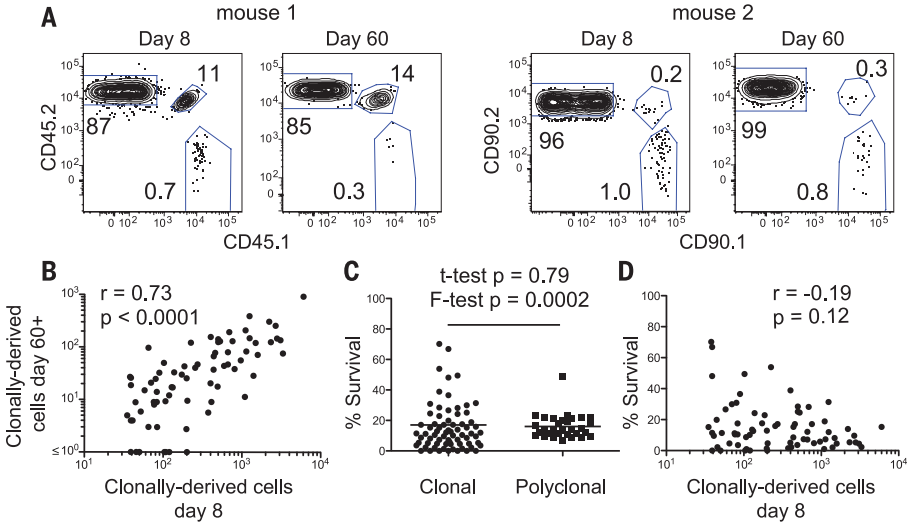


Fig. 2. Nearly all clonal effector cell populations produce memory cell populations. (**A**) LLOp:I-A^b tetramer–binding CD4$^+$ T cells from two different B6 mice that received 7 × 10^5 CD4$^+$ T cells from eight unique CD45 and CD90 congenic strains, identified by partial splenectomy and tetramer-based cell enrichment 8 days and 60 days after *L. monocytogenes* infection. Each mouse contained a recipient-derived polyclonal (CD45.2/2 for mouse 1 or CD90.2/2 for mouse 2) and two donor-derived clonal populations (mouse 1, CD45.1/2 and CD45.1/1; mouse 2, CD90.1/2 and CD90.1/1). (**B**) Number of cells produced by different single naïve cells at day 8 and day 60 or 62 after infection. (**C**) Percent survival between day 8 and day 60 or 62 after infection for different donor-derived clonal or recipient-derived polyclonal effector cell populations. Note that one clone, with a calculated percent survival of 149%, is not shown. (**D**) Number of effector cells produced by different single naïve cells at day 8 versus the percentage that survived on day 60 or 62. Statistical values in (B) and (D) were calculated with the Spearman correlation test and in (C) with Student's *t* test for unpaired samples or an F test of equality of variances. Pooled results from two independent experiments are shown.

(fig. S2), as previously reported (*15*, *16*). Thus, after contracting, memory cells retain the phenotype of their effector cell predecessors, except that CXCR5^{++} PD-1^{+} cells lose PD-1.

We then examined the recall responses of clonal memory cell populations. Limiting numbers of CD4^{+} T cells from uninfected congenic strains were transferred into B6 mice, which were then infected with *L. monocytogenes*. Sixty-five donor-derived clonal LLOp:I-A^{b} tetramer–binding memory cell populations, ranging from 6 to 1010 cells and averaging about 40 cells, were detected by partial splenectomy and cell enrichment 60 days later (Fig. 4, A and B). Seven days after another *L. monocytogenes* infection, clonal memory cell populations expanded by a factor of about 15 (Fig. 4, A and B) to produce an average of about 600 effector cells (Fig. 4C), which tended to have the same CXCR5 phenotype as their memory cell predecessors (Fig. 4, C and D). Thus, clonal memory cell populations expanded during a recall infection, albeit less well than naïve cells, and produced effector cell subsets like themselves.

These results indicate that essentially all naïve T cells in a polyclonal repertoire that respond to a bacterial p:MHC II ligand by producing effector cells also produce memory cells. Although we have evidence that the tetramer used here detects many of the T cells with TCRs specific for this ligand (*17*), it should be noted that some p:MHC II–specific T cells do not bind to the relevant tetramer, presumably due to expression of low-affinity TCRs (*18*). Thus, although all naïve CD4^{+} T cells with TCRs that bind p:MHC II tetramer can become memory cells, it remains to be seen whether this conclusion applies to any p:MHC II–specific cells that do not.

Although the nature of the TCR signal experienced by individual naïve clones could influence their effector cell fate (*12*), the present results suggest that all TCRs can support memory cell formation, although some may be better at it than others (*4*–*6*). The observation that a clonal memory cell population was very likely to

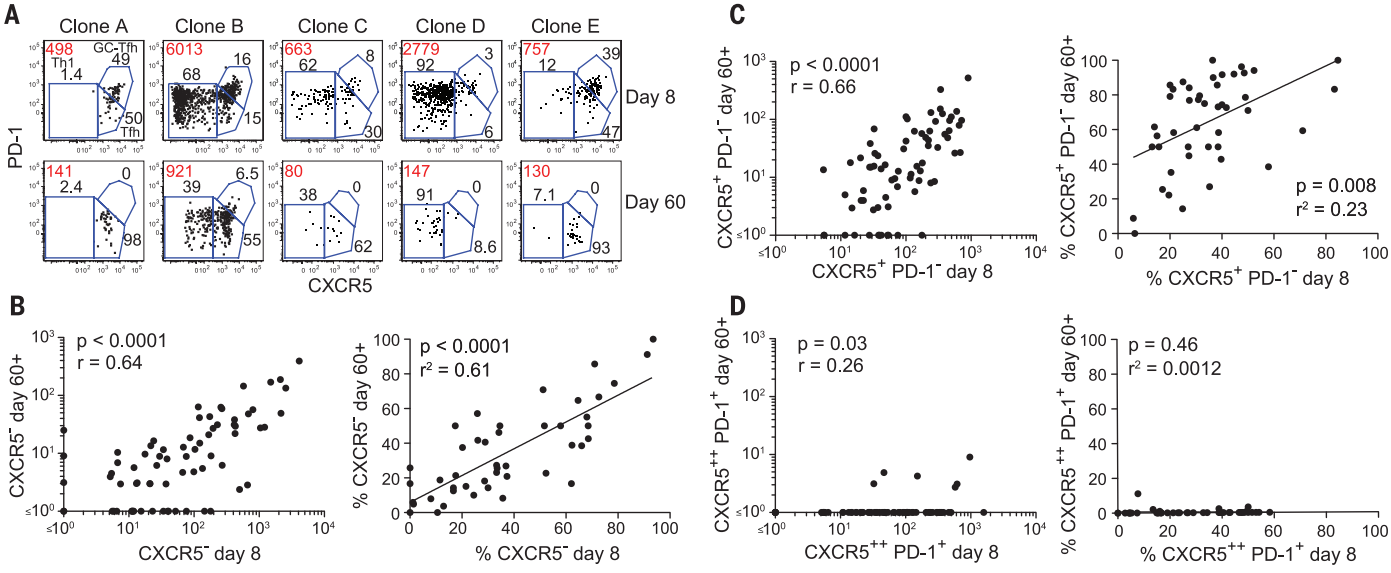


Fig. 3. Memory cells retain the CXCR5^{-} and CXCR5^{+} phenotype of effector cells. (**A**) Identification of T_H1, T_{FH}, and GC-T_{FH} effector cells in different clonal populations of CD44^{high} LLOp:I-A^{b} tetramer–binding cells on day 8 and day 60 after infection. Red values indicate the absolute number of cells in each population; black values indicate the percentages of each subset. (**B** to **D**) Left graph: Numbers of CXCR5^{-} (B), CXCR5^{+} PD-1^{-} (C), or CXCR5^{++} PD-1^{+} (D) cells in clonal populations at day 8 and day 60 or 62 after infection. Statistical values were calculated with the Spearman correlation test. Right graph: Percentages of cells in LLOp:I-A^{b} tetramer–binding clonal populations that were CXCR5^{-} (B), CXCR5^{+} (C), or CXCR5^{++} PD-1^{+} (D) on day 8 plotted versus the percentages of those subpopulations 60 to 62 days after infection. Each dot represents a clonal population. Only populations in which five or more events were recovered at day 60 or 62 were included to optimize the meaningfulness of the percentage values. Statistical values and trend lines from linear regression analyses are shown. Each dot represents a single clonal population. Pooled results from two independent experiments are shown.

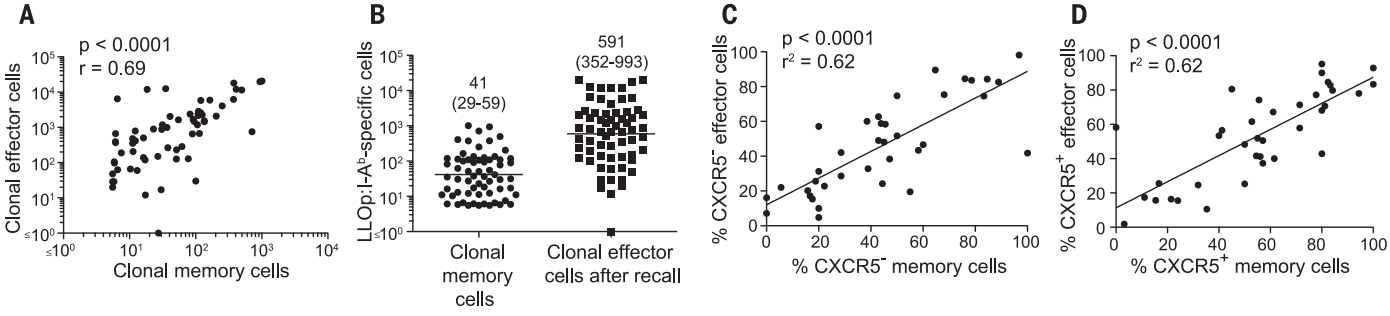


Fig. 4. Memory cells produce effector cells with a similar phenotype. (**A**) Numbers of LLOp:I-A^{b} tetramer–binding memory cells in 65 clonal populations plotted versus the number of effector cells produced from those populations 7 days after a second infection. (**B**) Numbers of LLOp:I-A^{b} tetramer–binding memory cells in 65 clonal populations before or 7 days after a second infection. Geometric mean values with 95% confidence intervals in parentheses are shown. (**C** and **D**) Percentages of CXCR5^{-} or CXCR5^{+} memory cells in individual clonal populations plotted versus the percentages of CXCR5^{-} or CXCR5^{+} effector cells generated from those populations after secondary infection. Statistical values and trend lines from linear regression analyses are shown. Pooled results from three independent experiments are shown.

have the same helper cell subset ratio as its predecessor population is consistent with each effector cell in the population having the same chance of becoming a memory cell. This model is consistent with studies of $CD8^+$ T cells indicating that memory cells arise from the effector cell pool by a TCR-independent stochastic process (*14*, *19*–*21*).

Our finding that a clonal $CD4^+$ memory T cell population tended to produce an effector cell population with the same subset composition after recall suggests that a $CXCR5^-$ memory cell produces $CXCR5^-$ effector cells and that a $CXCR5^+$ memory cell produces $CXCR5^+$ effector cells. Thus, although we (*10*) and others (*15*) have found that bulk $CXCR5^+$ memory cells can produce $CXCR5^-$ and $CXCR5^+$ effector cells, the present results fit the suggestion that both $CXCR5^+$ and $CXCR5^-$ cells are relatively lineage-committed (*15*). An advantage of this process is that the helper cell subset diversity of the effector cell pool is carried into the memory cell pool and retained thereafter.

REFERENCES AND NOTES

1. R. Ahmed, D. Gray, *Science* **272**, 54–60 (1996).
2. S. C. Jameson, D. Masopust, *Immunity* **31**, 859–871 (2009).
3. M. Pepper, M. K. Jenkins, *Nat. Immunol.* **12**, 467–471 (2011).
4. C. Kim, T. Wilson, K. F. Fischer, M. A. Williams, *Immunity* **39**, 508–520 (2013).
5. M. A. Williams, E. V. Ravkov, M. J. Bevan, *Immunity* **28**, 533–545 (2008).
6. P. A. Savage, J. J. Boniface, M. M. Davis, *Immunity* **10**, 485–492 (1999).
7. C. Stemberger *et al.*, *Immunity* **27**, 985–997 (2007).
8. C. Gerlach *et al.*, *J. Exp. Med.* **207**, 1235–1246 (2010).
9. J. J. Moon *et al.*, *Immunity* **27**, 203–213 (2007).
10. M. Pepper, A. J. Pagán, B. Z. Igyártó, J. J. Taylor, M. K. Jenkins, *Immunity* **35**, 583–595 (2011).
11. S. Crotty, *Annu. Rev. Immunol.* **29**, 621–663 (2011).
12. N. J. Tubo *et al.*, *Cell* **153**, 785–796 (2013).
13. C. Taswell, *J. Immunol.* **126**, 1614–1619 (1981).
14. V. R. Buchholz *et al.*, *Science* **340**, 630–635 (2013).
15. J. S. Hale *et al.*, *Immunity* **38**, 805–817 (2013).
16. K. Lüthje *et al.*, *Nat. Immunol.* **13**, 491–498 (2012).
17. R. W. Nelson *et al.*, *Immunity* **42**, 95–107 (2015).
18. R. J. Martinez, B. D. Evavold, *Front. Immunol.* **6**, 468 (2015).
19. J. N. Blattman, D. J. Sourdive, K. Murali-Krishna, R. Ahmed, J. D. Altman, *J. Immunol.* **165**, 6081–6090 (2000).
20. C. Gerlach *et al.*, *Science* **340**, 635–639 (2013).
21. P. Graef *et al.*, *Immunity* **41**, 116–126 (2014).

ACKNOWLEDGMENTS

We thank S. Jameson and D. Masopust for critical discussions and reading the manuscript and J. Walter for help with mouse breeding and screening. The data presented in this manuscript are tabulated in the main paper and in the supplementary materials. Supported by NIH grants R01 AI039614 (M.K.J.), R01 AI106791 (B.T.F.), and F32 AI107995 (N.J.T.).

SUPPLEMENTARY MATERIALS

www.sciencemag.org/content/351/6272/511/suppl/DC1
Materials and Methods
Figs. S1 and S2
References (*22*, *23*)

17 July 2015; accepted 23 December 2015
10.1126/science.aad0483

SEX CHROMOSOME

Two genes substitute for the mouse Y chromosome for spermatogenesis and reproduction

Yasuhiro Yamauchi,[1]* Jonathan M. Riel,[1]* Victor A. Ruthig,[1]* Eglė A. Ortega,[1] Michael J. Mitchell,[2] Monika A. Ward[1]†

The mammalian Y chromosome is considered a symbol of maleness, as it encodes a gene driving male sex determination, *Sry*, as well as a battery of other genes important for male reproduction. We previously demonstrated in the mouse that successful assisted reproduction can be achieved when the Y gene contribution is limited to only two genes, *Sry* and spermatogonial proliferation factor *Eif2s3y*. Here, we replaced *Sry* by transgenic activation of its downstream target *Sox9*, and *Eif2s3y*, by transgenic overexpression of its X chromosome–encoded homolog *Eif2s3x*. The resulting males with no Y chromosome genes produced haploid male gametes and sired offspring after assisted reproduction. Our findings support the existence of functional redundancy between the Y chromosome genes and their homologs encoded on other chromosomes.

Many sexual characteristics are influenced by sex chromosome constitution, with mammalian females typically carrying XX and males XY. We recently reported that in the mouse, only two Y-chromosome genes—testis-determinant *Sry* and spermatogonial proliferation factor *Eif2s3y*—are needed for successful assisted reproduction (*1*). Here, we asked if these two genes could be replaced by transgenic activation of their homologs encoded on other chromosomes.

For *Sry* replacement, we chose *Sox9* (*Sry*-related high-mobility–group box gene 9), a direct target of SRY (*2*). Prior work showed that transgenic overexpression of *Sox9* driven by the *Wt1* promoter results in female-to-male sex reversal in XX mice (*3*). We placed the *Wt1-Sox9* transgene in the context of a single X chromosome carrying the *Eif2s3y* transgene (fig. S1A) (*4*) and found that it generated males (X^EO*Sox9*). In these males, the Y-chromosome gene contribution is limited to *Eif2s3y* (table S1).

XO*Sry* males, which carry an autosomally encoded *Sry* transgene, develop testes containing spermatogonia that are unable to proliferate, which results in seminiferous tubules appearing empty when compared with those from males with an intact Y chromosome (XY) (Fig. 1, A and B). This defect can be overcome by transgenic *Eif2s3y* addition to the X chromosome (X^EO*Sry*) (table S1 and fig. S4A) (*1*, *5*). To replace *Eif2s3y*, we transgenically overexpressed its X chromosome–encoded homolog, *Eif2s3x* (fig. S2). We then placed the *Eif2s3x* transgene in the context of XO*Sry* (fig. S1B and supplementary text). The resulting XO*Sry*,*Eif2s3x* males (carrying autosomally encoded *Sry* and *Eif2s3x* transgenes) had the Y-chromosome contribution limited to *Sry* (table S1).

X^EO*Sox9* and XO*Sry*,*Eif2s3x* males had small testes (fig. S3), but spermatogenesis was initiated and progressed through meiosis and arrested at the round spermatid stage (fig. S4, B and C). Spermatogonia/Sertoli ratios in X^EO*Sox9* and XO*Sry*,*Eif2s3x* and spermatid/Sertoli ratio in X^EO*Sox9* were comparable to X^EO*Sry* but lower than those in XY (Fig. 1, D and E). Round spermatids in XO*Sry*,*Eif2s3x* were dramatically depleted; X^EO*Sry* and XY had 10 and 88 times as many, respectively (Fig. 1E and table S2). The spermatids from both X^EO*Sox9* and XO*Sry*,*Eif2s3x* males were functional in assisted fertilization, and live offspring were obtained after embryo transfer (Table 1).

We next tested whether spermatogenesis can take place in males with a complete absence of Y-chromosome genes. We used the same transgenes that were successful in single–Y gene substitutions (*Wt1-Sox9* and *Eif2s3x* Tg1) to generate mice transgenic for *Sox9* and *Eif2s3x* in the XO context (XO*Sox9*,*Eif2s3x*) (fig. S1C and table S1) The majority (35 out of 48) of XO*Sox9*,*Eif2s3x* males had testicular defects and essentially no germ cells (fig. S5 and supplementary text). In the remaining males, spermatogonial proliferation arrest was overcome (Fig. 1C and fig. S5), and spermatogenesis progression was comparable to that of XO*Sry*,*Eif2s3x* (Fig. 1, D and E, and table S2). Using assisted reproduction [round spermatid injection (ROSI)], we injected oocytes with spermatids from 13 males and obtained zygotes with two well-developed pronuclei and normal two-cell embryos (fig. S6, A to C, and movie S1). Embryos from 11 males were used for transfer. Ten resulted in pregnancy, and nine yielded offspring (Table 1). Among the males that yielded progeny, there were F_1, F_2, and F_3 generation XO*Sox9*,*Eif2s3x* ROSI males (fig. S6D). ROSI offspring from males with one or no Y-chromosome

[1]Institute for Biogenesis Research, John A. Burns School of Medicine, University of Hawaii, 1960 East-West Road, Honolulu, HI 96822, USA. [2]Aix-Marseille Université, INSERM, GMGF UMR_S 910, 13385 Marseille, France.
*These authors contributed equally to this work.
†Corresponding author. E-mail: mward@hawaii.edu

Downloaded from on January 31, 2016

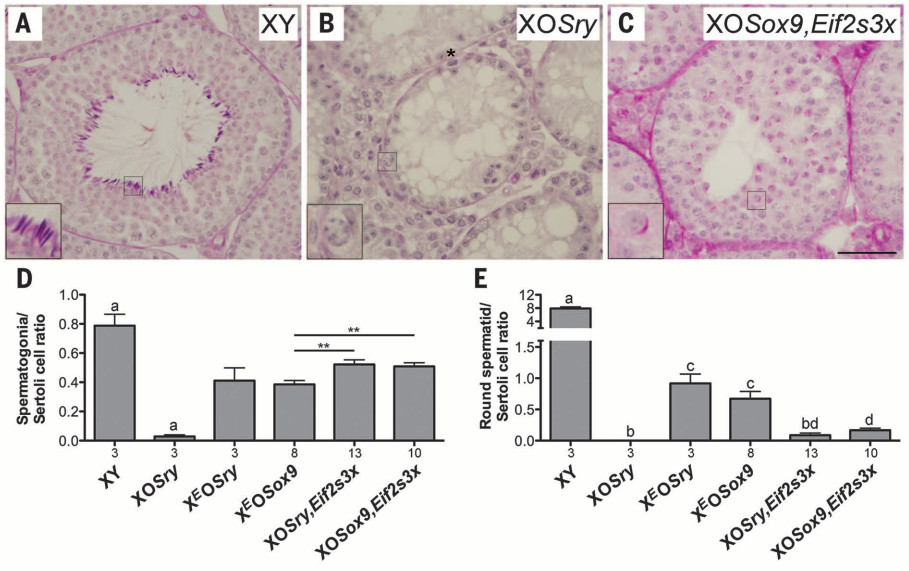


Fig. 1. Testis histology analysis. Tubules of periodic acid–Schiff–hematoxylin–stained sections of testis from XY (**A**), XO*Sry* (**B**), and XO*Sox9,Eif2s3x* (**C**) males. XY have normal spermatogenesis with expected germ cell types present, including step 16 spermatids [inset (A)]. XO*Sry* have spermatogonial proliferation arrest, resulting in tubules lacking germ cells except for occasional normal [inset (B)] and abnormal (*) spermatogonia. XO*Sox9,Eif2s3x* have meiotic and postmeiotic arrests that occasionally allow formation of round spermatids [insets (C)], arresting at step 7. Scale bar, 50 μm; insets, ×3 magnification. (**D** and **E**) Quantitative analysis of spermatogenesis progression. Bars are averages ± SEM, with *n* under the *x* axis. Statistical significance (*t* test): (D) bars marked with [a] are different from all others ($P < 0.05$), **$P < 0.01$; (E) bars with different letters are significantly different ($P < 0.05$).

Table 1. The results of ROSI with spermatids from males with a single or no Y-chromosome genes. Column heads 2 to 4: Males with round spermatids identifiable in live testicular cell suspension out of males examined. Males yielding progeny out of the number of males that yielded embryos used for embryo transfer and induced pregnancy. Live offspring as a percentage of embryos transferred. Statistical significance (Fisher's exact test, $P < 0.05$): [a]Different from all others.

Male genotype	Y gene contribution	Males with round spermatids (%) (no.)	Males yielding progeny	Live offspring (%) (no.)
X^{E}OSox9	*Eif2s3y*	80 (8/10)	7/8	15.7 (18/115)
XO*Sry,Eif2s3x*	*Sry*	55 (17/31)	16/17	22.5 (57/253)
XO*Sox9,Eif2s3x*	None	27 (13/48)[a]	9/10	20.7 (46/222)
XY control	Intact Y	100 (6/6)	6/6	25.0 (22/88)

genes were all normal and healthy (figs. S7 to S9 and supplementary text).

The quantification of *Eif2s3x/y* transcripts in males transgenic for *Eif2s3y* or *Eif2s3x* revealed a correlation between spermatogenesis progression and *Eif2s3x/y* expression level (Fig. 2, figs. S10 to S12, and supplementary text). All transgenic males had their respective transgene transcript levels elevated when compared with XY (Fig. 2, A and B). Compared with *Eif2s3x* transgenic males, *Eif2s3y* transgenic males showed higher *Eif2s3x/y* transcript levels (Fig. 2C) and increased incidence of round spermatids (Fig. 1E). When spermatogenesis and *Eif2s3x* expression were examined in XO*Sry,Eif2s3x* males with varying numbers of *Eif2s3x* transgene copies, one (Tg2 and Tg6) and four (Tg1), no differences in spermatogonia/Sertoli cell ratio were observed, but round spermatids were found only in Tg1 males, in which *Eif2s3x* transcript levels are 2.4 to 2.9 times those in Tg2 and Tg6 males (Fig. 2, D to F, and fig. S4, D to G).

We have shown that a male mouse without any Y-chromosome genes but with transgenically activated *Sox9* and *Eif2s3x* can generate haploid gametes and father offspring with the help of assisted fertilization. *Sox9* is not unique in being able to take over the *Sry* function in sex determination. Manipulation of expression of other genes can lead to sex-fate change [reviewed in (*6*–*8*)]. A surrogate sex-determination mechanism can also be activated without human input, as shown by two rodent species that lost the Y chromosome and *Sry* (*9*, *10*).

Eif2s3y and *Eif2s3x* represent a typical, formerly autosomal, single-copy, X-Y homologous gene pair and were hypothesized to have interchangeable function (*1*, *5*). Our data support this hypothesis: A single additional copy of *Eif2s3x* can functionally replace *Eif2s3y* in spermatogenesis initiation. For progression through meiosis, however, at least four *Eif2s3x* transgene copies are necessary, and the number of global *Eif2s3x/y* transcripts must reach a certain threshold. Our data also suggest that *Eif2s3x/y* may play roles in gonad formation. We observed severe abnormalities of mature testes, indicative of impaired gonadal development, in XO*Sox9,Eif2s3x* but not X^{E}O*Sox9* males. Because the global *Eif2s3x/y* expression is lower in the former, this suggests that a critical level of *Eif2s3x/y* may be required for efficient testis differentiation.

Our data support a model where *Eif2s3y* and *Eif2s3x* are functionally interchangeable in spermatogenesis, but each homolog has evolved a distinct expression level. *Eif2s3y* transcript amounts are ~5 to 7 times those in premeiotic and meiotic cells (*11*), which explains why the addition of one *Eif2s3x* transgene copy could not replace the function of endogenous *Eif2s3y* in driving spermatogenesis through meiosis. Our finding that a single *Eif2s3x* transgene copy was sufficient to substitute for *Eif2s3y* in overcoming spermatogonial proliferation arrest suggests that the strong *Eif2s3y* expression in spermatogonia is required for the subsequent meiotic stages but not for mitotic proliferation. Our observations contradict the accepted dogma of X-Y gene pairs evolving by decay on the Y chromosome and compensation on the X chromosome (*12*), because here, it is a beneficial overexpression of the Y gene *Eif2s3y* and not its X homolog that appears to have evolved to meet the needs of spermatogenesis. This might be the result of a selective advantage during oogenesis for reduced *Eif2s3x* levels or a selection for male germ cell beneficial effects on the Y chromosome.

It is generally believed that widely expressed genes on the human Y chromosome with X homologs that escape X inactivation are dosage-sensitive (*13*). Dosage sensitivity explains why genes are

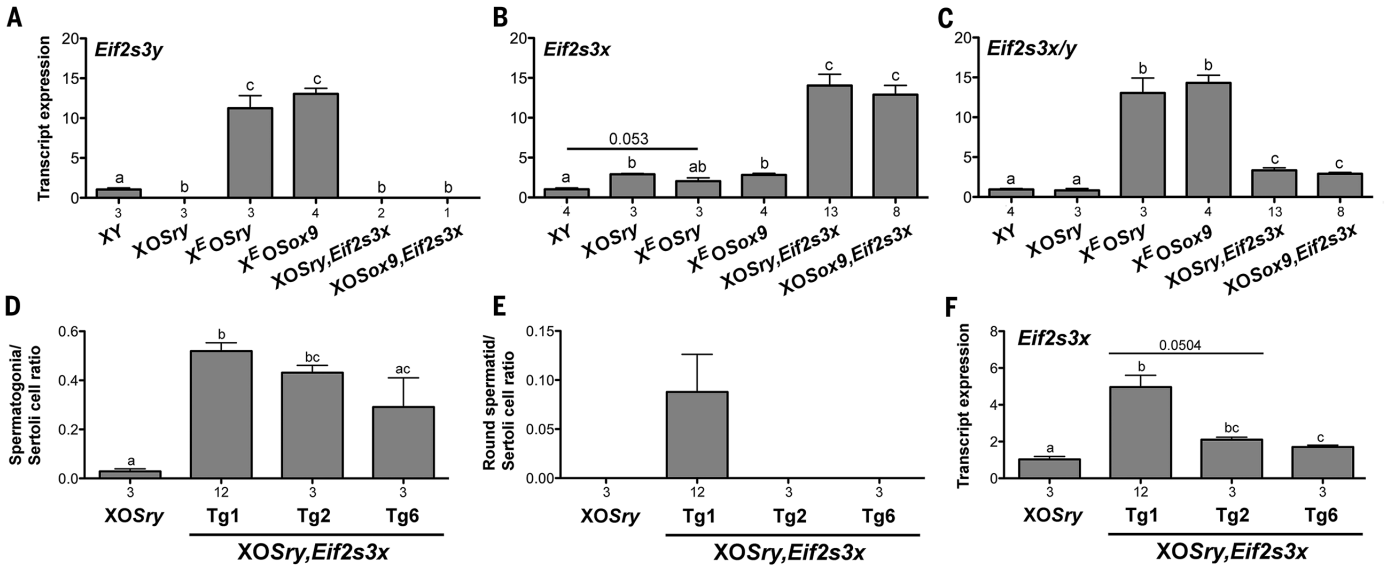


Fig. 2. Relation between *Eif2s3x/y* expression and spermatogenesis progression. (**A** to **C**) Transcript levels of endogenous and transgenic spermatogonial proliferation factors quantified by real-time polymerase chain reaction with *Actb* as a loading control and XY serving as reference control. (**D** to **F**) Analysis of spermatogenesis progression (D and E) and *Eif2s3x* expression (F) in XO*Sry,Eif2s3x* males with 4 (Tg1) and 1 (Tg2 and Tg6) *Eif2s3x* transgene copies. Means ± SEM, with *n* under the *x* axis; bars with different letters are statistically different (*t* test, $P < 0.05$).

conserved on the Y chromosome: A certain combined X-Y dose is critical at certain stages in certain tissues, and the X-gene dose cannot simply be increased globally to compensate for the loss of the Y gene because this would have detrimental effects in females. To lose the Y gene safely, the X gene, or the genome, or the developmental systems must adapt. Possible strategies might include incremental increases in X-gene dosage, relaxing constraints on dose-sensing, or retrogenes (*14*). The mouse *Eif2s3x/y* gene pair is not sensitive to overexpression; substantial elevation of *Eif2s3y* (*5*) or *Eif2s3x* in the XY context (this study) has no obvious somatic effects, nor does it affect spermatogenesis and fertility. These findings suggest that dosage sensitivity may appear mainly in association with underexpression and/or may vary between different X-Y gene pairs.

Altogether, our analyses of the *Eif2s3x/y* gene pair support their importance for spermatogenesis. It will now be imperative to explore the mechanisms whereby *Eif2s3x/y* factors exert their functions during testicular development and spermatogenesis. Our work also paves the way and prompts future evaluations of other ancestral X-Y gene pairs to clarify the dosage requirements for spermatogenesis and beyond. Finally, our demonstration that offspring can be obtained from males with no Y-chromosome genes shows that for assisted reproduction in the mouse, the Y chromosome is no longer necessary. However, there is extensive evidence from both phenotype characterization (*15*–*17*) and genomic analyses (*13*, *14*, *18*) unequivocally supporting the importance of Y-chromosome genes for normal, unassisted fertilization. So, although our data demonstrate that it is possible to bypass the requirement for the Y chromosome in male assisted reproduction, the Y clearly remains the genetic determinant of full natural masculinity.

REFERENCES AND NOTES

1. Y. Yamauchi, J. M. Riel, Z. Stoytcheva, M. A. Ward, *Science* **343**, 69–72 (2014).
2. R. Sekido, R. Lovell-Badge, *Nature* **453**, 930–934 (2008).
3. V. P. Vidal, M. C. Chaboissier, D. G. de Rooij, A. Schedl, *Nat. Genet.* **28**, 216–217 (2001).
4. Materials and methods and further details are available as supporting material on *Science* Online.
5. S. Mazeyrat *et al.*, *Nat. Genet.* **29**, 49–53 (2001).
6. S. Eggers, T. Ohnesorg, A. Sinclair, *Nat. Rev. Endocrinol.* **10**, 673–683 (2014).
7. A. Quinn, P. Koopman, *Semin. Reprod. Med.* **30**, 351–363 (2012).
8. N. Warr, A. Greenfield, *Dev. Biol.* **1**, 559–577 (2012).
9. W. Just *et al.*, *Nat. Genet.* **11**, 117–118 (1995).
10. S. Soullier, C. Hanni, F. Catzeflis, P. Berta, V. Laudet, *Mamm. Genome* **9**, 590–592 (1998).
11. H. Gan *et al.*, *Nat. Commun.* **4**, 1995 (2013).
12. K. Jegalian, D. C. Page, *Nature* **394**, 776–780 (1998).
13. D. W. Bellott *et al.*, *Nature* **508**, 494–499 (2014).
14. J. F. Hughes, H. Skaletsky, N. Koutseva, T. Pyntikova, D. C. Page, *Genome Biol.* **16**, 104 (2015).
15. J. Cocquet *et al.*, *PLOS Biol.* **7**, e1000244 (2009).
16. J. M. Riel *et al.*, *J. Cell Sci.* **126**, 803–813 (2013).
17. Y. Yamauchi *et al.*, *Biol. Reprod.* **81**, 353–361 (2009).
18. Y. Q. Soh *et al.*, *Cell* **159**, 800–813 (2014).

ACKNOWLEDGMENTS

The work was supported by NIH HD072380 and Hawaii Community Foundation 14ADVC-64546 grants to M.A.W. and INSERM core funding to M.J.M.

SUPPLEMENTARY MATERIALS

www.sciencemag.org/content/351/6272/514/suppl/DC1
Materials and Methods
Supplementary Text
Figs. S1 to S12
Tables S1 to S4
References (*19*–*50*)
Movie S1

4 August 2015; accepted 14 December 2015
10.1126/science.aad1795

NEW ENGLAND BioLabs® Inc.



In the know, wherever you go.

Introducing the NEBpubs™ app from New England Biolabs.

Looking for an easy and more environmentally-friendly way to catch up on your favorite NEB publications? Try the NEBpubs app! Available for both iPad® and Android™, the app contains interactive editions of our NEB Expressions newsletter, as well as all of our popular technical guides and product brochures. As if that weren't enough, you'll also get access to exclusive videos, animations, audio clips and other interactive content. *The NEBpubs app keeps you in the know, wherever you go!*

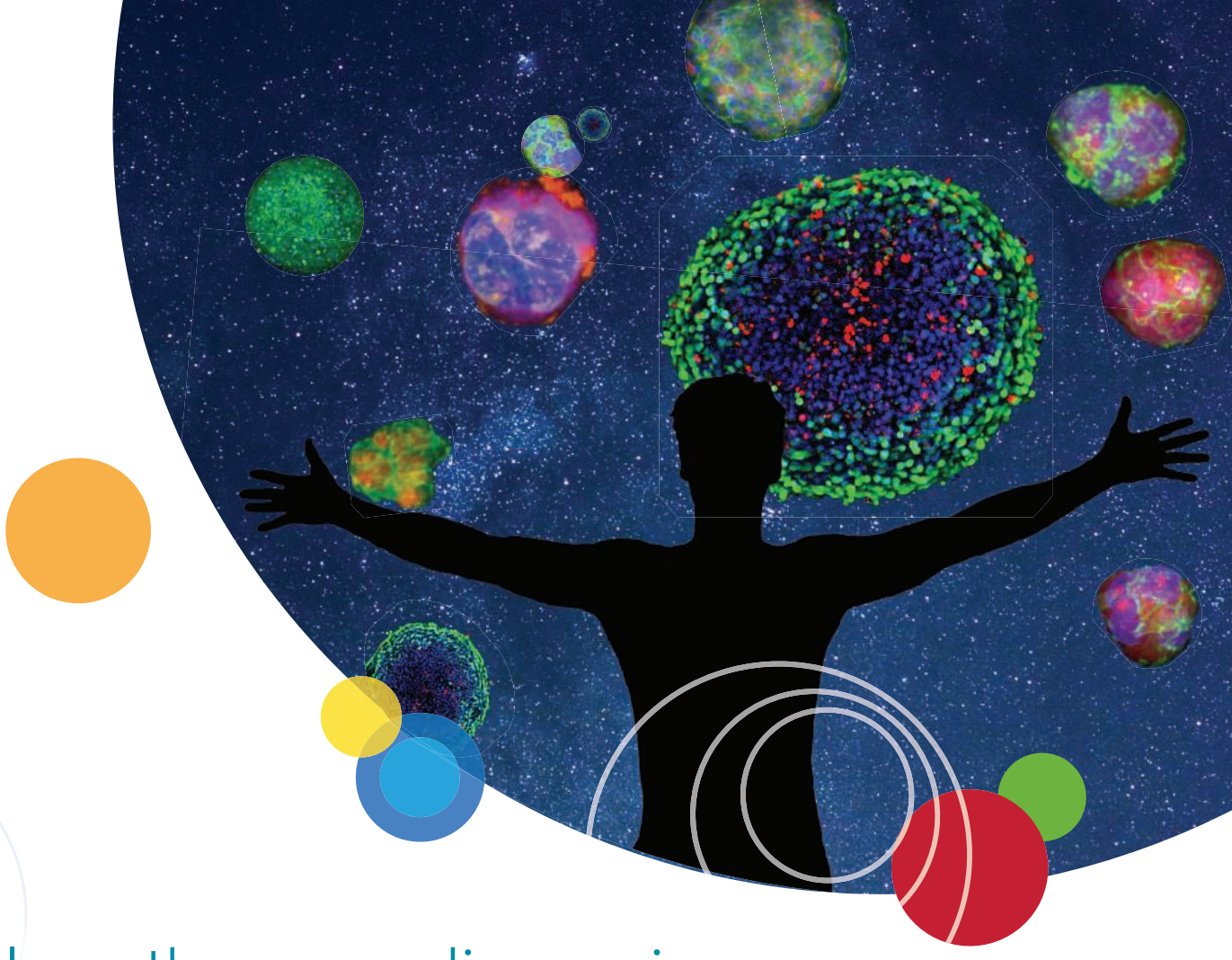
> *"The NEBpubs app is stellar. It's as beautiful and complete as you would expect from NEB – the same quality you get in their catalogs and publications...I'm a big fan of the NEB Expressions, so having them downloadable and available offline is helpful."*
>
> – Jason, Assistant Teaching Professor, University of Missouri

Get started today: www.neb.com/NEBpubs

Download on the App Store

GET IT ON Google play

NEW ENGLAND BIOLABS® and NEB® are registered trademarks of New England Biolabs, Inc. NEBPUBS™ is a trademark of New England Biolabs, Inc.
APPLE® and iPAD® are registered trademarks of Apple, Inc. GOOGLE PLAY™ and ANDROID™ are trademarks of Google, Inc.



Explore the new dimension

The confocal system for your complex biology

Explore the complexities of biology faster while generating better results. With our new ImageXpress® Micro Confocal High-Content Imaging System, you can run 3D cellular assays and obtain confocal results—at a speed you'd only expect from widefield screening. Easily quantify images and generate statistically relevant data by selecting an optical geometry from crisp confocal or whole-well widefield options to match your application requirements. Built on the reliable, field-proven ImageXpress Micro platform, the ImageXpress Micro Confocal is our most versatile system yet.



ImageXpress® Micro Confocal system

Discover more.

moleculardevices.com/IXMConfocal

MOLECULAR DEVICES

Unleash your brilliance™

For Research Use Only. Not for use in diagnostic procedures.

© 2015 Molecular Devices, LLC. All Rights Reserved. The trademarks mentioned herein are the property of Molecular Devices, LLC or their respective owners.

AACR Annual Meeting

American Association for Cancer Research

2016 • NEW ORLEANS

APRIL 16-20, 2016
ERNEST N. MORIAL CONVENTION CENTER
NEW ORLEANS, LA



For more information visit
www.AACR.org/AACR2016

Delivering Cures Through Cancer Science



Join us in New Orleans

for the best cancer science and medicine meeting in the world... the AACR Annual Meeting 2016!

You are invited to stretch your boundaries, form collaborations, attend sessions outside of your own area of expertise, and learn how to apply exciting new concepts, tools, and techniques to your own research.

Get your fill of ground-breaking cancer science each day, and then enjoy the great sounds, food, and culture that is New Orleans.

If you can only attend one cancer science meeting this year, the AACR's Annual Meeting is it!

Be sure to register early to take advantage of reduced rates!

Become a Member!

Join the AACR and enjoy substantially reduced registration rates, the privilege of sponsoring an abstract for the Annual Meeting, funding and award opportunities, and much more.

We look forward to seeing you in New Orleans!

CALLING ALL SCIENTISTS, PHILOSOPHERS, MATHEMATICIANS, CARDIOLOGISTS, TECHNOLOGISTS, VISIONARIES, STATISTICIANS, GAMERS, STUDENTS, RETIREES, TINKERERS AND ANYONE ELSE WHO MAY HAVE THE IDEA THAT'S GOING TO END CORONARY HEART DISEASE.

We're awarding $75 million to the idea that's going to end coronary heart disease and its consequences. If you have the thinking and leadership to bring one brave idea to life, this is your opportunity to join the list of visionaries who have made great strides in coronary heart disease research. Visit **onebraveidea.com** to get started.

ONE BRAVE IDEA™

A fund co-founded by:

American Heart Association.

verily

With significant support from:

AstraZeneca

FOCUS ON CAREERS

FACULTY



Responsibly conducting research

Responsible conduct of research (RCR) is every scientist's obligation, say researchers who have made RCR part of their scholarship. To promote high-quality science with lasting impact, these experts recommend individual actions and institutional policies that will create a culture of RCR.

See the full story on page 519.

Upcoming Features

Postdoc Careers—March 25
Cancer Research Careers—April 8
Regional Focus: China—June 24

Produced by the *Science*/AAAS Custom Publishing Office

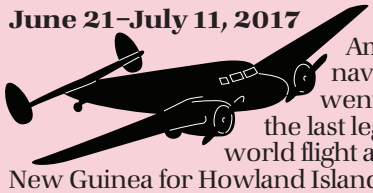
AAAS *Travels*

In Search of

AMELIA EARHART

Explore one of the greatest mysteries of all time!
On the 80th Anniversary of Amelia's World Flight & Disappearance!

June 21–July 11, 2017



On July 2, 1937, Amelia Earhart and her navigator Fred Noonan went missing on one of the last legs of their round the world flight after they departed New Guinea for Howland Island. Our colleagues at the International Group for Historic Aircraft Recovery (TIGHAR), believe they turned their Electra south and landed at Nikumaroro Island. On board the *Reef Endeavour,* we'll sail north from Fiji for 1,000 miles, stopping at Rotuma and Funafuti islands en route to Niku. We will join TIGHAR scientists in their research at Niku and look for artifacts which may indicate Amelia and Fred did land there! From $8,995 + air.

For a detailed brochure, call (800) 252-4910
All prices are per person twin share + air

BETCHART EXPEDITIONS INC.
17050 Montebello Rd, Cupertino, CA 95014
Email: AAASInfo@betchartexpeditions.com
www.betchartexpeditions.com

Antibiotic Sensitivity Testing

The mASTer (measuring antibiotic susceptibility testing easily and rapidly) software saves microbiologists hours of work by reproducibly measuring zones around antibiotic discs on antibiotic susceptibility testing (AST) plates and then automatically producing a bacteria's antibiotic susceptible, intermediate, or resistant (SIR) category. The versatile mASTer software can be used to analyze AST plate images generated by a Synbiosis ProtoCOL 3 automated zone measurement system or by a Syngene G:BOX image analyzer. Using a ProtoCOL 3 system with the new mASTer software allows scientists to work in a high-throughput batch mode to accurately measure zones around antibiotic sensitivity discs. With the G:BOX, microbiologists simply generate monochrome images of their AST plates and import them into the mASTer software. The mASTer software will, at the touch of a button, automatically measure inhibition zones on the true-to-life images and compare the results to data from all the tested microbes that have breakpoint values in the European Committee on Antimicrobial Susceptibility Testing (EUCAST) database.

Synbiosis
For info: +44-(0)-1223-727125
www.syngene.com

Ductless Balance Enclosures

Ideal for areas with restricted bench space, the AirClean Systems' popular PowderSafe Type A ductless balance enclosures have been further expanded to include the AC705, a smaller 24-inch wide model. Based on AirClean Systems' proven PowderSafe Type A design, the new AC705 provides operator protection from exposure to harmful powders and particulates, without disturbing balance readings. Each PowderSafe AC705 balance enclosure features an electrostatically-charged prefilter and high-efficiency particulate arrestance (HEPA) filtration for fine particulate capture. A mini-helic air flow gauge, HEPA filter-change indicator light, and integral polypropylene base are also standard. PowderSafe Type A ductless balance enclosures are manufactured in the United States and are shipped fully assembled. The installed HEPA filtration on each enclosure is leak-tested prior to shipment, making it ready for use upon arrival without on-site certification.

AirClean Systems
For info: 800-849-0472
www.aircleansystems.com



LED Illuminator

X-Cite TURBO is a new multiwavelength light-emitting diode (LED) fluorescence illuminator for microscopy imaging and detection applications. Featuring the patent-pending LaserLED Hybrid Drive, X-Cite TURBO provides maximum excitation power for all standard color wavelengths. The new X-Cite TURBO enables precise control by balancing illumination intensities between six popular wavelengths to protect samples from photodamage. Original equipment manufacturers (OEMs) and microscopists are able to define the exact bandwidth of light desired to reach the fluorophore for maximum excitation efficiency. X-Cite TURBO enables individual or simultaneous excitation of all fluorophores ranging from 4',6-diamidino-2-phenylindole (DAPI) to cyanine 5 (Cy5), or fluorescence proteins from cyan fluorescence protein (CFP) to mCherry, making it suitable for conducting a variety of live or fixed-cell imaging and detection experiments. X-Cite TURBO also features the valuable benefits of LED technology such as long lifetimes, mercury-free operation, virtually zero maintenance, and instant on/off capabilities. Additionally, the intensity of each of the six LEDs can be controlled independently through analog signals or PC control interface.

Excelitas Technologies
For info: 800-775-6786
www.excelitas.com

Adjustable Rigid Post Mounts

The HZP Series adjustable rigid post mounts provide a simple, flexible, stable, and low-cost solution for electophysiology applications. Compatible with upright and inverted microscopes and available in four different heights, the Prior HZP series is designed to work with Sensapex zero-drift solid state and other common micromanipulators. The HZP series offers a 60° sliding dovetail for smooth, stable positioning and requires no tools for height and rotational adjustment. Compatible with 1/4-20 and 6 mm optical breadboards, the HZP adjustable rigid post mounts are available with a micromanipulator platform, a platform for Prior standard sample holders, or a 110 mm diameter circular sample holder for recording chambers and standard microscope manual stage inserts.

Prior Scientific
For info: 800-877-2234
www.prior.com

Mutation Enrichment Kits

ICEme Mutation Enrichment Kits allow researchers to supercharge the sequencing platforms already present in their labs, including Sanger, next-generation sequencing (NGS), and droplet digital polymerase chain reaction (ddPCR), and achieve greatly improved detection. The kits leverage the distinctive performance attributes of multiplexed ice cold PCR (MX-ICP) technology to help cancer researchers accelerate the discovery of biomarkers, aid cancer research, and eventually improve cancer patient diagnosis and treatment. The kits work well with virtually any type of patient sample, including tissue, blood, plasma, urine, and other biofluids. MX-ICP technology is also nonallele specific, amplifying all mutations in the region under investigation. It delivers ultrahigh sensitivity, providing up to a 500-fold increase in mutation detection compared to most current methods, with levels of detection routinely achievable down to 0.01%. The kits are easily customizable for use with either single mutations or in combination—researchers can select the mutations they want. The initial menu includes 17 clinically relevant, actionable mutations that are associated with various cancers.

Transgenomic
For info: 888-813-7253
www.transgenomic.com

Electronically submit your new product description or product literature information! Go to www.sciencemag.org/products/newproducts.dtl for more information.

Newly offered instrumentation, apparatus, and laboratory materials of interest to researchers in all disciplines in academic, industrial, and governmental organizations are featured in this space. Emphasis is given to purpose, chief characteristics, and availability of products and materials. Endorsement by *Science* or AAAS of any products or materials mentioned is not implied. Additional information may be obtained from the manufacturer or supplier.



Join AAAS. Get instant access to *Science*. Support all of the sciences.

When you subscribe to *Science*, you become part of the American Association for the Advancement of Science (AAAS), a nonprofit community of more than 100,000 members worldwide who believe in the power of science to make the world a better place. AAAS is hard at work promoting science in government, schools, and in the public commons around the globe.

AAAS's award-winning journal *Science* offers the top peer-reviewed research across multiple disciplines. With your subscription, you'll get:

- 51 weeks of home delivery of *Science*
- Instant online retrieval of every *Science* article ever published, dating back to 1880
- Full access to the *Science* mobile site and apps
- Career advice, webinars, blogs and fascinating features exclusively for AAAS members
- Members-only newsletters, and much more

With increasing public skepticism about science–and public funding for research more uncertain than ever–our work has never been more important. Join hands with us today!

Visit promo.aaas.org/joinaaas. Together, we can make a difference.

Science
AAAS



THIS TEAM REVEALS THE FORCES BEHIND LIVING SHAPE

Photo: Laurent Julliand • théra

- **Tissue Architecture and Plasticity** is their name.
- **Morphogenesis mechanics** is the topic of their groundbreaking science.
- ***Drosophila*** is their model organism.
- **The Developmental Biology Institute of Marseille, France**, is their playfield.

Thomas Lecuit is their leader.
He pioneered the study of epithelial dynamics in whole organisms.

He is the 2015 laureate of the Liliane Bettencourt Prize for Life Sciences.

BETTENCOURT
SCHUELLER
FOUNDATION

The Liliane Bettencourt Prize for Life Sciences rewards a European researcher under the age of 45.

It has been awarded every year since 1997 to scientists recognized within the community for the quality of their international publications, the promising prospects of their projects and the leadership demonstrated in mobilising an entire team.

Created by a family, the Foundation trusts in people and their capacities, emphasizing inititative, creativity, quality and openness.

Its convictions define its spirit and ways of working – in the common interest, not for profit, and with social responsibility in mind.

27-29 rue des Poissonniers • 92200 Neuilly-sur-Seine • France
sciences@fondationbs.org

Find out more about Thomas Lecuit, the Bettencourt Schueller Foundation's purpose and this year's awards at ***www.fondationbs.org***



Science Careers Advertising

For full advertising details, go to ScienceCareers.org and click For Employers, or call one of our representatives.

Tracy Holmes
Worldwide Associate Director
Science Careers
Phone: +44 (0) 1223 326525

THE AMERICAS

E-mail: advertise@sciencecareers.org

Fax: +1 (202) 289 6742

Tina Burks
Phone: +1 (202) 326 6577

Nancy Toema
Phone: +1 (202) 326 6578

Online Job Posting Questions
Phone: +1 (202) 312 6375

EUROPE / INDIA / AUSTRALIA / NEW ZEALAND / REST OF WORLD

E-mail: ads@science-int.co.uk

Fax: +44 (0) 1223 326532

Sarah Lelarge
Phone: +44 (0) 1223 326527

Kelly Grace
Phone: +44 (0) 1223 326528

Online Job Posting Questions
Phone: +44 (0) 1223 326528

JAPAN

Katsuyoshi Fukamizu (Tokyo)
E-mail: kfukamizu@aaas.org
Phone: +81 3 3219 5777

Hiroyuki Mashiki (Kyoto)
E-mail: hmashiki@aaas.org
Phone: +81 75 823 1109

CHINA / KOREA / SINGAPORE / TAIWAN / THAILAND

Ruolei Wu
Phone: +86 186 0082 9345
E-mail: rwu@aaas.org

All ads submitted for publication must comply with applicable U.S. and non-U.S. laws. *Science* reserves the right to refuse any advertisement at its sole discretion for any reason, including without limitation for offensive language or inappropriate content, and all advertising is subject to publisher approval. *Science* encourages our readers to alert us to any ads that they feel may be discriminatory or offensive.

ScienceCareers
FROM THE JOURNAL SCIENCE AAAS

ScienceCareers.org

SANFORD RESEARCH

ASSOCIATE SCIENTIST/ASSISTANT PROFESSOR CHILDREN'S HEALTH RESEARCH CENTER, SANFORD RESEARCH

The Children's Health Research Center (CHRC, Sioux Falls, SD http://www.sanfordresearch.org/researchcenters/childrenshealth/), invites applications from researchers for full time faculty at the rank of Associate Scientist within Sanford Research (http://www.sanfordresearch.org/) with commensurate rank of Assistant Professor in the Department of Pediatrics of the Sanford School of Medicine at The University of South Dakota. An historic $400 million gift by philanthropist Denny Sanford has allowed for expansion of Sanford Research and development of the CHRC, an energetic and collegial research community focused on pediatric research.

We seek outstanding scientists with research programs on the underlying mechanisms and/or treatment of congenital defects, developmental disorders, pediatric diseases and regenerative cellular therapies. Applicants should hold a PhD, MD or MD/PhD degree and complement the existing strengths and the interdisciplinary and collaborative nature of the CHRC. Additionally, Physician Scientists are encouraged to apply. Candidates will be expected to develop independent research programs and secure extramural funding.

Significant institutional support, including modern laboratory space and state-of-the-art facilities, will be provided at the Sanford Center. In addition, a comprehensive compensation package will be tailored to the individual's qualifications.

Sanford Health is an Equal Opportunity/Affirmative Action Employer. Candidates should submit a single PDF including a detailed *curriculum vitae*, description of research experience and future research plans with specific details on the relevance of their research to pediatric research. Candidates should also submit at least three letters of recommendation. Incomplete candidate packages will not be accepted.

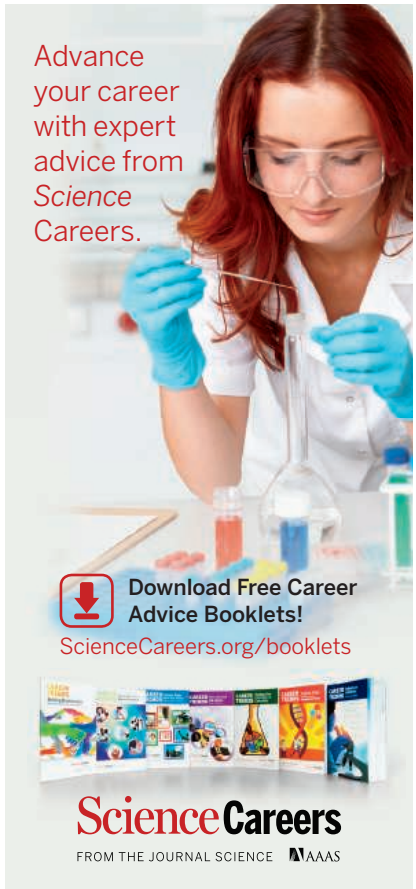
All application materials should be sent by email to:
Faculty Recruitment Committee; Chairs: Drs. Kyle Roux, Jill Weimer and Kurt Griffin
Children's Health Research Center at Sanford Research
and Department of Pediatrics at Sanford School of Medicine of The University of South Dakota
2301 E. 60th Street North, Sioux Falls, SD 57104
Telephone: 605-312-6004
Email: researchrecruitment@sanfordhealth.org

FACULTY POSITIONS

COLUMBUS STATE UNIVERSITY ASSISTANT PROFESSOR POSITION

Columbus State University Department of Biology in Columbus, GA invites applications for a tenure-track position as an organismic biologist at the rank of Assistant Professor to begin in August 2016. Teaching duties include undergraduate courses in anatomy and physiology, organismic biology, and animal physiology with the expectation to develop additional undergraduate and graduate courses in the candidate's area of specialty. The candidate is expected to establish an active research program, advise undergraduate and graduate students, and provide professional service to the university and the community. For details and to apply visit website: **https://columbusstate.peopleadmin.com/**. Review of applications will begin immediately will continue until the position is filled. Find more information about the department at website: **https://bio.columbusstate.edu**.

Post Your Jobs
1 million candidates*
151,000 job applications*
Reach Scientists.
Fill Positions.
*Jan–Dec 2014
ScienceCareers
employers.sciencecareers.org





Responsibly conducting research

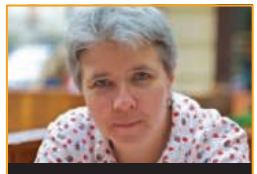
High-profile retractions of papers for falsification, misrepresentation, and dishonest reviews are a blow to science. They add urgency to ongoing campaigns for responsible conduct of research (RCR). RCR is every scientist's obligation, say researchers who have made RCR part of their scholarship. To promote high-quality science with lasting impact, these experts recommend individual actions and institutional policies that will create a culture of RCR. **By Chris Tachibana**

Outright scientific fraud is fortunately rare. More pervasive and arguably more damaging to science is hastily conducted, poorly reported, irreproducible research. To combat this problem, prominent organizations have launched campaigns to raise awareness about it, explore its root causes, and promote RCR resources. For example, *Science* helped develop the Transparency and Openness Promotion (TOP) guidelines. The American Society for Cell Biology is behind the draft of the San Francisco Declaration on Research Assessment (DORA). An international initiative has formed the Enhancing the QUAlity and Transparency Of health Research (EQUATOR) Network. And an initiative from *The Lancet* is fighting waste in biomedical research.

These and other programs address an expanding catalog of RCR issues. The list of topics is overwhelming. It includes validation of reagents, secure and transparent data handling, full reporting of studies including negative results, proper assignment of authorship, and open access to publications. But we can meet these challenges, say researchers with years of RCR experience, if we all take steps to promote best research and publication practices. We should start with our own work, then encourage trainees, peers, and our institution.

Create a responsible culture

It all begins with attitude, says **Virginia Barbour,** chair of the Committee on Publication Ethics (COPE). "The bottom line," she says, "is that the culture of the group and the institution determines how people conduct their research." From the moment you walk into the lab, she says, practice transparency: "Expect that everything you do is public. Make sure that other people can look at your work and know exactly what you did." Leaders promote transparency by regularly communicating with junior researchers, encouraging open discussions throughout the group, and taking RCR policies seriously. For example, Australia, where Barbour resides, follows the Australian Code for the Responsible Conduct of Research. Once you have that culture in place, says Barbour, layer on specific elements such as data management, recordkeeping, and publication plans.


Virginia Barbour

Preparation is important. "Before you start experiments," says Barbour, "think about how you will manage your data, notebook, images, and analysis software associated with the project." Authorship is one of the biggest challenges that COPE deals with, Barbour says, and should also be addressed at the beginning of a study. Be clear about the contribution of each person considered for authorship and remember to credit junior researchers. "You and your collaborators might not agree in the beginning about who will be authors and their order," she says, "but at least agree on the process of deciding authorship." This initial investment will pay off when you write up results. When protocols and procedures are in place from the beginning, accurate reporting at the end is easier.

Barbour was a founding editor of the open-access journal *PLOS Medicine* and is now executive officer for the Australasian Open Access Support Group. Researchers understand that open access promotes equity by making results available to all scientists and showing taxpayers the products of public funding, says Barbour. However, early career researchers in particular can feel torn between the demand for publications in certain journals and the open access publication model.

To increase the accessibility of scientific publications, many funding agencies now require articles to be publicly archived, for example in PubMed Central. Australian funders demand at least deposition of the author-accepted manuscript in an institutional repository. Some universities, including Harvard and the University of California San Francisco, have policies and repositories for this purpose. These are all steps toward recognizing and rewarding high-quality science that is clearly documented and can be validated and verified, says Barbour: "Research that is done well and reported well. That's what we should be aiming for." cont.>

PHOTOS: (FROM LEFT) © SHUTTERSTOCK.COM/ERGE; LARRY PEIPERL

"Just knowing RCR rules does not guarantee ethical behavior. Wanting to be ethical is the key." — Ioanna Semendeferi


Semendeferi (left) and Pavlidis

Keep up with RCR developments

Maintaining a culture of responsible research means keeping an eye on evolving RCR issues. **Francis Macrina,** vice president for research and innovation at Virginia Commonwealth University (VCU), has tracked RCR changes since he started an RCR course in the 1980s, before the National Institutes of Health and other funders began requiring ethics instruction for many trainees. He still teaches the course, and his experience and case studies are collected in his textbook on scientific integrity. Macrina has seen RCR grow to include a focus on data transparency, treatment, and storage; verification of cell lines, antibodies, and other reagents; parameters for working with the media; and the expansion of publication guidelines including "dual-use" biosecurity reporting for results that might be used for weapons development. Referring to the TOP Guidelines, he says, "We'll also probably see these entering practice incrementally."

To get an overview of current RCR requirements and issues in your field, Macrina suggests starting with journal author instructions. COPE and the International Committee of Medical Journal Editors have general publishing guidelines. Discipline-specific information is available from professional organizations such as the Society for Neuroscience and the American Chemical Society.

Macrina's office at VCU oversees industry collaborations, which raise additional RCR considerations. Examples include how long a company can delay manuscript submission for intellectual property review and whether students should work on industry-sponsored projects. "VCU has a corporate-sponsored research policy," Macrina says, so academic scientists thinking about an industry partnership should check with their technology transfer or commercialization center about similar documents. Experts at these centers can provide background, guidance, and advocacy in developing partnership agreements.

Companies want to collaborate with scientists who apply best practices because RCR is critical to the science-based industry, says **Christopher J. Roberts,** associate director of computational biology at Biogen Idec. When developing a drug or device, he explains, everything has to be absolutely dependable. "If you can't replicate something or get reliable results from a preclinical assay that you'll be running repeatedly," he says, "you'll never get a drug that works in the clinical phase." Companies also understand that peer-reviewed articles are important for the career development of their own scientists and their university collaborators, so many have established publication policies. However, the closer you get to a product, Roberts says, the more constraints you'll find on publishing. This is why, for university collaborations, Roberts says, "We set up legal agreements in advance that spell out intellectual property considerations and a publication strategy and timeline."

Train new scientists in RCR

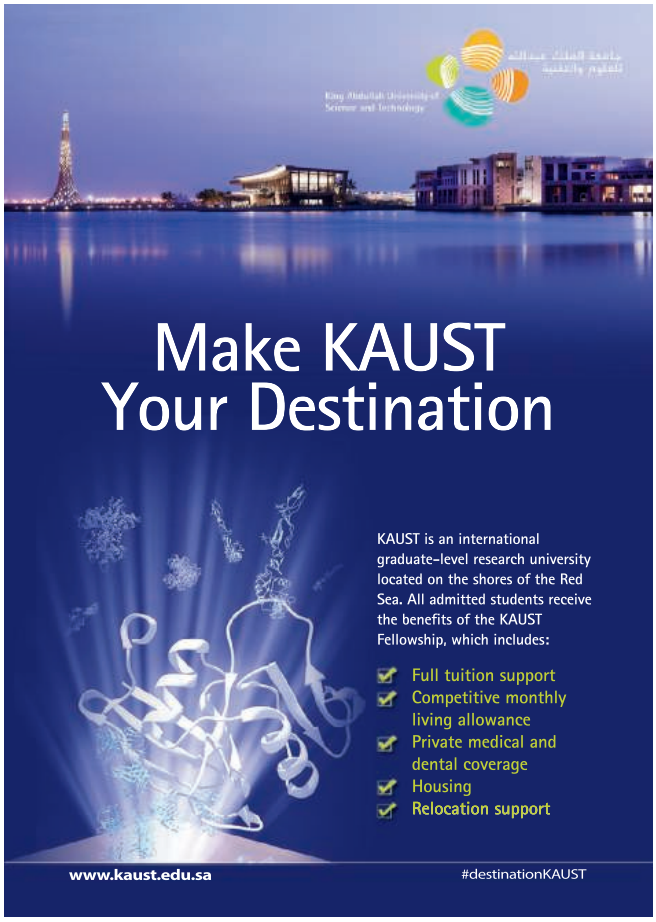
To achieve the aim of a ubiquitous culture of RCR, early career researchers need to be trained in RCR principles. Scientists have always learned their craft from mentors, but the faster pace and increased complexity of research now demands more formal training in best practices. A comprehensive, multimethod, history-based approach to RCR training is underway at the University of Houston. Associate Instructional and Research Professor **Ioanna Semendeferi** of the Department of Physics led development of a three-credit course with validated evaluation methods supported by the National Science Foundation. The core principle of the course is that best practices follow when scientists internalize ethical values. "Just knowing RCR rules does not guarantee ethical behavior," says Semendeferi. "Wanting to be ethical is the key."

Ioannis Pavlidis, Computational Physiology Lab director, co-teaches the course and helped develop it. "Semendeferi's approach is [to] lecture with visual elements like movies and documentaries that add emotional richness and cultivate empathy," he says. Course activities include in-class debates, a peer-review exercise supervised by a senior scientist, observing research with animals and human participants, and interpreting science ethics commentaries in national newspapers. The project also organizes a public seminar series on science history and ethics.

Semendeferi and Pavlidis recommend general science ethics courses that mix students from engineering, humanities, and social and natural sciences. "Everyone coming together is an education by itself," says Semendeferi. She says that hearing different viewpoints makes students aware of the decisions involved in doing ethical science and of their personal responsibility for their work. **Stephanie Watts,** professor of pharmacology and toxicology and assistant dean of the graduate school at Michigan State University (MSU), has had the same experience in a workshop series she coordinates that takes a practical approach to RCR issues. Watts says when students from multiple disciplines and countries hold discussions, they often spontaneously raise questions about expectations and norms in other fields and cultures. Examples are honorary authorship, which might be expected in some countries but against journal guidelines, or an engineer's impulse to precisely duplicate published text about methods, which can result in self-plagiarism. "We recognize that different parts of the world have different rules," says Watts, "So we talk about having conversations at the beginning of a collaboration about data sharing, authorship, and other publication issues. We talk about how plagiarism is stealing someone else's work, and no society allows stealing."

Watts and Pavlidis say teaching RCR has influenced their own research. "Reading and thinking about these issues has made me a better mentor," says Watts. "I talk cont.>

PHOTO: PROFESSOR BETTY SMOCOVITIS



Karolinska Institutet

Stockholms läns landsting

CIMED announces Junior and Senior Investigator grants within medical research

Center for Innovative Medicine (CIMED) at Karolinska Institutet South Campus supported by the Stockholm County Council (SLL), announces 5-year Junior and Senior Investigator grants in medical research and innovation involving basic, translational or clinical research.

For more information please visit:
cimed.ki.se

The closing date for applications is:
April 4th 2016



WE BELIEVE GRAND CHALLENGES REQUIRE BOLD ACTIONS.

We believe in the relentless pursuit of big ideas. In thinking ahead of the curve. We believe in individual strength and the power of collaboration. And in making tomorrow what we dream it can be. We believe in advancing the common good with uncommon will.

MSU's Global Impact Initiative is a bold endeavor designed to accelerate the pace of discovery through the creation of more than 100 new faculty positions in some of the most promising—and critical—fields of research, including energy, health, education, the environment, national security, and global development. **Join us.**

SPARTANS WILL.

msu.edu/globalimpact

MICHIGAN STATE UNIVERSITY

Featured Participants

Australasian Open Access Support Group
aoasg.org.au

Biogen Idec
www.biogen.com

Michigan State University
www.msu.edu

University of Houston
www.uh.edu

Virginia Commonwealth University
www.vcu.edu

Additional Resources

Australian Code for the Responsible Conduct of Research
www.nhmrc.gov.au/guidelines-publications/r39

Committee on Publication Ethics (COPE)
publicationethics.org/resources/guidelines

Enhancing the QUAlity and Transparency Of health Research (EQUATOR) Network
www.equator-network.org

International Committee of Medical Journal Editors (ICMJE)
www.icmje.org/recommendations

San Francisco Declaration on Research Assessment (DORA)
am.ascb.org/dora

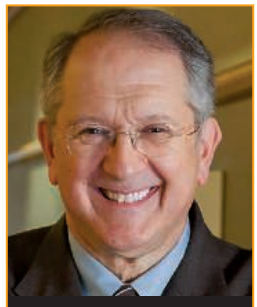
Transparency and Openness Promotion (TOP) Guidelines
cos.io/top

with lab members often so I know what they're doing. I see raw data from the start to the end of a project and we all interrogate each other in lab meetings about how we got our data and what they mean." Watts says keeping close track of everyone's work is just part of her job. "I tell them it's not because I don't trust them but to make sure we agree on the approach and what we see in the data. It's an RCR issue."

Teaching RCR has also affected Pavlidis's research on methods to measure physiological variables, such as for sleep, exercise, and dexterity. "We handle a lot of data," he says, "so we try to be transparent about it." For a project on measuring drivers' responses under stress, data are posted online as they accumulate. "Open data sharing lets everyone trace our conclusions from A to Z," he says. His group practices team science, cultivating a culture of mutual respect and credit sharing that recognizes both intellectual and technical contributions. Everyone understands the arrangement from the beginning, he says: For a given project, technical contributors get first credit in methods papers, while theoretical publications highlight other team members.

Promote RCR in departments and institutions

Formal courses mean that students, postdocs, and faculty who teach RCR are well versed in current issues in best research practices. For senior faculty educated before RCR training requirements came about, Watts says getting involved in an RCR course is a good introduction and can be fun. For the MSU workshops, Watts recruits colleagues as speakers, and students choose faculty members to be their research integrity consultants—their sounding board for RCR discussions. At VCU, Macrina recruits two or three faculty members per session to facilitate case discussions and gives them a one-hour training session on the basics of the course material.


Francis Macrina

However, even this time commitment might seem like a burden to overworked faculty. Watts leads her own research group, so she sympathizes with scientists who say they already spend up to 40 percent of their time on regulatory work. To handle the paperwork, she recommends taking advantage of institutional offices that help with Institutional Review Board proposals and radiation safety requirements, for example. But for scientists to stay motivated in the face of increasing regulations, widespread changes in culture and attitudes are needed. When Watts feels overwhelmed by regulations, she tells herself: "It's a privilege to have a lab and I'm lucky to be doing this work supported by taxpayer dollars. You want to do your science right, so your colleagues trust your work and you trust theirs."

Macrina agrees, and he questions the value of data that can't be reproduced. Although every new requirement adds bureaucracy, he says, "It's all about public trust." Trust is critical for the reputation of the researcher, the institution, and science in general. "It sounds like a cliché," he says, "but if we want research to have an impact, people need to trust researchers."

For culture change at the institutional level, we need to align hiring and promotion practices with RCR. Pavlidis and Semendeferi recommend rewarding scientists for mentoring, especially in RCR. Semendeferi says, "Just demanding particular behaviors without eliminating the conditions that lead to unethical practices will not solve the issues." We can all contribute to change, she says: "Individual scientists have the ability and power to make a difference."

The message that paper counts and journal impact factors don't represent true research value is reaching the academy. Macrina warns that moving away from these simple measures will take time. "Determining research quality isn't easy," he says. "Hiring committees have to seek and gather evidence to evaluate each publication, instead of just counting papers in high-impact journals." However, he is encouraged by initiatives like DORA, and by scientific leaders like National Medal of Science awardee Bruce Alberts who publicly criticize using impact factors to assess research productivity. Watts notes that these discussions are already having an effect. "I understand that young scientists feel pressured to move quickly and produce high-impact publications," she says. "But I'm involved in a job search right now and I'm looking for people who do their work with integrity, can finish what they start, and do solid science that others can build on—that's who I want to hire."

Chris Tachibana is a science writer based in Seattle, USA and Copenhagen, Denmark.

DOI: 10.1126/science.opms.r1600161

PHOTO: COURTESY OF VCU OFFICE OF RESEARCH AND INNOVATION

Vice President
Clinical Research Operations

The Vice President of Clinical Research Operations will report to the system's Chief Academic Officer and will serve as an integral leader for the growth, development and future success of research operations within the overall Dartmouth-Hitchcock system. Ideally, the individual fulfilling this role will combine their leadership shills, entrepreneurial spirit and industry insight into a dynamic, positive force for the future of clinical research at Dartmouth-Hitchcock (D-H). This leader will also collaborate with and provide services to affiliated D-H institutions conducting clinical research and trials. The VP will play a visible role toward creating requisite governance, leadership and reporting structures as well as industry best practice processes, controls and enablers necessary to achieve clinical trials operational efficiency, financial recovery and ongoing research compliance obligations.

Candidates are requested to apply on our recruitment site or contact:
Janice Kilfeather-Mackey (Janice.D.Kilfeather-Mackey@Hitchcock.ORG)

DHproviders.org/VPClinicalResearch

Dartmouth-Hitchcock is a national leader in healthcare delivery innovation that serves a patient population of more than 1.9 million. This unique area of the Northeast offers an unmatched quality of life in a beautiful, quintessential New England setting. Home to the prestigious Ivy League Dartmouth College, the local area offers a vibrant, academic and professional community rich with arts, outdoor activities and accessibility to major metropolitan hubs like Boston, New York and Montreal.

Dartmouth-Hitchcock

Learn more about Dartmouth-Hitchcock at:
dhproviders.org

imagine ***innovative*** medicine

The mission of the Clinical Trials Office at Dartmouth-Hitchcock is to facilitate the conduct of high-quality clinical trials by providing a centralized infrastructure to enhance patient safety, promote quality research, ensure fiscal and regulatory compliance, and encourage clinical translation collaborations. The CTO provides administrative, fiscal, and regulatory support for more than 150 clinical trials that test new therapeutics and medical devices.

Core Funding:
Core Funding from the National Cancer Institute is $3.1 million per year. NCCC has more than 30 consecutive years of funding from the NCI.

Research Funding:
Research Funding to Cancer Center Members: $62 million in National Institute of Health (NIH), NCI, and other grants and contracts 200+ Research Projects

Clinical Trials:
Over 150 open clinical trials, including Cancer Center-initiated clinical trials, national multi-center trials, and pharmaceutical-funded trials.



St. Jude Children's Research Hospital
ALSAC • Danny Thomas, Founder

FACULTY POSITIONS
Department of Immunology

The Department of Immunology seeks applicants for up to two faculty positions at all levels (Assistant, Associate, or Full) in areas of research exploring the cell biology of the immune system. Preference will be given to applicants with research programs in cancer immunotherapy or immunometabolism. St. Jude offers a remarkable opportunity to perform cutting edge research with outstanding institutional support and exceptional core facilities in an environment of open collaboration. Successful applicants will present a vibrant research program with potential for interaction within the department and institution.

Interested applicants should send CV, a letter of research interests, and contact information for three references to:

Douglas R. Green
Chair, Dept. Immunology
St. Jude Children's Research Hospital
362 Danny Thomas Place MS351
Memphis, TN 38105
Douglas.Green@stjude.org

EOE/Minorities/Females/Vet/Disability/
Sexual Orientation/Gender Identity

The University of Texas Medical Branch
Faculty in Experimental and Computational Biophysics
Sealy Center for Structural Biology & Molecular Biophysics

UTMB seeks faculty applicants at all levels in experimental and computational biophysics in the Sealy Center for Structural Biology and Molecular Biophysics (SCSBMB). The Center supports a graduate program in molecular biophysics and five excellent resource laboratories in Cryo-EM, NMR, X-ray, Computation and Solution Biophysics, each with a PhD-level manager. For details see: http://www.scsb.utmb.edu/

The successful candidate will be a highly motivated individual with a PhD, MD or equivalent degree, a strong publication record, and for senior faculty candidates, a record of independent, well-funded grant support. The ideal candidate will have research interests in the structure, novel mechanisms and functions of bio-molecules. Candidates for these positions will likely also hold appointment in one of the basic science departments at UTMB, where they should have or seek overlap with the highly collaborative, established biomedical research community in the basic science departments, centers and programs of excellence. These include the Institute for Human Infections and Immunity, which includes the Galveston National Laboratory, Center for Tropical Diseases, Center for Biodefense and Emerging Infectious Diseases, and the Sealy Center for Vaccine Development. Outstanding collaborative research opportunities are also available through the Institute for Translational Sciences, the Sealy Center for Cancer Cell Biology, the Sealy Center for Environmental Health and Medicine, the Sealy Center on Aging, the George P. and Cynthia Woods Mitchell Center for Neurodegenerative Diseases, the Moody Center for Brain and Spinal Cord Injury Research, the Sealy Center for Molecular Medicine and the Chemical Biology Program. In addition, a wide variety of outstanding core services are available, including recombinant DNA services, genomics, proteomics, high-throughput drug screening, mass spectrometry, and protein expression and purification. Excellent collaborative opportunities also exist through UTMB's participation in the Gulf Coast Consortia and the Keck Center for Interdisciplinary Bioscience, as well as its membership in the Texas Medical Center, one of the world's largest medical centers.

Applicants are requested to submit electronically: a cover letter expressing interest in being considered, a curriculum vitae, current funding, a summary of research accomplishments, and future goals to mail to: **SCSBMB.recruiting@UTMB.edu**

Direct inquiries to **Dr. B. Montgomery Pettitt**, **mpettitt@utmb.edu**, **409-772-0723**.

UTMB Health strives to provide equal opportunity employment without regard to race, color, national origin, sex, age, religion, disability, sexual orientation, gender identity or expression, genetic information or veteran status. As a VEVRAA Federal Contractor, UTMB Health takes affirmative action to hire and advance women, minorities, protected veterans and individuals with disabilities.

utmb Health

Western University
OF HEALTH SCIENCES
The discipline of learning. The art of caring.

ASSISTANT/ASSOCIATE PROFESSOR
DEPARTMENT OF MEDICAL ANATOMICAL SCIENCES

Western University of Health Sciences, a thriving center for human health care and veterinary medicine education, is growing and along with our site for the College of Osteopathic Medicine of the Pacific Northwest (COMP-NW) in Lebanon, Oregon.

The College of Osteopathic Medicine of the Pacific invites applications for **two** positions in the **Department of Medical Anatomical Sciences**. These are full-time, 12-month, tenure-track positions at the Assistant Professor/ Associate Professor/ rank dependent upon qualifications. One position is available on our Pomona campus and one on our Lebanon, Oregon campus. The Department is responsible for the teaching of medical gross anatomy, histology, neuroanatomy and embryology. Applicants should submit a cover letter expressing their interest and qualifications along with a curriculum vitae, current support, and three references to:

Craig Kuehn, Ph.D.
Director, Medical Gross Anatomy
Department of Medical Anatomical Sciences
Western University of Health Sciences
College of Osteopathic Medicine of the Pacific
309 E. Second St.
Pomona, CA 91766-1854
Office: 909-469-5248
Cell: 909-731-1351
Email: ckuehn@westernu.edu

Western University of Health Sciences is an equal opportunity employer.

The INNO+ Scholarship in Personalized Medicine

A number of INNO+ 2 year master level scholarships in Medicine with Industrial Specialization, with focus on cancer classification are available at School of Medicine, Aalborg University, Denmark.

The scholarships will only be awarded to top-class students from Brazil, India, China, South Korea, the USA or Japan.

Learn more at www.smh.aau.dk

AALBORG UNIVERSITY
DENMARK

Los Alamos
NATIONAL LABORATORY
EST. 1943

Los Alamos National Laboratory (LANL), a multidisciplinary research institution engaged in strategic science on behalf of national security, has several opportunities available for Postdocs on LANL's Foldamer Team.

PROTEIN AND POLYMER MODELING, MOLECULAR BIOLOGY AND BIOPHYSICS POSTDOCS
ORGANIC AND MATERIALS SYNTHESIS POSTDOCS

Jobs IRC47781, IRC47278, IRC44995 and IRC47983

Postdoctoral Fellows will collaborate on a large multi-disciplinary project to synthesize, characterize, and quantify diverse libraries of non-peptide biopolymers that fold like proteins and show functional, predictable binding and catalytic properties (Foldamers).

The successful applicants will have PhDs in Organic/Polymer Chemistry, Computational Biology/Polymer Physics, Molecular Biology, or closely related fields. The Ph.D. degree must be completed prior to beginning any position at LANL and awarded within the past five years.

Applicants for the organic and materials synthesis positions must possess advanced knowledge of organic synthesis and design as applied to preparation of organic molecules. Expertise in purification, isolation, and characterization of small molecules and variable size polymers is essential.

The computational positions require advanced application and model development in molecular structure modeling such as Rosetta, Quantum DFT, Macro-molecular dynamics, polymer dynamics, structure, and function.

The molecular biology positions require experience in design of assays for physiological property selection, sorting, and expertise in characterization methods including GFP tags, fluorescence, CD, and sequencing and/or mass spectrometry. Experience crossing experimentation, molecular design, and characterization will be favored.

Applicants must submit: A cover letter and CV with publication list to Dr. Charlie Strauss (PI) (cemS@lanl.gov) and Dr. Robert F. Williams (rfw@lanl.gov) and apply online at http://jobs.lanl.gov.

EOE

Assistant and Associate Professor of Systems Pharmacology and Translational Therapeutics

Perelman School of Medicine
University of Pennsylvania

The Department of Pharmacology at the **Perelman School of Medicine** at the **University of Pennsylvania** seeks candidates for several Assistant or Associate Professor positions in the tenure track. Rank will be commensurate with experience. The successful applicant will have experience in the field of systems pharmacology, neuropharmacology, pharmacomicrobiome, biologics, mechanism of pain, RNA, or cellular therapeutics. Responsibilities include establishing robust independent funding for their research program. Applicants must have a Ph.D. and/or M.D. degree and demonstrated excellent qualifications in research.

The Department is part of a highly collaborative research community that integrates disciplines from basic, translational, and clinical pharmacology with focus areas including neuropharmacology, cardiovascular and cancer pharmacology and other disciplines.

The University of Pennsylvania, founded by Benjamin Franklin, is a world-class research institution located near the center of Philadelphia. All of Penn's twelve schools are located within walking distance of one another. The Perelman School of Medicine at the University of Pennsylvania is one of the top ranked medical schools in the nation for research and NIH funding.

We seek candidates who embrace and reflect diversity in the broadest sense. The University of Pennsylvania is an EOE. Minorities/Women/Individuals with disabilities/ Protected Veterans are encouraged to apply.

Apply online at:
https://www.med.upenn.edu/apps/faculty_ad/index.php/g/d4209

Florida State University

Translational Health and Human Neuroscience Applications of Functional Magnetic Resonance Imaging

As part of a strategic faculty hiring initiative in Brain Health & Disease, Florida State University invites applications for an open-rank, tenure-track faculty position with joint appointments in the departments of Psychology (College of Arts and Sciences) and Biomedical Sciences (College of Medicine). We invite nominations and applications from researchers with expertise in fMRI. Specific areas of research include but are not limited to the study of normal and abnormal behavioral and cognitive functions across the life span and brain mechanisms underlying medical, psychiatric, neurodevelopmental, and neurodegenerative disorders.

A successful candidate is expected to have a synergistic impact on existing research programs in the University's departments and interdisciplinary centers and to contribute to teaching and mentoring of students. Sustained pursuit of individual and collaborative externally-funded research projects is an explicit goal of this hiring initiative. Applicants should currently hold external funding and demonstrate a strong history of grant funding. This position offers a highly competitive salary and start-up package, state-of-the-art research space, and access to world-class instrumentation and facilities in academic and interdisciplinary units, including the Institute for Successful Longevity, the Interdisciplinary Neuroscience Program, and the National High Magnetic Field Laboratory (NHMFL). This latter unit has an extensive research portfolio aimed at pushing the limits of resolution in magnetic resonance spectroscopy and imaging.

FSU features a brand-new research-dedicated neuroimaging center housed in a 2200-sq-foot suite expressly designed for human imaging. This center will feature a newly installed 3T Siemens Prisma scanner with 32- and 64-channel head coils and will be fully equipped for advanced imaging. Comprehensive support facilities are planned to include simultaneous EEG and peripheral physiology recording systems, VPixx HD LED projector (with 3D functions), eye-tracker, and state-of-the-art computing suite. Exceptional technical support and collaborations will be provided through the NHMFL.

Florida State University is classified as a Carnegie RU/VH (very high research activity) institution with a student population approaching 42,000 (including highly ranked doctoral programs in psychology, biomedical sciences, and related disciplines). The University continues to make considerable investments in research infrastructure in the sciences and engineering disciplines. The University is located in Tallahassee, the capital of Florida, where residents have access to a broad range of cultural amenities afforded by the presence of three institutions of higher learning. The region boasts an abundance of springs, lakes and rivers as well as pristine beaches on the Gulf of Mexico.

Applicants are asked to provide a *single document* in PDF format containing a letter of application, a full CV (with links to recent publications), a two page narrative describing their research interests, and a brief teaching statement. Applications must be sent electronically to **pro-brain-initiative2016.search@fsu.edu**. Applicants should also arrange to have three letters of recommendation sent in electronic format to **pro-brain-initiative2016.letters@fsu.edu**. The search committee will begin reviewing applications starting **March 15th, 2016** and will continue to review new applications until the position is filled.

Florida State University is committed to the diversity of its faculty, staff, and students, and to sustaining a work and learning environment that is inclusive. Women, minorities, and people with disabilities are encouraged to apply. FSU is an Equal Opportunity/Access/Affirmative Action/Pro Disabled and Veteran Employer. FSU's Equal Opportunity Statement can be viewed at: http://www.hr.fsu.edu/PDF/Publications/diversity/EEO_Statement.pdf. As an agency of the State of Florida, information shared with Florida State University is subject to disclosure under the Florida Public Records law, unless specifically exempted.

John Innes Centre

INDEPENDENT RESEARCH FELLOWSHIPS

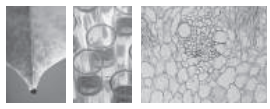
The John Innes Centre (JIC), Norwich, UK is a world leading centre of excellence in plant and microbial sciences based on the Norwich Research Park. We are inviting applications from outstanding researchers who either hold, or wish to apply for Independent Research Fellowships [such as a BBSRC David Phillips Fellowship (http://www.bbsrc.ac.uk/funding/fellowships/david-phillips.aspx), or a Royal Society University Research Fellowship (http://royalsociety.org/grants/schemes/university-research/)], to attend a Conference at the JIC on 18th April 2016. At the meeting you will be able to present a talk about your proposed area of research and to discuss your proposals, the development of your group and your future career plans in depth with senior JIC Scientists.

After the Conference we will select and mentor outstanding candidates in writing Fellowship applications and/or offer the opportunity to move existing Fellowships to the JIC. Considerable additional resources will be provided to Fellows by the Centre.

Further details and particulars can be found at http://www.jic.ac.uk/training-careers/training/fellowships/independent-research-fellows-conference/

Please e-mail a 2-page summary of your research plan, a copy of your CV and arrange for three letters of recommendation to be emailed to dawn.rivett@nbi.ac.uk by 11th March 2016.

The John Innes Centre is a registered charity (No223852) grant-aided by the Biotechnology and Biological Sciences Research Council and is an Equal Opportunities Employer and supports flexible working.



UIC University of Illinois at Chicago

Assistant/Associate Professor - Physiology and Biophysics

The Dept. of Physiology and Biophysics of the College of Medicine at the University of Illinois at Chicago is seeking outstanding candidates for tenure track faculty positions at the Asst. and Assoc. Professor levels. UIC offers an exciting intellectual environment undergoing growth in several areas of research, strong training programs, outstanding core facilities, & wonderful opportunities for collaboration in the Chicago community.

We seek candidates whose research programs can leverage interdisciplinary approaches for the study of molecular, cellular & whole animal physiology and pathophysiology. Candidates with a record of innovative & collaborative research in vascular biology, tumor biology, systems biology or metabolism are encouraged to apply.

Applicants must have a Ph.D. and/or M.D., postdoc. exp., strong publication record, and potential for extramural funding at the Asst. Professor level or significant current extramural funding at the Assoc. Professor level. The successful candidates will be expected to establish & maintain an extramurally funded research program, and participate in teaching at the graduate & professional health science levels. Highly competitive salary & start-up packages commensurate with qualifications and experience are available.

To apply, please visit: **https://jobs.uic.edu/job-board** & select the position from the list of openings. Please upload a curriculum vitae with a brief statement of research interests, proposal for ongoing & future research (2-3 pages), and the names & contact information for 3 references. For fullest consideration, the application must be received by **February 16, 2016**.

The University of Illinois at Chicago is an Equal Opportunity, Affirmative Action employer. Minorities, women, veterans and individuals with disabilities are encouraged to apply. The University of Illinois may conduct background checks on all job candidates upon acceptance of a contingent offer. Background checks will be performed in compliance with the Fair Credit Reporting Act.

UNIVERSITY OF SOUTH CAROLINA

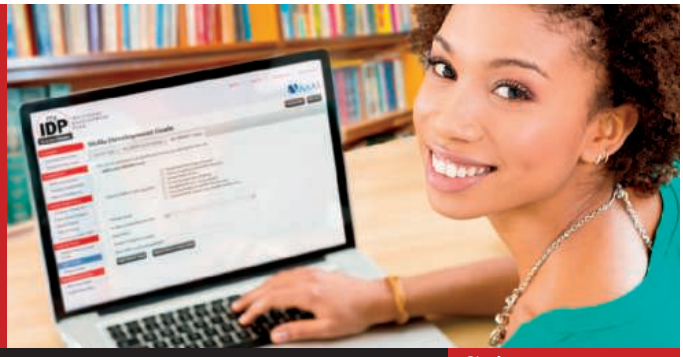
Director, Functional Genomics and Viral Vector Core

Individual sought to oversee the day-to-day operations of the Functional Genomics Core (FGC) (www.sccp.sc.edu/functional_genomics_core) of the NIH-supported Center for Targeted Therapeutics (www.sccp.sc.edu/ctt) and the Viral Vector Core (VVC) (http://ppn.med.sc.edu/vector.core.asp) at the University of South Carolina (USC). The appointment will be made at the level of a Research Assistant or Research Associate Professor at the USC School of Medicine, depending on experience. Responsibilities include interaction with investigators, plus overseeing and participating in the various services provided by the Functional Genomics Core (based at the USC College of Pharmacy) and Viral Vector Core (based at the USC School of Medicine). These laboratories produce genetically modified viral vectors and vector libraries designed to alter gene expression in vitro and in vivo, and conduct gene expression profiling and measurements. The services are provided for investigators both within and outside of the university. A PhD and at least five years of experience in viral vectors and genetic modification of mammalian cells is required. Experience in gene expression profiling and use of viral vectors in vivo is desired. The candidate will join a collegial and collaborative environment with focus areas in neurobiology, cancer, and cardiovascular research.

To apply please submit a single electronic file (PDF or Word) that includes a cover letter summarizing qualifications, curriculum vitae and publication list, a statement of experience and professional goals, and contact information for four references. The file should be attached to an e-mail message sent to **Dr. Marlene Wilson** at **director.search@uscmed.sc.edu** with Core Director Search as the subject. Review of applications will begin **February 1, 2016** and continue until the position is filled.

The University of South Carolina is an AA/EOE.

myIDP:
A career plan customized for you, by you.



For your career in science, there's only one Science

my IDP ScienceCareers

Recommended by leading professional societies and the NIH

Features in myIDP include:

- Exercises to help you examine your skills, interests, and values
- A list of 20 scientific career paths with a prediction of which ones best fit your skills and interests
- A tool for setting strategic goals for the coming year, with optional reminders to keep you on track
- Articles and resources to guide you through the process
- Options to save materials online and print them for further review and discussion
- Ability to select which portion of your IDP you wish to share with advisors, mentors, or others
- A certificate of completion for users that finish myIDP.

Visit the website and start planning today!
myIDP.sciencecareers.org

ScienceCareers In partnership with:

FASEB · UCSF University of California San Francisco · Medical College of Wisconsin · Burroughs Wellcome Fund



AAAS is here –
helping scientists achieve career sucess.

Every month, over 400,000 students and scientists visit ScienceCareers.org in search of the information, advice, and opportunities they need to take the next step in their careers.

A complete career resource, free to the public, *Science* Careers offers hundreds of career development articles, webinars and downloadable booklets filled with practical advice, a community forum providing answers to career questions, and thousands of job listings in academia, government, and industry. As a AAAS member, your dues help AAAS make this service available to the scientific community. If you're not a member, join us. Together we can make a difference.

To learn more, visit
aaas.org/plusyou/sciencecareers

AAAS + U = Δ

international network Institut Pasteur

AGENCE UNIVERSITAIRE DE LA FRANCOPHONIE

Joint International Call for Applications AUF - Institut Pasteur for Leaders of 4-year research groups within the Institut Pasteur International Network

Agence Universitaire de la Francophonie (AUF) and Institut Pasteur are jointly launching an international call for applications for future leaders of 4-Year Groups (G4) within the Institut Pasteur International Network (RIIP) in Sub-Saharan Africa and Southeast Asia (Cameroon, Côte d'Ivoire, Guinea, Madagascar, Niger, Senegal, the Central African Republic, Cambodia, China, Korea, Laos and Vietnam). The young scientist leading the group must propose an innovative and ambitious international research programme in infectious, tropical or neglected diseases.

Closing date for applications: 31 March 2016

See more: http://www.pasteur.fr/en/international/international-network-courses/4-year-group

Online Applications exclusively: http://g4.pasteur-international.org

UNIVERSITY OF IOWA HEALTH CARE

ASSOCIATE OR FULL PROFESSOR

The University of Iowa Carver College of Medicine is seeking a full-time faculty member in the Department of Surgery, Division of Gastrointestinal, Minimally-Invasive, and Bariatric Surgery at the level of Associate or Full Professor in the tenure-track. The successful candidate for this position will be a member of the Fraternal Order of Eagles Diabetes Research Center (FOEDRC) and the University of Iowa Obesity Research and Education Initiative (OREI). New faculty in the OREI will complement the University's existing expertise in this University intercollegiate, multidisciplinary initiative. Participation in the FOEDRC and OREI will be an important component in performance evaluations. In addition, the new hire may be eligible for appointment as Vice Chair of Research for the Department of Surgery, appointment to a basic science department, as well as appointment to the Dr. Edward and Dordana Mason Professorship.

Education Requirement: Candidates must possess a MD and/or PhD (or equivalent). **Required Qualifications:** Candidates must have an established record of research excellence, including a record of sustained external research funding with R01 funding being highly desirable, and ongoing scholarly productivity. Candidates must have experience working effectively in a diverse environment and should have excellent interpersonal and leadership skills.

To apply for this position visit the University of Iowa website: **http://jobs.uiowa.edu**, requisition **#68045**

The University of Iowa is an Equal Opportunity/Affirmative Action Employer. All qualified applicants are encouraged to apply and will receive consideration for employment free from discrimination on the basis of race, creed, color, national origin, age, sex, pregnancy, sexual orientation, gender identity, genetic information, religion, associational preference, status as a qualified individual with a disability, or status as a protected veteran.

University of Minnesota Medical School

Director, Minnesota Institute on the Biology of Aging and Metabolism

As a component of the medical discovery team initiative at the University of Minnesota Medical School, exceptional scientists are invited to apply for a tenured faculty position at the full professor level as the founding director of the Minnesota Institute for the Biology of Aging and Metabolism (iBAM). This State of Minnesota funded initiative is designed to develop centers of excellence in targeted areas relevant to the mission of the Medical School and University. The successful candidate is expected to maintain their active and vibrant research program in the biology of aging, to develop the Institute and its research themes, to recruit new investigators to the Institute and to work with the leadership of the Medical School and University to develop philanthropy around healthspan research. Preference will be given to scientists focusing on the molecular and cellular basis of aging and is expected to complement existing strength in genome stability, energy metabolism and proteostasis.

Applicants must apply online at: **http://www1.umn.edu/ohr/employment/**. Click on the appropriate tab under **"Search & Apply for Openings"**, enter **307216** into the **"Keywords"** field, then click the "Search" tab. Applicants should attach a cover letter, curriculum vitae, a description of their research program and a list of 3 potential references. Minimum qualifications include an M.D. or Ph.D. degree (or equivalent) and a track record of academic leadership and experience in leading interdisciplinary teams of scientists. Review of applications will begin immediately and continue until the position is filled. More information concerning the medical discovery team initiative and this position can be found at http://www.med.umn.edu/research/medical-discovery-teams.

The University of Minnesota provides equal access to and opportunity in its programs, facilities, and employment without regard to race, color, creed, religion, national origin, gender, age, marital status, disability, public assistance status, veteran status, sexual orientation, gender identity, or gender expression. The University supports the work-life balance of its faculty and especially encourages applications from women and members of under-represented groups.

ScienceCareers online @sciencecareers.org



For recruitment in science, there's only one Science

Fantastic Recruiting Opportunity!

POSTDOC CAREERS | March 25, 2016

Be sure to promote your openings to the thousands of scientists who will be reading *Science* to find out about the latest postdoc opportunities.

Reserve ads by March 8 to guarantee space.



Produced by the *Science*/AAAS Custom Publishing Office.

SCIENCECAREERS.ORG

ScienceCareers
FROM THE JOURNAL SCIENCE AAAS

To book your ad: **advertise@sciencecareers.org**

The Americas
+202-326-6582

Japan
+81-3-3219-5777

Europe/RoW
+44 (0) 1223-326500

China/Korea/Singapore/Taiwan
+86-186-0082 9345

Download the *Science* Careers jobs app from Science



Jobs are updated 24/7

Search thousands of jobs on your schedule

Receive push notifications per your job search criteria

Get a job on the go.

Search worldwide for thousands of scientific jobs in academia, industry, and government. The application process is seamless, linking you directly to job postings from your customized push notifications.

Scan this code to download app or visit **apps.sciencemag.org** for information.

ScienceCareers | AAAS
FROM THE JOURNAL SCIENCE

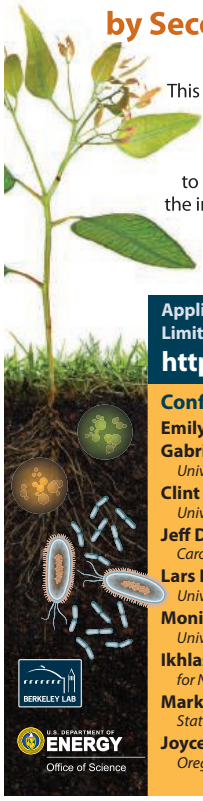
ScienceCcareers.org

MEETINGS

JGI JOINT GENOME INSTITUTE
A DOE OFFICE OF SCIENCE USER FACILITY

Microbial and Plant Systems Modulated by Secondary Metabolites Meeting

May 2–4, 2016 • Walnut Creek, CA



This meeting, hosted by the U.S. Department of Energy Joint Genome Institute, will bring together those interested in the role of secondary metabolites in plant-microbe and microbe-microbe interactions to discuss approaches for studying and manipulating the impact of secondary metabolites on environmental systems. Participants will also learn about JGI capabilities—large-scale DNA sequencing, synthesis and data mining—available to them.

Applications accepted through February 29, 2016. Limited to the first 80 participants. Apply here:
http://bit.ly/JGI-Metabolites

Confirmed speakers include:

Emily Balskus, *Harvard*
Gabriele Berg, *Graz University of Technology*
Clint Chapple, *Purdue University*
Jeff Dangl, *University of North Carolina, Chapel Hill*
Lars Dietrich, *Columbia University*
Monica Höfte, *Ghent University*
Ikhlas Khan, *National Center for Natural Products Research*
Mark Lange, *Washington State University*
Joyce Loper, *USDA-ARS, Oregon State University*
Bradley Moor, *Scripps Institution of Oceanography*
Sarah O'Connor, *John Innes Centre, UK*
Anne Osbourn, *John Innes Centre, UK*
Reuben Peters, *Iowa State University*
Jos Raaijmakers, *NIOO Wageningen*
Mohammad Seyedsayamdost, *Princeton University*
Lloyd Sumner, *The Samuel Roberts Noble Foundation*
Dorothea Tholl, *Virginia Tech University*
Julia Vorholt, *ETH Zurich*

BERKELEY LAB
U.S. DEPARTMENT OF ENERGY
Office of Science

16-JGI-2383

Join the Conversation!

Twitter is a great way to connect with AAAS members and staff about the issues that matter to you most. Be a part of the discussion while staying up-to-date on the latest news and information about your personal member benefits.

Follow us @AAASmember and join the conversation with #AAAS

AAAS MEMBERCENTRAL
MemberCentral.aaas.org

POSTDOCTORAL OPPORTUNITIES

POSTDOCTORAL POSITION available to study mechanisms regulating mammalian oogenesis and early embryogenesis. Studies involve a combination of advanced embryology, cell biology and molecular techniques, including microsurgical nuclear transfer, genetic analyses, transcriptome and pathway analysis, protein expression studies, epigenetic studies, and methods for manipulating gene expression. Experience in microsurgery, microinjection, embryo manipulation or molecular biology preferred. Send curriculum vitae and references to **Dr. Keith Latham, Department of Animal Science, Michigan State University, 474 S. Shaw Lane, East Lansing, MI 48824; telephone 517-353-7750; email: lathamk1@msu.edu**. *Michigan State University is an Equal Opportunity Employer.*

Post your jobs Fast and Easy



ScienceCareers
employers.sciencecareers.org

POSITIONS OPEN

THE UNIVERSITY OF ARIZONA CANCER CENTER

A Postdoctoral Research position working with Dr. Andrew S. Kraft, Director of the University of Arizona Cancer Center in Tucson, Arizona is available. The research will focus on investigating the ability of the Pim protein kinases to control the growth and metastasis of cancer, e.g. prostate, using knock-out and knock-in mice, cell culture, and novel small molecule kinase inhibitors (MCB 34:2517, 2014, Oncogene 34: 3728, 2015). Research will investigate the control of signaling pathways; identify substrates, and the interaction of Pim with other protein kinases, including AKT and mTOR. A strong background in protein chemistry, molecular and cellular biology, and experience working with mice is needed.

Applicants should submit cover letter, curriculum vitae, and the names of three references via the following website: www.uacareers.com and seek job #A20142

Outstanding UA benefits include health, dental, and vision insurance plans; life insurance and disability programs; paid vacation, sick leave, and holidays; UA/ASU/NAU tuition reduction for the employee and qualified family members; state and optional retirement plans; access to UA recreation and cultural activities; and more!

The University of Arizona is an EEO/AA employer-M/W/D/V.

By **Jörgen Johansson**

Battling the bureaucracy hydra

"How hard can it be to write a contract?" I asked myself. After all, I had already overcome some long odds. Seven weeks earlier—just days before I was to fly to Brussels for the second evaluation phase of a European Research Council (ERC) Starting Grant application—the Icelandic volcano Eyjafjallajökull erupted, throwing enough ash into the sky to essentially halt European air traffic. Yet my flight from Sweden, where I was an assistant professor at Umeå University, was one of the few not grounded. Then, when I arrived at ERC headquarters and entered the hot, airless meeting room to present my proposed work, the chairperson told me, "You have 10 minutes—sharp." I finished in 9 minutes and 59 seconds. "This must be a good sign," I told myself.

I turned out to be right. In the middle of the summer holidays, I learned that I received the grant! But the contract negotiations had to start immediately. With 19 different documents amounting to more than 150 pages to read or fill out, the contract process seemed like a many-headed bureaucratic hydra. I had to convert the text and budget of my application into a legal document, but my knowledge of legalese was limited, so I enlisted help from administrators and lawyers at my university. Eight weeks later, my team at Umeå and ERC officers in Brussels had exchanged many emails and documents, 15 people had been mobilized, and I had sacrificed a large part of my vacation, but the contract was signed.

A couple of months later, I realized that I needed to temporarily hire an outside person to bring in some specific expertise. The ERC officer said I would have to amend the painstakingly negotiated contract and asked me, "Do you really need to do this?" Any sensible person would have realized that such a statement meant problems, but I somehow missed the not-so-subtle message. After once again going through the lengthy contract process, I had an amended contract.

A year later the hydra returned, hidden in a discreet email entitled "Advanced Notice Letter," alerting me to the fast-approaching deadline for my first financial report. A failure to have the report approved would prevent me from receiving further funding, but meeting all the requirements laid out in the 36-page user guide seemed almost impossibly complicated. Again, a fierce communication between Umeå and Brussels began. Through a strategy that amounted to trial and error, and with the help of supportive ERC officials, the report was approved, and I could turn my attention back to research.



"The hydra returned at unpleasantly regular intervals."

The hydra returned at unpleasantly regular intervals, demanding its share of sacrifice. I have now finished the ERC project and completed four financial reports and two scientific reports. In addition, three different external auditing firms have scrutinized the project because auditing is required once a certain budget threshold is reached.

My ERC adventure helped me build up my research group and produce good science, and it has meant an enormous amount to me. But fighting the hydra has taken its toll. Certainly large grants require some control measures, but I don't think that cutting the number of reports and audits by half would have been irresponsible—and it would have allowed me to spend more of my time on the research the grant was meant to fund. But on the positive side, the experience helped me become more patient and stress resistant, and I now know that I have many helpful colleagues who can support me.

So what advice can I offer for others facing the hydra? First, before even applying for a grant, carefully plan how you'd like to spend the money to avoid time-consuming amendments. Second, the administrators helping you with the process are probably much more experienced in dealing with these situations than you are, so listen to their advice. Third, don't despair. Even if the requirements are complicated and lengthy, you will get through them—with the assistance of those more expert than you. Then you can return to the real reason you became a scientist and get back to the research. ■

Jörgen Johansson is a professor in the Department of Molecular Biology and a member of the Laboratory for Molecular Infection Medicine Sweden at Umeå University. Send your story to SciCareerEditor@aaas.org.

ILLUSTRATION: ROBERT NEUBECKER

Downloaded from on January 31, 2016

Published by AAAS